

AD-A182 996

DTIC FILE COPY

AGARD-CP-401

AGARD-CP-401

AGARD

ADVISORY GROUP FOR AEROSPACE RESEARCH & DEVELOPMENT

7 RUE ANCELLE 92200 NEUILLY SUR SEINE FRANCE

AGARD CONFERENCE PROCEEDINGS No.401

Transonic and Supersonic Phenomena in Turbomachines

Copyright Clearance Center
Inc. 222 Rosewood Drive
Danvers, MA 01923
01923-1831
01923-1831
01923-1831

RECEIVED
MAY 13 1987
A

NORTH ATLANTIC TREATY ORGANIZATION



DISTRIBUTION AND AVAILABILITY
ON BACK COVER

400043

87 5 10 140

COMPONENT PART NOTICE

THIS PAPER IS A COMPONENT PART OF THE FOLLOWING COMPILATION REPORT:

TITLE: Transonic and Supersonic Phenomena in Turbomachines: Proceedings of the
Propulsion and Energetics (68th)(B) Specialists' Meeting Held in Munich,
Germany on 10-12 September 1986.

TO ORDER THE COMPLETE COMPILATION REPORT, USE AD-A182 996

THE COMPONENT PART IS PROVIDED HERE TO ALLOW USERS ACCESS TO INDIVIDUALLY
AUTHORED SECTIONS OF PROCEEDING, ANNALS, SYMPOSIA, ETC. HOWEVER, THE COMPONENT
SHOULD BE CONSIDERED WITHIN THE CONTEXT OF THE OVERALL COMPILATION REPORT AND
NOT AS A STAND-ALONE TECHNICAL REPORT.

THE FOLLOWING COMPONENT PART NUMBERS COMPRISE THE COMPILATION REPORT:

AD#: AD-P005 506 thru AD-P005 522. AD#: _____

AD#: _____ AD#: _____

AD#: _____ AD#: _____

Accession For	
NTIS GRA&I	<input checked="" type="checkbox"/>
DTIC TAB	<input type="checkbox"/>
Unannounced	<input type="checkbox"/>
Justification	
By _____	
Distribution/	
Availability Codes	
Dist	Avail and/or Special
A-1	

DTIC
ELECTE
S **D**
AUG 17 1987
A

DTIC FORM 463
MAR 85

This document has been approved
for public release and sale; its
distribution is unlimited.

OPI: DTIC-TID

AGARD-CP-401

NORTH ATLANTIC TREATY ORGANIZATION
ADVISORY GROUP FOR AEROSPACE RESEARCH AND DEVELOPMENT
(ORGANISATION DU TRAITE DE L'ATLANTIQUE NORD)

AGARD Conference Proceedings No. 401
TRANSONIC AND SUPERSONIC PHENOMENA IN TURBOMACHINES

Papers presented at the Propulsion and Energetics 68th (B) Specialists' Meeting,
held in Munich, Germany, 10-12 September 1986.

THE MISSION OF AGARD

The mission of AGARD is to bring together the leading personalities of the NATO nations in the fields of science and technology relating to aerospace for the following purposes:

- Exchanging of scientific and technical information;
- Continuously stimulating advances in the aerospace sciences relevant to strengthening the common defence posture;
- Improving the co-operation among member nations in aerospace research and development;
- Providing scientific and technical advice and assistance to the Military Committee in the field of aerospace research and development (with particular regard to its military application);
- Rendering scientific and technical assistance, as requested, to other NATO bodies and to member nations in connection with research and development problems in the aerospace field;
- Providing assistance to member nations for the purpose of increasing their scientific and technical potential;
- Recommending effective ways for the member nations to use their research and development capabilities for the common benefit of the NATO community.

The highest authority within AGARD is the National Delegates Board consisting of officially appointed senior representatives from each member nation. The mission of AGARD is carried out through the Panels which are composed of experts appointed by the National Delegates, the Consultant and Exchange Programme and the Aerospace Applications Studies Programme. The results of AGARD work are reported to the member nations and the NATO Authorities through the AGARD series of publications of which this is one.

Participation in AGARD activities is by invitation only and is normally limited to citizens of the NATO nations.

The content of this publication has been reproduced
directly from material supplied by AGARD or the authors.

Published March 1987

Copyright © AGARD 1987
All Rights Reserved

ISBN 92-835-0413-5



Printed by Specialised Printing Services Limited
40 Chigwell Lane, Loughborough, Leicestershire LE10 3TZ

RECENT PUBLICATIONS OF THE PROPULSION AND ENERGETICS PANEL

Conference Proceedings

Testing and Measurement Techniques in Heat Transfer and Combustion
AGARD Conference Proceedings No.281, 55th A Meeting, May 1980

Centrifugal Compressors, Flow Phenomena and Performance
AGARD Conference Proceedings No.282, 55th B Meeting, May 1980

Turbine Engine Testing
AGARD Conference Proceedings No.293, 56th Meeting, Sep/October 1980

Helicopter Propulsion Systems
AGARD Conference Proceedings No.302, 57th Meeting, May 1981

Ramjets and Ramrockets for Military Applications
AGARD Conference Proceedings No.307, 58th Meeting, October 1981

Problems in Bearings and Lubrication
AGARD Conference Proceedings No.323, 59th Meeting, May/June 1982

Engine Handling
AGARD Conference Proceedings No.324, 60th Meeting, October 1982

Viscous Effects in Turbomachines
AGARD Conference Proceedings No.351, 61st A Meeting, June 1983

Auxiliary Power Systems
AGARD Conference Proceedings 352, 61st B Meeting, May 1983

Combustion Problems in Turbine Engines
AGARD Conference Proceedings 353, 62nd Meeting, October 1983

Hazard Studies for Solid Propellant Rocket Motors
AGARD Conference Proceedings 367, 63rd A Meeting, May/June 1984

Engine Cyclic Durability by Analysis and Testing
AGARD Conference Proceedings No.368, 63rd B Meeting, May/June 1984

Gears and Power Transmission Systems for Helicopters and Turboprops
AGARD Conference Proceedings No.369, 64th Meeting October 1984

Heat Transfer and Cooling in Gas Turbines
AGARD Conference Proceedings No.390, 65th Meeting, May 1985

Smokeless Propellants
AGARD Conference Proceedings No.391, 66th A Meeting, September 1985

Interior Ballistics of Guns
AGARD Conference Proceedings No.392, 66th B Meeting, September 1985

Advanced Instrumentation for Aero Engine Components
AGARD Conference Proceedings No.399, 67th Meeting, May 1986

Engine Response to Distorted Inflow Conditions
AGARD Conference Proceedings No.400, 68th A Meeting, September 1986

Approved	
By	
Date	
Initials	
Signature	
Stamp	
Handwritten	

Working Group Reports

Aircraft Fire Safety

AGARD Advisory Report 132, Vol.1 and Vol.2. Results of WG11 (September and November 1979)

Turbulent Transport Phenomena (in English and French)

AGARD Advisory Report 150. Results of WG 09 (February 1980)

Through Flow Calculations in Axial Turbomachines

AGARD Advisory Report 175. Results of WG 12 (October 1981)

Alternative Jet Engine Fuels

AGARD Advisory Report 181, Vol.1 and Vol.2. Results of WG 13 (July 1982)

Suitable Averaging Techniques in Non-Uniform Internal Flows

AGARD Advisory Report 182 (in English and French). Results of WG 14 (June/August 1983)

Producibility and Cost Studies of Aviation Kerosines

AGARD Advisory Report 227. Results of WG 16 (June 1985)

Performance of Rocket Motors with Metalized Propellants

AGARD Advisory Report 230. Results of WG 17 (September 1986)

Lecture Series

Non-Destructive Inspection Methods for Propulsion Systems and Components

AGARD LS 103 (April 1979)

The Application of Design to Cost and Life Cycle Cost to Aircraft Engines

AGARD LS 107 (May 1980)

Microcomputer Applications in Power and Propulsion Systems

AGARD LS 113 (April 1981)

Aircraft Fire Safety

AGARD LS 123 (June 1982)

Operation and Performance Measurement of Engines in Sea Level Test Facilities

AGARD LS 127 (April 1984)

Ramjet and Ramrocket Propulsion Systems for Missiles

AGARD LS 136 (September 1984)

3-D Computation Techniques Applied to Internal Flows in Propulsion Systems

AGARD LS 140 (June 1985)

Engine Airframe Integration for Rotorcraft

AGARD LS 148 (June 1986)

Other Publications

Airbreathing Engine Test Facility Register

AGARD AG 269 (July 1981)

THEME

The increase of speed is a promising possibility for improving the performance of gas turbine engines. In order to maintain high efficiency and reliability of advanced engines, containing large portions of supersonic flow, a deep understanding of the influence of supersonic and transonic phenomena is essential. The present Specialists' Meeting aimed at providing a contribution to this goal.

The scope included: experimental data on shock structures, shock induced losses including shock boundary layer interactions, computational results, and blade design methods. The meeting offered a forum for highly qualified specialists to discuss their views and the latest results of their investigations, and for development engineers to be informed on the state-of-the-art.

• • • • •

L'augmentation de la vitesse offre des possibilités prometteuses pour améliorer les performances des turbomachines. Pour maintenir le rendement élevé et la fiabilité des moteurs avancés, utilisant largement l'écoulement supersonique, il est essentiel de bien comprendre l'influence des phénomènes supersoniques et transsoniques. Cette réunion de spécialistes a aidé à atteindre cet objectif.

Les domaines étudiés comprennent: données expérimentales sur les structures de choc, sur les pertes dues aux ondes de choc y compris les interactions ondes de choc — couche limite, sur les résultats de calcul, et sur les méthodes de conception des aubes. Cette réunion constitua un forum pour les spécialistes hautement qualifiés où ils purent discuter leurs points de vue et les derniers résultats de leurs recherches, et pour les ingénieurs de développement qui peuvent se tenir au courant de l'état actuel de la technique.

PROPULSION AND ENERGETICS PANEL

Chairman: Professor H. Wittenberg
Delft University of Technology
Dept. of Aerospace Engineering
Kluyverweg 1
2629 HS Delft, Netherlands

Deputy Chairman: Dr W.L. MacMillan
EMF Communication Satellite
Defence Research Establishment
Ottawa
Ontario, Canada K1A 0Z4

PROGRAMME COMMITTEE

Professor Ch. Hirsch (Chairman)
Vrije Universiteit Brussel
Dienst Stromingsmechanica
Pleinlaan 2, 1050 Brussel, Belgium

Professor C. Casci
Direttore del Dipartimento di Energetica
Politecnico di Milano
Piazza Leonardo da Vinci 32
20133 Milano, Italy

Mr J. Fabri
ONERA
29 Avenue de la Division Leclerc
92320 Châtillon sous Bagneux, France

Professor L. Fottner
Universität der Bundeswehr
Institut für Strahlantriebe
Werner Heisenbergweg 39
8014 Neubiberg, Germany

Mr D.L. Martlew
Ministry of Defence (PE)
Royal Aircraft Establishment, Pyestock
Farnborough, Hants GU14 0LS, England

Professor H.H. Saravanamurtoo
Chairman, Mechanical and Aeronautical
Engineering — Carleton University
Ottawa, Ontario K1S 5B6, Canada

Professor A. Uçer
Middle East Technical University
O D T O, Mahina, Muh. Bahumu
Ankara, Turkey

HOST NATION COORDINATOR

Professor L. Fottner

PANEL

Dr E. Richter
AGARD-NATO
7 rue Anecle
92200 Neuilly sur Seine
France

ACKNOWLEDGEMENT

The Propulsion and Energetics Panel wishes to express its thanks to the National Delegates from the Federal Republic of Germany for the invitation to hold this meeting in Munich, and for the facilities and personnel which made the meeting possible.

CONTENTS

	Page
RECENT PUBLICATIONS OF PEP	iii
THEME	v
PROPULSION AND ENERGETICS PANEL	vi
	Reference
<u>SESSION I - EXPERIMENTAL DATA AND SHOCK STRUCTURES</u>	
ETUDES FONDAMENTALES SUR LES INTERACTIONS ONDE DE CHOC - COUCHE LIMITE DANS UN CANAL TRIDIMENSIONNEL par R.Benay, T.Pot et J.Delery	1
SHOCK STRUCTURE MEASURED IN A TRANSONIC FAN USING LASER ANEMOMETRY by J.R.Wood, A.J.Strazisar and P.S.Simonyi	2
WAKE AND SHOCK INTERACTIONS IN A TRANSONIC TURBINE STAGE by D.L.Schultz, A.B.Johnson, D.A.Ashworth and M.J.Rigby	3
THE BOUNDARY LAYER BEHAVIOUR OF HIGHLY LOADED COMPRESSOR CASCADE AT TRANSONIC FLOW CONDITIONS by H.Hobetsiel and N.J.Seyb	4
<u>SESSION II - SHOCK INDUCED LOSSES INCLUDING SHOCK BOUNDARY LAYER INTERACTION</u>	
VORTEX SHEDDING IN COMPRESSOR BLADE WAKES by A.I.Epstein, J.B.Gertz, P.R.Owen and M.B.Giles	5
Paper 6 withdrawn	
EXPERIMENTAL OBSERVATIONS ON AN UNSTEADY, NORMAL SHOCK/BOUNDARY LAYER INTERACTION by J.A.Edwards and L.C.Squire	7
MEASURED AND PREDICTED LOSS GENERATION IN TRANSONIC TURBINE BLADING by W.N.Dawes, J.J.Camus, L.P.Xu and C.G.Graham	8
INFLUENCE OF SHOCK AND BOUNDARY LOSSES ON THE PERFORMANCE OF HIGHLY LOADED SUPERSONIC AXIAL FLOW COMPRESSORS by E.D.Breichhausen and H.E.Gallus	9
ANALYSE DES PERTES DUES AUX ONDES DE CHOC par A.Fourmeau et A.Le Meur	10
EXPERIMENTAL INVESTIGATIONS ON SHOCK LOSSES OF TRANSONIC AND SUPERSONIC COMPRESSOR CASCADES by H.A.Schreiber	11
OPTIMIZATION OF A TRANSONIC FLOW RADIAL VANED DIFFUSER by S.Colonnaoui and R.Van den Braembouche	12
METHODE NUMERIQUE D'INTERACTION VISQUEUX-NON VISQUEUX POUR LES ECOULEMENTS INTERNES DECOLLES ET L'INTERACTION COUCHE LIMITE - ONDE DE CHOC par J.C.Le Ballour et D.Bisler	13

SESSION III - COMPUTATIONAL RESULTS**CALCUL TRIDIMENSIONNEL DANS LES AUBAGES DE TURBO-MACHINES AVEC
NAGEOIRE**

par T.Derrien

14

Paper 15 withdrawn

**A QUASI THREE DIMENSIONAL METHOD FOR THE CALCULATION OF TRANSONIC
FLOWS IN TURBOMACHINES**

by J.Haller

16

TRANSONIC THREE-DIMENSIONAL INVISCID CALCULATIONS IN TURBOMACHINES

by F.Bassi and M.Savini

17

Paper 18 withdrawn

**COMPUTATION OF TRANSONIC 2D-CASCADE FLOW AND COMPARISON WITH
EXPERIMENTS**

by H.J.Dietrichs, H.W.Happel and K.Lehmann

19

**A NUMERICAL STUDY OF UNSTEADY FLOW EFFECTS IN A SUPERSONIC COMPRESSOR
CASCADE**

by S.M.Richardson

20

**A NUMERICAL STUDY OF THE 3D FLOWFIELD IN A TRANSONIC COMPRESSOR
ROTOR WITH A MODELLING OF THE TIP CLEARANCE FLOW**

by W.N.Dawes

21

**CALCUL D'ECOULEMENTS INTERNES A GRAND NOMBRE DE REYNOLDS PAR
RESOLUTION NUMERIQUE DES EQUATIONS DE NAVIER-STOKES**

par L.Cambier, B.Escande et J.P.Veuillot

22

SESSION IV - BLADE DESIGN METHODS**SOME TURBOMACHINERY BLADE PASSAGE ANALYSIS METHODS - RETROSPECT
AND PROSPECT**

by D.Carragher and T.R.Kington

23

Paper 24 withdrawn

DETERMINE DE LA REGION DE CAPTATION D'UNE GRILLE D'AUBES SUPERSONIQUE

par G.Mesure

25

**DOWNSTREAM FLOW ANGLE CORRELATIONS FOR TURBINE CASCADES IN
SUBSONIC AND TRANSONIC FLOW CONDITIONS**

by W.Riem, P.Dalbert, P.A.Glass and H.J.Helmermann

26

**A SHOCK LOSS MODEL FOR SUPERCRITICAL SUBSONIC FLOWS IN TRANSONIC
AXIAL FLOW COMPRESSORS**

by R.J.Dunker

27

**COMPARISON BETWEEN INVERSE DESIGN (PVD) AIRFOILS AND STANDARD SERIES
AIRFOILS FOR HIGH LOADED AXIAL TURBINE NOZZLE APPLICATION**

by M.Horrmann and M.Schmidt

28

ETUDES FONDAMENTALES SUR LES INTERACTIONS ONDE DE CHOC-COUCHE LIMITE
DANS UN CANAL TRIDIMENSIONNEL

par

R. BENAY, T. POT et J. DELERY

Office National d'Etudes et de Recherches Aéronautiques (ONERA)
29, avenue de la Division Leclerc, 92320 CHATILLON, France

SOMMAIRE

Les renseignements expérimentaux détaillés sur l'interaction onde de choc-couche limite en écoulement tridimensionnel sont encore relativement rares. Cette constatation a amené l'ONERA à entreprendre une expérimentation ayant pour but de fournir une documentation aussi complète que possible sur un écoulement tridimensionnel transsonique avec chocs à l'intérieur d'un canal. Le montage d'essai adopté est un canal dont la section d'entrée est de 100 x 120 mm. Une boussole en flèche est disposée sur la paroi inférieure du canal dont les trois autres faces sont planes. En fonctionnement, un écoulement supersonique est amorcé et des recompressions par choc se forment dans la partie descendante de la boussole. L'écoulement a été analysé en utilisant, en particulier, un vélocimètre laser à trois composantes.

Les essais ont notamment révélé l'existence d'un écoulement fortement tridimensionnel dont la structure est très différente de celle observée dans les écoulements à l'intérieur de canaux bidimensionnels. Ainsi, la présente étude expérimentale a mis en évidence le fait qu'en présence du fort gradient de pression adverse que constitue le choc, une couche limite tridimensionnelle a moins tendance à s'écarter qu'une couche limite bidimensionnelle, l'écoulement ayant la possibilité de se réorganiser d'une manière beaucoup plus complexe selon les trois directions de l'espace.

Les renseignements précis ainsi obtenus sont exploités en vue d'aboutir à une meilleure compréhension physique des phénomènes. Ils constituent en outre une base de données pour valider les modèles de calcul en cours de développement.

FUNDAMENTAL STUDIES ON SHOCK-WAVE/BOUNDARY-LAYER INTERACTIONS IN A 3-D CHANNEL

SUMMARY

Detailed experimental data on shock-wave/boundary-layer interaction in 3-D flows is still relatively scarce. This fact has brought ONERA to undertake experiments in view of producing as complete a literature as possible on a three-dimensional transonic channel flow with shock. The test set-up is a channel with a 100mmx120mm inlet section. The lower wall of the channel is humped while the other three faces are flat. In operation, a continuous supersonic flow is started and shock recompressions formed on the descending part of the hump. The flow in the interaction region has been carefully analyzed by using, in particular, a three-color LDV system.

The tests brought out a strongly 3-dimensional flow structured very differently from the one observed in 2-D channel flows. The present experimental study thus revealed the fact that in the presence of the strong adverse pressure gradient of the shock, a 3-D boundary layer tends to thicken less than a 2-D boundary layer, since the flow can reorganize in a much more complex fashion in the three directions of space.

The precise data obtained from this have been analyzed to arrive at a better understanding of the phenomena from a physical point of view, and also constitute a data base for validating the calculation models being developed.

1 - INTRODUCTION

Les interactions entre les ondes de choc se formant dans un canal aux vitesses transsoniques ou supersoniques et les couches limites se développent sur les parois ont, comme on le sait, des répercussions déterminantes sur le fonctionnement aérodynamique du dispositif, que ce soit une prise d'air, un diffuseur ou une grille d'aubes. Les interactions ont des effets particulièrement néfastes quand elles entraînent le décollement des couches limites. Il peut en résulter des pertes de performances considérables avec, le plus souvent, l'apparition d'instabilités à grande échelle extrêmement nuisibles.

D'où l'effort de recherches très important consacré aux interactions choc-couche limite avec comme objectif de mieux comprendre le physique de ces phénomènes, de les modéliser correctement et de développer des techniques de contrôle permettant de prévenir leurs conséquences négatives [1].

Sans entrer plus avant dans un examen approfondi des problèmes d'interaction choc-couche limite (le lecteur intéressé pourra se reporter aux références [2,3,4] pour des renseignements beaucoup

plus complète) signalons que des progrès très substantiels ont été accomplis ces dernières années dans l'analyse expérimentale et surtout dans la modélisation de ces phénomènes en écoulement bidimensionnel que ce soit par l'utilisation de méthodes de couplage fluide parfait/fluide visqueux [5 à 8] ou par résolution des équations complètes de Navier-Stokes moyennées en temps [9,10,11].

Toutefois, dans la pratique la plus courante, hormis quelques dispositifs à symétrie de révolution (tuyères propulsives ou certaines prises d'air, par exemple), les écoulements sont très généralement tridimensionnels. Le problème de l'interaction devient alors nettement plus complexe et, déjà sur le plan de la compréhension physique des phénomènes, on se heurte à de grosses difficultés dans l'interprétation de l'observation [12,13,14]. Quant à la prévision théorique, ses possibilités sont encore limitées, bien que les progrès de la modélisation par résolution des équations de Navier-Stokes soient rapides [15,16,17].

Les objectifs principaux de l'étude de base faisant l'objet de la présente communication sont les suivants :

- 1 - en premier lieu, donner une description physique aussi complète que possible de l'écoulement transsonique dans un canal tridimensionnel ;
- 11 - en second lieu, constituer un ensemble de données bien documenté et détaillé pour évaluer les méthodes de calcul existantes ou en cours de développement.

Les expériences ont été effectuées volontairement sur une configuration statique de forme simple de manière à éviter les difficultés de mesure rencontrées dans les essais sur turbomachines réelles [18]. Cette situation plus confortable permet, comme nous le verrons, de décrire avec beaucoup de finesse un écoulement dont la structure est déjà d'une grande complexité. L'étude présentée est une extension au tridimensionnel des recherches nombreuses déjà effectuées à l'ONERA sur les écoulements transsoniques en canal bidimensionnel [19].

2 - DISPOSITIF EXPERIMENTAL ET TECHNIQUES D'INVESTIGATION -

2.1 - Montage d'essai - Définition du canal -

La photographie de la figure 1 donne une vue d'ensemble du dispositif expérimental. Celui-ci consiste, pour l'essentiel, en une veine subsonique-supersonique dont la paroi supérieure est plane et dont la paroi inférieure porte une "bosse" dont la géométrie est définie dans ce qui suit. Les deux faces latérales du canal sont constituées de glaces planes. L'envergure de la veine est de 122mm et sa hauteur, dans la section d'entrée, est de 100mm. La forme et les dimensions de la bosse sont précisées fig.2. Elle comporte, en amont, une partie rectiligne dont la pente, relativement à l'horizontale, est d'environ 7°. Cette première portion, qui donne au canal sa forme pratiquement bidimensionnelle, est suivie d'un contour à pente évolutive, d'abord circulaire convexe (rayon égal à 100mm), puis circulaire concave (rayon égal à 100mm). Les deux arcs de cercle sont définis de manière à assurer la continuité des pentes en leur point de raccord ainsi qu'en leurs contacts avec les parties amont et aval rectilignes. L'effet tridimensionnel est obtenu en donnant à la ligne formant le sommet de la bosse une direction de 30° par rapport à l'écoulement amont (flèche de 30°). La hauteur maximale de la bosse est de 20mm et sa longueur totale de 153mm. En aval de la ligne de crête la géométrie est cylindrique.

L'écoulement subsonique en provenance de l'amont s'accélère dans la partie convergente de la veine pour atteindre l'état critique au col du col de la bosse qui constitue un col. En aval, l'écoulement devient supersonique ; puis, en raison d'un effet de blocage produit par un densité ρ , il se ralentit en étant le siège d'ondes de choc interagissant fortement avec les couches limites qui se développent sur les quatre faces de la veine.

Le second col, dont l'ouverture est réglable, est amont à l'entrée de la veine, comme le montre la photographie de la figure 1. Outre l'effet de blocage, ce col limite l'écoulement assés des perturbations de pression provenant des cavitations aval de la soufflerie qui seraient une source d'instabilités parasites.

La forme du canal a été définie avec le souci de faciliter sa représentation dans les méthodes de calcul en évitant, en particulier, les discontinuités ou variations trop rapides de pentes qui sont sources à l'origine de difficultés de maillage. En revanche, comme nous allons le voir, l'écoulement transsonique ainsi généré est fortement tridimensionnel et beaucoup plus complexe que la plupart de ceux étudiés jusqu'à présent [20 à 22, voir aussi 4].

Le montage d'essai est installé dans une soufflerie continue, du type Eiffel, alimentée par de l'air atmosphérique détaché sous les conditions géométriques : pression $P_0 = 0,92.10^5$ Pa, température $T_0 = 290K$. Le nombre de Reynolds, calculé pour l'état critique et en prenant comme longueur de référence la hauteur du col (soit $l = 80mm$) a pour valeur $11,3.10^5$. Dans ces conditions, les couches limites sont pleinement turbulentes au niveau des interactions.

2.2 - Moyens de qualification de l'écoulement -

Les parois inférieure et supérieure de la veine sont équipées chacune de 250 orifices de pression statique dont la plupart sont implantés dans les zones de forte interaction, comme indiqué fig.2.

Les écoulements persistents, sur les quatre faces du canal, ont été décrits à partir de spectres obtenus par la technique de l'écouit visqueux.

Les mesures de champ ont été effectuées à l'aide d'un vélocimètre laser à 3 composantes dont nous allons décrire les caractéristiques essentielles ainsi que le mode de fonctionnement adopté pour les premiers essais.

L'appareil, dont la figure 3 donne le schéma de principe, a été mis au point par la Direction de la Physique Générale de l'ONERA en liaison avec le Groupe Mesures Laser de la Direction de l'Aérodynamique (pour plus de détails, voir la référence [28]).

Le vélocimètre est équipé de deux lasers à Argon identiques pouvant émettre une puissance maximale toutes raies de 15W. Le premier fonctionne en mono-raie violette (longueur d'onde $\lambda = 0,4765 \mu\text{m}$) sous une puissance de 3W. Le second est utilisé en toutes raies sous 6W et son faisceau est divisé par un jeu de lames dichroïques semi-transparentes en deux couleurs : le vert ($\lambda = 0,5145 \mu\text{m}$) et le bleu ($\lambda = 0,488 \mu\text{m}$).

Les trois paires de faisceaux qui résultent de la traversée des trois diviseurs (DV₁, DV₂ et DV₃, voir Fig.3) sont focalisées pour constituer le volume de mesure dont le diamètre utile est d'environ 400 μm . Dans la présente configuration, les rayonnements bleu et vert sont émis dans un plan horizontal selon une direction faisant un angle de 25,17° par rapport à l'axe OY dirigé selon l'envergure du montage (voir Fig.4). Leur interférence donne deux systèmes de franges l'un horizontal (le bleu) et l'autre vertical (le vert) contenus dans un plan perpendiculaire à la direction d'émission. Le rayonnement violet est également émis dans un plan horizontal selon une direction inclinée à 23,33° par rapport à l'axe OY. Il produit un réseau de franges verticales situées dans un plan normal à cette direction.

Ainsi, le vecteur vitesse est mesuré dans un système d'axes dont l'un est vertical, OZ, et dont les deux autres, OX₁ et OX₂, contenus dans un plan horizontal, font entre eux un angle de 48,50°. Des formules élémentaires permettent d'exprimer les composantes du vecteur vitesse dans le système d'axes adopté (OX, OY, OZ) défini Fig.4.

Les réglages utilisés conduisent aux valeurs suivantes pour les interférences : 37,34 μm pour le bleu, 38,61 μm pour le vert et 35,93 μm pour le violet.

Afin de permettre au système de détecter l'orientation de la composante de vitesse mesurée, les six faisceaux traversent des cellules de Bragg induisant un défilement des franges à l'intérieur du volume de mesure, dont la fréquence de modulation est de 7,5MHz pour le bleu et le violet et de 10MHz pour le vert.

La partie réception est constituée de deux télescopes Cassegrain de 200mm d'ouverture de manière à collecter un maximum de rayonnement diffusé par les particules traversant le volume de mesure. Le premier comporte des filtres interférentiels qui permettent d'extraire et de séparer les rayonnements vert et bleu de la lumière qu'il recueille. Le deuxième télescope sélectionne, de la même manière, le violet. Les rayonnements ainsi séparés sont envoyés sur trois photomultiplicateurs. Les signaux qu'ils délivrent entrent dans des compteurs DISA 55L dont les sorties numériques sont connectées à un système d'acquisition par l'intermédiaire d'un numériseur simultané. Cet appareil permet de s'assurer que les trois mesures de vitesse effectuées sont bien relatives à la même particule qui vient de traverser le volume de mesure. La fenêtre de ce numériseur est ici réglée à 1 μs .

Le système peut fonctionner, soit en diffusion avant, soit en rétrodiffusion. Dans les présents essais, le mode de diffusion avant, qui procure un rapport signal sur bruit beaucoup plus important, a été adopté. Alors les ensembles d'émission et de réception sont montés sur deux tables animées de déplacements précis (incertitude de 0,05mm) selon trois directions perpendiculaires. Elles sont pilotées par un ordinateur qui coordonne leurs mouvements de manière à ce que l'optique collectrice suive le volume de mesure au cours de son déplacement.

Afin d'obtenir un taux d'acquisition suffisant, surtout dans les régions tourbillonnaires, l'écoulement était ensémené par des gouttelettes de paraffine injectées par une canne placée dans la chambre de tranquillisation de la soufflerie.

La photographie de la figure 5 montre le vélocimètre laser installé de part et d'autre de la soufflerie. Sur la partie gauche de la photo, on voit l'ensemble émission avec ses deux sources laser et les deux optiques de focalisation visant respectivement à 25,17° et 23,33° par rapport à la normale à la veine. À droite de la soufflerie, on distingue les deux télescopes Cassegrain équipant la partie réception.

En chaque point de mesure, il était procédé à l'enregistrement des trois composantes de la vitesse instantanée sur un échantillon de 2000 événements correspondant à la traversée du volume de mesure par 2000 particules (soit au total : $3 \times 2000 = 6000$ valeurs instantanées pour u, v, w, composantes selon OX, OY, OZ respectivement). L'ordinateur associé au vélocimètre permet d'obtenir en léger décalé les termes statistiques les plus usuels ; à savoir, pour trois variables fluctuantes x et y, z :

$$\text{— les valeurs moyennes : } \bar{x} = \frac{1}{N} \sum_{i=1}^N x_i ; \bar{y} = \frac{1}{N} \sum_{i=1}^N y_i ; \bar{z} = \frac{1}{N} \sum_{i=1}^N z_i$$

$$\text{— les écarts types : } \sigma_x = \left[\frac{1}{N} \sum_{i=1}^N (x_i - \bar{x})^2 \right]^{1/2} ; \sigma_y = \dots ; \sigma_z = \dots$$

$$\text{— les corrélations croisées : } \overline{xy} = \frac{1}{N} \sum_{i=1}^N (x_i - \bar{x})(y_i - \bar{y}) ; \overline{xz} = \dots ; \overline{yz} = \dots$$

Les six quantités $\sigma_x, \dots, \overline{xy}, \dots$ sont identifiées aux composantes distinctes du tenseur de Reynolds qui caractérisent les propriétés de la turbulence.

Dans cette communication, nous ferons uniquement état des résultats relatifs au champ moyen.

3 - DESCRIPTION DE L'ÉCOULEMENT DANS LE CANAL -

3.1 - Répartition de pression à la paroi -

Dans ce qui va suivre, nous désignerons par A la paroi latérale du canal située à gauche pour un observateur placé face au vent. Cette face, comme le montre la figure 2, contient le sommet le plus en aval de la bosse. L'autre paroi latérale sera appelée B.

Considérons, en premier lieu, les répartitions de pression relevées sur les parois haute et basse de la veine. Afin d'être plus parlants, les résultats sont présentés en nombre de Mach "pariétal" M_p , M_p se déduisant du rapport p/p_0 par la relation de détente isentropique (hormis les cas de décollement très étendus, M_p s'identifie pratiquement avec le nombre de Mach à la frontière de la couche limite).

La figure 6 présente les répartitions longitudinales $M_p(x)$ pour 5 positions en envergure. Le caractère fortement tridimensionnel de l'écoulement apparaît immédiatement à la vue de ces courbes.

Examinons d'abord les répartitions sur la bosse (Fig. 6a). A l'amont (à $X = 200$ mm, par exemple), l'étalement des courbes résulte directement de la géométrie du canal. L'écoulement est moins rapide près de la face A (qui, rappelons-le, contient l'origine de l'axe transversal Y) qu'il ne l'est à proximité de la face B, le sommet de la bosse étant en effet plus reculé en A qu'en B. Les nombres de Mach les plus élevés sont atteints dans le centre du canal où le maximum de M_p est voisin de 2,1. Latéralement quand on tend vers A ou B, M_p diminue rapidement, les maxima locaux s'étaguant entre 1,45 et 1,70. Il est à noter que, excepté dans le milieu du canal, les recompressions, en aval du maximum de M_p , ne traduisent pas l'existence d'un choc, mais au contraire sont progressives, évolution jamais observée en écoulement bidimensionnel. De telles tendances traduisent l'existence de décollements tridimensionnels marqués par un étalement des compressions. Plus en aval, le nombre de Mach continue à décroître lentement jusqu'à des valeurs proches de l'unité.

Sur la paroi supérieure (voir Fig. 6b), on observe des phénomènes analogues. Le nombre de Mach maximal $M_p = 1,92$ est observé dans la tranche $Y = 45$ mm. Toutefois, contrairement à ce qui se passe sur la face A, l'existence d'une onde de choc, occupant la plus grande partie de l'envergure du canal, est ici clairement décelable. Seule la répartition à $Y = 13$ mm a une allure nettement différente, certainement en raison de la présence du gros décollement qui se forme au raccord entre la face A et la paroi supérieure, comme le mettent en évidence les visualisations pariétales analysées plus bas (voir §3.2). Les figures 7a et 7b donnent des représentations en perspective qui permettent de mieux visualiser les répartitions de M_p sur les parois inférieures et supérieures. On observe bien, pour les deux parois, la survitesse au voisinage de $Y = 45$ mm qui subsiste d'ailleurs en aval du choc où elle est vraisemblablement due à la formation d'un tourbillon vigoureux (voir §3.3). Également, le caractère quasi bidimensionnel de la distribution de pression pariétale sur une bonne partie de la paroi supérieure apparaît nettement.

Les répartitions de pression renseignent assez peu sur la structure de l'écoulement. Hormis des situations flagrantes, en tridimensionnel, il est pratiquement impossible de conclure, à partir de leur seul examen, sur l'existence ou non de décollements. Pour cela, il faut faire appel à une étude de la structure de l'écoulement pariétal.

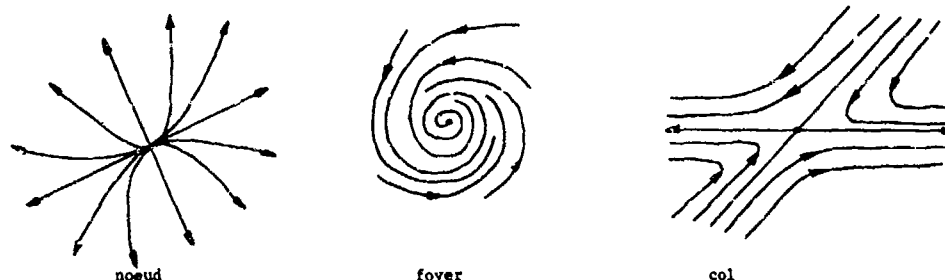
3.2 - Propriétés de l'écoulement pariétal -

Les spectres pariétaux obtenus par séduit visqueux constituent une aide précieuse et quasi-indispensable à la compréhension physique des écoulements tridimensionnels, surtout lorsque des décollements se produisent. Les traces d'séduit observées peuvent en effet être assimilées, avec un bon degré de confiance, aux lignes de courant pariétales de l'écoulement réel. De telles lignes sont définies comme la limite, quand la distance à la paroi tend vers zéro, des lignes de courant et elles s'identifient avec les lignes de frottement qui sont les lignes de force du champ de vecteurs constitué par le frottement pariétal. C'est l'examen attentif de la topologie des lignes de frottement, et plus spécialement l'observation des points singuliers (foyers, noeuds, cols) révélée par leur réseau, qui permet le plus sûrement de définir le concept de décollement - ou mieux de séparation - en écoulement tridimensionnel où cette notion est loin d'être aussi claire qu'en bidimensionnel.

L'interprétation des spectres pariétaux s'appuie sur l'analyse de LICHNEROWICZ [29,30] inspirée des travaux de LICHNEROWICZ sur les singularités des systèmes d'équations différentielles [31] (voir aussi LICHNEROWICZ [32]).

Rappelons ici, brièvement, que dans le réseau des lignes de courant pariétales, on met en évidence l'existence de points singuliers isolés où les vecteurs frottement et tourbillon s'annulent. Parmi ces points, il faut distinguer (voir schéma ci-dessous) :

- I - les points d'attachement ou de séparation) où toutes les lignes de frottement, sauf une, sont tangentes à une direction commune ;
- II - les foyers où il n'existe pas de tangente commune ; une infinité de lignes de courant s'enroulent autour de ce point ;
- III - les cols par où passent seulement deux lignes de frottement pariétal et toutes les autres lignes évitent le point singulier en s'inclinant pour prendre la direction de l'une, ou de l'autre, de ces directions particulières.



Points singuliers d'un écoulement pariétal

On est ensuite amené à introduire le concept fondamental de ligne de séparation (S) comme étant une ligne de frottement passant par un col. Une telle ligne, qui joue un rôle essentiel dans la définition du décollement en écoulement tridimensionnel, a en effet la propriété de séparer les lignes pariétales en deux familles de telle façon que ces lignes tendent à s'en rapprocher indéfiniment sans jamais la traverser ni avoir de contact avec elle (pour plus ample information, voir [30] et [32]).

Ces éléments vont nous servir à interpréter rationnellement les visualisations pariétales sur les quatre faces du canal dont les figures 8a à 8d montrent des photographies. Dans la discussion de ces résultats, nous considérerons également les schémas dessinés Fig.9. Ils représentent certaines lignes de frottement pariétal ainsi que les points singuliers du spectre. Ils ont été établis d'après les photographies et un examen direct des visualisations en cours d'essai qui révèle des détails et des indications (sens de reflux de l'écoulement pariétal, par exemple) perdus après la prise de vue. Les schémas, bien qu'ayant surtout valeur qualitative, respectent néanmoins sensiblement les proportions de la réalité.

L'examen de l'écoulement sur la bousse (voir Figs.8a et 9a) montre, en premier lieu, l'existence de deux foyers F1 et F2 bien visibles dans la moitié gauche du canal. La ligne de séparation (S1), passant par le col C1 et s'enroulant autour de F1 et F2, constitue une "barrière" située approximativement au pied de l'onde de choc oblique qui se propage dans l'écoulement extérieur (voir 14.) plus bas).

Les lignes de frottement, venant de l'amont et contenues dans le domaine limité par la ligne de séparation (S1) passent par le col C2, vont s'enrouler autour, soit de F1, soit de F2, selon qu'elles sont situées d'un côté ou de l'autre de la ligne de séparation (S1) qui passe à la fois par C1 et C2. Une partie de ces lignes contourne la barrière (S1) en s'incurvant brusquement.

La structure constituée de (S1), (S2) et des deux foyers F1 et F2 est classiquement observée dans les interactions choc-couche limite en canal avec effet tridimensionnel [33,34].

Dans une telle situation, (S1) peut être associée sans ambiguïté à un décollement bien caractérisé, l'écoulement au voisinage immédiat de (S1) "quittant" la paroi selon le mécanisme décrit par LIGHTHILL [32]. De son côté, la ligne de séparation (S2) est, elle, une ligne d'attachement - ou de recollement - en ce sens qu'un peu au-dessus de (S2) le fluide extérieur "plonge" en direction de la paroi. Ainsi, C1 et C2 sont respectivement des cols de décollement et d'attachement. Cette brève discussion met bien l'accent sur la distinction qu'il convient de faire entre ligne de séparation et ligne de décollement.

L'enroulement autour de foyers, tels que F1 ou F2, est la trace sur la paroi d'un tourbillon s'échappant dans l'écoulement extérieur. Une ligne de séparation est, elle, la trace d'une surface de séparation - ou nappe de décollement - qui s'enroule autour du centre de la structure tourbillonnaire.

Revenant au schéma de la figure 9b, on observe que les lignes de frottement en provenance de l'amont se partagent en deux familles.

Les unes, proches de la face A s'écoulent continuellement de l'amont vers l'aval.

Les autres, voisines de A, se séparent à leur tour en deux sous-ensembles :

- celles comprises entre (S2) et la ligne de séparation (S4), aboutissant au demi-col C3, continuent leur chemin vers l'aval,
- celles situées entre A et (S4) vont s'enrouler autour d'un troisième foyer F3 pour former un "tourbillon" délimité par la ligne de séparation (S3) issue du demi-col C4.

Considérons maintenant la face A (voir Figs.8b et 9b) sur laquelle la structure de l'écoulement pariétal est particulièrement complexe. Ainsi, nous distinguons sans difficulté la ligne de séparation (S4) associée au large décollement se formant sur A. La ligne (S4) est issue du demi-col C3, globalement conforme avec C4 et formant avec ce dernier un col complet. (S4) va s'enrouler autour du foyer F4 situé près de la paroi supérieure. Dans cette configuration, toutes les lignes de frottement venant de l'amont s'enroulent autour de F4 pour constituer la grosse structure spirale bien visible sur la photographie de la figure 8b. Le partage entre les lignes en provenance de l'amont et celles "avalées" par le tourbillon est assuré par la ligne de séparation (S7) issue du demi-col C6.

Tout l'écoulement amont "disparaissant" dans le foyer F4, le champ aval doit être alimenté par un ou plusieurs noeuds. Dans le cas présent, on met ainsi en évidence le noeud N1, situé près de la paroi inférieure, et le demi-noeud N2 dans le coin entre A et la paroi supérieure. Il s'établit alors en aval de (S6) une structure extrêmement complexe dont le dessin résulte d'observations très attentives et d'une interprétation se guidant sur des règles topologiques. Nous ne décrirons pas l'écoulement représenté en détail, ce qui serait fastidieux. Mentionnons simplement, en plus des noeuds N1 et N2 :

- les deux foyers F5 et F6 ;
- les cols C7, C8 et C10 ;
- le demi-col C9 sur la paroi inférieure.

L'écoulement comporte un grand nombre de lignes de séparation (représentées en trait renforcé sur le dessin) que nous ne repèrerons pas spécialement. Distinguons quand même les lignes (S8) et (S9) qui séparent l'écoulement allant vers l'aval de celui refluant vers l'amont pour "disparaître" dans les foyers F4, F5 et F6.

L'examen se poursuit par la considération de l'écoulement sur la paroi supérieure (voir Figs. 8c et 9c). En étant cette fois encore plus bref, nous distinguons ici :

- 3 foyers : F7, F8 et F9 ;
- 3 cols : C11, C12 et C13 ;
- 2 demi-cols : C14 et C15 ;
- 2 demi-noeuds : N3 et N4.

Il est à noter que C15 et N4 sont à associer respectivement avec C6 et N2 pour constituer un col et un noeud complets. La ligne de séparation (S10) passant par C11, dont une branche s'enroule autour de F7 et l'autre autour de F8, correspond au décollement induit par le choc quasi-normal que l'on observe, dans la moitié supérieure du canal, sur la plus grande partie de l'envergure (voir les répartitions de pression de la figure 7 et les courbes iso-Mach de la figure 11). La structure allongée, organisée autour de F9, est à mettre en correspondance avec le gros "tourbillon" observé sur la face A, dans sa partie haute. Le foyer F8 est alimenté à la fois par des lignes de frottement venant de l'amont et des lignes issues du demi-noeud N3. D'une manière analogue, F9 reçoit une partie de son alimentation du demi-noeud N4.

Enfin, les figures 8d et 9d montrent l'écoulement sur la face latérale B. Ici, la structure du spectre pariétal est sensiblement plus simple. On distingue, principalement, la ligne de séparation (S12), passant par le col C16, qui sépare les lignes de frottement s'enroulant autour du foyer F10 de celles poursuivant leur chemin vers l'aval. F10 est aussi alimenté par des lignes naissant au demi-noeud N5. La ligne de séparation (S13) fait la démarcation entre le fluide pariétal venu de l'amont et celui issu de N5. Une des branches de (S13) s'enroule autour de F10 en même temps que la ligne de séparation (S14) venant du demi-col C17.

Réunissant les demi-noeuds et les demi-cols en correspondance, et sachant qu'un foyer est topologiquement équivalent à un noeud, le dénombrement de tous les points singuliers représentés conduit à la relation :

$$\sum \text{noeuds} - \sum \text{cols} = 13 - 13 = 0$$

qui doit être satisfaite par les singularités réparties sur une telle surface.

3.3 - Structure du champ extérieur moyen -

Le volume exploré au vélocimètre laser à trois composantes est représenté sur la figure 4. Il couvre toute la hauteur de la voûte et s'étend de $X = 250$ à $X = 590$ mm, c'est-à-dire inclut la région d'interaction forte. Les explorations ont été exécutées selon des lignes verticales, espacées en X de 10 mm, et contenues dans 3 plans longitudinaux de coordonnées $Y = 30, 45$ et 75 mm. Ainsi, seule la partie centrale de l'écoulement, sur une largeur représentant la moitié de l'envergure du canal, a pu être sondée. En effet, il s'est avéré impossible d'effectuer des mesures à moins de 30 mm des parois latérales, les photomultiplicateurs étant alors éblouis par les réflexions sur les glaces. Au total, les échantillons de 2 000 valeurs du vecteur vitesse instantané ont été prélevés en 6 C.O points environ.

Les figures 10a à 10c montrent une représentation du champ sous forme de tracés de projections du vecteur vitesse moyen dans les 3 plans longitudinaux YZ. L'examen de ces résultats met en évidence les caractéristiques suivantes :

Dans la partie amont du domaine, l'écoulement supersonique s'accélère, en même temps que la section du canal s'agrandit, la vitesse étant plus grande près de la bosse ; ce qui est normal en vertu de l'effet de courbure. La couche limite, dont l'épaisseur est voisine de 4 mm, est difficile à mettre en évidence, le vélocimètre ne donnant pas de mesures significatives à une distance d'une paroi inférieure à 1,5 mm, en approche tangentielle.

Partant du plan $Y = 30$ mm (le plus proche de la face A) et en considérant ce qui se passe près de la bosse, on observe, à partir de $X = 280$ mm, un fort épaississement de la couche limite dont les profils sont très crénelés jusqu'à $X = 310$ mm (voir Fig. 10a). Ce comportement est à mettre en relation avec le spectre pariétal dessiné Fig. 9a. On y voit que le plan $Y = 30$ mm traverse la zone décollée comprise entre les lignes de séparation (S1) et (S2). En aval, les profils se remplissent rapidement, la couche dissipative renaît très épaisse.

La tendance est accentuée dans le plan $Y = 45$ mm (voir Fig. 10b) où à $X = 290$ mm, la distribution de vitesse comporte, très près de la paroi, une zone de reflux. En fait, ce plan traverse le décollement

dans la partie où il est le plus étendu, c'est-à-dire entre les cols C1 et C2. Pour $Y = 60\text{mm}$ (voir Fig.10c), les profils sont nettement moins déformés, le plan passant près du bord extérieur du tourbillon centré sur F2. Si pour $Y = 45$ et 30mm , on n'observe pas de reflux, malgré la direction prise par les lignes de courant pariétales entre (S1) et (S2), c'est que le courant de retour est trop mince pour pouvoir être détecté par l'appareillage utilisé.

Il est à noter qu'en bidimensionnel, pour les mêmes nombres de Mach avant choc que ceux rencontrés ici, il se formerait un courant de retour beaucoup plus fort que l'on détecterait aisément [19]. Cette différence de comportement fondamentale provient du fait, qu'en tridimensionnel, l'écoulement a la possibilité de "fuir" latéralement d'où le plus souvent un étalement et un affaiblissement des interactions.

Les plans situés à $Y = 75$ et 90mm (voir Figs.10d et 10e) passent au delà de (S1) si bien que l'épaississement de la couche limite est maintenant modeste. En même temps, l'intensité du choc tend à diminuer, comme le montrent les distributions du nombre de Mach M_p (voir Figs.6a et 7a).

Près de la paroi supérieure, les champs de vecteurs mettent en évidence un phénomène similaire dont l'origine est plus en aval en raison de la position plus reculée de l'onde de choc (voir Figs.6b et 7b). Se reportant au schéma de la figure 9c, on voit que le plan $Y = 30\text{mm}$ (Fig.10a) traverse une région, comprise entre les lignes de séparation (S10) et (S11) où l'écoulement est fortement ralenti sans qu'il y ait formation d'un tourbillon. En se rapprochant du plan médian du canal ($Y = 45\text{mm}$ puis $Y = 60\text{mm}$, voir Figs.10b et 10c), les explorations pénètrent dans la région de forte interaction où naît le tourbillon intense centré autour du foyer F7. Les profils de vitesse sont alors très évidés, une zone de reflux étant maintenant clairement détectée aux abscisses $X = 350$ et 360mm dans le plan $Y = 60\text{mm}$. Encore plus loin de la face A, pour $Y = 75$ et 90mm , le courant de retour disparaît, mais la déformation des profils est encore extrêmement prononcée en raison de la proximité du grand décollement organisé autour de F9.

La structure de l'écoulement de fluide parfait, extérieur aux couches dissipatives, est mise en évidence par les tracés de lignes iso-Mach présentés Figs.11a à 11e.

Pour les 5 plans considérés, on observe nettement une structure de chocs en lambda comportant, un choc de tête oblique (λ_1), un choc quasi-normal intense (λ_2), occupant à peu près la moitié du canal, le pied du lambda (λ_3), très peu intense, étant à peine discernable (l'épaississement des chocs (λ_3) est causé par le logiciel de tracé des courbes iso qui interpole linéairement entre les points de mesures, ici trop espacés en X pour "capturer" convenablement les discontinuités orientées selon OZ). Le choc oblique (λ_1) est bien marqué dans les plans $Y = 30, 45$ et 60mm . A $Y = 90\text{mm}$, il s'est considérablement affaibli et semble être remplacé par une compression continue, ce que confirment les mesures à la paroi (voir Figs.6a et 7a). Il est à noter que la position en X des pieds des ondes de choc (λ_1) aussi bien que (λ_2) ne varie pratiquement pas d'un plan Y à l'autre, ce qui montre que ces chocs sont peu inclinés par rapport à la vitesse à l'entrée du canal. Il serait bien sûr très instructif de faire des mesures plus près des parois latérales de manière à préciser la structure des chocs dans les coins.

Les figures 12a à 12e représentent les projections des vecteurs vitesse dans des plans transversaux YZ (noter que l'échelle des vecteurs est plus grande que pour le tracé du champ longitudinal dans les plans ZX).

Le premier résultat (voir Fig.12a) est relatif au plan situé à $X = 260\text{mm}$, c'est-à-dire qu'il correspond au champ des vitesses immédiatement en amont du système de chocs. D'une manière générale, à cette station, sous l'effet de la bosse l'écoulement transversal se fait de la face A vers la face B et présente une composante plongeante. Egalement, on observe que la composante de vitesse transversale est beaucoup plus importante près de la bosse que dans la zone externe du champ.

A partir de $X = 280\text{mm}$ (voir Fig.12b), il se produit un changement important dans la structure du champ transversal au voisinage de la bosse en raison de l'influence de l'onde de choc. Ainsi, pour les explorations à $Y = 75$ et 90mm (les plus proches de la face B) l'écoulement, près de la paroi et au dessous d'une discontinuité qui est manifestement la trace de l'onde de choc λ_1 , tend à changer de sens et à se faire de B vers A. Ce comportement s'accroît au fur et à mesure que l'on s'éloigne vers l'aval, comme le montre la figure 12e relative au plan situé à $X = 320\text{mm}$. Le reflux de B vers A se fait maintenant sentir aussi pour l'exploration située à $Y = 45\text{mm}$, sur une distance très courte au voisinage immédiat de la paroi. En revanche, pour $Y = 30\text{mm}$, l'écoulement se fait toujours de A vers B. On distingue également le passage de l'onde de choc (λ_1) qui intersecte les quatre lignes d'exploration $Y = 45, 60, 75$ et 90mm . Pour $X = 350\text{mm}$ (voir Fig.12d), le champ de vitesse extérieur ne contient plus de discontinuité, le plan YZ considéré se situant en aval du système de chocs (λ_1). Le mouvement de rotation, près de la bosse, s'est amplifié si bien qu'il affecte maintenant la ligne $Y = 30\text{mm}$. Un phénomène analogue se développe dans le voisinage de la paroi supérieure où, pour $Y = 75$ et 90mm , l'écoulement très près de la surface se fait de B vers A.

Les mêmes caractéristiques, mais accentuées, sont visibles dans le plan le plus aval, situé à $X = 390\text{mm}$ (voir Fig.12e). Simultanément, on assiste à une diminution générale de l'amplitude de la composante transversale, surtout dans la partie centrale du champ et dans les régions les plus proches de la face B. Cette tendance traduit l'alignement de l'ensemble de l'écoulement selon l'axe longitudinal du canal dont la section est redevenue constante.

Les figures 13a à 13h montrent des tracés des lignes d'égale valeur du module de la composante de la vitesse dans des plans transversaux YZ . En amont des ondes de choc (plan à $X = 260\text{mm}$, Fig.13a) les courbes ont une allure régulière qui traduit la détente dans la partie divergente du canal. Les stations $X = 280$ et 290mm (Figs.13b et 13c) sont juste en aval du pied du choc oblique (λ_1) dont on distingue parfaitement la trace dans le champ des lignes iso. En même temps, près de la paroi, on voit se former une structure, constituée de courbes fermées, correspondant au décollement provoqué par (λ_1).

En allant vers l'aval (Figs.13d, e, f), la trace de (\bar{u}) s'éloigne progressivement de la bosse. A $X = 330\text{mm}$ (Fig.13f), elle est située un peu au dessus du milieu du canal. Dans cette section, au contact de la paroi supérieure, apparaît un noyau coïncidant avec l'origine de l'interaction provoquée par le choc (\bar{u}) . Encore plus loin, pour $X = 340$ et 390mm (Figs.13g et 13h), le plan passe en aval des chocs. Les deux structures associées aux larges décollements sont particulièrement bien visibles.

Une exploitation plus poussée de ces résultats, en vue d'une part de mettre en évidence la structure des pseudo lignes de courant associées au mouvement transversal et d'autre part d'établir la continuité avec les spectres pariétaux, nécessitera des mesures complémentaires, plus près des parois latérales, et selon des lignes Y plus rapprochées.

4 - CONCLUSION -

L'écoulement résultant d'une interaction onde de choc-couche limite turbulente se produisant dans un canal transsonique de géométrie tridimensionnelle a été qualifié de manière détaillée au moyen de mesures de pression à la paroi, de visualisations pariétales par enduit visqueux et de sondages de champ par vélocimétrie laser à trois composantes.

Les spectres pariétaux, relevés sur les quatre faces du canal, révèlent une structure extrêmement complexe caractérisée par l'existence de nombreuses lignes de séparation et de plusieurs foyers, traces sur la paroi de tourbillons s'échappant dans l'écoulement extérieur.

Les sondages au vélocimètre laser mettent d'abord en évidence l'existence de chocs constituant un système en λ , analogue à ce qui est observé en bidimensionnel. Toutefois, de larges différences existent avec le cas plan, notamment au voisinage des parois latérales du canal où les chocs tendent à être remplacés par des compressions continues. Les explorations montrent ensuite la formation de deux régions décollées, l'une sur la paroi inférieure, l'autre sur la paroi supérieure, dont la naissance coïncide avec les pieds des ondes de choc. Ces zones sont marquées par un fort épaissement de la couche limite avec évidemment important des profils de vitesse longitudinaux. Toutefois, la destabilisation est moindre que dans le cas bidimensionnel, l'écoulement ayant ici la possibilité de s'écouler latéralement, atténuant ainsi l'effet des gradients de pression antagonistes.

Les présents essais doivent permettre une meilleure compréhension physique des interactions complexes se produisant dans un canal transsonique tridimensionnel. Ils peuvent également servir à la validation des codes de calcul résolvant les équations de Navier-Stokes en fournissant un ensemble de données expérimentales bien documenté.

Néanmoins, une exploitation plus poussée des résultats disponibles et des mesures complémentaires s'avèrent nécessaires pour se faire une image vraiment claire de l'écoulement, notamment de son organisation dans des plans transversaux.

REFERENCES -

- 1 - DELERY, J. "L'interaction onde de choc-couche limite turbulente et son contrôle." AGARD-CP n°363 (1984) ; du même auteur "Shock-wave/turbulent boundary-layer interaction and its control". *Prog. in Aerospace Sciences*, Vol.22, pp.209-280 (1985).
- 2 - LEBLANC, R. "Recent progress in shock-wave/boundary layer interaction." VKI-LS-64 on Transonic Blade to Blade Flow in Axial Turbomachinery" (1976).
- 3 - STANENSKY, E. "Wechselwirkung Zwischen Ausströmung und Grenzschicht an transsonischen Profilen." Thèse de Docteur-Ingenieur, D-83, Berlin (1981).
- 4 - DELERY, J. et MARVIN, J.G. "Turbulent shock-wave/boundary-layer interaction." AGARDograph n°280 (1986).
- 5 - CALVERT, W.J. "An inviscid-viscous interaction treatment to predict the blade-to-blade performance of axial compressors with leading edge normal shock wave." ASME Paper n° 82-GT-135 (1982).
- 6 - MEAUME, G. et DELERY, J. "Méthode de couplage pour le calcul en mode inverse des écoulements internes transsoniques avec onde de choc." AGARD-CP n°331 et ONERA TF n°1983-62.
- 7 - WHITFIELD, D.L. et THOMAS, J.L. "Transonic viscous inviscid interactions using Euler and inverse boundary-layer equations." *Computational Methods in Viscous Flows in Recent Advances in Numerical Methods in Fluids*, W.G. Nabeshi, Editor, Pitman Press (1983).
- 8 - LE BALLEUR, J.C. et BLAISE, D. "Calculs des écoulements internes décollés et de l'interaction couche limite-onde de choc par couplage visqueux-non visqueux." *La Recherche Aérospatiale*, n°1983-4.
- 9 - JOHNSON, D.A. et KING, L.S. "A new turbulence closure model for boundary-layer flow with strong adverse pressure gradients and separation." AIAA Paper n°84-0173 (1984).
- 10 - VANDROMME, D. et MA NINH M. "Physical analysis of turbulent boundary-layer/shock-wave interactions using second order closure predictions." Symposium IUTAM sur "Turbulent Shear Layer/Shock-Wave Interactions, 9-12 Septembre 1985, Palaiseau, France, Springer Verlag (1986).

- 11 - CAMBIER, L., ESCANDE, B. et VEUILLOT, J.P. "Calcul d'écoulements internes à grand nombre de Reynolds par résolution numérique des équations de Navier-Stokes." AGARD PEP 68th Specialist Meeting, 10-12 Septembre 1986, Neubiberg, Germany.
- 12 - PEAKE, D.J. et TOBAK, M. "Three-dimensional interactions and vortical flows with emphasis on high speeds." AGARDograph 252 (1980).
- 13 - HERNUNG, H.G. "The vortex skeleton model for three-dimensional steady flows". AGARD-CP N°342 (1983).
- 14 - BENAY, R. et POT, T. "Interaction onde de choc/couche limite turbulente en écoulement de canal tridimensionnel". 22ème Colloque d'Aérodynamique Appliquée de l'AAAF, 13-15 Novembre 1985, Lille, France et ONERA-TP n°1985-151.
- 15 - LIU, M.-S., SHAMROTH, S.J. et Mc DONALD, H. "Numerical solutions of Navier-Stokes equations for compressible turbulent two/three dimensional flows in the terminal shock region of an inlet/diffuser". NASA CR n°3723 (1983).
- 16 - WEINBERG, B.C., YANG, R.-J., Mc DONALD, H. et SHAMROTH, S.J. "Calculations of two and three dimensional transonic cascade flow fields using the Navier-Stokes equations." Journal of Engineering for Gas Turbines and Power, Vol.108, pp.93-102 (1986).
- 17 - DAMES, W.N. "Computation of off-design flows in a transonic compressor rotor". Journal of Engineering for Gas Turbines and Power, Vol. 108, pp.144-150 (1986).
- 18 - PRINCE, D.C., Jr "Three dimensional shock structures for transonic/supersonic compressor rotors". Journal of Aircraft, vol.17, n°1, pp.28-37 (1980).
- 19 - DELERY, J. "Experimental investigation of turbulent properties in transonic shock/boundary layer interactions." AIAA Journal, Vol.21, n°2, pp.180-185 (Fév. 1983) ; voir aussi AIAA Paper n°81-185 (Juin 1981).
- 20 - OSKAM, B., VAS, I.E. et BOGDONOFF, S.M. "Mach 3 oblique shock-wave/turbulent boundary layer interactions in three dimensions." AIAA Paper n°75-336 (Juillet 1976).
- 21 - SKITTLES, G.S., PERKINS, J.J. et BOGDONOFF, S.M. "Investigation of three dimensional shock/boundary-layer interactions at swept compression corners." AIAA Journal, vol.18, n°7 (Juillet 1980).
- 22 - KUSSOV, M.I., VIEGAS, J.R. et HORSTMAN, G.C. "An experimental and numerical investigation of a 3D shock separated turbulent boundary layer." AIAA Journal, vol.18, n°12 (Décembre 1980).
- 23 - DOLLING, D.S. "Comparison of sharp and blunt fin-induced shock-wave/turbulent boundary-layer interaction". AIAA Journal, Vol.20, n°10, pp.1385-1391 (1982).
- 24 - DEGREZ, G. et GINOUX, J.J. "Three dimensional observed shock wave laminar boundary layer interaction at Mach 2.25". AIAA Paper n°83-1755 (1983).
- 25 - LU, F.K. et SKITTLES, G.S. "Conical similarity of shock/boundary-layer interactions generated by swept fins." AIAA Paper n°83-1756 (1983).
- 26 - JUNKOWICH, M.S. "Flow visualization studies of a 2-D shock/boundary layer interaction in the presence of a non-uniform approach boundary-layer". AIAA Paper n°84-1560 (1984).
- 27 - CHOU, J.N., CHILDS, M.K. et WONG, K.S. "An experimental study of three dimensional shock-wave/turbulent boundary-layer interactions in a supersonic flow." AIAA Paper n°83-1566 (1983).
- 28 - BOUTIER, A., D'NUMIERES, G. et SOULEVANT, D. "Three dimensional laser velocimetry : a review." 2nd International Symposium on Application of Laser Anemometry to Fluid Mechanics, Lisbon, 2-5 Juillet 1984 et ONERA TP 1984-43.
- 29 - LEGENDRE, R. "Écoulement au voisinage de la pointe avant d'une aile à forte flèche aux incidences moyennes". La Recherche Aérospatiale, n°30, pp.3-6 (1952).
- 30 - LEGENDRE, R. "Lignes de courant d'un écoulement permanent. Décollement et séparation." La Recherche Aérospatiale n°1977-6 (1977).
- 31 - POINCARÉ, H. "Les points singuliers des équations différentielles". C.R. Académie des Sciences, 13-2-1882 et Oeuvres Complètes (Vol.1).
- 32 - LIGHTHILL, M.J. "Attachment and separation in three-dimensional flows." Section II 2-6 of Laminar Boundary Layers, Oxford University Press, pp.72-82 (1963).
- 33 - GREEN, J.E. "Interactions between shock-waves and turbulent boundary layers". NAE-TR n°6908 (1969) ; voir aussi Prog. in Aerospace Sciences, Vol.11 (1971).
- 34 - REDA, D.C. et MURPHY, M.D. "Shock-wave/turbulent boundary-layer interactions in rectangular channels". AIAA Paper, n°72-715 (1972).

 Zones équipées de prises de pression
cotes en millimètres

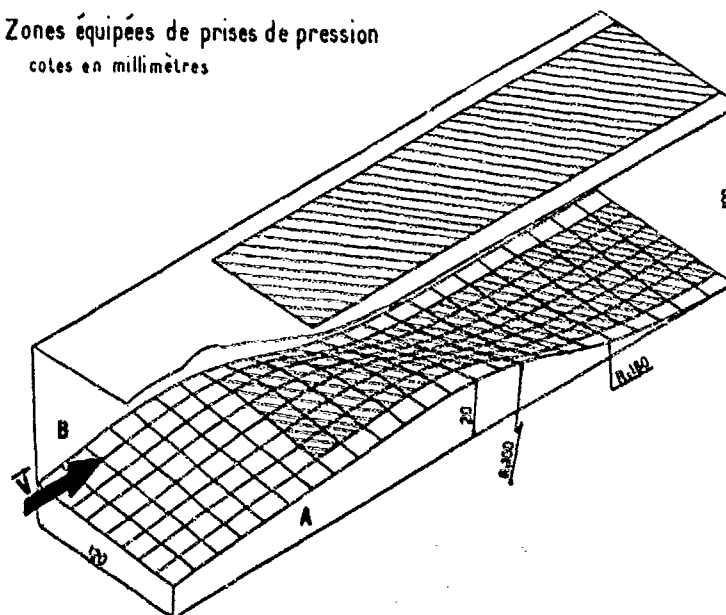
[illegible]

Fig 2 : Schéma de principe du vélocimètre laser

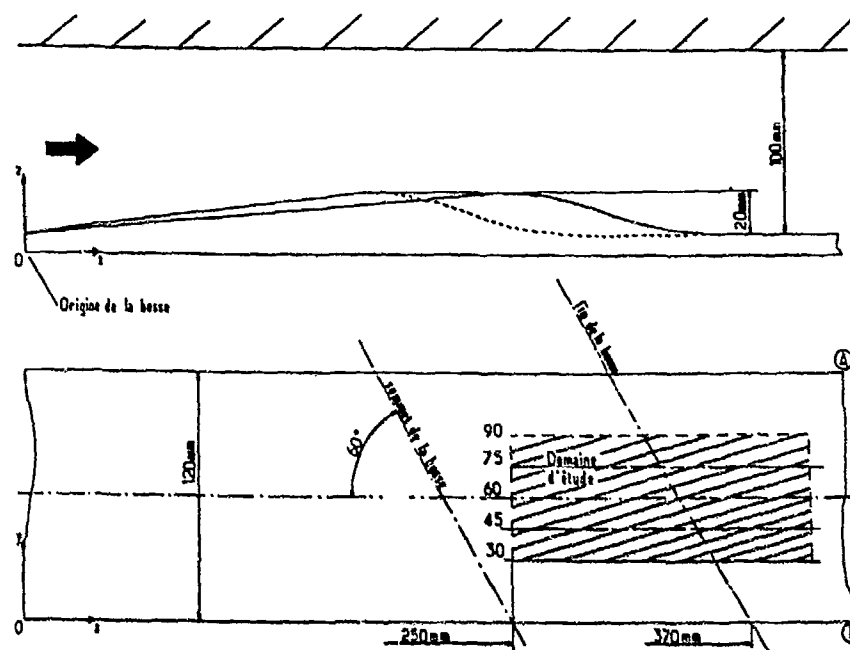


Fig 4 : Définition du système d'axes et du domaine d'exploration



Fig 5 : Installation du vélocimètre laser sur le lit d'essai

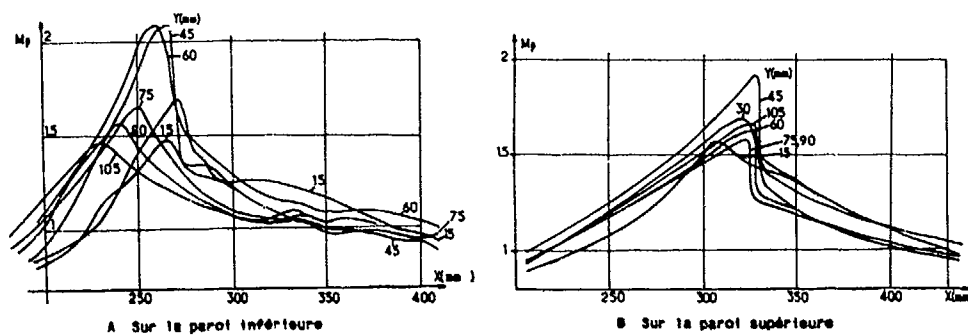


Fig 6 : Répartition du nombre de Mach pariétal

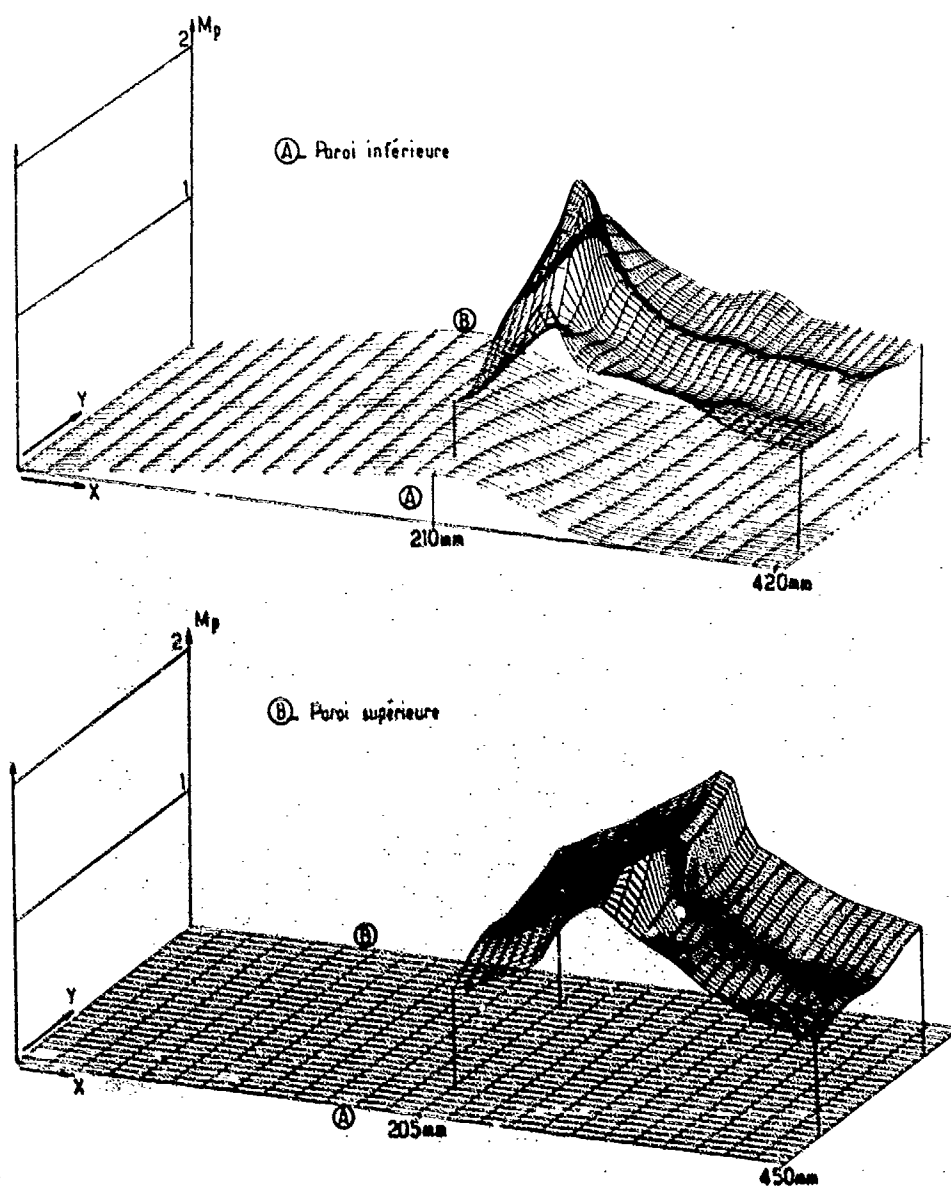
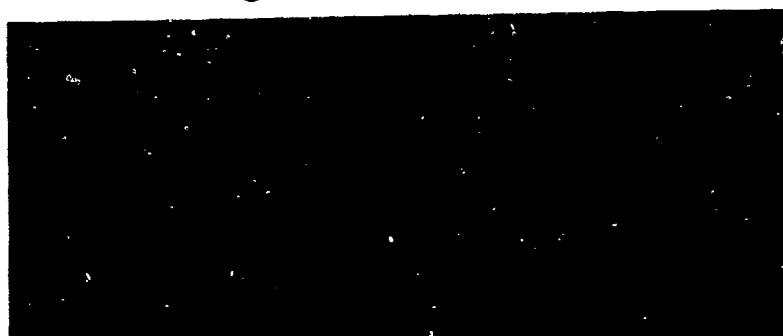


Fig 7 : Vue perspective de la répartition du nombre de Mach pariétal



(A) Sur la paroi inférieure



(B) Sur la paroi A



(C) Sur la paroi supérieure



(D) Sur la paroi B

Fig 8 : Visualisation de l'écoulement partiel

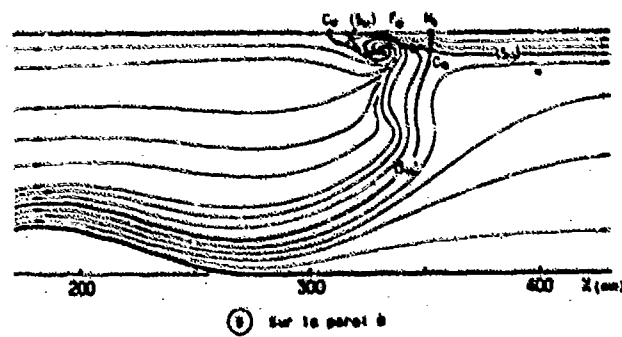
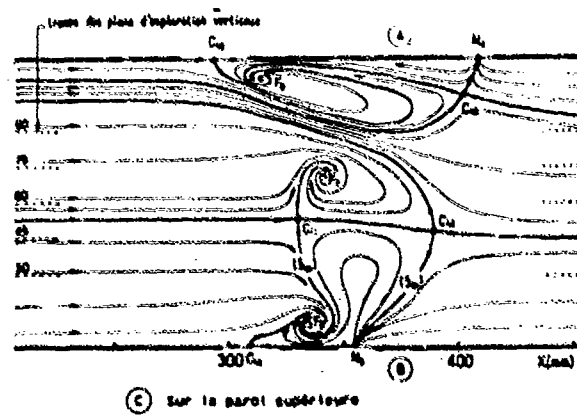
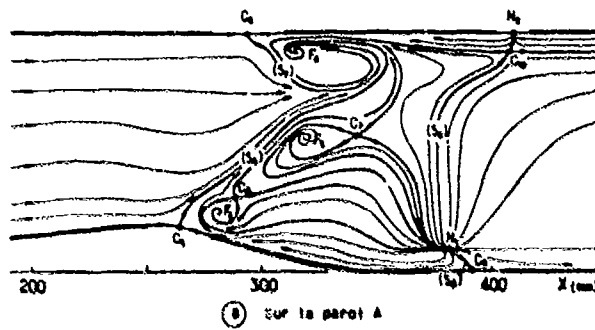
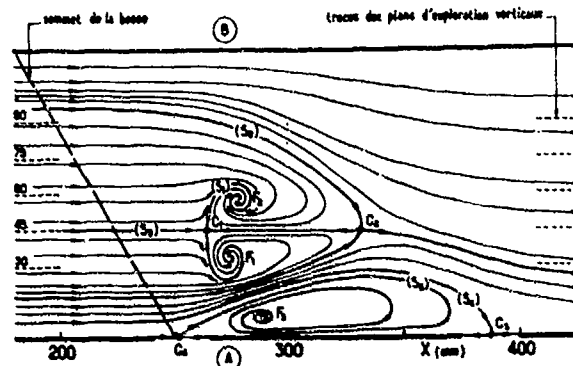


Fig 8 : Schéma de l'écoulement pariétal

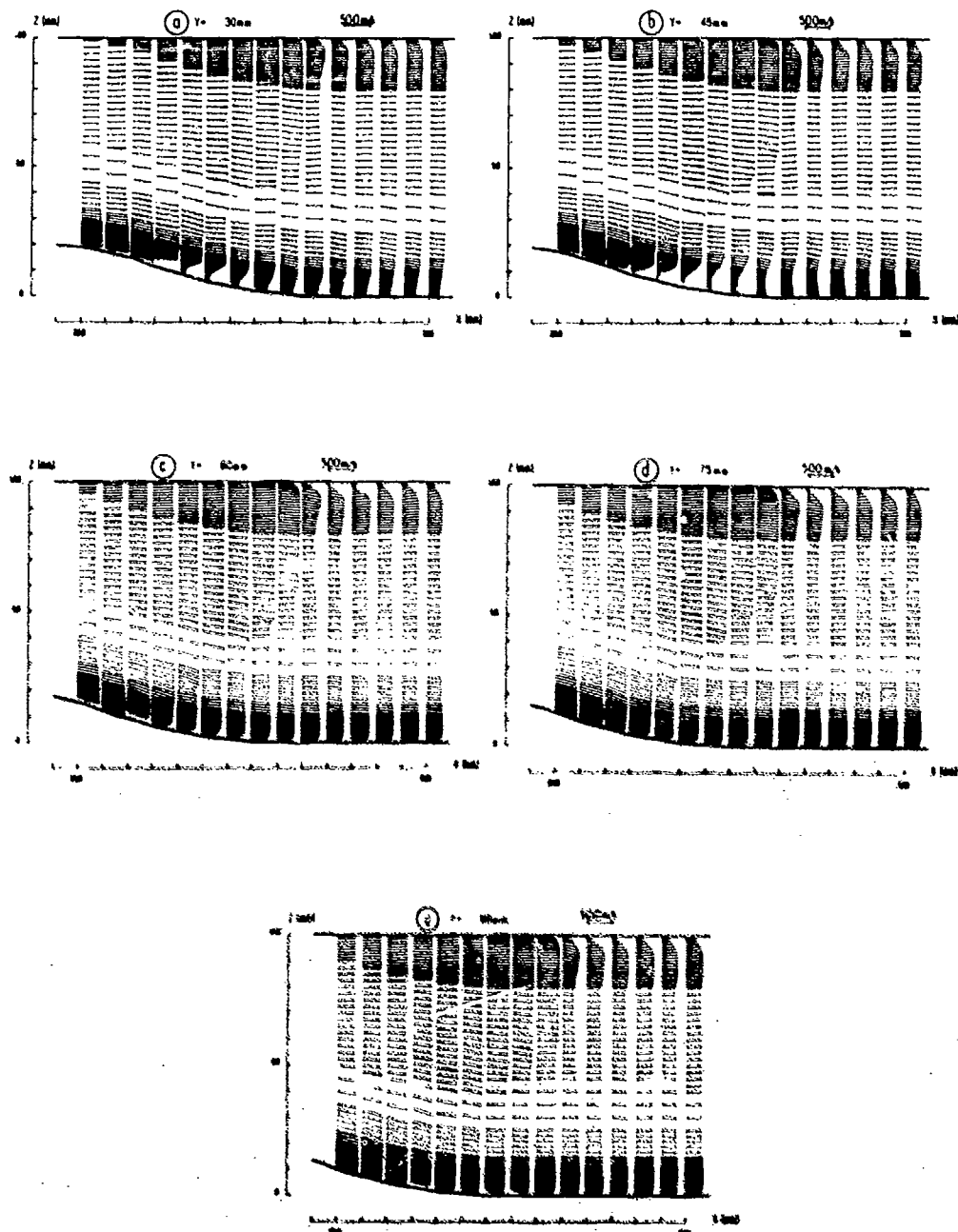


Fig 10: Projections and vector's velocity data to plan longitudinal

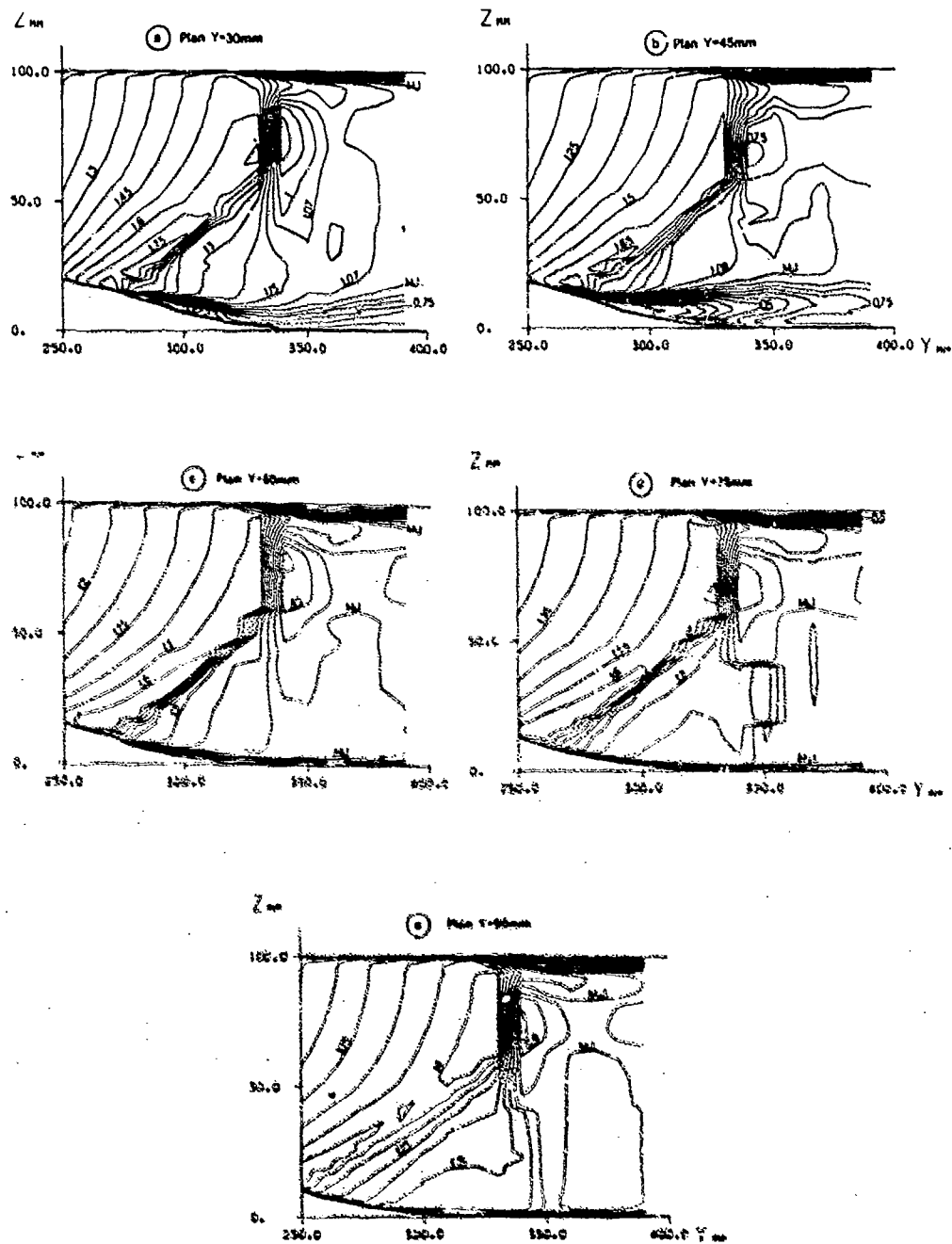


Fig 11 : Représentation du signal 140-MHz

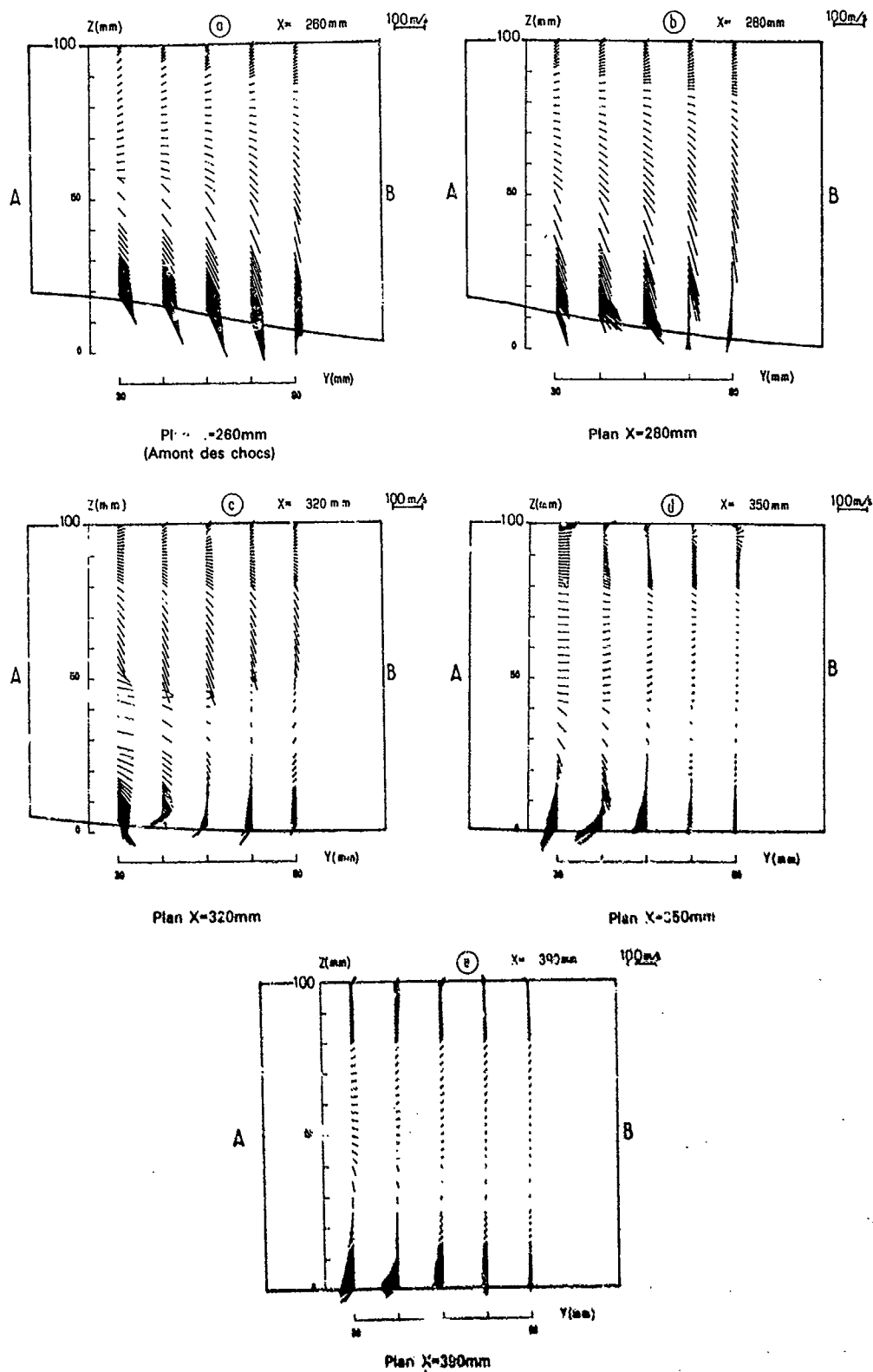


Fig 12 Composante des vecteurs vitesse dans des plans transversaux

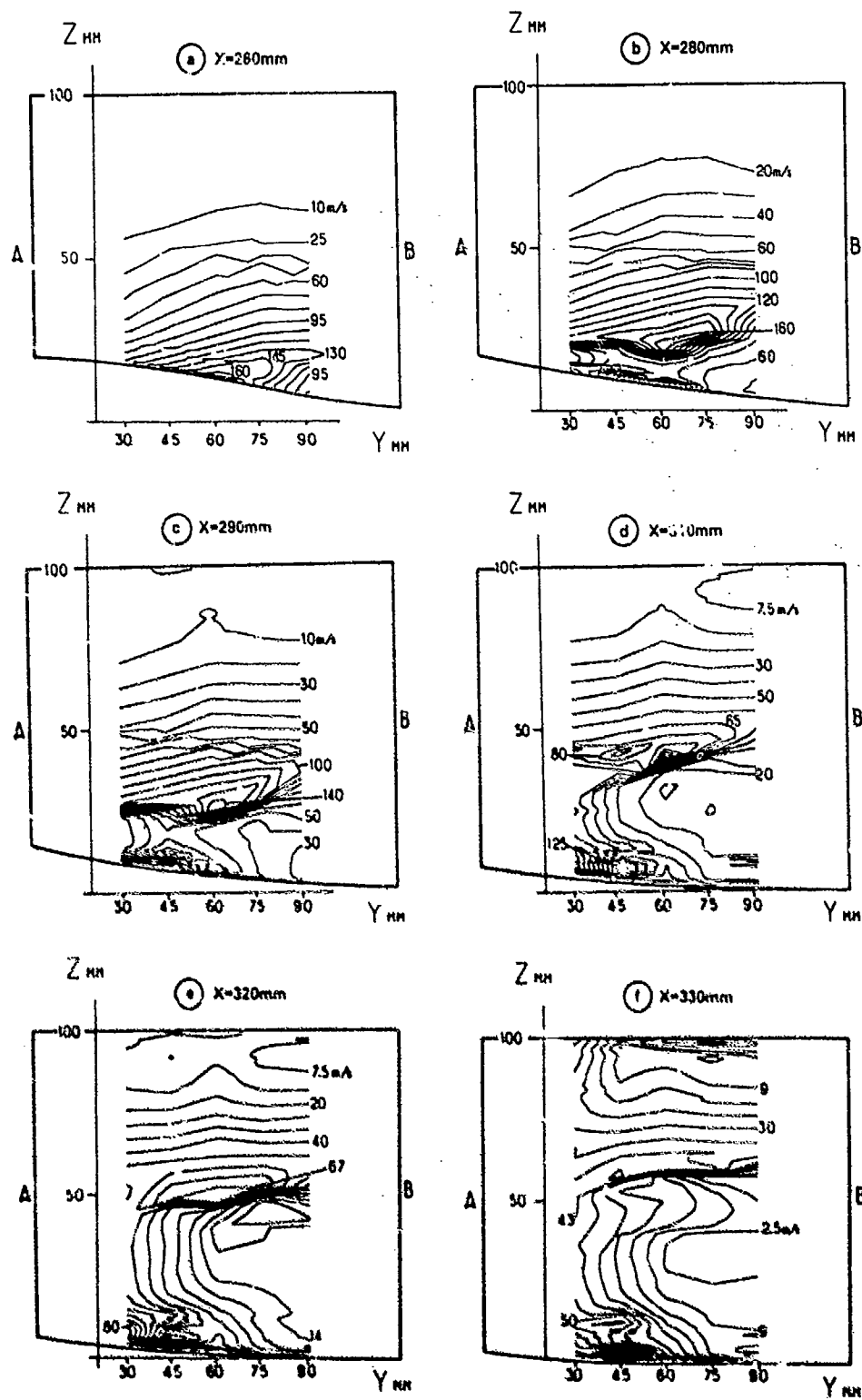


Fig 18 : lignes d'égalité valeur du module de la composante de vitesse dans des plans transversaux

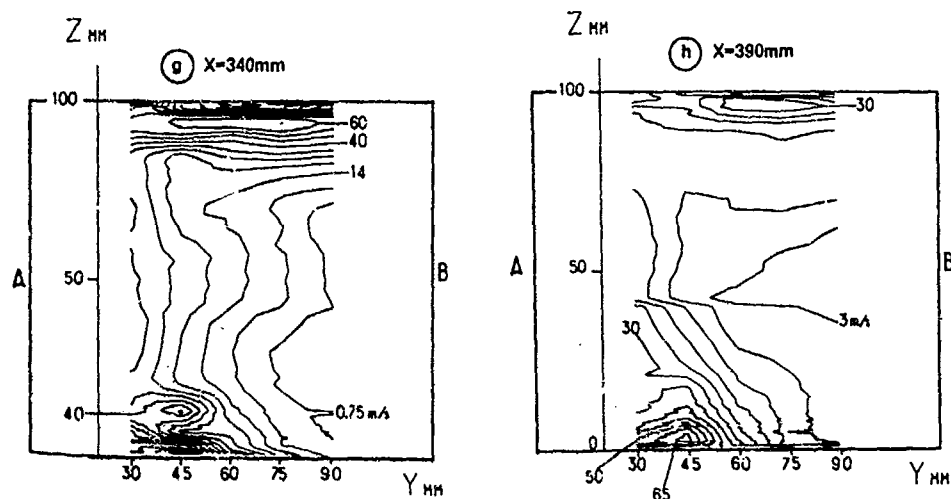


Fig 13 : Lignes d'égale valeur du module de la composante de vitesse dans des plans transversaux

DISCUSSION

P. Ramette, Fr

1. Avez vous observé des fluctuations de l'écoulement dans le temps? (battement des ondes de choc, etc.)
2. L'analyse instationnaire de l'écoulement que vous allez faire vous permettra-t-elle d'analyser à la fois la turbulence de l'écoulement et les fluctuations avec une échelle de temps plus grande?

Author's Reply

1. Un battement de l'onde de choc est effectivement perceptible dans les mesures effectuées, il se traduit par un léger étagement de celle-ci dans les résultats des mesures. Toutefois, ce phénomène est à petite échelle, il n'y a pas de phénomène à grande échelle (nous rappelons que l'écoulement désiré devait être stationnaire dans un premier temps).
2. Bien que l'écoulement soit en principe sensiblement stationnaire, une analyse instationnaire des signaux issus des capteurs de pression est possible. Il est en outre probablement envisageable d'étudier, avec le même montage, une configuration franchement instationnaire, au prix éventuellement de quelques modifications à étudier.

H.B. Weyer, Ne

An important question of accuracy of LDV is related to the seed particles which must follow the flow rather exactly. Have you proved that your particles follow accurately the flow, particularly when crossing the shock waves?

Author's Reply

At ONERA we already have long experience of LDV measurements. So the accuracy of measurements and the capability of the particles to follow the flow were tested many years ago. It appeared that in the transonic domain, the particles lag due to the inertial effects is negligible even when crossing a shock. The diameter of the particles used (generally incense smoke) is less than 5 μm .

J. Moore, US

On Figure 10, the velocity vectors are in the channel direction. I did not see any reverse flow. Was this because there was any or because you could not distinguish back flow with the measurement technique?

Author's Reply

It is possible to distinguish reverse flow with our LDV system which is equipped with Bragg cells. It is not possible to observe the area of negative velocities on the pictures presented because of the scale used, the negative velocities being small in modulus compared with the other ones and the region of reversed flow very thin.

K.D. Papailiou, Gr

This is a very important experiment in a domain where data are lacking. I would like to ask the following questions:

1. Was unsteadiness observed in the experiment and how did you cope with it?
2. How close can you measure near the solid wall and how can you circumvent the difficulty of measuring when the solid wall is forming a "bump"?

3. How did you choose your geometry?
4. Can you make any comments on the accuracy of the measurements?

Author's Reply

1. The aim of the experiment was to obtain a configuration which is as steady as possible. Actually we observed small scale fluctuations of the shock location that can hardly be avoided in such an experiment.
2. It was possible to do measurements at a distance of two millimetres from the wall in the region of the bump and 1.5 millimetres in the flat zone (downstream). It was necessary to modify the inclination of the beams and the orientation of the collecting optics for performing the measurements in the vicinity of the bump.
3. The geometry was chosen for fulfilling the two following conditions:
 - to obtain a three dimensional flow
 - this three dimensional flow had to be obtained with a geometry as simple as possible, the surface being entirely defined with analytical formulas. The smoothness of the surface must facilitate future calculations of the flow.
4. The accuracy of measurements of transonic flows with LDV was tested many years ago at ONERA in 2D cases by comparison with other kinds of measurements. It was established that the accuracy is better than 1%.

SHOCK STRUCTURE MEASURED IN A TRANSONIC FAN USING LASER ANEMOMETRY

Jerry R. Wood and Anthony J. Strazisar
National Aeronautics and Space Administration
Lewis Research Center
Cleveland, Ohio 44135, USA
and
P. Susan Simonyi
Sverdrup Technology, Inc.
Middleburg Heights, Ohio 44130, USA

laser fringe

SUMMARY

Shock structure measurements acquired in a low aspect ratio transonic fan rotor are presented and analyzed. The rotor aspect ratio is 1.36 and the design tip relative Mach number is 1.38. The rotor flowfield was surveyed at near maximum efficiency and near stall operating conditions. Intra-blade velocity measurements acquired with a laser fringe anemometer on blade-to-blade planes in the supersonic region from 10 to 40 percent span are presented. The three-dimensional shock surface determined from the velocity measurements is used to determine the shock surface normal Mach number in order to properly calculate the ideal shock jump conditions. The ideal jump conditions are calculated based upon the Mach numbers measured on a surface of revolution and based upon the normal Mach number to indicate the importance of accounting for shock three dimensionality in turbomachinery design. Comparison of the shock locations with those predicted by a 3D Euler code showed very good agreement and indicated the usefulness of integrating computational and experimental work to enhance understanding of the flow physics occurring in transonic turbomachinery passages.

INTRODUCTION

Advanced fans and core compressor inlet stages feature low aspect ratio, highly loaded rotors which operate in the transonic regime. Much of the total pressure rise which occurs in these rotors is due to the rotor passage shock. Accurate models of the passage shock are therefore required for use in the blade design process.

Until recent years, the classic Miller-Lewis-Hartman shock model has been used in many blade design systems. This model is based on the assumption that the shock surface is normal to a blade-to-blade streamsurface and is oriented normal to the suction surface of the rotor blade. Prince [1] and Mennerstrom [2] have attempted to refine this model to include the effects of shock obliquity in both the blade-to-blade and spanwise direction. The refined models are based on analysis of high-response rotor tip static pressure measurements and empirical arguments.

As part of a NASA Lewis Research Center program aimed at obtaining detailed flowfield measurements within turbomachinery blade rows, a transonic axial fan rotor has been extensively surveyed using laser anemometry. Results from this effort include detailed velocity surveys through the rotor passage shock system. An analysis of this data is the subject of this report. The shock surface shape and orientation are presented for the near stall and peak efficiency operating conditions. Several qualitative features of the rotor passage shock are found to be in agreement with empirical arguments set forth by Prince [1]. The shock jump conditions are calculated for the three dimensional shock and are compared to those obtained when spanwise obliquity of the shock is neglected. The results indicate that spanwise obliquity of the shock must be taken into account in order to obtain accurate predictions of the shock strength. The results are also consistent with the laser anemometer measurements which indicate that the shock strength is weaker than one would expect if one assumes that the shock surface is normal to a blade-to-blade streamsurface. The shock locations on the suction surface are compared to isomach lines obtained from a numerical calculation of the three dimensional Euler equations coupled with a two dimensional boundary layer code. The agreement in terms of spanwise lean is excellent.

COMPRESSOR ROTOR

The test vehicle for the present study is a low aspect ratio fan rotor. The rotor design pressure ratio is 1.63 at a mass flow of 33.25 kg/s. The tip relative Mach number is 1.38 at the design tip speed of 129 m/s. The rotor has 22 blades, an aspect ratio of 1.36 (based on average span/root axial chord), an inlet tip diameter of 51.3 cm, and an inlet hub/tip radius ratio of 0.375. The rotor tip clearance at design speed is 6.3 mm. The rotor does not have a part-span shroud which is typically found in fan rotors of higher aspect ratio. Details of the rotor aerodynamic design are given in [3].

The results reported herein were obtained in a rotor-only configuration with no inlet guide vane or stator installed. The rotor-only design speed operating line is shown in Figure 1. Massflow rate is measured across a calibrated orifice located far upstream of the fan rotor. The rotor total pressure rise and efficiency are measured using conventional pressure and temperature survey instrumentation.

INSTRUMENTATION

The laser fringe anemometer (LFA) system used in the present investigation is a single-channel, dual-beam system with an on-axis backscatter light collection scheme and has previously been described in detail in [4] and [5]. Access to the compressor flowfield is through a 3 mm thick glass window. The window curvature conforms to the rotor outer flowpath, thereby minimizing disturbances to the tip region flow. Fluorescent seed particles with a nominal diameter of 1-1.4 microns are spray atomized and injected into the flow stream through a 6 mm pressure and temperature survey instrumentation is used to control the on-line operating condition set point.

The LFA measurement locations in the meridional plane and in the blade-to-blade plane at 10 percent span are shown in Figure 2. Conventional pressure and temperature data are obtained at stations 1 and 2 in the figure. LFA measurements are acquired along conical measurement surfaces edges. These conical surfaces are generated by straight-line interpolation between design streamlines radii which are known at stations 1 and 2 and at the blade edges. Measurement locations are distributed axially at 20 percent chord intervals from -100 percent to -25 percent chord, at -10 percent chord, and at 2.5 percent chord intervals from -5 percent chord to 10 percent chord. For the near stall operating condition, measurement locations are distributed at 10 percent chord intervals from 10 percent chord to the rotor trailing edge. For the peak efficiency operating condition, the measurement locations are distributed at 2.5 percent chord intervals from 10 percent chord to the rotor trailing edge. The increased axial density of measurement locations used at peak efficiency is required in order to resolve two-shock systems which occur within the rotor at backpressure levels at and below the peak efficiency operating point.

The circumferential location of each LFA velocity measurement relative to the rotor is determined by assigning the measurement to a "window" formed by adjacent pulses generated by a variable frequency clock that is phase-locked to the rotor rotational speed. All measurements that occur within a measurement window are averaged together and assigned to the center of the window. The clock frequency is set to generate 50 measurement windows across a blade pitch. LFA measurements are acquired across 17 of the 22 rotor blade passages. A typical data collection run consists of collecting 60,000 velocity measurements at each axial survey location. This yields approximately 70 measurements in each individual measurement window and results in a circumferential velocity profile in each of 17 individual blade passages. These 17 profiles are spatially averaged together to form an "average" blade passage velocity profile. The mean velocity calculated in each of the 50 measurement windows in this "average" profile is therefore based on approximately 1200 measurements.

Velocity magnitude and flow angle are determined using measurements acquired at two different angular orientations of the fringe system at each axial survey location. Just prior to performing a complete flowfield survey, screening runs are made to determine the axial distribution of the pitchwise-averaged flow angle along the measurement streamsurface. The fringe orientations which are used at each axial survey location are then chosen so as to bracket the local pitchwise-averaged absolute flow angle by 20 degrees.

SEED PARTICLE LAG EFFECTS

The velocity measured immediately downstream of a shock is known to be higher than the true gas velocity because the seed particles have finite inertia and cannot follow the high deceleration rates across a shock. This phenomena is known as seed particle lag. The extent of the region in which seed particle lag effects are present and the magnitude of the lag are functions of the seed particle size and the shock strength. The particle size and shock strength parameters in the present work are nearly identical in value to those of an earlier investigation [4], in which seed particle lag effects were studied. Results from [4] indicate that for a normal shock at an upstream Mach number of 1.4 the velocity measured behind the shock lags behind the true velocity for a streamwise distance of 12 mm, which corresponds to 12 percent of aerodynamic chord for the present rotor. Within this lag region, the measured velocity is given approximately by

$$V_p = V_{g1} + (V_{g1} - V_{g2}) * \exp(-X/L) \quad (1)$$

where V_p is the measured seed particle velocity, V_{g1} and V_{g2} are the true gas velocities upstream and downstream of the shock, respectively, X is the streamwise distance downstream of the shock, and L is the lag distance.

Schodl [6] has investigated the effects of particle size on the Mach number distribution measured across a shock by comparing measurements acquired with a laser transit anemometer across an axial compressor rotor how shock for a range of particle sizes. He found that although the post-shock Mach number distribution is dependent on particle size, the point at which the Mach number first begins to change rapidly is independent of particle size. Therefore, when determining the shock location in the present study, the point at which the measured Mach number first begins to change is considered to be an accurate and consistent indicator of the shock location.

DETERMINATION OF SHOCK SURFACE LOCATION

The shock location is determined on each measurement surface between 10 and 40 percent span by inspecting blade-to-blade distributions of relative Mach number at each axial measurement point as well as streamwise distributions of Mach number at constant pitch relative to the blade suction surface. Typical blade-to-blade and streamwise Mach number distributions are shown in Figure 3, along with the shock location. The measurements shown in this figure were acquired on the 30 percent span measurement surface for the peak efficiency operating condition. Both the blade-to-blade and streamwise Mach number distributions indicate the existence of a two-shock system within the rotor. The second shock occurs only at each pressure level at or below the peak efficiency operating point and rarely shows up as clearly in blade-to-blade plots as it does in Figure 3. Streamwise plots of relative Mach number are found to provide a much more sensitive indication of the second shock location. In order to improve the spatial resolution of the streamwise Mach number distributions, LFA surveys are taken every 2.5 percent of rotor chord at the peak efficiency operating condition.

The locus of shock location data points determined using the above procedure is shown for the peak efficiency and near stall operating conditions in Figures 4 and 5, respectively. The shock is shown extending from the suction surface to its intersection near the blade leading edge with a line extrapolated from the blade mean camber line. Only the front shock is shown at each span for the peak efficiency condition. At the near stall flow there appeared to be a weak front lambda shock near the blade suction surface followed by a stronger rear lag. The shock plots for near stall reflect only the rear portion of the lambda which produced the majority of the flow deceleration. The uncertainty in the shock location is on the order of two measurement windows (4 percent of rotor pitch) in the circumferential direction and one percent of rotor chord in the streamwise direction. The solid curve in each figure is determined by a least-squares polynomial curve fit of the shock location data points. This curve fit is performed in order to obtain an analytically smooth description of the shock in the blade-to-blade streamsurface. Eleven points along the shock face are determined from the fitted curve for use in plotting the three-dimensional shock surface shape and in performing calculations of the shock jump conditions.

The shock shapes at 10 percent through 40 percent span are consistent with the model proposed by Fringe [1] in that they are approximately axial over most of the passage width before turning to normal at the suction surface. At 10, 20 and 30 percent spans the intersection of the axial and normal portions of the shock occurs at approximately 75, 76 and 81 percent passage width, respectively. This compares quite well to Fringe's estimate of 80 percent passage width. Shock stand-off distances at these spans are approximately 2.3 percent chord. At 40, 50 and 60 percent spans, the stand-off distances are approximately 1.6, 2.9 and 3.4 percent of chord, respectively. The estimated error in determining stand-off distance is about 1.7 percent of chord.

CALCULATION OF JUMP CONDITIONS ACROSS THE SHOCK

In order to calculate the jump conditions across the shock which satisfy the relations for conservation of mass, normal momentum, tangential momentum, and energy together with the requirement that the entropy does not decrease, it is necessary to determine the normal vector to the three dimensional shock surface in the rotor passage. The normal is calculated by assuming that the shock surface can be described by some function

$$G(\theta, R, Z) = 0 = \theta - F(R, Z) \quad (2)$$

where θ , R , Z are the axes for a cylindrical coordinate system. Consequently,

$$\theta = F(R, Z) \quad (3)$$

The normal vector, \hat{n} , can be obtained by

$$\hat{n} = \frac{\nabla G}{[\nabla G \cdot \nabla G]^{1/2}} = \frac{\hat{e}_\theta - R \frac{\partial \theta}{\partial R} \hat{e}_R - R \frac{\partial \theta}{\partial Z} \hat{e}_Z}{[1 + (R \frac{\partial \theta}{\partial R})^2 + (R \frac{\partial \theta}{\partial Z})^2]^{1/2}} \quad (4)$$

where \hat{e}_θ , \hat{e}_R , and \hat{e}_Z are the unit vectors in the cylindrical coordinate system. The partial derivatives are obtained using numerical differentiation.

The shock face Mach numbers were obtained from the velocity components measured in the θ, Z plane and assuming the radial velocity ahead of the shock could be calculated from the measured axial component of velocity and the design streamline slopes for the rotor. The maximum design streamline slope was -8.5 degrees at 10 percent span from the tip which did not significantly change the Mach number. The Mach number component normal to the surface is obtained from

$$M_n = \vec{M} \cdot \hat{n} \quad (5)$$

where the Mach vector, \vec{M} , has the same direction as the velocity vector and the same magnitude as the Mach number. The component of the Mach vector tangent to the shock is obtained from

$$\vec{M}_t = \vec{M} - M_n \hat{n} \quad (6)$$

With the speed of sound before the shock, the velocity component tangent to the shock surface c_t can be obtained. With the normal and tangential components known before the shock, the conservation laws can be applied to yield the after shock conditions.

In order to demonstrate the importance of considering the three dimensional nature of the shock, the after shock conditions were also calculated with the shock assumed to be perpendicular to the conical surface of revolution on which the measurements were taken. The "perceived" normal Mach number which would be obtained if only the two dimensional nature of the shock were considered was calculated in a manner similar to that used to calculate the true normal Mach number. The normal velocity calculated after the shock using the normal Mach number and the normal velocity after the shock using the "perceived", or two dimensional, normal Mach number were used to calculate the Mach number and total conditions after the shock for each case. Although in the frame of reference of the rotor the total temperature across the shock is constant, the total temperature across the shock in the laboratory, or absolute, frame of reference is not constant. A significant increase in total pressure and total temperature occurs across the shock along with a corresponding increase in entropy. The total pressure ratio and the associated isentropic efficiency of the compression across the shock was calculated to demonstrate the difference in calculated rotor work done by assuming a two dimensional shock when the actual shock is three dimensional. The isentropic efficiency, η , was calculated from

$$\eta = \frac{PR - 1}{PR - 1 - \frac{\gamma}{\gamma - 1} (TR - 1)} \quad (7)$$

where PR is the total pressure ratio and TR is the total temperature ratio across the shock in the absolute frame of reference and γ is the specific heat ratio.

QUALITATIVE DESCRIPTION OF THE SHOCK SURFACE

Two earlier investigations have attempted to visualize the three dimensional shock surface. This goal is quite difficult to achieve due to the three-dimensional nature of both the rotor blade and the shock itself. In [1] holograms were acquired from a transonic axial fan rotor. A three-dimensional image of the shock surface and blade passage was obtained by reconstructing the hologram within two blades held in a fixture in the laboratory. A pointer was then placed on the shock surface by using parallax while viewing the hologram and blade pair. The pointer locations were then used to place a piece of plastic film within the blade passage at the shock surface location. Photographs of the blade pair with the plastic film attached are included in [7]. In an earlier investigation of the present data [8], plots of the shock locations determined at each span were "stacked" together to obtain a quasi-three dimensional view of the shock surface. This view represented the shock as seen from a single perspective.

In the present work, three dimensional graphics is used to qualitatively study the shock surface shape. The eleven points determined from curve fits of the shock location data in each of the six blade-to-blade measurement surfaces are combined to form an eleven-by-six grid which describes the shock surface shape. This grid is combined with coordinates of the blade section and pressure surfaces to form a composite graphics image in which the shock appears in the proper orientation relative to the blade. By using surface shading and hidden line techniques as well as coordinate rotation about three orthogonal axes, the shock surface can be studied on a graphics workstation from several different viewing angles. Selected views of the near stall and peak efficiency shock surfaces are shown in Figures 6 and 7, respectively.

Since surface shading could not be illustrated in a black and white format, a mesh plot of figures 6 and 7 was chosen for this report. Although Mach number contours are not visible on the mesh plots the three dimensional characteristics of the shock surface can be shown. The figures illustrate such qualitative features of the shock as spanwise location, spanwise distance of the shock surface from the blade's leading edge, and the overall structure of the shock surface. A comparison of the shock structure between the two operating conditions can easily be made by viewing figures 6 and 7. Three dimensional graphics has proven to be a powerful method of studying the shock surface shape. The technique, however, is most effective when one views the three dimensional image on a graphics workstation.

RESULTS FOR THE JUMP CALCULATIONS ACROSS THE SHOCK

The calculations for the jump conditions across the shock were done only for the shock loci presented and did not attempt to consider the change through a multiple shock system. The results for the near stall flow rate are presented in figures 8 through 10 and show the calculations for the jump conditions across the shock when the actual three dimensional nature of the shock is considered and when the shock is considered to be two dimensional i.e. the shock is perpendicular to the conical surface of revolution. The calculation of the post-shock Mach number for 10, 30 and 50 percent span from the tip is shown in figure 8. The three dimensional nature of the shock is most evident for 50 percent span where the 3D calculation yields an after shock Mach number which is generally 0.20 to 0.25 higher than the 2D calculation. At thirty percent span the difference is between 0.15 and 0.17. At ten percent span the shock is two dimensional except for a slight three dimensional effect near the leading edge which is due to the lean of the leading edge in the streamwise direction. The total pressure rise calculated across the shock in the laboratory frame of reference is shown in figure 9. A large pressure rise occurs across the bow shock for each percent span with the tip shock producing a calculated pressure ratio of 1.37 and the 50 percent span location producing a pressure ratio 1.06. The two dimensional calculation consistently produces more indicated pressure ratio than does the three dimensional calculation. The isentropic efficiency of the compression process across the shock is shown in figure 10. The isentropic efficiency calculated for the two dimensional shock is lower than that calculated for the 3D shock which is consistent with the pressure rise calculated with each method.

Results calculated for the peak efficiency flow point are shown in figure 11 for the calculated Mach number change only since the calculated pressure rise and efficiency followed the same trends as those observed for the near stall flow rate. For 10 percent span the shock is essentially two dimensional up to about 50 percent of the distance along the face of the shock from the leading edge to the suction surface with three dimensional effects occurring over the last 50 percent of the passage. Whereas the two dimensional calculations indicate after shock Mach numbers appreciably less than sonic, the three dimensional calculation indicates after shock Mach numbers that are generally greater than sonic. There is considerably less three dimensional effect at 30 percent span and comparable three dimensional effects at 30 percent and 50 percent spans. The location of the shock foot at peak efficiency is very sensitive to small changes in flow and the large difference in the three dimensional effects at 10 percent and 20 percent may be due in part to difficulty in establishing identical operating conditions for all the percent span locations which were measured on different days.

The three dimensionality of the shock has considerable effect on the assumption that the flow can be treated as streamsurfaces for analysis with either two dimensional or quasi-three dimensional computer codes. At 30 percent span near the leading edge, the flow into the shock is inclined at about -2.8 degrees to the axial direction. After the shock the calculated flow has an inclination of about +9.8 degrees to the axial direction. This also has ramifications on the measured velocities behind the shock since the measurements are taken on the design streamsurface of revolution. Obviously, some of the particles measured downstream of the shock crossed the shock at a different spanwise location than that at which they are being measured after the shock.

Chordwise plots of relative Mach number are shown in Figure 12a for the near stall flow rate for the midpitch position for 10, 30 and 50 percent spans and in Figure 12b for the peak efficiency flow at 20, 30 and 50 percent pitch for 10 percent span. Also shown are the results from the jump calculations across the shock. For the near stall flow at the 10 percent span location the shock is two dimensional and both the 3D and 2D calculations yield an after shock Mach number of about 0.85 at 22 percent chord compared to a measured value of about 0.94 at 40 percent chord. If particle lag is considered then the particles should have reached terminal velocity at about 34 percent chord. Since no detailed data were taken in the 30-40 percent chord range it is not possible to determine where the particle deceleration ceased; however, it would appear that they would have attained an after shock velocity corresponding to about Mach 0.95 to 1.0 at the 34 percent chord location. At 30 percent span the shock is three dimensional with the 3D calculation yielding an after shock Mach number of 0.94 and the 2D calculation yielding a value of 0.79. The experimental data shows an after shock Mach number of about 0.97 at 12 percent chord downstream of the shock. At 50 percent span the shock is also three dimensional with the 3D calculation yielding 1.14 and the 2D calculation yielding 0.84 Mach number. At 12 percent chord downstream of the shock the Mach number from the data appears to be about 0.94. Inspection of the deceleration of the flow from 20 percent to 44 percent chord indicates the passage is increasing in area so that part of the difference between the 3D calculation and the estimated value at 10 percent chord may be due to an increase in flow area in the streamwise direction from the location of the shock to the passage exit.

In (9) the LFA data for this rotor were compared to the results obtained with the 3D Euler computer code described in (10). Comparisons of the calculations with the experimental data indicated that from 10 to 70 percent span the code gave results which described quite well the locations of the shocks when compared to near-surface Mach numbers in the blade-to-blade plane. Figure (13) shows the projection of the suction surface of the blade onto a meridional plane with the shock locations from the present data and the isomach lines determined from the calculations. In addition to the original views given in (10) for the peak efficiency and near stall flow, an additional result from the code is included for a flow rate slightly smaller than the peak efficiency flow. Peak efficiency flow rate from the experiment was 98.9 percent of the maximum flow rate measured for the rotor. The calculation previously presented for peak efficiency was for a flow rate of 99.9 percent of the maximum flow rate predicted by the computer code for the rotor. In (10) the difference in maximum predicted flow and maximum experimental flow was quoted as 0.84 percent. It was also stated that calculations were made at 98.4 percent flow and 99.8 percent flow and that significantly different locations were predicted for the shock at 10 percent span. The results for the calculations at 98.4 percent flow are also shown on the figure and compared to the measured shock locations. For both flows the three dimensional nature of the shock along the suction surface is well predicted with the best fit being for a flow rate between 98.4 and 99.8 percent of maximum flow. Comparison of the calculated isomach lines and the measured shock locations are also shown for the near stall point. The predicted three dimensional nature of the shock agrees well with the data.

Figure (14) shows the results obtained from the code in the blade-to-blade plane for 10 percent span. As stated in (9) the shock location calculated on the suction surface for 98.4 percent flow moved about 15 percent chord from that calculated at 99.8 percent flow. Figure (14) shows the transition of the flow from a two shock system to a single shock in going from 98.8 to 99.8 percent flow. This type of shock structure more nearly matches the model proposed by Henningson (2) than that proposed by Prince (1). This large movement of the shock at the near peak efficiency flow point for a small change in flow rate (0.8 percent or 0.38 ft/sec) requires watching experimental and computational flow rates very accurately in order to make valid comparisons. It also emphasizes the difficulty of mapping this rotor at many spanwise stations for a flow rate near peak efficiency.

CONCLUDING REMARKS

The present paper has defined the shock structure inside the rotating passage of a low aspect ratio transonic fan at a flow rate near peak efficiency and near stall using detailed data obtained with a laser fringe anemometer. Because of the severe distortion of the shock surface at the peak efficiency flow, it is quite beneficial to qualitatively study the shock structure using three dimensional graphics in an interactive mode. It was also shown that once the shock surface is defined, the normal shock jump conditions can be used to calculate after shock Mach numbers. When particle lag across the shock is considered, the agreement with data was shown to be good. At the near stall flow where the density of the LFA measurements was not as high as that used for the peak efficiency flow, the agreement was not quite as good between the jump calculations and the after shock Mach numbers. Overall the jump calculations indicate the importance of including the three dimensional nature of the shock in interpreting the experimental data. It also emphasizes the need to account for the three dimensionality of the shock as proposed by Prince [1] and Wannerstrom [2] in the design of turbomachinery passages. The total pressure ratio calculated across the shock indicated that a significant portion of the rotor total pressure rise is produced by the shock and that the efficiency of this compression process is quite high.

Comparison of the shock locations with those predicted by a 3D Euler code showed very good agreement and indicated the usefulness of integrating computational and experimental work to enhance understanding of the flow physics occurring in transonic turbomachinery passages.

References

1. Prince, D.C. Jr., "Three-Dimensional Shock Structure For Transonic/Supersonic Compressor Rotors," AIAA Journal of Aircraft, Vol. 17, No. 1, Jan. 1980, pp. 28-37.
2. Wannerstrom, A.J. and Putterbaugh, S.L., "A Three-Dimensional Model for the Prediction of Shock Losses in Compressor Blade Rows," ASME Paper No. 83-GT-216, 1983.
3. Urasek, D.C., Gorrell, W.T. and Cunnann, W.S., "Performance of a Two-Stage Fan Having Low Aspect Ratio First-Stage Rotor Blading," NASA TP-1493 and AVRADCOM TR 78-49, Aug. 1979.
4. Powell, J.A., Strazisar, A.J. and Seasholtz, R.G., "Efficient Laser Anemometer for Intra-Rotor Flow Mapping in Turbomachinery," ASME Journal of Engineering for Power, Vol. 103, No. 2, Apr. 1981, pp. 424-429.
5. Strazisar, A.J. and Powell, J.A., "Laser Anemometer Measurements in a Transonic Axial Flow Compressor Rotor," ASME Journal of Engineering for Power, Vol. 103, No. 2, Apr. 1981, pp. 430-437.
6. Schodl, R.G., "A Laser-Two-Focus (L2F) Velocimeter for Automatic Flow Vector Measurements in the Rotating Components of Turbomachines," ASME Journal of Fluids Engineering, Vol. 102, Dec. 1980, pp. 412-419.
7. Muerker, R. F., Kobayashi, R. J., Heflinger, L. O., and Ware, T.C., "Application of Holography to Flow Visualization Within Rotating Compressor Blade Row," NASA CR-121264, Feb. 1974.
8. Strazisar, A.J., "Investigation of Flow Phenomena in a Transonic Fan Rotor Using Laser Anemometry," ASME Journal of Engineering for Gas Turbines and Power, Vol. 107, No. 2, Apr. 1985, pp. 427-435.
9. Pieraga, M. J. and Wood, J. R., "Investigation of the Three-Dimensional Flow Field Within a Transonic Fan Rotor: Experiment and Analysis," ASME Journal of Engineering for Gas Turbines and Power, Vol. 107, No. 2, Apr. 1985, pp. 436-449.
10. Denton, J. D., "An Improved Time Marching Method for Turbomachinery Calculations," ASME Paper 82-GT-239, 1982.

DISCUSSION

J. Chauvin

(1) Do the measurements give information about unsteadiness of the flow, especially about the shock foot motion at the suction surface? Have you information on the flow turbulence?

(2) How close to the stall line was the near stall point?

Author's Reply

In general only the components of velocity and the standard deviation of the velocity histogram were stored because of memory limitations in the dedicated computer. Some data were taken and individual measurements for each window were stored so individual histograms could be studied. Some of this data was discussed by Strazisar [8] and did demonstrate movement of the shock at the 28 percent chord location for 18 percent span at the near stall flow. More data was taken in this "data capture mode" but was not taken in sufficient detail to allow study of the shock foot movement. Increased memory capacity on our dedicated computer at NASA Lewis will allow us to do more detailed mappings in order to study shock unsteadiness in the future.

The near stall flow rate was 92.6 percent of the maximum measured flow for the rotor. Unstable operation of the rotor occurred at 91.6 percent of maximum measured flow rate.

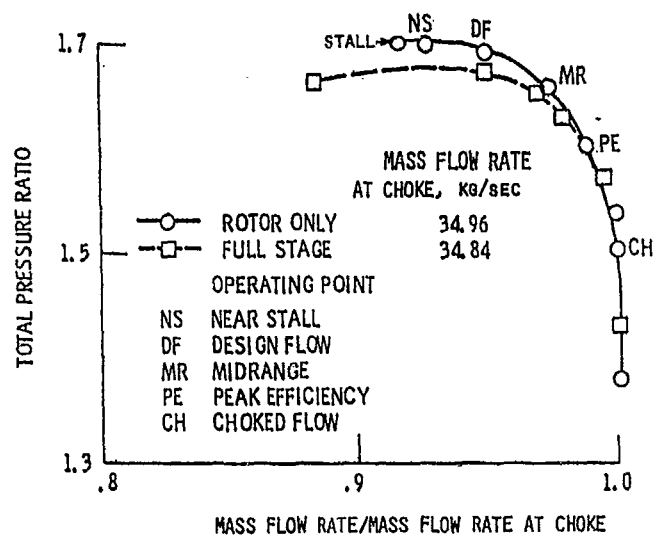


Figure 1.- Rotor design speed operating line.

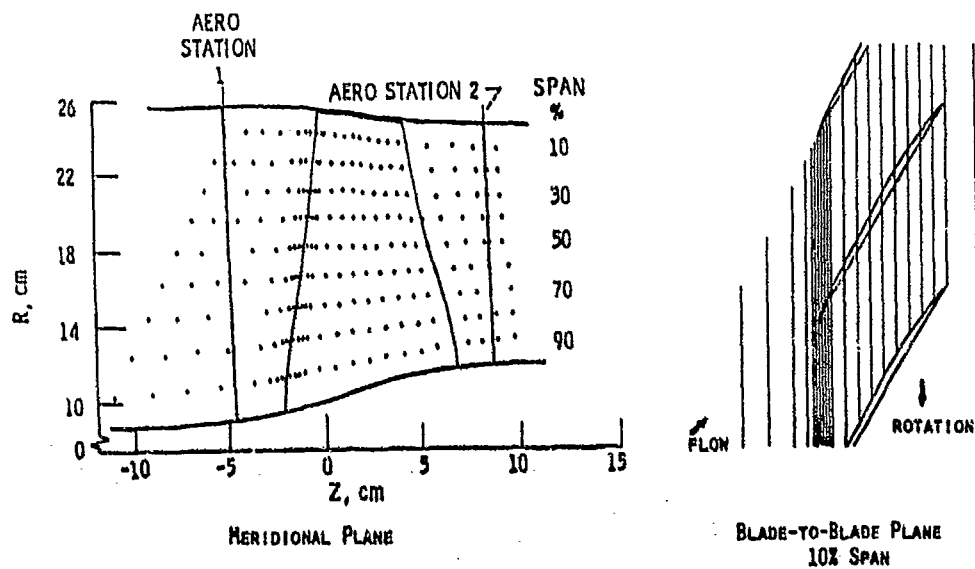


FIGURE 2. - TYPICAL LASER FRINGE ANEMOMETER MEASUREMENT POINTS AND AERODYNAMIC SURVEY LOCATIONS

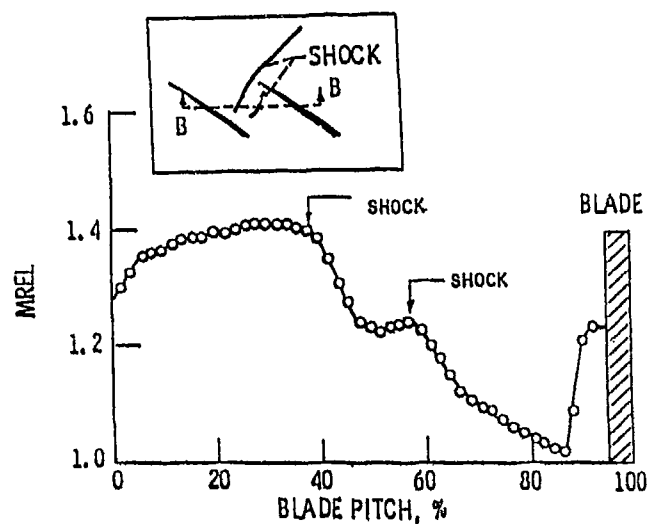


FIGURE 3A. - Blade-to-blade distribution (view B-B of relative Mach number at 30% span, 30% chord at peak efficiency.

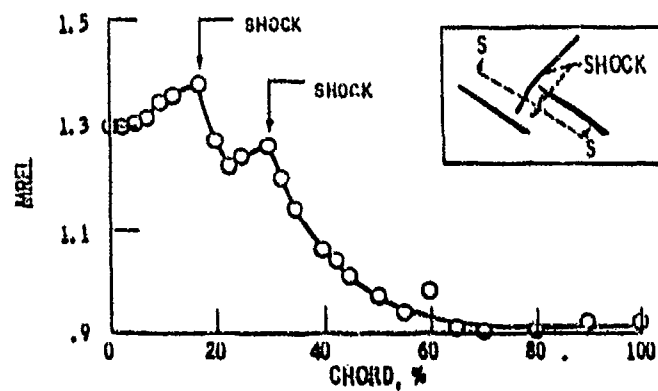


FIGURE 3B. - Streamwise distribution (view S-S) of relative Mach number at 30% span, 60% blade pitch from the suction surface at peak efficiency.

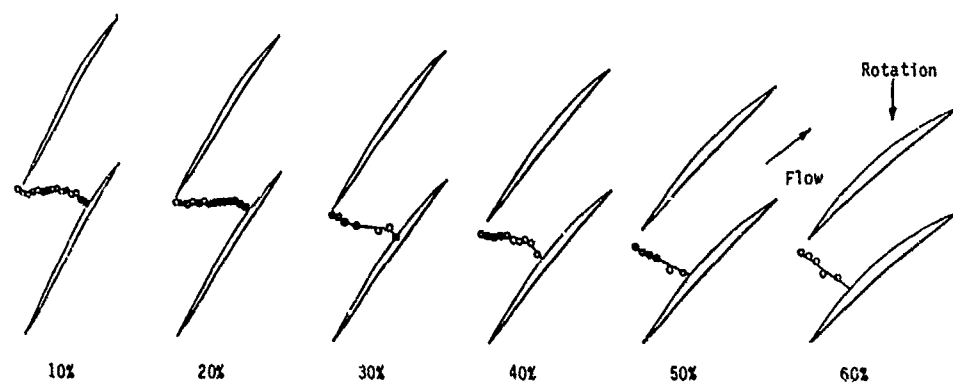


Figure 4. - Shock location in blade-to-blade plane for six spanwise locations at Near Stall Flow Rate.

o - Shock Location
 - - Curvefit of Data

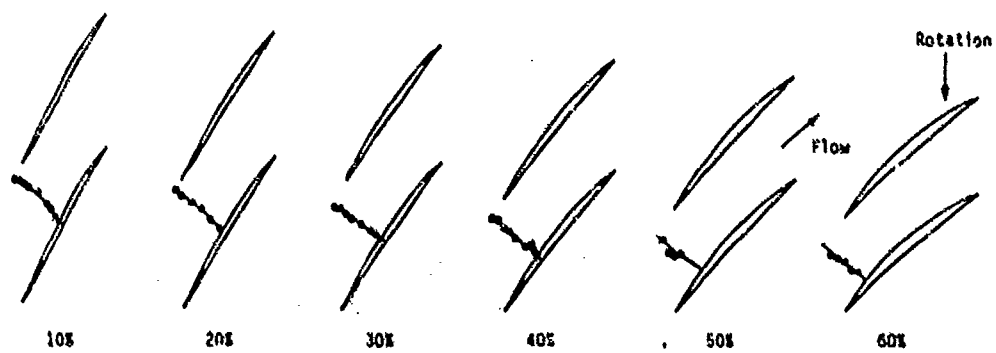


Figure 5. - Shock location in blade-to-blade plane for six spanwise locations at Peak Efficiency Flow Rate.

o - Shock Location
 - - Curvefit of Data

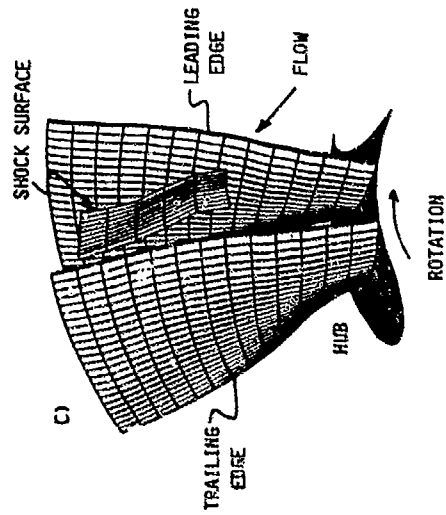
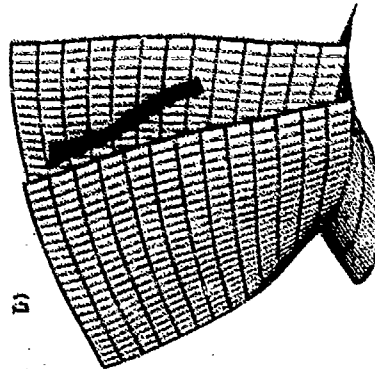
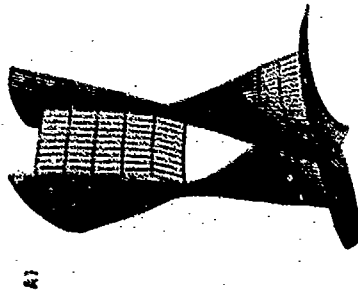
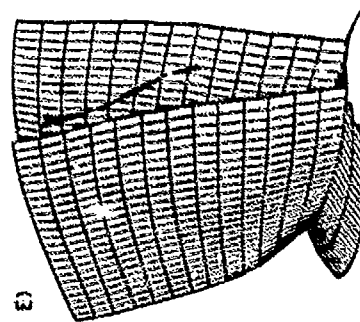
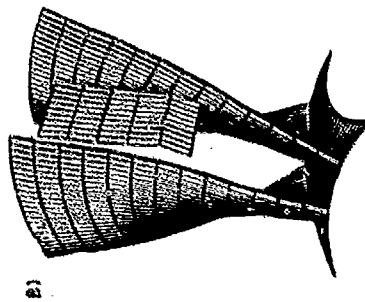


FIGURE 5. - THREE DIMENSIONAL VIEWS OF THE SHOCK SURFACE AT THE NEAR STALL FLOW RATE. VIEWS B THROUGH E ARE ROTATED APPROXIMATELY 20 DEGREES ABOUT A RADIAL LINE



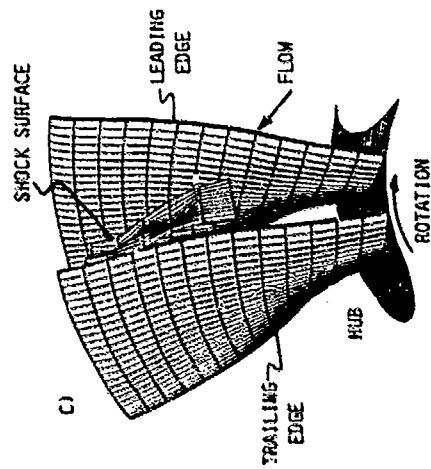
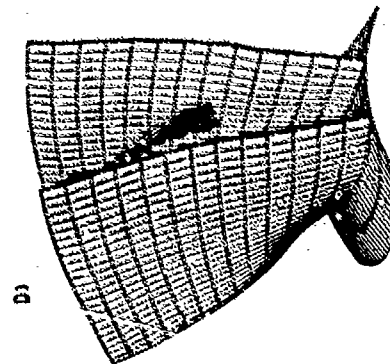
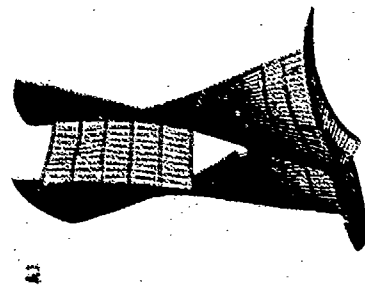
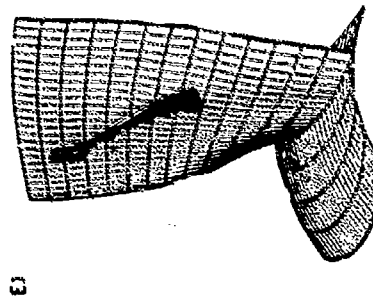
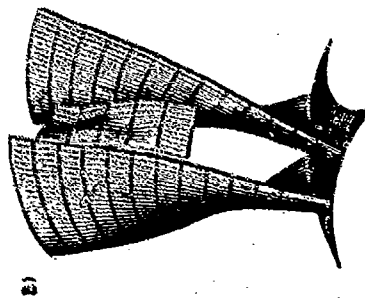


FIGURE 7. - THREE DIMENSIONAL VIEWS OF THE SHOCK SURFACE AT THE PEAK EFFICIENCY FLOW RATE. VIEWS B THROUGH E ARE ROTATED APPROXIMATELY 20 DEGREES ABOUT A RADIAL LINE



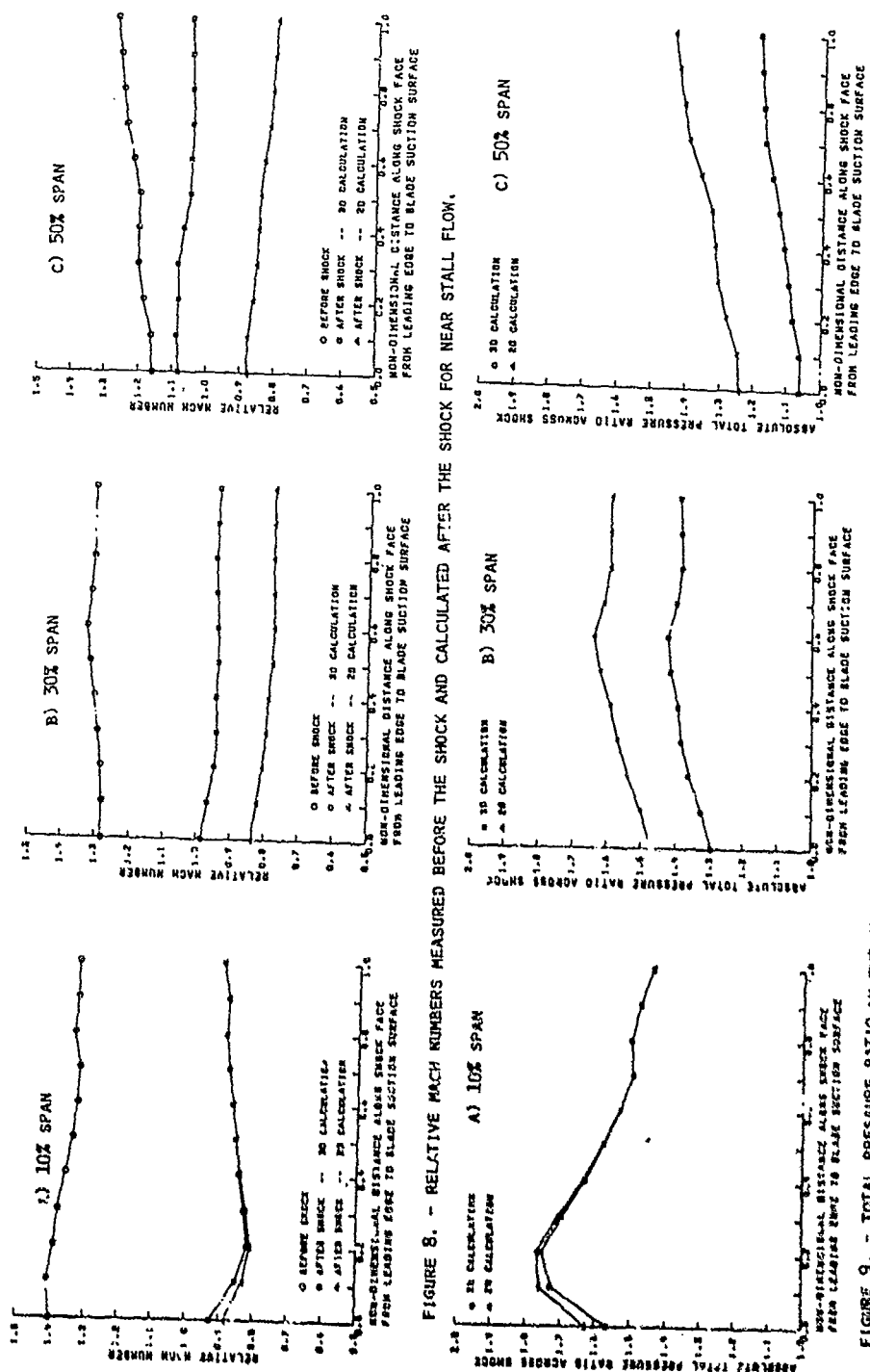


FIGURE 8. - RELATIVE MACH NUMBERS MEASURED BEFORE THE SHOCK AND CALCULATED AFTER THE SHOCK FOR NEAR STALL FLOW.

FIGURE 9. - TOTAL PRESSURE RATIO IN THE ABSOLUTE REFERENCE FRAME CALCULATED ACROSS THE SHOCK FOR NEAR STALL FLOW.

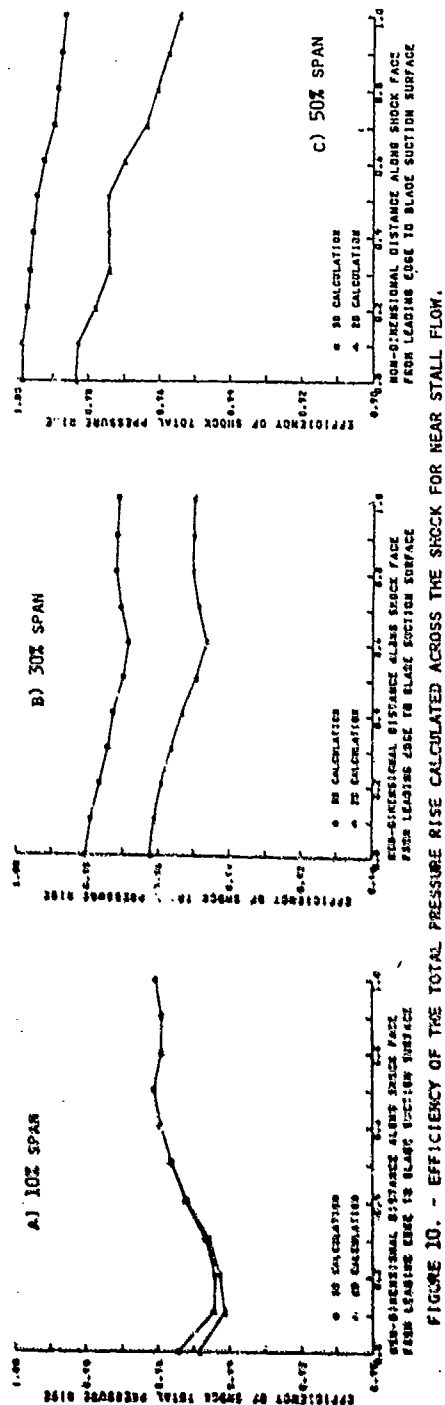


FIGURE 10. - EFFICIENCY OF THE TOTAL PRESSURE RISE CALCULATED ACROSS THE SHOCK FOR NEAR STALL FLOW.

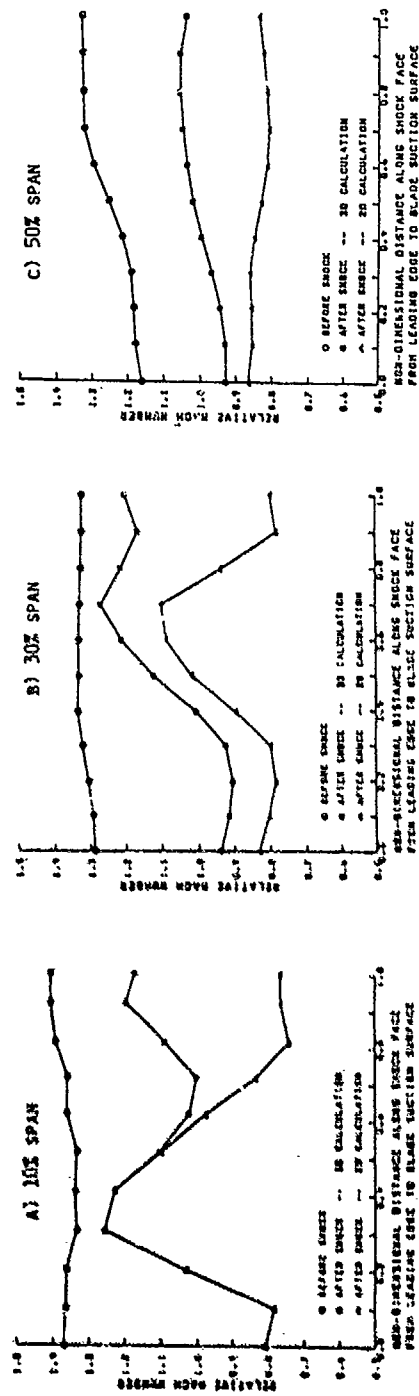


FIGURE 11. - RELATIVE MACH NUMBERS MEASURED BEFORE THE SHOCK AND CALCULATED AFTER THE SHOCK FOR PEAK EFFICIENCY FLOWS.

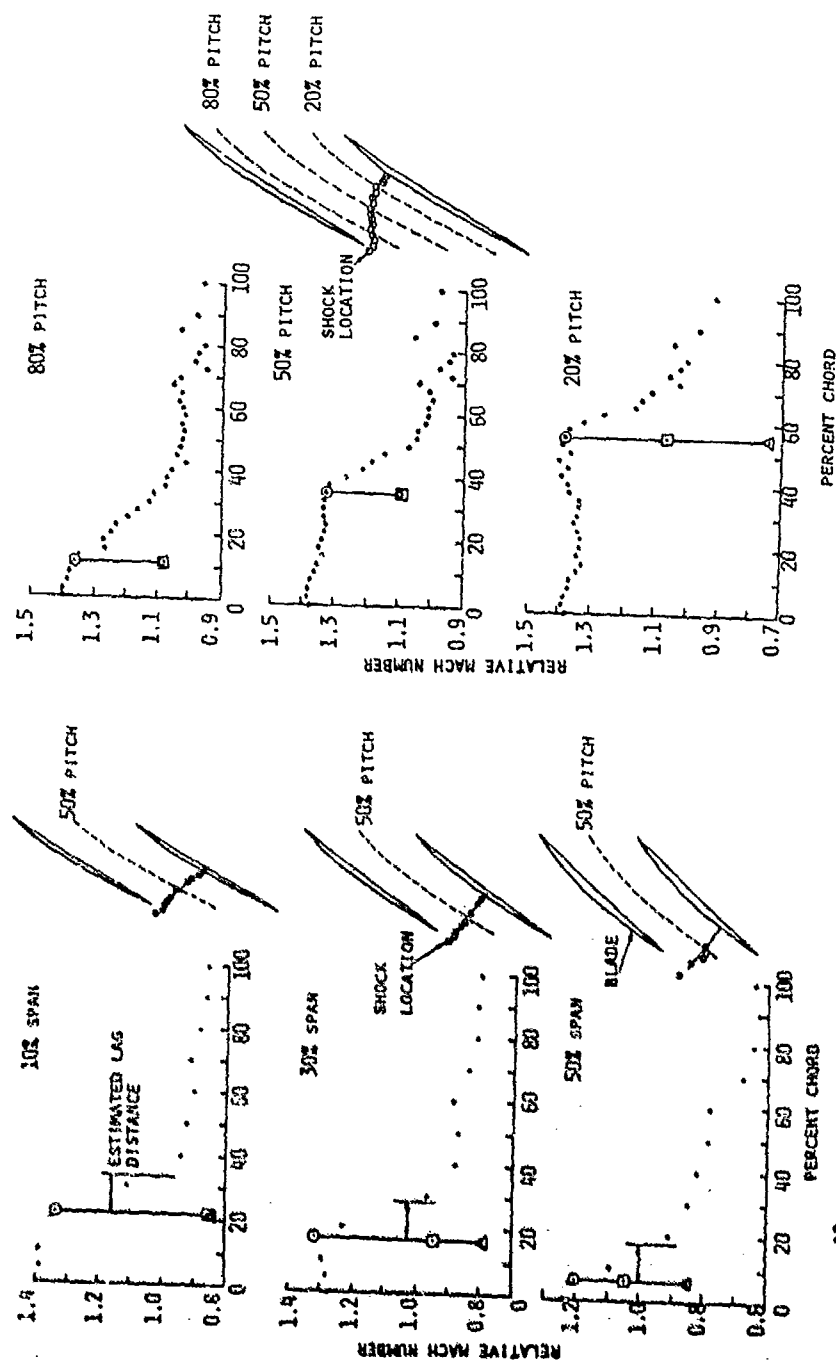


FIGURE 12A. - CHORDWISE PLOTS OF RELATIVE MACH NUMBER AT 50% PITCH FOR THE NEAR STALL FLOW RATE AT 10%, 30%, AND 50% SPAN.
 ○ - DATA; □ - BEFORE SHOCK; ▣ - AFTER SHOCK -- 3D CALCULATION
 ▴ - AFTER SHOCK -- 2D CALCULATION

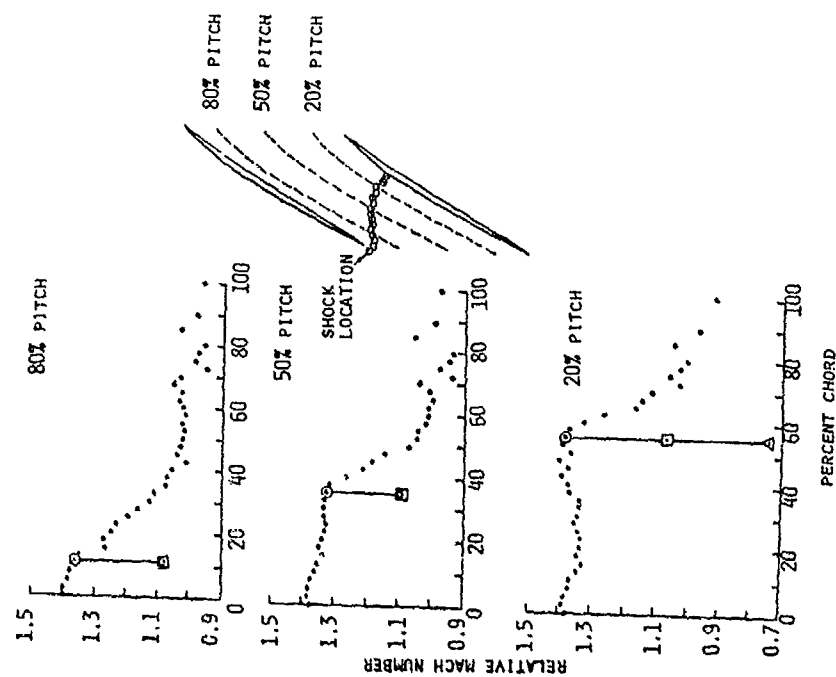


FIGURE 12B. - CHORDWISE PLOTS OF RELATIVE MACH NUMBER AT 10% SPAN FOR THE PEAK EFFICIENCY FLOW RATE AT 20%, 50%, AND 80% PITCH FROM THE SUCTION SURFACE.
 ○ - DATA; □ - BEFORE SHOCK; ▣ - AFTER SHOCK -- 3D CALCULATION
 ▴ - AFTER SHOCK -- 2D CALCULATION

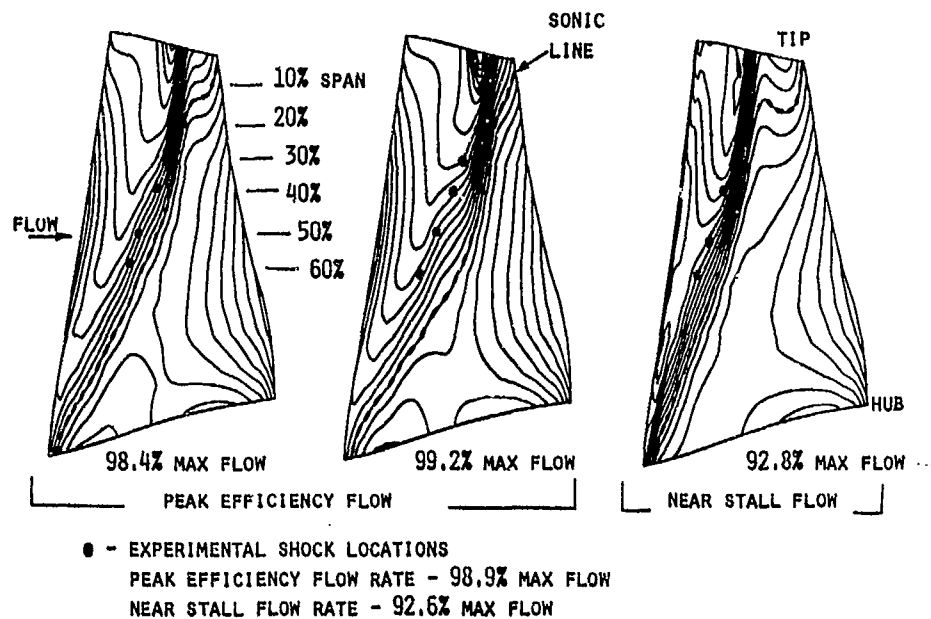


FIGURE 13. - COMPARISON OF SHOCK LOCATIONS ON THE BLADE SUCTION SURFACE FOR PEAK EFFICIENCY AND NEAR STALL FLOW RATES WITH ISOMACH LINES FROM A 3D EULER CALCULATION.

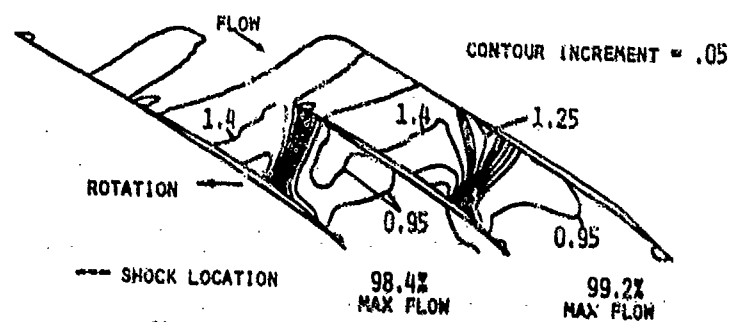


FIGURE 14. - ISOMACH LINES FROM A 3D EULER CALCULATION SHOWING TRANSITION FROM AN OBLIQUE SHOCK/PASSAGE SHOCK AT 99.2% MAXIMUM FLOW TO A SINGLE SHOCK AT 98.4% MAXIMUM FLOW AT 10% SPAN.

DISCUSSION

J. Fabri, Fr

Comment: From tests performed at ONERA by visualisation of flow fields in transonic or supersonic compressors, it appears that the leading edge shock wave is absolutely steady until near stall conditions. The downstream shock wave may be fluctuating at open throttle conditions.

WAKE AND SHOCK INTERACTIONS IN A TRANSONIC TURBINE STAGE

by

D.L.Schultz and A.B.Johnson
Dept. of Engineering Sciences
Oxford University
Oxford OX1 3PJ, UK

D.A.Ashworth and M.J.Rigby
Rolls Royce
Derby, UK

and

J.E.LaGraff
Syracuse University
N.Y., USA

Abstract

The strong trailing-edge shock waves from the nozzle guide vanes of transonic turbine stages can give rise to interactions with the downstream rotor which are significantly more severe than is the case with lower pressure ratio stages. It is therefore important to study such effects in detail both from the point of view of stage power output and more importantly from that of heat transfer rates. A study has been made of a transonic rotor profile in a static cascade in which the effect of shock wave interaction is simulated by means of an array of bars rotating at the correct speed and spacing upstream of the stationary rotor blades. Detailed heat transfer rate measurements made with rapid response gauges enable the wake and shock phenomena to be separated.

Nomenclature

C_2 = NGV exit velocity, relative bar velocity
 C_t = Tangential (or true) chord
 k = Thermal conductivity (W/mK)
 \dot{q} = Heat transfer rate (W/m²)
 M = Isentropic Mach Number (based on local static pressure and inlet total pressure)
 Nu = Nusselt Number
 Re = Reynolds Number (based on inlet total conditions, isentropic exit Mach Number and tangential chord)
 s = Blade surface perimeter
 t = Time
 T = Temperature (K)
 Tu = Turbulence level = u'/\bar{U}
 u' = Fluctuating velocity (m/s)
 U = Velocity (m/s)
 V = Rotor relative velocity, cascade inlet velocity
 x = Surface distance from the leading edge stagnation point
 y_b = Distance in the pitch-wise direction from the spanwise datum position
 β = Gas angle (measured from the axial direction)

Subscripts

- = Freestream
 o = Total
 i, e = Inlet, Outlet
 meas = Measuring point
 h, m, t = Hub, mean, tip (or tangential in chord definition)
 rel = Relative bar condition

Introduction

The effects of unsteady flows caused by rotor blade/NGV interactions and the disturbance to the potential flow due to rotor blade motion are arousing increasing interest as attempts are made by turbine designers to improve their predictions of performance. Previous work by Doorly¹⁻³ and Dunn⁴⁻⁶ has shown the significant effect of NGV-rotor interaction on heat transfer rates associated with the effect of the turbulent NGV wake on the rotor boundary layer as the blade passes through the wake. Doorly's studies have identified the fluid dynamic phenomena associated with the interaction employing a stationary linear cascade and an array of bars rotated off-axis upstream of the blades in such a way as to generate a set of wakes which pass over an instrumented stationary blade. Dunn's studies, on the other hand, involved a complete rotor behind an NGV ring. An extensive study of unsteady secondary flow vortices in a turbine rotor stage has been made by Binder et al.¹¹⁻¹³. Laser two-focus velocimetry was used to track the distortion and migration of the NGV passage vortex as it passed through the rotor blade ring. Simultaneous measurements of mean velocity and turbulence level were made. It was found that the turbulence level arising from this vortex was raised considerably by the cutting action of the rotor blades and this effect was ascribed by Binder et al. to the break-up of the vortex itself. The experiments were carried out in a steady flow turbine rig so that the long sampling times required for accurate L2F measurements were readily attainable. Hodson¹⁴ has also investigated the blade-wake interaction measuring unsteady blade pressures on a large-scale rotating rig in a manner similar to that at UTRC where Dring and his colleagues¹⁵⁻¹⁷ have studied blade boundary layers using a rotor axis fixed hot wire anemometer.

The work reported in the present study has been carried out in a linear cascade of the blades of a transonic stage where the NGV exit Mach Number is generally higher than that used by Doorly or Dunn and in which the strong recompression shocks in the wake have a more important effect on the boundary layer and hence on the heat transfer rates. The rotor profile is the same as that currently fitted to the MIT transient blowdown facility described by Epstein et al.¹⁸ so that direct comparisons will be possible between the two different approaches.

Experimental Apparatus

The measurements were carried out in the isentropic light piston cascade described by Schultz et al.¹⁹ in which a short duration (~ 0.5 sec.) flow is produced at the correct full-scale engine Reynolds and blade exit Mach Numbers and at the correctly scaled gas/wall temperature ratio. The simulation employed, i.e. stationary rotor and moving wakes has advantages in terms of simplicity over the fully rotating experiment in so far as Schlieren techniques may be employed to locate shock waves and boundary layer separations (induced, it will be seen, by the incident shock wave). It must be emphasised, however, that the following effects are not simulated:

1. Temperature gradients in the wake due either to a film cooled NGV or the heat transfer to the vane as a whole.
2. The differential effects of buoyancy forces on the cooled wake and the mainstream flow.
3. Distortion of the NGV passage flow by the rotor blockage.
4. The influence of unsteady secondary flows over both the rotor root and the tip region.

The simulation is, in effect, valid only for mid-blade height flow but is believed to be valuable nevertheless in that it enables the relevant fluid dynamic phenomena to be isolated and studied in some detail. The arrangement of the linear cascade, the rotating disc and stranded steel cables is illustrated in Fig. 1(a). A more complete description is given by Ashworth et al.²⁰ and it suffices here to record that the aerodynamic design of the prototype cold air turbine in which a 61 blade rotor spins at 9004 RPM behind an NGV ring of 16 vanes is correctly simulated by having a disc carrying 16 radial bars (stranded cable) and a turbine scaling factor cascade/cold air turbine of 1.3247. The NGV trailing edge diameter was 1.2192 mm and the nearest suitable cable diameter of 1.6151 mm was chosen for convenience. The plane of the array of the bars was located 14.333 mm upstream of the cascade blade leading edge line. Experiments reported by Doorly¹⁻³ have shown that a wake velocity profile similar to that from an NGV can be produced by a circular cylinder of diameter equal to that of the vane trailing

edge. The cascade has a span of 50 mm at blade inlet and 56.095 mm at exit with the expansion on one side only as illustrated in Fig. 1(a). A turbulence grid 208 mm upstream of the cascade provides a level of u'/\bar{U} of approximately 3%. Upstream and downstream static and total pressures were measured routinely to establish the correct cascade operating conditions and are reported in more detail by Ashworth et al.¹². The operating conditions at the nominal engine design point are given below.

The heat transfer gauges used in this study are conventional thin film surface resistance thermometers widely used for the determination of heat transfer rate in short duration facilities¹³. Data from 22 such gauges were stored in a digital transient recorder sampling up to 16 channels at 500 kHz for each channel or were input directly to the A/D converter at a slower rate of 400 Hz for some of the 64 available A/D channels when time average data only were required, also used for measurements such as inlet and exit static pressures. The locations of these heat transfer gauges on the blade are shown in Fig. 2(a) and given in terms of the surface length 'x' to perimeter 's' from the stagnation point. A more detailed study of the reaction of the suction surface boundary layer to both freestream turbulence and the wake-passing phenomena is also reported below. For this study another blade was instrumented with thin film gauges which were only 4 mm long as compared to 10 mm for the previous tests, and were more closely spaced around the profile, as shown in Fig. 2(b). The model points in Fig. 2(b) are those referred to in Fig. 6. Surface pressures were measured in a time-averaged manner using Sensym semiconductor transducers type LX-1620D operating in a differential mode as reported in more detail by Ashworth et al.¹². Baseline experimental results have been reported by Ashworth et al. but for clarity some of this data is referred to in the present paper. The velocity triangle for the steady nominal design case is shown in Fig. 1(b) which includes the effect of the reduced NGV exit wake velocity C_2' on the rotor inlet angle β_1 .

Experimental Results

Mean Heat Transfer Without Wake Interaction

A comparison of baseline data with no rotor/wake interaction is given in Fig. 3(a) for the two cases of low ($< 0.5\%$) freestream turbulence and with a turbulence level of approximately 3%. It will be seen that the turbulence generated by the bar grid is sufficient to bring the region of boundary layer transition forward from about 50% x/s on the pressure surface and 50% x/s on the suction surface to 10% and 30% respectively. All of this data was taken at the nominal design cascade operating conditions:

$$\begin{aligned} T_{\text{total}} &= 432 \text{ K} \\ M_{\text{exit}} &= 1.18 \end{aligned}$$

(based on isentropic inlet total and pitchwise averaged exit static pressures)

$$Re = 0.419 \times 10^6$$

$$\beta_1 = 38.04^\circ$$

The circled numbers refer to heat transfer gauges identified in Fig. 2(a). The heat transfer rate is presented in terms of a non-dimensional Nusselt Number, defined as:

$$Nu = \frac{q_{\text{meas}}}{(T_s - T_{\text{meas}}) k} \frac{U_\infty}{k}$$

Instantaneous and Mean Heat Transfer with Wake Interaction

The heat transfer rate to the blade with the additional effect of wake interaction is illustrated in Figs. 3(b) and 3(c) for both cases of effectively zero freestream turbulence and $\sim 3\% u'/\bar{U}$. From Fig. 3(c) it will be seen that there is an overall increase in heat transfer rate over both the pressure and suction surfaces. The pressure surface heat transfer is enhanced over practically the whole length although the dominant effect is observed for values of x/s $< 70\%$. On the pressure surface the effect of wake interaction persists to about x/s $\sim 10\%$. Examples of instantaneous heat transfer rates are inset in the figure and a more extensive 'atlas' of results is given in Ashworth et al.¹². The heat transfer rates with wake interaction and with effectively zero freestream turbulence are shown in Fig. 3(b). As expected there is a marked increase in the level of heat transfer rate over almost the entire pressure

and suction surfaces. Examples of instantaneous values of heat transfer rate are inset and these also illustrate the increase over the undisturbed case.

Mean Effects of Inlet Incidence Angle on Heat Transfer Rate and Pressure Distribution

As is illustrated in Fig. 1(b) the passage of the reduced velocity wake through the rotor blading gives rise to a time varying change of incidence angle. Although this change is associated with the blade-wake interaction there is nevertheless a time-averaged effect which leads to quite marked variations, particularly on the suction surface heat transfer rate and pressure distribution. Considering first the heat transfer rate, Fig. 4(a), illustrates the more prolonged region of laminar heat transfer rate associated with a decreased incidence of -10° from design value of 38.06° . Studies at an increased incidence of 63.06° were carried out for off-design performance purposes only and although reported here for reference are not a part of the overall wake-blade interaction experiments. The unsteady incidence effects caused by the wake velocity deficit are not correctly simulated by measurements made in the steady state but it is probable that the nature of the transient changes, at least near the leading edge, are in line with those shown. Similar remarks apply to the effect of a decreased incidence on Mach Number distribution around the blade, Fig. 4(b), the overall result being a reduction of Mach Number, i.e. unloading of the crown of the suction surface, $x/s < 40\%$.

Measurement of the Unsteady Disturbance at Inlet

In order to understand the unsteady phenomena caused by the bar-passing apparatus, a sketch of the expected inlet disturbances in the simulation and the engine is given in Fig. 5(a). The velocity triangles are matched by setting the correct bar velocity and matching the cascade inlet velocity to the rotor relative velocity. The intermittent perturbations to the inlet flow caused by the simulation are shown for the high freestream turbulence case in Fig. 5(b) in terms of hot-wire output from the probe mounted in the freestream inlet plane at mid-passage, and surface stagnation point measurements of pressure and heat transfer rate. Both these results and the detailed measurements on the suction surface are presented from tests using the bar-passing apparatus described above with just 2 bars fitted, as opposed to the 16 bars necessary to model the correct blade passing frequency of the cold-air turbine design. This enables individual bar-passing events to be separated in time, since it is difficult to tell whether events were merging together from the 16 bar experiments alone. This data is normalised with respect to 2 cycles of the bar-passing event, so that it is possible to relate information from different runs in terms of cycle fraction. The signals show a background turbulent level extending over about 60% of the cycle characterised by a similar type of signal to that obtained with no rotating bars. All three signals have a periodic component at bar-passing frequency with two characteristic parts:

(i) Over about 6% of the cycle rapid changes in level of the order of 5 to 10 μ s rise and fall times are observed. The pressure signal varies by $\pm 25\%$ and the heat transfer rate by approximately $\pm 30\%$. This disturbance is attributed to shock waves generated as the bar sweeps past the cascade. By examination of Schlieren photographs of this flow, examples of which are given in Fig. 7, the nature of the NOV simulated shock structure can be determined. Clearly two shocks are associated with one bar-passing event, the bow and recompression shocks that would be expected at the bar relative Mach Number in steady flow. The separation time between these shocks is approximately 75 μ s, marked as Δt_s in Fig. 5(b), and is seen to correspond to the time interval between the sharp falls in level to the adjacent sharp peak.

(ii) Following these rapidly changing events, a second less marked change in level associated with the wake is also visible over about 10% of the cycle, marked as the "wake" region in Fig. 5(b).

Time-Resolved Heat Transfer Rate Measurements on the Suction Surface

The nature of the reaction of otherwise laminar boundary layers to both a higher level of isotropic freestream turbulence, and to the intermittent disturbances caused by the wake and shock/boundary layer interactions was investigated in more detail using the instrumented suction surface shown in Fig. 2(b), and these results are presented in Fig. 6.

(a) Natural Transition of the Suction Surface Boundary Layer

Wide bandwidth heat transfer signals obtained from the surface thin film gauges clearly illustrate the important differences between the low and high freestream turbulence cases as shown in the high frequency traces of Fig. 6(a). There is a constant spacing of 5 mm between the thin film gauge results shown, starting with gauge 3 at an x/s value of 0.12 through to gauge 15 at $x/s = 0.63$. The low turbulence case (Run 5723) remains quiet (laminar) throughout the entire measuring range of the transient data (to $x/s = 0.63$). The surface heat transfer for the high freestream turbulence case, while starting somewhat higher than the laminar case, becomes increasingly dominated by sharp transient events (consistent with the theory of turbulent spot development, growth, and gradual merger as proposed by Emmons²² and verified by many others (e.g. Schubauer and Klebanoff²³). These spots, which raise the heat transfer coefficient instantaneously to high turbulent levels, continue to grow and merge until finally the Nusselt Number signals become increasingly characterized by the "steady" turbulent levels. It is clearly seen that by the $x/s = 0.63$ station the flow is at the turbulent level more than half of the time but drops precisely to the undisturbed laminar values between the turbulent events. In other tests conducted at $1.5 \times Re$ design, the boundary layer was fully turbulent at this location.

The physical process of turbulent spot breakdown to turbulence can be seen in Fig. 6(a). The growth and rearward convection of individual turbulent spots is clearly seen as they move along the blade surface. The spot signals grow in height and width as the spots cover more of each succeeding thin film gauge and shift in time downstream. This breakdown process is quantified in more detail in Ashworth²² where intermittency levels are estimated from the digital time records and spot convection rates are estimated from cross-correlation analysis of adjoining thin film signals.

(b) Detailed Wake and Shock Interaction Effects

It is possible to analyse the reaction of the blade boundary layer to the wake and shock perturbations with 2 bars rotating by investigation of the sequence of time-resolved Nusselt Number plots given in Fig. 6(b), (c) and (d). The high freestream turbulence case with wakes and shocks present (Fig. 6(b)) is markedly different to the naturally transitional boundary layer (Fig. 6(a)) over the first 35% of the surface, with similar rapid rises and falls in Nusselt Number to the perturbations evident in Fig. 5. This shock related event occurs on the early suction surface due to a shock/boundary layer interaction starting at gauge 9, close to the crown of the suction surface. Examination of the Schlieren photographs (Fig. 7) indicates that the shocks first interact with the boundary layer near to gauge 9, the reflection point moving towards the leading-edge as the bar moves in the same direction. This is visible on the early gauges on Fig. 6(b), occurring first on gauge 9 then moving gradually through gauges 7 and 5 and finally showing on gauge 3. The rapid drop in surface Nusselt Number is attributed to an unsteady separation and the rise to a turbulent re-attachment both caused by the shock boundary layer interaction. The effect of the wake is not clearly discernable in Fig. 6(b) and to aid in identification of this the bars were rotated at a lower speed such that the bar relative Mach Number was subsonic. The results of this are shown as Fig. 6(c) with a much more clearly identifiable enhancement in heat transfer due to this wake. This extends to the later gauges of the surface causing the boundary layer to be fully turbulent over the extent of the wake. In Fig. 6(d) the background turbulence was reduced to less than 0.04 and the periodic disturbances due to the bar-passing events are more clearly evident. The early suction surface has shock-related phenomena extending well into the cycle period with apparent oscillations in Nusselt Number moving with the shock. Also apparent from Fig. 6(d) is the intermittent nature of the turbulence induced in the boundary layer by the wake and shock interaction, as the boundary layer clearly returns to its undisturbed laminar value between the periodic events. The heat transfer enhancement due to the wake is clearly evident along the whole surface.

In summary, it appears that the state of the turbine boundary layer seems to be controlled by the level of freestream turbulence except during the time for which the shock and wake actually pass through the cascade passage.

Schlieren Photographs of the Wake and Shock Interaction

In Fig. 7 Schlieren photographs showing four passages of the cascade (marked A to D) are presented for five instants in the bar-passing cycle. This reflected Schlieren technique gives changes in tone corresponding to the integrated effects of density gradient across the span of the cascade, so that events running normal to the tunnel sidewall show up most clearly. With no bars present the general mid-tone appearance varies most at the trailing-edge shocks with some effects due to the high accelerations near to the leading-edges. The photographs in Fig. 7 are from the 2 bar tests, as the pictures become somewhat confusing in the high-frequency wake-passing case. The position of the bar is shown corresponding to time 1, 26 μ s before the bar reaches its datum position at 90° to the tunnel sidewall. The tip of the bar enters and leaves the cascade when the bar radial line is inclined at $\pm 45^\circ$ to its datum position, but over the range of photographs shown this angle varies from -3° to 17° thus amounting to 11% of the cycle between bar-passing events. The shock and wake events are evident in all of these photographs as is detailed here for each of the times in Fig. 7:

1. The bow shock is visible in passage C as a thin horizontal line just touching the crown of the suction surface. The curved end of this shock is due to refraction from the leading-edge of the upper blade of this passage, as the shock was chopped here as the bar swept by, vertically downwards from the point of view of these photographs. Some weak shock activity is evident in passage D, as will be discussed below. Passage C contains some reflected shock activity associated with the bar recompression shock. The wake can be seen as a mottled region in passage A covering more than half of the passage.
2. 71 μ s later the bow shock has passed the lower blade leading-edge of passage C and is now being refracted from this point. The recompression shock is now in passage C, with its distorted shape due to reflection effects. The wake is now visible in both passages A and B.
3. After another 65 μ s the bow shock has nearly left the lower passage (D), with a quite strong reflected shock visible as a series of arcs, due to the three-dimensional nature of the shock as will be described below. The recompression shock is close to the leading-edge of the upper blade of passage D, also reflected across the passage. The wake is steadily encroaching in to the two upper passages (A and B).
4. The reflection of the recompression shock in passage C is still evident, and the refraction of the same shock in the lower passage is now overlapping with the reflection of the bow shock, which now also is reflecting again from the pressure surface. The wake is now starting to appear in passage C.
5. A short time (30 μ s) later the shock activity has almost cleared passage C, save for some weak secondary reflections of the recompression shock still evident, surprisingly reflecting again off the suction surface. It is assumed that these weaker shock interactions would not have much effect on the boundary layer state, but could cause some of the oscillations in heat transfer noticeable only in the cases where M_{rel} (the bar relative Mach Number corresponding to U_{rel}) is transonic.

Predictions of the Wake and Shock Positions

2-Dimensional Wake Predictions

For the five times corresponding to the Schlieren photographs shown in Fig. 7, predictions of the wake position were calculated, the results of which are shown in Fig. 8. The wake itself is almost 2-dimensional in form, varying mainly in height across the span due to the 3-dimensional bar geometry, so that only a 2-dimensional calculation is necessary. The procedure follows that described in Doory²², now fully automated and allowing for the spreading of the wake by using a width proportional to the square-root of the distance from the bar along the line of U_{rel} with the constant of proportionality derived from a database of wake measurements. The prediction procedure is as follows:

- (i) A prediction of the flowfield velocity is made, in this case using the Denton scheme¹⁴ and stored by the program.
- (ii) U_{rel} is calculated (assumed constant across the span), the center-line of the undistorted wake is calculated from the specified bar position and the width added.
- (iii) The wake is shifted back in time so that the bar will return to its correct position following the marching process of the prediction routine.
- (iv) From this initial position elements of the wake are convected by small time steps using the local velocity interpolated from the prediction until the bar reaches the specified location. The differential velocities in the flowfield cause distortion of the wake along its length and across its width as it is accelerated through the passage.

This simple scheme, which could be incorporated in the blade design process, agrees well with the positions of the wake on the Schlieren photographs, so that the fraction of time that the heat transfer rate to the surface is affected by the wake could be calculated and included in the intermittency term of a prediction. It also demonstrates that to the level of our measuring ability second-order effects such as the "negative jet" effect do not significantly affect the wake position, as referred to in Doorly¹⁵, and that the assumption that this flow unsteadiness may be superimposed on the steady flowfield is a valid approximation.

Quasi-3-Dimensional Shock Prediction

Although it was possible to model the wake in 2-dimensional terms, the shock structure associated with the transonic nature of the bar (as M_{rel} varies from 1.06 at the hub to 1.25 at the tip) is not strictly 2-dimensional, as has been seen in the Schlieren photographs (Fig. 7). An attempt was made to predict the positions of the bow and recompression shocks due to the bar in order to allow trajectory rate calculations to be made relating to the heat transfer measurements, and to aid in understanding phenomena observed in the Schlieren photographs. An example of such a prediction is presented as Fig. 9. The prediction is based on the assumption that for a small element of the bar the flow is 2-dimensional with respect to the plane containing U_{rel} and normal to the bar axis, a quasi-3-dimensional approach described in detail in Ashworth¹⁶. As U_{rel} varies in both magnitude and direction, so does the associated shock structure, and unlike the wake, this variation should be accounted for. The method of prediction was computerized as follows:

- (i) For assumed constant inlet conditions and a specified position of the bar M_{rel} is calculated and its direction determined.
- (ii) The equation of the bow shock in the 2-dimensional plane described above is derived from M_{rel} using the method described in Shapiro¹⁷, shock properties and turning angles obtained by curve-fit equations where necessary over a range of Mach Number from 1.0 to 1.5.
- (iii) The recompression shock is assumed to be straight and inclined at the Mach angle ($\sin^{-1} 1/M_{rel}$) to the direction of M_{rel} , with a virtual origin two diameters downstream of the bar.
- (iv) The shocks are chopped and refracted if they are downstream of the blade axial leading-edge point, with allowance made for regeneration of the shock as it moves away from this point.
- (v) Finally the points of intersection with the blade suction surface are calculated, and the shocks are simply reflected from an origin mid-way between the two intersection points.

Comparison with the Schlieren photographs is encouraging, the position shown in Fig. 9 corresponding to time 1 in Fig. 7., and it is hoped that information from this simplified model will prove useful as an aid to understanding the complex shock movements in turbine passages, in spite of the many simplifying assumptions made in this prediction (such as allowing for no variation of the freestream velocity).

Conclusions

It has been established during the course of this study that the Isentropic Light Piston Tunnel facility combined with the wide bandwidth/high sampling rate heat transfer instrumentation has proved capable of tracking very rapidly progressing unsteady events in a transonic boundary layer. Operating

under a simulated unsteady gas turbine rotor environment, sensitive detection and precision tracking of transient shock, wake and boundary layer transitional events was accomplished.

A second major outcome of this study was the observation that the strong unsteady interaction of a double shock and a simulated NGV wake with the rotor boundary layer did not have any measurable "long-term" effects apart from the strong excursion in heat transfer associated with the actual passing of the shocks and wake. The heat transfer fluctuation levels were essentially unchanged far removed from the disturbance (in time) and nearly identical at the rearmost measuring point except for a turbulent patch associated with the shock/wake event itself.

The interaction of the shocks and wake with the rotor establishes in more detail the earlier observation of Ashworth et al.¹⁴ and Doorly and Oldfield⁴ of strong changes in local heat transfer coefficient. The tracking of the interaction over the surface could be followed with some precision with the time resolution of the instrumentation used.

Predictions of the positions of both the wake and shock structures caused by the bar are most encouraging, as they are based on simplified models easily incorporated in the design process, unlike many other methods which are too unwieldy for turbine designers to use. They both are based on superimposing the unsteady structures on existing steady-state information, and as such agree well with measured data.

Acknowledgements

This work has been carried out with the support of the Procurement Executive, Ministry of Defence, and also Rolls-Royce plc to whom the authors are grateful for permission to publish this paper. The authors wish to acknowledge the assistance of M. L. G. Oldfield and K. J. Grindrod during the experiments, and to thank Dr. J. D. Denton for providing his time-marching code. Professor LaGriff would also like to acknowledge the financial support of the U.S. Air Force Office of Scientific Research under grant number 85-0293 and the Division of International Programs of the National Science Foundation under grant number INT-8509407.

References

- Doorly, D. J. and Oldfield, M. L. G., "Simulation of Wake Passing in a Stationary Turbine Rotor Cascade", J. Eng. for Gas Turbines and Power, ASME, Vol. 107, pp. 998-1006, 1985.
- Doorly, D. J. and Oldfield, M. L. G., "Simulation of the Effects of Shock Wave Passing on a Turbine Rotor Blade", ASME Paper No. 85-GT-112, 1985.
- Doorly, D. J., Oldfield, M. L. G. and Scrivener, C. T. J., "Wake Passing in a Turbine Rotor Cascade", AGARD CP-390, pp. 7.1-7.18, 6th May, 1985.
- Dunn, M. G. and Hause, A., "Measurement of Heat Flux and Pressure in a Turbine Stage", ASME J. Eng. for Power, Vol. 104, pp. 215-223, 1982.
- Dunn, M. G., Lukis, G., Ursio, M., Neimans, R. J., Orszulik, S. and Kay, W. J., "Instrumentation for Gas Turbine Research in Short Duration Facilities", Aerospace Congress, Long Beach, CA, Paper No. 841504, 15th - 18th October, 1984.
- Dunn, M. G., Ree, W. J. and Holt, J. L., "Measurement and Analysis of Heat-Flux Data in a Turbine Stage", Parts I and II, J. Eng. for Power, Vol. 106, No. 1, January, 1984.
- Dunn, M. G., Martin, H. L. and Stanek, M. J., "Heat Flux and Pressure Measurements and Comparison with Prediction for a Low Aspect Ratio Turbine Stage", ASME Paper No. 86-GT-79.
- Dunn, M. G., "Heat Flux Measurements for a Rotor of a Full-Stage Turbine: Part I - Time-Averaged Results", ASME Paper No. 86-GT-77.
- Dunn, M. G., George, M. K., Rae, M. J., Woodward, S. H., Moller, J. C. and Seymour, P. J., "Heat-Flux Measurements for the Rotor of a Full-Stage Turbine: Part II - Description of Analysis Technique and Typical Time-Resolved Measurements", ASME Paper No. 86-GT-78.
- Dunn, M. G., "Experimental Measurements of Heat-Flux Distributions in a Turbine Stage with Upstream Disturbances", Advanced Earth-to-Orbit Propulsion Technology Conference, Huntsville, Alabama, 13th - 15th May, 1986.
- Binder, A., Forster, W., "Turbulence Production due to Secondary Vortex Cutting in a Turbine Rotor", ASME Paper No. 85-GT-13.
- Binder, A., Forster, W., Mach, K. and Rogge, N., "Unsteady Flow Interaction Caused by Stator Secondary Vortices in a Turbine Rotor", ASME Paper No. 86-GT-343.
- Hodson, H. P., "An Inviscid Blade-to-Blade Prediction of Wake Generated Unsteady Flows", ASME Paper No. 84-GT-189, 1984.

14. Dring, R. P. and Joslyn, H. D., "The Relative Eddy in Axial Turbine Rotor Passages", ASME Paper No. 83-GT-22, 1983.
15. Dring, R. P., Joslyn, H. D., Hardin, L. W. and Wagner, J. H., "Turbine Rotor-Stator Interaction", ASME J. Eng. for Power, Vol. 104, pp. 729-742, 1982.
16. Epstein, A. H., Guenette, G. R. and Norton, R. J. G., "The MIT Blowdown Turbine Facility", ASME Paper No. 84-GT-116, 1984.
17. Schultz, D. L., Jones, T. V., Oldfield, M. L. G. and Daniels, L. C., "A New Transient Cascade Facility for the Measurement of Heat Transfer Rates", AGARD CP-219, 1977.
18. Ashworth, D. A., LaGraff, J. E., Schultz, D. L. and Grindrod, K. J., "Unsteady Aerodynamic and Heat Transfer Processes in a Transonic Turbine Stage", ASME Paper No. 85-GT-128, 1985.
19. Schultz, D. L. and Jones, T. V., "Heat Transfer Measurements in Short Duration Hypersonic Facilities", AGARDGRAPH No. 165, 1973.
20. Emmons, H. W., "The Laminar-Turbulent Transition in a Boundary Layer - Part I", J. Aero. Sci., Vol. 18, No. 7, July, 1951.
21. Schubauer, G. B. and Klebanoff, P. S., "Contributions on the Mechanics of Boundary Layer Transition", NACA Report 1289, 1956.
22. Ashworth, D. A., LaGraff, J. E., and Schultz, D. L., "Unsteady Interaction Effects on a Transitional Turbine Blade Boundary Layer", Paper to be presented at the Joint ASME/JSME Gas Turbine Conference, March, 1987.
23. Doorly, D. J., "A Study of the Effect of Wake Passing on Turbine Blades", D.Phil. Thesis, University of Oxford, 1983.
24. Denton, J. D., "An Improved Time-Marching Method for Turbomachinery Flow Calculation", ASME J. Eng. for Power, Vol. 105, pp. 514-530, 1983.
25. Ashworth, D. A., "Unsteady Wake and Shock Interactions on a Transonic Turbine Blade", D.Phil. Thesis, University of Oxford, 1986.
26. Shapiro, A. H., "The Dynamics and Thermodynamics of Compressible Fluid Flow", Ronald Press, Vol. 1, pp. 854-865, 1954.

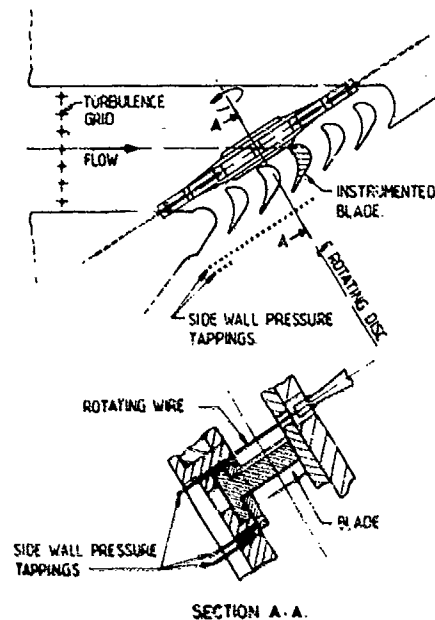


Fig. 1(a) Arrangement of the rotating bar wake generator and cascade.

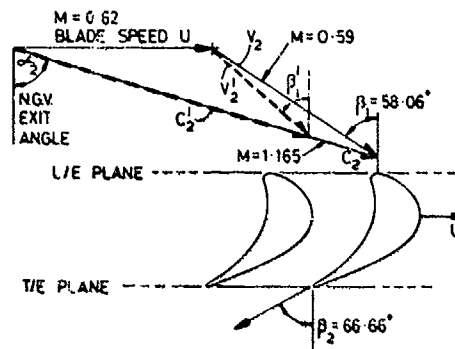
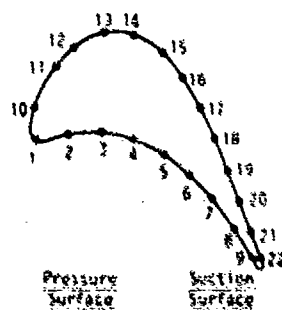
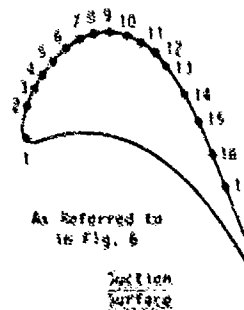


Fig. 1(b) Velocity triangles at inlet for the steady nominal design case at mid-span, showing the reduced incidence caused by the deficit in the wake.



Pressure Surface		Suction Surface	
Model Point	x/s	Model Point	x/s
1	0.00	10	0.08
2	0.12	11	0.10
3	0.24	12	0.24
4	0.36	13	0.31
5	0.48	14	0.39
6	0.59	15	0.46
7	0.71	16	0.53
8	0.84	17	0.61
9	0.96	18	0.68
		19	0.75
		20	0.83
		21	0.90
		22	0.96

(a)



As Referred to in Fig. 6.

Model Point	x/s
1	0.03
2	0.08
3	0.12
4	0.15
5	0.19
6	0.24
7	0.28
8	0.31
9	0.35
10	0.39
11	0.43
12	0.47
13	0.51
14	0.55
15	0.65
16	0.73
17	0.81

(b)

Fig. 2(a) Co-ordinates of the original heat transfer gauges on the blade profile.

Fig. 2(b) Co-ordinates of the heat transfer gauges for the detailed suction surface study, referred to in Fig. 6.

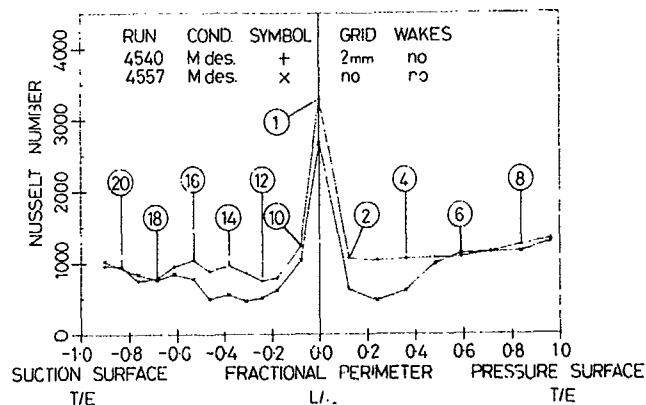


Fig. 3(a) Effect of freestream turbulence level on mean heat transfer rate without wakes for the nominal design case, $M_2 = 1.18$, $Re = 0.919E6$.

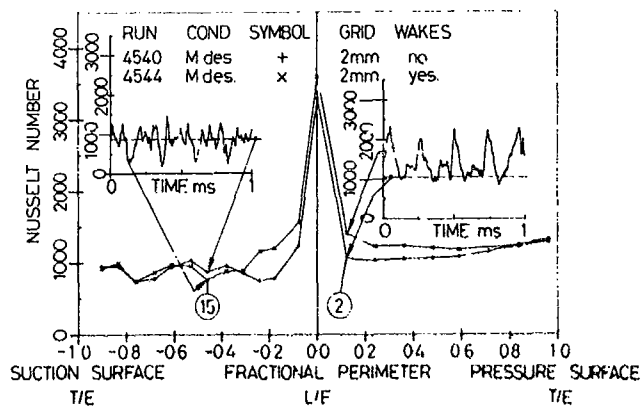


Fig. 3(b) Effect of wake and shock interaction on mean heat transfer rate at the high freestream turbulence case ($\sim 3\%$) and design operating conditions. Inset are typical transient recorder signals for the 16 bar experiment at two x/w locations showing a 1 ms interval of the record together with the time-averaged values without the wake and shock interactions.

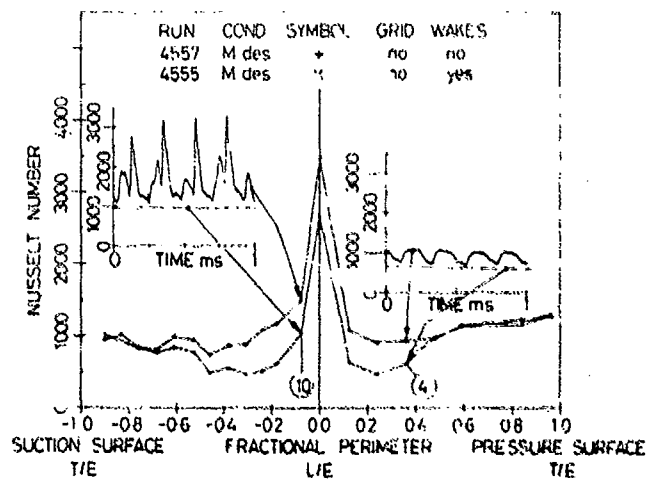


Fig. 3(c) Effect of wake and shock interaction on mean heat transfer rate for the low freestream turbulence case ($< .8\%$), otherwise as in Fig. 3(b).

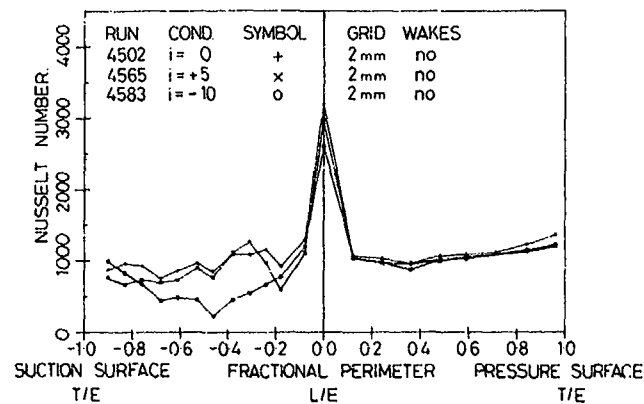


Fig. 4(a) Effect of incidence variation on mean heat transfer rate at the nominal design case ($M_2 = 1.18$, $Re = 0.919E6$) with no wake and shock interaction.

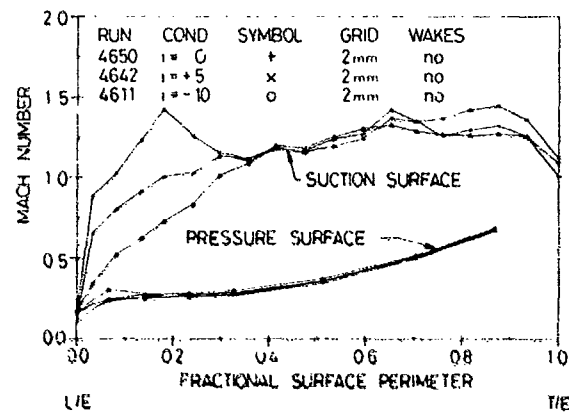


Fig. 4(b) Effect of incidence variation on mean surface isentropic Mach Number at the nominal design case ($M_2 = 1.18$, $Re = 0.919E6$).

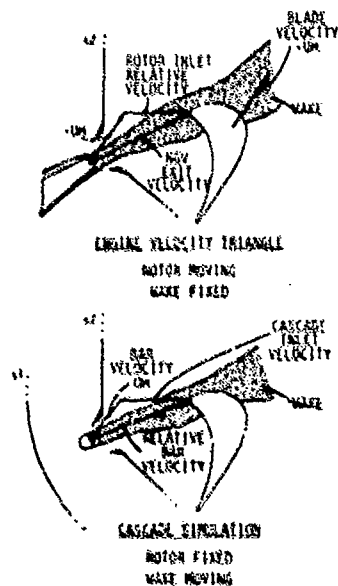


Fig. 5(a) Illustration of the comparative velocity triangles for the engine and cascade simulation of the NGV/rotor interaction.

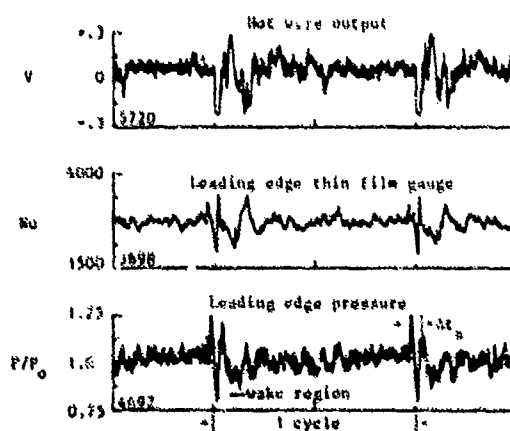


Fig. 5(b) Measurements of the unsteady disturbance at inlet by a hot-wire in the freestream and heat transfer and pressure measurements at the stagnation point.

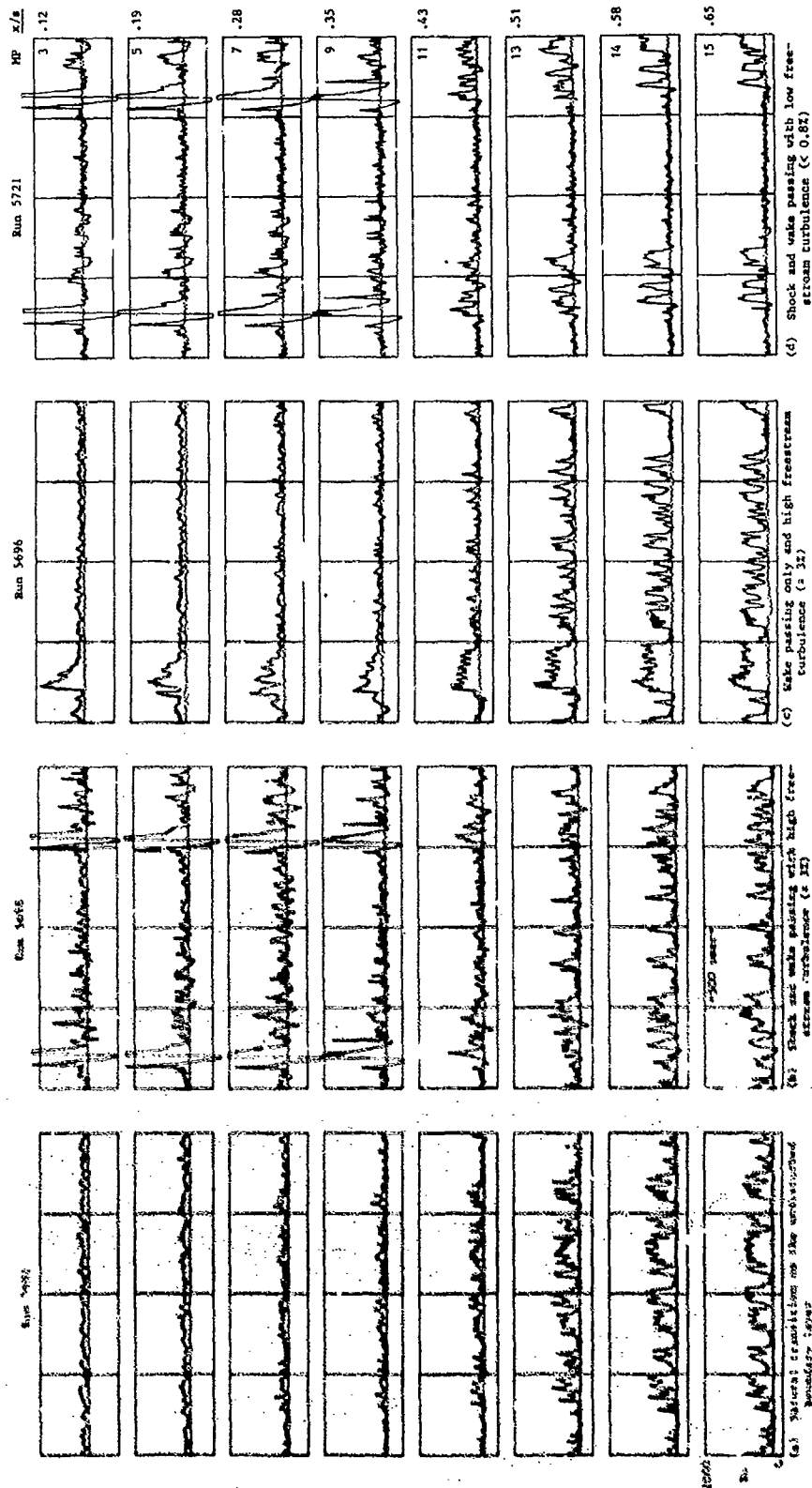


Fig. 6 Detailed time-resolved heat transfer rate measurements to the blade suction surface. The dotted lines are the baseline undisturbed results for the low freestream turbulence case ($\approx 12\%$, Run 5723).

A dark, high-contrast, black and white photograph showing a close-up of a textured surface, possibly a wall or ceiling. A large, dark, irregular shape, which appears to be a shadow or a hole, dominates the center of the frame. The surrounding areas are lighter and show a grainy, mottled texture. The overall image is very dark and has a grainy, high-contrast quality.

1: T = -26 us

[illegible]

Path of Rotation of the Uars

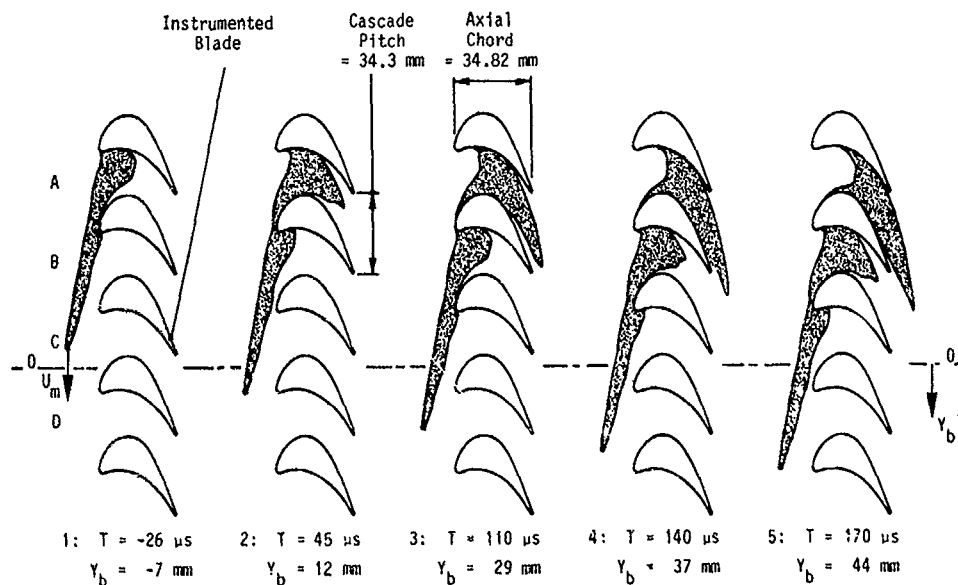


Fig. 8 Predicted wake positions at times corresponding to the Schlieren photographs in Fig. 7. The two lines for each time are the leading and trailing edges of the highly turbulent wake region.

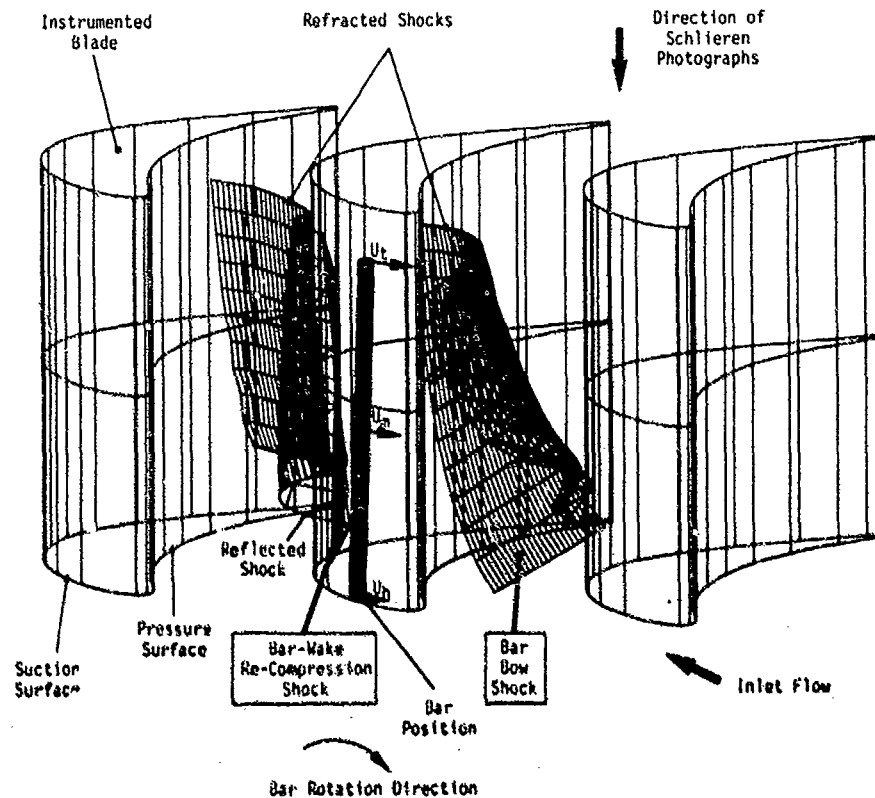


Fig. 9 Predicted shock position corresponding to time 2 of Fig. 7, with the bar inclined at -2° to its datum position. Only the half of the shocks downstream of the bar are shown for clarity. The refraction and reflection of both shocks can be seen, with the re-compression shock more 2-dimensional in form than the detached bow shock, due to stand-off distance variation with bar relative Mach Number. Both shocks are weaker towards the hub due to the lower Mach Number there, with the bow shock strength less than the re-compression shock strength at each radius.

DISCUSSION


P. Ramette, Fr

The wake is induced, in your experiment, by a bar with a diameter corresponding to the nozzle trailing-edge section, which is symmetrical, while the nozzle wake is non-symmetrical. Consequently, you do not have the same gradients. How representative of a nozzle wake effect is your experiment?

Author's Reply

The work reported here is the follow-up of work carried out on a different profile, with a lower relative bar Mach Number, as reported by Doorly²⁷. Prior to these tests, static tests were carried out by inserting a bar in a cascade with NGV's mounted in the same test section. It was therefore possible to traverse both bar and nozzle wakes and it was noted that the bar wake was quite representative of the NGV wakes. The larger momentum deficit corresponding to the suction side boundary layer that one would expect to contribute to the asymmetry did not appear to be significant and we assumed the same to be true for our cascade. It is worth noting that the weaker shock in the experiments reported by Doorly¹⁻³ only caused a boundary separation once the shock passed the leading edge of the blade. It is very interesting that quite different results can be obtained from similar experiments with only a few parameters altered, the most important of which is the shock strength.

²⁷Doorly, D.J., "A Study of the Effect of Wake Passing on Turbine Blades", D. Phil Thesis, University of Oxford, 1983.



by

H. Hoheisel⁺ and N.J. Seyb⁺⁺

*Deutsche Forschungs- und Versuchsanstalt für Luft- und Raumfahrt (DFVLR), Institut für Entwurfsaerodynamik, Braunschweig, Germany

The design of efficient blade profiles for gas turbine compressors can no longer be effectively carried out through the use of correlations of 2D-cascade data. For the description of the real flow field three dimensional effects have to be taken into account. Modern theoretical calculation methods which involve the determination of blade profile pressure distribution and the associated boundary layer parameters, are now becoming accepted practice. However before the engine designer can have confidence in these new methods the predicted performance must be demonstrated to be in good agreement with experimental data. It is the purpose of the work reported in this contribution to present an accurate set of experimental measurements of blade profile pressure distributions and boundary layer parameters under quasi-3D-flow conditions and to compare these with the predicted performance for a high deflection transonic compressor cascade. It is shown that for conditions near minimum loss incidence the agreement between measured and predicted values is achieved to an adequate engineering standard and that the two most important aspects, choking flow and boundary layer separation ($H_{12} > 2.8$) are well predicted. Also the data presented could be used to further update and improve the current prediction methods.

NOMENCLATURE

c	chord	$n^+ = n \cdot w_1 / v$	non-dimensional distance from surface
C_{pi}	static pressure coefficient	ρ	density
e	standard location of traverse plane	τ	shear stress
h	test section height	U	axial velocity density ratio (AVOR)
H, H_{12}, H_{32}	boundary layer shape factors		
\ln	logarithm to base e		
M_a	Mach number		
p	static pressure		
P_o	total pressure		
Re	Raynolds number based on inlet condition		
Re_{δ_2}	Raynolds number based on δ_2		
s	blade spacing		
t	blade thickness		
Tu_i	degree of turbulence at cascade inlet		
x, y	rectangular coordinates		
w	velocity		
$w^+ = w/w_\infty$	non-dimensional velocity		
β, θ_s	flow angle and blade angle (see fig. 6)		
ΔS	turning angle		
δ_1, δ_2	displacement and momentum thickness		
C_{Pi}	total pressure loss coefficient		
y	coordinate normal to blade surface		

Subscripts	
1, 2	for quantities in front and behind the cascade
-	free stream, edge of boundary layer
cr	critical values
l	local values
p	frictionless flow given from measurement $p = p(\eta)$
pw	frictionless flow given from measurement $p = p'(\eta=0) = P_u$
PS	pressure side
SS	suction side
S	separation
TP	traverse plane, test point (VN)
t	turbulent
w	wall

1. INTRODUCTION

The design of blade profiles for turbo-machines is becoming more and more demanding as a result of the requirement for reduced fuel consumption and more compact higher performance engines. Thus blades with lower losses and/or a greater work potential are an essential future requirement but these objectives must not be achieved at the expense of mechanical reliability. The actual target for a blade design will depend upon the engine type; for a long range civil transport efficiency and reliability are all important whereas with a military fighter high performance and minimum engine weight may be the prime objective. It is towards the latter performance that the work described in this paper is aimed as the lessons learnt will have direct relevance to the more lightly loaded but higher efficiency civil target.

Blade design methods have until recently relied upon simple 2D correlations of cascade experimental results for the choice of incidence, space/chord ratio, deviation, choke margin, working range etc. using blades with a geometric profile description. These methods have many obvious disadvantages particularly since modern turbo-machines demand blade profiles which are often well outside the limits of existing correlations and are no longer adequately modelled by 2D cascade tests. Thus to achieve the best overall performance a more sophisticated blade profile design method is essential. Such methods are now available and they involve the determination of the blade profile pressure distribution and an assessment of the associated boundary layer. In particular, in the blade design process, it is essential to define a blade on which boundary layer separation is avoided or at least minimized.

In setting up the mathematical model to represent the above procedures a large number of assumptions must be made and it is therefore essential to check that an adequate representation of the real flow has been achieved. It is the purpose of the work reported in this contribution to obtain comprehensive and accurate experimental data under quasi-3D-flow conditions against which to validate the above blade design procedures and to establish their suitability as an engineering design tool. The experimental target chosen for this investigation was a cascade having a design point inflow Mach number of 0.85 and flow turning of 50° since this represents a typical requirement for the hub sections of current compressors, (see figure 1). The experiments were performed on the chosen cascade in the High Speed Cascade Wind Tunnel of the DFVLR Braunschweig.

2. DESCRIPTION OF BLADE PROFILE DESIGN AND PERFORMANCE ASSESSMENT

2.1 Prediction procedures

Modern methods of blade profile design are in general based upon the determination of the surface pressure distribution as a step in obtaining the related boundary layer characteristics. There are many such theoretical methods available e.g. (1), (2), (3), (4), which can range from a quasi-3D-time marching method with a linked boundary layer model to a fully 3D viscous procedure. The method used in this contribution represents the flow as indicated in figure 2a (i.e. quasi 3D) with an inviscid core, the characteristics of which are determined by time marching methods described by Carrhar and Kingston (20). The boundary layer is represented as described below. The time marching technique integrates the time dependant equations of motion with respect to time until a steady state solution is obtained. The equations are solved in a finite volume form using a grid of quasi streamlines which are intersected by pitchwise lines-typically 20 quasi streamlines and up to 100 equally spaced pitchwise lines are specified. This time marching calculation is used iteratively with the boundary layer calculation which, when combined with the blade profile, defines the effective flow boundary.

An aspect of major importance is the variation of stream tube thickness at all stations axially through the cascade. This variation in stream tube thickness, in the axial direction, can have any specified variation although for the predictions discussed below a linear variation as shown in figure 2a has been used. The real axial variation of stream tube thickness is difficult to determine experimentally, but theoretical investigations reported by Stark/Noheisel (5) showed a possibility to define the axial velocity density ratio δ for comparison of predicted and measured results. These results are supported by 3D inviscid time marching calculations for the cascade considered in this contribution. Figure 2b demonstrates a comparison of results obtained by the two different methods, for the incompressible flow condition by the method of (5) and for the actual Mach number of $Ma_1 = 0.6$ using a 3D-time marching method. The agreement of the so called "transition function" is very good and confirms the dominant influence of the aspect ratio of the blade. As was found in (6) no Mach number influence for $Ma \leq 0.8$ can be identified from the present results. It will be noted that there is an approximate linear variation of stream tube thickness from inlet traverse plane to exit traverse plane for the investigated cascade which has a blade aspect ratio of $h/c = 1.75$.

2.2. Boundary layer method

The assessment of the boundary layer characteristics is the main objective of the calculations as it is only in this way that the blade performance can be judged. An essential point of this assessment is the determination of the change "point" between laminar and turbulent boundary layers and the manner in which the boundary layer reacts at this point. There are basically three possibilities

- (i) change to a turbulent layer without separation (transition)
- (ii) separate and then reattach immediately as a turbulent layer
- (iii) separate completely or reattach after a significant bubble.

The transition and laminar separation prediction methods used are based on the correlations shown in figure 3. Concerning the transition, these correlations account for local values of pressure gradient λ , laminar boundary layer state Re_{δ_2} and local turbulence level [7]. Figure 3b is used, when laminar separation is predicted, to determine whether or not reattachment can be assumed to follow immediately or complete separation is the more likely event. This curve must be considered somewhat speculative as it contains only the local pressure gradient and boundary layer state just upstream of the separation point, where as other parameters such as turbulence level etc. could have a major influence [8].

The methods used to determine the turbulent boundary layer parameters are those of Truckenbrodt [9] but with two changes. The first being that the numerical constant "A" in the momentum thickness equation given in [7] as

$$\frac{\delta_2}{c} = \left(\frac{w}{w_1}\right)^{-3} \left[c_t + \left(\frac{0.037}{Re_c^{1/5}}\right)^{7/6} \int_{x_t/c}^{x/c} \left(\frac{w}{w_1}\right)^{10/3} d(x/c) \right]^{6/7} \quad (1)$$

has been increased from $A = 0.037$ to 0.07 . The value c_t is given as

$$c_t = \left[\frac{\delta_2}{c} \left(\frac{w_t}{w_1}\right)^3 \right]^{7/6} \quad (2)$$

The second modification is related to the subsidiary shape factor correlation

$$H = f(H_{12}) \quad (3)$$

The method relies on a relationship between the calculated subsidiary shape factor H and the shape factor H_{12} for the determination of H_{12} and δ_2 . Preliminary predictions for one experimental test condition indicated that the original curve of figure 4 underpredicted the values of H_{12} (and hence δ_1) and that a revised curve resulted in much better agreement with the present experiments. This revised curve was then used for all the subsequent predictions.

The inviscid-viscous interaction model described will thus produce the boundary layer parameters at the blade trailing edge. A method, which follows Stewart's analysis [10], was then used to compute the mean outlet air angle and the total pressure loss.

3. EXPERIMENTAL INVESTIGATION

3.1 Apparatus and cascade geometry

The experimental investigations were carried out in the High Speed Cascade Wind Tunnel of the DFVLR at Braunschweig [11], now in operation at Munich [12], [13]. The tunnel was installed in a tank which could be evacuated from 1 to 0.05 bar (see figure 5). An independent variation of Mach number and Reynolds number was possible. The degree of turbulence was mainly $Tu_1 = 4\%$ and could be achieved using grids of crossed bars upstream of the cascade [14]. Only some investigations were carried out on a lower turbulence level of about $Tu_1 = 1\%$ using no grids. The tunnel had a test section width of $b = 300$ mm and an adjustable height of 250 to 500 mm depending on the inlet angle.

The investigations were carried out on a so called "V2 double circular arc blade" designed to achieve 50° of deflection at an inlet Mach number of $Ma_1 = 0.85$ (figure 6). The coordinates of the blade shape are given in table 1, with a chord of $c = 80$ mm resulting in an aspect ratio of $h/c = 3.75$. Wake traverse measurements (total pressure, static pressure and outlet flow angle) at midspan position were performed with a wedge type probe [11] located at 30% of chord axially downstream of the blade trailing edge plane. Surface pressure distributions also at midspan position were measured using static pressure tapings on the suction and the pressure sides of the blades adjacent to the centre blade.

Boundary layer measurements at midspan position of the blade were carried out at different positions of the blade suction surface and in some cases on pressure surface but near the trailing edge only. These boundary layer measurements were done using a two-finger probe specially developed for boundary layer measurements of the highly loaded compressor cascade V2. The probe measures the static pressure up to a wall distance of 1.60 mm, the height of the flattened Pitot probe amounts to 0.15 mm. The probe was calibrated for Mach and Reynolds number, flow angle and turbulence level. Corrections were applied from these calibrations on the basis of a comparison with flat plate experiments [13] and with measurements by a laser-Doppler anemometer respectively [16].

Changes in AVDR through a cascade can be obtained by varying the amount of air removed through porous side walls. Two side wall conditions were applied in the present investigation, solid and porous (sketch 8 in fig. 6). When applying different side wall con-

conditions it is necessary to achieve the same stream tube contraction at midspan of the cascade. To control this, the pressure distribution on blade surface indicates the local variation of stream tube thickness. However, under certain circumstances the axial distribution of stream tube thickness can have a dramatic influence on cascade performance as evidenced by prediction and test results respectively. After a series of careful calibration tests sufficient agreement between the solid and porous side wall conditions on the mid-span blade pressure distribution has been achieved. Figure 7 demonstrates two results for the case of a subcritical and a supercritical flow condition respectively. Only very small differences especially in the front part were observed. Very good agreement was achieved also on inlet and exit angle for the two different side wall configurations. Further discussion of this topic is given in reference [5] and [6].

3.2 Data evaluation

The wake data were evaluated by transforming the non-homogeneous flow in the measuring plane into an equivalent homogeneous flow by applying the laws of conservation [17]. This evaluation leads to the total pressure loss coefficient which is defined as

$$\zeta_{V1} = \frac{P_{O1} - P_{O2}}{P_{O1} - P_1} \quad (4)$$

the turning angle

$$\Delta\beta = \beta_1 - \beta_2 \quad (5)$$

and the axial velocity density ratio (AVDR)

$$\Omega = \frac{\rho_2 \cdot w_2 \cdot \sin \beta_2}{\rho_1 \cdot w_1 \cdot \sin \beta_1} \quad (6)$$

In quasi-three-dimensional flows with axial velocity variations shown in fig. 2b, the results depend on the location of the traverse plane. Therefore, they are regarded as local values (index 1). Final values at upstream and downstream infinity respectively may be predicted from the local values using the transition function (see fig. 2).

For the pressure distribution a non-dimensional coefficient is defined as

$$c_{p1} = \frac{p(x/c) - p_1}{P_{O1} - P_1} \quad (7)$$

The boundary layer data were evaluated applying a new definition of the integral values [18], which takes the varying static pressure within the boundary layer into account. For this method "called evaluation C3" the displacement thickness is given by

$$\delta_1 = \int_0^\delta \left(\frac{\rho_p \cdot w_p}{\rho_{pw} \cdot w_{pw}} - \frac{\rho(\eta) \cdot w(\eta)}{\rho_{pw} \cdot w_{pw}} \right) d\eta \quad (8)$$

and the momentum thickness

$$\delta_2 = \int_0^\delta \frac{\rho(\eta) \cdot w(\eta)}{\rho_{pw} \cdot w_{pw}} \left(\frac{w_p}{w_{pw}} - \frac{w(\eta)}{w_{pw}} \right) d\eta \quad (9)$$

Under the assumption of constant static pressure across the boundary layer "called evaluation A" the equs. (8) and (9) lead to the standard definition, e.g. for the momentum thickness

$$\delta_2 = \int_0^\delta \frac{\rho(\eta) \cdot w(\eta)}{\rho_\infty \cdot w_\infty} \left(1 - \frac{w(\eta)}{w_\infty} \right) d\eta \quad (10)$$

The degree of turbulence in the inlet plane is defined as

$$Tu_1 = \frac{\sqrt{w_1'^2}}{w_1} \quad (11)$$

where w_1' is the fluctuating velocity component in the direction of w_1 obtained from a single hot-wire probe placed normal to the free stream velocity.

3.3 Cascade performance

A comprehensive test programme comprising wake and pressure distribution measurements for a number of inlet angles, Mach numbers and AVDR-values lead to the cascade performance. Figure 8 demonstrates the influence of AVDR on turning angle and loss coefficient for different Mach numbers at constant inlet angle. For the design Mach number $Ma_\infty = 0.85$ the minimum losses will be achieved at a flow condition of relatively high acceleration

which characterizes the performance of the present cascade V2. This loss characteristic is the result mainly of the suction side boundary layer behaviour as shown in figure 9. In this diagram the regions where separation or choked conditions occur are marked. Similar plots of the loss coefficient at different inlet angles lead to the cascade performance plotted in figure 10 as loss coefficient versus inlet angle at the constant Mach number $Ma_1 = 0.8$. At this high Mach number the inlet angle for minimum loss will be strongly influenced by the AVDR-value. Taking these effects into consideration the boundary layer investigations were undertaken for the following flow conditions:

1. Near maximum deceleration w_2/w_1 (stalled condition, α_{min})
2. At minimum losses, ζ_{Vmin}
3. Choke separation, α_{max} -values.

The boundary layer test programme can be seen from figure 9 at $\beta_1 = 49.5^\circ$, and for different incidence angles from figure 10, where the inlet angles are marked by arrow. Only boundary layer results of the suction side will be presented.

4. COMPARISON OF PREDICTION AND EXPERIMENTAL RESULTS

4.1 Influence of pressure gradient on boundary layer

As mentioned before two different data evaluation methods were applied to the boundary layer measurements. Figure 11 shows for an arbitrary test condition the boundary layer velocity profiles on the suction side with constant (closed symbols, evaluation A) and with variable static pressure (open symbols, evaluation C3) within the boundary layer. The variation of static pressure (diagram B) yields higher nondimensional velocities compared with the evaluation taking the wall static pressure as constant throughout the boundary layer. The main reason for this is a lower reference velocity at the edge of the boundary layer. Therefore, the variable static pressure can alter the integral boundary layer results up to 15%. The corresponding deviation of the integral values for some cases of the present boundary layer investigations can be taken from table 2 and 3 respectively. For comparison of the measurements with the prediction, test data from evaluation C3 (variable static pressure) has been used.

4.2 Influence of turbulence on "transition"

In the test programme a wide range of test conditions has been covered, see section 3, in order to obtain the total range of boundary layer conditions. Figure 12 illustrates the effect of two different inflow turbulence levels (4% and 1%) for two different Mach numbers. Using the methods of section 2a laminar separation followed by immediate reattachment is predicted (indicated by the arrows) and this is nearly consistent with the experimental results for the case of high turbulence (4%). At the lower level of turbulence some form of laminar separation bubble appears to exist causing a deviation in the pressure distribution. Thus it is concluded that turbulence must have a significant effect on the existence and extent of laminar separation bubbles and must be included in any bubble prediction correlation. If a laminar separation bubble exists the correlations of transition are rather uncertain, as was found on turbine cascade investigations (19), therefore further experimental data are required to achieve more confidence in the prediction of transition.

4.3 Surface pressure distribution and boundary layer parameters

Figure 13 shows a comparison between predicted and measured blade surface pressure distribution for three inlet Mach numbers near minimum loss operating conditions ($\alpha_1 = 1.20$, fig. 13a) and for a higher deceleration rate w_2/w_1 ($\alpha_1 = 1.20$, fig. 13b) respectively. The comparison is shown to be acceptable, with the exception of the leading edge region on suction surface at supercritical inlet Mach number. There, the measured acceleration is shifted upstream presumably because of different stream tube thickness between measured and predicted flow condition.

The measured boundary layer velocity profiles at the same flow conditions as the pressure distributions are shown in figure 14. It will be seen that for all Mach numbers boundary layer separation occurs at $\alpha_1 < 1.20$ somewhere between 88% and 99% chord. This behaviour is in agreement with the measured pressure distribution results. The beginning of the boundary layer separation at $\alpha_1 = 1.20$ is limited to 98% chord.

The predicted and measured local boundary integral values at the same flow conditions as before are shown in figure 15. The agreement between predicted and measured values is also shown to be acceptable. At the design Mach number $Ma_1 = 0.85$ higher momentum thicknesses are indicated compared with the predicted results. In the prediction no shock boundary layer interference is considered, which can be assumed from the measured pressure distribution seen in figure 13 and schlieren measurements not shown here. These results when compared with the information of figure 14 indicate that turbulent boundary layer separation will occur at shape factors H_{12} in excess of 2.8. The presented boundary layer data are only a selection from the total test programme but they give confidence in the prediction method used.

It should be noted that all the predictions carried out above were made at design in-

cidence and near minimum loss conditions. However, it is necessary, when producing a blade design for engine application to determine the operating range in terms of incidence capability and flow choke margin. For the highly loaded blades being considered in this contribution considerable difficulty was experienced in achieving acceptable predicted results at these off design conditions. The discrepancies are generally accepted to be due to the inability of the time marching methods to adequately model the flow when large local variations in pressure gradient exist and the boundary layer procedure to be a realistic representation when large regions of separated flow are present. Some experimental results for these off design conditions are included in table 3.

4.4 Overall performance

The predicted overall performance in terms of trailing edge boundary layer parameters and total loss coefficients is compared with measured values in figure 16 and 17 respectively for a selected number of test cases. Taking into account that this is a very heavily loaded cascade a reasonably good agreement is illustrated except near choking conditions where the predicted losses are seen to be lower than the measured values. In these cases shock-boundary layer interaction and the stream tube height both have an important influence on the measured and predicted results. Thus at high transonic Mach numbers an accurate simulation of the shock/boundary layer interaction and local flow conditions (AVDR and inflow angle) must be specified. The choking flow Mach number is however predicted with reasonable accuracy because the throat is near the leading edge where the influence of local AVDR and boundary layer with respect to the overall performance is small.

The predicted losses of fig. 17 reflect the error in the trailing edge boundary layer parameters δ , and δ , shown in fig. 16. For example, in the case of 0.6 Mach number both boundary layer parameters are underpredicted at low AVDR and overpredicted at high AVDR. The result is that there is a change in tendency in the calculated losses when compared with the measured values. However using the measured boundary layer parameters for calculating the losses results in a tendency in agreement with the measurements. This example shows the sensitivity on these flow conditions.

4.5 Additional boundary layer analysis

The velocity profiles of turbulent boundary layer are described by the "law of the wall". Checking this behaviour on some of the present results, the influence of Mach number is shown in figure 18. As an important statement can be drawn that the wake region starts early compared with results without strong pressure gradients at n^+ -values in excess of 100, and no Mach number influence can be observed.

The method of Truckenbrodt [9] with some limited modifications, as described in section 2, has been used for turbulent boundary layer calculations reported in this note. There is however the possibility of using the measured data derived in the experimental programme to investigate whether improvements to the method are possible. In this integral boundary layer method it is assumed that there is a unique relationship between the shape factors H_{12} and H_{32} . The current experimental results are plotted in figure 19 together with the curve by Truckenbrodt for incompressible flow condition. The experimental data in the upper diagram show results at design incidence on different Mach numbers and in the lower diagram at a constant Mach number of $Ma = 0.8$ for different incidences. The data correspond to different chord positions x/c and n -values for the attached turbulent flow conditions and lie clearly above the theoretical curve. A better representation of the present test results could be produced by

$$H_{32} = \frac{4 H_{12}}{3 H_{12} - 1} + 0.1 \cdot Ma \quad (12)$$

A comparison of this equation with the test results is shown in figure 20, where the inlet Mach number was used to correlate the experimental data with eq. (12).

Further the Truckenbrodt method relies on the substitution of the subsidiary shape factor L defined as

$$L = \ln H = \int_{H_{32}}^{H_{12}} \frac{dH_{32}}{(H_{12} - 1)H_{32}} \quad (13)$$

where H_{32} is the value for flow with zero pressure gradient. Substitution of equation (12) into (13) then produces a relationship between H_{12} and H or H and H_{12} and this new dependence is plotted for different values of H_{12} in figure 21 and is compared with the revised curve used for all boundary layer calculations reported in this contribution. For turbulent boundary layer a mean value of $H_{12} = 1.3$ is generally in use. The present results are better correlated by a value of $H_{12} = 1.4$ which leads to the relationship for the case of $Ma = 0$

$$H = \frac{0.875}{H_{32}} \cdot \frac{1}{\sqrt{2 - H_{32}}} \quad (14)$$

The constant 0.875 changes to 0.816 if $H_{12} = 1.3$ is applied. The new relationship $H_{12}(H)$ shows a small influence of the Mach number which was not considered in the present method. Furthermore the new function is not identical with the revised curve used in the present investigation, but for attached flow ($H_{12} < 2.8$) the differences are small. The above discussion of additional boundary layer analysis is included to illustrate that the presented experimental data could easily be applied to derive improved boundary layer prediction methods for high subsonic Mach numbers.

5. CONCLUSIONS

The contribution describes theoretical and experimental investigations of the boundary layer and loss behaviour on a high turning DCA-compressor cascade to achieve 50° of deflection up to 0.85 inlet Mach numbers. The objective of this investigation was to obtain detailed data to check theoretical blade profile design methods which are being developed. For the present investigation a time marching method was used to predict the blade pressure distribution. This was iteratively coupled with a boundary layer integral method to predict the boundary layer integral parameters and the total losses. The experiments were carried out in the High Speed Cascade Wind Tunnel of the DFVLR Braunschweig to obtain the cascade characteristics and boundary layer parameters. The investigations led to the following conclusions:

1. The predicted blade pressure distributions and choking flow limits are in good agreement with the experiments near design inflow angles.
2. In the case of good agreement between predicted and measured pressure distribution, an acceptable agreement can be achieved between the predicted and measured boundary layer parameters.
3. The boundary layer measurements confirm in principle the boundary layer integral method used. From these measurements a modification was derived which gave adequate agreement between predicted and measured boundary layer parameters up to 0.85 Mach numbers and thus permitted the determination of the turbulent boundary layer separation ($H_{12} > 2.8$).
4. The theoretical method used in this investigation is unsatisfactory for performance assessment at conditions remote from the design point operation.
5. The presented experimental data could be applied to derive improved boundary layer prediction methods at both design and off design conditions.

ACKNOWLEDGMENT

The authors wish to thank Rolls-Royce plc and DFVLR for permission to publish this material. The assistance of P. Geisler, G. Iaskowski and D. Scoltock during the measurements and the data evaluation is also appreciated. The opinions expressed in this paper are those of the authors and are not necessarily those of Rolls-Royce plc.

REFERENCES

- (1) Mease, G.
Viscous-Inviscid Flow Interaction Methods Shock Boundary Layer Interaction
ONERA T.P. no 1984-114
- (2) Schäfer, O., Frühauf, H.H., Bauer, P., Giguère, M.
Application of a Navier-Stokes Analysis to Flow Through Plane Cascades
AD85 Paper 85-07-56, 1986
- (3) Janaseni, P., Hirsch, Ch.
A Viscid-Inviscid Interaction Procedure for Two Dimensional Cascades
AGARD-CP-351, 1983
- (4) Calvert, W.J., Herbert, M.V.
An Inviscid-Viscous Interaction Method to Predict the Blade-to-Blade Performance of Axial Compressors
Aeronautical Quarterly, August 1980, pp. 173-196
- (5) Stark, U., Noheisel, H.
The Combined Effect of Axial Velocity Density Ratio and Aspect Ratio on Compressor Cascade Performance
Trans. of the ASME, Jour. Eng. for Power, Jan. 1981, Vol. 103 pp 247-255
- (6) Noheisel, H.
Die Verluste an Verdichtergitter bei unterschiedlichen Schaufelhöhenverhältnissen in Quasi-zweidimensionaler Strömung
VDI-Bericht Nr. 424, 1981, S. 131-142
- (7) Seyb, W.J.
The Role of Boundary Layers in Axial Flow Compressor Loss and the Prediction of their Effects
AGARDograph No. 164, 1972, pp. 241-279

- [8] Roberts, W.B.
The Effect of Reynolds Number and Laminar Separation on Axial Cascade Performance
ASME-Paper 74-GT-68, 1974
- [9] Truckenbrodt, E.
Ein Quadraturverfahren zur Berechnung der laminaren und turbulenten Reibungsschicht
bei ebener und rotationssymmetrischer Strömung
Ing.-Archiv XX BD. Heft 4, S. 211-228
see also: H. Schlichting Boundary-Layer Theory, Sixth Edition 1968, Mc Graw-Hill
Book Company London, Verlag G. Braun Karlsruhe
- [10] Stewart, W.L.
Analysis of two-dimensional compressible flow loss characteristics downstream of
turbomachine blade rows in term of basic boundary layer characteristics
NACA TN 3515, 1955
- [11] Hoheisel, H., Klock, R.
Zwanzig Jahre Hochgeschwindigkeits-Gitterwindkanal des Instituts für Aerodynamik
der DFVLR Raunschwieg
Zeitschr. Flugwiss. Weltraumforsch., Vol. 1, No. 1 (1977) pp 17-29
- [12] Sturm, W., Fottner, L.
The High-Speed Cascade Wind-Tunnel of the German Armed Forces University Munich
Paper presented at the 8th Symposium on Measuring Techniques for Transonic and
Supersonic Flows in Cascades and Turbomachines Oct. 1985, Genua, Italy
- [13] Hoheisel, H.
Der Hochgeschwindigkeits-Gitterwindkanal - immer noch eine wichtige Versuchsanlage
für Untersuchungen an Turbomaschinenbeschaufelungen
DFVLR-Mitt. 86-11 (1986)
- [14] Klock, R., Laskowski, G., Hoheisel, H.
Die Erzeugung höherer Turbulenzgrade in der Meßstrecke des Hochgeschwindigkeits-
Gitterwindkanals, Braunschweig zur Simulation turbomaschinenähnlicher Bedingungen
DFVLR-FB 82-25 (1982) see also GSA-TT815 (1983)
- [15] Hoeger, M., Hoheisel, H.
On the accuracy of boundary layer measurements in cascades at high subsonic speeds.
7th Symposium on measuring techniques for transonic and supersonic flow in cascades
and turbomachines, Aachen (1983)
Mitt. 1/84 Inst. Strahlantriebe RWTH Aachen 1984
- [16] Hoheisel, H., Hoeger, M., Meyer, P., Koeber, G.
A comparison of laser-Doppler anemometry and probe measurement within the boundary
layer of an airfoil at supersonic flow.
Laser Anemometry in Fluid Mechanics, Second Symposium, Lisbon-Instituto
Superio Technico, Lisbon-Portugal 1985
- [17] Anack, J.
Anwendung der transsonischen Ähnlichkeitsregel auf die Strömung durch ebene Schau-
felgitter, VDI-Forschungshft 540 (1970) pp 14-28
- [18] Klock, R.
Auswertung von Grenzschichtmessungen in zweidimensionaler kompressibler Unterschall-
strömung mit Druckgradient in der Grenzschicht
DFVLR-Mitt. 82-14 (1982)
- [19] Hoheisel, H., Klock, R., Lichtfuß, H.J., Fottner, L.
Influence of free stream turbulence and blade pressure gradient on boundary layer
and loss behaviour of turbine cascades
ASME-Paper No. 84-GT-234, 1984
- [20] Carrhar, D., Kingston, T.R.
Some Turbomachinery Blade Passage Analysis Methods - Retrospect and Prospect
AGARD 66th (8) Specialists' Meeting of FFR on Transonic and Supersonic Phenomena in
Turbomachines, Munich, Germany, 10-12 Sept. 1986

x/c	y_{PS}/c	x/c	y_{SS}/c
0	0.0049	0	0.0049
0.0003	0.0033	0.0014	0.0082
0.0012	0.0017	0.0020	0.0087
0.0020	0.0009	0.0054	0.0112
0.0040	0.0001	0.0120	0.0156
0.0066	0.0003	0.0254	0.0244
0.0103	0.0018	0.0355	0.0309
0.0196	0.0034	0.0665	0.0493
0.0242	0.0071	0.1017	0.0683
0.0335	0.0106	0.1341	0.0840
0.0662	0.0222	0.1672	0.0983
0.0992	0.0329	0.2007	0.1113
0.1325	0.0428	0.2348	0.1229
0.1660	0.0519	0.2655	0.1320
0.1997	0.0601	0.3004	0.1409
0.2336	0.0674	0.3317	0.1576
0.2677	0.0738	0.3672	0.1538
0.3020	0.0793	0.3989	0.1581
0.3314	0.0834	0.4348	0.1615
0.3659	0.0873	0.4667	0.1633
0.4005	0.0903	0.4988	0.1639
0.4351	0.0924	$r_L/c =$	0.0049
0.4698	0.0936	$r_T/c =$	0.0049
0.4995	0.0940		

Table 1:
Profile Coordinates (nominal)

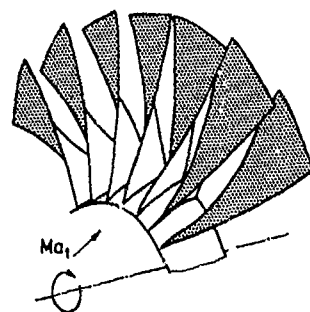
SS, $Re_1 = 4.1 \times 10^5$, $Re_2 = 5 \times 10^5$												
VM	θ_1 (°)	Re_1	α	x/l	t_1 (mm)	t_2 (mm)	H_{12}	H_{22}	Re_{12}	Re_{22}	VM	DU
11145	15.5	0.3	1.00	0.88	1.078	1.044	2.894	1.476	5328	8353		
152				0.78	0.915	0.871	1.844	1.392	2494			
200				0.42	0.478	0.275	1.239	1.032	1769			
11144			1.20	0.88	1.346	0.634	2.124	1.395	3335	8356		
174				0.88	0.894	0.412	2.048	1.451	2971			
151				0.78	0.634	0.302	1.811	1.388	1838			
167				0.42	0.361	0.228	1.566	1.255	1327			
199				0.42	0.238	0.124	1.357	1.050	912			
11149			1.032	0.88	1.793	1.072	4.471	1.584	6510	9359		
154				0.78	1.667	0.848	2.982	1.575	3419			
134				0.42	0.369	0.200	1.844	1.204	1270			
11148			1.085	0.88	1.042	1.084	2.782	1.530	5700	9354		
155				0.78	0.879	0.484	1.894	1.442	2573			
197				0.42	0.411	0.192	2.145	1.454	1254			
11146			1.20	0.88	1.847	0.594	2.687	1.595	3610	9360		
173				0.88	0.831	0.429	1.950	1.447	2343			
153				0.78	0.611	0.286	1.638	1.427	1712			
168				0.42	0.449	0.244	1.835	1.211	1586			
189				0.42	0.263	0.118	2.231	1.435	815			
11147			1.28	0.88	1.749	0.540	2.349	1.687	2826	9354		
154				0.78	0.666	0.258	1.810	1.498	1617			
189				0.42	0.340	0.119	2.457	1.424	850			
11184			0.6	1.12	0.88	1.942	0.780	1.057	1.569	1891	8342	
177				0.88	1.940	0.685	1.833	1.561	1607			
159				0.78	1.145	0.529	2.125	1.723	2930			
172				0.42	0.688	0.361	2.250	1.618	2343			
190				0.42	0.422	0.204	2.101	1.486	1509			
11150			1.20	0.88	2.919	0.781	2.889	1.547	3935	8344		
159				0.78	0.783	0.422	1.883	1.707	2435			
191				0.42	0.423	0.214	1.947	1.480	1403			
11103			1.22	0.88	1.930	1.368	2.573	1.639	2638	9358		
175				0.88	1.104	0.922	1.848	1.717	2447			
160				0.78	1.146	0.845	1.831	1.729	2138			
149				0.42	0.827	0.486	1.773	1.744	1403			
192				0.42	0.421	0.184	2.163	1.508	1142			
11181			0.85	1.13	0.88	1.458	1.174	1.941	1.574	6110	8338	
162				0.78	1.424	0.616	1.184	1.607	4571			
197				0.42	0.491	0.260	1.883	1.733	1904			
11180			1.16	0.88	1.804	1.105	1.804	1.574	5789	8340		
178				0.88	1.206	0.981	2.145	1.627	3643			
162				0.78	1.189	0.782	2.023	1.682	3370			
171				0.42	0.830	0.481	1.894	1.730	2432			
194				0.42	0.491	0.244	1.895	1.700	1572			
1.179			1.20	0.88	2.693	1.397	2.787	1.689	7590	8341		
164				0.78	1.405	0.888	1.609	1.730	5146			
193				0.42	0.519	0.212	2.150	1.541	1417			
11182			1.21	0.88	1.116	1.235	1.125	1.640	12681	8342		
179				0.88	1.123	0.808	1.100	1.633	12441			
164				0.78	1.427	1.193	1.174	1.694	8910			
170				0.42	0.832	0.632	1.414	1.632	5668			
194				0.42	0.372	0.150	1.040	1.497	1011			

Table 2:
Test Results
(Evaluation A)

SS, $Tu_1 = 44$; $Re_1 = 5 \cdot 10^5$													
TP BLN	δ_1 (°)	Re_{δ_1}	α	$\pi/1$	δ_1 (mm)	δ_2 (mm)	H_{12}	H_{22}	Re_{δ_2}	$\Delta\theta$ (°)	ζ_{PI}	TP PDM	
11270 273 774 277	47,5	0,8	1,083	0,94	3,513	0,693	5,074	1,543	3474	45,2	0,0461	8325	
				0,88	1,418	0,549	2,580	1,553	2820				
				0,78	0,784	0,379	2,074	1,638	2085				
				0,62	0,485	0,248	1,956	1,694	1509				
				0,42	0,327	0,154	2,128	1,685	1011				
11271 275 276 277 279			1,17	0,98	4,209	1,511	2,785	1,625	8184	46,0	0,0880	8321	
				0,88	2,190	1,073	2,042	1,660	6047				
				0,78	1,415	0,761	1,859	1,704	4473				
				0,62	0,847	0,444	1,908	1,727	2827				
				0,42	0,883	0,178	4,955	1,444	1237				
11145 152 200	49,5	0,3	1,07	0,98	3,193	1,088	2,936	1,484	5334	45,8	0,0435	8353	
				0,78	0,947	0,495	1,913	1,604	2581				
				0,42	0,467	0,270	1,729	1,644	1770				
11144 151 199			1,20	0,98	1,352	0,623	2,168	1,578	3242	49,0	0,0335	8356	
				0,78	0,404	0,252	1,604	1,726	1544				
				0,42	0,293	0,131	2,244	1,623	946				
11149 156 186			0,6	1,032	0,98	4,745	1,102	4,307	1,530	5553	46,5	0,0550	7355
					0,78	1,660	0,616	2,695	1,548	3214			
					0,42	0,365	0,196	1,864	1,709	1244			
11148 155 187			1,095	0,98	3,134	1,042	3,008	1,495	5274	47,5	0,0470	7356	
				0,78	0,872	0,447	1,952	1,616	2424				
				0,42	0,407	0,189	2,156	1,642	1252				
11146 177 153 168 188			1,20	0,98	1,812	0,656	2,762	1,571	3381	49,1	0,0374	7360	
				0,88	0,819	0,410	1,999	1,632	2252				
				0,78	0,331	0,213	1,554	1,747	1264				
				0,62	0,432	0,215	1,917	1,482	1396				
				0,42	0,272	0,116	2,270	1,633	804				
11147 154 189		1,28	0,98	1,269	0,516	2,367	1,549	2859	49,8	0,0349	7354		
			0,78	0,454	0,246	1,849	1,687	1538					
			0,42	0,339	0,118	2,887	1,534	846					
11184 177 159 172 190			0,8	1,12	0,98	3,958	0,770	5,143	1,543	3874	47,1	0,0458	8343
					0,88	1,845	0,659	2,952	1,531	3369			
					0,78	1,088	0,481	2,260	1,595	2570			
					0,62	0,842	0,373	2,261	1,624	2207			
					0,42	0,427	0,202	2,119	1,698	1289			
11190 158 191		1,20	0,98	2,931	0,715	4,100	1,534	3696	47,9	0,0468	8344		
			0,78	0,721	0,367	1,962	1,641	2094					
			0,42	0,420	0,211	1,892	1,635	1395					
11183 175 160 145 182			1,27	0,98	3,367	1,258	2,677	1,604	4938	46,8	0,0845	7358	
				0,88	1,581	0,811	1,849	1,659	4434				
				0,78	1,408	0,714	1,974	1,678	4282				
				0,62	0,752	0,407	1,846	1,729	2415				
				0,42	0,633	0,161	3,928	1,495	1118				

SS, $Tu_1 = 44$, $Re_1 = 5 \cdot 10^5$													
TP BLN	δ_1 (°)	Re_1	α	$\pi/1$	δ_1 (mm)	δ_2 (mm)	H_{12}	H_{22}	Re_{62}	$\Delta\theta$ (°)	ζ_{PT}	TP PCM	
11181 141 197	48,5	0,85	1,13	0,98	4,435	1,110	4,116	1,551	5853	47,3	0,0577	8338	
				0,78	1,754	0,738	2,313	1,604	4047				
				0,42	0,488	0,233	1,920	1,751	1477				
11180 154 162 171 196		0,6	1,16	0,98	4,200	1,055	3,880	1,552	5429	47,3	0,0413	8340	
				0,88	2,121	0,847	2,504	1,574	4442				
				0,78	1,345	0,745	2,101	1,654	4082				
				0,62	0,842	0,416	1,839	1,706	2546				
				0,42	0,487	0,235	2,036	1,719	1717				
11179 143 195		0,6	1,20	0,98	3,819	1,281	2,981	1,547	4193	47,8	0,0379	8341	
				0,78	1,401	0,710	1,972	1,637	4041				
				0,42	0,359	0,207	2,892	1,574	1382				
11182 176 164 150 188		0,6	1,21	0,98	3,000	1,523	2,735	1,614	4668	49,1	0,1432	8342	
				0,88	4,468	1,788	2,596	1,527	10736				
				0,78	2,386	1,392	2,218	1,565	8456				
				0,62	2,653	0,783	2,823	1,582	5027				
				0,42	0,334	0,156	4,755	1,552	1048				
11256 255 262	50,5	0,7	1,28	0,98	2,589	0,713	3,534	1,870	3475	50,8	0,0453	8338	
				0,78	0,209	0,438	2,388	1,598	2375				
				0,42	0,619	0,207	2,086	1,655	1335				
11252 253 256 262		0,6	1,12	0,98	1,425	1,627	2,781	1,675	13813	51,9	0,1173	8339	
				0,78	1,541	0,848	1,751	1,738	11120				
				0,62	1,860	1,027	1,737	1,737	5932				
				0,42	1,127	0,599	1,882	1,680	2681				
11253 256 259 268		0,6	1,36	0,98	2,589	0,710	3,642	1,847	3723	50,8	0,0452	7359	
				0,78	0,873	0,414	2,116	1,646	2396				
				0,62	0,511	0,285	1,923	1,719	1628				
				0,42	0,344	0,171	1,848	1,731	1162				
11252 255 259 262	50,5	0,6	1,04	0,98	0,891	2,734	1,631	1,639	18118	50,1	0,1291	7365	
				0,88	4,884	1,402	2,782	1,599	12723				
				0,78	1,089	0,710	1,731	1,655	1556				
				0,62	1,009	0,633	1,848	1,689	9070				
				0,42	2,238	1,234	1,678	1,731	4926				
11251 250 270 276		0,6	1,25	0,98	4,718	1,023	4,911	1,547	5419	51,6	0,0907	7357	
				0,78	1,673	0,684	2,446	1,570	2781				
				0,62	0,859	0,223	2,042	1,640	2067				
11253 256 259 262		0,6	1,23	0,98	1,626	1,634	1,823	1,619	15906	53,7	0,1884	7368	
				0,88	5,004	1,626	2,042	1,672	12115				
				0,78	1,320	1,387	1,878	1,685	9927				
				0,62	1,420	0,535	1,813	1,718	7881				
				0,42	1,502	0,923	1,748	1,776	5763				
11254 259 268		0,6	1,35	0,98	1,224	0,918	1,407	1,516	5261	53,0	0,0486	7351	
				0,78	1,132	0,599	1,860	1,682	2472				
				0,62	0,483	0,246	1,817	1,780	1573				

Table 1: Test Results (Evaluation C3)



Cascade Condition at the Hub:
Inlet Mach number $Ma_1 > 0.8$
Deflection $\Delta\theta \approx 50^\circ$
Spacing $s/c \approx 0.60$

Figure 1: Compressor Rotor

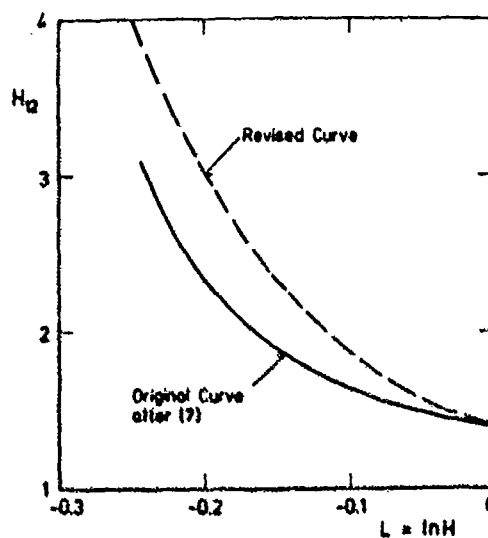


Figure 4: Shape Factor Correlation

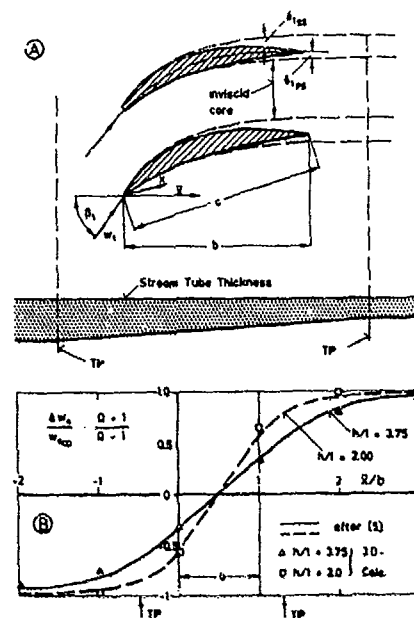
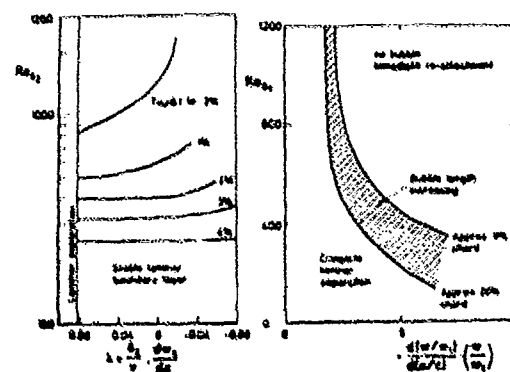
Figure 2: (A) Quasi 3D-Model
(B) Transition Function

Figure 3: Correlation of Laminar Boundary Layer Transition

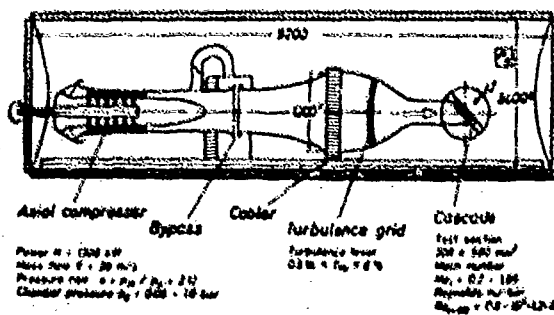
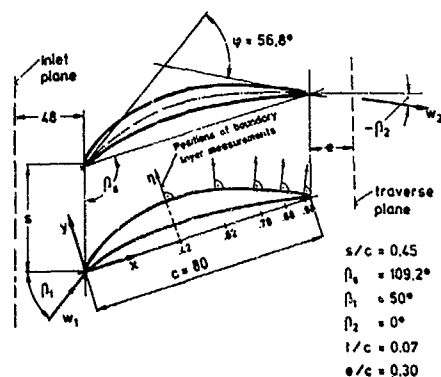


Figure 5: High Speed Cascade Windtunnel

① Cascade Geometry V2



⑧ Side Wall Conditions

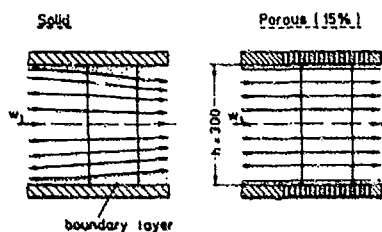


Figure 6: Cascade Geometry V2 and Test Section Side Wall Conditions

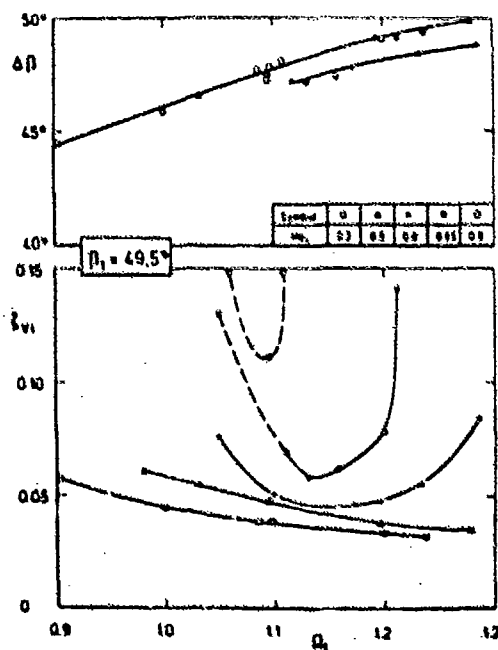


Figure 6: Effect of AVDR on Measured Cascade Performance on Different Mach Number, $M_1 = 49.5^{\circ}$

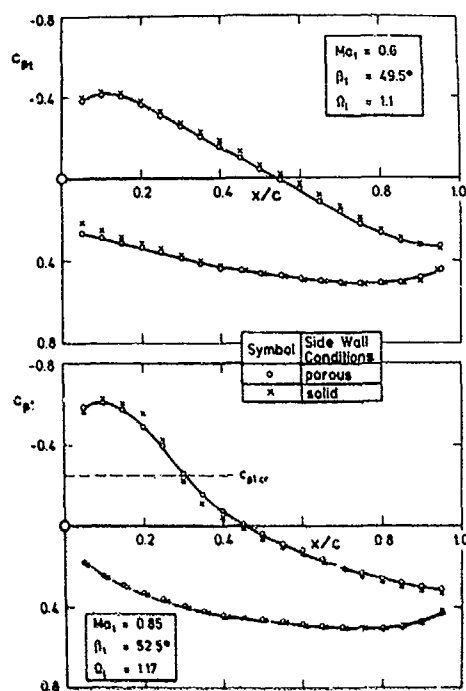
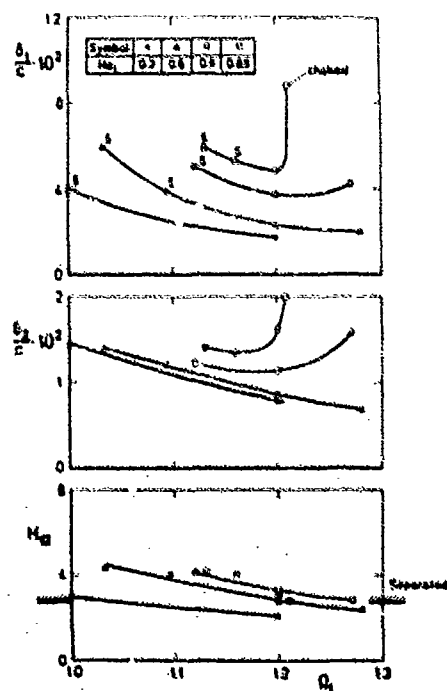


Figure 7: Effect of Side Wall Condition on Measured Blade Pressure Distribution



**Figure 9: Boundary Layer Parameter,
Section Surface $\theta_1 = 49.5^\circ$
Measurement at $x/c = 0.98$**

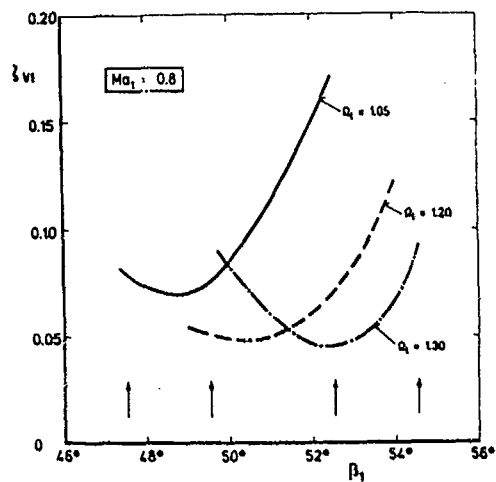


Figure 10: Effect of Inlet Angle on Measured Cascade Performance at Different Values of AVDR, $Ma_1 = 0.8$

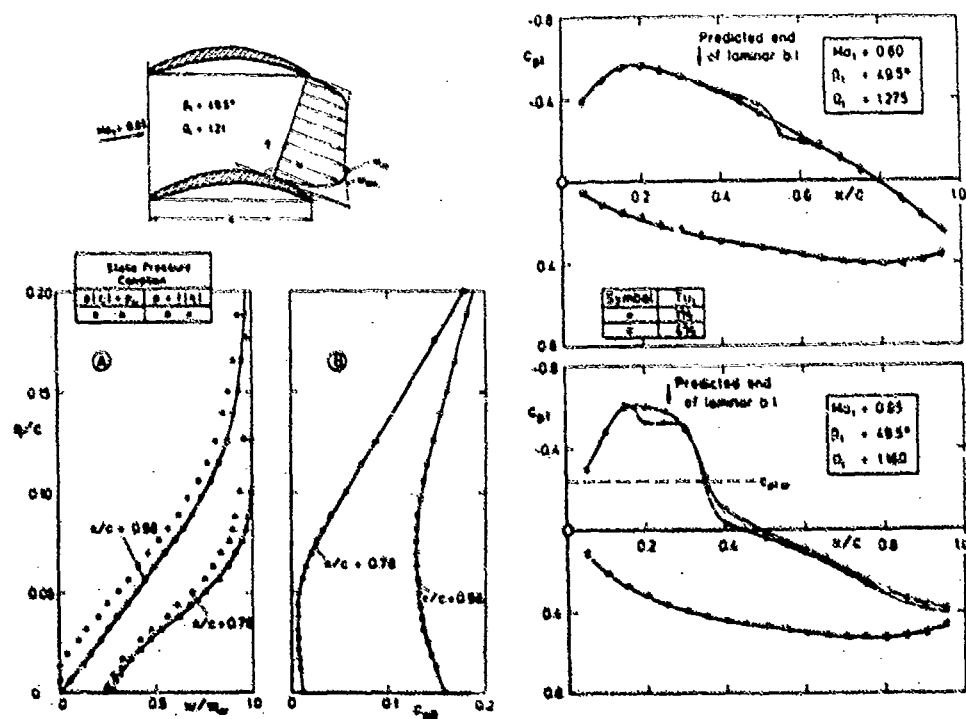


Figure 11: Boundary Layer Velocity Profiles and Static Pressure, Suction Surface

Figure 12: Effect of Free Stream Turbulence on Measured Blade Pressure Distribution

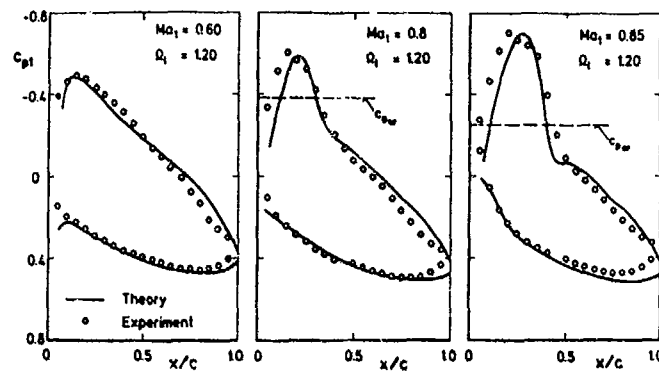


Figure 13a:
Pressure Distribution
Influence of Mach Number
 $\alpha_1 = 49.5^\circ$ $\alpha_1 = 1.20$
Comparison Theorie-Experiment

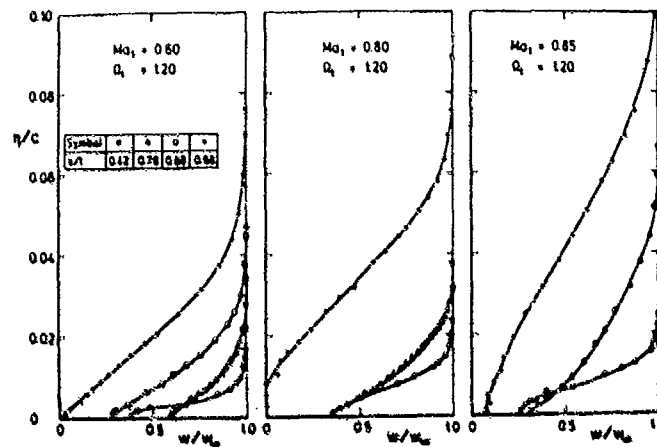


Figure 14a:
Boundary Layer Velocity
Profiles, Suction Surface,
 $\alpha_1 = 49.5^\circ$ $\alpha_1 = 1.20$

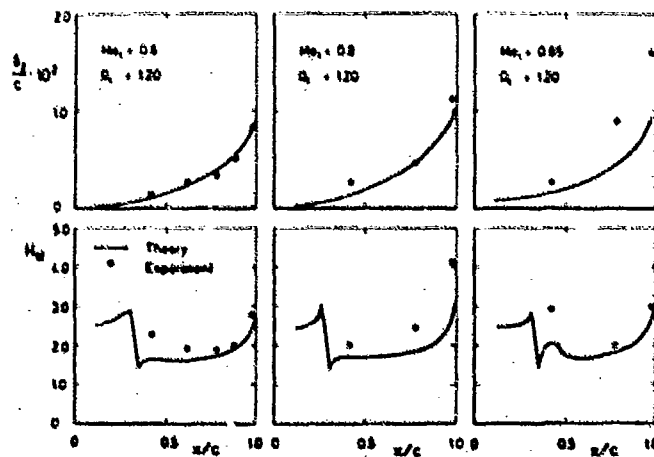


Figure 15a:
Local Boundary Layer
Parameters, Suction Surface
 $\alpha_1 = 49.5^\circ$ $\alpha_1 = 1.20$

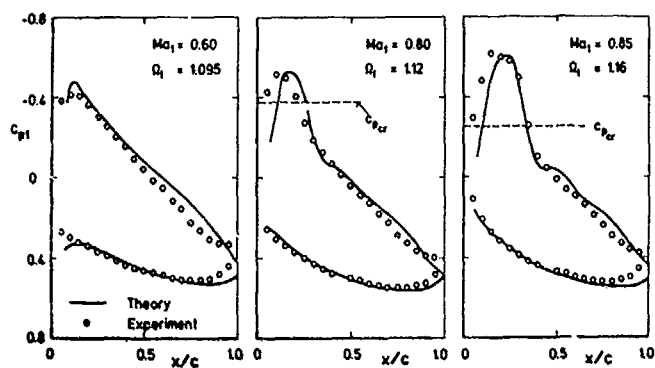


Figure 13b:

Pressure Distribution,
Influence of Mach Number
 $\beta_1 = 49.5^\circ$ $\rho_1 < 1.20$;
Comparison Theory-Experiment

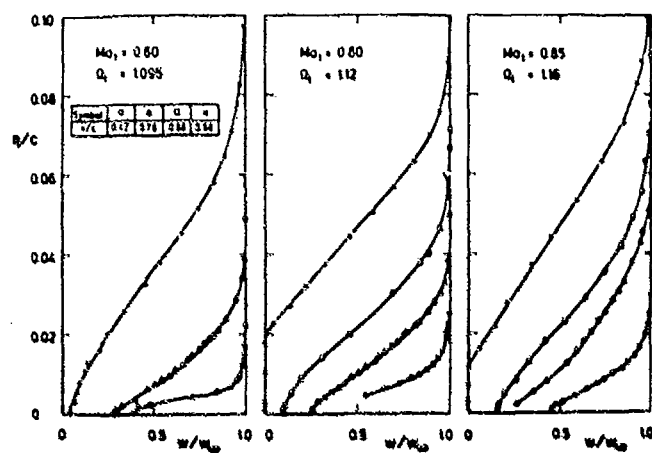


Figure 14b:

Boundary Layer Velocity
Profiles, Suction Surface,
 $\beta_1 = 49.5^\circ$ $\rho_1 < 1.20$

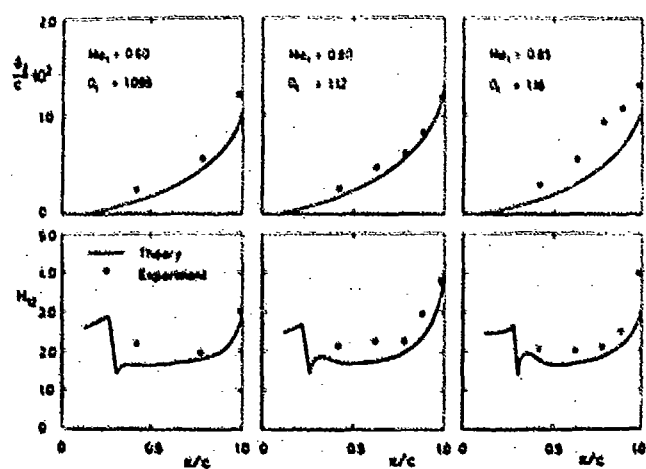


Figure 15b:

Local Boundary Layer
Parameters, Suction Surface
 $\beta_1 = 49.5^\circ$ $\rho_1 < 1.20$

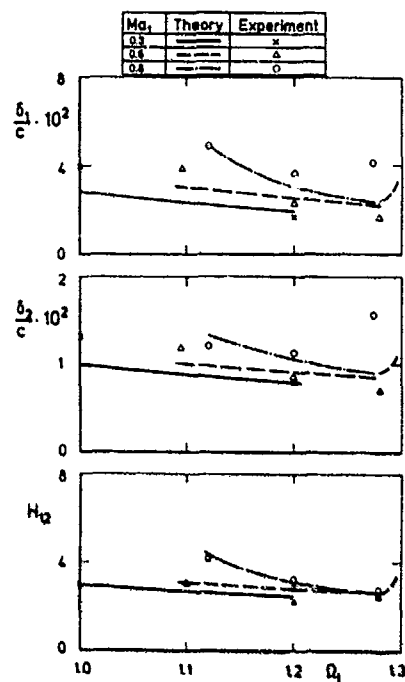


Figure 16: Boundary Layer Parameter at Trailing Edge $\beta_1 = 49.5^\circ$

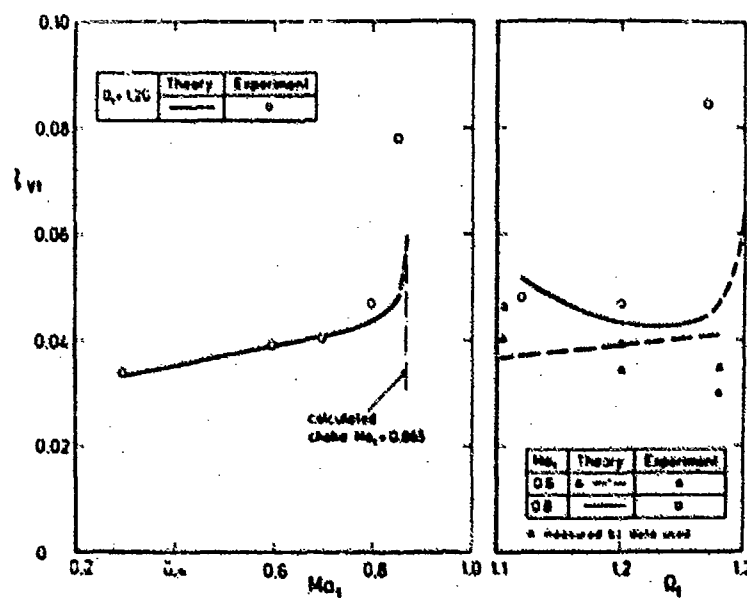


Figure 17: Loss Coefficient at $\beta_1 = 49.5^\circ$, Comparison Theory - Experiment

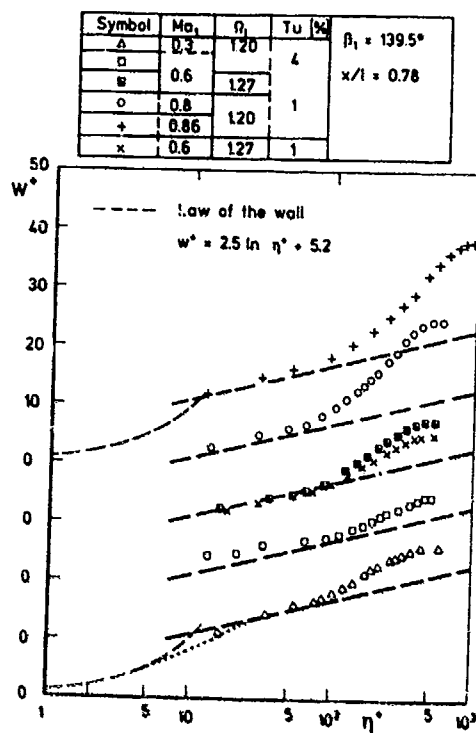


Figure 18: Measured Boundary Layer Velocity Profiles, Law of the Wall Correlation

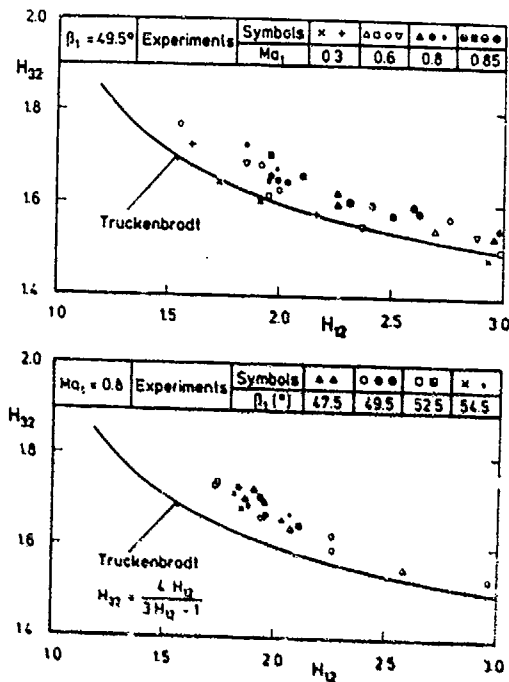


Figure 19: Boundary Layer Shape Factors, Comparison Theory - Experiments

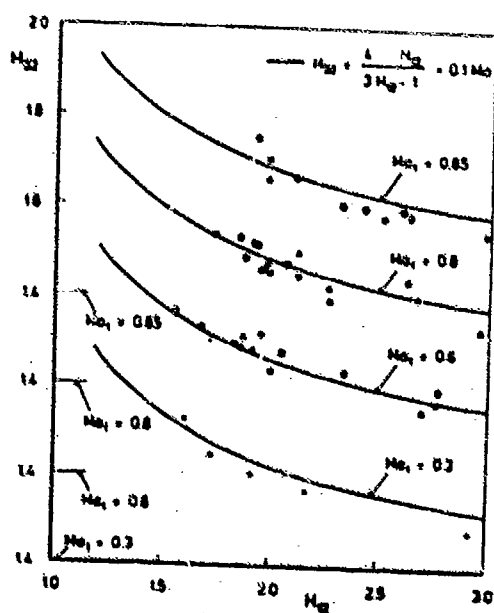


Figure 20: Modified Boundary Layer Shape Factors Comparison Theory - Experiments

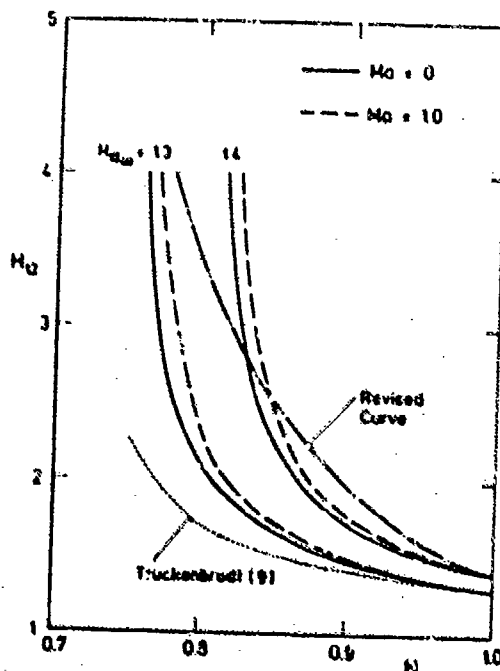


Figure 21: New Shape Factors

VORTEX SHEDDING IN COMPRESSOR BLADE WAKES

A.H. Epstein, J.B. Gertz, P.R. Owen and M.B. Giles
Gas Turbine Laboratory
Massachusetts Institute of Technology
Cambridge, MA 02139 USA

SUMMARY

The wakes of highly loaded axial compressor blades have often been considered to be turbulent, unstructured flows. Recent work has suggested that the blade wakes are in fact dominated by a vortex street-like structure. This paper reviews the work on wake structure at MIT, presents the results of a viscous numerical simulation, compares the blade wake vortices to those shed from a cylinder, and discusses the implications of the wake structure on compressor performance. In particular, a two-dimensional, time accurate, viscous calculation shows both a periodic wake structure and time variations in the passage shock strength. The numerical calculations are compared to laser anemometer and high frequency response probe data. The effect of the wake structure on the entropy production and apparent adiabatic efficiency of the compressor rotor is discussed.

1. INTRODUCTION

Although bluff bodies and low speed airfoils have long been known to shed vortices into their wakes, the wakes of high speed, high Reynolds number turbomachinery blading have generally been considered to be turbulent and unstructured. Usually, the wake is described only in terms of a time averaged velocity profile. This is consistent with the view that, assuming uniform inflow and excepting turbulence, the flow in the frame moving with the compressor rotor is uniform and that variations observed in the stationary frame are primarily due to blade geometric differences. This view, however, is erroneous in detail with practical import for compressor design.

There is a considerable body of experimental data which shows that blunt trailing edge airfoils typical to turbines shed vortex streets [1], [2], [3]. Recent work has shown that a similar phenomenon may occur in sharp trailing edge transonic compressors as well [4].

If we assume for the moment that high speed compressor blade wakes can consist of a vortex street-like structure, then a number of questions immediately become relevant. These include: do all blade wakes contain vortices; why are the vortices rarely observed experimentally; how are the vortex streets formed and what is their structure; and what is the practical importance of the wake structure to the compressor designer? We will address the last question first so as to provide a groundwork for the discussions which follow.

In the context of high efficiency, high performance transonic compressors and fans, the influence of the wake temporal and spatial structure for a given time averaged velocity defect can be surprisingly large. The wake structure can influence the compressor aerodynamics, noise, and structural integrity. Vortex shedding decreases the blade row efficiency (higher base drag and shock loss, increased unsteadiness) and induces artifacts in standard measurement techniques. An increased level of unsteadiness into following blade rows can increase the loss there and alter the mass flow characteristic, independently of whether that blade row is itself shedding vortices. The interaction of the shed vortex street with subsequent blade rows is also a source of noise. Obviously, the unsteady loading due to the vortex streets and related phenomena can have deleterious effects on the structural integrity of a compressor when the aerodynamic excitation frequencies coincide with those which are structurally important. The blade wake structure also influences compressor design and analysis in that it represents a physical phenomenon not usually modelled (either because the analysis is inviscid or steady state). Thus, the design intent may not represent a physically realizable system.

This paper is an extension of previous work in which the presence of vortex streets was inferred from experimental measurements and their effect on the blade shock system discussed [4], [5]. Here, we review that work, discuss the effects of vortex streets on the temperature distribution within the flow, note the influence of the wake structure on conventional aerodynamic performance measurements, present the results of an ab initio numerical simulation showing similar behavior, and suggest areas for further investigation.

2. REVIEW OF EXPERIMENTAL OBSERVATIONS

Flow visualization studies have demonstrated the existence of vortex streets in the wakes of transonic flat plate and turbine airfoil cascades [1], [2], [3] but, excepting the special case of acoustic resonance enhanced shedding [6], [7], shedding in high speed compressor airfoils had not been conclusively reported. Hot wire measurements in the wakes of controlled diffusion airfoil cascades yielded ambiguous results [8] with one configuration showing evidence of periodicity in the wake while

another did not. In the context of hydrofoils, Blake [9] suggested that all bodies shed but may do so in a discontinuous fashion, i.e., shed in bursts. Lack of phase coherence between the bursts would then tend to obscure the shedding when examined with spectral analysis techniques. This is consistent with the observation that the least ambiguous information has been instantaneous flow visualizations.

Time resolved measurements in the outflow of 3 transonic compressor rotors operating near the compressors' peak efficiency points revealed high frequency (3 to 4 times blade passing) total pressure and temperature fluctuations of substantial amplitude in the core flow between the wakes, as well as large fluctuations in the wake strength of any particular blade [5], Fig. 1. Similar observations were made in three different single stage transonic compressors in three different test facilities using a variety of high frequency response probe types [11]. The machines differed in design intent (both commercial fan and high speed military designs were included), but all operated at high rotor efficiency (above 90%). The outflow of all three rotors demonstrated similar types and degrees of rotor relative unsteadiness, the unsteadiness being maximum near the design or maximum efficiency operating point. This indicates that rotor relative unsteadiness is a common phenomenon in transonic compressors.

A laser anemometer physically measures one or more components of the instantaneous velocity at a point in space. Because of the relatively high level of turbulence common to turbomachinery, the instantaneous velocity measurements are usually averaged and the result presented as the average velocity at that point (Fig. 2a). The velocity statistics at the point can also be examined however (although this is not commonly done), and can be presented in terms of a probability density distribution (PDD), a histogram showing the number of observations made at each value of velocity. For a turbulent flow, the shape of this histogram should be Gaussian. Laser anemometer measurements in the vicinity of the passage shock have shown a bimodal velocity distribution indicative of a shock moving to either side of the measurement point [10]. These observations were explained in terms of small (0.5% of axial chord) motion of the passage shock about its mean position. Vortex shedding in the blade wake was advanced as a possible driver of this motion [5].

Subsequent laser anemometer measurements in the rotor wakes revealed that the velocity distributions were bimodal there as well; i.e., two velocities were equally likely with almost no measurements observed at the "average" velocity as it would be normally derived from such data [4], Fig. 2. Simultaneous time resolved temperature and pressure probe measurements in the rotor outflow showed unsteadiness relative to the rotor at two time scales. One was the high frequency disturbances mentioned above. The second appeared primarily as a modulation of the wake flow with frequency components on the order of 1/2 to 3 times shaft rotational speed. This modulation could not be explained in terms of blade to blade geometric differences since the fluctuations were primarily aperiodic with rotor rotation (and thus not locked to the geometry) and were several times the magnitude of the periodic disturbances. A striking feature of the disturbances themselves was the large total temperature fluctuations in the wakes--13-5% of the mean total temperature (i.e., 10-20°C)--indicating local regions of intense cooling and heating. The instantaneous adiabatic efficiency calculated from these measurements showed a concomitant variation with some local regions appearing as over 100%. These temporal fluctuations and laser anemometer measurements were explained as resulting from a vortex street structure in the blade wakes. The over 100% efficiency observations have yet to be explained.

3. DESCRIPTIONS OF THE BLADE WAKE AND VORTEX STREET

In the previous work, the wake was modeled as two staggered rectilinear rows of Rankine vortices of opposite sign in a uniform freestream [11]. The vortices consist of an inner region with a forced-vortex core and an outer region following the irrotational flowfield of a classic von Karman vortex street. This model was fit to the laser anemometer data so that the time averaged velocity profile and the statistical distribution of velocities (the probability density distribution) in the wake would match. The vortex size and strength were adjusted to fit the velocity profile while the ratio of the streamwise vortex spacing (Λ) to the distance between vortex rows (H) determined the velocity statistics (see Fig. 3).

As can be seen in Fig. 3, the model fits the data relatively well, which is a consistency check. The model prediction of a shedding frequency of 16.2 kHz is quite close to the 14-15 kHz inferred from the core flow pressure fluctuations. Furthermore, the model readily explains the high level of fluctuations observed in the wake with the high frequency response probes. This is an artifact of sampling caused by the random position of the vortices in the wakes as the compressor revolves past the probe location. Figure 4 compares the absolute frame rotor outflow total pressure fluctuations predicted by the model with measurements.

While the vortex street model in [11] does a good job of explaining many of the experimental observations, it is a static model, describing the wake state only at a particular axial station. Thus, it contains no information on the vortex formation process, its evolution or decay. At this time we know of no published analytical model describing this process in detail.

4. DYNAMIC ENERGY REDISTRIBUTION

One of the more interesting implications of identifying the structure of the wake of a transonic compressor blade as containing a vortex street is that the unsteady pressure field in the blade relative frame can redistribute thermal energy. The vortex street propagates at a velocity different from that of the mean flow and entrains fluid into and through the wake. As the entrained fluid passes through the pressure field of the vortex, its total enthalpy can be changed. In essence, the vortex street can be thought of as an array of tiny turbomachines!

The dynamics of this problem have been addressed by McCune [12] with a straightforward unsteady energy equation analysis. He shows that the pressure field fluctuations from the vortices change the total temperature distribution in the fluid and that this effect scales with the square of the freestream Mach number. At Mach 1, the vortices are predicted to produce a temperature fluctuation of 3-5% of the freestream total temperature, quite close to the observed value. This scaling with Mach number explains why the effect was first noticed in a high speed machine (tip relative Mach number of 2.2).

Kurosaka et al. treat the problem in terms of the general Eckert-Weise effect [13] in which the recovery factor at the rear of a shedding right circular cylinder can be negative and the wake centerline cooled to below the freestream inflow value, showing that this is the result of vortex street behavior [14]. A key point is that this cooling by the vortices is observed with steady state instrumentation, i.e., the average centerline temperature is depressed. There must, of course, be a concomitant increase in total temperature in the surrounding flow outside the wake. Kurosaka also demonstrated that the vortex shedding and temperature separation can be significantly enhanced with acoustic feedback, essentially extending acoustic resonance work to include energy separation [6], [7].

The intense, localized hot and cold spots generated by the vortex street explain the large, abrupt temperature fluctuations observed in the time resolved total temperature measurements of the compressor wakes.

5. WAKE STRUCTURE EFFECTS ON APPARENT COMPRESSOR EFFICIENCY

An earlier work on high frequency passage shock motion driven by vortex shedding identified three mechanisms by which the loss in the compressor could increase [5]. The first is the increase in entropy rise across a shock wave undergoing small periodic axial motion compared to that for a steady shock at the same average approach Mach number. This change was quite small, amounting to only a 0.1 to 0.2 percent decrease of adiabatic efficiency in the rotor studied. The second loss source was the small scale nonuniformities in total pressure generated by the oscillating shock wave. In this case, it was assumed that due to the small spatial extent of the perturbation (1/8-1/4 chord), the enthalpy would not be recovered as pressure rise in the diffusion process in the stator but rather appear as a mixing loss downstream. This loss was calculated to be of the same order as the wake mixing loss, about 1% (10% of the total measured stage loss). The third loss mechanism is the amplification of the spatial nonuniformities in the stage outflow, discussed above, by the shock system in a following transonic stage. This loss was estimated to be 2 to 3 times as great as that in the first stage, i.e., 2 to 3 percent of stage adiabatic efficiency.

In this section we wish to discuss not additional thermodynamic loss mechanisms (i.e., production of entropy), but rather apparent losses, artifacts induced in the measurement processes and their interpretation by the periodic nature of the wake structure. If not properly accounted for, these artifacts can result in an erroneous estimate of compressor performance.

Before doing so, however, we wish to point out a simple curiosity. Adiabatic efficiency is often used to express turbomachine loss (entropy production). In an unsteady flow, however, the change in adiabatic efficiency need not be congruent with the entropy production, as it must in a steady flow.

To illustrate this, we will define the local adiabatic efficiency, η , in the usual manner relating the total pressure, P_t , and total temperature, T_t , ratios in the absolute (laboratory) frame as follows,

$$\eta = \frac{\left(\frac{P_{t2}}{P_{t1}}\right)^{\frac{\gamma-1}{\gamma}}}{\left(\frac{T_{t2}}{T_{t1}}\right)} - 1 \quad (1)$$

where the subscripts 1 and 2 denote stations upstream and downstream of the rotor blade. Station 1 is assumed to have uniform conditions of total temperature and pressure as would be the case with the first stage of a compressor. Station 2 consists of a freestream region with the blade wakes represented by vortex streets as modelled in [11], with the total pressure and temperature contours as shown in Figs. 5 and 6. The

change in entropy, S , from station 1 to station 2 may be expressed as,

$$e^{-(S_2-S_1)/c_p} = \frac{\left(\frac{P_{t2}}{P_{t1}}\right)^{\frac{\gamma-1}{\gamma}}}{\left(\frac{T_{t2}}{T_{t1}}\right)_{\text{abs}}} \quad (2)$$

This can be seen in Fig. 7 for the vortex model with a freestream stagnation temperature ratio of 1.175. As expected, the entropy variation is zero in the regions outside the vortex cores since the model allows only variation in the vortex cores themselves.

Equation (1) for the efficiency may now be re-written by eliminating the stagnation pressure ratio using Eq. (2).

$$\eta = \frac{\left(\frac{T_{t2}}{T_{t1}}\right)_{\text{abs}}^{-(S_2-S_1)/c_p} - 1}{\left(\frac{T_{t2}}{T_{t1}}\right)_{\text{abs}}} \quad (3)$$

If there is no change in entropy from station 1 to station 2 then the efficiency is exactly 1.0 regardless of the variations in total temperature. However, if between stations 1 and 2 there is some loss mechanism (such as a normal shock) so that $S_2 > S_1$ in the freestream region, then the efficiency will be less than 1.0 and, in fact, will vary through the vortex street as the total temperature varies. This will be the case even outside the vortex cores in the wake where the flow is modelled to be irrotational and is inviscid. In these regions the entropy does not vary as shown in Fig. 7. This means that the value of entropy outside the vortex core is constant and so the value of (S_2-S_1) is constant as well. Now since the flow in the absolute frame is unsteady (with or without vortex shedding) and the gradient of entropy is zero outside the cores, the total temperature must vary according to Crocco's theorem which may be written as follows,

$$T \nabla S = \frac{1}{c_p} \nabla \left(\frac{1}{2} V^2 \right) + \frac{\partial T}{\partial t} \quad (4)$$

In the regions outside the vortex cores this reduces to,

$$c_p \frac{\partial T}{\partial t} = -\frac{\partial \left(\frac{1}{2} V^2 \right)}{\partial t} \quad (5)$$

This implies that the total pressure must vary so as to keep (S_2-S_1) constant. In any case, since (S_2-S_1) is constant and T_{t2}/T_{t1} varies throughout the vortex street, the efficiency will vary as well, even though the entropy is constant! This can be seen by comparing Figs. 7 and 8. The efficiency is not congruent with the entropy change. Because of the energy separation mechanisms discussed in section 4, the total temperature in local regions can be greater or less than that of the freestream. Thus, there are regions in which the efficiency is greater than the freestream value. It should be pointed out, however, that no matter how large the variations in total temperature, the efficiency will always be less than one, since by Eq. (3), S_2-S_1 is always greater than zero.

It is important to note that this difference between entropy rise and efficiency is due to the unsteadiness in the absolute frame, not the blade relative frame, and thus is not dependent on the state of the blade wake. Rather, it is common to all transonic and supersonic machinings. The practical significance of this observation has yet to be elucidated but the authors find it interesting.

The structure of the compressor blade wakes can make a difference in the aerodynamic efficiency as commonly measured with aerodynamic probes in the rotor outflow. To illustrate this, we will consider two transonic compressor rotors with the same geometry, true mass averaged total pressure and temperature rise, and, therefore, the same mixed out adiabatic efficiency. One blade will be assumed to have a classic turbulent wake while the other's wake will consist of a vortex street with the same average velocity defect. In other words, the wakes as measured by conventional laser anemometry techniques would appear identical. Conventional, low frequency response probes are then used to accurately measure the true time average of the total temperature and pressure at the rotor outflow. (Since this is a two-dimensional analysis, the area averaged quantities measured by probes are actually line averages.) The probes are assumed to be free from dynamic effects. We will take the average flow conditions at the rotor blade row exit plane to be those measured in a transonic rotor (4), Table 1. Note that the total temperature is higher in the flow outside the wakes in the vortex street case compared to that in the turbulent wake case. This is required since the vortex street depresses the wake centerline temperature but the total energy flux out of the blade row must be the same in both cases.

TABLE 1
ROTOR EXIT CONDITIONS ASSUMED FOR MIXING CALCULATION

Freestream	Vortex Wake	Turbulent Wake
Total pressure ratio	1.646	1.646
Total temperature ratio	1.175	1.170
Absolute exit flow angle	45°	45°
Wake width/Passage width	0.260	0.260

Table 2 shows the resultant average flow condition calculated with the two wake states. Results are given both close to the rotor (the measurements were made at 130% of the axial chord) where the wake structures are distinct, and far downstream where the wakes have totally mixed out. The mass averaged quantities agree at both stations of course. The time averages close to the rotor do not, however. The time average of the vortex street wake case is quite close to the mass average (probably by coincidence) but the turbulent wake case efficiency is measured at over 1% low. (The difference between time or area and mass averages is well known. The point is that the low frequency response probes can only measure the time average.) Far downstream, the mass averaged efficiency has decreased by 1/2% (which is why probe stations are normally placed as far downstream as possible).

TABLE 2
ROTOR OUTFLOW AVERAGE LABORATORY FRAME CONDITIONS

Near Rotor (130% Axial Chord)	Vortex Wake	Turbulent Wake
Mass averaged total pressure ratio	1.644	1.642
Mass averaged total temperature ratio	1.175	1.175
Mass averaged adiabatic efficiency	0.873	0.871
Probe indicated total pressure ratio	1.644	1.641
Probe indicated total temperature ratio	1.175	1.177
Probe indicated adiabatic efficiency	0.872	0.859
Far Downstream (Mixed Out)		
Total pressure ratio	1.646	1.645
Total temperature ratio	1.177	1.176
Adiabatic efficiency	0.866	0.867

If the wake structure were always the same, the difference in measured efficiencies due to the structure could be mixed in with empirical probe calibration factors and thus be calibrated out (in theory). If, however, a small change in blade design or turbomachine operating point were to alter the wake structure alone, there would be an erroneous change in measured aerodynamic efficiency, an error of over 1% for the stage studied here. In other words, a change in the wake structure can appear as a change in stage efficiency, even though the momentum and thermal energy flux through the machine (the pressure and temperature rise) have not changed. This error would disappear if the measurements were made with sufficient time resolution to resolve the wake structure.

Thus, wake structure can introduce artifacts in the measurement of compressor performance, introducing apparent changes not representative of the state of the fluid exiting the machine. Because the magnitude of the temperature separation in the vortex street scales with the square of the Mach number, this effect should be most important for transonic and supersonic turbomachines. The argument should hold true for turbine flows as well, but this has not been verified.

6. NUMERICAL SIMULATION OF COMPRESSOR BLADE WAKE STRUCTURE

To further investigate the compressor wake structure, the flow through a single blade passage was simulated with a computational fluid dynamic (CFD) technique. A two-dimensional, time accurate, Reynolds averaged, explicit Navier-Stokes calculation was done with a relatively fine grid and very small time step to insure good spatial and temporal resolution. The midspan airfoil geometry of the transonic rotor measured in [4] was used. To accommodate supersonic inflow limitations in the code, the inlet relative Mach number was reduced from the 1.17 of the measurement condition to 0.9 for the calculation. Inlet total conditions were adjusted to keep the Reynolds number based on axial chord at 1.2×10^6 . The inlet flow at the upstream boundary is specified as uniform. Thus, there is no external excitation or periodicity, only that generated in the flow by the blade itself. More details on the calculation can be found in [15].

The primary observation made from this ab initio calculation is that vortices are shed into the blade wake. Figure 9 is a plot of instantaneous velocity vectors in the blade relative frame near the trailing edge. It shows the vortex structure in the

wake as well as a separated region on the suction surface. (The vector length denotes the magnitude of the local flow velocity, the orientation the flow direction.) Only two vortices are readily seen here due to the change in vortex core translational velocity as the vortices propagate downstream. This has the effect of blurring the flow structure in any frame other than that moving with the cores. A similar problem in visualizing the vortices was encountered in the modelling effort [11]. In both cases, the ready identification of the vortex structure is strongly dependent on the frame of reference chosen, making the vortex street fairly elusive and hard to see.

The shedding periodicity shows up quite clearly in the calculated trailing edge static pressure, Fig. 10. Also of interest is the lower frequency present which modulates both the amplitude and the frequency of the vortex shedding. This is quite similar to low frequency modulation observed in the experimental measurements [11]. In the simulation, the lower frequency correlates with the motion of the separation point along the suction surface and with axial motion of the passage shock, and thus may be a shock boundary layer interaction, Fig. 11. There is also a 30% fluctuation in blade moment at this frequency, which is low enough (~ 300 Hz) to be of concern to the structural designer. The exact cause of this low frequency movement of the separation point is not yet clear but appears quite similar to instabilities observed in high speed diffusers.

The modulation of the vortex shedding frequency by the low frequency oscillation was considerable, a factor of two. The strength of the vortices varied inversely with the shedding frequency. The shedding frequency range from the CFD calculation is compared with those inferred from the laser anemometer probability density distributions and from the core flow-shock motion fluctuations in Fig. 12. These three estimates are completely independent and show quite good agreement. The large fluctuations in frequency shown in the numerical simulation tend to explain the difficulty encountered in extracting a single, unambiguous frequency estimate from the experimental measurements. Fluctuations of this magnitude may also blur the bimodal anemometer histograms.

The blade relative total pressure in the numerical simulation as would be measured with a fixed laboratory frame probe as the rotor passes is compared with measurements [11] in Fig. 13. The qualitative agreement is excellent. The calculation clearly captures the wake modulation evident in the measurements.

The high frequency jitter of the passage shock at the shedding frequency inferred in [5] is not observed in the calculation. However, since the predicted shock motion is no more than one grid cell size and the numerics spread the shock over five grid points, this is not surprising. A calculation with a much finer grid size would be required in order to address this problem properly.

Overall, the numerical, CFD simulation agrees extremely well with the experimental observations and the analytical model. The one area in which the numerical simulation does not add information is the decay of the wake structure as it is convected downstream since the numerical damping overwhelms most physical dissipation mechanisms.

7. DISCUSSION AND CONCLUSIONS

Considerable effort has traditionally been spent on establishing the proper parameter with which to correlate vortex shedding. A Strouhal number based on trailing edge thickness is commonly used, especially for blunt trailing edge bodies [2], [3], [9]. For compressor blades, the wake displacement thickness has been suggested as a more realistic correlation [5]. Since the wakes of compressor blades are relatively thick compared to the trailing edge, the difference between the correlations using the different parameters is considerable, a factor of four in frequency. For the blade section studied here, a frequency of 15 kHz is predicted using the wake thickness, matching both the experimental and numerical results.

The modulation of the frequency and strength of the vortex shedding observed in the CFD calculation is extremely important for the interpretation of experimental measurements. The presence of the modulation considerably complicates the practical problem of vortex detection in rotating machinery. The impact on laser anemometry techniques and spectral analysis methods needs to be quantitatively assessed.

Examination of the details of the numerical simulation as well as classical vortex shedding analysis [16] suggests that the process may be considerably more complex than can be represented by a simple Strouhal number. Many shedding processes may compete and the separation zone observed in the simulation certainly plays a part. A more complete discussion of vortex formation and evolution will be the subject of a later paper.

This work has tended to treat the compressor blade and vortex street in isolation when in reality it is part of a very complex environment. Acoustic feedback has been shown to both enhance shedding and alter the frequency [7], [13], [18]. There are many mechanisms involving inter-blade row interactions for forcing the shedding as well. The possibility of phase locking between blades is also evident [17]. Clearly much work can be done in this area.

Another area needing more investigation is the three-dimensional wake structure in real turbomachines. Although it is often dangerous to generalize from two to three

dimensions, we will point out that if the vortices have considerable spanwise extent, they can serve as an extremely powerful mechanism for the radial transport of fluid--complicating the evaluation of the radial work and efficiency distributions. Work with cylinder shedding has shown that external forcing (acoustic in this case) can enhance the spanwise coherence [18].

In this paper we have made the following observations concerning the structure of compressor blade flow and wakes:

1. The wakes of high Reynolds number, transonic compressor blades can consist of shed vortex streets. This is confirmed by measurement, modelling, and numerical simulation.
2. The shedding frequency and strength are sensitive to the environment.
3. The vortex street can depress the wake temperature.
4. The importance of the wake structure increases with the square of the freestream Mach number.
5. Wake structure can influence the measurement of compressor efficiency.
6. Changes in wake structure can be mistaken for changes in compressor performance.
7. The wake structure can drive the blade shock system, inducing loss.
8. The wake structure can be influenced by other fluid dynamic instabilities present in a blade passage which themselves may be important for performance and structural dynamic reasons.

Overall, vortex shedding in transonic compressor blade wakes can have significant influence on compressor behavior.

8. REFERENCES

1. Davies, M.R.D. and Bryanston-Cross, P.J., "Holographic Measurements and Theoretical Predictions of Unsteady Flow in a Transonic Annular Cascade," J. Eng. for Power, Vol. 107, No. 2, 1985.
2. Heinemann, H.J. and Butefisch, K.A., "Determination of the Vortex Shedding Frequency of Cascades With Different Trailing Edge Thicknesses," AGARD CP-227, 1977, pp. 35-1 to 35-10.
3. Heinemann, H.J., Lawaczek, O., Butefisch, K.A., "V. Karman Vortices and Their Frequency Determination in the Wakes of Profiles in the Sub- and Transonic Regimes," IUTAM Symposium, 1976, pp. 75-82.
4. Hathaway, M.D., Gertz, J.B., Epstein, A.H. and Strazisar, A.J., "Rotor Wake Characteristics of a Transonic Axial Flow Fan," AIAA Paper 85-1133, July 1985.
5. Ng, W.G. and Epstein, A.H., "Unsteady Losses in Transonic Compressors," J. Eng. for Power, Vol. 107, No. 2, 1985.
6. Cumpsty, N.A. and Whitehead, D.S., "The Excitation of Acoustic Resonances By Vortex Shedding," J. Sound Vib., Vol. 18, No. 3, 1971.
7. Parker, R., "An Investigation of Acoustic Resonance Effects in an Axial Flow Compressor Stage," J. Sound Vib., Vol. 8, No. 2, 1968.
8. Hobbs, D.E., et al., "Experimental Investigation of Compressor Cascade Wakes," ASME 82-GT-299, April 1982.
9. Blake, W.K., "Excitation of Plates and Hydrofoils by Trailing Edge Flows," J. of Vib., Acoustics, Stress, & Rel. in Des., Vol. 106, July 1984.
10. Strazisar, A.J., "Investigation of Flow Phenomena in a Transonic Fan Rotor Using a Laser Anemometer," J. of Eng. Power, Vol. 107, No. 2, April 1985.
11. Gertz, J.B., "Unsteady Design Point Flow Phenomena in Transonic Compressors," MIT Ph.D. Thesis, September 1985.
12. McCune, J.E., "Theoretical Modelling of Stability and Unsteadiness in Transonic Compressor Flow Fields," Annual Technical Report to AFOSR, "Fluid Dynamics of High Performance Turbomachines," MIT GTL, November 1985.
13. Eckert, E.R.G., "Energy Separation in Fluid Streams," Int. Comm. Heat Mass Transfer, Vol. 13, 1986, pp. 127-143.

14. Kurosaka, M., Gertz, J., Graham, Goodman, J.R., Sundarem, Riner, W.C. and Kuroda, H., "Energy Separation in a Vortex Street," in publication, J. Fluid Mech., 1986.
15. Owen, P.R., "Computational Simulation of Unsteady Flow in a Transonic Compressor Rotor," MIT S.M. Thesis, September 1986.
16. Morkovin, M.V., "Flow Around Circular Cylinder - A Kaleidoscope of Challenging Fluid Phenomena," in Symposium on Fully Separated Flows, A.G. Hansen, Ed., ASME, New York, 1964.
17. Camus, J.J. and Bryanston-Cross, P.J., "1 MHz Bandwidth, Real Time Schlieren Techniques in a Linear Cascade," Proc. of Symposium Measurement Techniques in Transonic and Supersonic Flows in Cascades and Turbomachines, Lyon, 1981.
18. Blevins, R.D., "The Effect of Sound on Vortex Shedding From Cylinders," J. Fluid Mech., Vol. 161, 1985, pp. 217-237.

9. ACKNOWLEDGEMENTS

The authors would like to thank Mr. R. Haines for assistance with the numerical simulation (he wrote the code), and E.M. Greitzer for many useful discussions. This work was supported in part by the U.S. Air Force Office of Scientific Research and the NASA Lewis Research Center.

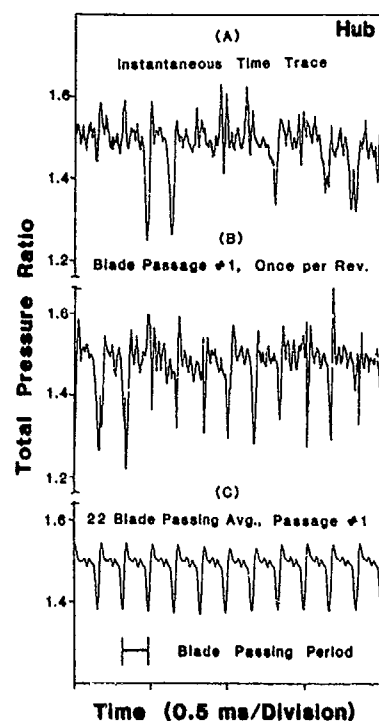
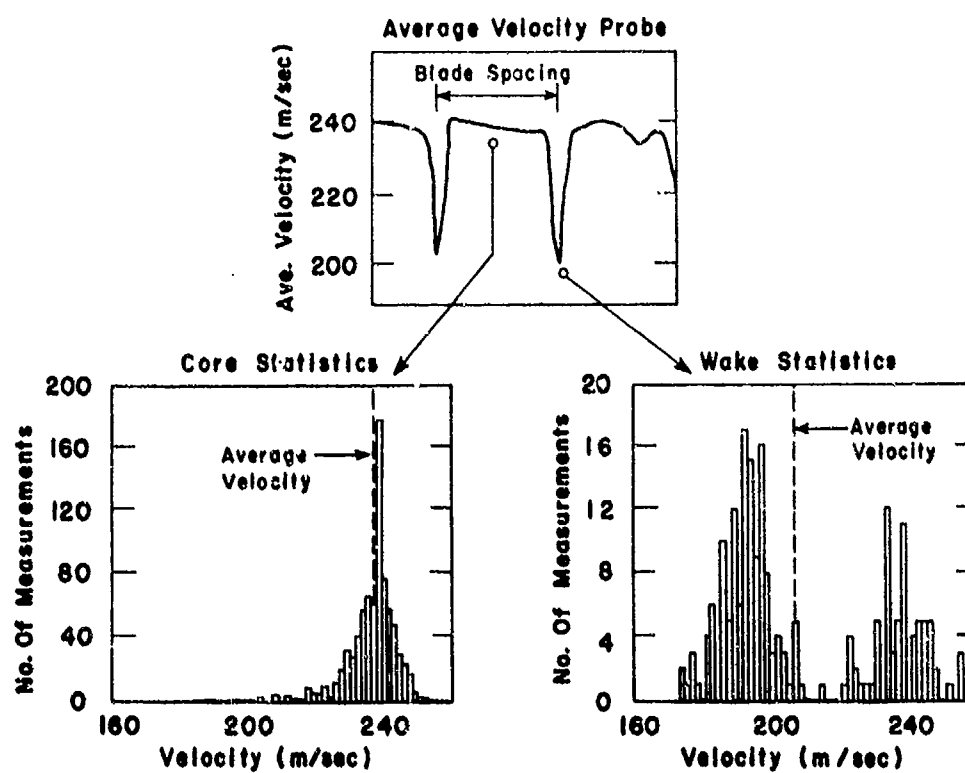


Fig. 1: Transonic compressor rotor exit total pressure near hub: (A) instantaneous measurement, (B) an individual blade passage as seen once per revolution, and (C) an ensemble average of that individual passage, from [5]

Fig. 2: Laser anemometer measurement of the outflow from a transonic compressor rotor: (A) average velocity profile, (B) histogram of velocity statistics in core flow showing Gaussian profile characteristic of turbulence, and (C) velocity statistics in wake showing bimodal distribution attributed to vortex street, from [4] (below)



5-10

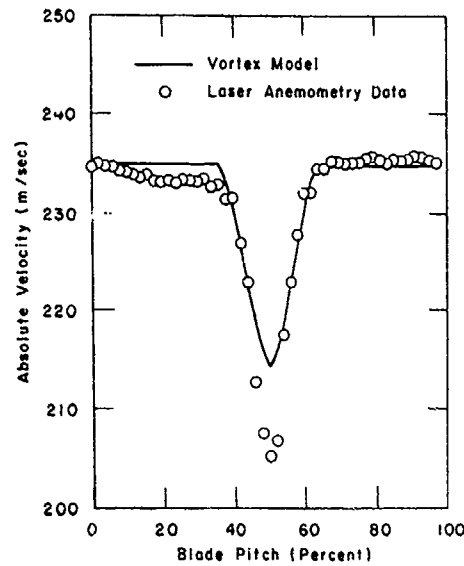


Fig. 3: Comparison of mean absolute velocity measured by a laser anemometer in a rotor blade passage with that from the average of the vortex street model [4]

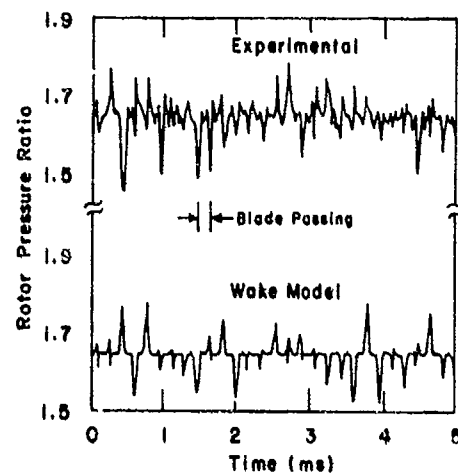


Fig. 4: A comparison of the time resolved rotor exit absolute total pressure with that predicted by the vortex street model, from [11]

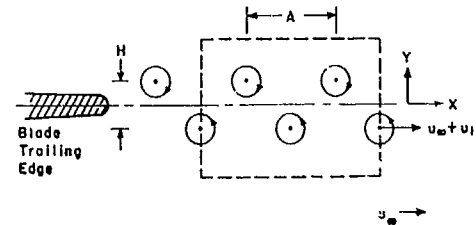


Fig. 5: A schematic representation of the vortex street geometry used in the model. The box delineates the region illustrated in Figs. 6, 7 and 8.

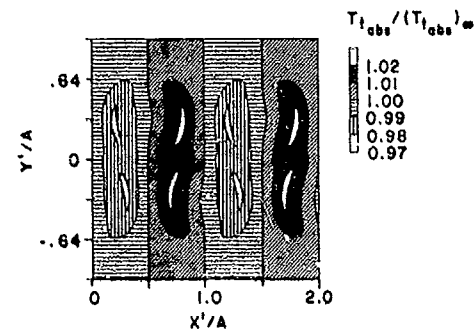


Fig. 6a: A contour plot of absolute total temperature contours predicted by wake model

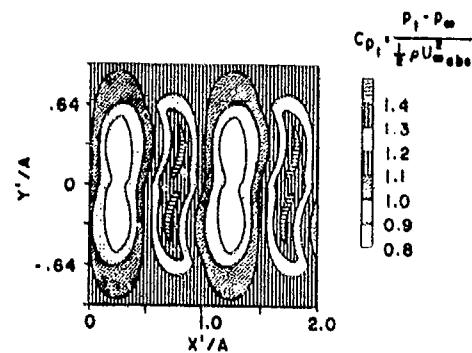


Fig. 6b: A contour plot of absolute total pressure contours predicted by wake model

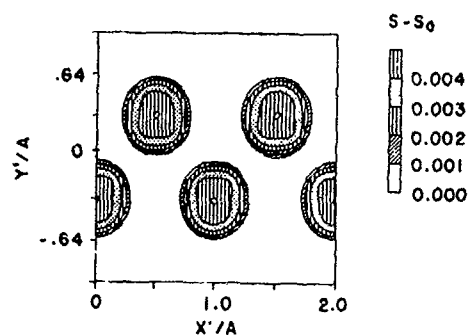


Fig. 7: Contours of entropy rise from wake model. Note that the entropy is essentially constant outside the vortex cores

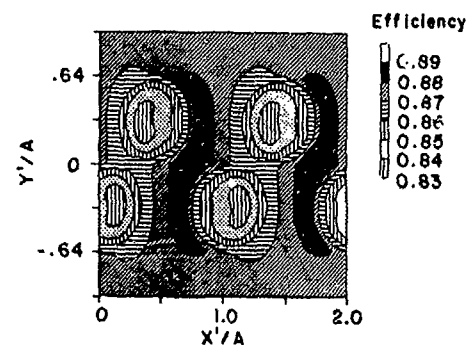


Fig. 8: Contours of adiabatic efficiency from the wake model. Note that these regions are not congruent with the entropy change in Fig. 7 and that there are regions of adiabatic efficiency indicated as above that of the freestream.

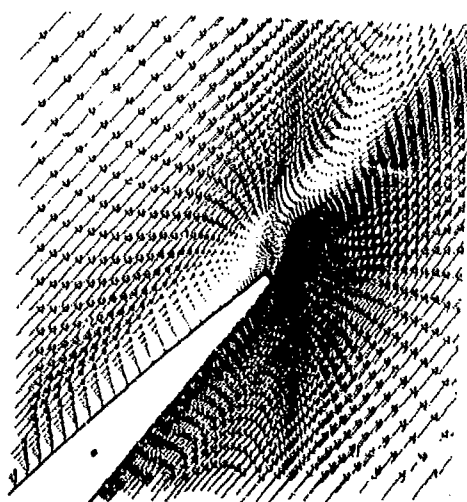


Fig. 9: Instantaneous vector plot (arrow orientation is velocity direction, length is velocity magnitude) of the trailing edge region of a transonic airfoil calculated with a 2-D time accurate Navier-Stokes code. Note the separated region on the suction surface and the vortices shed into the wake.

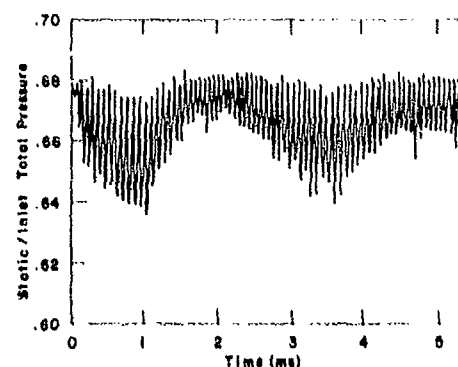


Fig. 10: Static pressure history at trailing edge of a transonic airfoil. Note the periodicity due to vortex shedding and the modulation of that shedding by a lower frequency disturbance.

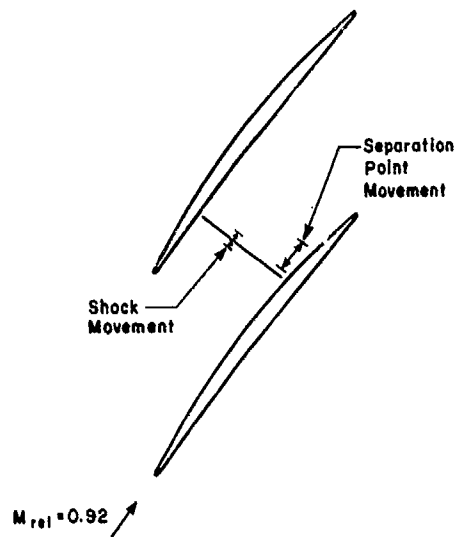


Fig. 11: The numerical simulation shows a correlation between the passage shock motion and the separation point movement

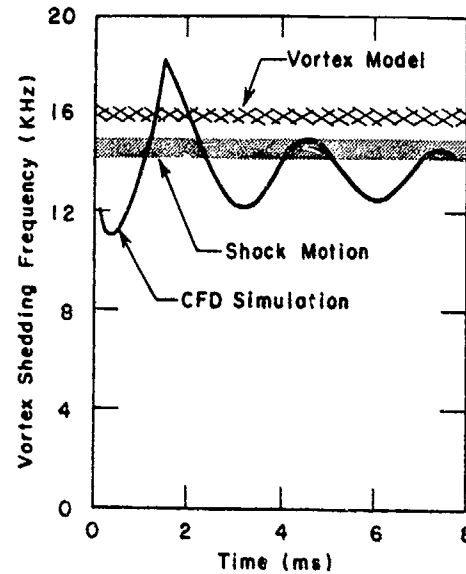


Fig. 12: A comparison of the shedding frequency predicted by the CFD simulation with those inferred from measurements

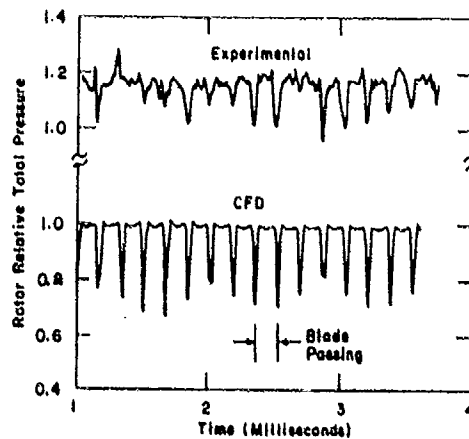


Fig. 13: A comparison of the rotor relative total pressure time history measured in a transonic compressor with that predicted by the CFD simulation

DISCUSSION

P. Ramette, Fr

Have you compared your Navier-Stokes calculations of the vortex streets with other calculations like Random Vortex Method or large Eddy Simulation methods?

Author's Reply

2 points

1. Some large Eddy Simulation work, done at Wright-Patterson AFB for cylinders is just about to be published and shows similar effects in the wake of a cylinder at Mach = 0.7.
2. Even if our computer uses a Reynolds averaged simulation, it is a very time consuming calculation as you have to simulate not only the high frequencies, but something 15--20 times less. The calculations shown are hopefully the first of many. Even if relatively crude, they agree with the experiments.


H.B. Weyer, Ne

In similar measurements within a transonic compressor using Laser Transient Velocimeter, we found that vortex shedding frequency within the rotor blade wakes depends among other things, upon the blade passing frequency of the succeeding stator. What is your idea on this finding?

Author's Reply

We know that one can change and force the frequency of vortex shedding through an external perturbation. By coincidence in many compressor stages, because of the way the blade number is fixed to avoid noise, you are very close to being in an odd harmonic of the blade passing by the stator. I think this is a strong forcing function. We plan to put the potential forcing function in the numerical simulation and see what we get.

Another point coming from your publications is that if you can see vortex cores in a stationary frame with a laser velocimeter, it means that the potential field of the stator is not only setting the frequency, but also locking the phase of shedding. This has implications for the measurement and on the errors in performance evaluation.



✓
EXPERIMENTAL OBSERVATIONS ON AN UNSTEADY, NORMAL
SHOCK/BOUNDARY LAYER INTERACTION

by

J.A. Edwards and L.C. Squire
Cambridge University Engineering Department
Cambridge CB2 1PZ, UK

ABSTRACT

An experiment is described in which a normal shock interacts with the natural turbulent wall boundary layer in a parallel sided duct at Mach 1.3 and 1.5. The shock wave is vibrated in symmetric fashion by a rotating cam mounted in the tunnel diffuser. The design of this experiment, particularly the efforts to obtain a pure forcing signal, is discussed. Shock motion analysis at reduced frequencies of order 0.2 to 2 and amplitude parameters of 2% to 20% (based on equivalent chord) is presented. Unsteady surface pressure measurements under the interaction have been made and demonstrate that there is negligible phase change between the shock motion and the surface pressures. It appears reasonable to utilise quasi-steady assumptions in the calculation of the surface pressures at the low frequency conditions tested.

1. INTRODUCTION

Theoretical studies directed at unsteady problems in inlets and turbomachinery have until recently generally assumed inviscid flow (e.g. Refs. [1], [2], [3], [4], [5], [6], [7], [8]). However, it has long been known that unsteady viscous effects are extremely important in cascades. Even in the relatively simple problem of inlet diffuser flows, inviscid analyses form an incomplete basis for the correlation of experimental data [9], [10], [11], [12], [13]. More recently, Liou and Coakley [14] have attempted a numerical simulation of the forced and self-excited flow in a transonic inlet diffuser, examined experimentally by Sabjen and co-workers [Refs. 9-13], using the Reynolds-averaged Navier-Stokes equations. While good agreement between the analysis and experiment was achieved for the cases of forced oscillation, there is a case for extending the range of experimental data beyond those parameters considered by Sabjen et al.

The objectives of our experiments are to consider more closely the detail of the unsteady viscous-inviscid interaction than has been hitherto attempted. We therefore have chosen a simpler geometry for our initial experiments than that studied in Ref. [9-13] although there are considerable areas in which we have benefitted from this work. The two-dimensional interaction of a shock wave with a naturally grown flat plate boundary layer which is then forced in a symmetrical manner is studied. The parameters of interest in turbomachines differ slightly from those in inlets, and differ from engine to engine. We therefore have chosen a fairly wide range of conditions over which our simulation will, hopefully, provide data of general interest. Since we are primarily interested in the viscous behaviour we use boundary layer thickness as our length scale. In this context we define a reduced frequency and shock motion amplitude parameter based on equivalent chord by assuming that on the full scale blade at the shock interaction position the boundary layer thickness is of order (chord $\times 10^{-2}$). The amplitude parameter is defined as the ratio of shock displacement to equivalent chord.

In this paper we consider the behaviour of unsteady shock motion in a parallel sided duct at Mach 1.32 and 1.53. A comparison of the flow at these Mach numbers is of interest, since we may expect (for the steady flow case) that the boundary layer will remain attached at Mach 1.3 but be beyond the point of incipient separation at Mach 1.5 [15]. The design of the experiment to enable us to achieve a range of reduced frequencies and shock amplitude parameters is discussed and shock motion results are

presented. At Mach 1.5, reduced frequencies of order 0.2 to 2 are attainable with the natural tunnel boundary layer and amplitude parameters of 2% to 20% at a reduced frequency of order 1, are demonstrated. Unsteady surface pressure measurements under the shock/turbulent boundary layer interaction at Mach 1.5 are presented. The results are compared with a simple theoretical approach.

2. EXPERIMENTAL DETAILS

2.1 Operating Conditions of Tunnel

Intermittent running facility (up to 1 min. run time)

Working section Mach number	1.53	1.32
boundary layer thickness	5.6mm	5.5mm(measured from schlieren)
Po stagnation pressure	135kPa	129kPa
To stagnation temperature	296 \pm 4°K	-
TW wall temperature	292 \pm 5°K	-
Reynolds number	1.9x10 ⁷ /m	2.1x10 ⁷ /m
Working section width	114mm	
height	152mm	

2.2 Description of Experiment

A rotating cam was installed centrally in the diffuser of the tunnel (Fig. 1). This was used to vibrate a normal shock situated in the working section by creating a periodic variation in the back pressure. Shock frequencies of up to 240 Hz. were obtained. The rotation speed of the cam was measured by a magnetic transducer and was checked independently with a calibrated tachometer. To vary the forcing pressure disturbance a number of cams were manufactured (Fig. 2). Five cams of equilateral triangle section, with face dimensions varying from 19mm to 25mm, were tested at both Mach 1.3 and 1.5. Cams of double wedge section with dimensions 38mm x 25mm and 51mm x 25mm were tested at Mach 1.5.

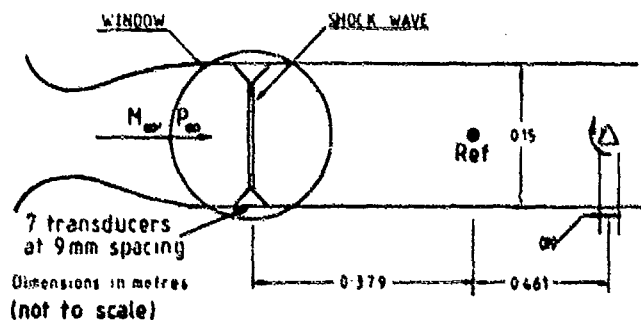


Fig.1 Experimental configuration

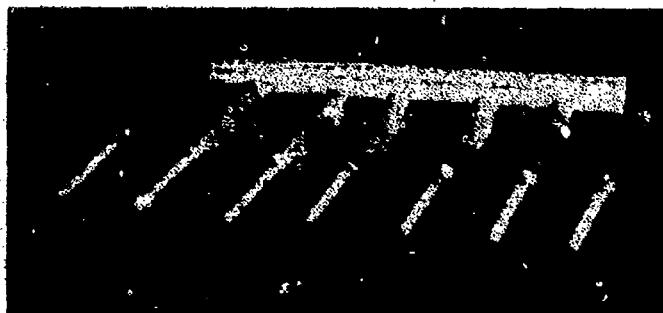


Fig.2 Cams used to provide the downstream pressure fluctuations

The mean shock position was set at the window centre by adjusting the tunnel stagnation pressure. The tunnel is controlled manually. It was found that while the stagnation pressure could be monitored accurately (± 0.5 mm Hg) by the use of a transducer, it was more effective to control the shock position by the use of a video-schlieren system (Fig. 3). In this way, with a "steady" shock, ie without the cam rotating, random movement of the shock could be constrained to within reasonable limits of the selected mean position (Fig. 4). The shock position was monitored using a Reticon LC11 line scan camera with an array of 256 diodes in a similar way to that described by Sabjen and Crites[16]. It is known that this technique gives an accurate representation of the shock position[17]. An image of the horizontal centreline of the working section up to 160 mm long was cast on the face of the camera. The poorest resolution of the system was thus theoretically 0.625 mm. In practice there was found to be an error of ± 1 pixel (photodiode). The light intensity was attenuated optically so that the camera responded to only two pixels across the image. The linearity and accuracy of the system was checked by placing strips of black tape across the working section at known distances from the upstream end of the window. By varying the magnification and restricting the scan length the accuracy of the system could be varied between ± 1 mm and ± 0.2 mm (depending on shock motion amplitude).

Unsteady pressure measurements were made using Kulite XCQ-062 transducers. The forcing reference pressure was monitored on the tunnel sidewall at the point marked Ref in Fig. 1. Seven transducers were mounted flush on the floor of the working section as shown in Fig. 1. The stagnation pressure was also measured using a transducer mounted in the settling chamber. The pressure and shock position data were captured on a mini-computer for storage and subsequent analysis.

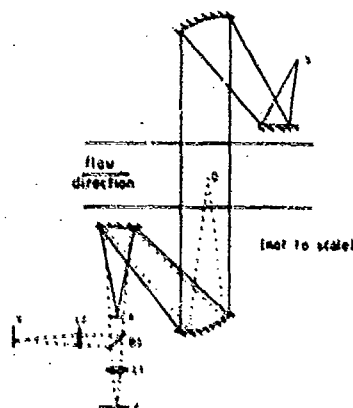


Fig.3 Optical arrangement for simultaneous tunnel drive and flow visualization

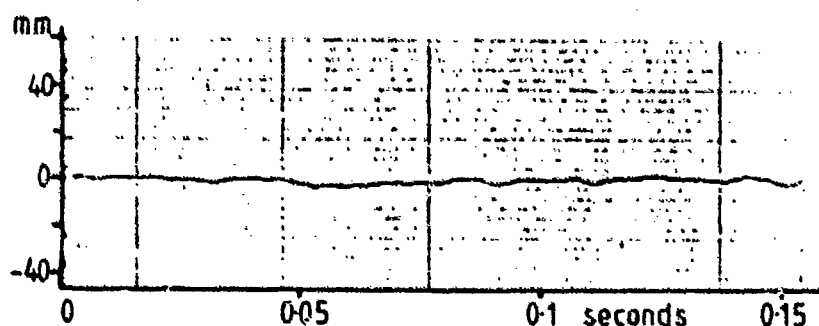
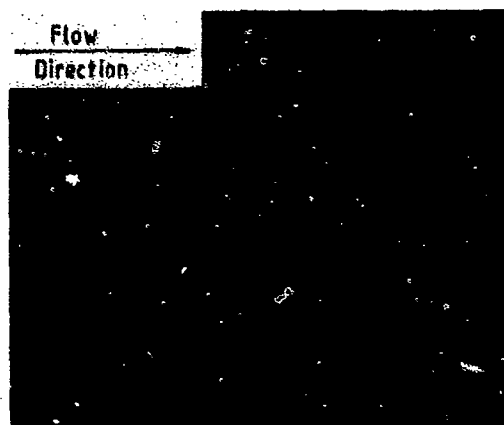


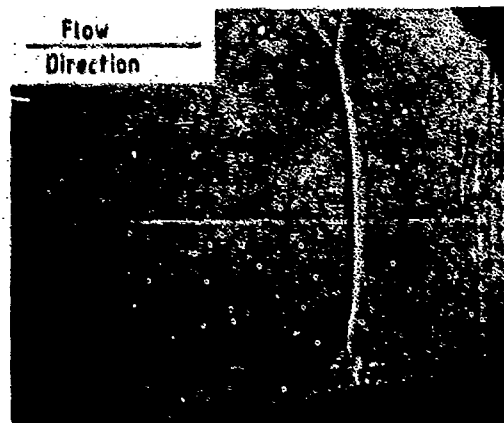
Fig.4 Steady shock output from the Line Scan Camera ($M = 1.5$)

3. RESULTS

Spark shadowgraph photographs of the interaction region at Mach 1.5 with the shock "steady" and forced at a nominal frequency of 100Hz. are shown in Fig. 5. Downstream of the leading foot of the lambda (the "viscous ramp" [18]), the region of high density gradient in the shear layer rises from the surface, leaving a region of low density gradient close to the wall. One can observe an apparent reduction in the intensity of the optical structures close to the wall, downstream of the interaction. However, it is not possible to tell whether there is actually a separation point underneath the shock wave, although, from the results of Sawyer and Long [13] at the same Mach number and similar free stream Reynolds number ($10 \times 10^6/m$), we might expect a separation bubble to exist and to extend for perhaps 5 boundary-layer thicknesses downstream of the shock. Photographs at Mach 1.3 are shown in Fig. 6. In this case the boundary layer thickens but does not separate.

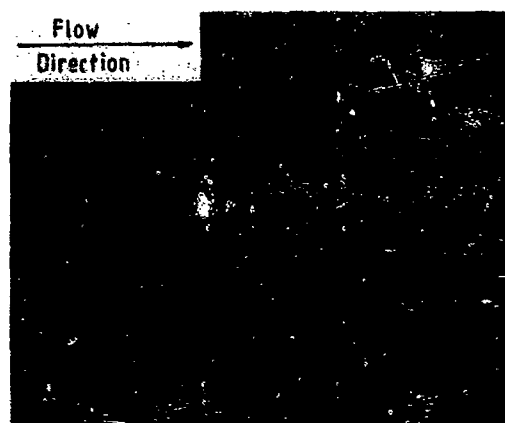


(a) Shock steady

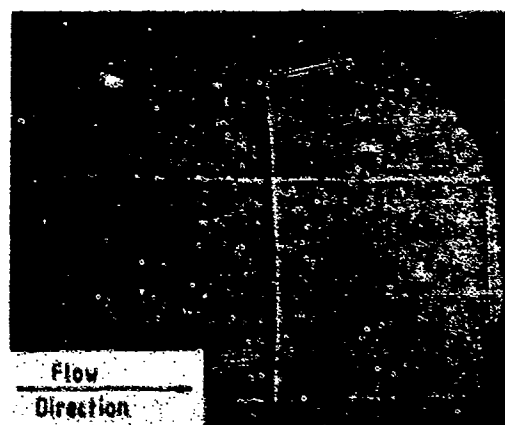


(b) Shock oscillating at 95 Hz

Fig. 5 Shadowgraph photographs at Mach 1.5



(a) Shock steady



(b) Shock oscillating at 100 Hz

Fig. 6 Shadowgraph photographs at Mach 1.3

Figs. 7, 8 and 9 show the shock wave motion and the forcing pressure time histories at Mach 1.3 and a nominal frequency of 100 Hz, for the 15mm triangular cam and the two double wedge cams. As the pressure disturbance increases the increasing distortion in both forcing pressure and shock motion can be observed. Power spectra of the forcing pressure signals are shown in Fig. 10(a). (The scales are arbitrary, but each is related to the same datum.) Note also the reduction in actual frequency as the pressure loading increases. Actual frequencies (the frequency of the fundamental as measured from the power spectra) are used in the results that follow. To attempt to clean up these signals a 38mm x 25mm cam of sinusoidal section was manufactured. The power spectrum of the forcing pressure signal is shown in Fig. 10(b). There is a significant improvement in the form of the frequency spectrum, only pure harmonics of the fundamental are evident and the loading on the cam is reduced. Further improvements can only be achieved by taking account of the aerodynamic properties (e.g. asymmetric wake shedding) on the cam.

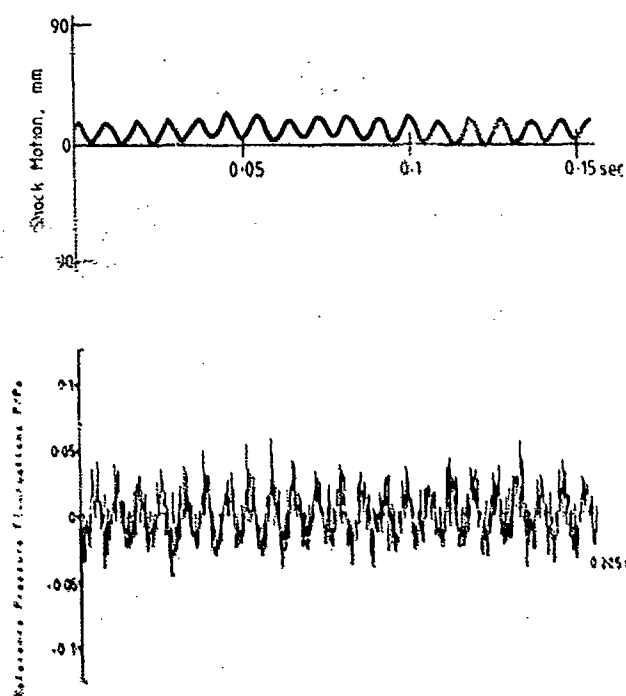


Fig. 7 Shock motion and reference pressure forced with the 19 mm triangular section cam at a nominal frequency of 100 Hz

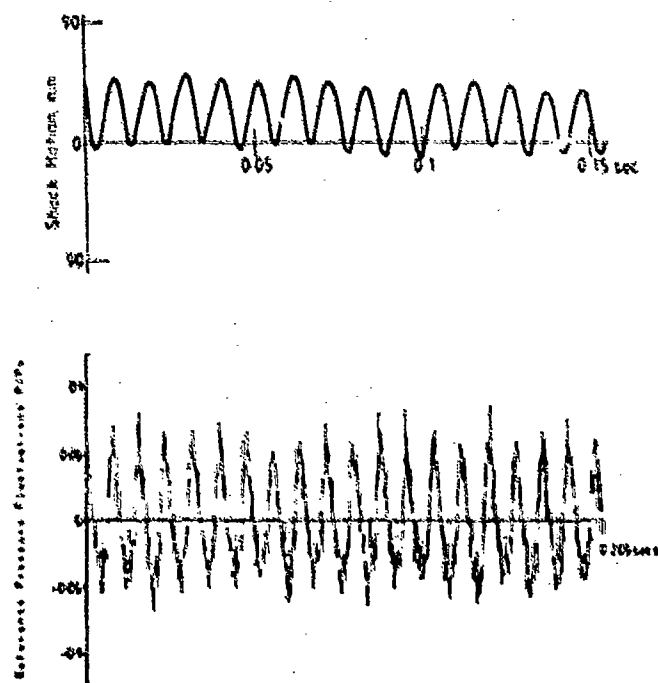


Fig. 8 Shock motion and reference pressure forced with the 38 x 25 mm double wedge section cam at a nominal frequency of 100 Hz

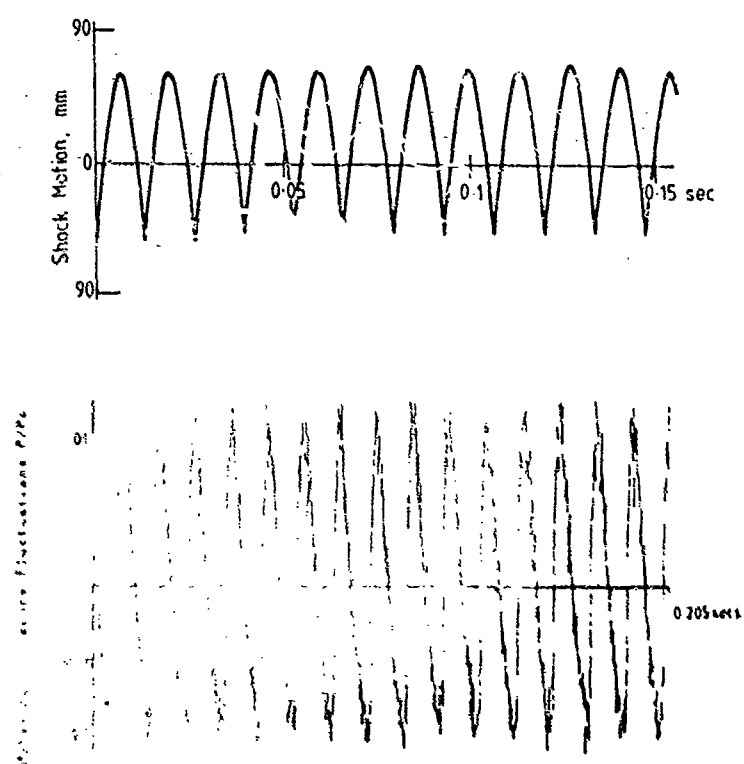


Fig. 9 Shock motion and reference pressure forced with the 51 × 23 mm double wedge section cam at a nominal frequency of 100 Hz

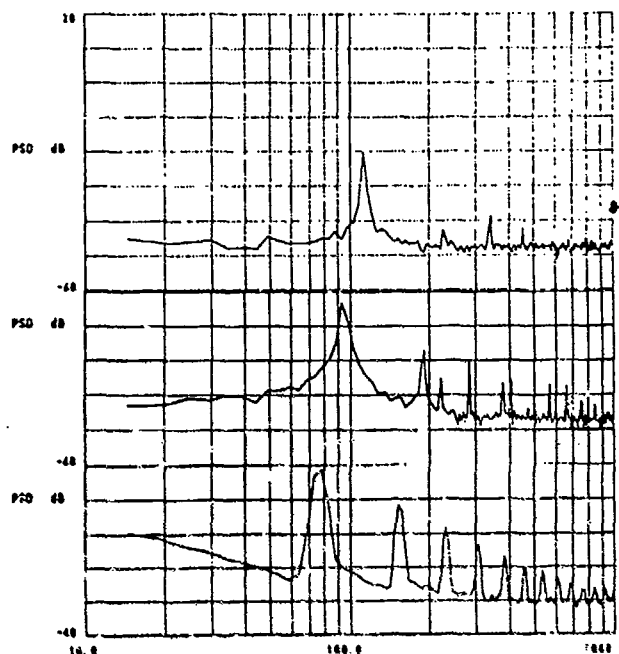


Fig.10(a) Power spectral density traces corresponding to Figs. 7, 8 and 9 (arbitrary scale)

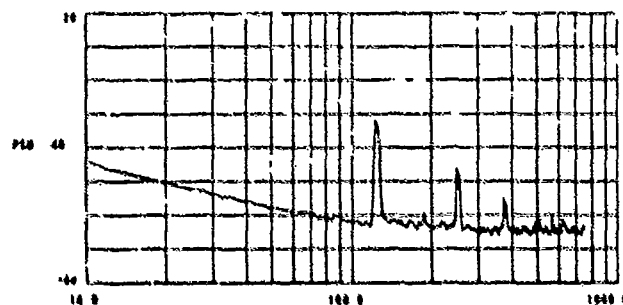


Fig.10(b) Power spectral density trace of 38 x 25 mm sinusoidal section cam

Fig. 11 shows the variation in shock wave amplitude at $M=1.31$ for the various triangular section cams. These are compared with the shock wave amplitudes predicted using the asymptotic theory of Refs. [2-4]. It should be noted that the asymptotic description of the flow requires $1-M^2$ to be a small parameter, and we might therefore expect that agreement at Mach 1.3 would be poor. Nevertheless, as can be seen from

Fig. 11, the agreement is excellent. We expect agreement to be less good at Mach 1.5 since the asymptotic representation of the shock wave is not valid, and, as can be seen from Fig. 12, the relative shock Mach number at the higher forcing pressure fluctuations can no longer be assumed constant. It is interesting to note that, for the 51mm x 25mm double wedge section cam, there is a significant difference in shock Mach number with frequency and with direction of travel. The difference with frequency is due to a reduction in the rms forcing pressure, while the difference with travel direction is due to a small extent to the work done by the shock against the flow but in the main is due to the forcing wave shape. Note that at 80Hz, the rms forcing pressure is 17.5% of the free stream dynamic pressure and the total shock wave excursion scales to 19.3% chord. This particular case leads to the observation (based on quasi-steady arguments) that for the downstream travelling wave we might expect the flow to be attached ($M<1.4$), while for the upstream travelling wave we would expect the flow to be heavily separated ($M>1.6$). The variation in shock wave amplitude for each of the cases together with the predicted amplitudes for the 19mm and 25mm triangular cams are shown in Fig. 13.

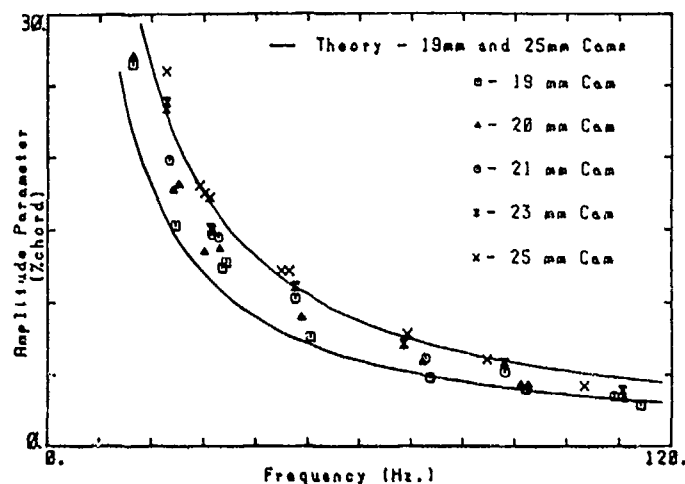


Fig.11 Shock motion peak-peak amplitudes forced by the triangular section cams at Mach 1.32

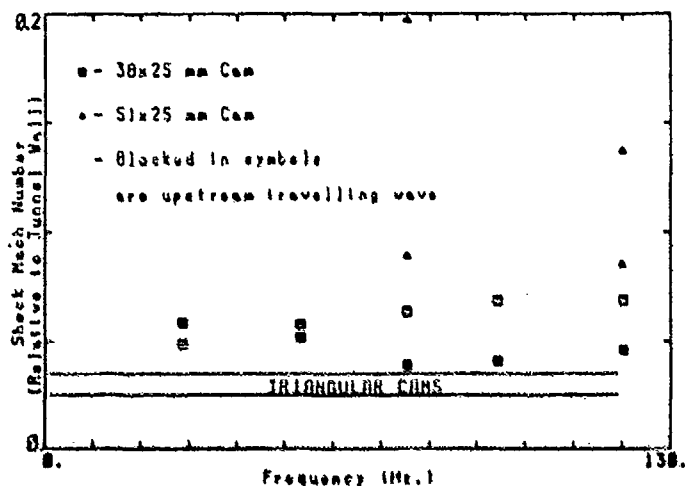


Fig.12 Peak shock wave Mach numbers at Mach 1.5

Time mean surface pressure measurements under the interaction at Mach 1.5 with no downstream forcing are shown in Fig. 14. These are compared with the data of Seddon[19]. Note the rapid rise of the surface pressure at the start of the interaction followed by a decreasing pressure gradient downstream of the viscous ramp. Unsteady surface pressure time history data for the 19mm triangular section cam are shown in Fig. 15. The effect of the pressure gradient distribution shown in Fig. 14 can clearly be observed in the surface pressure response. The variation of surface pressure fluctuation with frequency is shown in Fig. 16. As the frequency increases and hence the shock motion amplitude decreases the pressure fluctuation decreases. The pressure fluctuations decrease away from the start of the viscous ramp due to the decreasing static pressure gradient. Under the separation hubble, at 57 Hz, the measured pressure fluctuation is less than that in the undisturbed boundary layer (cf. Fig. 5).

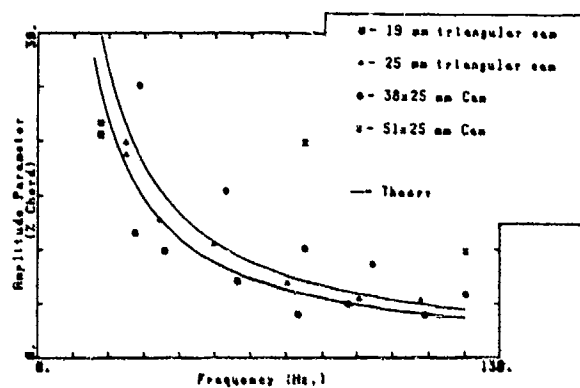
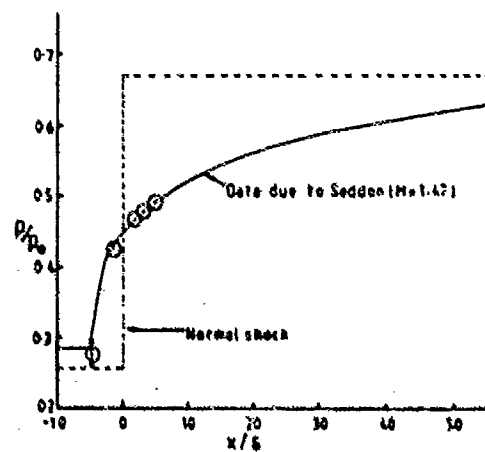


Fig.13 Shock motion peak-peak amplitudes forced by the various cams at Mach 1.5

Fig.14 Time-mean surface pressures under the shock/boundary-layer interaction ($M = 1.5$)

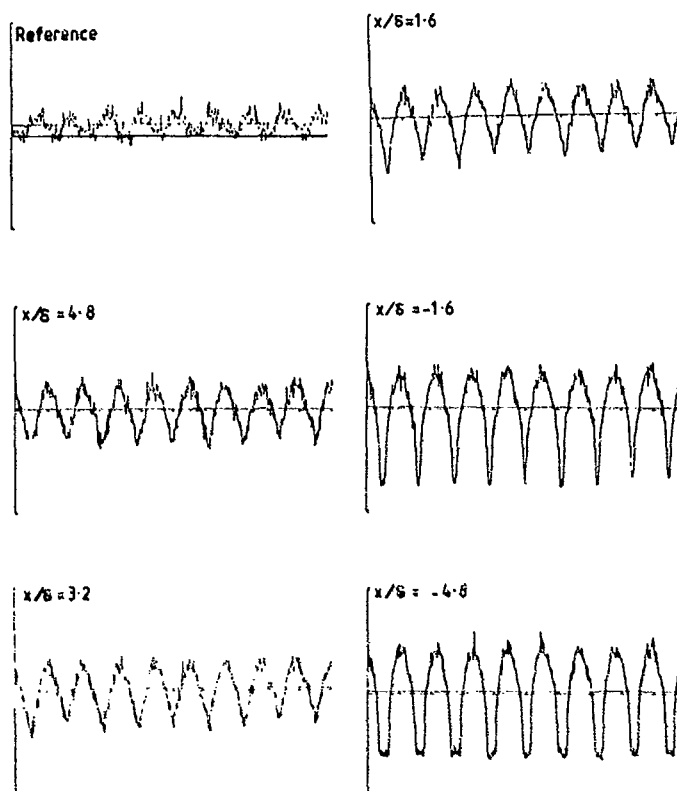


Fig.15 Unsteady surface pressure time history data under the interaction with the shock forced at 17.7 Hz. ($M = 1.5$)

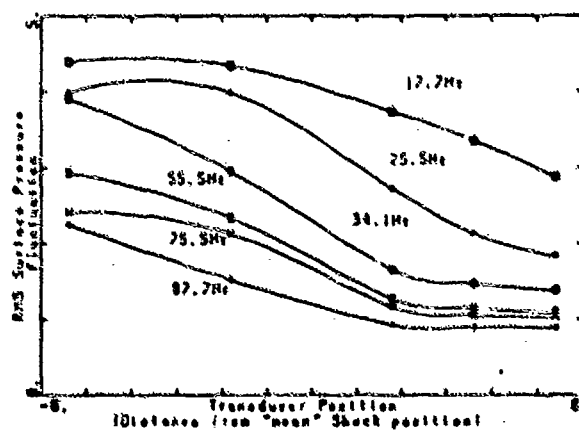


Fig.16 Root mean square surface pressure fluctuations under the interaction ($M = 1.5$)

The relationship between the shock position and surface pressure under the interaction is shown in Fig. 17 at a nominal forced frequency of 40 Hz. (arbitrary vertical scales) after digital filtering with a second order Butterworth filter to clarify the comparison. Shock motion is shown as positive upstream. Analysis of the signals shows a negligible phase difference between surface pressure and shock motion. This is in agreement with the results of Sabjen et al. [12]. It is found that quasi-steady calculations of the surface pressure are applicable.

The phase change between the forcing pressure at the reference point and the measured surface pressures at a particular x station at Mach 1.5 is shown in Fig. 18. A least squares straight line has been fitted through the first five experimental points. The slope of this line is due to the effect of the time lag between the reference station and the mean shock position. It has been demonstrated above that at low frequency there is no phase change between the shock position and the surface pressure. However, at 100 Hz. the phase change begins to deviate from the straight line, indicating that non-quasi-steady effects are appearing. We surmise that at reduced frequencies of 0.75 or less, the flow may be considered quasi-steady in this experiment.

The calculated phase of the shock wave motion with respect to the reference station shows poor agreement with the experiment. The error in phase is approximately 30° when the time lag is calculated with the assumptions that the forcing pressure is an acoustic disturbance and that the static temperature immediately downstream of the shock wave is given by the normal shock relations and subsequently varies linearly to the conditions at the reference point. Better agreement is obtained if we discard the assumption that the pressure signals are transmitted through the core flow but instead, are transmitted through the boundary layer. This point has been raised to demonstrate the difficulty in applying simple calculation methods to such flowfields. Firstly, the flow downstream of the shockwave is non-uniform. We can appeal to the findings of Sawyer and Long[15] that, in the steady flow case, the flow has not stabilised after 100 boundary-layer thicknesses downstream, the slip line and velocity gradients in the inviscid flow still being distinguishable. This is well beyond the reference point in our experiment. In cases in which a strong viscous-inviscid interaction occurs (whether or not flow separation is present) a more sophisticated approach is required. Secondly, as has also been concluded by Sabjen et al.[12], the modelling of perturbations in the forced oscillation case as acoustic waves may not be acceptable.

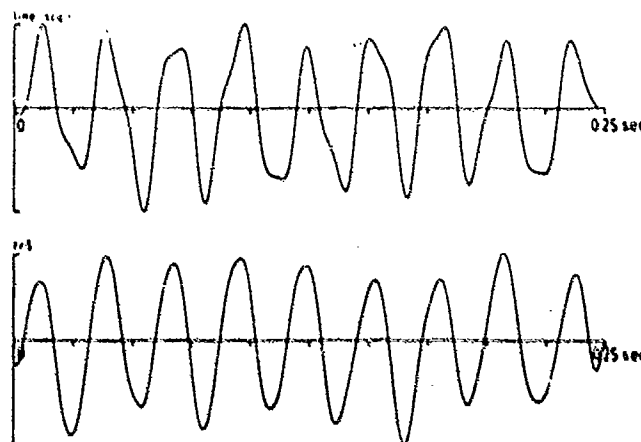


Fig.17 Local shock position and surface pressure fluctuations at $x/\delta = -1.6$ ($M = 1.5$)

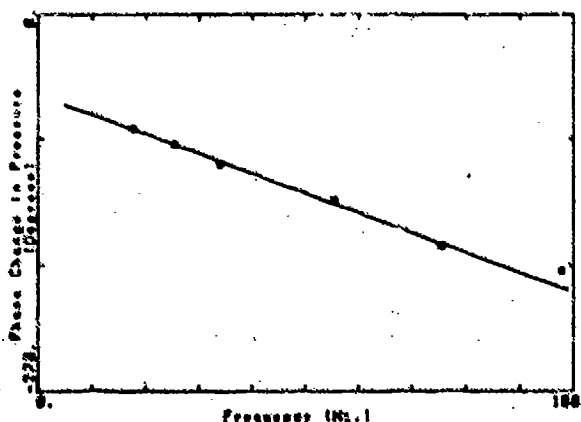


Fig.18 Phase change between the surface pressure at $x/\delta = 1.6$ and the forcing pressure ($M = 1.5$)

4. CONCLUDING REMARKS

The objectives of the design of our experiment, namely, to provide a symmetrically, forced oscillation over a wide range of conditions for a two-dimensional shock/boundary layer interaction on a flat plate, have been demonstrated. Reduced frequencies of order 0.2 to 2 with amplitude parameters of 2% to 20% chord at reduced frequencies from order 0.2 to 0.8 have been achieved.

The generation of a pure forcing disturbance is desirable from the point of view of the validation of theoretical and numerical methods but is difficult in practice. The best approach may be to provide a sinusoidal variation in downstream blockage by movement of the outer walls, however, a reasonably "clean" signal has been demonstrated.

The amplitude parameter is important in flowfields where the boundary layer is close to shock induced separation due to the relationship between amplitude and local shock strength. In such a case one could generate a periodically separating flowfield with obvious similarities to stall flutter. In the case of curved surfaces typical in a cascade of compressor blades it is also possible to envisage the case of a stall flutter occurring due to a low frequency, relatively high pressure disturbance generated downstream of the cascade.

For the purposes of the prediction of shock motion amplitudes to engineering accuracy, the simple asymptotic method has proved to be surprisingly good at high transonic Mach numbers ($M=1.3$), at least in the context of this experiment. This is outside the bounds over which the theory would be expected to apply. However, there are difficulties with phase prediction and this is an extremely important phenomenon, for which prediction methods are essential. Work is still required on the determination of acoustic paths.

Given the details of the shock motion the unsteady surface pressures may be calculated from a knowledge of the steady surface pressure distribution. Certainly this is true of a flat plate boundary-layer for reduced frequencies of $O(0.4)$ and possibly up to reduced frequencies of 0.7 or higher.

The authors are grateful to Rolls Royce Plc. (Derby) in the support of this work.

5. REFERENCES

1. Hurrell, H.G., "Analysis of Shock Motion in Ducts During Disturbances in Downstream Pressure", NACA TN 4090, 1957
2. Richey, G.K. and Adamson, T.C. Jr., "Analysis of Unsteady Transonic Channel Flow with Shock Waves", AIAA Journal, Vol.14, Aug. 1976, pp.1054-1061
3. Messiter, A.F. and Adamson, T.C. Jr., "Asymptotic Solutions for Nonsteady Transonic Channel Flows", Symposium Transonicum II, ed. K. Oswatich and B. Rues, Springer-Verlag, 1976, pp.41-48
4. Chan, J. S.-K. and Adamson, T.C. Jr., "Unsteady Transonic Flows with Shock Waves in an Asymmetric Channel", AIAA Journal, Vol.16, April 1978, pp.377-384
5. Adamson, T.C. Jr., Messiter, A.F. and Lieu, M.S., "Large Amplitude Shock-Wave Motion in Two-Dimensional Transonic Channel Flow", AIAA Journal, Vol.16, Dec. 1978, pp.1240-1247
6. Messiter, A.F. and Adamson, T.C. Jr., "Forced Oscillations of Transonic Channel and Inlet Flows with Shock Waves", AIAA Journal, Vol.22, Nov. 1984, pp.1590-1597
7. Whitehead, D.S., "The Calculation of Steady and Unsteady Transonic Flows in Cascades", Cambridge University Engineering Department, Report CUED/A-Turbo/TR 116, 1982
8. Barton, H.A., Maqvi, M.M. and Newton, S.G., "An Evaluation of a Finite Element Calculation Method for Unsteady Transonic Flows against Cascade Test Data", IUTAM Symposium "Unsteady Aerodynamics of Turbomachines and Propellers", Cambridge, Sept. 1984
9. Sabjen M., Kroutil J.C. and Chen C.P., "A High-Speed Schlieren Investigation of Diffuser Flows with Dynamic Distortion", AIAA Paper 77-875, 1977.
10. Chen C.P., Sabjen M. and Kroutil J.C., "Shock-Wave Oscillations in a Transonic Diffuser Flow", AIAAJ vol. 17, pp 1076-1083, 1979.
11. Sabjen M. and Kroutil J.C., "Effects of Initial Boundary-Layer Thickness on Transonic Diffuser Flows", AIAAJ vol. 19, pp 1386-1393, Nov. 1981.

12. Sabjen M., Bogar T.J. and Kroutil J.C., "Forced Oscillation Experiments in Supercritical Diffuser Flows with Applications to Ramjet Instabilities.", AIAA Paper 81-1487, 1981.
13. Bogar T.J., Sabjen M. and Kroutil J.C., "Characteristic Frequencies of Transonic Diffuser Flow Oscillations.", AIAAJ, Vol. 21, pp 1232-1240, 1983.
14. Liou, M-S. and Coakley, T.J., "Numerical Simulations of Unsteady Transonic Flow in Diffusers", AIAA Journal, Vol.22, Aug. 1984, pp.1139-1145
15. Sawyer W.G. and Long, Carol J., "A Study of Normal Shock-Wave Turbulent Boundary-Layer Interaction at Mach Numbers of 1.3, 1.4 and 1.5.", RAE TR 82099, 1982
16. Sabjen M. and Crites R.C., "Real Time Optical Measurement of Time Dependent Shock Position.", AIAAJ Vol. 17, pp910-912, 1979
17. Roos, F.W. and Bogar, T.J., "Direct Comparison of Hot-Film Probe and Optical Techniques for Sensing Shock-Wave Motion", AIAA Paper 81-0157, 1981
18. Sirieix, M., Delery, J. and Stanewsky, E., "High-Reynolds Number Boundary-Layer Shock-Wave Interaction in Transonic Flow", Lecture Notes in Physics, Vol.148, Springer Verlag, 1981, pp149-214
19. Seddon, J., "The Flow Produced by Interaction of a Turbulent Boundary Layer with a Normal Shock Wave of Strength Sufficient to Cause Separation", RAE TM Aero 667, 1960

DISCUSSION

P.Ramette, Fr

How do you explain that the asymptotic theory is giving good results for a Mach number of 1.32, for which asymptotic theory should not be used?

Author's Reply

One would normally expect that in such an asymptotic expansion, one should take second and third order terms. We were quite surprised that it worked. The results however, are not very good for phase. Phase prediction is a rather difficult problem. We are not sure at this stage why the asymptotic theory does not predict the phase. I suspect that taking a larger number of terms in the asymptotic expansion might give better results at that point of view.

P.Ferrand, Fr

We are particularly interested in your results as we work on choke flutter in turbomachines. We have made a model based on a linear theory which allowed us to study the influence of various parameters. From the results it appears that the fluctuations of the flow, downstream of the shock had a negligible effect on the phase of the shock motion. Your results confirm the quasi-steady effects of these perturbations on the shock. However we have established the dominant influence of the upstream perturbations on the phase, especially in the throat area. The phenomena are not quasi-steady any more. It would be interesting to set up an experiment imposing flow fluctuations upstream of the shock.

Author's Reply

I agree with your comments. It is not simple, with our configuration, to generate well established disturbances upstream. Additionally, we are interested in the effects of the shock movement on the interaction with the boundary layer itself. If one were to disturb the shock from upstream, we would also disturb the boundary layer upstream, and that we prefer not to do.

MEASURED AND PREDICTED LOSS GENERATION IN TRANSONIC TURBINE BLADING

W.N. Dawes, J-J Camus, L.P. Xu and C.G. Graham
 Whittle Laboratory Rolls-Royce PLC,
 Cambridge University P.O. Box 3,
 Madingley Road Filton,
 Cambridge CB3 0DY, U.K. Bristol BS12 7QE

SUMMARY

For a typical transonic turbine rotor blade, designed for use with coolant ejection, the trailing edge, or base loss is three to four times the profile boundary layer loss. The base region of such a profile is dominated by viscous effects and it seems essential to attack the problem of loss prediction by solving the compressible Navier-Stokes equations. However, such an approach is inevitably compromised by both numerical accuracy and turbulence modelling constraints.

This paper describes a Navier-Stokes solver written for 2D blade-blade flows and employing a simple two-layer mixing length eddy viscosity model. Then, measured and predicted losses and base pressures are presented for two transonic rotor blades and attempts are made to assess the capabilities of the Navier-Stokes solver and to outline areas for future work.

1. INTRODUCTION

Gas turbine blades usually, for reasons of stressing or cooling have thick trailing edges. The static pressure just downstream of the trailing edge is typically lower than the adjacent free stream and this base pressure is thought of as being associated with a performance penalty called base drag or base loss. With subsonic exit velocities, the base pressure and near-wake region seem strongly influenced by periodic vortex shedding [1]; indeed this vortex shedding may be more significant than turbulence in the lateral transport of axial momentum in the near wake. By contrast, with supersonic exit velocities this vortex shedding may be suppressed [2] (although some measurements do indicate a vortex street downstream of a strong shock system [3]). Instead a characteristic triangular base region forms downstream of the blunt trailing edge with an associated shock-expansion system [4]. The details of this complex, viscous dominated, region can influence the flow over much of the aft region of the blade suction surface. The overall properties of the blade row, in particular the losses, are largely determined by the flow in the base region.

The 2D, or cascade, loss of a turbine blade, is thought of as consisting of both base loss and profile loss. For a typical high speed gas turbine rotor blade, designed for use with TE coolant ejection, the base loss may be three to four times the profile loss. The problem of modelling the base flow region is thus fundamental to the problem of modelling flows past blading. Numerical simulations using either the potential formulation or the Euler equations must apply explicitly (or implicitly) a Kutta condition at the trailing edge in order to get the blade circulation correct. However, a suitable condition is by no means obvious for a blunt trailing edge. In the context of the inviscid Euler equations of motion, a modelling of the base flow region has been achieved by adding some sort of cusp to the trailing edge to represent the base triangle and adjusting its position iteratively to produce an isobaric zone with the pressure in it given by some base pressure correlation [5]. However, the accuracy of the final solution is at the mercy of the abilities of the correlation. Faige [6] redesigned the aft suction surface profile of a transonic gas turbine rotor blade to reduce the scale of the shock-boundary layer interaction and hence to reduce the profile loss. He used an inviscid Euler solver, run in inverse mode, with a simple TE cusp, to perform the redesign. Although he was indeed successful in reducing the profile loss, the base loss was much increased by a much lower than expected base pressure, and the overall blade 2D loss was little changed.

Numerical simulations using the full compressible Navier-Stokes equations do not, at least in principle, suffer from these difficulties, and should be capable of true predictions. The current paper presents some solutions for the transonic flows past two gas turbine rotor blades obtained using a Navier-Stokes solver developed recently by the first author. The objectives are partly to predict the blade losses and base pressures and their variation with exit Mach number but also to assess the current capability of Navier-Stokes solvers.

In the following sections a brief outline will be given of the Navier-Stokes solution procedure and then the solutions obtained will be presented and discussed. The results are compared with density interferograms, blade surface pressure and loss measurements.

2. NAVIER-STOKES SOLUTION PROCEDURE

The flowfield is described by the two-dimensional isenthalpic time-dependent equations of motion written in integral form:

$$\frac{\partial}{\partial t} \oint_{VOL} \bar{U} dVOL = \oint_{AREA} R \cdot dAREA \quad (1)$$

where

$$\bar{U} = \begin{bmatrix} \rho \\ \rho u \\ \rho v \end{bmatrix} \quad R = \begin{bmatrix} \rho \bar{q} \\ \rho u \bar{q} + \bar{\tau} \hat{i}_x \\ \rho v \bar{q} + \bar{\tau} \hat{i}_y \end{bmatrix}$$

with $\bar{q} = u \hat{i}_x + v \hat{i}_y$ $\bar{\tau} = \sigma_x \hat{i}_x \hat{i}_x + \tau_{xy} \hat{i}_x \hat{i}_y + \tau_{yx} \hat{i}_y \hat{i}_x + \sigma_y \hat{i}_y \hat{i}_y$
 \hat{i}_x and \hat{i}_y are unit vectors and the stress tensor $\bar{\tau}$ has components

$$\sigma_x = p - \mu \left(\frac{4}{3} u_x - \frac{2}{3} v_y \right)$$

$$\sigma_y = p - \mu \left(\frac{4}{3} v_y - \frac{2}{3} u_x \right)$$

$$\tau_{xy} = \mu (u_y + v_x)$$

where $\mu = (1 + \mu_T)/Re$ and for isenthalpic flow $p = (\gamma - 1/\gamma) \rho (h_0 - (u^2 + v^2)/2)$.

Turbulence is introduced by the coefficient μ_T and modelled, for expediency, by a simple two layer mixing length model. Transition is forced to occur at specified locations on the blade. The model has two layers in which the eddy viscosity, μ_T , is given by

$$\mu_T = \begin{cases} (\mu_T)_{inner} & Y \leq Y_{crossover} \\ (\mu_T)_{outer} & Y > Y_{crossover} \end{cases} \quad (2)$$

where Y is the normal distance from the nearest wall and $Y_{crossover}$ is the smallest value of Y at which values from the inner and outer formulae are equal. In the inner region

$$(\mu_T)_{inner} = \epsilon l^2 |B| \quad (3)$$

where $l = \kappa Y (1 - e^{-Y/A^*})$ (4)

$|B|$ is the magnitude of the vorticity and

$$Y^* = \frac{u^2}{u_w^2} \quad \frac{v^2}{v_w^2} \quad (5)$$

In the outer region

$$(\mu_T)_{outer} = C_{CL} \cdot P_{WAKE} \cdot P_{KLEN} \quad (6)$$

where

$$P_{WAKE} = \text{AMIN}(V_{MAX} V_{MAX}^*, C_{WX} V_{MAX}^{u_{DIFF}/V_{MAX}}) \quad (7)$$

The quantities P_{MAX} and V_{MAX} are determined from the function

$$F(Y) = Y |B| (1 - e^{-Y/A^*}) \quad (8)$$

V_{MAX} is the maximum value of $F(Y)$ in a given profile and Y_{MAX} the value of Y at which the maximum occurs. Thus the model length scale is determined from the vorticity distribution. The Klebanoff intermittency factor is given by

$$P_{KLEN} = 1 / \left[1 + 9.5 \left(\frac{C_{KLEN} Y}{V_{MAX}} \right)^2 \right] \quad (9)$$

The value of u_{DIFF} is the difference between maximum and minimum velocities in the given profile.

The outer formulation is used in wakes and in attached and separated boundary layers. Transition must be simulated by ad hoc means; in the current effort by specifying the actual location of the transition point on the blade.

The various constants are taken as:

$$\begin{aligned} A^* &= 26 \\ C_{CL} &= 0.02688 \\ C_{KLSB} &= 0.3 \\ k &= 0.41 \\ C_{WK} &= 0.25 \end{aligned} \quad (10)$$

The flowfield is divided into a large number of arbitrary non-orthogonal finite volume computational cells. The flow equations are discretised on this mesh with flow variables stored at cell centres. Values of the variables on cell faces are found by assuming that they vary linearly between cell centres. Viscous derivatives on cell faces are evaluated by defining a local non-orthogonal co-ordinate system. The full stress tensor is retained. The system of equations are marched forward to an asymptotic steady solution using the implicit iterative replacement (or deferred correction) algorithm described in more detail in [8] and [9], to which the interested reader is referred.

The algorithm has the block matrix-vector form:

$$(I - \frac{\Delta t}{\Delta VOL} M) \Delta \bar{u} = \frac{\Delta t}{\Delta VOL} (L_H + D_1 + CV)^n \quad (11)$$

where

$$\Delta \bar{u} = \bar{u}^{n+1} - \bar{u}^n$$

$$L_H = \sum_{\text{cells}} R_i (\Delta A_{ix} \hat{i}_x + \Delta A_{iy} \hat{i}_y) \quad \text{is essentially second order accurate centred representation of the integral flux operator}$$

D_1 is a defect operator chosen to be essentially the difference between an upwind and a centred representation of the flux terms and added to enhance robustness and iterative stability

$CV^n = (1-\omega) CV^{n-1} + \omega(D_1 - D_2)$ is a correction factor designed to progressively remove the defect operator and force a higher accuracy steady solution (ω is a relaxation parameter typically 0.1)

and

D_2 is a residual smoothing operator which limits the cell Reynolds number (its typically 10^{-4} to 10^{-6}) and contains a numerical filter to control the shock capture (without affecting boundary layers or wakes) [8]

The block five diagonal matrix M , on the LHS of equation (11) represents the conventional linearised reflection of the non-linear RNS operators (obtained by replacing $u^{n+1} = u^n + \frac{1}{2} \Delta u$, $\frac{\partial}{\partial x} = \frac{\partial}{\partial x} + \frac{1}{2} \frac{\partial}{\partial x}$, etc.). The matrix $(I - \frac{\Delta t}{\Delta VOL} M)$ is factored into two tridiagonal matrices for efficient inversion. The asymptotic steady solution, taken as $\Delta u = 0$ is

$$L_H + D_1 + D_2 = 0 \quad (12)$$

It should be stressed that the residual smoothing provided by D_2 is carefully controlled and is in fact effectively set to zero in regions dominated by physical viscous effects.

The boundary conditions are fixed flow angle and stagnation pressure at inflow, fixed static pressure at outflow and zero slip velocity on the blade surfaces. Pressure on blade surfaces is extrapolated from interior cells and although options exist in the code for the use of wall functions to reduce grid resolution requirements in the near-blade region, all the solutions presented here employ a sufficiently fine mesh to resolve the blade boundary layers down to laminar sublayer scale. This has been shown [9] to be important if loss predictions are to be attempted.

The algorithm is used with spatially varying time steps to enhance convergence rate and a typical solution requires 400-600 time steps at a processing rate of 10^{-3} s/pu seconds per point per time step on a Perkin Elmer 3230 mini-system (10^{-3} seconds per point per time step on an IBM 3081 mainframe).

3. BLADE DETAILS AND COMPUTATIONAL MESHES

Two turbine blade profiles were chosen for the present study. Both were high pressure turbine rotor sections with thick coolable trailing edges, but operated here with no coolant flow. The main difference between the blades is the TE thicknesses.

The first blade, designated RD, was tested by Haller [10]; details of the blade geometry are available in [10]. The key parameters are

Pitch/chord	0.842
inlet angle	-56.75°
exit angle	+64.65°
stagger angle	29.6°
TE radius/chord	1.41

The blade was tested over a range of exit isentropic Mach numbers from 0.9 to 1.2 with a nominal Reynolds number (on chord) of 0.9×10^6 .

The second blade, designated RG, was tested by Paige [6]. The key parameters are

Chord	41.1 mm
Stagger	39.8°
Pitch/chord	0.824
inlet angle	-59.1°
Exit angle	+71.5°
TE radius/chord	1.91

For the test results that are presented here, the isentropic exit Reynolds number, based on blade chord, was 0.7×10^6 . The blade was tested over a range of exit isentropic Mach numbers from 0.8 to 1.2.

The TE thickness of RG is about 50% greater than that of RD.

The Navier-Stokes solutions were obtained on an H-mesh with mesh lines exponentially refined towards blade surfaces to fully resolve the blade boundary layers. For the RD blade, 41×30 mesh was used with seven cells around the trailing edge circumference. A general view of the mesh is given in Figure 1, and a detail view of the mesh near the trailing edge is given in Figure 2. This mesh required about 1.2 Mbytes of storage using 12 bit real numbers. A similar mesh was employed for RG.

4. PRESENTATION AND DISCUSSION OF RESULTS

4.1 Blade-blade flowfield and blade surface properties

Generally good agreement was obtained between predicted and measured blade-blade flowfields and blade surface pressures over the whole range of flows considered. For economy of space only a few examples will be presented here.

4.1.1. RD blade

Fringes of constant density measured for the blade RD using holographic interferometry [10] are shown in Figure 3 for an isentropic exit Mach number of 0.9 for which the flow is entirely subsonic. Figure 4 shows contours of density predicted by the Navier-Stokes solver (the contour interval is the same as that in the interferogram). The agreement is good: all the features present in the interferogram are successfully resolved.

Measured density fringes are shown in Figure 5 for an isentropic exit Mach number of 1.20. The shock-expansion system associated with the trailing edge is apparent. The strong expansion generated as the flow turns from the pressure surface around the trailing edge is quickly followed by an oblique shock which passes across the blade passage and interacts with the suction surface boundary layer. Surface oil-flow studies [10] show that the boundary layer separates, with re-attachment indicated just upstream of the trailing edge. Figure 6 shows density contours (again with the same interval as in the measurements) predicted by the Navier-Stokes solver. The agreement with the measurements within the blade passage is striking, particularly the resolution of the passage shock. In the predictions the shock interaction separates the suction surface boundary layer, but re-attachment does not occur upstream of the trailing edge. Consequently the trailing edge shock on the suction side is missing from the predictions.

Predicted blade surface isentropic Mach numbers are compared with measurements in Figures 7 and 8 for exit Mach numbers of 0.90 and 1.20 respectively. The agreement is very satisfactory.

4.1.2 RG blade

Figure 9 shows predicted contours of Mach number for a case with zero incidence and design exit Mach number of 1.15. The shock-suction surface boundary layer interaction is strong enough to cause separation with re-attachment just upstream of the trailing edge.

Figures 10 and 11 compare predicted and measured blade surface isentropic Mach numbers for zero incidence and $+10^\circ$ incidence respectively and at exit Mach numbers of 1.15 and 1.10. The agreement is satisfactory.

Both predictions and measurements [6] indicate that the interaction of the trailing edge shock with the suction surface boundary layer is sufficient to cause a small separation bubble. This bubble grows with increased exit Mach number until at speeds higher than design re-attachment does not occur upstream of the trailing edge. In addition in the runs at $+10^\circ$ incidence, a large separation bubble (from 15 to 35% axial chord) is present associated with the leading edge overspeed.

4.2 Blade losses and base pressures

4.2.1 RD blade

Blade losses were computed over a range of exit Mach numbers assuming turbulent boundary layers because film cooling slots in the suction surface of the experimental blade promote early transition. The predicted loss coefficients $(p_{01} - p_{02})/(p_{02} - p_2)$ are compared with those measured in Figure 12. The measured losses show a dramatic increase as the exit Mach number becomes supersonic, rising from around 4% at $M_2 = 0.9$ to 9% at $M_2 = 1.2$. The predicted loss variation follows this trend but with somewhat higher level (losses rising from around 5.5% at $M_2 = 0.9$ to 11.5% at $M_2 = 1.2$).

Predicted and measured base pressures are compared in Figure 13. Over the range of Mach numbers considered the predicted base pressures are lower than those measured and this is consistent with the overprediction of losses. The low values of predicted base pressure imply too much mixing near the trailing edge and hence too rapid entrainment of fluid into the wake [12]. To test this hypothesis, the computations were repeated for the 1.20 exit Mach number case assuming the flow to be entirely laminar. As shown in Figures 12 and 13 the predicted base pressure is indeed increased by the reduced trailing edge mixing and the predicted losses reduced. However, the predicted loss is still some 2% points higher than that measured. This remaining discrepancy which persists right down to subsonic exit Mach numbers must be attributed to the inevitable numerical errors associated with satisfying the conservation equations only to a certain discrete level.

4.2.2 RG blade: zero incidence

The variation with exit Mach number of predicted and measured loss coefficients is shown in Figure 14 for the RG blade at zero incidence. For these computations, the blade boundary layers were assumed to be laminar the way to the trailing edge. The predicted losses are greater than those measured for subsonic exit Mach numbers and lower for supersonic exit. This trend is consistent with the variation of predicted measured base pressures, Figure 15, which show the predicted base pressure to be too low for subsonic exit and too high for supersonic exit. In terms of trailing edge modelling this implies that there is too much mixing for subsonic exit Mach numbers (as was observed for RD) but too little mixing for the supersonic exit cases.

Experimental observation suggests that at the design exit Mach number of 1.15 the suction surface boundary layer remains laminar until interaction with the passage shock causes separation followed by turbulent re-attachment. In the numerical simulations, the transition location is simply specified as an input variable. Figure 16 shows, for design exit Mach number, the predicted variations of loss coefficient and base pressure with suction surface transition location. The predicted losses increase as transition is moved towards the leading edge but the base pressure is very little altered. This contrasts with the predictions for the RD blade where, for supersonic exit velocities, base pressure, as well as loss, were sensitive to transition location. This suggests that the increased trailing edge thickness of RG relative to RD (50% thicker) renders the base flow less sensitive to the character of the boundary layers and that the variation of loss with transition location for RG must be associated with blade profile loss, rather than TE loss.

4.3. RG blade at $+10^\circ$ incidence

The variations with exit Mach number of predicted and measured loss coefficients and base pressures are shown in Figures 17 and 18 for the RG blade operated at $+10^\circ$ incidence. The computations were performed using laminar boundary layers. The much higher level of loss at subsonic speeds (compared with the zero incidence case) are due to separation bubbles on the suction surface from about 15 to 35% axial chord caused by the leading edge overspeed.

As in the earlier cases considered, a consistent picture emerges of: predicted base pressures lower than measured over predicted loss levels are higher, and vice versa; loss levels over predicted by 1 to 2% points with respect to measurement for subsonic

exit velocities; loss levels more closely predicted for the cases with supersonic exit velocities.

5. CONCLUDING DISCUSSION

In the flow past turbine blades there is a relatively weak coupling between the inviscid flow and the boundary layer flow. (Unlike compressor blading where this coupling is strong and dominates the flowfield character). Consequently, it is straightforward to achieve good agreement between predicted and measured blade surface pressures. The quality of loss prediction is determined by how well the Navier-Stokes solver allows the boundary layer flow (including the small separations) to respond to the imposed pressure field and by how well the solver limits the impact of numerical error. The Navier-Stokes solver used in the present study predicts well the trends in loss coefficient when compared to the measurements but with discrepancies in level. Several points may be drawn from the comparisons made:

(i) the predicted combinations of loss and base pressure are consistent. When predicted losses were higher than measurement, the base pressures were lower, and vice versa. Globally the base pressure results from mass momentum and energy balances ("mixing out"). Locally this conservation takes place by strong mixing (dissipation) in the trailing edge region. The stronger the mixing the more vigorous the entrainment and the lower the base pressure. Some of the discrepancies between predictions and measurements seem to be due to poorly predicted mixing levels [12]; this is hardly surprising for the cases run with turbulent boundary layers when considering the crude turbulence modelling employed. Additionally, the predictions do not resolve the vortex shedding, from the trailing edge at subsonic speeds (because the time marching time step size is bigger than the shedding time scales) and so one of the potential mixing mechanisms is missing.

(ii) at subsonic exit velocities the predicted loss level is systematically higher than that measured (1 to 2% points high). Much of this discrepancy must represent numerical error. Quite apart from issues such as mesh size and quality and formal truncation error, numerical error in total pressure is inevitable (Dr. J.D. Denton - Private Communication). The numerical scheme satisfies the conservation equation for mass momentum and energy exactly (at some discrete level), but total pressure (i.e. loss) is derived from the solution; combining properties which are consistent only on a discrete level is similar to the classic irreversible mixing of two streams of fluid with different velocities and is bound to lead to loss generation. The way round the problem may be to solve the equation for entropy transport and production as well as the equations of mass momentum and energy conservation. Rather than being redundant, the total pressure equation is used to monitor the accuracy of the main solution procedure. Encouraging work is already proceeding along these lines.

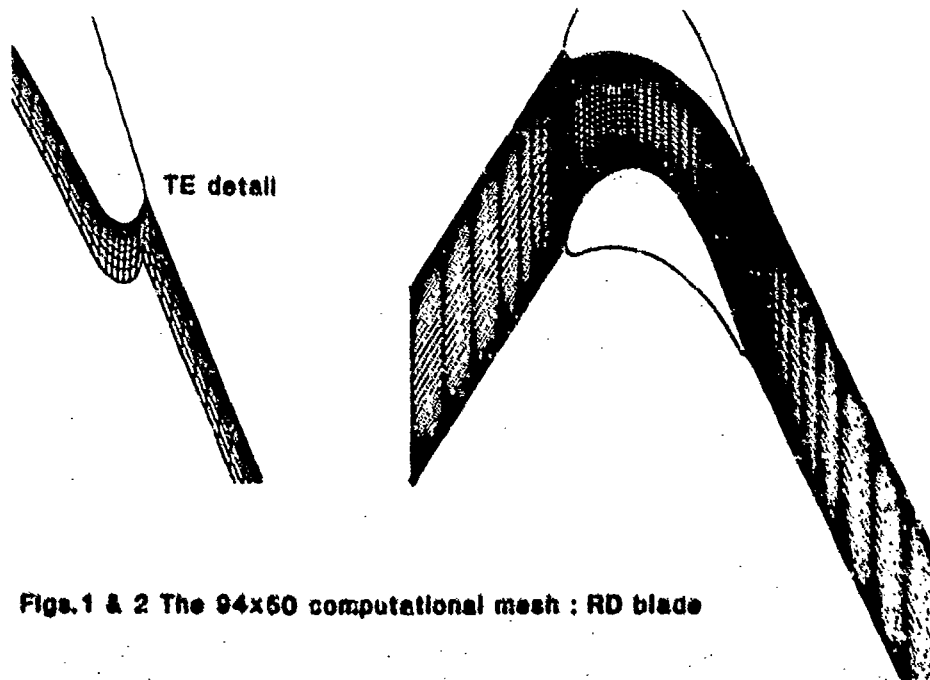
(iii) predicted and measured loss levels rise dramatically for supersonic exit Mach numbers. Whether predicted losses are higher than measurement or not depends on the actual exit Mach number at which the predicted rise occurs; the predicted point of loss increase is early for RD and late for RG. The rise in losses is partly due to separation of the suction surface boundary layer but also due to the transition point moving on the blade surface. More work is needed on transition modelling in the context of Navier-Stokes solvers.

6. ACKNOWLEDGMENTS

J.-J. Camue and L.P. Xu thank Rolls-Royce, Plc, for their sponsorship of the experimental part of this work and Rolls-Royce personnel for essential discussion.

REFERENCES

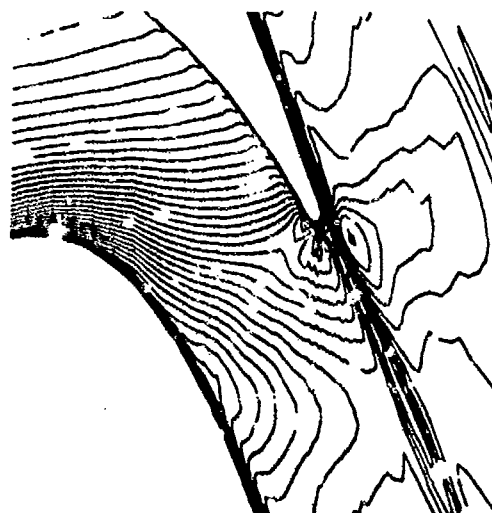
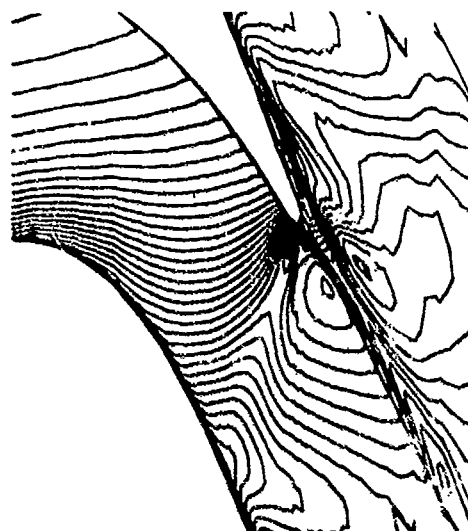
- [1] Paterson, R.W., and Weingold, H.G. Experimental investigation of a simulated compressor airfoil trailing edge flowfield
AIAA Paper 84-0101, 1984.
- [2] Lawaczeck, O., Heinemann, H-J, von Karman Vortex Streets in the wakes of subsonic and transonic cascades
AGARD-CP-177, Paper No. 28, 1976.
- [3] Richards, P.H., and Brown, R.G.W. Measurements in shear layers in transonic flows with a laser transit anemometer.
J. Phys. D. Appl. Phys., 15, 1982.
- [4] Sieverding, C., Decuyper, M., Colpin, J., and Amana, O. Model tests for the detailed investigation of the trailing edge flow in convergent transonic turbine cascades.
ASME Paper 76-GT-30, 1976.
- [5] Singh, U.K. Computation of transonic flows in and about turbine cascades with viscous effects.
ASME Paper 84-GT-18, 1984.
- [6] Paige, R.W. A computational method for the aerodynamic design of transonic turbine blades Ph.D. Dissertation, Cambridge Univ., 1983.
- [7] Baldwin, B., and Lomax, H. Thin layer approximation and algebraic model for separated turbulent flows.
AIAA Paper 78-257, 1978.
- [8] Dawes, W.N. Computation of off-design flow in a transonic compressor rotor.
ASME Paper 85-GT-1, ASME Gas Turbine Conference, Houston, 1985.
- [9] Dawes, W.N. Application of full Navier-Stokes Solvers to Turbomachinery Flow Problems. VKI Lecture Series 1986-02. Numerical Techniques for Viscous Flow Calculations in Turbomachinery Bladings. Jan 1986.
- [10] Haller, B.R. The effects of film cooling upon the aerodynamic performance of transonic turbine blades.
Ph.D. Thesis, Cambridge Univ. 1980.
- [11] Bryanston-Cross, P.J., Lang, T., Oldfield, M.L.G., and Norton, R.J.G., Interferometric measurements in a turbine cascade using image-plane holography.
ASME J. of Eng. for Power, Vol. 103, 1981.
- [12] Xu, L., The base pressure and trailing edge loss of transonic turbine blades
Ph. D. Dissertation, Cambridge Univ., 1986.



Figs.1 & 2 The 94x60 computational mesh : RD blade



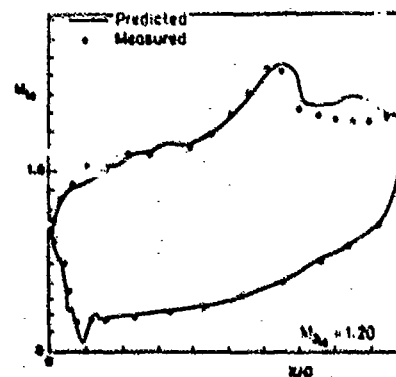
measured

 $M_2=0.90$ 

predicted

 $M_2=1.20$

Figs.3-6 Measured and predicted density contours : RD blade



Figs.7 & 8 Measured and predicted blade surface isentropic Mach numbers : RD blade

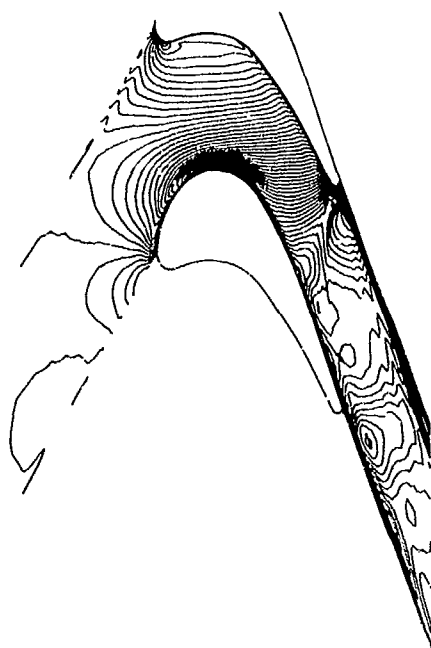
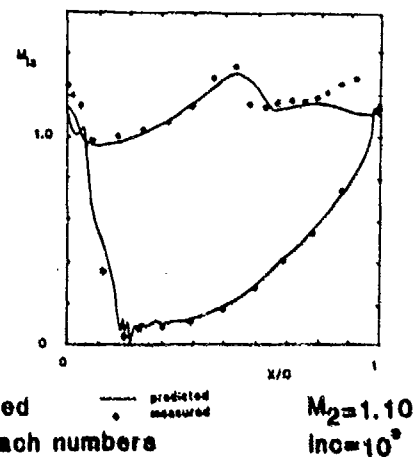
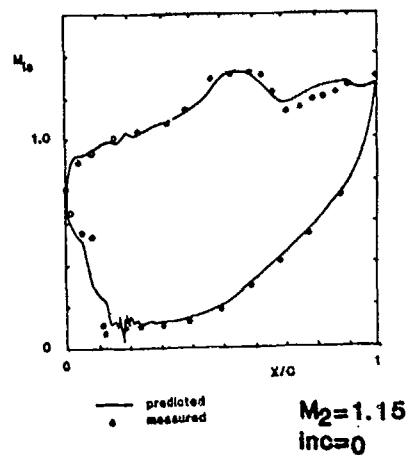
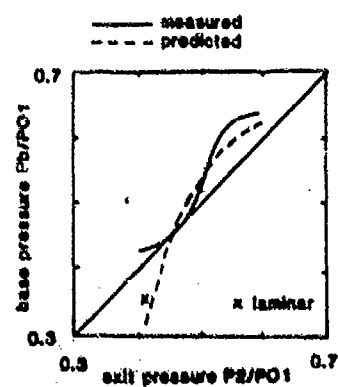
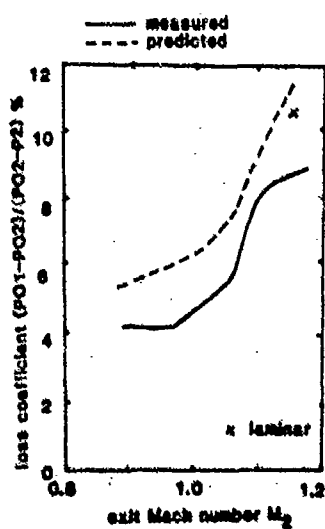


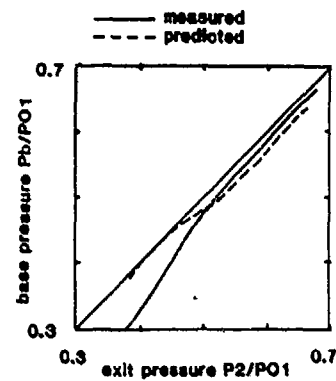
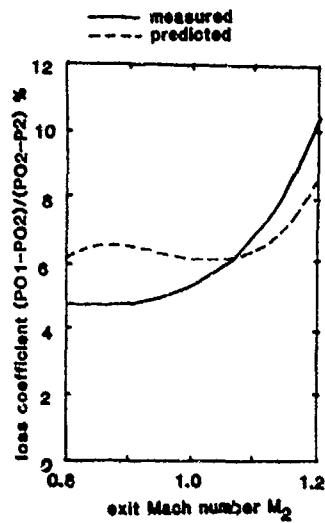
Fig.9 RG : predicted Mach numbers
 $M_2=1.15$ $\text{inc}=0$
 (interval 0.025)



Figs.10 & 11 RG : predicted and measured
 blade surface isentropic Mach numbers

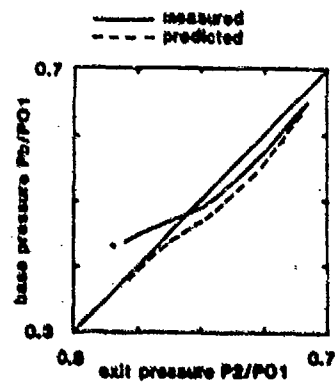
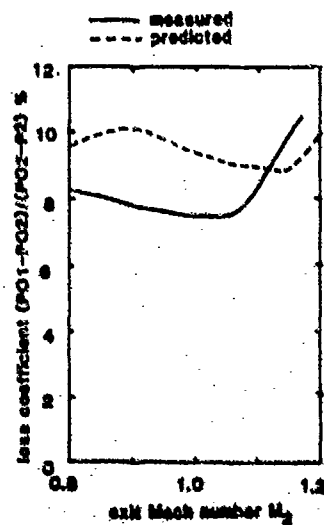
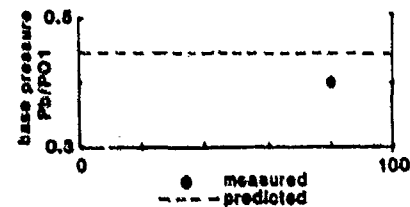
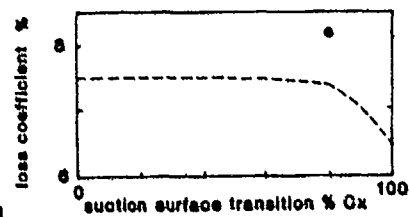


Figs.12 & 13 RD : predicted and measured loss coefficients and base pressures



Figs. 14 & 15 RG : predicted and measured loss coefficients and base pressures
- incidence 0

Fig. 16 RG : variation of predicted loss coefficient and base pressure
with suction surface transition location - $M_2 = 1.15$



Figs. 17 & 18 RG : predicted and measured loss coefficients and base pressures
- incidence 10 degrees

DISCUSSION

J. Chauvin, Fr

The differences between measured and calculated total pressure are of the order of 1%. Are you sure that this is larger than the measurement accuracy?

Author's Reply

I am not sure that the discrepancy between measured and predicted total pressures is larger than experimental accuracy for supersonic exit velocities. Nevertheless, I think that numerical error (false total pressure loss) may be responsible for discrepancies of around 1% point, firstly because the discrepancy between measured and predicted loss levels is systematic and secondly because false total pressure loss is inevitable in non-uniform flows (especially at the blade leading edge).

J. Moore, US

You are comparing 2-D calculation with what must have been at some point a 3-D flow. Could that account in part for the differences between measurement and calculation?

Author's Reply

I could have believed that but if you sum the entropy generation it tends to explain levels of discrepancy that I see in the results. The problem is probably false total pressure generation.

J. Moore, US

Have you ever tried just simply turning the viscosity off?

Author's Reply

It is easier said than done. You write a program with a certain philosophy. I cannot turn the viscosity off.

J. Moore, US

You could multiply it by 0.1.

Author's Reply

Yes, you can run at enormous Re numbers but you still have non-negligible levels of pressure loss, principally at the leading edge.

J. Moore, US

When you say at the L.E., is that the same problem that J. Denton has?

Author's Reply

It is not appropriate for me to discuss Denton's approach. Leading edge is the place where you have the largest gradients in pressure, larger than in shocks. It is the last place where you would expect the H-mesh to be applicable.

J. Moore, US

So it is the mesh which is giving you trouble.

Author's Reply

The mesh at the leading edge contributes to false entropy production. Elsewhere the mesh is satisfactory.



AD-P005 512

INFLUENCE OF SHOCK AND BOUNDARY-LAYER LOSSES
ON THE PERFORMANCE OF HIGHLY LOADED SUPERSONIC
AXIAL FLOW COMPRESSORS

K. D. Broichhausen

and

H. E. Gallus

Motoren- und Turbinen-Union
München GmbH
Dachauer Str. 665

Institut für Strahlantriebe
und Turboelasmaschinen RWTH Aachen
Templergraben 56

8000 München 50, Germany

5100 Aachen, Germany

SUMMARY

Performance and losses of trans/supersonic axial flow compressors are influenced by shock structure, shock-boundary layer interactions and boundary layer separation. The combination of these phenomena and their effects on the flow characteristics of supersonic compressors are discussed in the presented contribution. For this purpose experimental results are compared with theoretical approaches involving different semi-empirical correlations for shock and boundary layer losses, for separation and flow deviation. By an appropriate combination of these models the flow characteristics of supersonic compressors are interpreted and the performance of such compressors is successfully reproduced in a wide range. Finally, generally valuable statements on the design of highly loaded supersonic compressors are derived and possible perspectives are described.

SYMBOLS

A	area	c	absolute velocity
D	diffusion factor	F	area rotor entrance
M	Mach number	n	rot. speed
p	stat. pressure	p_t	total pressure
r	radius	Re	Reynolds number
R	Gas constant	t	pitch
T_{rot}	rotalpy	u	circumferential velocity
w	relative velocity	x_0, y_0	coordinates bow shock
α	absolute flow angle	β	relative flow angle
γ	ratio of spec. heats	σ	solidity
ω	loss coefficient		

SUBSCRIPTS

O	design	1,2,3	axial position
abs	absolute system	h	hub
P	profile, pressure side	rel	relative system
S	suction side	t	tip
TM	tandem mean position		

SUPERSCRIPTS

\sim	downstream shock	*	critical data
--------	------------------	---	---------------

1. INTRODUCTION

Regarding the extreme increase in stage pressure ratio of the next jet-engine generation, the application of supersonic compressors again is considered. In the past different attempts on the realization of supersonic compressors were made:

With respect to impulse-type-rotors with totally supersonic flow, remarkable standards were reached at the end of the NACA research period /1/, at CNERA /2/, at the AFARL /3/ and the RWTH-Aachen /4/. In all cases, however, the deceleration of the flow in the stators was connected with a strong decrease in efficiency. A more even distribution of the static pressure rise in rotor and stator was achieved by the development of rotors with strong passage shocks and tandem-stators /5, 6, 7/. With these components high pressure ratios ($\pi_t = 3.5$) have been reached in combination with satisfying efficiencies ($\eta_t = 82\%$).

These results, specially for the rotors, are based on well established design methods /4, 7/. The theoretical description of the off-design performance, however, up to now encounters major difficulties by a lack of experimental data and insight into the aerodynamics of supersonic compressors.

Therefore the performance data of different supersonic compressors (Fig. 1) have been compiled. The main geometry of these compressors is outlined in table 1. In the following, some characteristic results of these extensive investigations are compared with a performance prediction method. For this theoretical approach a loss model, consistent for all investigated supersonic components, is described and the dominating influence of compression shocks and viscous effects is discussed. A more detailed discussion of measuring techniques and theory is presented in /8/.

2. SURVEY ON THE BASIC COMPUTATIONAL METHODS

For the detailed analysis of the whole flow field at off-design conditions a streamline-curvature through flow method /7/ is used. To determine the overall performance of the compressor more efficiently, this code is reduced to a single representative streamline and applied as a pitch-line duct flow technique. In the case of the supersonic compressor components it is not sufficient to establish control-surfaces at entrance and at the exit of each blade row (Fig. 2). Additionally the influence of the blockage caused by finite blade thickness has to be considered. To cover this effect supplementary computational planes have to be positioned inside of rotor and stator.

For the tandem-stators the effective flow through area of each partial channel is represented by two control planes at entrance and exit of the overlapping part of the cascade. The flow conditions at the entrance of the second blade row are determined by a simplified SI-surface calculation corresponding to /7/. Assuming isentropic flow downstream of the leading edge shock system, the velocity and the Mach number upstream of the two channels yields applying the conservation of energy and circulation on the coarse grid, shown in Fig. 3:

$$\frac{c_{0, s-1H}}{c_{1,1}} = \frac{c_{1H}}{c_{1,1}} = \frac{1}{4} \frac{1 - \cos \alpha_{1H}}{\Delta s_{1H}} \quad \tan \alpha_{1H} = 2 \frac{\sin \alpha_1^*}{\cos \alpha_1^*}$$

$$M_{0, s-1H}^2 = \frac{c_{0, s-1H}^2}{c_{1,1}^2} M_{1,1}^2 \left\{ 1 + \frac{\gamma-1}{2} M_{1,1}^2 \left(1 - \frac{c_{0, s-1H}^2}{c_{1,1}^2} \right) \right\}$$

Regarding the leading edge blockage, at the entrance of the rotor the span is imposing certain radial effects: choking occurs not over the whole channel cross section but on discrete circumferential domains with transonic inlet flow. This is illustrated by Fig. 4 where the percentual amount of local choking (related to the overall inlet cross section) is plotted for different speeds. As a parameter the relative leading edge thickness related to the pitch is varied. Corresponding to this graph, an overall choking occurs only for a leading edge thickness greater than 1.2% of the pitch and in a rather narrow range of rotational speed. However, partial choking has to be considered even for very thin blades and within a remarkable range of rotor speeds. It extends from local choking near the tip at low speeds over partial choking near midspan to local choking near the hub at higher rotor speeds.

3. SHOCK- AND LOSS-MODELLING

3.1 Boundary-Layer Losses

The losses caused by the viscosity of the fluid can be attributed to boundary layers at the hub, the casing and the blades. For design tasks the profile boundary-layers are determined by a boundary-layer calculation. The integral method used is described in /9/. In case of performance prediction the complexity of the calculation is reduced determining the profile losses utilizing the loss model proposed by Monnerat *et al.* /10/. Considering also a radial shift of the streamlines it gives a correlation of the loss coefficient ω /11/ and the aerodynamic loading of the profile indicated by the diffusion factor D (Fig. 5) for different spans.

As the supersonic compressors have low aspect and high hub-tip-ratios, the losses for rotor and stator are taken for the near wall region of the Monnerat correlation indicated by screening in Fig. 5.

3.2 Shock-Boundary-Layer Interaction

In the case of supersonic and transonic flow in the blade passages the interaction between shocks and boundary layers has to be taken into account. In the impingement zone of the shocks the boundary layers have to undergo a sudden pressure rise, which leads to an increase of the boundary layer thickness or even to shock-induced separation. This aerodynamic loading of the boundary layer is dealt by a semiempirical approach [7], which is implemented in the integral-equations boundary layer code. In the interaction region the characteristic distributions of wall pressure rise, momentum thickness and shape factor, revealed by a series of experiments, are described unitary in dimensionless form using the conservation laws for the impingement zone. This procedure is experimentally validated for shock-upstream Mach numbers up to 1.4.

Applying a duct flow calculation a detailed analysis of the boundary layer is impossible. The losses due to weak shock-boundary-layer interaction are assumed to be included in the Monserrat loss correlation. An additional integral loss is however calculated when the shock forces the boundary-layers to separate. The separation itself is indicated by an interpolation of the data of Donaldson and Lange [12]:

$$\frac{\beta}{\rho_1} < 1 + K_1 \times M_{rel}^2 + Re_x^{-K_2}$$

$$K_1 = 2.25 ; K_2 = -1/5 \text{ (turbulent)}$$

$$K_1 = 0.7 ; K_2 = -1/2 \text{ (laminar)}$$

If separation occurs, it is assumed, that the separated boundary layer generates a critical through flow cross section inside of the blade passage and the flow downstream decelerates from $M = 1$ to the effective outlet cross section of the cascade according to a Carnot-diffusion process [13]:

$$\frac{W_{cl}}{W^*} = \frac{x R T_{rot} + \frac{x-1}{2} u_{cl}^2 + \frac{x-1}{2} W_{cl}^2}{(A_{cl}/A^*) d^2 + x W^2}$$

3.3 Boundary-Layer Blockage

The displacement of the flow by the boundary-layers is able to choke the flow in the blade passage. This effect is reproduced considering the influence of the overall losses on the local Mach number.

Considering only commonly used deviation correlations, the numerical simulation shows specially at part speed conditions and high back pressure, that the losses of the shock induced boundary-layer separation may cause passage choking to occur in the rotors. The experiments however indicate that in these cases the "unique incidence" [14] mass flow is swallowed even with a spanwise supersonic relative velocity at the rotor entrance. The exit flow angle according to the experiments obviously is adjusted for separated boundary layer up to critical conditions in the exit plane of the rotor.

If, however, loss induced choking is indicated without any boundary-layer separation, the entering mass flow defined by the "unique incidence" condition is unable to pass the critical cross section any longer. In reality the compressor would run into an unsteady choking process.

Only in case of an inlet flow with subsonic relative velocity near the hub, the inlet flow is reduced iteratively corresponding to the choking mass flow at the rotor exit.

3.4 Shock Losses

In supersonic compressors the shock losses contribute significantly to the overall losses and a detailed representation of the shocks is essential for a successful prediction of the flow field and the off-design performance. Thus, for design purposes the 3-D shock structures are determined by a fitting procedure, described in [7, 9]. With a view to the loss prediction at off-design speed again a simplifying model is used. The losses are assumed to be generated either by a bow shock or a passage shock. The shape and the intensity of the hyperbolic bow shock (i.e. X_{sh}, Y_{sh} in Fig. 6) is determined corresponding to Moockel [15] by conservation of mass and energy within the subsonic region in front of the blade leading edge (screened in Fig. 6). The shape of the stagnation streamline is found applying the continuity equation between the undisturbed inlet flow conditions and an arbitrary left running characteristic i emanating from the suction side.

The losses of the shock system appearing in the blade passage are represented by a single normal leading-edge shock [10]. The shock Mach number is the mean between the inlet value and the conditions at the shock impingement point on the suction side, determined by a Prandtl-Meyer expansion.

The bow-shock losses have to be considered only for blades with strong suction side camber (impulse-type-rotor). In this case and for design speed these losses are still low compared to the losses of the normal leading-edge shock (Fig. 6 b). The bow-shock losses, however, contribute remarkably to the overall losses at low speed conditions.

If the flow is throttled by increased backpressure or in consequence of the blade passage geometry, an additional shock system is stabilized within the blade channel. The additional losses are simulated by a normal passage shock, whose position is varied according to the back pressure. For this purpose the Mach number distribution in the blade passage is assumed to change corresponding to the variation of the flow through area.

4. PERFORMANCE ANALYSIS

4.1 Supersonic Compressor Rotors

4.1.1 Overall Entrance and Exit Flow Properties

The inlet flow conditions of the investigated rotors (Fig. 1) can be discussed comparing the absolute Mach number variation for different rotor speeds (Fig. 7a, b). In case of the impulse-type rotor in the whole range of investigated rotational speeds the inlet flow corresponds to the unique incidence condition at mid-span.

Examining the shock rotor the unique incidence condition predicts a Mach number which is too high at low speed operation (thin line in Fig. 7b). This mass-flow reduction is caused by the blockage of the blades, which are wedge shaped near the leading edge. Considering this geometrical blockage as qualitatively described in Fig. 4 the variation of the axial Mach number with rotor speed is reproduced more accurately. In conformity with the remarks on choking caused by boundary-layer blockage, this adjustment of the massflow can no longer occur with relative supersonic flow near the hub.

The rotor exit flow conditions are compared by means of the speed dependent variation of the relative Mach number (Fig. 8a, b) and the absolute flow angle (Fig. 9a, b) measured with reference to the circumferential direction.

For unthrottled flow the relative Mach number in the exit of the impulse-type rotor is increasing with rotor speed nearly comparable to the isentropic increase. In correspondence the absolute flow angle decreases continuously.

In the case of high backpressure the data at the exit of the impulse-type rotor show two different ranges with increasing speed. At lower speeds ($n/n_0 < 0.8$) in accordance with semiconductor measurements in the compressor casing the presented loss- and shock models reveal, that the front wave is strongly detached in consequence of the curved suction side and the low Mach numbers. The pressure rise in the blade passage shock, stabilized by the back pressure is small and the boundary-layers remain attached. Thus, even with high back pressure and a position of the passage shock near the spill point, the relative exit flow velocity increases with rotor speed.

Above $n/n_0 = 0.8$ the strong passage shock causes a separation of the suction side boundary-layer. The additional losses are responsible for a slightly subsonic relative exit Mach number, nearly constant with increasing rotor speed up to the design point.

Contrary to the impulse-type rotor the shock-rotor has a decreasing blade passage cross section. Because of this converging geometry and additional shock losses even for unthrottled flow the exit Mach number for different speeds differs significantly from the one found at the impulse-type rotor.

At maximum back pressure the exit Mach number of the shock-rotor decreases slightly increasing the rotor speed at low speed conditions ($n/n_0 < 0.83$). This is caused by the mass-flow reduction due to leading edge blockage (Fig. 7b). The resulting change of the mean incidence angle brings upon an increase of the through-flow area ratio across the rotor and thus for subsonic passage flow a deceleration of the flow with increased rotor speed.

If shock induced boundary-layer separation occurs ($n/n_0 > 0.83$) the computer simulation of the flow indicates choking at the rotor exit. Corresponding to the discussed correlations (Ch. 3.3) the relative flow angle is adjusted discontinuously till sonic exit flow is generated. Experimental data and the computed course (dashed line Fig. 8b, 9b) consequently show for high back pressure a sudden increase of relative Mach number and absolute flow angle at the exit of the shock-rotor.

4.1.2 Composition of the Losses

A detailed comparison of the loss coefficients, measured at the rotor exit and the data computed by the described procedure is given for different speeds and backpressures in Fig. 10. The computed overall losses are subdivided into the shares due to friction (P), bow-shock (K), passage shock (S) and shock induced separation (A).

Corresponding to higher diffusion the frictional losses generally increase with higher back pressures. The losses induced by the bow-shock contribute to the overall losses only in the case of the impulse-type rotor (strong suction side camber). They increase slightly for the lower rotational speed because of a strong bow-shock detachment at still high Mach numbers. The bow-shock losses of the shock-rotor with a straight suction side are negligible in comparison with the magnitude of the other loss sources.

If the impulse-type rotor is throttled a remarkable increase of the losses is obvious. This has to be attributed to the losses of the additional passage shock and shock induced separation.

At design speed and low back pressure the overall losses are extremely small. No separation is indicated. The shock losses are caused by the leading edge shock. Increasing the back pressure a strong shock is stabilized in the rotor channel, which leads to a separation of the boundary layers. At spill point conditions the throttling shock and the passage branch of the leading edge shock coincide. Only one shock is considered for the determination of the rotor losses. At lower speed the composition of the overall losses is comparable.

The relative flow in the shock-rotor at design speed and lowest back pressure is already throttled because of the converging blade passage. This causes remarkable shock losses. They are represented in the model correlation again by assuming an additional strong shock. Increasing the backpressure this shock moves forward. The shock losses slightly decrease because of the Mach number distribution in the rotor blade passage. In case of maximum throttling the leading edge shock, which according to Mises represents the shock losses in the supersonic part of the flow and the throttle shock coincide again and the losses decrease.

In all cases the passage shock produces separation. Because of the converging blade passage geometry this separation losses for design speed are small in comparison to the impulse type rotor.

4.1.3 Radial Distributions at Rotor Exit

The radial distribution of the flow is achieved incorporating the described loss correlations in a streamline curvature algorithm. Only the separation losses are treated more distinctive: For the core region these losses are determined using the flow-through area limited by two adjacent SI-surfaces and the blade surface resp. the periodic boundaries downstream of the blading. Near hub and casing the additional losses are represented by a purely 2-D Carnot diffusion without accounting for the radial thickness of the annular stream tube. As Fig. 11, 12 demonstrate the procedure, already discussed with regard to the mean-line computation, also represents the spanwise distribution of the rotor exit flow at different speeds and back pressures in good accordance with the experiments. An isentropic calculation however fails especially in the case of high back pressure.

4.2 Supersonic Compressor Stages

The capability of the presented loss models for the performance prediction of supersonic compressor stages is demonstrated here for a combination of shock-rotor and tandem-stator. Additional examples are discussed in /8/.

In the case under consideration the flow is supersonic at the entrance of the stator. As the axial wall pressure distribution in Fig. 13 indicates for low back pressure operation, the flow is still accelerated across the stator.

Increasing the back pressure an axisymmetric ring-shock, generating subsonic axial flow, is positioned in the diffuser /16/. This shock is pushed into the stator passage with stronger throttling until it is stabilized for maximum back pressure in the entrance region nearly perpendicular to the flow direction. The rotor flow remains uninfluenced by this throttling procedure. The flow pattern in the investigated tandem stators thus can be characterized by three different situations:

- supersonic flow within the blade passage in case of low backpressure operation,
- moderate back pressure with a strong compression shock in the stator, e. g. at the entrance of the second blade row,
- maximum back pressure with a strong shock in the entrance region and subsequent subsonic flow.

For a computational reproduction of the stator flow the loss model and its structure remains unchanged compared with the computation of the rotor flow.

In case of entirely supersonic flow the losses are described by the Monneret model. This includes the weak passage shocks being represented by a single strong entrance shock. The diffusion factor and thus the blade losses are determined separately for the first and second blade row. The inlet velocities to the second passage are calculated as described in Ch. 2.

If the throttling shock is stabilized inside of the stator passage, the losses caused by shock induced separation are again modelled by a Carnot-diffusion. For the calculation of the corresponding critical data it is necessary to include all losses occurring from stator entrance up to the position of the critical passage cross section.

The comparison of the measured losses and the results of the described loss model (Fig. 14) validates the introduced simplifications. The low losses for supersonic stator flow consist of shock and viscosity losses for both blade rows. Increasing the back pressure moderately the losses for the first blade row remain constant. The boundary-layer separation induced by the throttling shock in the second blade row causes a sharp increase of the overall losses. With the stator running at spill-point condition, these separation losses are reduced remarkably by the special passage geometry. As also the losses of the second blade row are to be attributed only to a subsonic diffusion, for maximum back pressure again the total loss reaches a minimum.

The stage performance data calculated with the described technique and the measured values are compared in Fig. 15, 16. Without back pressure the exit Mach number is supersonic. Reducing it by throttling to subsonic magnitudes, in the tandem-cascade a deceleration of the flow from an entrance Mach number of about 1.5 to an exhaust value of .5 is achieved. This corresponds to a stage static pressure rise of 3.2%.

In analogy to the loss coefficients a drop of the total pressure is registered and computed for medium throttling. The further increase of the back pressure finally yields a total pressure ratio of 1. The mass flow rate of 21 kg/sec in accordance to the experiment is determined by the unique incidence condition of the rotor. The corresponding stage efficiency turns out to be 82%.

5. CONCLUSIONS

For any application of supersonic compressors the performance of these components at off-design speed is a central aspect. In the presented paper experimental and computational results are discussed with respect to a prediction of the performance of supersonic compressors. It is shown that a theoretical approach succeeds if in addition to the commonly used loss correlations the following phenomena with significant influence are considered.

- bow-shock induced losses
- additional shock losses induced by back pressure rise
- shock induced separation
- blade passage and loss induced choking

If these effects are represented correctly a consistent model algorithm can be established which is valid for low aspect-ratio supersonic compressors. Taking not into consideration the discussed aerodynamic features of supersonic

compressors for low speed conditions at a new design, severe problems can be encountered during the starting procedure.

Based on this experience future efforts can either concentrate on further improvement of efficiency and axial length or cope with new conceptions of supersonic compressors implying a remarkable increase of pressure rise by a design with diagonal pitch line.

6. REFERENCES

- /1/ Klapproth, J. F.:
"A Review of Supersonic Compressor Development", Transactions of ASME - Journal of Engineering for Power, 1961
- /2/ Paulon, J., Reboux, J., Savrano, R.:
"Comparison of test results obtained on plane and annular, fixed or rotating supersonic blade cascades", ASME-Paper 74-GT-49
- /3/ Wennerstrom, A. J., Buzzel, W. A., De Rose, R. D.:
"Test of a Supersonic Axial Compressor Stage Incorporating Splitter Vanes in the Rotor", ARL TR 75-0165, 1975
- /4/ Simon, H.:
"Anwendung verschiedener Berechnungsverfahren zur Auslegung eines Überschallverdichter-Laufrades und dessen experimentelle Untersuchung", Diss. RWTH Aachen, 1973
- /5/ Simon, H., Bohn, D.:
"Experimental Investigations of a Recently Developed Supersonic Compressor Stage (Rotor and Stage Performance)", ASME Paper 74-GT-116, 1974
- /6/ Gallus, H. E., Bohn, D., Broichhausen, K.-D.:
"Theoretische und experimentelle Ergebnisse der Untersuchungen an zwei unterschiedlichen Überschallverdichterstufen", Jahrb. DGLR 76-166, 1976
- /7/ Broichhausen, K.-D., Gallus, H. E.:
"Theoretical and Experimental Analysis of the Flow through Supersonic Compressor Rotors", AIAA Journal, Vol. 20, No. 8, 1982
- /8/ Broichhausen, K.-D.:
"Betriebsverhalten von supersonischen Axialverdichtern", Habil., RWTH Aachen, 1986
- /9/ Broichhausen, K.-D., Gallus, H. E.:
"Three-Dimensional Effects in Supersonic and Transonic Rotors - an Experimental and Computational Study", ASME Paper 82-GT-278
- /10/ Monnerat, N. T., Keenan, M. J., Tremm, P. C.:
"Design Report: Single-Stage Evaluation of Highly-Loaded High-Mach-Number Compressor Stages", NASA CR-77362, 1969
- /11/ Johnson, A., Ballock, R. D. (Ed.):
"Aerodynamic Design of Axial-Flow Compressors", NASA SP-36, 1965
- /12/ Donaldson, C., Lange, R. H.:
"Study of the Pressure Rise Across Shock Waves Required to Separate Laminar and Turbulent Boundary Layers", NACA TN 2700, 1952
- /13/ Hirsch, Ch., Denton, J. D. (Ed.):
"Through Flow Calculations in Axial Turbomachines", AGARD AR 175, 1981
- /14/ Lichtfuß, H.-J., Starken, H.:
"Supersonic Cascade Flow", Progress in Aerospace Science, Vol. 15, 1974
- /15/ Moehrel, W. E.:
"Approximate Method for Predicting Form and Location of Detached Shock Waves on Cones and Spheres", NACA TN 2004, 1950
- /16/ Bohn, D.:
"Untersuchung zweier verschiedener axialer Überschallverdichterstufen unter besonderer Berücksichtigung der Wechselwirkungen zwischen Lauf- und Leitrad", Diss. RWTH Aachen, 1977

ACKNOWLEDGEMENTS

The presented investigations were supported by the "Deutsche Forschungsgemeinschaft". The researching "Institut für Strömungs- und Turbomaschinen, RWTH Aachen" and the authors like to express their sincerest thanks for this promotion.

		impulse-type	shock	tandem-stator	
		rotor	rotor	cascade 1	cascade 2
stagger	/°/	38.5	38.8	18.5	1.
chord	/mm/	113.	115.8	64.5	61.7
solidity	/-/	2.37	2.427	3.25	3.13
max. thickness	/mm/	5.2	7.8	5.5	4.6
aspect ratio	/ /	0.312	0.309	0.226	0.373

Table 1: Survey on blading-data

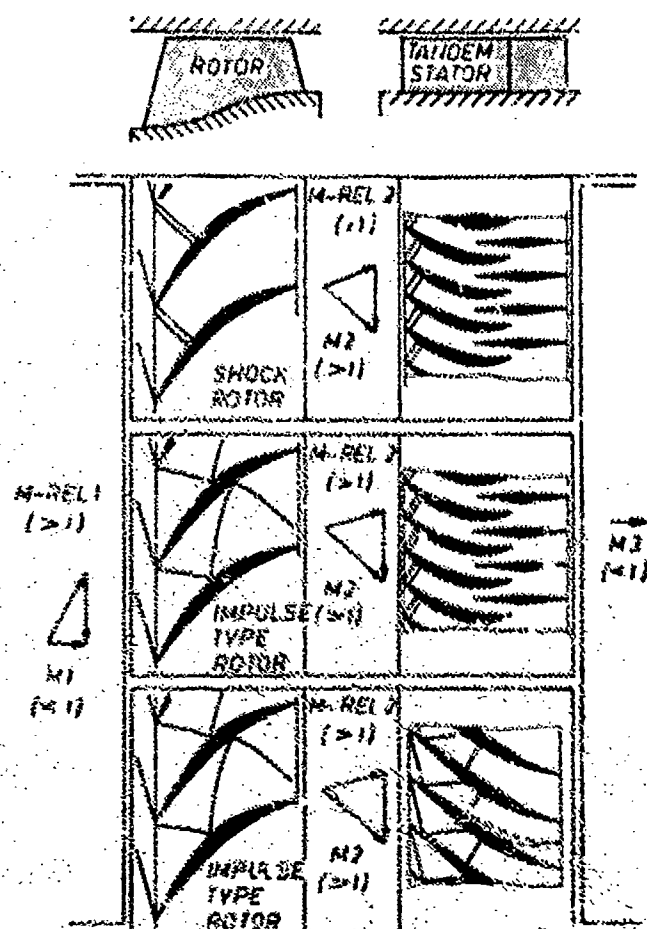


Fig. A: Geometry on the investigated supersonic compressor stages

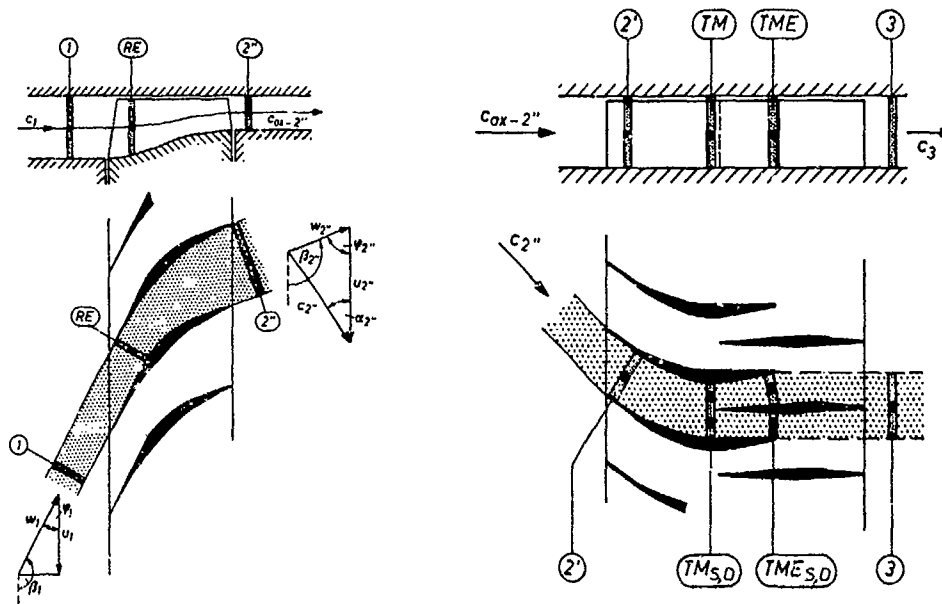


Fig. 2: Control-surfaces for the pitch-line rotor and stator calculation

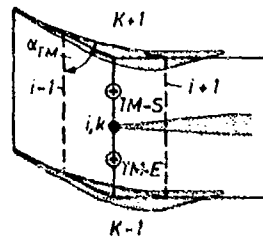


Fig. 3: Simplified grid for the determination of flow conditions at entrance of the second tandem-blade row

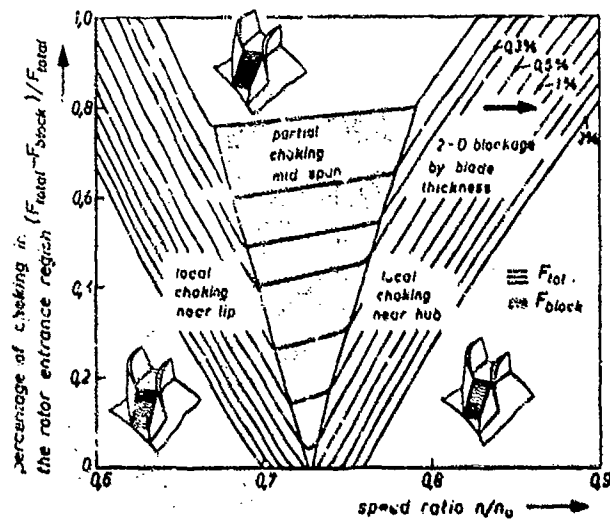


Fig. 4: Blockage by finite blade thickness

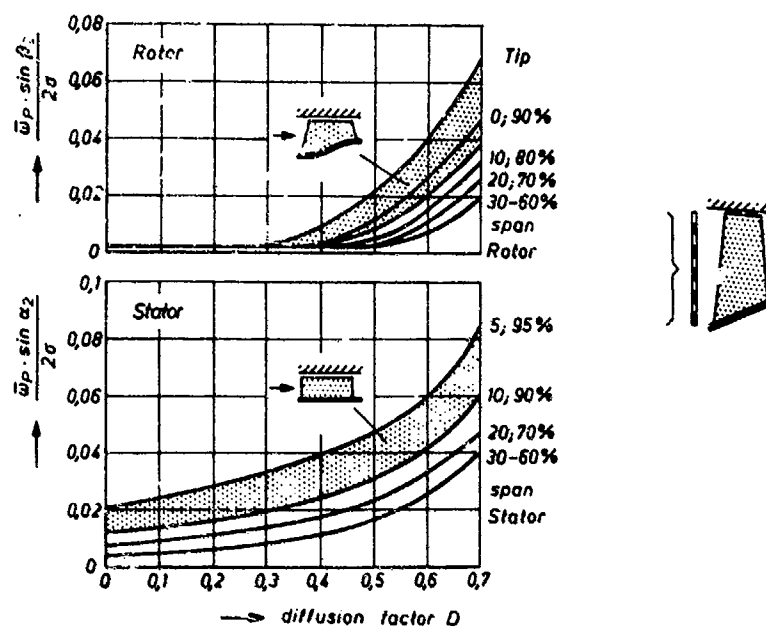


Fig. 5: Loss-correlation by Monsarrat

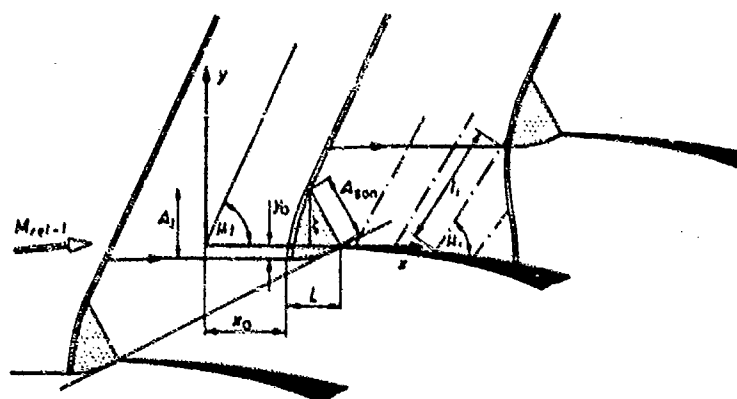


Fig. 6a: Scheme of bow-shock system

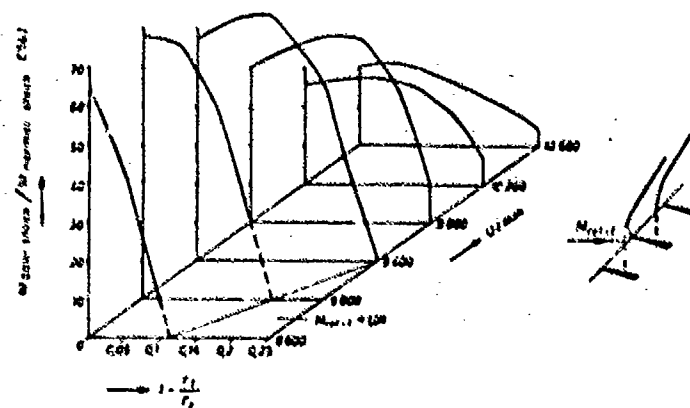


Fig. 6b: Bow-shock induced losses

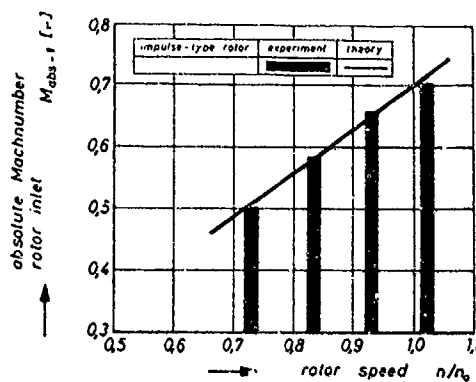


Fig. 7a: Absolute Mach number at entrance of the impulse-type rotor

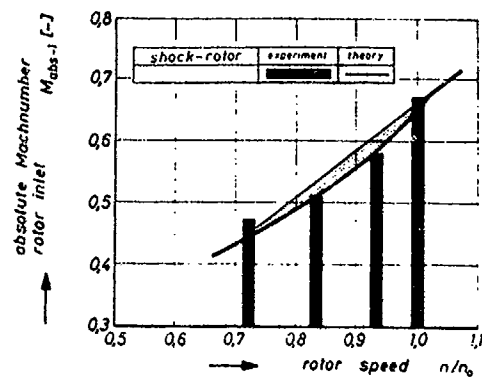


Fig. 7b: Absolute Mach number at entrance of the shock-rotor

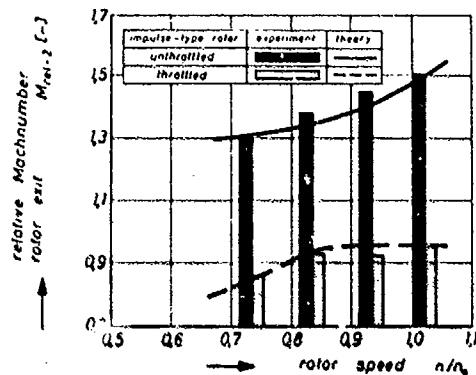


Fig. 8a: Relative Mach number at the exit of the impulse-type rotor

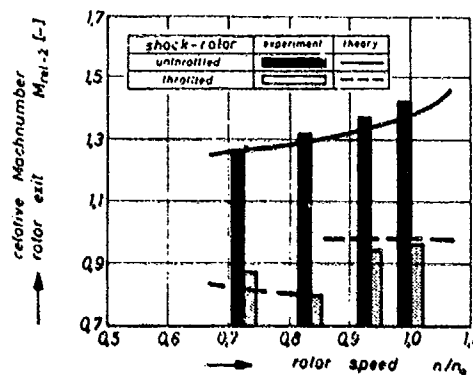


Fig. 8b: Relative Mach number at the exit of the shock-rotor

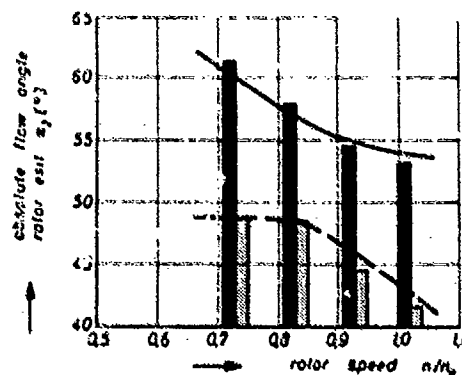


Fig. 9a: Absolute flow angle at the exit of the impulse-type rotor

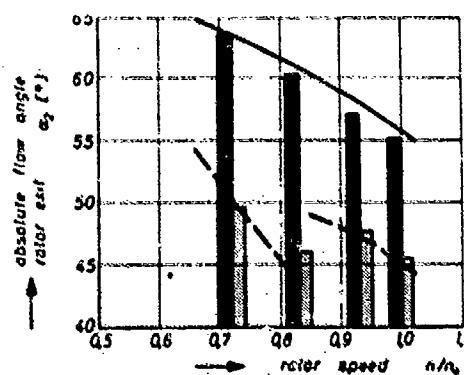


Fig. 9b: Absolute flow angle at the exit of the shock-rotor

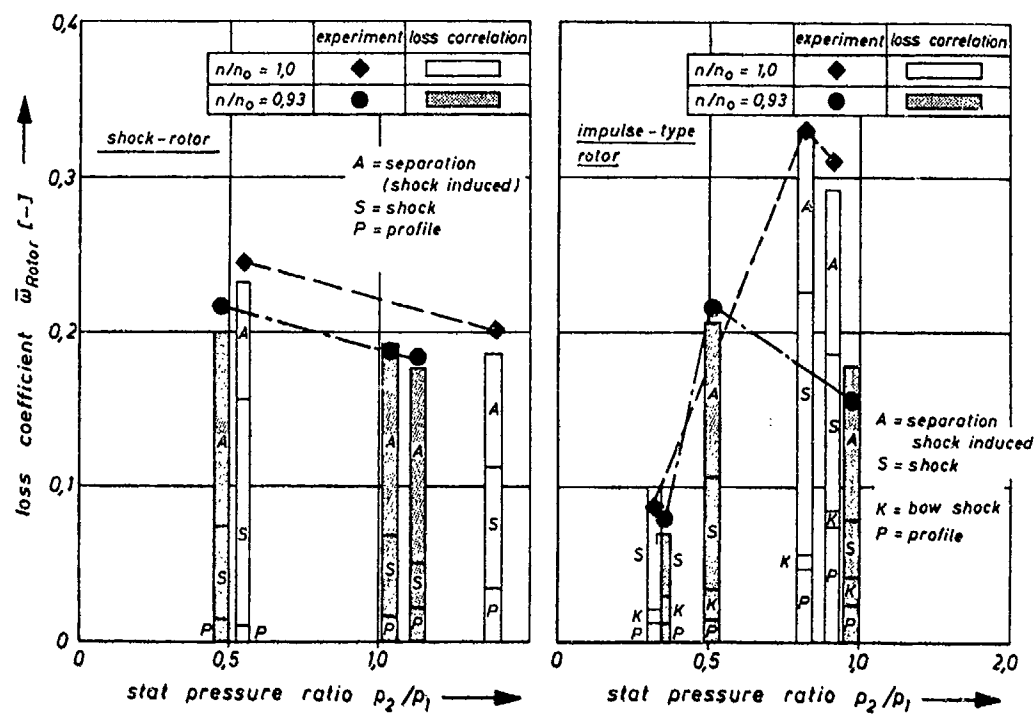


Fig. 10: Overall losses of supersonic rotors

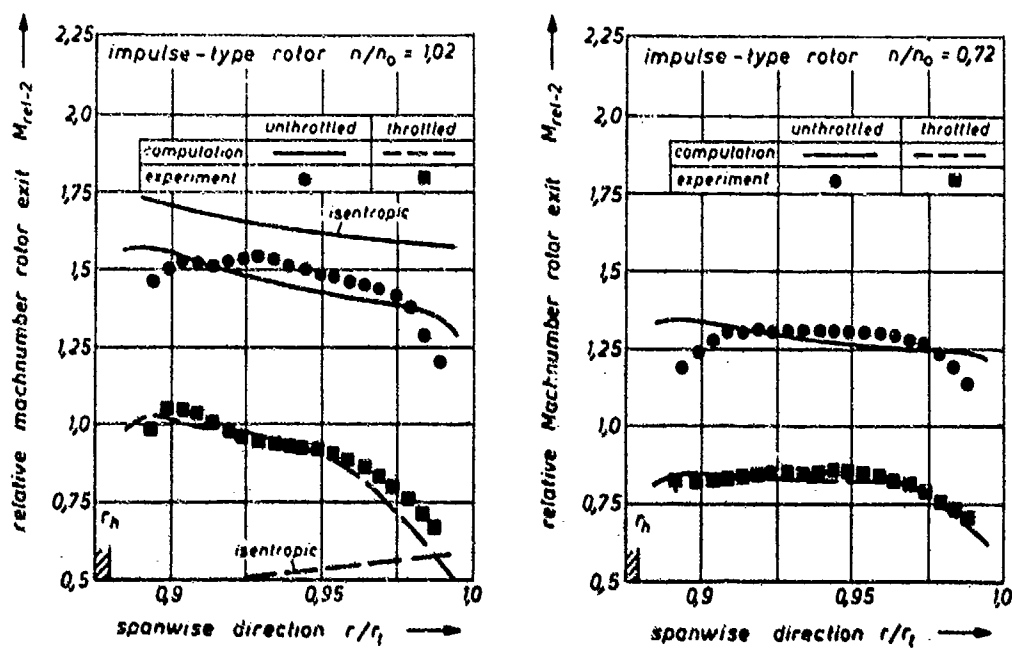


Fig. 11: Radial distribution of the relative exit Mach number (impulse-type rotor)

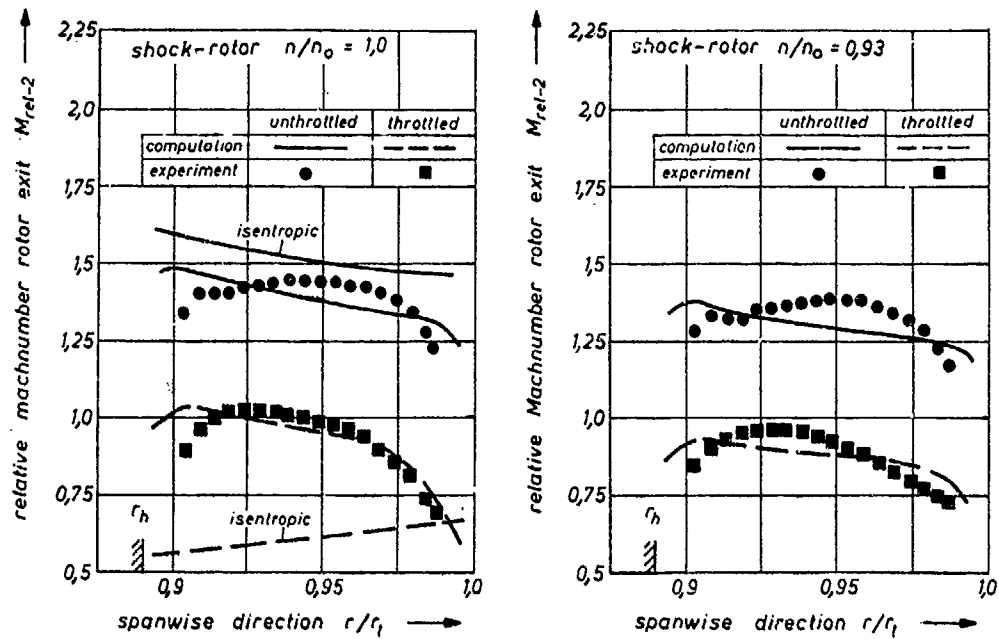


Fig. 12: Radial distribution of the relative exit Mach number (shock-rotor)

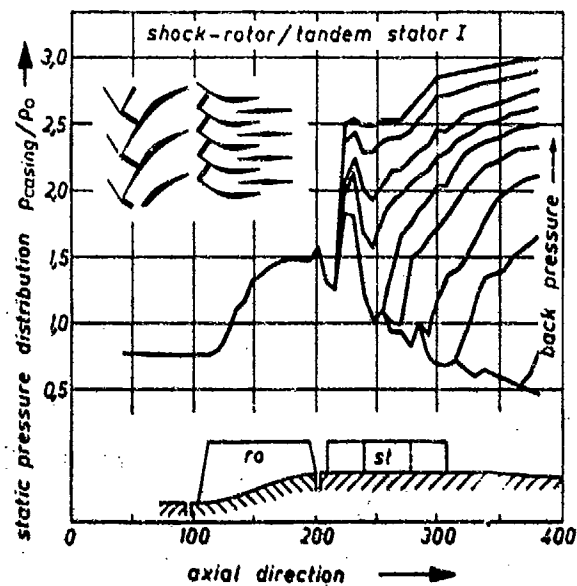


Fig. 13: Axial wall pressure distribution of a supersonic compressor stage

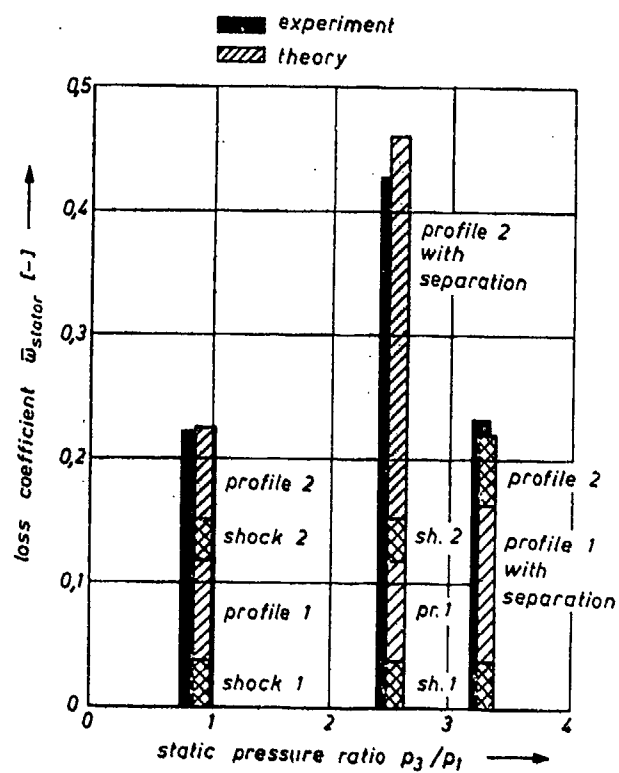


Fig. 14: Losses in tandem-stators

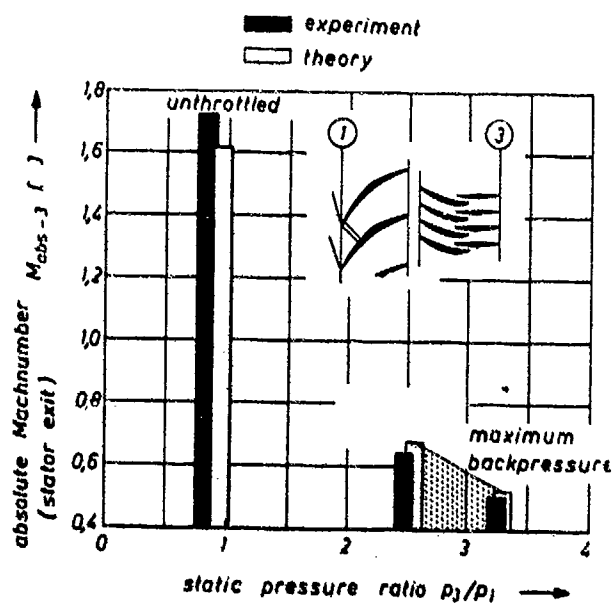


Fig. 15: Supersonic compressor stages: Exit Mach number for different back pressure

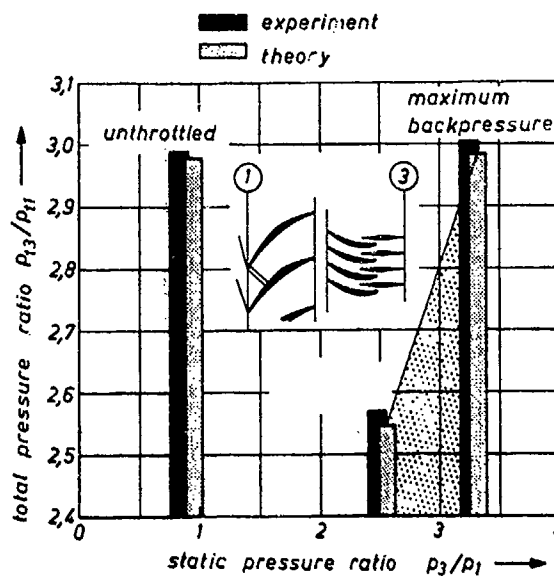


Fig. 16: Supersonic compressor stages Pressure characteristic

DISCUSSION

F. Leboeuf, Fr

In which way are you handling the unique incidence and choking conditions for a particular streamline in your through flow calculations?

Author's Reply

We have two computer codes: the first is a mid-span streamline code, which calculates the integrated choked area over the radius and diminishes the effective frontal area of the rotor accordingly. The second code is a streamline curvature code where we first look at choking for each streamline, and decrease the mass flow if span-wise choking occurs, and the Mach number is not totally supersonic across the span.

F. Leboeuf, Fr

Is your code able to handle, for one stream tube, multistage compressors?

Author's Reply

We have applied the code to a rotor-stator combination with several stator blade rows. I would think that we can do it for two stages, although we have not done it yet. It is just a matter of introducing more "ifs" in the program.

ANALYSE DES PERTES DUES AUX ONDES DE CHOC *

par Antoine FOURMAUX et Alain LE MEUR

Office National d'Etudes et de Recherches Aérospatiales
29, avenue de la Division Leclerc
92320 - CHATILLON SOUS BAGNEUX

RESUME

Dans la conception de turbomachines de technologie avancée, l'un des soucis constants est la réduction des pertes induites par les phénomènes aérodynamiques.

Très schématiquement, ces pertes ont trois origines :

- 1 - Pertes liées au choc de bord d'attaque
- 2 - Pertes liées au choc principal de recompression
- 3 - Pertes de frottement, liées à l'évolution des couches limites.

Pour des conditions d'entrée et de sortie données, un dessin judicieux des profils utilisés peut permettre d'obtenir un niveau minimum de pertes. Afin de guider le dessin de profils à performances optimales, divers travaux à dominante expérimentale ont été menés récemment à l'ONERA, et cet article se propose d'en présenter les résultats essentiels :

- choc de bord d'attaque : influence de la forme du bord d'attaque sur la trace du choc et son impact sur l'extrados de l'aube inférieure ;
- analyse expérimentale détaillée d'un montage simulant un seul canal intersube, et destinée à valider certains principes sur l'interaction onde de choc - couche limite en turbomachines,
- analyse expérimentale globale d'une grille d'aubes dont les profils ont été conçus spécialement pour minimiser les pertes liées au choc de recompression et les pertes visqueuses.

Tous ces travaux concernent des écoulements bidimensionnels. Un accent particulier sera mis sur l'utilisation alternée des méthodes théoriques de calcul et des méthodes expérimentales.

ABSTRACT

SHOCK WAVES LOSSES ANALYSIS

In advanced technology turbomachinery design, reducing aerodynamic losses is an important matter. Schematically, these losses have 3 origins :

- 1 - losses related to the leading-edge shock
- 2 - losses related to the main-compression shock
- 3 - friction losses, related to the boundary layer evolutions.

For given inlet and outlet conditions, a judicious designing of the blade profiles may induce a minimum loss level. In order to successfully conclude such a design, some rather experimental work has recently been carried out in ONERA, the main results of which will be presented in this paper :

- leading edge shock : the influence of the leading edge shape on the shock and on its impingement on the lower blade suction surface,
- experimental analysis of a single blade-to-blade passage in order to validate certain principles concerning shock/boundary layer interaction,
- experimental analysis of a cascade in which the blade profile is specially designed to minimize the losses.

All these projects were done on two dimensional flow. The alternate use of theoretical and experimental methods will be emphasized.

* Travail effectué sous contrat SNECMA

I. INTRODUCTION

Ce papier a pour but principal de donner une analyse, aussi détaillée que possible, des pertes dues aux ondes de choc. En effet dans la conception des turbomachines de technologie avancée, l'un des soucis constants est la réduction des pertes induites par les phénomènes aérodynamiques.

Très schématiquement, ces pertes ont trois origines :

- 1 - Pertes liées au choc de bord d'attaque,
- 2 - Pertes liées au choc principal de recompression,
- 3 - Pertes liées à la viscosité du fluide (frottement) y compris l'interaction avec le choc principal.

Pour des conditions d'entrée et de sortie données, un dessin judicieux des profils utilisés peut permettre d'obtenir un niveau minimum de pertes. Afin de guider le dessin de profils à performances optimales, divers travaux à dominante expérimentale ont été menés récemment à l'ONERA, et cet article se propose d'en présenter les résultats essentiels :

- choc de bord d'attaque : influence de la forme du bord d'attaque sur la trace du choc et son impact sur l'extrados de l'aube inférieure ;
- analyse expérimentale détaillée d'un montage simulant un seul canal interaube, et destinée à valider certains principes sur l'interaction onde de choc - couche limite en turbomachines ;
- analyse expérimentale globale d'une grille d'aubes dont les profils ont été conçus spécialement pour minimiser les pertes liées au choc de recompression et les pertes visqueuses.

Tous ces travaux concernent des écoulements bidimensionnels. Un accent particulier sera mis sur l'utilisation alternée des méthodes théoriques de calcul et des méthodes expérimentales.

II. EFFETS DUS AU CHOC DETACHE DU BORD D'ATTAQUE

2.1. Rappel des phénomènes

Il est bien connu qu'un écoulement supersonique attaquant un obstacle qui présente un nez émoussé provoque une onde de choc qui se détache devant celui-ci. L'écoulement aval comporte alors dans la région frontale un domaine mixte subsonique-transsonique plus ou moins compliqué [1].

Cette onde de choc est accompagnée d'une augmentation d'entropie liée au nombre de Mach incident et à l'épaisseur de bord d'attaque. Cela se traduit par une baisse de la pression d'arrêt différente pour chaque filet de courant.

Ces pertes sont théoriquement prises en compte par les méthodes qui résolvent les équations d'Euler mais sont en fait souvent ignorées quand le type de maillage utilisé n'est pas suffisamment raffiné au bord d'attaque, ce qui est pratiquement toujours le cas pour les aubes supersoniques. C'est pourquoi, dans une étude spécifique, l'on avait dissocié le phénomène du choc détaché du calcul complet de l'écoulement autour d'une coupe, de façon à l'étudier seul et de connaître ainsi son influence propre sur les performances de cette coupe [2].

Dans le cas d'une grille d'aubes (figure 1), la présence de bords d'attaque arrondis (plutôt que pointus) entraîne une modification de l'écoulement amont par l'apparition de pertes supplémentaires dues au choc détaché.

Si de plus, on peut appliquer à la grille le concept d'incidence unique, un bord d'attaque émoussé tend à augmenter l'angle amont, par modification géométrique de la zone de captation. On rappelle ici simplement que ce phénomène d'incidence unique résulte de l'indépendance du domaine amont par rapport au domaine aval - cette indépendance existant sous certaines conditions décrites en [3] -.

Bien que tous ces phénomènes soient intimement liés, l'effet d'un bord d'attaque arrondi par rapport à un B.A. pointu peut être dédoublé :

- tout d'abord un effet dû à l'augmentation des pertes à travers le choc de bord d'attaque : le débit maximum est réduit, et l'incidence unique voit sa valeur augmenter,
- ensuite un effet directement dû à la modification de la géométrie : l'incidence unique augmente. Cet effet a été analysé par Starken [4], dans une étude systématique de l'influence de l'épaisseur d'aube en forme de plaques (l'épaisseur du bord d'attaque étant rapportée au pas de la grille).

Dans cette étude, seule une toute petite partie des pertes est prise en compte et c'est essentiellement l'effet de la géométrie qui apparaît sur les résultats proposés sous forme d'ébauches très utiles pour avoir une bonne approximation de l'influence du rayon de bord d'attaque.

L'étude déjà citée en référence [2] fait ressortir l'effet du cumul des pertes dû aux branches montantes des ondes de choc détachées qui remontent l'écoulement. Cette perte chiffrable correspond à une variation de l'incidence unique par rapport à un cas où les aubes seraient pointues. Toutefois cet effet ne se fait vraiment sentir que pour des nombres de Mach égaux ou supérieurs à 1,4. Ainsi en toute rigueur il faut cumuler les deux effets (géométrie et pertes) pour obtenir une estimation correcte de l'incidence unique.

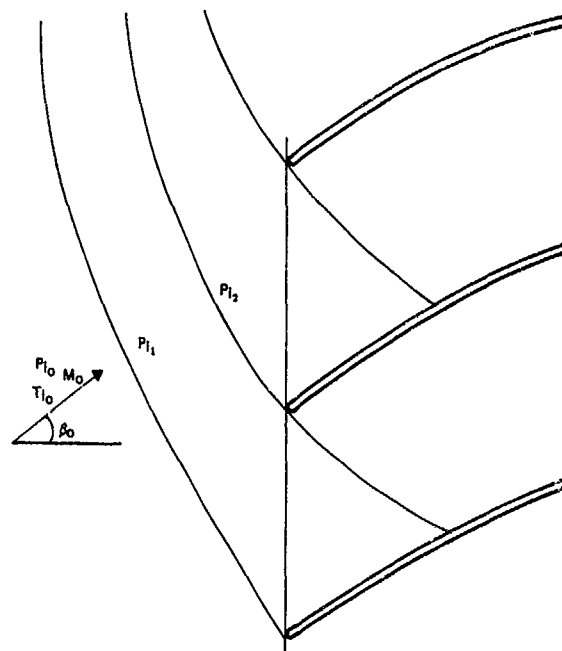


Fig. 1. CONFIGURATION DU SYSTEME D'ONDE DETACHEE DANS UNE GRILLE D'AUBE

2.2. Rappel du principe d'estimation des pertes de bord d'attaque

Le calcul, comme il est indiqué dans [2] consiste d'abord à déterminer aussi finement que possible le champ de l'écoulement créé autour d'une plaque plane isolée pour un nombre de Mach à l'infini amont et une épaisseur donnée.

A cet effet on utilise un calcul pseudo-stationnaire dans la région du bord d'attaque suffisamment loin de la ligne sonique pour que le champ de vitesse résultant soit franchement supersonique. Le calcul est alors poursuivi par la méthode des caractéristiques.

En se plaçant suffisamment loin en aval de façon à ce que le choc soit devenu évanescent, on peut alors obtenir par intégration de la pression d'arrêt locale $P_1(\psi)$ la perte moyenne relative d'un tube de courant de débit Q capté sur une hauteur h à partir de la plaque selon la formule indiquée sur la planche n° 2.

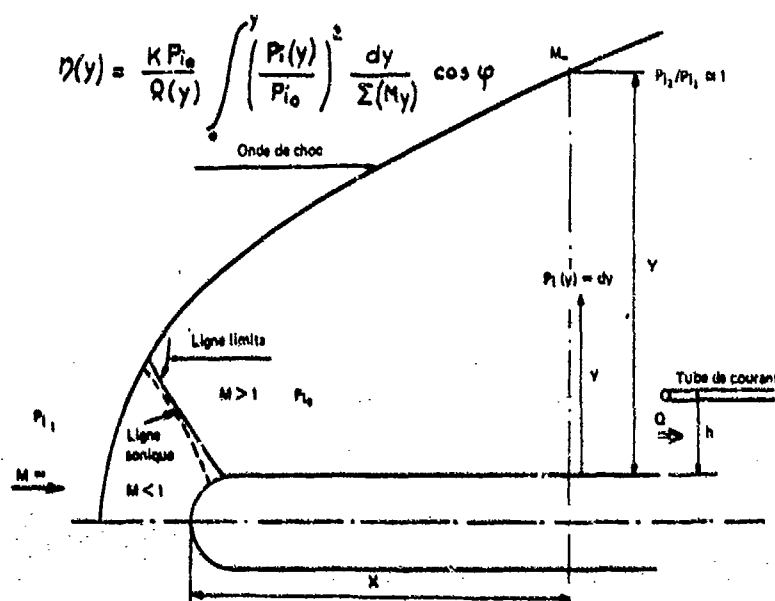


Fig. 2. SCHEMA DE PRINCIPLE DU CALCUL DE LA PERTE DE PRESSION D'ARRÉT

2.3. Application aux coupes d'aubes supersoniques

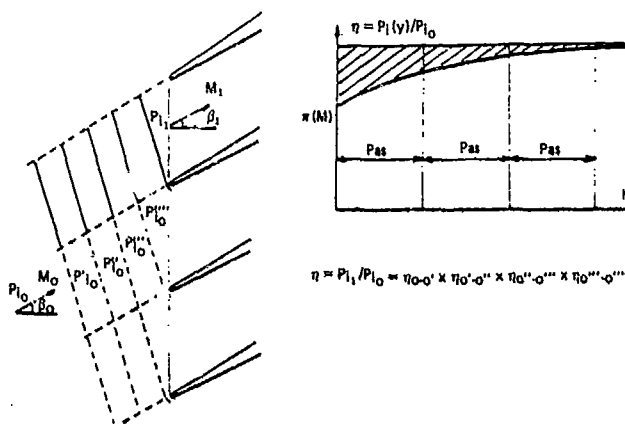
Les résultats obtenus par la méthode rappelée ci-dessus sont appliqués aux coupes d'aubes supersoniques ; deux cas distincts sont alors à envisager.

2.3.1. Pertes à l'entrée de la grille

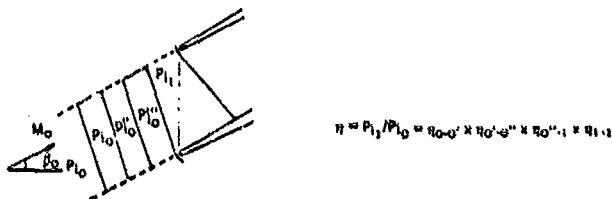
Dans le cas d'une grille d'aubes, il y a lieu de considérer toutes les branches ou parties de branches concernant chaque canal interaube. La planche 3a illustre bien cet effet où l'on voit que pour un tube de courant il faut prendre en compte toutes les parties de branches d'ondes de choc successives. Le calcul montre que seules quatre ou cinq branches sont à considérer au maximum.

2.3.2. Pertes totales provoquées par l'onde de choc

Pour connaître la perte totale dans une grille d'aube provoquée par l'onde de choc détachée au bord d'attaque, il faut tenir compte en outre selon la configuration étudiée de la branche inférieure du choc issue du bord d'attaque de l'aube supérieure (planche 3b). Comme il est indiqué dans [2] l'on admettra en première approximation que le supplément de perte provoqué par la branche inférieure est égal à celui donné par la branche supérieure du choc.



3a. PERTE A L'ENTREE D'UNE GRILLE D'AUBE



3b. PERTE TOTALE PROVOQUEE DANS UNE GRILLE PAR L'ONDE DE CHOC DETACHEE

Fig. 3.

Les résultats prenant en compte les différentes branches d'onde de choc pour un rapport R/λ donné sont représentés sur la planche n° 4.

3. ANALYSE THEORIQUE ET EXPERIMENTALE DE L'INTERACTION CHOC-COUCHE LIMITE DANS UN CANAL TRANSONIQUE (Nonocanal)

3.1. But recherché

Le but de cette opération peut être résumé en deux points principaux :

- tout d'abord la recherche théorique d'un profil minimisant les pertes dues aux effets visqueux dans un canal de grille d'aubes transsonique,
- ensuite, la validation expérimentale des idées et des méthodes de calcul mises en oeuvre dans l'approche numérique.

L'optimisation d'un profil doit être envisagée globalement : la géométrie générale du canal gouverne évidemment l'ensemble de l'écoulement, mais des phénomènes locaux tels que détachement de choc de bord d'attaque, épaississement des couches limites, ont une importance non négligeable lorsqu'il s'agit d'augmenter l'efficacité de la grille. La complexité du problème est accrue par le fait que tous ces éléments réagissent les uns sur les autres.

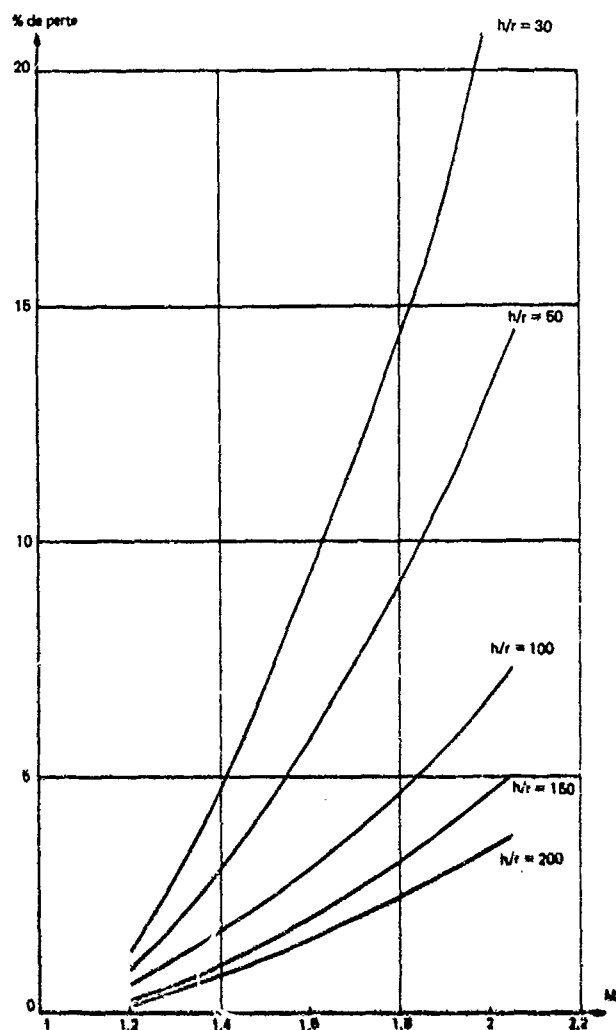


Fig. 4. ABACUS DES PERTES TOTALES PROVOQUEES PAR L'ONDE DE CHOC DETACHEE DANS LE CANAL INTERAURE

Ici, nous nous sommes plutôt attachés à concevoir une géométrie du canal qui, compte tenu du développement des couches limites, minimise l'intensité du choc principal de compression. L'effet espéré est double :

- réduction des pertes au travers du choc,
- réduction des pertes visqueuses par non-décollement des couches limites entrées et intrados.

3.2. Conception du profil

3.2.1. Partie amont du canal

La partie amont du canal est construite selon des règles simples :

- concevoir une géométrie minimisant les survitesses tout en étant réaliste (épaisseur suffisante, hauteur de canal permettant l'amorçage de l'écoulement),
- utiliser la compression due au choc oblique de bord d'attaque pour ralentir sur l'entrées l'écoulement avant le choc principal.

Un calcul de fluide parfait, en mode direct dans cette partie du canal fournirait alors la répartition de la vitesse sur l'entrados du profil. Un calcul de couche limite (en mode direct. Méthode intégrale, régime laminaire) permet alors d'évaluer les caractéristiques de la couche limite au niveau de l'impact du choc oblique issu du bord d'attaque supérieur. A cet endroit, on admet une transition ponctuelle avec des relations empiriques de saut des grandeurs intégrales.

Ensuite la couche limite turbulente est calculée (en mode direct) sur un court plateau, jusqu'à un point choisi arbitrairement comme étant le début d'interaction.

3.2.2. Géométrie de l'extrados dans la zone d'interaction

La couche limite attachée est donc connue juste à l'amont de l'interaction. De là, un calcul en mode inverse est mené. La donnée de ce calcul est une évolution du coefficient de frottement pariétal en fonction de l'abscisse curviligne. Dans la région du choc, le choix de cette évolution est fait en utilisant divers critères empiriques [5]. Deux résultats importants sont issus de ce calcul :

- une répartition de vitesse sur la partie a de l'extrados, dans laquelle une forte compression traduit l'impact du choc principal fig. 5,
- une évolution de l'épaisseur de déplacement de la couche limite (qui sera utilisée pour déterminer la géométrie réelle du canal).

La répartition de vitesse ci-dessus est alors introduite comme donnée d'un calcul de fluide parfait en mode inverse. Dans ce type de calcul, le débit est conservé, et l'on obtient la géométrie de la ligne de courant correspondant à la paroi matérielle de l'extrados déplacée de δ^* (épaisseur de déplacement de la couche limite).

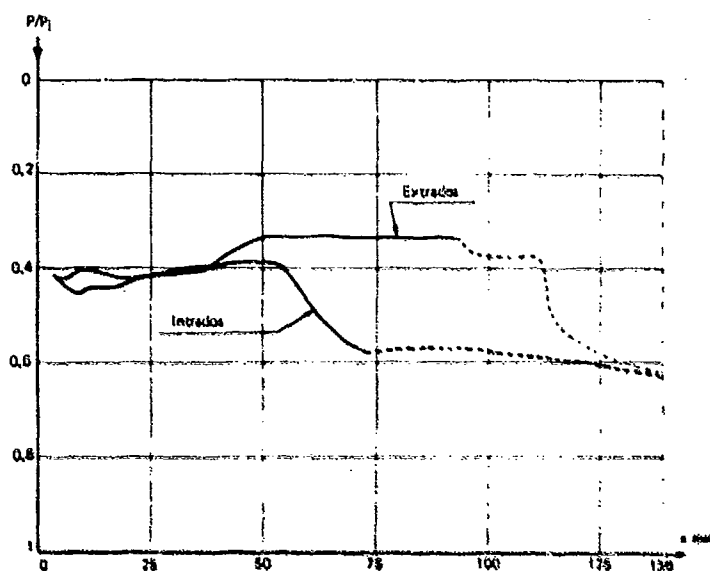


Fig. 5. PROFIL DE PRESSION IMPOSÉE SUR UNE PARTIE DE L'EXTRADOS ET DE L'INTRADOS INDICÉ EN TRAIT MIXTE POUR LE CALCUL INVERSE

3.2.3. Obtention du profil final

La paroi supérieure du canal -qui simule l'intrados- a été déterminée par retouches successives à l'aide du calcul fluide parfait en mode semi-inverse (mode inverse pour la partie subsonique en aval du choc). L'épaisseur de déplacement sur cette paroi est fournie par un calcul de couche-limite en mode direct.

La géométrie définitive du canal est enfin obtenue en translatant de l'épaisseur de déplacement δ^* les parois fictives déduites des calculs en fluide parfait.

L'aspect final du canal est présenté sur la fig. 6.

3.3. Vérification expérimentale

3.3.1. Présentation de la maquette

3.3.1.1. Echelle

L'échelle de la maquette a été choisie telle que :

- les conditions géométriques de la soufflerie utilisée donnent un nombre de Reynolds proche de ceux rencontrés dans les machines réelles,
- les dimensions réelles des couches limites soient mesurables par les moyens classiques disponibles.

En conséquence, les caractéristiques principales du montage et des essais sont les suivantes :

Conditions géométriques : $M_0 = 1,30$
 (soufflerie 53 G4) $P_0 = 400.000 \text{ Pa}$
 $T_0 = 315 \text{ K}$

Maquette : $pas = 0,150 \text{ m}$
 $corde = 0,250 \text{ m}$
 $ouverture = 0,300 \text{ m}$

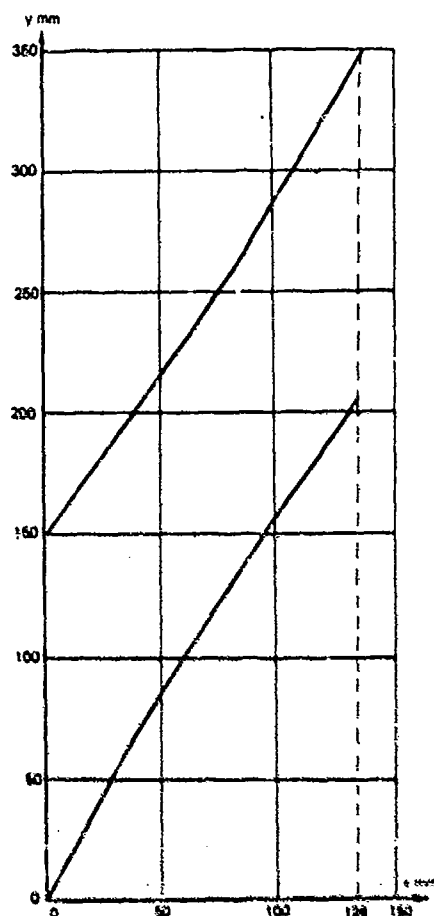


Fig. 6. GEOMETRIE DU NOUVEAU CANAL

3.3.1.2. Moyens de mesure

La maquette est équipée de 122 prises de pression statique, pour une détermination expérimentale précise des répartitions de pression entrées et intrados, à la fois dans le plan médian, et dans des plans latéraux (pour vérifier la bidimensionalité de l'écoulement dans la zone centrale).

Dans la couche limite, les profils de pression d'arrêt sont mesurés par une sonde de type piston.

Les conditions génératrices de l'écoulement (direction et nombre de Mach, pression génératrice) sont mesurées, à l'amont de la maquette, par une sonde miniature ($\varnothing 1,5$ mm) à 3 trous, et la température génératrice par un thermocouple dans la chambre de tranquillisation.

3.3.1.3. Essais préliminaires et réglages

Les essais préliminaires ont révélé quelques effets non prévus dus au choc de bord d'attaque : celui-ci est en réalité dévié et courbe avant de se transformer en choc quasi-oblique (fig. 7). Comme le but principal était de retrouver la même localisation de son impact sur l'extrados, une modification de la position relative des deux profils a dû être faite. La répartition de pression expérimentale sur l'extrados du profil reconçu alors de façon très satisfaisante la répartition de pression théorique prévue (fig. 8), alors que, sur l'intrados, des différences sensibles sont apparues.

3.3.1.4. Mesures de la couche limite sur l'extrados

La couche limite extrados a été sondée en différentes positions, à l'amont et dans la zone d'interaction, pour des régimes de fonctionnement vauels et dévaues (fig. 9).

Les profils de vitesse classiques (M_x/M_0) sont déduits des profils de pression d'arrêt mesurés (fig. 10).

On première intégration des profils de vitesse est ensuite effectuée à partir des résultats expérimentaux. Toutefois un tel type d'intégration peut être insuffisant et l'on manque d'information près de la paroi. Pour pallier cette lacune, on procède à un ajustement des profils expérimentaux par des profils théoriques (dits "de Colson"), puis l'intégration de ces profils est menée. Les différences relevées entre les résultats des deux intégrations ne sont réduites cependant assez faibles.

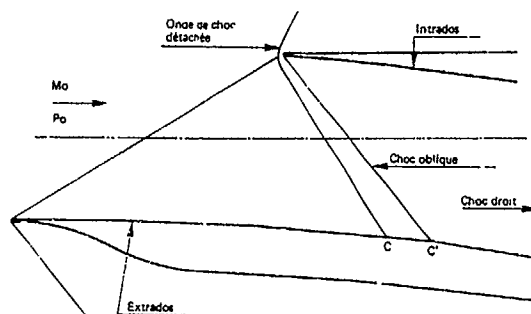


Fig. 7. CONFIGURATION DES ONDES DE CHOC DANS LE CANAL INTERAUBES

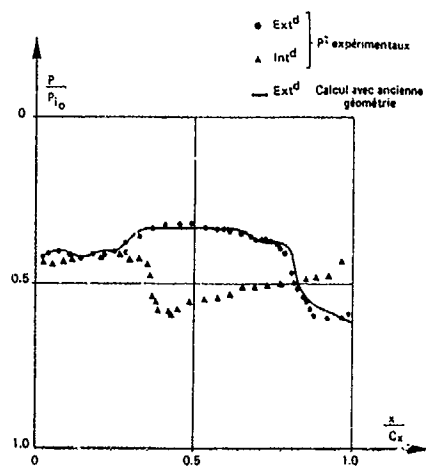


Fig. 8. REPARTITION DE PRESSION EXPERIMENTALE APRES DIFFERENTS REGLAGES

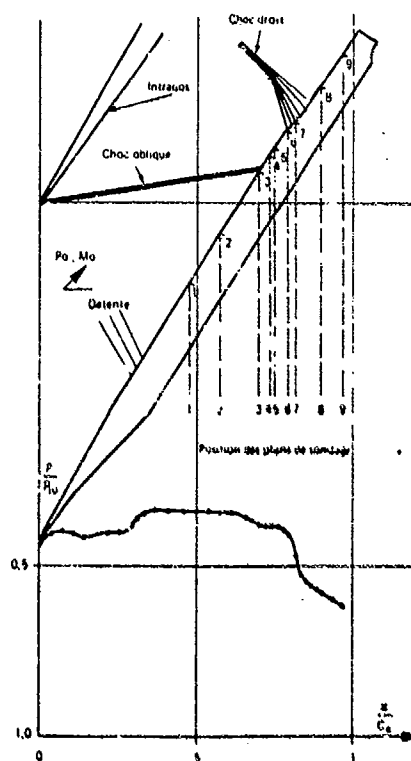


Fig. 9. CONFIGURATION DES PHENOMENES DANS LE MONO-CANAL

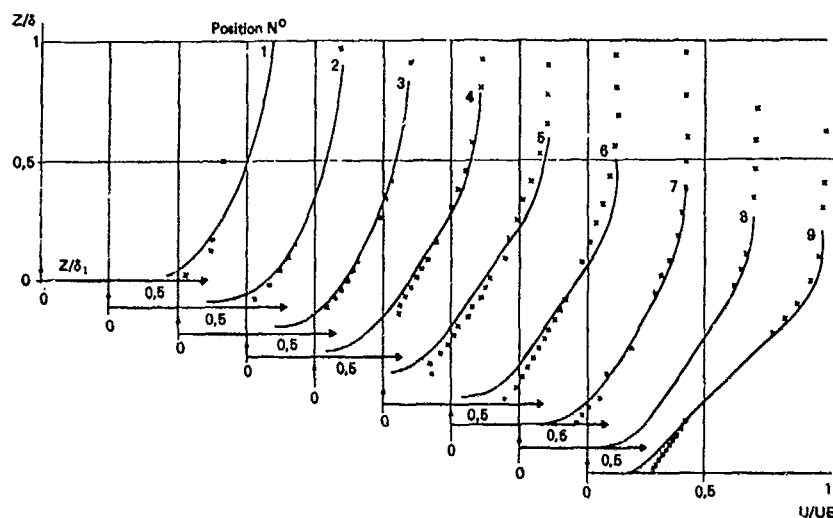


Fig. 10. PROFILES DE VITESSE - REGIME VANNE

Le principal résultat est présenté sur la fig. 11 où l'épaisseur de déplacement déduite de l'expérience est comparée à la pression théorique. Compte tenu des erreurs expérimentales (inévitables sur la mesure de phénomènes de dimensions aussi petites), on voit que l'accord est satisfaisant entre les valeurs expérimentales et la courbe théorique. Ces résultats montrent donc que les principes d'optimisation, utilisés pour la conception du profil, donnent des résultats intéressants.

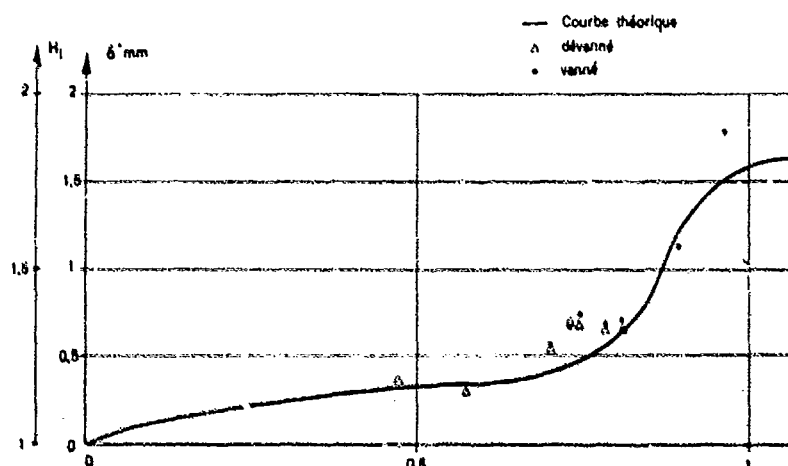


Fig. 11. EVOLUTION DE L'ÉPAISSEUR DE COUCHE LIMITE DE DÉPLACEMENT SUR L'EXTRADOS DU MONO-CANAL

4. ANALYSE EXPERIMENTALE D'UNE GRILLE D'AUBES OU LES PERTES SONT MINIMISEES

Cette troisième partie concerne une grille supersonique à haut rendement, et en particulier ses performances expérimentales.

En effet, l'accroissement des performances des turbomachines a conduit à avoir, dans les compresseurs, des niveaux de vitesse de plus en plus élevés, et l'on trouve fréquemment, dans les coupes de tête actuelles, un écoulement relatif amont supersonique, l'écoulement aval étant toujours subsonique. On a alors, dans le canal interaube, tout un système d'ondes de choc pouvant amener, si l'on ne prend pas certaines précautions, un décollement de la couche limite. C'est ainsi que l'on a souvent, dans les coupes d'aubes supersoniques, de très mauvais rendements dus aux pertes par choc et par effets visqueux.

Pour minimiser ces pertes, il est possible d'appliquer certains principes de construction, et si on se limite à un nombre de Mach relatif amont modéré, de l'ordre de 1,4, on peut obtenir des aubes supersoniques ayant un très haut rendement, proche du celui des aubes subsoniques.

4.1. Choix du profil

L'objectif principal à atteindre est le suivant : le nombre de Mach à l'amont du choc principal

de compression (choc droit) doit être au plus égal à 1,32 environ. Cette valeur correspond à un saut de pression au travers du choc tel que la couche limite ne décolle pas.

D'autres critères (tel que le critère d'amorçage) et différents paramètres (nombre de Mach et direction de l'écoulement amont, contraintes mécaniques), sont aussi pris en compte pour la définition du profil. Celle-ci a été réalisée à l'aide de méthode de calcul de fluide parfait, en faisant largement appel au mode inverse [6].

4.2. Résultats d'essai

A partir du profil précédent, une maquette de grille plane a été réalisée, puis essayée dans la soufflerie S5Ch de Chalais-Meudon. Le nombre de Mach amont est 1,42, et les essais ont été menés en vue d'obtenir un taux de compression supérieur à 2. Les réglages du vannage aval, et du niveau de la pression dans les caissons d'aspiration latéraux où débouchent les pièges à couche limite pariétaux, permettent de faire varier à la fois le rapport de pression statique de la grille et le niveau de la convergence de la veine.

Les résultats les plus importants, tirés des nombreux essais effectués, peuvent être résumés dans le tableau ci-après :

	taux de convergence	rapport de pression statique	rapport de pression d'arrêt
veine bidimensionnelle	1.00	2.10	0.954
	0.991	2.08	0.949
	0.992	1.9	0.933
veine divergente	1.031	2.2	0.955
	1.026	2.15	0.947
	1.036	1.84	0.922
	1.042	1.08	0.912
veine convergente	0.962	2	0.958
	0.969	2.015	0.951
	0.964	1.945	0.944

Il apparaît que les performances maximales atteintes en écoulement bidimensionnel correspondent à un taux de compression statique de 2,1 avec une efficacité de 0,954. Une coupe de roue mobile fonctionnant dans les mêmes conditions donnerait un taux de compression (absolu) de 1,92 avec un rendement isentropique de 0,926, c'est-à-dire des performances très élevées.

Une analyse rapide permet de décomposer les pertes de pressions d'arrêt qui sont de l'ordre de 5 % en trois parts à peu près égales :

- couches limites,
- choc oblique et choc droit (estimation à partir du calcul non visqueux),
- choc détaché de bord d'attaque (estimation d'après réf. [2]).

Il est très difficile de rechercher des pertes plus faibles ; en effet, les couches limites sont déjà très minces, pratiquement sans décollement compte tenu de la faible intensité du choc principal à l'extrados comme à l'intrados. Il est impossible de réduire davantage le nombre de Mach de ce choc principal (1,3 en moyenne) sans empêcher l'auto-amorçage de la grille.

En outre, il n'est guère plausible d'envisager au niveau des applications industrielles des profils ayant des bords d'attaque plus minces. Ainsi, les performances mesurées dans cette grille correspondent à des valeurs vraisemblablement optimales.

5. CONCLUSIONS

Afin d'apporter une aide à la conception des turbomachines ayant de bonnes performances, les différentes sources de pertes qui apparaissent dans l'écoulement à la traversée d'une grille d'aubes supersonique sont ici rappelées et analysées.

L'accent a été mis particulièrement sur les pertes dues à l'onde de choc détachée, provoquée par l'arondi du bord d'attaque.

Par ailleurs des principes d'optimisations ayant pour but de réduire l'intensité du choc principal et de son interaction avec la couche limite, ont été appliqués et validés dans le cas d'un canal interaube et d'une grille d'aubes supersonique.

REFERENCES

- (1) P. CARRIERE
Chocs et onde de choc (tome 1) publié sous la direction de André L. Jaumotte (Masson et Cie)
- (2) A. LE MEUR
Computation of blade cascade aerodynamic losses due to detached shock waves.
thèse ISAE, Paris, 6-11 juin 1983.

- [3] G. MEAUZE
Détermination de la région de captation d'une grille d'aube supersonique.
68th Specialists Meeting of the propulsion and energetics panel on "Transonic and supersonic phenomena in turbomachines"
10-12 Septembre 1986. Munich (RFA)
- [4] H. STARKEN, H. SCHREIBER, Z. YONGKING
Mass flow limitation of supersonic blade rows due to leading edge blockage.
ASME paper N. 84-67-233.
- [5] J. DELEURY
Recherches sur l'interaction onde de choc-couche limite turbulente
13ème Colloque d'Aérodynamique appliquée de l'AAF, Lyon 1976.
- [6] G. MEAUZE
Méthode de calcul aérodynamique inverse pseudo-instationnaire,
La Recherche Aérospatiale n° 1980-1.

AD-P005 513

EXPERIMENTAL INVESTIGATIONS ON SHOCK LOSSES OF TRANSONIC AND
SUPERSONIC COMPRESSOR CASCADES

H.A. Schreiber

DFVLR
Institut für Antriebstechnik
Postfach 90 60 58
5000 Köln 90, Germany

SUMMARY

The losses of transonic and supersonic compressor bladings are due to viscous effects and due to entropy rises in shock waves arising in the entrance regions and passages of the blades. Depending on inlet Mach number, inlet flow angle and back pressure the shock loss level reaches 40 to 70 percent of the overall losses. Most of the loss prediction models in use consider viscous and shock losses separately. However, very few quantitative experimental data of shock losses are available to verify these models.

In this paper a separation of the viscous and shock losses is performed by the analysis of wake measurements behind some compressor cascades. The cascade tests have been performed in the inlet Mach number range from 0.8 to 1.7. Detailed information is presented about the shock structure and the region of shock boundary layer interaction in the blade passage of a supersonic cascade obtained with the aid of laser anemometry.

NOMENCLATURE

AVDR	axial velocity density ratio = $\rho_2 w_2 \sin \beta_2 / (\rho_1 w_1 \sin \beta_1)$
h	streamtube height
l	blade chord length
M	Mach number
M _{is}	isentropic Mach number = $f(p/p_{t1})$
M ₀	Mach number upstream of shock wave
M	Mach number behind shock wave
p	static pressure
p _t	total pressure
p _t /p _{t0}	total pressure ratio across shock wave
c _p	blade pressure coefficient = $(p_{t1} - p) / (p_{t1} - p_1)$
Re	Reynolds number
r _{LE} /l	relative radius of the leading edge
t	blade pitch
t/l	pitch chord ratio
x _{LE}	distance downstream of the leading edge (x-axis tangential the blade surface at x _{LE} =100 mm; direction $\beta=150^\circ$)
x/l	relative blade chord
y	coordinate normal to x _{LE} -axis (Fig. 14)
y/h	normalized coordinate within the streamtube
β	flow angle with respect to cascade front
β_s	stagger angle
δ	flow deflection across shock wave $\delta = \Delta \beta_s - \Delta \beta$
η	coordinate in tangential direction
ω	total pressure loss coefficient = $(p_{t1} - p_{t2}) / (p_{t1} - p_1)$
ω_s	shock loss coefficient
θ	inclination of shock wave
ξ_2	distance of downstream traversing plane (normal to cascade exit plane)

INDICES

- 1 uniform inlet conditions
- 2 uniform outlet conditions
- 2' conditions in the downstream traversing plane

1. INTRODUCTION

Improvements of fan and compressor performance require a continuous increase of the aerodynamic loading of the stages. The components are designed for higher through flow velocities, higher rotational speeds and higher pressure increase of the blade rows. Due to this the velocities relative to the blades increase to transonic and supersonic speeds and shock waves occur in the entrance region and passages of the blade rows. Advances in the design of aerodynamically efficient blades are dependent on obtaining a comprehensive understanding of the loss mechanism of the transonic and supersonic flow fields with embedded shock waves. The shock wave pattern varies considerably with increasing velocities.

For transonic blade sections up to relative inlet Mach numbers of 1.0 principally a normal shock wave occurs in the front part of the blades. Even so-called supercritical blades, which are designed for shock free operation, may have at least weak shock waves.

At supersonic speeds (M>1.0) a detached bow shock develops in front of the blade leading edge passing over to an oblique shock which propagates upstream of the successive blades. At the blade passage entrance the bow wave passes over to a quasi normal or oblique passage shock. Depending on back pressure a second normal passage shock or oblique trailing edge shocks may occur at the rear part of the blades.

There are several papers, which deal with the determination of shock losses such as [1-6], however, they mostly describe only one single part of the shock waves as for example the bow wave or the first passage shock. However, in many applications the shock wave pattern is more complex. For example the structure of the shock wave and its strength at the blade passage entrance or within the blade passage is strongly influenced by the interaction with the blade surface boundary layer. The shock induces a boundary layer thickening or may even force the boundary layer to separate, and due to this the shock itself weakens in the vicinity of the blade surface.

To study all the complex transonic and supersonic phenomena with shock waves and shock wave boundary layer interaction, the cascade model is a rather simple but very useful tool. Due to the stationary flow and a good accessibility to the flow field, the fluid mechanic phenomena can be studied in all details.

In this paper cascade measurements are presented, which deal with the determination of shock losses in transonic and supersonic compressor rotor blade sections. The first part of the paper describes shock losses which have been analyzed from wake traverse measurements downstream of Multiple Circular Arc (MCA) blades ($M_1=0.8-1.2$) and so-called pre-compression blades ($M_1=1.3-1.7$).

The second part gives more detailed information about the shock structure and strength within the blade passage of a supersonic blade section with an upstream Mach number of 1.53 and a separated boundary layer.

The presented data may help to develop more realistic analytical and semi-empirical loss models, or they may be a basis for the verification of more sophisticated computational blade to blade methods considering shock waves and the effect of shock boundary layer interaction.

2. EXPERIMENTAL FACILITIES AND TEST CONDITIONS

The tests have been conducted in the cascade wind tunnels of the DFVLR in Cologne. The MCA blade sections were investigated in the transonic cascade facility [6,7], which provides an inlet Mach number variation from $M_1=0.2$ to 1.4. The pre-compression blades were tested in the supersonic cascade facility, which allows inlet Mach numbers from $M_1=1.3$ to 2.4. Both tunnels are closed loop, continuously running facilities equipped with flexible supersonic nozzles. Suction systems are available to remove the sidewall boundary layers within the blade passages. Wake flow measurements at midspan position were obtained by traversing a combination probe for static pressure, total pressure, and flow direction. Two neighbouring blades have been instrumented to measure the surface pressure distribution, one for the pressure surface and the other one for the suction surface. A Schlieren system allowed the observation of the shock wave pattern and helped to check the flow periodicity. A Laser-Two-Focus (L2F) velocimeter was used to analyse the transonic flow field within blade passages.

3. SHOCK LOSSES FROM WAKE ANALYSIS

3.1 Experimental Procedure

The measured total pressure losses in the traversing plane downstream of the cascade consist of all viscous losses and losses due to the entropy rise in the shock waves. The shock losses arise in all parts of the shock waves intersecting the stream tube enclosed by two periodic stream lines as sketched in Fig. 1.

In a measurement plane behind the cascade, which is not too far downstream, the shock losses can be recognized outside of the turbulent wake. Assuming a wake model as shown in Fig. 2, shock losses and viscous losses can be separated. This figure shows qualitatively, how the measured total pressure losses along one blade gap look like. If the extension of the viscous wake is known (point η_{sc} and η_{sp}), it is relatively easy to separate the losses. The assumption of a linear variation of the shock losses across the wake, as a first approximation, is sufficient to obtain the correct order of magnitude. The wake root points are approximately 20-50% left and right of the wake centre. The wake width is dependent on the streamwise distance to the cascade exit plane, but also on the magnitude of the losses itself. Due to thicker suction surface boundary layer or due to separation, normally the wake is asymmetric. In any case, the measurement plane should not be too far downstream. The reduced data presented here, have been obtained from traversing planes which are approximately half a gap or less axially downstream of the cascade exit plane ($\xi_2/t \leq 0.5$).

3.2 Transonic Blade Sections

As an example for transonic blade sections the results of two rotor blade sections, having MCA blades, will be presented here. The cascades have been derived from the rotor blades of a DFVLR transonic compressor stage, which was investigated in detail using advanced testing techniques [8]. The L030-4 cascade corresponds to the blade section at 45% and the L030-6 cascade to the 68% blade height section. The blades have a relatively low suction surface curvature and a blade camber of 14.9° and 7.86° respectively.

Generally transonic blade sections are designed for unchoked inlet flow conditions. In this case inlet Mach number and inlet flow angle are independent parameters and thus the arising shock losses are also a function of Mach number and flow angle. (Flow configurations with choked flow and reduced back pressure, where shocks exist behind the throat cross section, will not be analysed here.) The driving parameter, of course, is the upstream Mach number. With increasing inlet velocities, there is a gradual rise of the total pressure losses induced by the occurrence of shock waves in the entrance region of the blades. These shocks appear, when the flow around the blades becomes supercritical at a special inlet Mach number. With increasing Mach number, the local supersonic areas

on the blade suction surface also increase and the extending shocks move downstream up to a position near the leading edges of the adjacent blades. At sonic and supersonic speeds, these shocks are emanating from the cascade entrance area infinitely far upstream (see Fig. 1 and Schlieren photographs in Figs. 5 and 8).

Figures 3 and 6 show the measured overall losses and the separated shock losses for different inlet flow angles. The gradual rise of the overall losses with Mach number is primarily induced by the shock losses. The viscous losses, which are the difference between overall- and shock losses, seem to be not very much dependent on the inlet Mach number.

Increasing the incidence angle, the level of the shock losses rises continuously in the whole investigated Mach number range and it seems, that the viscous losses are not very much influenced. It is presumed however, that for the high positive incidence range, this type of wake analysis overpredicts the shock losses or that the measurement plane was too far downstream ($x/t \approx 0.45$).

A comparison of the losses for the L030-4 and L030-6 cascade shows no essential difference in the behaviour, but due to the higher front camber of the L030-4 blades, their shock loss level at sonic and supersonic inlet speeds is higher. The difference between these two blade section is clearly demonstrated in Figs. 4 and 7. Here the shock losses are calculated by a shock loss model similar to that one of Miller, Lewis, and Hartmann [1], but considers the influence of the detached bow shock wave and the influence of the inlet flow angle by a stagnation streamline shift [2,6].

The mechanism of inlet Mach number and inlet flow angle on the shock losses can be understood by looking to the blade pressure distribution and the corresponding Schlieren pictures in Figs. 5 and 8. The Mach numbers in front of the shock waves increase with inlet Mach number as well as with rising positive incidence. The blade pressure distributions also indicate, that at least for the subsonic cases, most of the flow expansion occurs near the blade leading edge. This, however, is very typical for profiles, which are rather thin and have low suction surface curvature. Rising the incidence angle, the shock waves in front of the blade passages become more normal and the intensity of the bow shock waves increases.

An always interesting question is, whether the shocks are unstable or not: The shock waves in the investigated flow range are very stable and no unsteady shock-wave boundary layer interactions have been observed. It is presumed, that the shock waves, which are relatively strong, have their well defined position in the flow field around the MCA blades.

3.3 Supersonic Blade Sections

The fundamental characteristic of supersonic cascades is a fixed relationship between inlet Mach number and inlet flow angle (unique incidence). Beyond a special upstream Mach number, when the supersonic flow of the blade passage is started, the inlet flow conditions are fixed and independent of the prescribed back pressure. Thus, the losses of the oblique shock waves and bow shocks ahead of the cascade are constant for a given inlet Mach number. However, the shock pattern within the blade passage and exit plane is dependent on the back pressure, and the resulting shock losses can vary considerably. The analysis of the investigated supersonic cascades presented below, however, will concentrate on flow conditions of maximum attainable back pressure only, because this normally corresponds to the design flow conditions.

ARL-SL19 cascade

The analysed supersonic compressor cascade was derived from a rotor blade section of a high-through-flow transonic axial compressor of the US Air Force Aero Propulsion Laboratory, Ohio [9]. This cascade, corresponding to streamline 19 of the compressor, initially was designed and tested by Detroit Diesel Allison (DDA) [10] and later investigated at ONERA and DVL in a joint program.

The essential design feature of this profile is a concave suction surface curvature in the front part of the blade, resulting in a deceleration of the flow already upstream of the blade passage. These so called pre-compression blades have lower Mach numbers ahead of the passage shock and therefore lower shock losses. The cascade has a design Mach number of 1.16, a blade camber of -2.89° , and an extreme thin leading edge ($x_c/l = 0.00128$). Due to the nearly pointed leading edge, the contribution of the detached bow shock to the losses is relatively small. The Schlieren picture in Fig. 9 provides an impression of the shock wave pattern of the ARL cascade at an inlet Mach number of approximately 1.43. It must be pointed out, however, that this Schlieren photo belongs to a test series, where no sidewall suction was provided and therefore maximum static pressure rise could not be achieved. Thus, the shock pattern in the exit region is not typical for the data presented below.

A characteristic feature of the pre-compression blades is an oblique shock wave, which develops in the blade entrance region in tangential direction. This so called pre-compression shock arises due to an overlapping of the left-hand running characteristics emanating from the concave blade contour. Its contribution to the shock losses, however, is rather small.

The main contribution results from the relatively strong first oblique passage shock and a second weak normal shock as sketched in the upper part of Fig. 10. Due to the strong pressure increase in the first passage shock, the suction surface boundary layer separates and a lambda shock develops above the separated region. This region of interaction increases on the one hand with rising inlet Mach numbers and on the other hand with increasing back pressure.

Fig. 10 provides the measured overall losses, the analysed shock losses, and the corresponding static pressure ratios of the ARL cascade for upstream Mach numbers up to 1.7. The continuous loss increase with Mach number, again, is primarily a function of the shock losses. For comparison, calculated shock losses are plotted into the diagram.

The upper solid curve represents the losses of a normal shock wave ahead of the blade passage and the lower dashed line an oblique shock wave with maximum attainable deflection and nearly sonic conditions ($M \approx 1.0$) behind the shock. For high inlet Mach numbers, the experimentally determined shock losses tend to the solution of an oblique shock, whereas the tests with Mach numbers less than 1.4 tend to the normal shock solution. This trend is meaningful, because the low Mach number tests tend to an unstated passage flow with a quasi normal shock at blade passage entrance.

Two typical blade Mach number distributions for an inlet Mach number of 1.35 and 1.6 respectively are provided in Fig. 11.

PAV-1.5 Cascade

The second supersonic cascade is also a pre-compression blade, but was designed especially for investigations on shock boundary layer interaction with separation. Its design Mach number is 1.5, it has a blade camber of $+0.39^\circ$, and a considerably thicker leading edge ($x_{LE}/l = 0.0025$). The front part is aerodynamically higher loaded and the first passage shock was designed to be oblique with a deflection to obtain $M = 1.0$ behind the shock.

Due to the higher loading, the measured overall losses and analysed shock losses are slightly higher (Fig. 12) than those of the ARL cascade. It is remarkable, that for this cascade the experimentally determined shock loss level tends to agree with the theoretical results of a normal shock at the blade passage entrance.

This result and the previous results indicate, that it is very important to adjust any shock loss model carefully to the real cascade geometry and the real shock pattern prescribed by the back pressure.

A sketch of the cascade and its shock wave location is provided in Fig. 12 and a Schlieren photograph at $M_1 = 1.5$ in Fig. 13. Again a lambda shock develops due to the boundary layer separation and a second weak normal shock stands in the rear passage. A detailed analysis of this shock pattern will be described in the following chapter.

One thing remains to be mentioned: the scattering of the losses in Fig. 12 is due to slightly different static pressure ratios, but also to different axial velocity density ratios (AVDR). The AVDR primarily influences the rear part of the passage and mainly influences the amount of the viscous losses.

4. PASSAGE SHOCK WAVE ANALYSIS

4.1 Test Model and Testing Technique

The PAV-1.5 cascade was designed having an oblique passage shock and separation of the suction surface boundary layer. To improve the measuring accessibility of the shock wave boundary layer interaction region and the boundary layer itself, the blade chord was selected to be 170 mm. Due to the limited size of the cascade wind tunnel test section ($H/b = 237/152$ mm), only three blades with an aspect ratio of 0.894 could be installed. For supersonic cascade flow, however, there is no essential problem to obtain a periodic cascade flow, because the periodic inlet flow pattern is fixed already behind the first blade passage [2]. The central blade was instrumented on the suction surface and the successive outer blade on the pressure surface.

Many of the classical shock wave boundary layer interaction experiments suffer from the problem of sidewall effects. The flow field at least behind the shock wave is strongly influenced by the thickening of the sidewall boundary layer, although a 2-dimensional flow field was desired. To overcome this problem, at least partly, a side-wall boundary layer suction was applied in the area, where the strong passage shock interacts with the wall shear layer. Due to suction, nearly 2-dimensional flow conditions at least at midspan position could be obtained (AVDR ≈ 1.0). A further advantage of this model is, that it simulates the flow field and the boundary layer thickness of a real transonic compressor blade section.

A Schlieren photograph of the cascade with the investigated shock wave location is shown in Fig. 13. The oblique shock and the lambda shock can be observed through trapezoidal suction holes of the plexiglas sidewalls.

Fig. 14 provides a drawing of the cascade and the horizontal measurement planes across the first passage shock (planes 1-8) and the second normal shock (planes 10-13). Using a non-automated Laser-Two-Focus anemometer (L2F) [11], velocity and flow angle measurements have been performed at midspan position. The non-automated version of the anemometer has some advantage measuring in the vicinity of shock waves, because the signals obtained can be analysed and interpreted directly by "hand". A mist of oil particles was introduced into the settling chamber to improve the rate of signals in the measurement volume. Due to the small size of the oil droplets (about $0.07 \mu m$ in mean diameter), they adequately follow the flow across shock waves.

4.2 Results and Discussion

Emphasis was placed on studying the flow field ahead and downstream of the passage shock waves to obtain a better understanding of the transonic flow and the shock strength. Furthermore the measurements near the blade surfaces shall provide some more information about the region of shock wave boundary layer interaction with separation.

The investigated test point had an inlet Mach number of 1.529, Mach numbers in front of the oblique shock and partly quasi normal shock wave in the order of 1.42 to 1.53, a static pressure ratio of 2.13, and an AVDR of 1.02. Fig. 15 shows the measured blade Mach number distribution together with the location, where the shock waves impinge the blade surface. The high pressure increase in the first passage shock forces a boundary layer separation at approximately $x = 108$ mm ($x/l = 0.635$) and the shock splits into a lambda shock system. The steep pressure increase at 63% blade chord of the suction

surface in Fig. 15 corresponds to the position, where the leading oblique shock of the lambda system enters the boundary layer and where separation occurs.

Fig. 16 shows the position of the shock waves, and the estimated thickness of the boundary layer. The indicated Mach numbers and flow deflections have been deduced from the measured velocity and flow angle distributions in the traversing planes 1 to 13, which are shown in Fig. 17 and 19.

First Passage Shock Wave

The results of planes 6 to 8 in Figs. 16 and 17b qualitatively confirm the assumed design goal of an oblique shock with a flow deflection, which provides a deceleration to sonic velocity. Unfortunately the data of plane 5 and 6 show some small discrepancies, which are assumed to be generated by some sidewall disturbances, coming from an upstream position. Also the results just behind the shock of section 5 have been slightly unsteady.

The overall shock pattern, however, was very stable and the L2F anemometer easily could resolve the strong decelerations across the shocks. The measured Mach numbers behind the shocks are very close to the calculated ones, assuming the theoretical shock relations together with the measured flow deflection (see data in Fig. 17).

Shock Wave Boundary Layer Interaction

The quasi normal part of the first passage shock (between plane 2 and 4) is established by the prescribed back pressure. This part already belongs to the area of strong shock-wave boundary layer interaction. The negative flow turning across the shock and the strong acceleration just behind the shock is primarily induced by the flow-direction and curvature at the edge of the separated boundary layer. The flow properties through the lambda shock in plane (1) (Fig. 17a) are in qualitatively good agreement to the findings of Seddon, East, Kooi, and Delery [12-15]. Only the velocity within the plateau between the shocks is constant and the acceleration behind the shock seems to be stronger.

Very typical for the lambda shock configuration is the stepwise deceleration from $M_0 = 1.53$ to 1.19 in the leading shock, and from 1.19 to about 0.97 in the rear quasi normal shock. The flow, however, quickly reaccelerates to about $M = 1.12$ within 2-3 mm. A comparison of the stepwise Mach number distribution to the measured Mach numbers on the blade surface is presented in Fig. 18. Behind the shock system, the Mach numbers on the surface and 3.6% of chord above the surface, are still supersonic.

Second Passage Shock Wave

The convex curvature in the front part of the blade pressure surface allows the passage flow to reaccelerate partly. The maximum Mach number is achieved, where the second passage shock meets the pressure surface at about 40% blade chord. Because the Mach number is about 1.33, the normal shock wave forces a weak local boundary layer separation, which has been detected with the aid of a surface flow visualization technique.

Fig. 19 shows the laser results of section 10 to 13. The strength of the shock weakens considerably from the pressure surface towards the suction surface and the shock vanishes, entering the edge of the separated boundary layer (Fig. 16).

Shock Wave Strength

In order to obtain a better understanding of the shock loss mechanism, the total pressure recovery of the different shocks is plotted separately in Fig. 20. The losses are generated by the outer bow shock and its oblique extension ahead of the cascade (1), the pre-compression shock (2), the first passage shock (3), and the rear passage shock (4). The detached bow shock (1) has a considerable contribution in the direct vicinity of the leading edge, as the calculated curve illustrates in the upper part of Fig. 20. The oblique pre-compression shock (2) is very weak, but decelerates the velocity in front of the leading edge from $M = 1.68$ to 1.42. Due to this, the contribution of the inner part of the detached bow shock is much smaller, but a strong discontinuity is established just ahead of the blade leading edge.

The strength of the two passage shocks (3 and 4) could be determined with the data obtained from the L2F-measurements. The highest amount of losses is produced in the quasi normal part of the first passage shock between about 18 to 45 percent of the blade channel height. The contribution of the lambda shock, the oblique passage shock and the rear normal shock (4) is much smaller.

In order to compare the estimated shock loss distribution to the measured overall losses, the accumulated but non-mixed-out shock losses are plotted together with the total pressure ratios obtained in the downstream traversing plane (Fig. 21). Remarkable is the discontinuity of the bow shock losses near the wake center and the relatively high amount of shock losses between $\eta/t = 1.18$ and 1.45 resulting from the normal part of the first passage shock.

CONCLUSIONS

The paper suggests, how to determine shock losses from downstream-flow measurements behind transonic and supersonic cascades. The obtained data show, that shock loss calculations should not be over-simplified but should be carefully modeled according to the real flow conditions. At least the influence of the most important parameters as inlet flow angle in the transonic flow range and the back pressure, which prescribes the passage shock wave location and strength in supersonic cascades, should be simulated carefully.

Passage shock analysis provides detailed information about the transonic flow field, the shock-wave location with the associated losses and an insight into the region of shock wave boundary layer interaction. The results demonstrate the dominant influence of the viscous flow in the rear part of the blade passage.

REFERENCES

- [1] Miller, G.R.; Lewis, G.W. and Hartmann, M.J.: "Shock Losses in Transonic Compressor Blade Rows", Transactions of the American Society of Mechanical Engineers, Vol. 83, Series 4, No. 3, pp. 235-242, July 1961.
- [2] Starken, H.: "Untersuchung der Strömung in ebenen Überschallverzögerungsgittern", DLR-Forschungsbericht 71-99 (1971).
- [3] Breugelmans, F.A.: "The Effect of Leading-Edge Thickness on the Bow Shock in Transonic Rotors", in "Transonic Flow Problems in Turbomachinery", edited by T.C. Adamson, jr.; M.F. Platzler (1977).
- [4] Le Meur, A.: "Computation of Blade Cascade Aerodynamic Losses due to Detached Shock Waves", 6th International Symposium on Air Breathing Engines, Paris, 1983.
- [5] York, R.E.; Woodard, H.S.: "Supersonic Compressor Cascades - An Analysis of the Entrance Region Flow Field Containing Detached Shock Waves", ASME Journal of Eng. for Power, pp. 247-257, April 1976.
- [6] Schreiber, H.A.; Starken, H.: "Experimental Cascade Analysis of a Transonic Compressor Rotor Blade Section", ASME Journal of Eng. for Gas Turbines and Power, Vol. 106, No. 2, April 1984.
- [7] Schreiber, H.A.; Starken, H.: "Evaluation of Blade Element Performance of Compressor Rotor Blade Cascades in the Transonic and Low Supersonic Flow Range", Fifth International Symposium on Air Breathing Engines, Bangalore, India, pp. 67 1-9, Febr. 1981.
- [8] Dunker, R.; Hungenberg, H.G.: "Transonic Axial Compressor Using Laser Anemometry and Unsteady Pressure Measurements", AIAA Journal, Vol. 18, No. 8, August 1980.
- [9] Wennerstrom, A.J.: "The Design and Evaluation of a High-Throug-Flow Transonic Axial Compressor", 6th International Symposium on Air Breathing Engines, Paris, 1983.
- [10] Fleeter, S.; Holtmann, R.L.; Mc Clure, R.B.; Sinnet, G.T.: "Experimental Investigation of a Supersonic Compressor Cascade", ARL TR 75-0208, Aerospace Research Laboratories, Wright-Patterson AFB, Ohio, June 1975.
- [11] Schodl, R.: "A Laser-Two-Focus (L2F) Velocimeter for Automatic Flow Vector Measurements in the Rotating Components of Turbomachines", Trans. ASME, J. Fluid Eng., Vol. 102, No. 4, 1980.
- [12] Seddon, J.: "The Flow Produced by Interaction of a Turbulent Boundary-Layer with a Normal Shock-Wave of Strength Sufficient to Cause Separation", ARC R&M 3502, 1960.
- [13] East, L.F.: "The Application of a Laser Anemometer to the Investigation of Shock Wave/Boundary Layer Interactions", RAE Tech. Memo, AERO 1666, see also AGARD-CP-193, Feb. 1976.
- [14] Kooi, J.W.: "Influence of the Free-Stream Mach Number on Transonic Shock-Wave/Boundary Layer Interactions", NLR MP-78013 U, May 1978.
- [15] Delery, J.; Marvin, J.G.: "Shock-Wave Boundary Layer Interactions", AGARD -ograph No. 280, 1986.

ACKNOWLEDGEMENT

The author gratefully acknowledges the technical support of Dr. R. Schodl, who provided the Laser-Two-Focus velocimeter.

Table 1
Geometrical parameters of the investigated cascades:

	L030-4	L030-6	ARL-SL19	PAV-1.5
c/l	0.621	0.678	0.634	0.650
l mm	90	90	85	170
δ°	138.51°	145.71°	146.93°	148.09°
d_{max}/l	0.030	0.04	0.0255	0.035
r_{max}/l	0.00403	0.00317	0.00128	0.0025
camber	14.9°	7.85°	- 2.89°	+ 0.39°

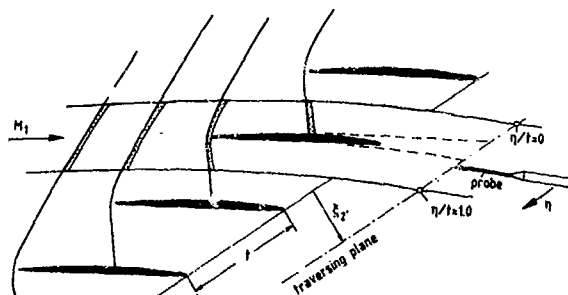


Fig. 1 Shock waves contributing to the losses measured downstream of the cascade

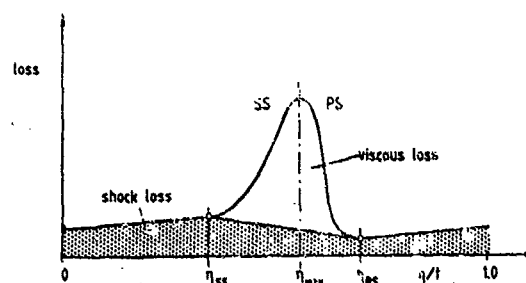


Fig. 2 Model to separate viscous and shock losses in the downstream measurement plane

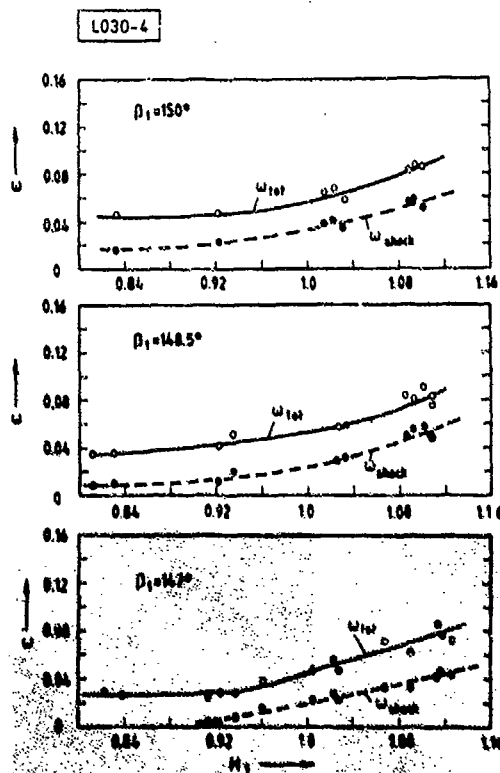


Fig. 3 Influence of inlet Mach number and inlet flow angle on measured total pressure losses and corresponding shock losses of the L030-4 cascade

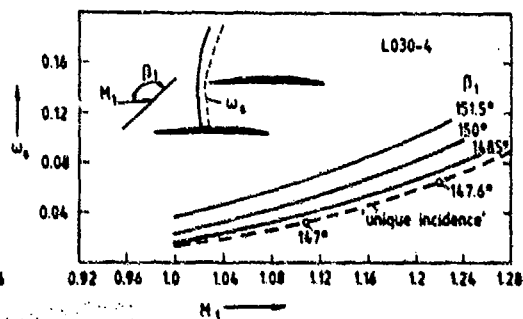


Fig. 4 Calculated losses of the normal passage shock depending on inlet Mach number and inlet flow angle of the L030-4 cascade

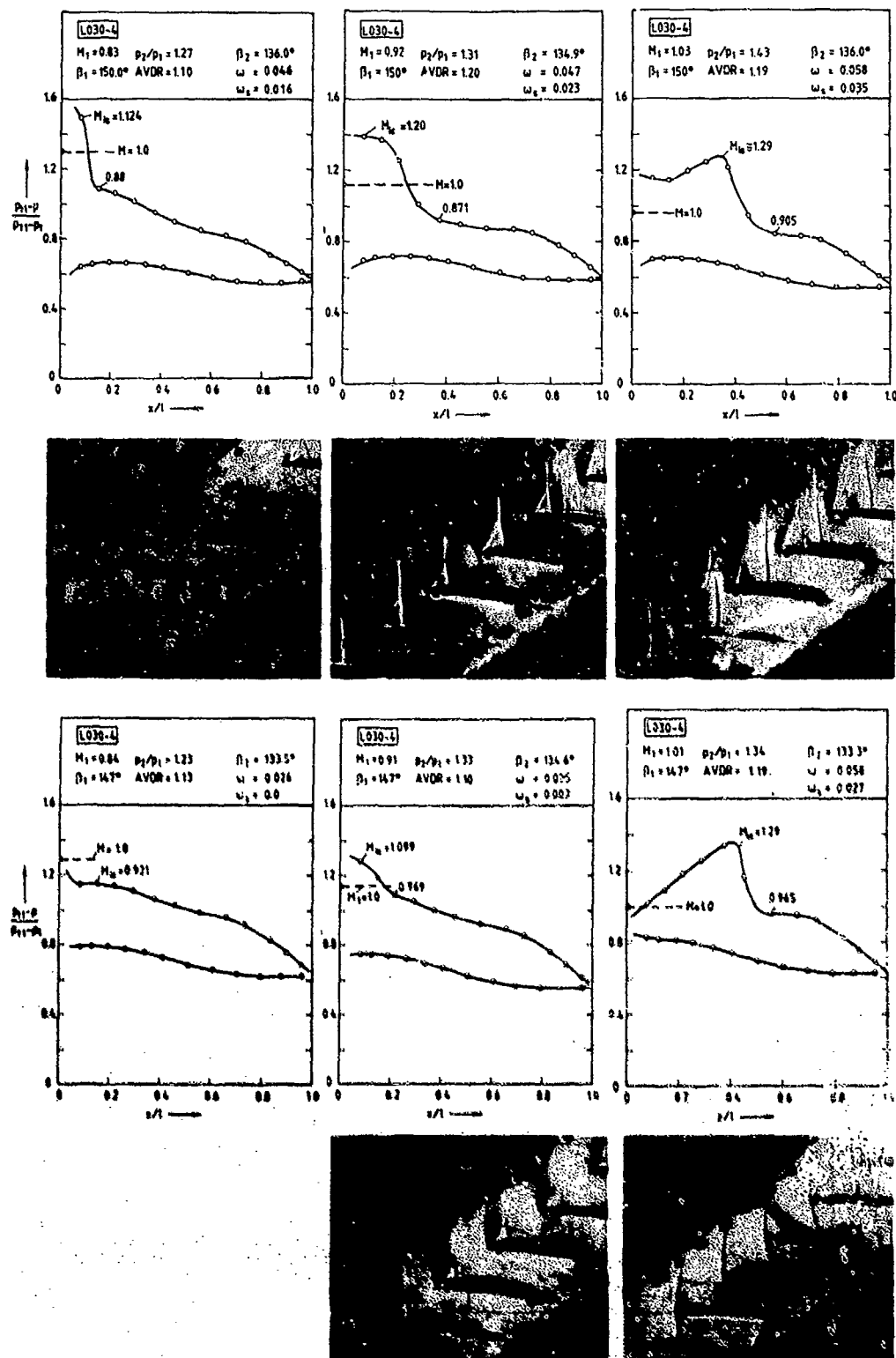


Fig. 5 Influence of inlet Mach number on blade pressure distribution and shock wave location of the L030-4 cascade (upper part: $\beta_1 = 150^\circ$; lower part: $\beta_1 = 147^\circ$)

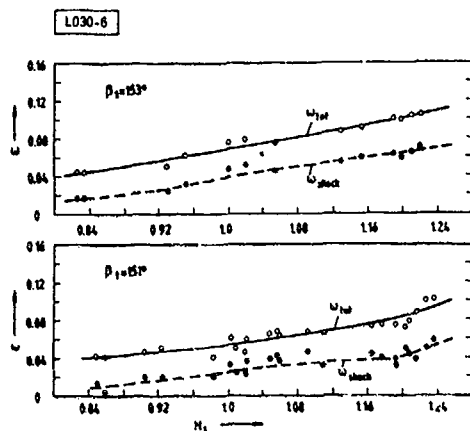


Fig. 6 Influence of inlet Mach number and inlet flow angle on measured total pressure losses and corresponding shock losses of the L030-6 cascade

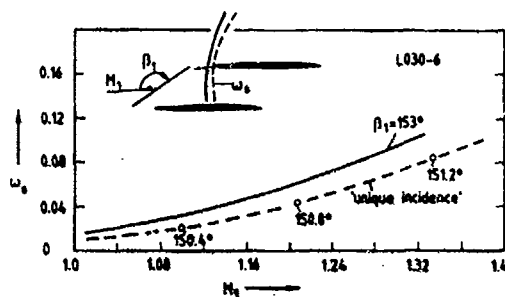


Fig. 7 Calculated losses of the normal passage shock depending on inlet Mach number and inlet flow angle of the L030-6 cascade

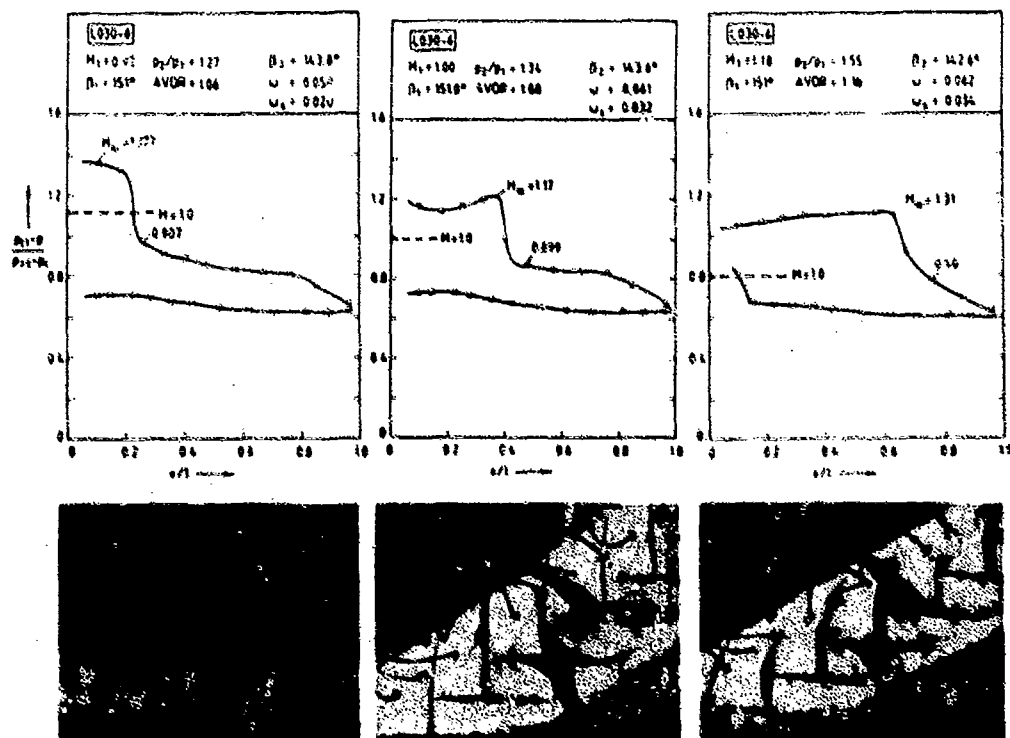


Fig. 8 Influence of inlet Mach number on blade pressure distribution and shock wave location of the L030-6 cascade at $\beta_1 = 15.1^\circ$

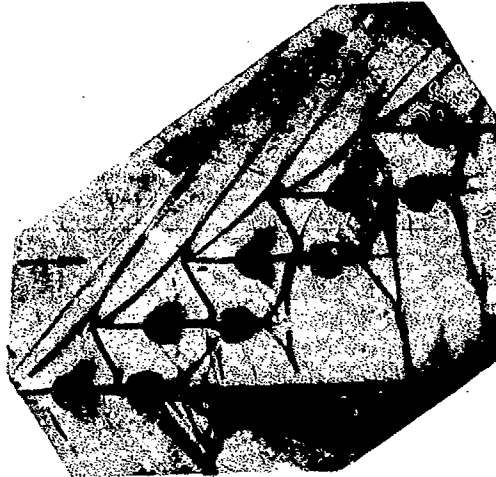


Fig. 9 Schlieren photograph of the ARL-SL19 cascade at $M_1=1.43$ and $p_2/p_1=1.35$

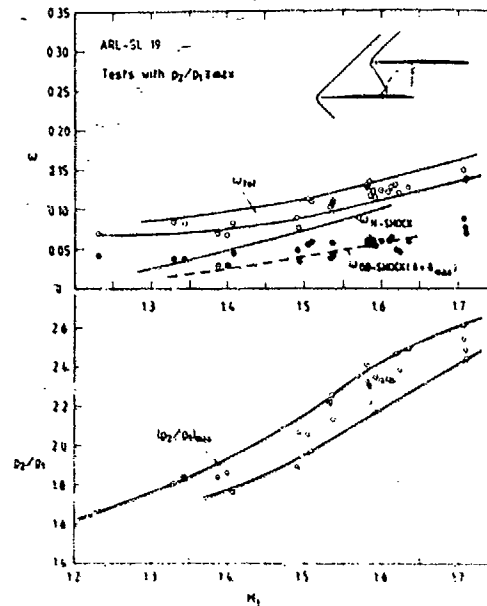


Fig. 10 Total pressure losses and corresponding shock losses (solid symbols) of the ARL-SL19 cascade at max. static pressure ratios

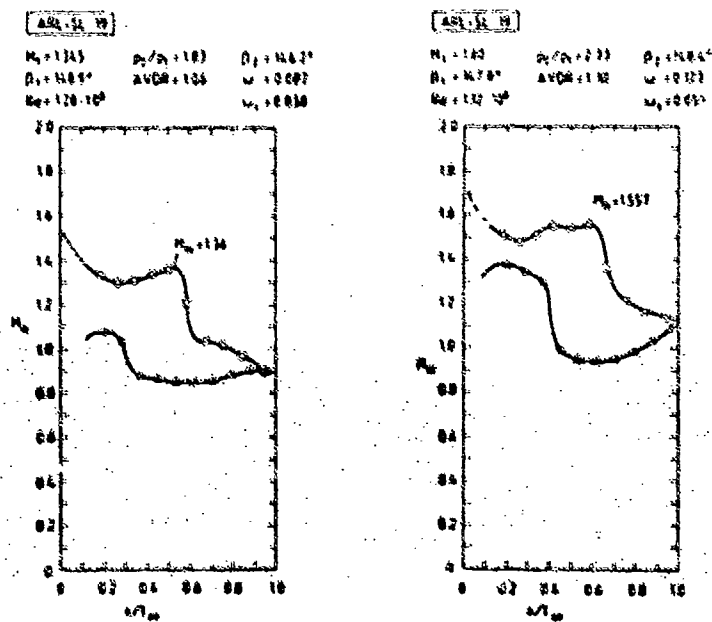


Fig. 11 Blade Mach number distribution of the ARL-SL19 cascade at $M_1=1.145$ and $M_1=1.60$

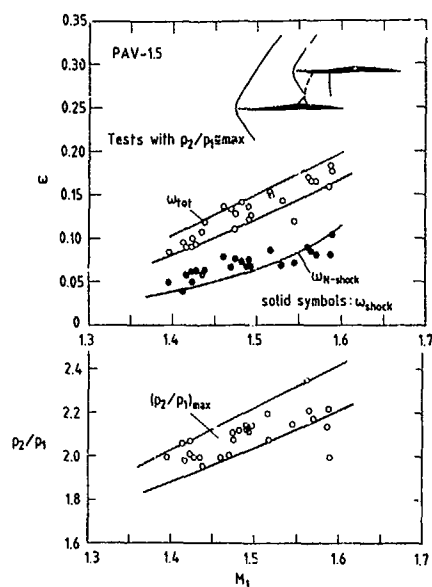


Fig. 12 Total pressure losses and corresponding shock losses of the PAV-1.5 cascade at max. static pressure ratios

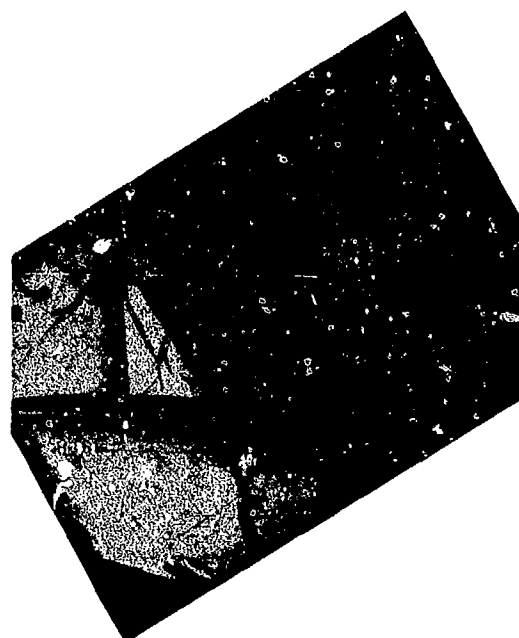


Fig. 13 Schlieren photograph of the PAV-1.5 cascade at $M_1=1.5$ and $p_2/p_1=2.1$ (trapezoidal holes for sidewall boundary layer suction)

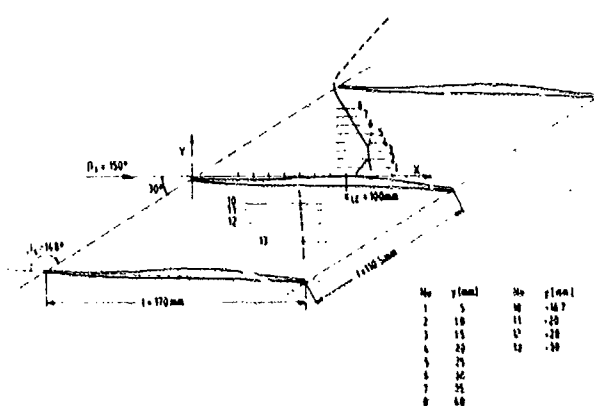


Fig. 14 Cascade geometry and L2F-measurement planes

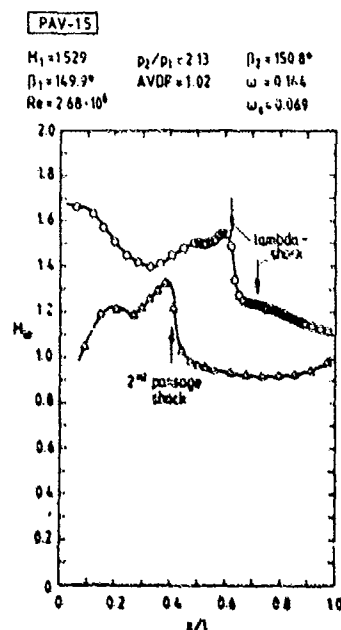


Fig. 15 Blade Mach number distribution of the PAV-1.5 cascade at $M_1=1.529$ corresponding to the L2F results in Figs. 17-19

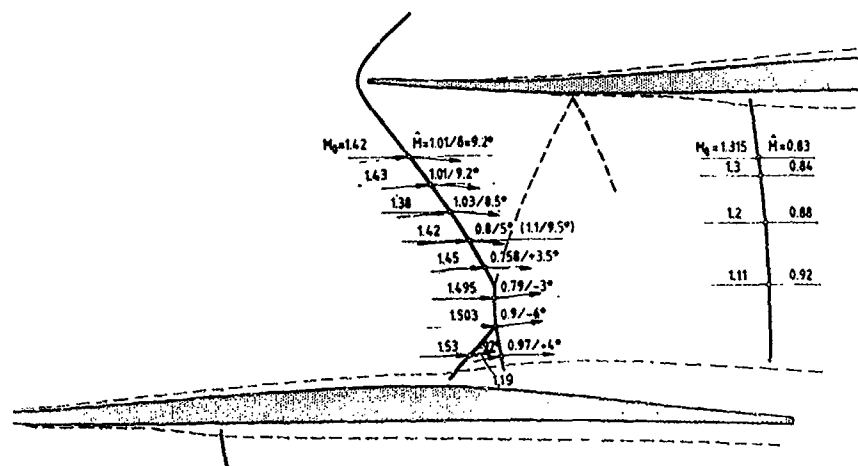


Fig. 16 Flow vectors upstream and downstream of passage shock waves deduced from L2P results ($M_1=1.529$, $p_2/p_1=2.13$)

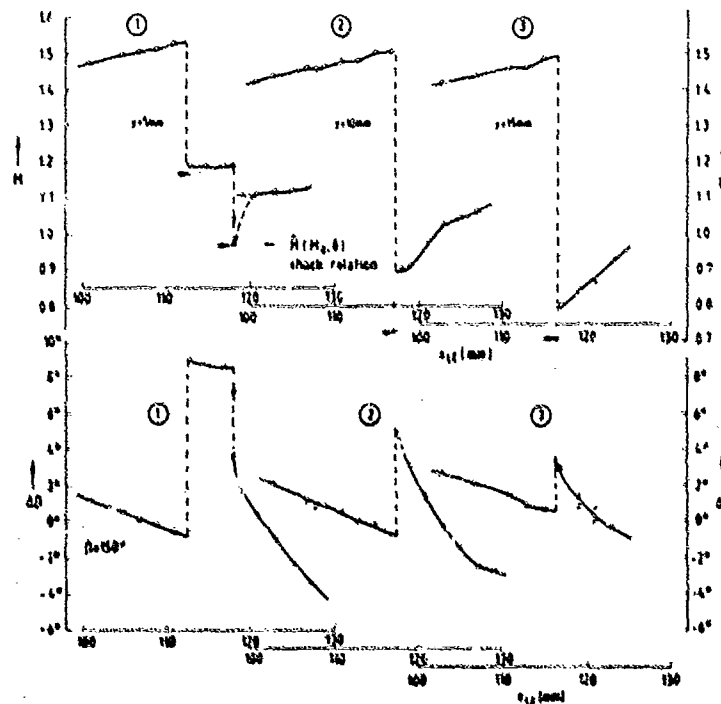


Fig. 17a Mach number and flow direction profiles across the first passage shock wave measured by L2P anemometer (planes see Fig. 14), $M_1=1.529$, $p_2/p_1=2.13$

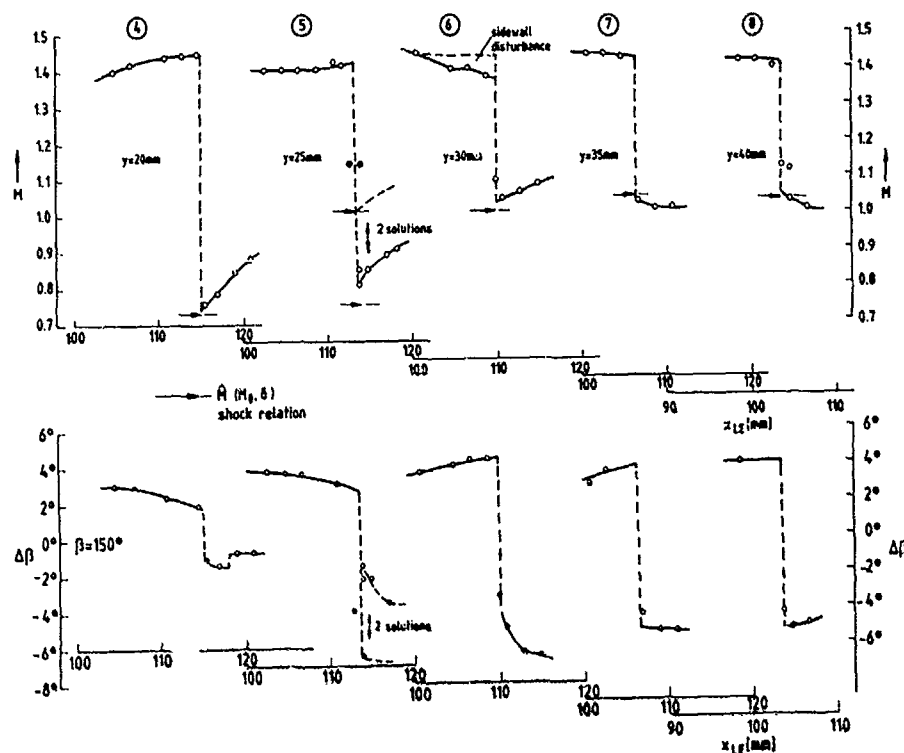


Fig. 17b Mach number and flow direction profiler across the first passage shock wave measured by LZF anemometer (planes see Fig. 14), $M_1=1.529$, $p_2/p_1=2.13$

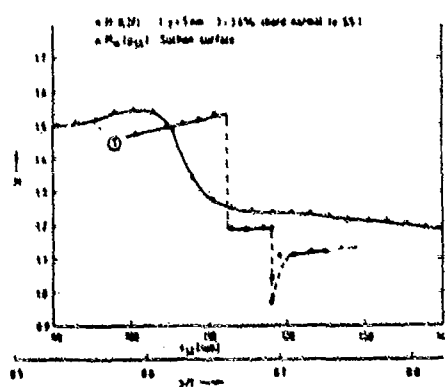


Fig. 18 Mach number profiles in the area of shock wave boundary layer interaction with separation - comparison of "wall" Mach numbers and Mach numbers 1-3.6% chord above the blade surface (plane 1), $M_1=1.529$, $p_2/p_1=2.13$

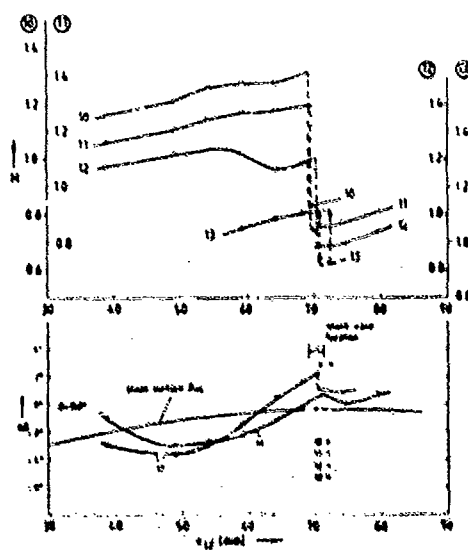


Fig. 19 Mach number and flow direction profiles across the second passage shock wave; see Fig. 14 ($M_1=1.529$, $p_2/p_1=2.13$)

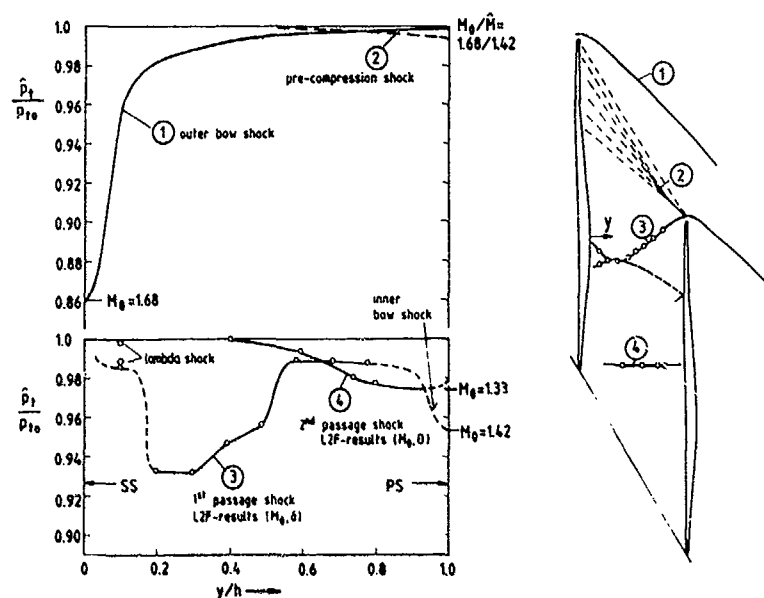


Fig. 20 Contribution of the different shock waves to the loss distribution across the blade passage of the PAV-1.5 cascade at $M_1=1.529$ and $p_1/p_2=2.13$

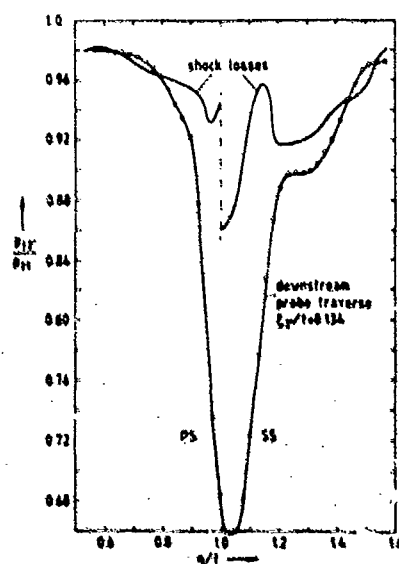


Fig. 21 Measured total pressure ratio behind the PAV-1.5 cascade ($M_1=1.529$, $p_1/p_2=2.13$) compared to the distribution of the non-mixed-out shock losses.

DISCUSSION

A.S.Üçer, Tu

Did you make any attempt to construct a shock loss model which may be used for performance prediction purposes?

Author's Reply

The theoretical results presented in Figures 4, 7, 10 and 12 are based on a shock loss model developed by Starken (2) which has been extended to consider the influence of the inlet flow angle.

The results of the transonic cascade measurements have been used to develop a shock loss model for inlet Mach numbers lower than 1.0, which is presented in paper 27. I personally hope that the experimental results obtained might be used to verify transonic blade to blade codes, because they automatically should predict the real shock structures.


J.Hourmouziadis, Ge

Figure 18 compares the wall Mach number distribution derived from static taps with the Mach number distribution 5 mm away from the wall from the laser measurements. Do you have an explanation for the fact that the double shock structure in the main flow does not show on the wall?

Author's Reply

Because the Mach number ahead of the first passage shock is greater than 1.53, the strong pressure increase induces a severe boundary layer separation. The lambda shock structure itself is a result of the interaction mechanism between the strong passage shock and the separated boundary layer. The L2F measurement across the lambda shock system has been performed just outside of the viscous layer. The pressure jump across the shocks weaken and finally disappears, when the shocks enter the boundary layer. I assume that, especially due to the strong separation, the pressure information of the shock is fully smeared off.

Due to the interaction mechanism the main pressure increase on the wall occurs relatively far upstream of the shock system.



OPTIMISATION OF A TRANSONIC FLOW RADIAL VANED DIFFUSER

Salvatore Colantuoni
Alfa Romeo Avio R&D
Napoli, Italy

René Van den Braembussche
von Karman Institute
Rhode St Genèse, Belgium

SUMMARY

The transonic flow in an existing radial vane diffuser has been analysed with a time dependent finite area calculation method. The calculated Mach number distribution indicates a strong bow shock upstream of the throat.

Based on this experience, new diffusers have been designed in order to optimize the Mach number distribution in the semi-vaneless space by designing for a shock-free deceleration. The best predictions are obtained with a modified version of the design method of Herbert and Came in which a radial change of diffuser width is incorporated.

Experimental results obtained with this optimised design show an important increase in range and confirm the shock-free deceleration of the flow. The difference between the calculated and measured pressure distribution can be explained by incidence effects due to an incorrect estimation of the boundary layer blockage on the lateral walls. Better predictions will be possible only if a more precise definition of the real flow conditions at the diffuser inlet becomes available.

LIST OF SYMBOLS

AK	half diffuser channel opening angle	α	vane angle measured from radial direction
AL	leading edge wedge angle	β	flow angle measured from radial direction
B	blockage factor (1-Blocked area/geometrical area)	π	pressure ratio
e	internal energy	ρ	density
F	flux term of the conservative Euler's system of equations		
G	flux term of the conservative Euler's system of equations		
h	corrected diffuser width		
l	non dimensional length along diffuser vane suction side		
m	mass flow		
M	Mach number		
p	static pressure		
r	radius		
s	cross section area of control volume		
t	time		
w	velocity vector		
x	meridional coordinate		
y	tangential coordinate		
2D	two dimensional		

Subscripts

2	diffuser inlet radius
le	leading edge position
t	time derivative
te	trailing edge position
th	throat position
tt	total to total
x	meridional component or derivative
y	tangential component or derivative

INTRODUCTION

High pressure ratio centrifugal compressors have transonic or supersonic flow at the impeller exit and the vane diffuser is the most efficient device to decelerate this flow and to transform the kinetic energy into static pressure rise.

Analytical models normally treat separately the zone of rapid adjustment upstream of the throat, where the isobaric lines change rapidly from almost parallel to the impeller exit to a direction perpendicular to the velocity vector, and the divergent channel, downstream of the throat where the flow is almost one-dimensional. It has been demonstrated that the diffuser data of Rundstadler [1] give an accurate prediction of the performance in the divergent channel if the throat Mach number and blockage are known. These conditions depend on the diffusion of the flow in the vaneless and semi-vaneless space. The stability of the transonic flow in this region also influences the operational range between surge and choke. The inlet region is therefore considered as a critical element in the design of a high performance compressor.

The study of the flow in this region is complicated due to:

- the three dimensional character of the flow because of the skewed boundary layers on the lateral walls;
- the unsteadiness of the inlet flow due to the non uniformity of the flow leaving the impeller;
- interaction between the impeller blade tip and the diffuser vanes;
- compressibility and shock wave-boundary layer interaction.

An experimental study of this flow on a compressor diffuser combination can account for all these effects, but it is more difficult to study separately the influence of blade geometry, inlet conditions or unsteadiness.

The research program, described here, intends to do a systematic study of the effect of blade shape on performances and range. One assumes here that the inlet flow is steady and uniform over the passage width. The boundary layer blockage on the lateral walls is accounted for by introducing a blockage factor.

The starting point has been the analysis of an existing compressor. The impeller vanes have 32° back-sweep at the exit. The diffuser vanes have a curved meanline and a constant normal thickness of 1.5 mm. They are tapered at the leading edge to a leading edge thickness of 0.5 mm. Although they were originally

designed to operate with a leading edge Mach number of 0.95, they are used in the actual configuration with leading edge Mach number above 1.05.

A theoretical analysis of the 2D inviscid flow field has been performed for this diffuser geometry (geom. 0). This initial step has been very useful to verify the application of the Euler solver on this type of cascade and, at the same time, to define the fluid dynamic behaviour of the flow in the existing geometry.

In order to evaluate possible improvements of the velocity distribution in the semi-vaneless space, a new diffuser has been designed, based on the method of Herbert and Came (geom. A).

Detailed flow studies suggested that this diffuser could be further improved using a modified design procedure (geom. B and C). Geometry C has been built and experimental results have been compared with the theoretical predictions.

THEORETICAL CALCULATION METHOD

The quasi three-dimensional time marching method, developed at the von Karman Institute, has been used to calculate the inviscid transonic flow in the semi-vaneless space.

The equations to be solved are the time dependent Euler equations expressing the mass-momentum- (in meridional and tangential direction) and energy-conservation laws. Written in a time dependent differential form using non-dimensional variables, these equations are :

$$W_t = F_x + G_y$$

$$W = \begin{pmatrix} \rho \\ u \\ v \\ e \end{pmatrix} \quad F = \begin{pmatrix} u \\ p+u^2/\rho \\ u v/\rho \\ (e+p) u/\rho \end{pmatrix} \quad G = \begin{pmatrix} v \\ u v/\rho \\ p+v^2/\rho \\ (e+p) v/\rho \end{pmatrix}$$

$$\text{where } u = \rho w_x \quad v = \rho w_y$$

The domain of calculation is defined by one of the blade passages and is extended upstream and downstream of the cascade by two pseudo-streamlines defined by $r.w. = \text{const.}$ The numerical domain (figure 1) is made up of several pseudo-streamlines and lines of constant radius. The pseudo-streamlines are uniformly spaced in the tangential direction. The spacing between the constant radius lines can change in a regular way between inlet and outlet. The intersection points of the pseudo-streamlines and constant radius lines define the corner points of the hexagonal control area. Applying Gauss' theorem on the space derivatives, one can evaluate the variation of the unknowns in the control volumes as a function of the corresponding convective fluxes through the surfaces :

$$S h W_t = - \int_{\partial S} (F h n_x + G h n_y) d\Omega$$

One assumes here that the variables remain constant over the selected control volumes. The third dimension, h , is the diffuser width, corrected for boundary layer blockage and varies only in the radial direction. The flow variables are defined at each node point. A linear variation of the flux along each line segment is assumed in order to evaluate the transport terms on the finite volumes. As the transport terms across the sides of the elements are applied to two adjacent volumes, the overall conservation is automatically satisfied during the calculation.

The time derivative is discretised by means of the corrected viscosity scheme. It has been shown that this scheme possesses very good qualities of convergence and stability [2,3].

As boundary conditions, one imposes a constant total pressure and uniform velocity (with given Mach number) at the diffuser inlet radius. For supersonic inlet Mach numbers, in which one is interested here, the inlet flow angle is defined by the unique incidence and is obtained by applying the periodicity condition upstream of the blades. At the outlet a static pressure is imposed corresponding to the different operating regimes of the diffuser. This pressure is different from the experimental value because one is only interested in the semi vaneless space and no correction of the blockage in the divergent channel is introduced.

ANALYSIS OF AN EXISTING DIFFUSER

The time dependent calculation program has first been applied to an existing diffuser of 25 blades with a leading edge to impeller exit radius ratio of 1.114 (geom. 0). The vane geometry and grid system are shown in figure 1. The calculations have been made for the four performance points (A,B,C,E) shown in figure 2. The corresponding diffuser inlet flow conditions are deduced from measurements by means of an analysis program. They are listed in table 1. The blockage, due to the boundary layers on the lateral walls, is deduced from the measurements at diffuser inlet and at throat section. A linear variation of the channel height is used in between.

Calculated iso-Mach lines corresponding to the four operation points are shown in figure 3. The diffuser absolute inlet Mach number changes only slightly with mass flow but the radial velocity component, and therefore also the flow angle, changes as a function of the operation point. This results in a change of the diffuser vane incidence and the corresponding change of the iso-Mach line pattern is shown

by test points A, B and C in figure 3. The throat Mach number increases from 0.8 to 1.0 when the mass flow changes from surge (point A) to choke (point C) resulting in a decrease of the semi-vaneless space static pressure rise coefficient. In test point E the calculations show the fully supersonic character of the flow and a bow shock at the blade leading edge. This type of bow shock, extending over the hole throat passage, is in agreement with experimental observations [4,5]. Previous analysis has shown the validity of this method since it correctly predicts the important features of the transonic flow at diffuser inlet.

It is the intention to use this compressor at higher rotational speeds so that the diffuser inlet Mach number will be higher and stronger bow shocks will occur upstream of the throat. The corresponding increase in boundary layer thickness will result in higher blockage and consequently will reduce the pressure recovery in the divergent channel. Alternative designs in which the vane suction side flow deceleration between leading edge and throat can be controlled are therefore studied.

NEW DIFFUSER DESIGNS

In order to evaluate possible improvements that can be obtained, a detailed investigation of the flow in alternative diffuser designs has been made. Special emphasis was put on the optimisation of the semi-vaneless space geometry. A prime requirement for the semi-vaneless space is to assure that the local Mach number on the vane suction side nowhere significantly increases above the leading edge value, either due to incidence or due to surface shape, in order to limit the strength of the bow shock upstream of the throat.

The design method for vaned diffusers, proposed by Herbert and Came [6], is summarized in figure 4. After definition of geometrical parameters such as:

- radius of leading edge and trailing edge location (r_{le} , r_{te})
- leading edge and trailing edge round-off radius
- number of vanes
- throat area and width
- incidence measured against the suction side
- leading edge wedge angle AL and channel divergence angle AK

curves are generated which fit in a smooth way polynomials through the points H, Z, D, P, Q, L, E.

The most important part in this study is the vane suction side shape and the location of the inflection point Z. According to Herbert and Came this point should be outside the suction side to avoid reacceleration of the flow upstream of the throat. However, once the vane leading edge angle and throat dimensions are fixed, there is not much freedom to choose the location of the inflection point.

The new designs have a reduced diffuser leading edge to impeller outlet radius ratio of 1.07 resulting in a higher leading edge Mach number. A smaller value may be dangerous for the integrity of the impeller blades because the interaction with the diffuser vanes becomes too strong. A larger value increases the vaneless space and can be at the origin of vaneless diffuser stall [7]. The throat area is the same as in the previous configuration.

In a first design (geom. A), the vane leading edge is connected to the throat by a fourth order polynomial. The tangent to the vane suction side at the leading edge is at 76° measured from the radial direction and the diffuser has 29 vanes.

The diffuser geometry and the flow field calculated for the operational point E, is shown in figure 5. The flow reaccelerates after the leading edge to a Mach number of 1.25 and the strong deceleration in front of the throat is an indication for a bow shock. This cannot be considered as a good design. The Mach number and angle distribution shown in figure 6 (geom. A) explains how the rapid variation of the suction side angle near the leading edge is responsible for the increase of suction side Mach number. The deceleration of the fluid takes place in the region of constant vane angle. Alternative vane shapes and blade setting angles will therefore be examined in the future designs.

In a second design (geom. B), a logarithmic spiral is fitted over the first 60% of the vane suction side, in order to obtain a vane shape which is close to the unperturbed free vortex flow (point H to Z on figure 4). A fourth order polynomial makes then a smooth connection to the downstream divergent channel (point Z to D). The number of vanes has been reduced to 25 to reduce the pressure gradient by increasing the flow path length between leading edge and throat. Another design choice is a meridional contraction between impeller exit and diffuser leading edge. This modification suggested by [8] may help to uniformise the axial velocity distribution at the diffuser leading edge. The diffuser width is 8 mm at the leading edge compared to 10.7 mm at the impeller exit.

The flow field relative to the operational point E is shown in figure 7. One observes a smaller reacceleration of the fluid downstream of the leading edge and the deceleration in front of the throat is again important, indicating an entry bow-shock. The Mach number distribution along the suction side (fig. 6 geom. B) shows a reacceleration of the fluid downstream of the inflection point Z due to change of flow angle to a more radial direction as shown by the suction side angle variation.

In order to minimize the suction side reacceleration a third design has been made (geom. C). The blade height was increased to 8.2 mm which allowed to decrease the throat width and to minimize the convex curvature of the blade shape downstream of the inflection point Z. The Mach number distribution calculated for the operation point E is shown in figure 8. Except for some local perturbations, no reacceleration around the vane leading edge is observed. The suction side Mach number decreases gradually towards the throat without bow shock. This gradual deceleration is clearly shown in figure 6 (geom. C), where one also observes a smoother variation of the vane angle.

The Mach number distribution has also been calculated for the same geometry at the operation points A and C. The comparison of the suction side Mach number distributions (figure 9) shows that a smooth variation remains for all operation points between surge and choke. At the surge point (A), the positive incidence results in a reacceleration of the flow downstream of the leading edge, followed by a smooth deceleration towards the throat Mach number. At the choking point (C), the incidence is smaller or negative and

the maximum Mach number is lower. The Mach number in the throat is higher, because of the larger mass flow, resulting in a lower suction side deceleration at choking mass flow.

COMPARISON WITH EXPERIMENTAL DATA

The diffuser design C has been built and instrumented with a series of static pressure tappings on the shroud side-wall as shown in figure 10. It has been observed in the past that such measurements seldom show steep pressure gradients corresponding to shocks. This can be explained either by the interaction of the shocks with the thick boundary layers on the lateral walls or by the unsteadiness of the flow upstream of the throat. Nine additional static pressure tappings, having 0.3 mm hole diameter, have been installed on the blade suction side at midheight. It is expected that local accelerations or decelerations and eventual shocks will be more easily detected here, because of the smaller boundary layer thickness.

The new performance curve is shown by the dashed line in figure 2. The choking limit is now at a 2% lower mass flow. It is not clear if this variation must be attributed to a difference in throat area, because of different blockage or manufacturing errors, or if it must be attributed to the fact that both measurements have been obtained on different facilities using different devices to measure the mass flow.

The new operating range between surge and choking is more than twice the original one. This improvement must be attributed to the more favorable velocity distribution on the suction side of the new diffuser blades.

Isopressure lines measured in three operation points on the 105% speed line are shown in figure 11. Near choke the static pressure on the suction side is everywhere higher than the impeller exit pressure and a smooth pressure rise between leading edge and throat is observed. At medium mass flow, the local pressure downstream of the leading edge first decreases to a level below the inlet pressure and increases towards the throat section.

There is no operating point for which the measured distribution agrees with the one predicted for the operating point E and shown in figure 12. The discrepancies can be explained by an overestimation of the boundary layer blockage at the diffuser inlet, resulting in an underestimation of the incidence during the calculations. In the experiments, the lowest incidence occurs at choking mass flow and the pressure distribution near the leading edge is very similar to the predicted one. Further downstream there is a discrepancy because the calculations are made for low back-pressure corresponding to unchoked conditions. At medium and surge mass flow the incidence is higher (less negative). The resulting reacceleration downstream of the leading edge is similar to the predicted incidence effect shown in figure 9. Closer to the throat, the pressure distribution is very similar to the predicted one. The pressure field is very sensitive to the incidence angle and better agreement is only possible with a more accurate prediction of the boundary layer blockage on the lateral walls.

The static pressure distribution along the vane suction side, predicted for the operating point E, is compared with the one measured at choking and at medium mass flow on figure 13. It shows that the predicted values are somewhere between the experimental curves for choking and medium mass flow. The data shown here are measured on the vane suction side and the amplitude of the variations is smaller than the one measured on the side wall. The variation however is not as smooth as the predicted one. It indicated a small discontinuity between the leading edge and the throat.

CONCLUSIONS

Previous calculations have shown that it is possible to design diffuser vanes with a smooth deceleration of the flow along the suction side. The main point is the control of the convex curvature between the inflection point Z and the throat.

Outside the design point this optimum velocity distribution can be perturbed because of an acceleration of the fluid, immediately downstream of the leading edge. This acceleration is strongly dependent on the incidence.

The flow is very sensitive to the boundary layer blockage on the side walls. An iterative procedure in which the boundary layer thickness is recalculated as a function of the predicted velocity distribution could result in a more precise prediction than with the linear variation used in the present calculation. However, the results will strongly depend on the diffuser inlet conditions, which are not well known at the moment.

ACKNOWLEDGEMENTS

The research described in this study paper is part of a five year research program at Alfa Romeo Avio on "Theoretical and experimental study on diffusers for high pressure ratio single-stage centrifugal compressors" and is sponsored by C.N.R. (Consiglio Nazionale delle Ricerche) under contract Nr : 83,00041,59.

The authors wish to acknowledge the efforts of the Alfa Romeo Avio R&D personnel who were involved in the design, instrumentation, testing and data reduction of the diffuser investigated. Particular thanks to Ing. Antonio Colella for his contribution in the calculations and to Mr. Salvatore Lamberti for instrumenting the diffuser.

REFERENCES

1. RUNDSTADLER, P. : Pressure recovery performances of straight channel, single plane divergence diffusers at high Mach numbers. Creare TN 88, 1969.
2. COUSTON, N.; McDONALD, P.; SMOLDEREN, J. : The damping surface technique for time-dependent solutions to fluid dynamic problems. VKI TN 109, 1975.

3. VAN HOVE, W. & ARTS, A. : Comparison of several finite difference schemes for time marching methods as applied to one dimensional nozzle flows.
VKI TN 132, 1979.
4. DEAN, R. : The fluid dynamic design of advanced centrifugal compressors.
VKI LS 66 : Advanced Radial Compressors, 1974
5. JAPIKSE, D. : The influence of the diffuser pressure fields on the range and durability of centrifugal compressor stages.
AGARD CP 282 : Centrifugal Compressors, Flow Phenomena and Performance, Paper 13, 1980.
6. CAME, P. & HERBERT, M. : Design and experimental performance of some high pressure ratio centrifugal compressors.
AGARD CP 282 : Centrifugal Compressors, Flow Phenomena and Performance, Paper 15, 1980.
7. FRIGNE, P. & VAN DEN BRAEMBUSSCHE, R. : Comparative study of subsynchronous rotating flow patterns in centrifugal compressors with vaneless diffusers.
NASA CP 2250 : Rotor Dynamic Instability Problems in High Performance Turbomachinery, 1982.
8. BEARD, M.; PRATT, C.; TIMMIS, P. : Recent experience on centrifugal compressors for small gas turbines.
ASME PAPER 78 GT 193, 1978.

TEST POINT	M_2	B_2	B_2	B_{th}
A	1.21	78.7	0.10	0.12
B	1.21	77.9	0.10	0.075
C	1.20	76.5	0.10	0.045
E	1.24	78.7	0.10	0.120

TABLE 1

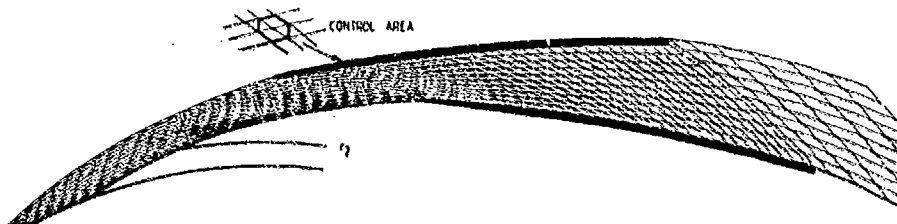


FIG. 1 - CONTROL AREA AND MESH DEFINITION

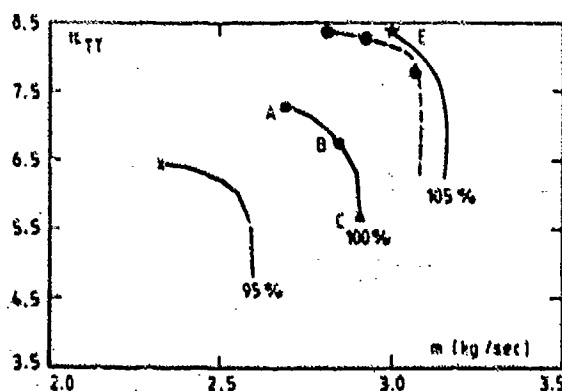


FIG. 2 - OVERALL COMPRESSOR PERFORMANCES

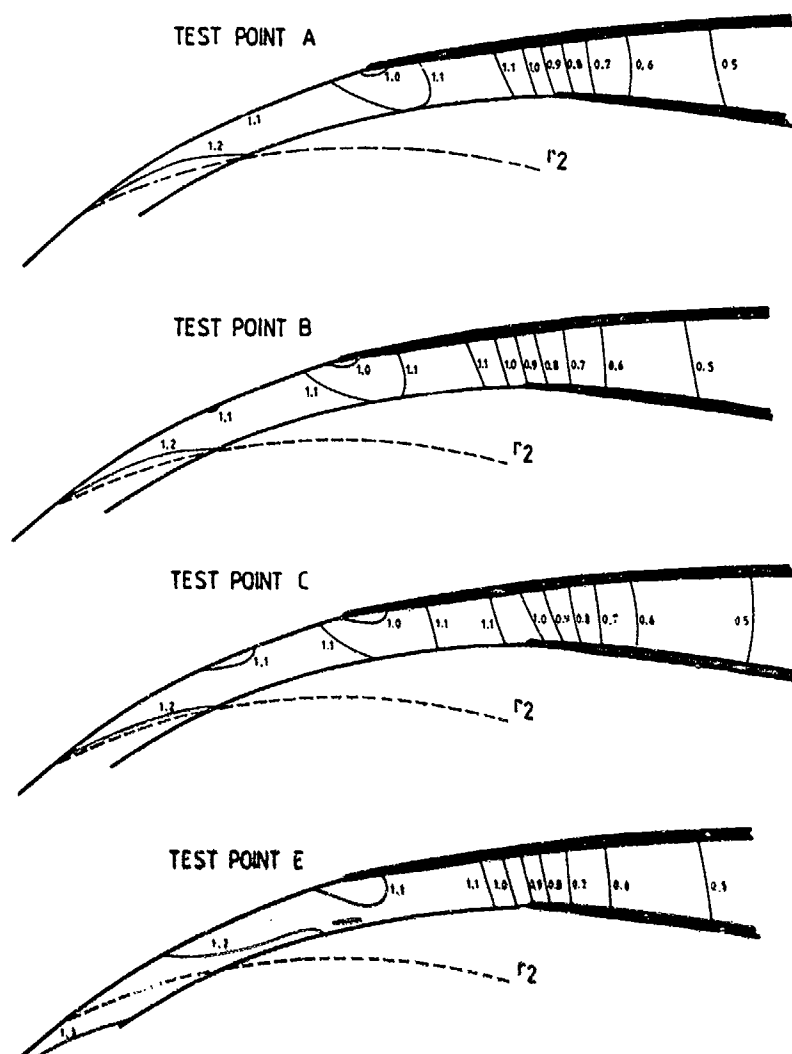


FIG. 3 - ISOMACH LINES

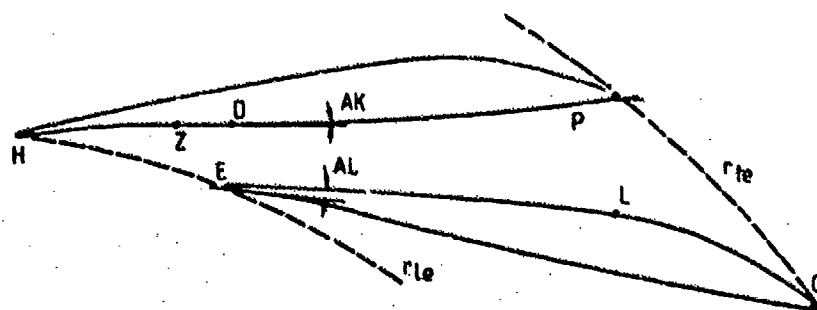


FIG. 4 - DEFINITION OF DIFFUSER VANES

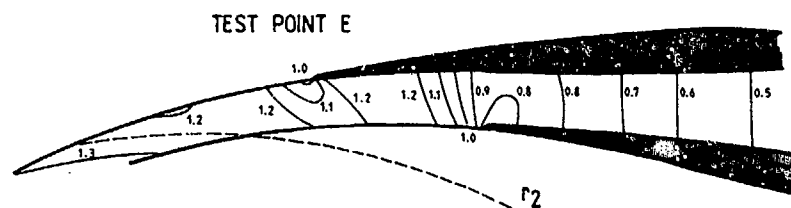


FIG. 5 - ISOMACH LINES FOR GEOM. A

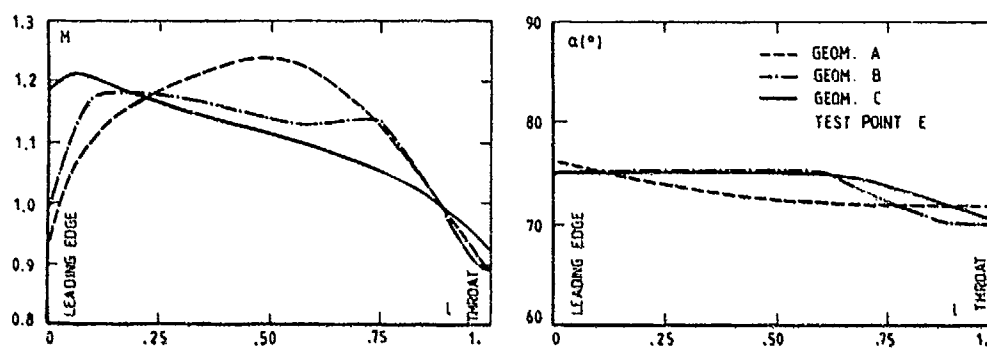


FIG. 6 - MACHNUMBER AND ANGLE DISTRIBUTION ALONG VANE SUCTION SIDE

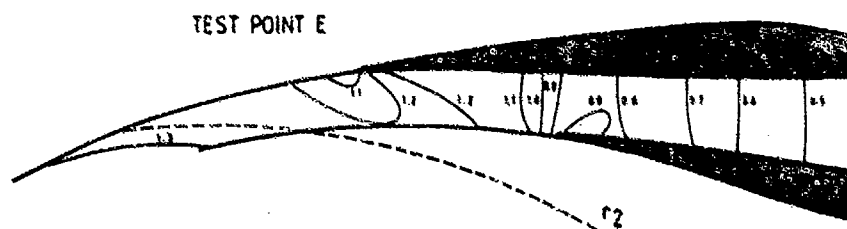


FIG. 7 - CALCULATED ISOMACH LINES (GEOM. B)

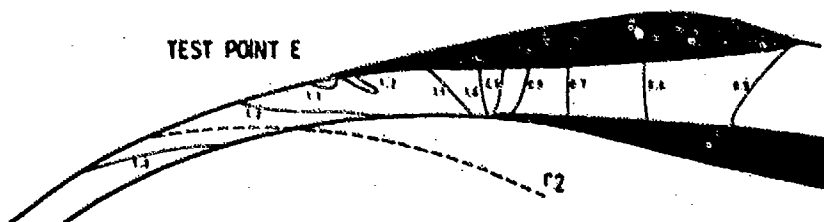


FIG. 8 - CALCULATED ISOMACH LINES (GEOM. C)

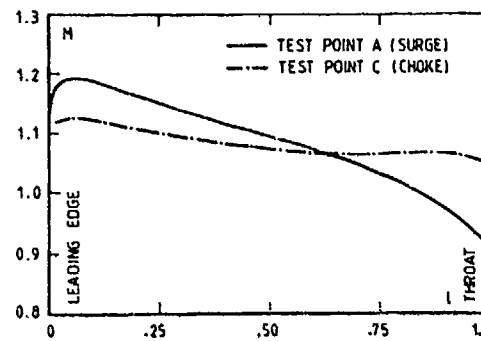


FIG. 9 - INFLUENCE OF INCIDENCE ON VANE SUCTION SIDE MACH NUMBER DISTRIBUTION

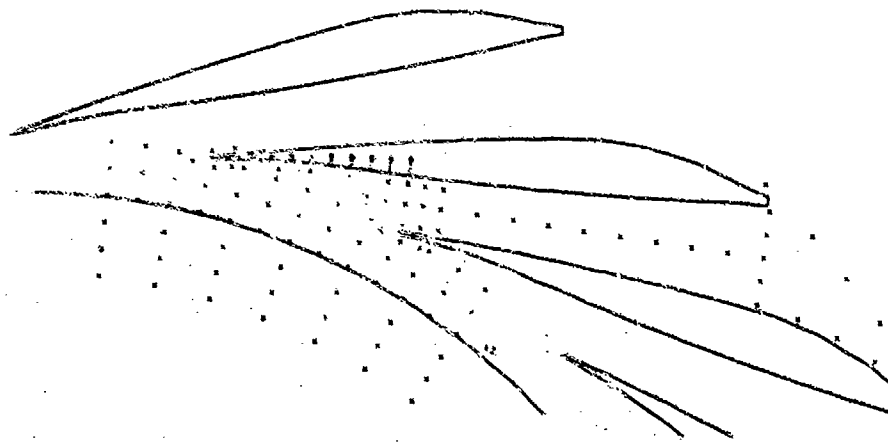


FIG. 10 - SHROUD AND VANE SUCTION SIDE STATIC PRESSURE TAPPINGS

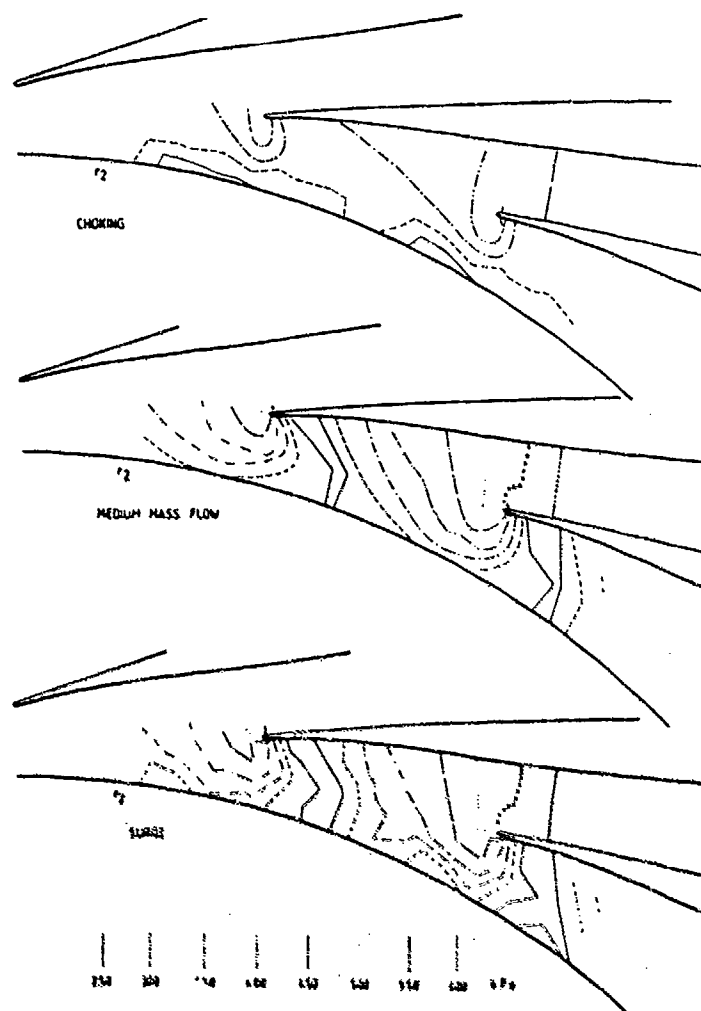


FIG. 11 - EXPERIMENTAL ISO PRESSURE LINES

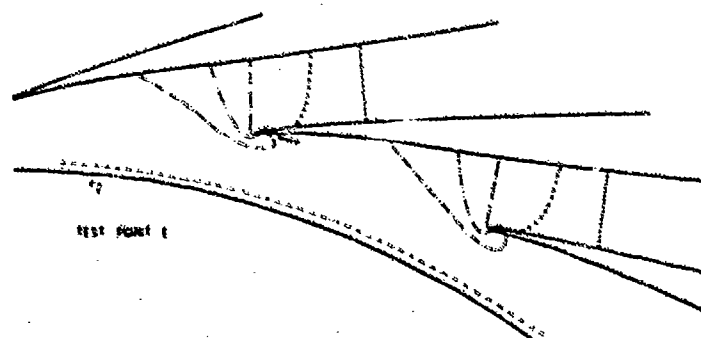


FIG. 12 - PREDICTED ISO PRESSURE LINES

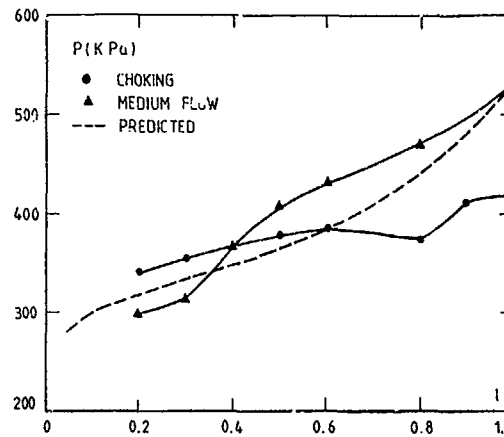


FIG. 13 - EXPERIMENTAL AND PREDICTED PRESSURE DISTRIBUTION ON THE DIFFUSER VANE SUCTION SIDE

DISCUSSION

A.S.Üçer, Tu

Could you give some information about the technique used for determining the fluid properties on blade boundary surfaces?

Author's Reply

A half control volume is placed on the blade boundaries, where zero flux is applied for mass and energy.

The pressure on the wall can then be calculated in the normal way, because the central point is on the wall. In this way, extrapolation of the pressure towards the wall can be avoided.



METHODE NUMERIQUE D'INTERACTION VISQUEUX-NON VISQUEUX POUR LES ECOULEMENTS INTERNES DECOLLES ET L'INTERACTION COUCHE LIMITE - ONDE DE CHOC (*)

J.C. LE BALLEUR et D. BLAISE

Office National d'Etudes et de Recherches Aérospatiales (ONERA)
BP 72, 92322 Châtillon Cedex, France.

Résumé

Une méthode de calcul des écoulements internes transsoniques décollés ainsi que l'interaction couche limite - onde de choc est présentée. Elle s'appuie sur le développement de résolutions numériques 'Indirectes' par interaction visqueux - non visqueux, bien conditionnées aux grands nombres de Reynolds.

Le fluide visqueux est calculé selon la théorie de 'Formulation Déficiente', ici simplifiée par des approximations de couches minces compatibles avec une résolution par méthode intégrale. Les méthodes numériques de couplage fort 'Directe' et 'Semi-Inverse', ainsi que les méthodes intégrales déficientes directe et inverse avec modèles de turbulence à 0-1- ou 2-équations de transport intégrales, qui avaient été proposées antérieurement pour le calcul des profils d'ailes, ont été généralisées aux écoulements internes où le fluide parfait nécessite un traitement des équations d'Euler.

Des résultats sont obtenus pour des écoulements turbulents dans des canaux transsoniques bloqués avec contre-pression comportant des interactions couche limite - onde de choc multiples, ainsi que des décollements naissants ou étendus. La méthode est également appliquée à l'interaction couche limite - onde de choc en supersonique, pour des rampes de compression ou des réflexions d'ondes de choc obliques. Les premiers résultats obtenus pour le calcul des écoulements visqueux de grille d'aubes sont présentés.

NUMERICAL VISCOUS-INVISCID INTERACTION METHOD FOR INTERNAL SEPARATED FLOWS AND SHOCK WAVE-BOUNDARY LAYER INTERACTION

Abstract

A calculation method for internal transonic separated flows, and for shock wave - boundary layer interactions, is presented. It is based on developments in 'Indirect' numerical solvers with viscous-inviscid splitting, well conditioned at high Reynolds numbers.

The viscous flows are calculated with the 'Defect Formulation' theory, here simplified with thin layer approximations compatible with an integral method. The 'Direct' and 'Semi-Inverse' strong coupling methods, and the direct and inverse defect integral methods with turbulence models involving 0-, 1-, or 2- integral transport equations, which have been previously suggested for airfoil flows, have been generalized to internal flows for which the inviscid field requires to use an Euler solver.

Results are obtained for turbulent flows in transonic choked channels with back-pressure, involving multiple shock wave - boundary layer interactions, and incipient or extensive separations. The method is also applied to supersonic shock wave - boundary layer interactions, for compression ramps or shock wave - reflexions. First results obtained for computing viscous flows in cascade are presented.

1 - Introduction

Les écoulements internes des turbomachines se caractérisent par des nombres de Reynolds élevés et par l'influence dominante de phénomènes de forte interaction visqueuse, décollements et interactions couche limite - onde de choc notamment. Le développement de méthodes numériques capables de déterminer complètement ces écoulements repose de ce fait, soit sur des méthodes de résolution "Directes" d'équations de type Navier-Stokes [1,2], soit sur des méthodes de résolution "Indirectes" par interaction visqueux-non visqueux plus spécifiquement conditionnées pour les grands nombres de Reynolds [1,3 à 10].

Les progrès des méthodes "Indirectes", voir par exemple Le Balleur [11,12], montrent que ces méthodes numériques ne sont pas limitées aux approximations de la couche limite, et que leur extension progressive devrait permettre d'obtenir à volonté, soit une résolution d'équations de couche limite généralisées avec couplage fort, soit une "résolution indirecte" d'équations de Navier-Stokes.

L'avantage intrinsèque des "méthodes indirectes" par interaction visqueux-non visqueux est celui d'un

conditionnement numérique d'autant plus efficace que le nombre de Reynolds est plus élevé, contrairement aux "méthodes Directes". Cet avantage est similaire à celui des techniques numériques de couche limite, les "méthodes Indirectes" visant précisément à généraliser les techniques numériques de couche limite pour résoudre les équations de Navier-Stokes.

Le second avantage des "méthodes Indirectes" est la possibilité, au moins dans une première étape de développement, d'introduire des équations et modélisations plus simplifiées que dans les "méthodes Directes", sans éliminer la capacité de traiter l'interaction choc - couche limite ou le décollement massif [12]. Un second objectif possible des "méthodes Indirectes" est de ce fait la recherche d'une réduction notable du coût de calcul à grand nombre de Reynolds.

En contre-partie de ces deux avantages, les "méthodes Indirectes" conduisent à une complexité numérique accrue par rapport aux "méthodes directes", notamment par la nécessité d'un opérateur numérique de "couplage fort" traitant l'interaction entre les opérateurs visqueux et non-visqueux.

La présente "méthode Indirecte", détaillée en [13,14] correspond à la théorie de "Formulation Déficitaire" proposée antérieurement [9,14]. Celle-ci est résolue avec approximations de couches minces et modélisation de méthode intégrale. La méthode "Semi-Inverse" de Le Balleur [15] est utilisée pour l'opérateur numérique de couplage fort.

Les résultats de cette première étape démontrent que le calcul des écoulements internes décollés par une "méthode Indirecte" est réalisable. Ils montrent en second lieu que la valeur prédictive de la présente méthode intégrale s'avère très encourageante. Elle devrait permettre à terme, moyennant un progrès sur les techniques numériques actuelles de type explicite utilisées pour les opérateurs "non-visqueux" et "couplage", de conduire à une méthode de calcul de coût minimal. Enfin la Méthode sous sa forme actuelle permet aussi d'envisager son extension à une résolution "Indirecte" d'équations de Navier-Stokes par "Formulation Déficitaire" et technique numérique de couplage.

2 - Formulation Déficitaire - Equations simplifiées résolues -

2.1 Formulation Déficitaire complète

Rappelons que la théorie de "Formulation Déficitaire", Le Balleur [9,14,17], dissocie le problème global en sous-problèmes numériques visqueux ("déficitaire") et non-visqueux ("pseudo-fluide parfait") dont les domaines de calcul se recouvrent et occupent tout l'espace. La dissociation n'étant pas unique, la "Formulation Déficitaire" est celle où le pseudo-fluide parfait satisfait les équations d'Euler, la viscosité ne contrôlant le pseudo-fluide parfait que par les conditions aux limites.

Désignant par \bar{F} , \bar{p} la pression et la densité, par \bar{U} , \bar{W} les composantes de la vitesse et par \bar{V} les termes de contraintes visqueuses en repère cartésien XOZ, par \bar{u} , \bar{w} et \bar{v} leurs homologues dans le repère curviligne orthogonal xOz tangent à la paroi ou à la ligne moyenne du sillage, les équations de Navier-Stokes :

$$\frac{\partial \bar{F}}{\partial X} + \frac{\partial \bar{G}}{\partial Z} = \bar{V} \quad , \quad \bar{F} = \begin{bmatrix} \bar{p} \bar{U} \\ \bar{p} \bar{U}^2 + \bar{p} \\ \bar{p} \bar{U} \bar{W} \end{bmatrix} , \quad \bar{G} = \begin{bmatrix} \bar{p} \bar{W} \\ \bar{p} \bar{U} \bar{W} \\ \bar{p} \bar{W}^2 + \bar{p} \end{bmatrix} \quad (1)$$

sont décomposées en un système équivalent de Formulation Déficitaire :

$$\frac{\partial \bar{F}}{\partial X} + \frac{\partial \bar{G}}{\partial Z} = 0 \quad (2)$$

$$\left\{ \begin{aligned} \frac{\partial}{\partial x} (\bar{F} - \bar{F}) + \frac{\partial}{\partial z} (\bar{G} - \bar{G}) + K (\bar{H} - \bar{H}) &= -\bar{V} \end{aligned} \right. \quad (3)$$

$$0 = \lim_{x \rightarrow \infty} (\bar{f} - \bar{f}) \quad , \quad \bar{f} = \{ \bar{u} , \bar{w} , \bar{p} , \bar{\rho} \} \quad (4)$$

$$\bar{F} = \begin{bmatrix} \bar{\rho} \bar{u} \\ \bar{\rho} \bar{u}^2 + \bar{p} \\ \bar{\rho} \bar{u} \bar{w} \end{bmatrix} , \quad \bar{G} = \begin{bmatrix} \bar{\rho} \bar{w} \\ \bar{\rho} \bar{u} \bar{w} \\ \bar{\rho} \bar{w}^2 + \bar{p} \end{bmatrix} , \quad \bar{H} = \begin{bmatrix} 0 \\ -\bar{p} \bar{u} \bar{w} \\ \bar{\rho} \bar{u}^2 + \bar{p} \end{bmatrix}$$

constitué d'un champ pseudo-fluide parfait $\bar{\rho}$, \bar{p} , \bar{U} , \bar{W} en coordonnées cartésiennes, vérifiant les équations d'Euler (2), et d'un système d'équations déficitaires (3) ainsi que d'équations de couplage fort (4), en coordonnées curvilignes, avec $h = 1 + Kx$, $K(x)$ étant la courbure de la paroi.

L'intégration exacte en x de l'équation de continuité déficitaire de (3), compte tenu du couplage fort (4),

fournit la condition "d'effet de déplacement" généralisée aux équations de Navier-Stokes :

$$\text{paroi : } \rho w_{(x,0)} = \frac{\partial}{\partial x} \int_0^{\infty} (\rho u - \bar{\rho} \bar{u}) dz \quad (5a)$$

$$\text{sillage : } \langle \rho w_{(x,0)} \rangle = \frac{\partial}{\partial x} \int_{-\infty}^{+\infty} (\rho u - \bar{\rho} \bar{u}) dz \quad (5b)$$

expression où $\langle f \rangle = f(x, 0^+) - f(x, 0^-)$. Cette condition aux limites exacte a permis d'éliminer l'écueil des couches limites "supercritiques" au sens de Crocco-Lees, voir Le Balleur [16]. Elle inclut la variation de ρu selon z , et suffit à déterminer le pseudo-fluide parfait dans l'approximation potentielle.

Lorsque les équations d'Euler complètes (2) sont résolues, la théorie des caractéristiques montre que la condition (5) n'est suffisante que dans les zones où le pseudo-fluide parfait présente une succion à la paroi ($w < 0$, normale Oz vers l'intérieur). Deux conditions doivent être ajoutées dans les zones où l'effet de déplacement impose une injection ($w > 0$) afin d'y fixer les niveaux d'entropie et d'enthalpie totale.

Comme il a déjà été indiqué, voir Le Balleur [10,11], un choix quelconque peut être effectué pour ces deux conditions supplémentaires dans le cas de la Formulation Déficitaire complète (2)(3)(4) mettant en jeu des équations de Navier-Stokes. En cas de modélisation simplifiée du système déficitaire (3) au contraire, ce choix est un degré de liberté supplémentaire pour minimiser les approximations de couche mince. Dans le cas présent, faute d'une étude plus précise, le choix empirique de dérivées normales nulles pour l'entropie et l'enthalpie totale du pseudo-fluide parfait (si $w > 0$) a été retenu.

2.2 - Equations simplifiées résolues

Admettant que l'approximation Navier-Stokes "Couche-Mince" est suffisante, les contraintes visqueuses sont réduites au terme de cisaillement τ . On réduit de plus les équations déficitaires par un développement asymptotique par rapport à l'épaisseur δ des couches visqueuses. Les équations déficitaires simplifiées au premier ordre sont alors :

$$\begin{cases} \frac{\partial}{\partial x} (\rho u - \bar{\rho} \bar{u}) + \frac{\partial}{\partial z} (\rho w - \bar{\rho} \bar{w}) = 0 \\ \frac{\partial}{\partial x} (\rho u^2 - \bar{\rho} \bar{u}^2) + \frac{\partial}{\partial z} (\rho u w - \bar{\rho} \bar{u} \bar{w}) = -\frac{\partial}{\partial x} (p - \bar{p}) - \frac{\partial \tau}{\partial z} \\ \frac{\partial}{\partial z} (p - \bar{p}) = 0 \end{cases} \quad (6)$$

Les équations intégrales déficitaires correspondantes obtenues par intégration selon z , complétées de l'équation déficitaire locale de quantité de mouvement en $z = \delta(x)$ (équation d'entraînement) sont alors :

$$\left\{ \frac{\partial}{\partial x} [\rho q \delta_1] - \rho w + \bar{\rho} \bar{w} \right\}_{(x,0)} = 0 \quad (7)$$

$$\left\{ \frac{\partial}{\partial x} [\rho q^2 (\delta_1 + \theta_{11})] - \rho u w + \bar{\rho} \bar{u} \bar{w} \right\}_{(x,0)} = \rho q^2 \frac{C_f}{2} \quad (8)$$

$$\left\{ \frac{d\delta}{dx} - \frac{w}{q} \right\}_{(x,0)} = \lambda E_{\eta} \quad (9)$$

$$\bar{p}(x, z) = p(x, z) \quad (10)$$

$$\text{avec : } \begin{cases} \delta_1 \rho q_{(x,0)} = \int_0^{\infty} |\rho u(x, z) - \bar{\rho} \bar{u}(x, z)| dz \\ (\delta_1 + \theta_{11}) \rho q^2_{(x,0)} = \int_0^{\infty} |\rho u^2(x, z) - \bar{\rho} \bar{u}^2(x, z)| dz \\ q^2 = u^2 + w^2, \quad \lambda E_{\eta} = \left[\frac{1}{\rho q} \frac{\partial \tau}{\partial z} \right]_{(x,0)} \end{cases} \quad (11)$$

Rappelons que, compte tenu du caractère "Déficientaire" des définitions (11) des épaisseurs intégrales, l'équation de continuité (7) est exacte, que les équations de quantité de mouvement (8)(10) ou d'entraînement (9) sont approchées à l'ordre δ près, et que l'approximation de premier ordre sur le gradient de pression normal (10) est déjà moins restrictive que les équations de Prandtl. Une correction de second ordre (12) peut en outre affiner à posteriori l'approximation du champ de pression à partir de la "courbure induite" $K''(x)$ de la surface de déplacement [18,9] :

$$\bar{p}(x,0) = p(x,0) - K''(x) (\delta_1 + \theta_{11}) \rho q_{(x,0)}^2 \quad (12)$$

Cette correction conduit, le long des sillages, à introduire dans le pseudo-fluide parfait une condition aux limites "d'effet de courbure" généralisée $\langle p(x,0) \rangle$, déduite de (12) par la continuité du champ de pression réel $\langle \bar{p}(x,0) \rangle = 0$. Il est à noter que les "courbures induites" au dessus du sillage $K''(x,0^+)$, et au dessous $K''(x,0^-)$, sont différentes, surtout dans le proche sillage [14].

2.3 - Fermeture turbulente

Les équations déficientes simplifiées (6), résolues sous la forme intégrale (7)(8)(9)(10), sont fermées par modélisation pour les couches turbulentes avec décollements étendus ($1 < H, < \infty$) proposée par Le Balleur en bidimensionnel [14,12], puis en tridimensionnel [17,10] et en instationnaire [18]. On admet que cette modélisation de type couche limite, qui détermine $\delta, C_f, \lambda E_v$ en fonction de δ_1, θ_{11} , reste applicable aux grandeurs "déficientes" de (11).

Les profils de vitesse turbulents moyens sont représentés par la description analytique à deux paramètres (δ, δ_{11}) suivante, où $x = \delta \eta$ et où δ_{11} est l'épaisseur de déplacement "incompressible" :

$$\bar{v} = q \cdot \left[1 - C_2 F \left(\frac{\eta - \eta^*}{1 - \eta^*} \right) + C_1 \text{Log} \eta \right] \quad (13)$$

$$\begin{cases} 1 - C_2 = C_1 \left[\text{Log} (R_1 \sqrt{|C_f|/2}) + 5.25 \times 0.41 \right], & C_1 = \frac{1}{0.41} \frac{C_f}{\sqrt{2|C_f|}} \\ F(X) = (1 - X^{4/3})^2, & F = 1 \text{ si } X < 0 \\ \eta^* = 0, & 0 < \delta_{11} < 0.44 \delta \\ \delta \eta^* = 4.598 (\delta_{11} - 0.44 \delta)^2, & 0.44 \delta < \delta_{11} < 0.69 \delta \\ \delta \eta^* = 2.299 (\delta_{11} - 0.505 \delta), & 0.69 \delta < \delta_{11} < \delta \end{cases} \quad (14)$$

Les profils (13)(14) généralisent les profils de Coles des écoulements attachés par la loi $\eta^*(\delta_{11}, \delta)$ qui modifie la fonction de sillage. La loi η^* élimine les vitesses de retour physiquement irréalistes qui apparaissent avec $\eta^* = 0$ pour les couches limites infiniment décollées et permet de calculer le cas extrême d'une couche de mélange isobare ($H, \rightarrow \infty$), voir [12]. Les profils de densité sont déduits des profils de vitesse dans l'hypothèse isoénergétique.

Dans le cas d'une turbulence d'équilibre, c'est à dire avec $\lambda(x) = 1$ dans l'équation d'entraînement (9), l'entraînement E_v est déduit de la modélisation des profils de vitesse par une fermeture algébrique du type longueur de mélange, de même que la dissipation intégrale d'énergie Φ_v , les expressions étant précisées références [14,12].

Dans le cas d'une turbulence hors-équilibre, si $\bar{k}(x), \bar{\epsilon}(x), \bar{\nu}(x)$ sont respectivement les valeurs moyennes entre $x=0$ et $x=\delta$ de l'énergie cinétique de turbulence $\bar{k}(x,z)$, de la dissipation locale d'énergie $\bar{\epsilon}(x,z)$ et de la contrainte de cisaillement de Reynolds $\bar{\nu}(x,z)$, l'écart à l'équilibre $\lambda(x)$ est fourni par la résolution d'une ou deux équations intégrales de transport simplifiées proposées précédemment [14] pour l'énergie \bar{k} et la contrainte de Reynolds $\bar{\nu}$

$$\begin{cases} \frac{D\bar{k}}{Dt} = 0.5 \frac{\bar{\nu}}{\bar{\nu}_m} \Phi_v \bar{\nu}^2 - \bar{\epsilon} \delta \\ \frac{D\bar{\epsilon}}{Dt} = 1.5 \frac{\bar{\epsilon} \delta}{\bar{k}} \left[\left(\frac{\bar{k}}{\bar{k}_m} \right)^2 \frac{\bar{\nu}_m}{\bar{\epsilon}} - \bar{\nu} \right] \\ \frac{\bar{\epsilon}}{\bar{\nu}_m} = \left(\frac{\bar{k}}{\bar{k}_m} \right)^{3/2}, \quad \lambda(x) = \frac{\bar{\nu}}{\bar{\nu}_m}, \quad \delta = (1 - \eta^*) \delta \end{cases} \quad (15)$$

les niveaux d'équilibre \bar{k}_{ii} , $\bar{\epsilon}_{ii}$, $\bar{\tau}_{ii}$ étant précisés dans la référence [14,12].

3 - Méthodes de résolutions numériques -

3.1 - Equations intégrales déficitaires

Supposant que l'enthalpie totale est constante, les équations de l'écoulement moyen (7)(8)(9) sont écrites en fonction de deux paramètres propres à la couche visqueuse $\delta(x)$ et $a(x) = \delta_{11}/\delta$, ainsi que de trois paramètres communs aux problèmes visqueux et non-visqueux, le nombre de Mach réduit $m = 0.5(\gamma-1)M^2$, la pression totale p_i , le rapport w/q . Pour ces trois paramètres, on note $(\bar{m}, \bar{p}_i, \bar{w}/q)_{(x,0)}$ les valeurs prises par les paramètres dans la résolution découplée du problème visqueux, par $(m, p_i, w/q)_{(x,0)}$ les valeurs prises par les paramètres dans le pseudo-fluide parfait, ces valeurs ne coïncidant qu'après convergence du couplage fort. Les équations de transport turbulent (15), semi-découplées, sont résolues séparément pour calculer l'écart à l'équilibre de la turbulence $\lambda(x)$. Le système des équations moyennes de rang 3 s'écrit alors :

$$\begin{cases} A_i'(\epsilon, m, \delta) \frac{\partial f'}{\partial x} = b' \\ f' = \left\{ \delta, \epsilon, m, \bar{p}_i \right\}, \quad b' = \left\{ \frac{\bar{w}}{q}, \frac{C_f}{2}, \lambda E \right\} \end{cases} \quad (16)$$

Le nombre d'inconnues étant de cinq $\{\delta, \epsilon, m, \bar{p}_i, \bar{w}\}$, la résolution de (16) peut être effectuée en couplant directement deux des paramètres communs aux problèmes visqueux et non-visqueux, la compatibilité du troisième paramètre commun devant cependant être rejetée sur la convergence ultérieure de l'algorithme de couplage fort :

$$\bar{p}_i = p_i, \quad \epsilon \frac{\bar{w}}{q} + (1-\epsilon) \frac{d\bar{m}}{dx} = \epsilon \frac{w}{q} + (1-\epsilon) \frac{dm}{dx} \quad (17)$$

Dans les zones éloignées du décollement (paramètres de forme $H_i < 1.8$), la résolution est effectuée en problème "Direct" ($\epsilon=0$), avec $\bar{m} = m$, $\bar{p}_i = p_i$, et découplage de la vitesse normale $\bar{w} \neq w$. Dans ce mode, où les inconnues \bar{m} et \bar{p}_i sont éliminées du système (16), on a pu montrer que le déterminant du sous-système final s'annule au décollement ($H_i = 2.7$) et que la singularité, liée à celle de Goldstein, ne peut être levée qu'à convergence du couplage, voir Le Balleur [16].

Dans les zones décollées ou proches du décollement (paramètres de forme $H_i > 1.8$), cette difficulté est évitée en adoptant une résolution en problème "Inverse" ($\epsilon=1$), le mode inverse choisi étant $\bar{w}/q = w/q$, $\bar{p}_i = p_i$, avec découplage de la vitesse et du Mach $\bar{q} \neq q$, $\bar{m} \neq m$. Il a pu être montré que ce mode n'est jamais singulier, même en supersonique, compte tenu de l'élimination des interactions "supercritiques" au sens de Crocco-Lees grâce à l'équation de couplage "défictaire" (7), voir Le Balleur [16].

Dans le mode Direct comme dans le mode Inverse, la résolution numérique est toujours effectuée en marchant d'amont en aval. Le détail des schémas numériques implicites, non-linéaires, mis au point pour intégrer le système (16), précis au premier ou au second ordre selon la taille des mailles, est précisé dans la référence [14].

3.2 - Equations intégrales de sillage

La modélisation par moitiés supérieures ($x > 0$) et inférieures ($x < 0$) des profils de vitesse moyenne de part et d'autre du minimum de vitesse se ramène à annuler C_f dans la représentation (13)(14). Ceci conduit à remplacer (16) par un système de rang double, voir [14].

$$\begin{cases} [A_i']_{(x^+, x^-)}^* \left[\frac{\partial f'}{\partial x} \right]^* = [b']^* \\ [b']^* = \left\{ \frac{w}{q} - \frac{\bar{p}\bar{w}}{\rho q}, \frac{\bar{p}\bar{w}}{\rho q} \left(1 - \frac{\bar{w}}{q} \right), \lambda E_w + \frac{\bar{p}\bar{w}}{\rho q} \right\}_{(x^+, x^-)} \\ \bar{w}_{(x^+, 0^+)} + w_{(x^-, 0^-)} = 0, \quad \bar{w}_{(x^+, 0^+)} - w_{(x^-, 0^-)} = 0 \end{cases} \quad (18)$$

Bien que la résolution exacte de (18) soit réalisable, voir [14], le fait que l'effet de courbure soit négligeable au premier ordre en vertu de (10), ce qui implique $\langle p(x, 0) \rangle = p(x, 0^+) - p(x, 0^-) = 0$, conduit

en écoulement isentropique à un calcul notablement simplifié où $q(x, 0^+) = q(x, 0^-)$, $m(x, 0^+) = m(x, 0^-)$, $a^+ = a^-$, $[A_j]^+ = [A_j]^-$. Par extension, si la discontinuité d'entropie du pseudo-fluide parfait sur la coupure du sillage reste modérée, une décomposition des équations (18) en parties symétrique et antisymétrique reste possible moyennant une certaine approximation, voir [14, 18] :

$$f^{\pm} = f + \frac{1}{2}(f^+ - f^-) \quad , \quad f = \frac{1}{2}(f^+ + f^-) \quad , \quad A^+ \simeq A^- \simeq A(f) \quad (19)$$

$$\begin{cases} A_{j(x,a)} \cdot \frac{\partial f^j}{\partial x} \simeq \delta^j \\ \delta^j = \left\{ \frac{1}{2} \left\langle \frac{w}{q} \right\rangle , 0 , \lambda E_{ij} \right\} \end{cases} \quad (20)$$

la partie symétrique (20) étant suffisante à elle seule pour déterminer l'effet de déplacement de première approximation. Le système (20) peut alors être traité de façon strictement analogue au système de couche limite (16).

3.3 - Fonction d'influence visqueuse

L'élimination des inconnues propres au problème visqueux $\delta(x)$ et $a(x)$ dans les systèmes (16) et (20) fournit une relation différentielle entre la vitesse normale $\psi(x, 0)$, la vitesse $\hat{q}(x, 0)$ et la pression totale $\hat{p}(x, 0)$:

$$\left\{ \frac{\psi}{q} = B^* \frac{1}{q} \frac{d\hat{q}}{dx} + C^* \frac{1}{p_i} \frac{d\hat{p}_i}{dx} + D^* \right\}_{(x,0)} \quad (21)$$

la vitesse normale ψ/q devant être remplacée par la discontinuité de vitesse normale $\langle \psi/q \rangle$ sur la coupure dans le cas d'un sillage. Cette relation, qui représente la condition aux limites appliquée à l'opérateur "pseudo-fluide parfait", caractérise l'opérateur "visqueux" dans le traitement numérique du couplage visqueux - non visqueux, voir Le Balleur [9, 12, 16, 18].

La relation montre que les rôles des variables ψ et \hat{q} ne sont pas asymétriques. Elle est fortement non-linéaire par le terme B^* qui est négatif dans les zones attachées, positif dans les zones décollées, et qui tend vers l'infini aux stations de décollement ou de recolllement. Le calcul de B^* est nécessaire pour contrôler la stabilité des algorithmes de couplage.

3.4 - Algorithmes numériques de couplage

Le couplage visqueux - non visqueux est obtenu selon les zones, soit par la méthode "Directe", soit par la méthode "Semi-Inverse" de Le Balleur [15]. Ces méthodes de relaxation pour le couplage, de nature explicite, avaient été originellement définies pour donner accès au calcul des écoulements décollés en régimes sub- ou super-soniques, ainsi que pour fournir automatiquement le contrôle de stabilité linéaire nécessaire par leur caractère explicite.

Toutefois, l'analyse de stabilité du fluide parfait vis à vis de conditions aux limites perturbées qui avaient été proposées [15] pour définir ces méthodes supposant la résolution d'équations stationnaires, un minimum de convergence de l'opérateur fluide parfait doit être assuré entre deux itérations de couplage. Ce minimum de convergence s'avère en pratique plus contraignant dans le cas du solveur Euler de type explicite actuellement utilisé (50 à 100 pas de temps), que dans le cas d'un solveur potentiel utilisant une technique de relaxation (5 à 10 itérations).

Dans les zones de couches visqueuses attachées où le problème visqueux est résolu en mode direct ($M_\infty < 1.8$), le couplage est traité par l'algorithme "Direct". Désignant par $w_{i,1}^n$, $q_{i,1}^n$, $\psi_{i,1}^n$ les valeurs discrétisées de $w(x, 0)$, $q(x, 0)$, $\psi(x, 0)$ à l'itération de couplage n et aux abscisses x_i , il s'écrit [15] :

$$\begin{cases} w_{i,1}^{n+1} - w_{i,1}^n = \omega \cdot \omega^D (\psi_{i,1}^n - \psi_{i,1}^n) \\ \omega_i^D = \omega_{\text{ext}} [\mu(x_i, \alpha_{\text{max}})] \\ 0 < \omega < 2 \end{cases} \quad (22)$$

$$\text{avec : } \begin{cases} \mu_{(x,0)} = \frac{\alpha B^*}{\beta} = R + jI, \quad \beta = \sqrt{1-M^2} \\ \omega_{\mu}(\mu) = \frac{1-R}{(1-R)^2 + I^2}, \quad \alpha_{\max} = \frac{\pi}{\Delta x_i} \end{cases} \quad (23)$$

Dans ces expressions $\omega_{i,1}$ représente l'estimation issue du système visqueux, donc de (21) avec $\hat{q} = q^*(x,0)$, $\hat{p}_i = p_i^*(x,0)$ et μ représente l'amplification de couplage non-relaxée [15], amplification tendant vers l'infini au décollement. L'algorithme (22) est capable de propager l'influence visqueuse d'aval en amont dans les zones supersoniques grâce à l'utilisation de schémas décentrés vers l'aval pour $(dm/dx)_{i,1}^*$ dans la relation (17), c'est à dire pour le couplage des dérivées de \hat{m} , \hat{q} avec $m_{i,1}^*$, $q_{i,1}^*$.

Dans les zones où le problème visqueux est résolu en mode inverse ($H_i > 1.8$), le couplage est traité par la méthode "Semi-Inverse". La correction sur $\omega_{i,1}^*$ est déduite des estimations visqueuses $\hat{q}(x,0)$ et non-visqueuses $q^*(x,0)$ et de leurs dérivées, discrétisées aux abscisses x_i . Elle s'écrit [15] :

$$\begin{cases} \omega_{i,1}^{*+1} - \omega_{i,1}^* = \omega_{i,1}^* \left[\frac{q^*}{\hat{q}} \frac{\partial \hat{q}}{\partial x} - \frac{\partial q^*}{\partial x} \right]_{i,1} + \omega_{i,1}^* \left[\frac{q^*}{\hat{q}} \frac{\partial^2 \hat{q}}{\partial x^2} - \frac{\partial^2 q^*}{\partial x^2} \right]_{i,1} \\ \omega_{i,1}^0 = \omega_{\mu} \left[\mu^{-1}(x_{i,1}, \alpha_{\max}) \right] \end{cases} \quad (24)$$

$$0 < \omega < 2$$

avec les expressions (23) de μ et ω_{μ} . Elle est utilisée sous la forme originelle [15] avec $\omega_{i,1}^A = \omega_{i,1}^0$, $\omega_{i,1}^S = 0$ aux noeuds subsoniques, $\omega_{i,1}^A = 0$, $\omega_{i,1}^S = \omega_{i,1}^0$ aux noeuds supersoniques. La dérivée seconde de q^* est en outre discrétisée avec un décentrement vers l'aval par rapport à la dérivée seconde de \hat{q} , ce qui augmente la vitesse de convergence (pour le nombre d'onde α_{\max}) et accentue la capacité à propager l'influence visqueuse vers l'amont dans les zones supersoniques.

4 - Résultats numériques -

La présente méthode de calcul a été mise en oeuvre ici en utilisant, pour la partie résolvant les équations d'Euler, la technique pseudo-stationnaire à enthalpie totale constante de Vivand, Veuillot [19], qui s'appuie essentiellement sur une adaptation du schéma explicite de Mac Cormack et sur un traitement des conditions aux limites par relations de compatibilité. Les itérations des algorithmes de couplage ont été menées en effectuant 50 pas de temps du solveur Euler par itération, avec la technique du critère CFL local.

La méthode a d'abord été développée pour le calcul des écoulements visqueux en canal plan. Les résultats ont permis de vérifier la capacité de la méthode à traiter le décollement étendu ainsi que les divers types d'interaction couche limite - onde de choc, en transsonique et en supersonique. Ils ont vérifié aussi que la présente "méthode Indirecte" d'interaction visqueux - non visqueux peut être utilisée sur des géométries quelconques avec interactions visqueuses multiples, aussi longtemps que les couches limites ne sont pas confluentes, les seules données nécessaires au calcul étant les mêmes que dans les "méthodes Directes" de résolution d'équations de Navier Stokes.

La méthode a ensuite été développée pour le calcul des écoulements visqueux de grilles d'aubes planes, dont les premiers résultats sont présentés ici.

4.1 - Conditions aux limites - Echelles de discrétisation

Les données sont constituées de la géométrie, des conditions à l'amont du fluide parfait et de la couche visqueuse. Elles sont complétées par une donnée à l'aval, celle de la contre-pression en transsonique, supposée ici uniforme dans la section de sortie, et celle du retour à une situation de faible interaction visqueuse à l'extrémité aval de la couche visqueuse en supersonique (gradient de pression longitudinal nul dans la couche visqueuse), une telle condition pouvant être remplacée par la donnée de la pression de caisson, dans le cas d'une tuyère sur- ou sous-détendue.

Outre les problèmes propres au traitement du couplage visqueux - non visqueux, tels que la condition d'entropie dans les zones où $w > 0$ ainsi que sa connexion avec le couplage du sillage, une contrainte importante dans ces calculs d'interactions visqueuses complexes est la nécessité d'utiliser des maillages suffisamment denses pour capturer numériquement les régions de compression des décollements turbulents, la taille des mailles devant être inférieure de moitié au moins à l'épaisseur locale de la couche visqueuse en début d'interaction.

Des maillages moins denses conduisent en effet soit à une divergence des algorithmes de couplage, soit de

toute manière à une résolution inexacte des phénomènes physiques, dominée par la dissipation numérique des schémas de calcul. Bien que moins contraignante que l'échelle de discrétisation en z nécessaire en cas de résolution des équations de Navier-Stokes, cette échelle de discrétisation minimale en x pour les problèmes d'interactions fortes turbulentes conduit à une difficulté pratique de maillage du champ de calcul. Elle conduit aussi à une pénalité notable, lorsque le maillage est uniformément dense, pour les techniques explicites des solveurs "Euler" et "couplage", notamment dans les cas présentant des zones quasi-soniques étendues. Le développement de solveurs non-explicites ainsi que de maillages auto-adaptables [14,13] est cependant envisageable.

4.2 - Canal transsonique symétrique

Cette configuration ainsi que celle du paragraphe 4.3 confrontent la présente méthode de calcul à des expériences d'interaction couche limite - onde de choc en transsonique effectuées à l'ONERA, Déléry [20]. Il s'agit ici d'une tuyère plane supersonique symétrique d'environ 120x100 mm de section, alimentée à une pression totale de 0.96 bar et une température totale de 300°K, dans laquelle la contre-pression induit une interaction choc droit - couche limite turbulente, sensiblement à $Mach=1.30$, avec un nombre de Reynolds fondé sur la vitesse locale ainsi que l'épaisseur δ de la couche limite en début d'interaction $Re_\delta \approx 2 \cdot 10^6$. L'interaction correspond environ au décollement naissant.

Dans le calcul, la couche limite à l'amont de la tuyère est supposée d'épaisseur négligeable. Par ailleurs, l'expérience faisant appel à un second col mobile ne conduisant pas à une contre-pression connue avec précision, la comparaison calcul - expérience est effectuée en ajustant finement la contre-pression théorique pour faire coïncider les zones de début d'interaction.

Le maillage utilisé comporte 180x27 noeuds. Des resserrements locaux du maillage en z le long de la paroi ainsi qu'en x à l'abscisse de début d'interaction conduisent dans cette zone à des cellules sensiblement carrées comportant environ 4 mailles par épaisseur de couche limite. La comparaison des lignes iso-densités calculées avec un interférogamme expérimental en teinte plate, figure 1, montre le très bon accord qualitatif obtenu, bien que le calcul soit effectué avec le modèle algébrique de turbulence.

La figure 2 montre les distributions de pression à la paroi calculées avec le modèle de turbulence algébrique et avec le modèle à 2 équations, ainsi qu'en fluide parfait. La contre-pression est identique dans les trois calculs $p = 0.655p_0$, l'écart avec la pression expérimentale pouvant être imputé aux effets des couches limites des parois latérales. On observe l'importance de la viscosité sur la position et sur l'intensité du choc, la perte de pression d'arrêt dans le pseudo-fluide parfait à l'aplomb du choc étant en outre éliminée au niveau de la paroi.

Le calcul avec modèle de turbulence à 2 équations intégrales améliore la prédiction de la pression et de l'épaisseur de déplacement, figures 2 et 3. L'examen des profils de vitesse, figures 4 et 5, montre cependant que cette amélioration est entachée d'une légère surestimation de la tendance au décollement, et que les performances des deux modèles restent globalement similaires en cas de décollement naissant.

4.3 - Canal transsonique dissymétrique

Cette configuration, figure 6, illustre les possibilités de calcul à la fois pour les écoulements complexes, sur des géométries quelconques avec interactions visqueuses multiples, et pour les décollements étendus conduisant à des paramètres de forme élevés (M , α 25). Les conditions génératrices et la section du canal étant sensiblement les mêmes qu'en 4.2, le décollement massif à l'échelle de la couche limite résulte d'une interaction onde de choc - couche limite turbulente à $Mach \approx 1.30$. Elle est induite par contre-pression dans un canal transsonique dissymétrique dont la paroi inférieure présente une bosse, la paroi supérieure étant plane. Le nombre de Reynolds local en début d'interaction basé sur l'épaisseur de la couche limite inférieure est environ $Re_\delta \approx 3.8 \cdot 10^6$.

Le maillage, de 200x40 noeuds, couvrant la zone $0.010 < x < 0.450m$, comprend deux resserrements dans la région du choc, figure 6, ajustés l'un au pied du choc sur la paroi supérieure, l'autre au pied du choc sur la paroi inférieure. Les lignes iso-densité calculées, figure 7, et iso-Mach, figure 8, visualisent l'écoulement. Le modèle algébrique se révélant conduire à une sous-estimation quasi-totale du décollement pour cet écoulement, le calcul est effectué avec le modèle à 2 équations, la contre-pression $p = 0.659p_0$, étant ajustée pour positionner le début d'interaction à la paroi inférieure.

La figure 10 compare à l'expérience les pressions calculées sur les parois supérieures et inférieures. Sur la paroi inférieure on peut noter un "overshoot" de compression anormal avant le plateau de pression de la zone décollée. Des recoupements avec divers calculs ont montré que cette anomalie, qui traduit la relative simplicité de la modélisation à 2 paramètres des profils de vitesse turbulente pour des zones à recompression rapide, ne constitue cependant qu'une insuffisance localisée du calcul. On observe en particulier que la sélection du modèle de turbulence à 2 équations, qui accentue l'overshoot localisé, conduit au contraire à une amélioration systématique des solutions ainsi que des pressions de décollement.

Les écarts de niveaux de pression plateau à la paroi inférieure, de contre-pression, ainsi que de positionnement du choc à la paroi supérieure, figure 10, traduisent sous forme globale les différentes sources

d'erreur, c'est à dire l'imperfection de la modélisation turbulente du calcul, l'influence parasite des couches limites sur les parois latérales dans l'expérience, l'hypothèse de pression uniforme dans la section de sortie du calcul, ainsi que l'ajustement de cette pression pour recalculer le début d'interaction à la paroi inférieure. Il semble difficile de différencier ces différents effets compte tenu de la sensibilité d'un tel écoulement transsonique à toute perturbation.

La figure 9 fournit la distribution de vitesse normale à la paroi inférieure dans le pseudo-fluide parfait, calculée à convergence du couplage fort, qui traduit l'effet de déplacement généralisé. La régularité des valeurs discrètes montre la bonne convergence du couplage. On note que la densité des noeuds dans la zone de compression, en amont du décollement, est suffisante pour résoudre effectivement l'interaction choc - couche limite. On note de plus les valeurs élevées induites par le décollement sur l'angle d'injection, ainsi que la discontinuité qui coïncide avec le point anguleux de la paroi.

Le caractère légèrement subsonique plutôt que légèrement supersonique du plateau de pression s'associe à une sous-évaluation de l'épaisseur de déplacement maximale, figure 11, et du paramètre de forme maximal, figure 12, ces deux grandeurs étant cependant similaires aux distributions expérimentales, et bien prédites en début d'interaction.

La comparaison à l'expérience des profils de vitesse moyenne le long de la paroi inférieure dans la zone de décollement - recollement, figure 13, montre qu'en dépit de ces imperfections une prédiction d'ensemble déjà satisfaisante est obtenue ici pour ce type d'écoulements turbulents complexes, si l'on se réfère à l'état de l'art mis en évidence par la Conférence Stanford-1981 pour des écoulements de même nature.

La comparaison à l'expérience des profils de cisaillement turbulent et d'énergie cinétique turbulente, figures 17 et 18, montre que le calcul fournit aussi une estimation déjà satisfaisante de la turbulence, compte tenu de la complexité du problème, en dépit de la simplicité relative de la modélisation. Les profils des figures 17-18 sont déduits des écarts à l'équilibre calculés par (15), indépendants de z , ainsi que des profils d'équilibre selon z associés à la vitesse moyenne par un modèle de longueur de mélange.

La courbe d'hysteresis de la turbulence pendant le processus de décollement - recollement, dans le diagramme "cisaillement turbulent maximal - paramètre de forme", figure 14, confirme ces résultats relativement satisfaisants, bien que la comparaison calcul - expérience se dégrade dans la zone de recollement. Enfin l'évolution en abscisse du maximum de cisaillement turbulent au travers de la couche visqueuse, figure 16, ainsi que du maximum d'énergie cinétique, figure 15, confirme l'accord qualitatif calcul - expérience.

4.4 - Rampe de compression supersonique

Cette configuration, figure 20, correspond aux expériences à très grands nombres de Reynolds de Settles, Fitzpatrick, Bogdonoff [21]. Elle permet de vérifier l'aptitude de la méthode à calculer un premier type d'interaction couche limite - onde de choc supersonique, ainsi qu'à traiter la propagation de l'influence visqueuse vers l'amont en régime supersonique élevé.

Le nombre de Mach amont est $M_\infty = 2.85$, le dièdre de la rampe $\Psi = 24^\circ$, le nombre de Reynolds basé sur l'épaisseur δ de la couche limite amont est $R_\delta \approx 1.45 \times 10^6$. Un maillage de 100×50 noeuds, couvrant le domaine $-75 < x < 145$, conduit à un pas d'espace de l'ordre de 0.254 dans la zone de début d'interaction. Le calcul est effectué avec le modèle de turbulence à 2 équations.

La comparaison à l'expérience de la pression calculée à la paroi, figure 21, montre un accord relativement satisfaisant. Il est cependant à noter que la correction de "courbure réduite" (12), qui était négligeable en transsonique, a dû être utilisée. Son importance apparaît par comparaison des pressions de premier et de second ordre, figure 21. Les lignes isobares du champ de pression de premier ordre, figure 19, confirment l'importance du gradient de pression normal (surestimé au 1^{er} ordre) au sein de la couche visqueuse. Le décollement est enfin visualisé par les lignes iso-Mach calculées, figure 20.

4.5 - Réflexion d'une onde de choc en supersonique

L'aptitude de la méthode au calcul de ce second type d'interaction couche limite onde de choc supersonique est analysée à $Mach = 1.92$, pour un nombre de Reynolds basé sur l'épaisseur de couche limite en début d'interaction $R_\delta \approx 6.7 \times 10^5$. Cette configuration a été étudiée expérimentalement à l'ONERA, Le Baller, Delery [22].

Le calcul est effectué pour un choc oblique de déflexion $\Psi = 8.25^\circ$ induit par un dièdre de la paroi supérieure d'un canal. Le maillage utilisé, de 200×50 noeuds, fournit des mailles de l'ordre de 0.254 en début d'interaction et présente un resserrement près de l'impact du choc incident.

Les courbes isobares du champ de pression de premier ordre, figure 22, montrent que ce resserrement est utile pour capturer la réflexion du choc en aval de la détente imposée par la continuité de la pression à la paroi en fluide visqueux. La figure 22 montre que le calcul restitue la propagation de l'influence visqueuse à l'amont de l'impact, et visualise en outre les gradients de pression normaux importants au sein de la couche visqueuse dans la zone d'interaction.

Il est à noter que cette configuration, comme celle de la rampe supersonique, correspondent à des couches limites "supercritiques" au sens de Crocco, pour lesquelles un calcul résolvant les équations de Prandtl couplées

à leur frontière extérieure (ou bien sur la surface de déplacement) serait en défaut. La présente méthode de calcul montre, par les lignes iso-Mach de la figure 23, que le phénomène est qualitativement décrit. On y note l'important épaississement de la zone subsonique, en pointillés. Le calcul, effectué avec le modèle de turbulence algébrique, prévoit un décollement modéré sous le choc. La figure 24 compare enfin à l'expérience la distribution de pression de second ordre à la paroi, ainsi que l'écart entre les pressions de premier et de second ordre.

4.6 - Grilles d'aubes supersoniques

Le calcul est effectué sur un canal interaube, traité par moitié de part et d'autre de l'aube et de la ligne moyenne du sillage, qui correspond à une coupure dans le pseudo-fluide parfait. La géométrie de ce sillage est déterminée par le couplage visqueux - non visqueux, voir [14], après un minimum de convergence de l'effet de déplacement. Elle est remise en cause toute les 50 à 100 itérations de couplage. Une condition de périodicité est appliquée dans le pseudo-fluide parfait entre les frontières supérieures et inférieures, qui coïncident par translation. Les frontières amont et aval sont choisies parallèles au front de la grille.

La figure 25 montre le type de maillage utilisé, à convergence du calcul. Le maillage comporte 400x32 noeuds, soit 400x16 pour chaque demi-canal interaube. Faute d'une auto-adaptation du maillage, une distribution uniformément dense en x de 200 noeuds sur l'aube a été choisie, la densité en x devant aussi rester élevée le long du sillage dans le cas où celui-ci est supersonique et où il interagit avec des chocs ou des déteintes. Ce maillage dense conduit sur l'aube à des mailles de 0.005 corde en x et 0.006 corde en z. Ceci est juste compatible avec l'échelle de résolution nécessaire aux phénomènes de début d'interactions choc - couche limite, à condition qu'aucune n'ait un positionnement trop proche du bord d'attaque.

Les calculs sont effectués avec couplage fort du sillage en effet de déplacement et en positionnement. Une condition de retour au régime d'interaction faible est imposée à l'extrémité aval du sillage dans le cas supersonique. Le positionnement correct du sillage est important pour le contrôle des conditions d'entropie le long de la coupure, liées au signe des vitesses normales, elles-mêmes fonction du positionnement. Faute de résoudre l'échelle du rayon de courbure de bord d'attaque, la couche limite est initiée au bord d'attaque à l'intrados et à l'extrados en la supposant laminaire et d'épaisseur nulle. La transition laminaire - turbulent est déclenchée à 0.5 pourcent de corde, sans surépaississement.

Le calcul des figures 25, 26 est effectué pour une grille d'aube supersonique d'encombrement axial L, de pas 1.62L, avec un calage $\alpha = 67^\circ$, pour un nombre de Mach amont $M \approx 1.55$. Le nombre de Reynolds, basé sur L et sur la vitesse du son critique, est $Re_L = 8 \cdot 10^6$. La contre-pression imposée est $p_{aw} = 0.30 p_{\infty}$.

La figure 25 montre les lignes iso-Mach calculées ainsi que les lignes isobares (pression de premier ordre). L'écoulement est totalement supersonique et attaché. Il présente une interaction choc - couche limite qui conduit au voisinage du décollement à l'intrados. Le positionnement du sillage, caractéristique de ce régime, peut être observé. La figure 26 montre enfin les distributions de nombre de Mach et de vitesse normale du pseudo-fluide parfait calculées à la paroi et sur le sillage, ainsi que les distributions d'épaisseur de déplacement, de quantité de mouvement et de paramètre de forme. On peut y noter l'interaction couche limite - onde de choc, ainsi que l'évolution complexe des grandeurs sur le sillage supersonique.

Bien que seuls quelques premiers essais de calcul, imparfaitement convergés, aient encore pu être réalisés pour des configurations de grilles supersoniques avec décollement, la capacité de la méthode à traiter les écoulements décollés en canal, ainsi que les résultats antérieurs obtenus sur les sillages décollés des profils d'ailes [15, 17], garantissent en principe la possibilité de simuler par la présente méthode les écoulements décollés complexes transsoniques ou supersoniques.

Les problèmes nouveaux propres aux grilles d'aubes observés dans ces quelques essais préliminaires semblent liés à la difficulté imposée par l'échelle très fine des phénomènes de décollement turbulent lorsque les interactions choc - couche limite se rapprochent de la partie amont de l'aube ($\Delta < 0.25$ à début d'interaction), échelle qui rendrait utile une technique d'auto-adaptation du maillage à la zone du pied de choc, ainsi que la présence de zones quasi-soniques étendues, qui sont pénalisantes sur maillages très fins pour la vitesse de convergence de l'algorithme numérique de couplage sous la forme actuelle.

5 - Conclusions

La présente méthode numérique généralisée aux écoulements internes décollés avec interactions choc - couche limite ainsi qu'aux grilles d'aubes la méthode de calcul qui avait été proposée antérieurement pour les profils d'ailes décollés.

Ces résultats montrent que le calcul des écoulements internes décollés par une "méthode indirecte" d'interaction visqueux-non visqueux spécifiquement conditionnée pour les nombres de Reynolds élevés est réalisable.

La présente étape indique la valeur prédictive très encourageante d'une résolution approchée avec modification par méthode intégrale pour les écoulements décollés complexes, cette approche pouvant permettre à terme, moyennant un progrès sur les techniques numériques actuelles, de conduire à une méthode de calcul de coût minimal.

L'étape actuelle permet aussi d'envisager son extension vers une résolution "indirecte" d'équations de Navier-Stokes par "Formulation Déficiente" et techniques numériques de couplage fort.

Références

- [1] LE BALLEUR J.C., PEYRETR., VIVIAND H. - Numerical studies in high Reynolds number aerodynamics - Computers and Fluids, Vol 8, n°1, p.1-30, (March 1980).
- [2] CAMBIER L., ESCANDE B., VEUILLOT J.P. - Calcul d'écoulements internes à grands nombres de Reynolds par résolution numérique des équations de Navier-Stokes - AGARD/PEP 68th meeting on transonic and supersonic phenomena in turbomachines, Munich (10-12 Sept. 80).
- [3] MELNIK R.E., BROOK J.W. - The computation of Viscid/Inviscid Interaction on airfoils with separated flow. - Proceed 3rd Symp. on Numerical and Physical Aspects of Aerodynamic Flows, Long Beach (Jan. 1985), T. Cebeci editor, Springer-Verlag 1986.
- [4] CARTER J.E., EDWARDS D.E., HAFEZ M.M. - Analysis of transonic shock-induced separation flow including normal pressure gradient. - Report AFOSR-TR-83-1283 (Oct. 1983).
- [5] WERLE M.J. - Compressor and turbine blades boundary layer separation. - AGARD-CP-351, Paper 9, Copenhagen (1983).
- [6] LOCK R.C., FIRMIN M.C.P. - Survey of techniques for estimating viscous effects in external aerodynamics. - RAE Tech. Memo. Aero. 1000 (1981).
- [7] WAI J.C., YOSHIHARA H. - Planar transonic airfoil computations with viscous interactions. - AGARD-CP-291, Paper 9, Colorado-Springs (1981).
- [8] VELDMAN A.E.P. - The calculation of incompressible boundary layers with strong viscous-inviscid interaction. - AGARD-CP-291, Paper 12, Colorado-Springs (1981).
- [9] LE BALLEUR J.C. - Computation of flows including strong viscous interactions with coupling methods. - AGARD-CP-291, General Introduction, Lecture 1, Colorado-Springs (1981), or ONERA TP 1980-121.
- [10] LE BALLEUR J.C. - Numerical flow calculation and viscous-inviscid interaction techniques. - Recent Advances in Numerical Methods in Fluids, Vol. 3 : Computational methods in viscous flows, p.419-450, W. Habashi editor, Pineridge Press (1984).
- [11] LE BALLEUR J.C. - Progress in computation of Viscous-Inviscid Interaction. - AGARD-CP-351, Paper 1, Copenhagen (1983).
- [12] LE BALLEUR J.C. - Viscous-inviscid interaction solvers and computation of highly separated flows. Proceedings of ICASE workshop on Vortex Dominated Flows, NASA Langley Field, USA, (July 9-10 1985), Springer-Verlag, to be published. (ONERA TP. 1985-4).
- [13] LE BALLEUR J.C., BLAISE D. - Computation of separated internal flows and shock wave-boundary layer interactions by viscous-inviscid interaction. - La Recherche Aéronautique 1985-4, p.211-227, English and French editions, (July 1985).
- [14] LE BALLEUR J.C. - Strong matching method for computing transonic viscous flows including wakes and separations. Lifting airfoils. - La Recherche Aéronautique 1981-3, p.21-45, English and French editions, (1981).
- [15] LE BALLEUR J.C. - Viscous-inviscid flow matching : Numerical method and applications to two-dimensional transonic and supersonic flows. - La Recherche Aéronautique 1978-2, p.87-76, (march 1978), English transl. ESA-TT-493.
- [16] LE BALLEUR J.C. - Viscous-inviscid flow matching : Analysis of the problem including separation and shock waves. - La Recherche Aéronautique 1977-6, p.349-358, (Nov. 1977), English translation ESA-TT-478.
- [17] LE BALLEUR J.C. - Numerical viscid-inviscid interaction in steady and unsteady flows. - Proceed. 2nd Symp. Numerical and Physical Aspects of Aerodynamic Flows, Long Beach (1983), Springer-Verlag, T. Cebeci editor, chap. 13, p.359-384 (1984), or ONERA-TP 1983-5.
- [18] LE BALLEUR J.C., GIROUDROUX-LAVIGNE P. - A semi-implicit and unsteady numerical method of viscous-inviscid interaction for transonic separated flows. - La Recherche Aéronautique 1984-1, p.5-37, English and French editions, (1984).
- [19] VIVIAND H., VEUILLOT J.P. - Méthodes Pseudo-instationnaires pour le calcul d'écoulements transsoniques. Publication ONERA n° 1978-4, English translation ESA-TT-548.
- [20] DELERY J. - Experimental investigation of turbulence properties in transonic shock/boundary layer interaction. - AIAA J., Vol. 21, n°2, (1983), p.180-185.
- [21] SETTLES T.J., FITZPATRICK T.J., HODGONOFF S.M. - Detailed study of attached and separated decomposition corner flowfield in high number supersonic flow. - AIAA J., Vol. 17, n°6, (1979), p.579.
- [22] LE BALLEUR J.C., DELERY J. - Etude expérimentale de l'interaction d'une onde de choc plane et d'une couche limite turbulente à $M_\infty = 1.92$. Rapport ONERA n°4/7078, (C.N. 1979).



DENSITE

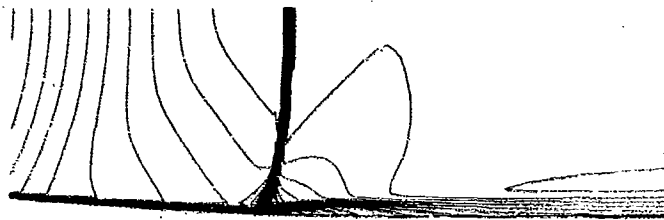


Fig. 1 - Canal symétrique, $M=1,30$. Comparaison calcul-expérience :
Lignes iso-densité et interférogamme en teinte plate.

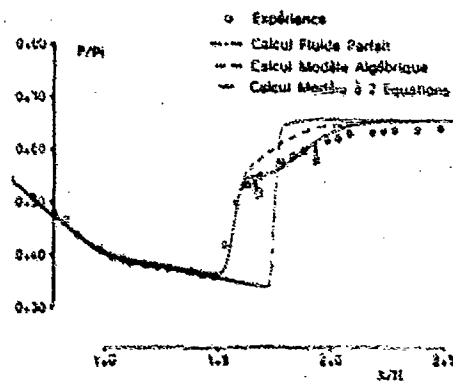


Fig. 2 - Canal symétrique, $M=1,30$.
Distribution de pression statique.

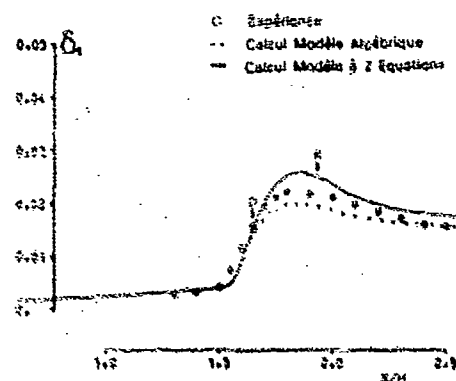


Fig. 3 - Canal symétrique, $M=1,30$.
Épaisseur de déplacement.

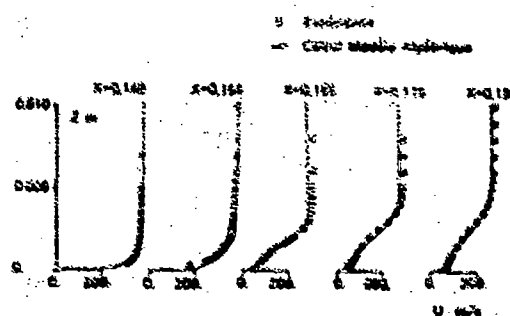


Fig. 4 - Canal symétrique, $M=1,30$. Profils de vitesse.
Calcul avec modèle algébrique de turbulence.

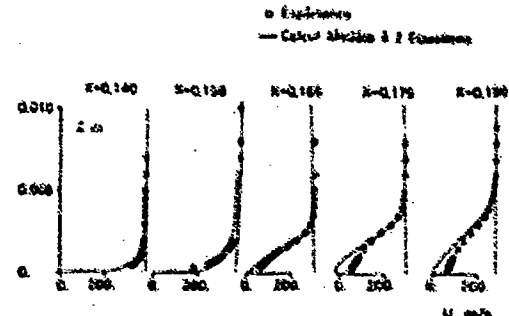


Fig. 5 - Canal symétrique, $M=1,30$. Profils de vitesse.
Calcul avec modèle de turbulence à 2 Equations.

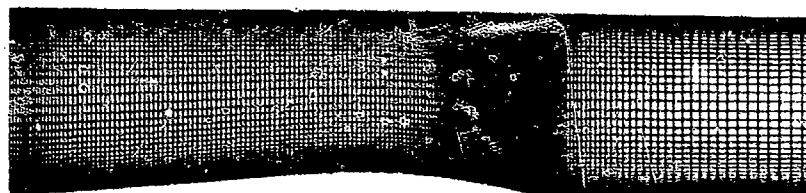


Fig. 6 - Canal dissymétrique . $M=1,36$.
Maillage: 200×40 .

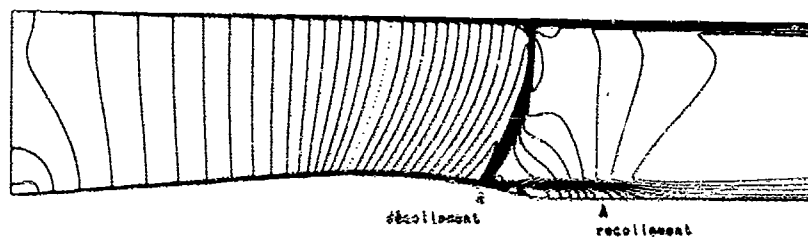


Fig. 7 - Canal dissymétrique . $M=1,36$.
Lignes Iso-densité.

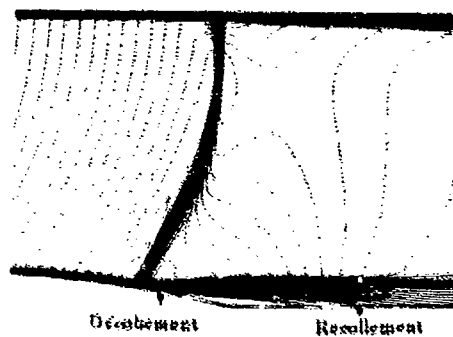


Fig. 8 - Canal dissymétrique . $M=1,36$.
Lignes Iso-Mach.

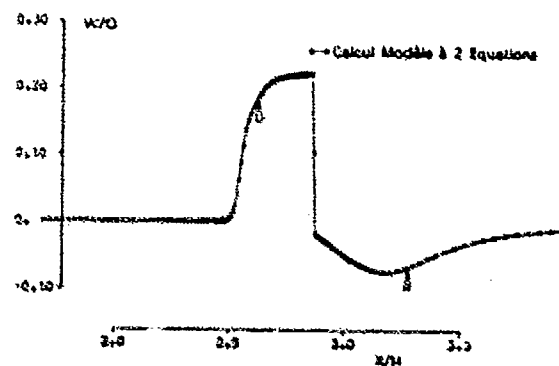


Fig. 9 - Canal dissymétrique . $M=1,36$.
Evolution de la vitesse normale
imposée au pseudo fluide parfait

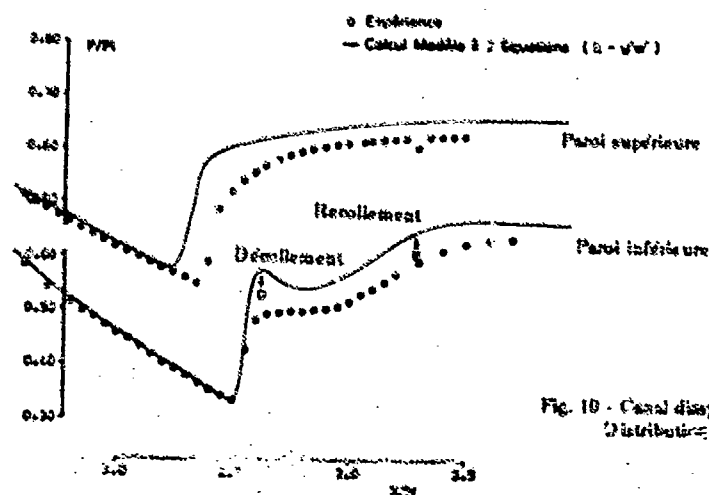


Fig. 10 - Canal dissymétrique . $M=1,36$.
Distribution de pression pariétale.

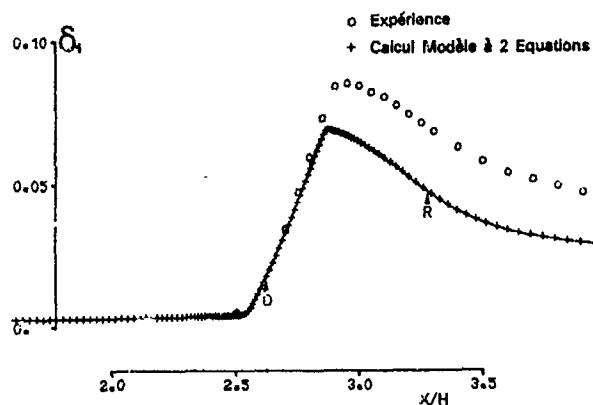


Fig. 11 - Canal dissymétrique . $M=1.36$.
Evolution de l'épaisseur de déplacement.

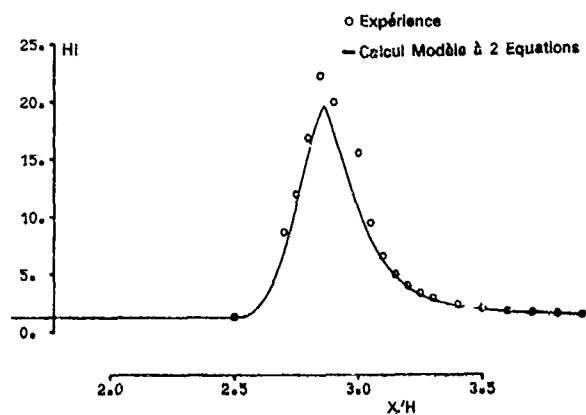


Fig. 12 - Canal dissymétrique . $M=1.36$.
Evolution du paramètre de forme incompressible

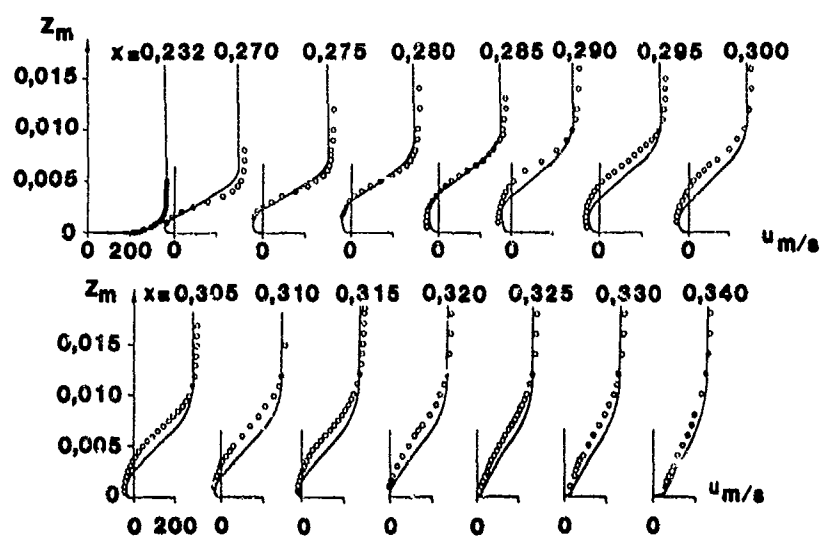


Fig. 13 - Canal dissymétrique . $M=1.36$.
Profils de vitesse moyenne.

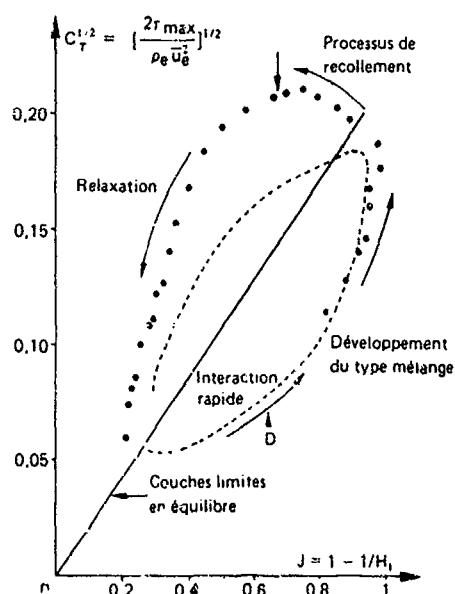


Fig. 14 - Canal dissymétrique . $M=1.36$.
Evolution du coefficient de cisaillement maximal
en fonction de H_1 : effet d'hystérésis sur la turbulence.

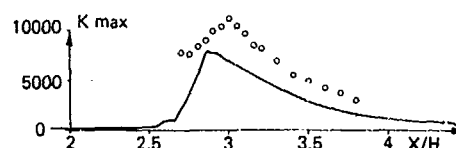


Fig. 15 - Canal dissymétrique . $M=1.36$.
Evolution de l'énergie turbulente maximale.

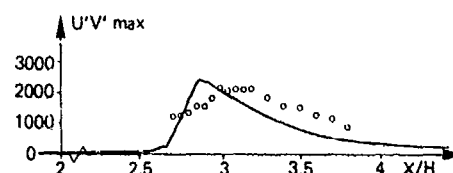


Fig. 16 - Canal dissymétrique . $M=1.36$.
Evolution du cisaillement turbulent maximal.

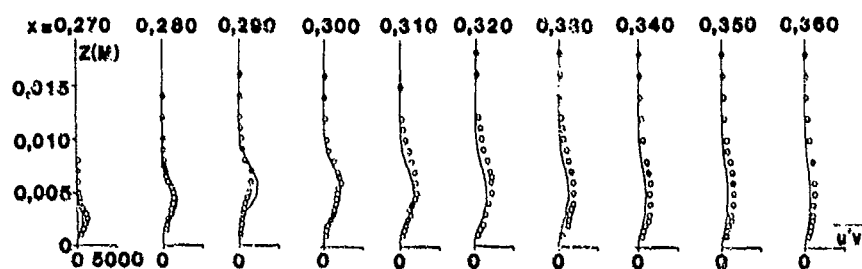


Fig. 17 - Canal dissymétrique . $M=1.36$.
Profils de cisaillement turbulent.

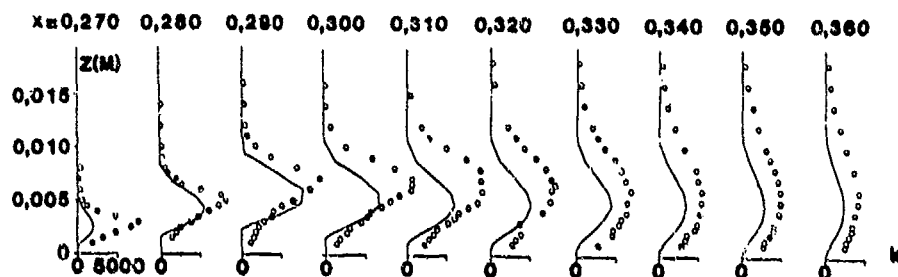


Fig. 18 - Canal dissymétrique . $M=1.36$.
Profils d'énergie turbulente.

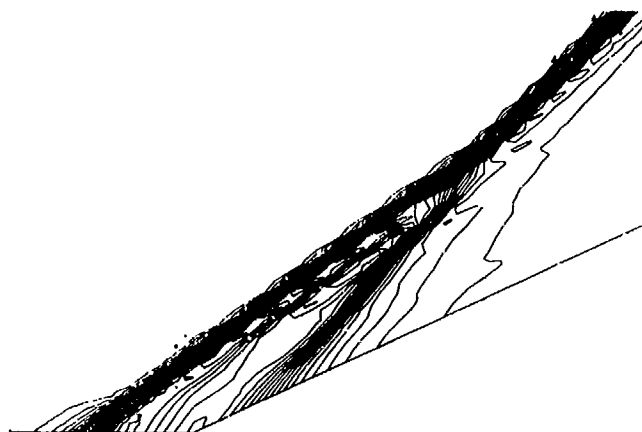


Fig. 19 - Rampe Supersonique . $M=2.85$. $\phi=24^\circ$. $R_\delta=1.4 \cdot 10^6$.
Lignes Isobares. (Approximation de 1^{er} ordre)

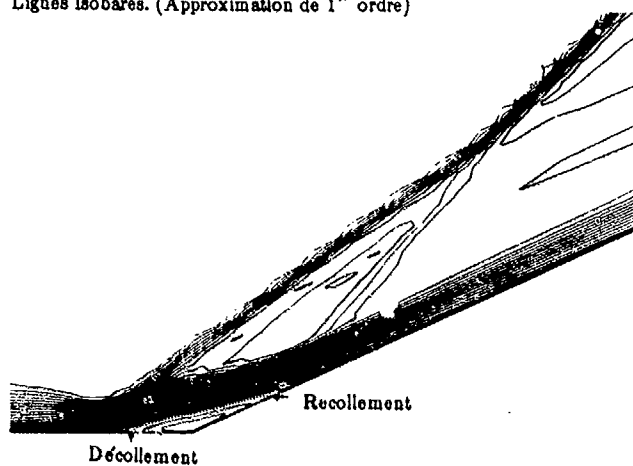


Fig. 20 - Rampe Supersonique . $M=2.85$. $\phi=24^\circ$. $R_\delta=1.4 \cdot 10^6$.
Lignes Iso-Mach.

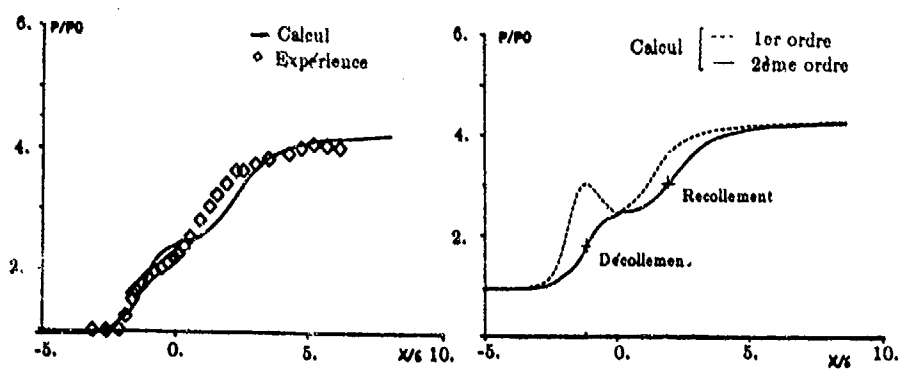


Fig. 21 - Rampe Supersonique . $M=2.85$. $\phi=24^\circ$. $R_\delta=1.4 \cdot 10^6$.
Distribution de pression à la paroi.

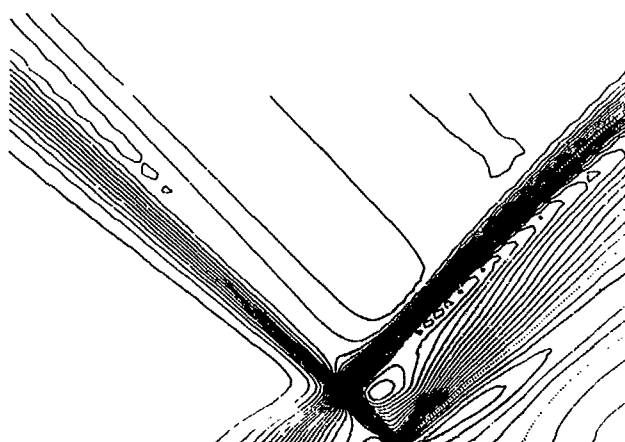


Fig. 22 - Interaction couche limite - onde de choc .
Lignes isobares. (Approximation de 1^{er} ordre)

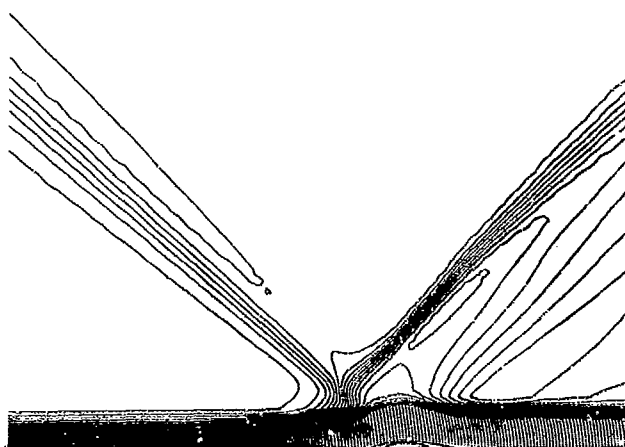


Fig. 23 - Interaction couche limite - onde de choc en supersonique .
 $M=1.92$, $\Phi=8.25^\circ$, $R_\delta=6.7 \cdot 10^4$. Lignes iso-Mach.

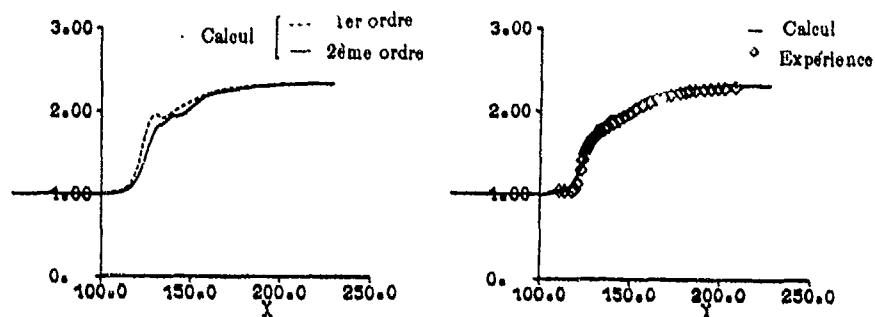


Fig. 24 - Interaction couche limite - onde de choc en supersonique .
 $M=1.92$, $\Phi=8.25^\circ$, $R_\delta=6.7 \cdot 10^4$. Distribution de pression à la paroi.

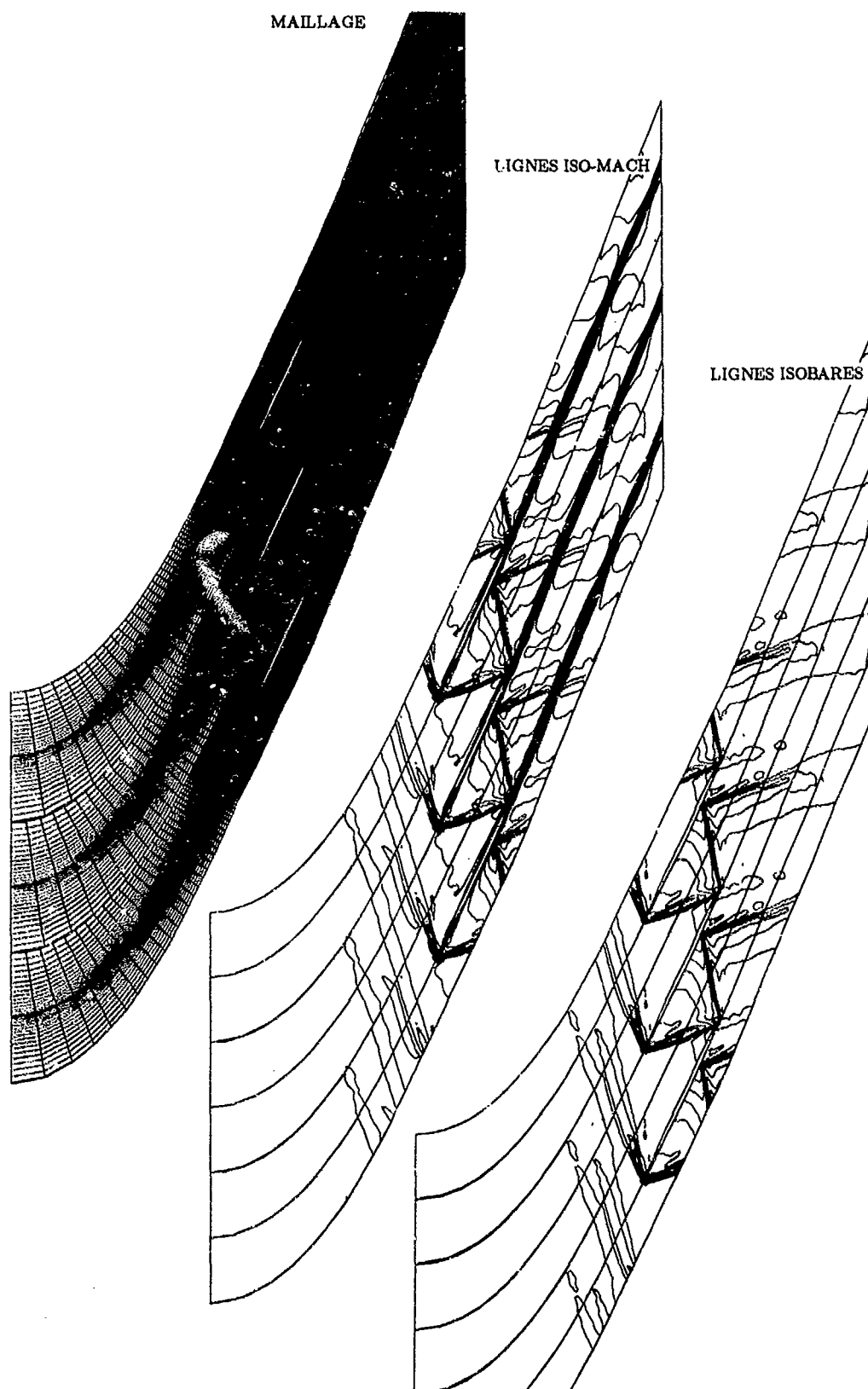


Fig. 25 - Calcul d'un écoulement visqueux de grille d'aube supersonique .

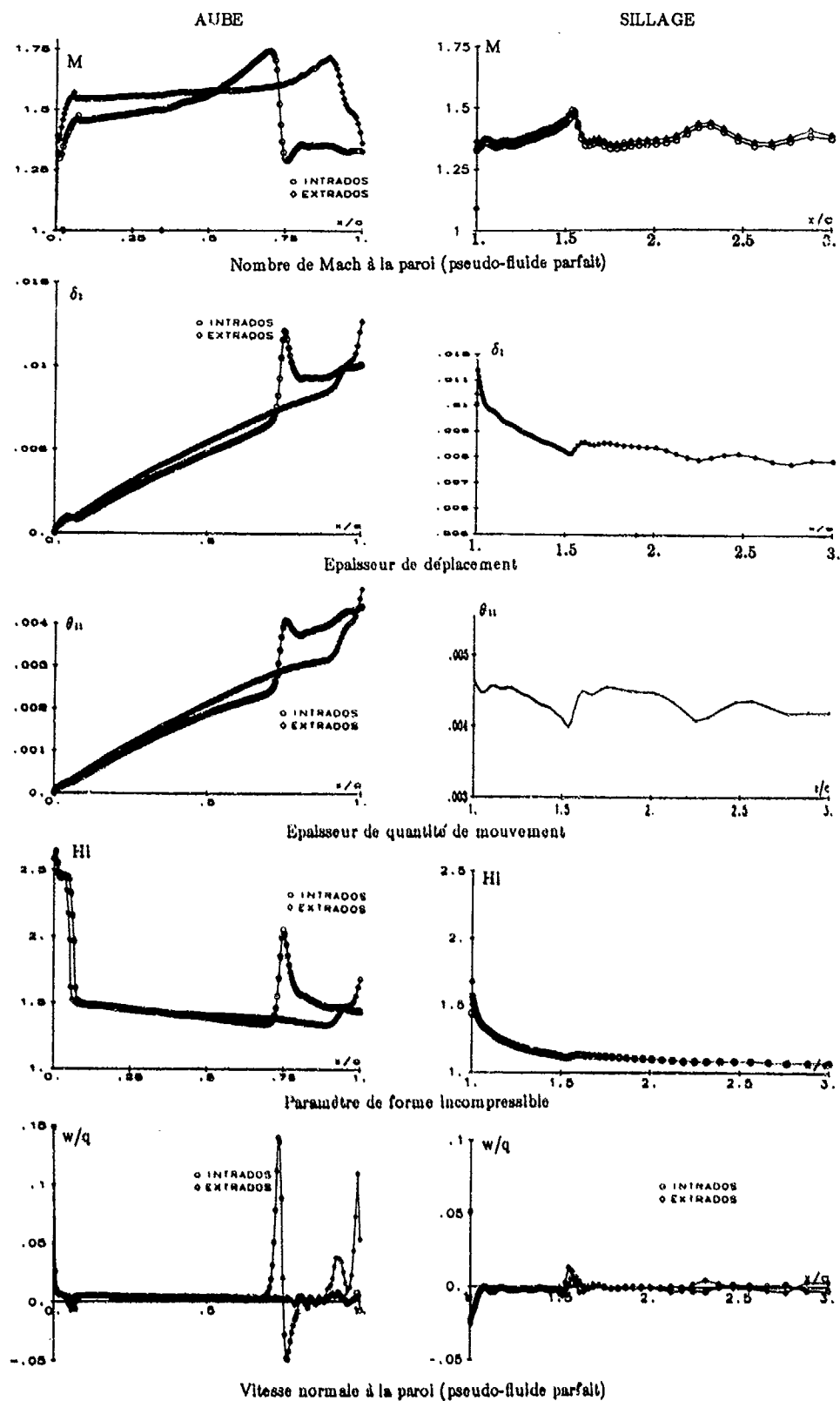


Fig. 26 - Calcul d'un écoulement visqueux de grille d'aube supersonique .

DISCUSSION

F. Leboeuf, Fr

1. Dans un canal interaube, comportant une zone visqueuse importante, où peut-on appliquer la relation de couplage entre les fluides visqueux et non-visqueux?
2. Comment adapter cette méthode dans le cas de canaux pour lequel l'écoulement est totalement visqueux?

Author's Reply

1. La dissociation en problèmes visqueux et non-visqueux étant effectuée avec recouvrement complet des deux domaines de calcul, le couplage entre le pseudo-fluide parfait et le fluide visqueux réel suppose simplement qu'il subsiste un noyau résiduel non-visqueux, aussi réduit soit-il, au centre du canal. La condition de raccordement "continu" (Matching) implique que les deux fluides s'identifient dans cette zone, au sein de laquelle peut-être arbitrairement placée la distance de la paroi qui est notée schématiquement z , dans les conditions de couplage fort. La "Formulation Déficitaire" proposée rend la solution totalement indépendante du choix précis de cette distance à la paroi, pourvu qu'elle se situe dans le noyau non-visqueux.
2. L'extension de la méthode au régime de conduite, lorsque l'écoulement est visqueux dans sa totalité, n'est pas envisagée ici. Les relations de couplage précédentes restent valides. En revanche, les équations d'Euler ne peuvent plus être appliquées au pseudo-fluide parfait. Bien qu'il ne soit probablement pas impossible d'étendre la Formulation Déficitaire à ces régimes, il n'est effectivement pas certain que ces régimes restent dans le domaine d'intérêt de la présente technique numérique.

Mr Kordulla, Gc

Your results are very impressive, therefore it is a pity that for the channel flow the agreement between predicted and measured pressure cannot be tuned. As far as I know the back pressure is prescribed. Therefore: why didn't you adjust the back pressure to the experimentally observed value?

Author's Reply

In fact, it was not possible, with the present ONERA experiment, to make an exact comparison between calculation and experiment by adjusting the two back-pressures. The experimental device is a small wind tunnel, with a roughly square section, where non-negligible three-dimensional effects are generated by the boundary layers on the side-walls, especially in transonic separated flow. The experiment is also controlled by adjusting the geometry of a second-throat whose contour is not exactly known, and which then cannot be included in the calculation. The upper and lower wall pressure measurements are restricted to a zone upstream of the second throat, and the pressure across the channel at the last measured station is not fully uniform. The calculation domain has been then continued farther downstream the second throat, and it is assumed that the back pressure is uniform across the exit section.

Due to the sensitivity of such a transonic flow to minor changes on boundary conditions, it was believed, within the present constraints, that the more valuable comparison with experiment was to match the beginnings of interaction (i.e. shock locations) for the inner wall, where the separation was studied, by adjusting arbitrarily the theoretical back-pressure. Of course, this choice concentrates the overall discrepancies due to the experimental 3D-interferences and to the limitations of the calculation on the comparison obtained for the back pressure and wall pressure.

J. Hourmouziadis, Gc

You did not make any approximation on the pressure field, like in the classical boundary layer theory that the pressure is constant across the boundary layer. Did you calculate the pressure field?

Author's Reply

We make an approximation which is of the first order and is not exactly the same as in the boundary layer theory, because we extend the inviscid flow up to the wall. In this case, the simplest approximation is to assume that the normal pressure gradient is not zero but is the same as in the inviscid field. This approximation is in fact implicitly made, as soon as you use integral methods. Looking carefully at the equations, you can see that the integral method gives a higher approximation than the finite difference equations of Prandtl. The difficulty is of course displaced to the closure relations.

CALCUL TRIDIMENSIONNEL DANS LES
AUBAGES DE TURBO-MACHINES AVEC NAGEOIRE

Par

T. DERRIEN

Société Nationale d'Etude et de Construction de Moteurs d'Aviation (SNECMA)
77550 MOISSY-CRAMAYEL
FRANCE

RESUME

On présentera ici une résolution numérique des équations d'Euler au travers d'un aubage de roue mobile pourvue d'une nageoire. On explicite la méthode par domaines, choisie pour sa simplicité de mise en oeuvre. L'analyse des résultats de calculs, à comparer avec ceux obtenus dans les mêmes conditions sur le même aubage sans nageoire, permettra de dégager les principales influences de la nageoire sur le champ aérodynamique.

INTRODUCTION

Le progrès des ordinateurs rendant aujourd'hui le coût d'un calcul tridimensionnel de fluide parfait abordable. D'autre part, cette modélisation est la première approche satisfaisante pour l'analyse des effets relatifs d'une nageoire non axisymétrique dans une roue de turbo-machine. Nous présenterons ici un développement des méthodes pseudo-instationnaires en usage depuis longtemps à l'ONERA (réf. 1, 2, 3) et à la SNECMA. Celui-ci est donc un exemple de la réponse à un problème industriel, au moyen d'outils validés.

A. FORMULATION

1. Equations dans le repère mobile

En partant des équations de la dynamique des gaz en repère fixe, où l'on néglige les tensions visqueuses ou dues à la gravité, on écrit :

$$(a) \quad \frac{dp}{dt} + \text{div}(\rho \vec{v}) = 0$$

$$(b) \quad \rho \frac{d\vec{v}}{dt} = - \text{grad } p$$

$$(c) \quad \rho \frac{dE}{dt} = - \text{div}(\rho \vec{v} E)$$

avec

$$E = C_v t + \frac{v^2}{2}$$

La transformation dans un repère relatif, entraîné avec l'aube dans un mouvement uniforme, peut s'écrire :

$$(a) \quad \frac{\partial \rho}{\partial t} + \operatorname{div}(\rho \vec{w}) = 0$$

$$(b) \quad \frac{d\vec{r}}{dt} = \frac{d\vec{w}}{dt} + \underbrace{2\vec{\Omega} \wedge \vec{w}}_{\text{Coriolis}} - \underbrace{\vec{\Omega}^2 \vec{r}}_{\text{entraînement}}$$

d'où :

$$(b) \Leftrightarrow \rho \frac{d\vec{w}}{dt} + 2\rho \vec{\Omega} \wedge \vec{w} - \rho \vec{\Omega}^2 \vec{r} + \vec{g} \rho = 0$$

$$\Leftrightarrow \frac{d(\rho \vec{w})}{dt} - \vec{w} \frac{d\rho}{dt} + 2\rho \vec{\Omega} \wedge \vec{w} - \rho \vec{\Omega}^2 \vec{r} + \vec{g} \rho = 0$$

Soit en introduisant (a') :

$$\frac{d(\rho \vec{w})}{dt} + \rho \vec{w} \operatorname{div} \vec{w} + 2\rho \vec{\Omega} \wedge \vec{w} - \rho \vec{\Omega}^2 \vec{r} + \vec{g} \rho = 0$$

et :

$$\frac{d(\rho \vec{w})}{dt} = \frac{\partial}{\partial t}(\rho \vec{w}) + \vec{w} \cdot \vec{\nabla}(\rho \vec{w})$$

soit :

$$\frac{\partial(\rho \vec{w})}{\partial t} + \vec{w} \cdot \vec{\nabla}(\rho \vec{w}) + \rho \vec{w} \operatorname{div} \vec{w} + 2\rho \vec{\Omega} \wedge \vec{w} - \rho \vec{\Omega}^2 \vec{r} + \vec{g} \rho = 0$$

or :

$$\operatorname{div}(\vec{u} \otimes \vec{v}) = (\operatorname{div} \vec{u}) \vec{v} + (\vec{u} \cdot \vec{\nabla}) \vec{v}$$

soit :

$$\operatorname{div}(\rho \vec{w} \otimes \vec{w}) = \rho \vec{w} (\operatorname{div} \vec{w}) + \vec{w} \cdot \vec{\nabla}(\rho \vec{w})$$

devient donc

$$\frac{\partial(\rho \vec{w})}{\partial t} + \operatorname{div}(\rho \vec{w} \otimes \vec{w} + p \vec{I}) = -2\rho \vec{\Omega} \wedge \vec{w} + \rho \vec{\Omega}^2 \vec{r}$$

L'équation de l'énergie (c) peut se transformer suivant

$$\rho \frac{dE}{dt} = -\operatorname{div}(\rho \vec{v}) ; \quad \vec{v} = \vec{w} + \vec{\Omega} \wedge \vec{r}$$

soit :

$$\frac{d}{dt}(\rho E) - E \frac{d\rho}{dt} = -\operatorname{div}(\rho(\vec{w} + \vec{\Omega} \wedge \vec{r}))$$

ou :

$$\frac{d}{dt}(\rho E) + \rho E \operatorname{div}(\vec{w}) = -\operatorname{div}(\rho(\vec{w} + \vec{\Omega} \wedge \vec{r}))$$

en utilisant $\operatorname{div} f \vec{v} = f \operatorname{div} \vec{v} + \vec{v} \cdot \vec{\nabla} f$, ceci s'écrit :

$$\frac{\partial}{\partial t}(\rho E) + \operatorname{div}(\rho E \vec{w}) + \operatorname{div}(\rho \vec{w}) = -\operatorname{div}(\rho \vec{\Omega} \wedge \vec{r})$$

ou :

$$\frac{\partial}{\partial t}(\rho(E - \frac{(\vec{\Omega} \wedge \vec{r})^2}{2})) + \operatorname{div}(\rho E + p) \vec{w} = \rho \vec{\Omega}^2 \vec{w} \cdot \vec{r}$$

soit :

$$\frac{\partial(\rho I - p)}{\partial t} + \operatorname{div}(\rho I) \vec{w} = 0$$

$$I = h + \frac{p}{\rho} + \frac{w^2 - (\vec{\Omega} \wedge \vec{r})^2}{2}$$

Ce qui conduit au système

$$\frac{\partial u}{\partial t} + \frac{\partial F(u)}{\partial x} + \frac{\partial G(u)}{\partial y} + \frac{\partial H(u)}{\partial z} = K(u)$$

$$U = \begin{pmatrix} p \\ p_u \\ p_r \\ p_w \\ p_{I-r} \end{pmatrix} \quad F(u) = \begin{pmatrix} p_u \\ p_{u-r} \\ p_{u-w} \\ p_{u-I} \end{pmatrix} \quad G(u) = \begin{pmatrix} p_r \\ p_{r-u} \\ p_{r-w} \\ p_{r-I} \end{pmatrix} \quad H(u) = \begin{pmatrix} p_w \\ p_{w-u} \\ p_{w-r} \\ p_{w-I} \end{pmatrix} \quad K(u) = \begin{pmatrix} 0 \\ 0 \\ 2p_{rw} + p_{u-r}^2 \\ -2p_{ru} + p_{u-w}^2 \\ 0 \end{pmatrix}$$

Cette formulation est celle qui sera effectivement discrétisée. On trouvera une forme conservatrice dans réf. 7.

2. Conditions aux limites

a) Les conditions aux limites sont les suivantes :

- périodicité (le seul canal inter-aube est traité)
- glissement - la vitesse sur les parois solides doit se trouver dans le plan tangent au solide. Cette condition se rencontre donc sur le moyeu, le carter, l'intrados et l'extrados de l'aube, et la nageoire.
- conditions d'alimentation à l'amont : La pression totale, la température totale et la direction absolue de l'écoulement à l'amont sont conservées pendant la durée du calcul.
- condition de pression aval : La pression statique au moyeu dans le plan est fixée - celle-ci sert donc à ajuster le vannage du compresseur. Le profil radial de pression statique qui sera imposé est issu d'un calcul simplifié de l'équilibre radial (pas de courbure des lignes de courant). Ce calcul est effectué à chaque itération.

b) Liens avec le calcul de l'écoulement méridien.

Le champ initial, et par conséquent les valeurs physiques qui seront conservées pendant le calcul, proviennent d'un calcul méridien, où le seul effet de blocage est dû à l'aube.

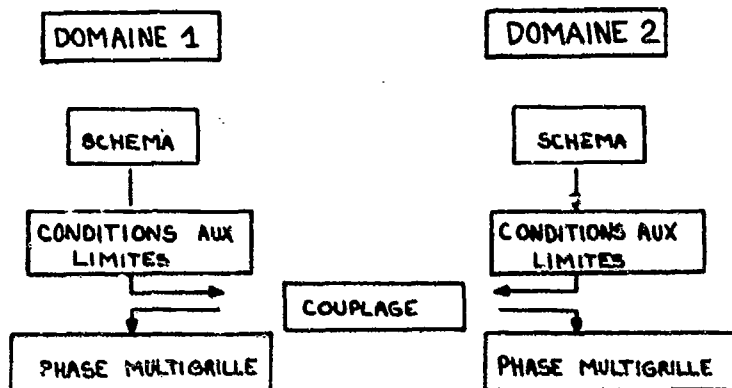
B. L'APPROCHE PAR SOUS-DOMAINES : SON IMPLEMENTATION

La résolution numérique des équations par une technique différences finies passe par l'élaboration d'un maillage. Dans le cas qui nous préoccupe, l'approche la plus simple consiste à créer 2 maillages adjoints remplissant le domaine de calcul, ayant donc des frontières communes. Un premier domaine est constitué, décrivant le canal inter-aube du moyeu à l'intrados nageoire, le second allant de l'extrados nageoire au carter.

La résolution numérique s'effectue suivant les étapes décrites ci-après :

- En supposant la solution connue au temps T^n , on applique le schéma d'avancement en temps à chaque domaine de calcul.
- Les conditions aux limites propres à chaque zone (glissement, périodicité, amont, aval) sont ensuite traitées.
- On effectue alors le couplage aux frontières communes des deux domaines, à l'aide des relations de compatibilité : A l'issue de cette phase, la détermination des variables de calcul sur ces frontières est unique.
- Puis l'on applique la phase multigrille d'accélération de convergence à chaque domaine de calcul.

Cette organisation est résumée dans le diagramme ci-dessous :



Nous allons maintenant expliciter chaque phase.

C. RESOLUTION NUMERIQUE

1. Pas d'avancement en temps

Nous adoptons ici le classique schéma de MacCormack, du type prédicteur-correcteur, que l'on écrit :

$$T^n, T^{n+1} = T^n + \Delta T$$

$$U^{n+1} = U^n - \Delta T \left(\frac{\partial^+ F^n}{\partial x} + \frac{\partial^+ G^n}{\partial y} + \frac{\partial^+ H^n}{\partial z} - K^n \right)$$

$$U^{n+1} = \frac{1}{2} \left(U^n + U^{n+1} - \Delta T \left(\frac{\partial^- F^{n+1}}{\partial x} + \frac{\partial^- G^{n+1}}{\partial y} + \frac{\partial^- H^{n+1}}{\partial z} - K^{n+1} \right) \right)$$

où $\partial^+ \partial^-$ désignent respectivement des dérivées décentrées avant et aval. Une viscosité artificielle est ajoutée et un lissage du quatrième ordre est effectué, à l'issue de cette séquence.

2. Conditions aux limites

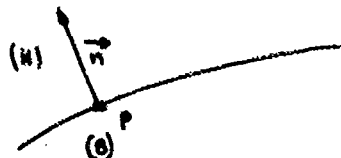
Toutes les conditions aux limites sont traitées grâce aux relations de compatibilité. Le lecteur trouvera une description détaillée de leur justification et de leur utilisation dans les références 4, 5, 6. Nous nous contentons de développer la méthode de couplage, dont l'utilisation est simple et fiable, en ce sens qu'elle n'induit pas d'oscillations parasites.

En effet, en supposant l'existence de deux valeurs

$$U_S = (P_S^{n+1}, U_S^{n+1}, V_S^{n+1}, W_S^{n+1}, T_S^{n+1}) \text{ et}$$

$$U_H = (P_H^{n+1}, U_H^{n+1}, V_H^{n+1}, W_H^{n+1}, T_H^{n+1})$$

issues du schéma en un même point P appartenant à deux domaines différents, ici (H) et (S). Soit \vec{n} la normale intérieure au domaine (H) au point P.



(ici u^*, v^*, w^* désignent les valeurs de la vitesse relative dans un repère orthonormé de premier vecteur \vec{w}^*).

Si u est supersonique, c'est le domaine amont qui impose son champ.

Si u est subsonique, $u > 0$, nous disposons de 5 relations de compatibilité.

$$(1) \quad -\rho u^{nn} + p^{nn} = -\rho u u_n^{nn} + p_n^{nn}$$

$$(2) \quad -v^{nn} = -v_n^{nn}$$

$$(3) \quad -w^{nn} = -w_n^{nn}$$

$$(4) \quad -\alpha^2 p^{nn} + p^{nn} = -\alpha^2 p_s^{nn} + p_s^{nn}$$

$$(5) \quad -\rho(-u^{nn}) + p^{nn} = -\rho(-u_s^{nn}) + p_s^{nn}$$

associées respectivement aux valeurs propres $(u^n, -u^n, -u^n, -u^n, (-u^n) - \alpha)$ du système linéarisé (réf 4.), la première l'étant dans le domaine (H), les quatre suivantes dans le domaine (S). Le système linéaire d'ordre 5 a un déterminant non nul, donc une solution unique, valeur qui est alors imposée au point P.

Notons que cette technique permet également de traiter le cas des frontières périodiques.

1. Accélération de la convergence

Une phase multigrille, développée à partir des travaux en bidimensionnel de Vuille et Guénilier à l'ONERA, et basée sur la formulation de REX HAN (réf. 3) a été implantée dans les codes tridimensionnels en usage à la SNECMA. La seule contrainte est de disposer d'un maillage ayant dans chaque direction un nombre de points égal à $K \times 2^m + 1$, K étant le même dans chaque direction. Les gains en temps CPU sont en moyenne de 33 % avec 3 grilles d'accélération. Ce faible résultat, à comparer au 70 % ou plus obtenu en bidimensionnel s'explique par :

- le calcul à chaque itération multigrille des coefficients d'interpolation, des volumes des cellules et des surfaces des mailles, ceci afin d'économiser de la place mémoire,
- du faible nombre de grilles d'accélération (3) en raison du nombre de points de maillage (337X1331).

D. PRÉSENTATION ET ANALYSE DES RÉSULTATS OBTENUS

Sous présentons dans les planches 1 à 3 les résultats de calcul obtenus avec le code "nageoire" à comparer avec les mêmes résultats obtenus avec une formulation et une résolution numérique identiques pour la même aube, dépourvue de nageoire. On mesure donc l'effet relatif de la nageoire sur des paramètres globaux (rendement, taux de compression...) ou locaux (répartitions de Mach, de pression...)

Si l'influence locale de la nageoire est évidente (fig 1. et suivantes), son effet global ne l'est pas moins.

On attribuera l'origine de celui-ci - malgré la relativement faible portance de la nageoire - à la forte distorsion des lignes de courant. Ces dernières subissent en effet l'influence de la distorsion de la nappe de choc - attachée, côté extrados, au bord de fuite de la nageoire.

Ceci se traduit par une modification de la déviation dans la partie supérieure de l'aube et au voisinage de la nageoire.

Par conséquent, la loi de travail des coupes est profondément affectée. En particulier, les coupes de tête, plus vannées, ont un meilleur rendement.

CONCLUSION

L'emploi d'un code tridimensionnel permet de mesurer l'effet relatif d'une nageoire sur l'écoulement dans un canal inter-aube.

La SNECMA utilise donc systématiquement cet outil dans le développement des aubes de soufflante munies de nageoires car il permet une bonne optimisation aérodynamique de la géométrie complète de l'aube.

REMERCIEMENTS

Je tiens à remercier G. MONFORT pour avoir le premier développé un code tridimensionnel instationnaire à la SNECMA.

Je tiens également à remercier tous les personnes ayant participé à la réalisation matérielle de ce document.

REFERENCES

- 1 - BROCHET J. - Numerical Computation of 3D transonic Internal Flows - La recherche Aérospatiale, n°5, 1980, pp. 301-315 (english Version).
- 2 - ENSERME M., BROCHET J. and BOISSEAU J.P. - low Cost 3D Flow Computations using a Mini system - AIAA J., Vol. 20, n° 11, 1982.
- 3 - BROCHET J., BOISSEAU J.P., ENSERME M., VEUILLOT J.P. - Calcul de l'écoulement tridimensionnel dans une roue axiale de soufflante. Mise en oeuvre sur un ordinateur parallèle 18^{ème} colloque d'Aérodynamique Appliquée - Fautiers, 18 - 20 Novembre 1981.
- 4 - CAMBIER L., GHASZI W., VEUILLOT J.P. and VIVIANO B. - Une approche par domaines pour le calcul d'écoulements compressibles - Computing Methods in Applied Sciences and Engineering V, North Holland, Amsterdam, 1982, pp. 423-446.
- 5 - VEUILLOT J.P. and CAMBIER L. A sub-Domain Approach for the Computation of Compressible Flows - Workshop IXIA sur "Les Méthodes Numériques pour les équations d'Euler pour les Fluides Compressibles Non visqueux" Rocquencourt, 7-9 Décembre 1981 - ONERA TP n° 1982 61.
- 6 - CAMBIER L., BESSON F. et VEUILLOT J.P. - Méthode multi domaines pour les équations d'Euler - Applications pour des aubes domaines avec recouvrement - La Recherche Aérospatiale
- 7 - VEUILLOT J.P., MEACZE G., A 3D Euler method for internal transonic flows computation with a multi-domain approach - Agard lecture series n° 140 paper n° 3.
- 8 - ROS-HO-WI - A multiple grid scheme for solving the Euler equations - AIAA Journal VOL 20 n° 11 nov - 1982 pp 1563 - 1571.

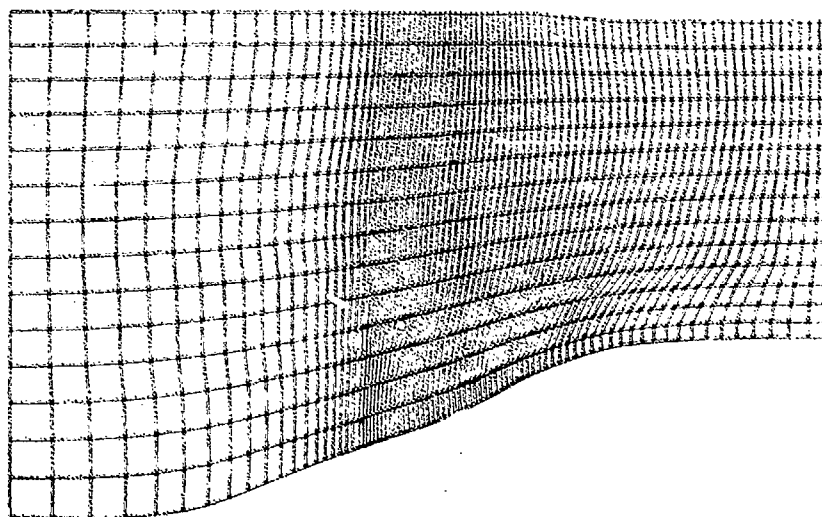
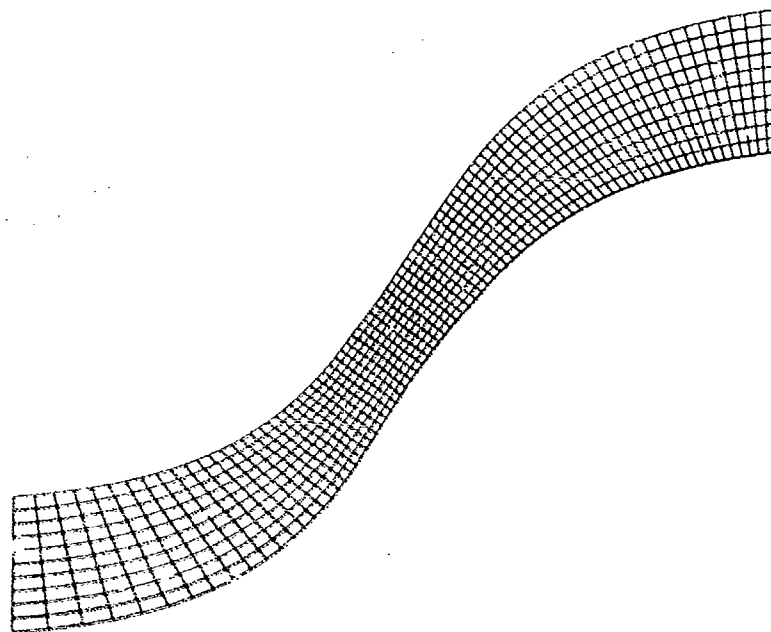


Fig 1. Railings - Can come negative

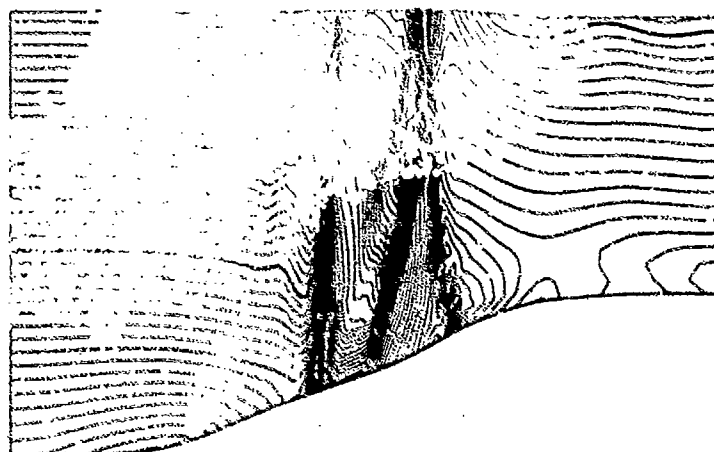
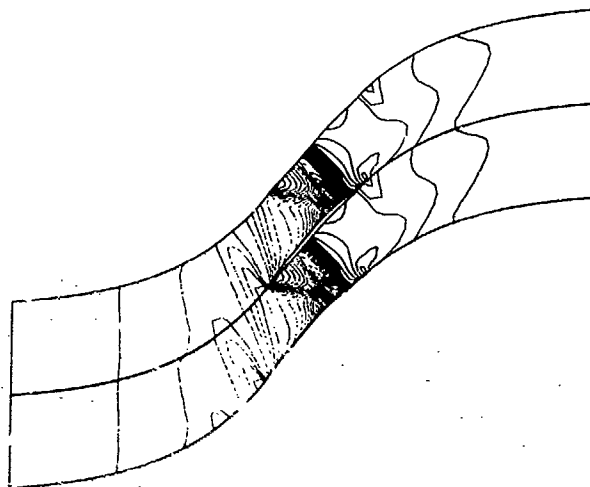


Fig 2. Lignes isolées - Cas sans régime

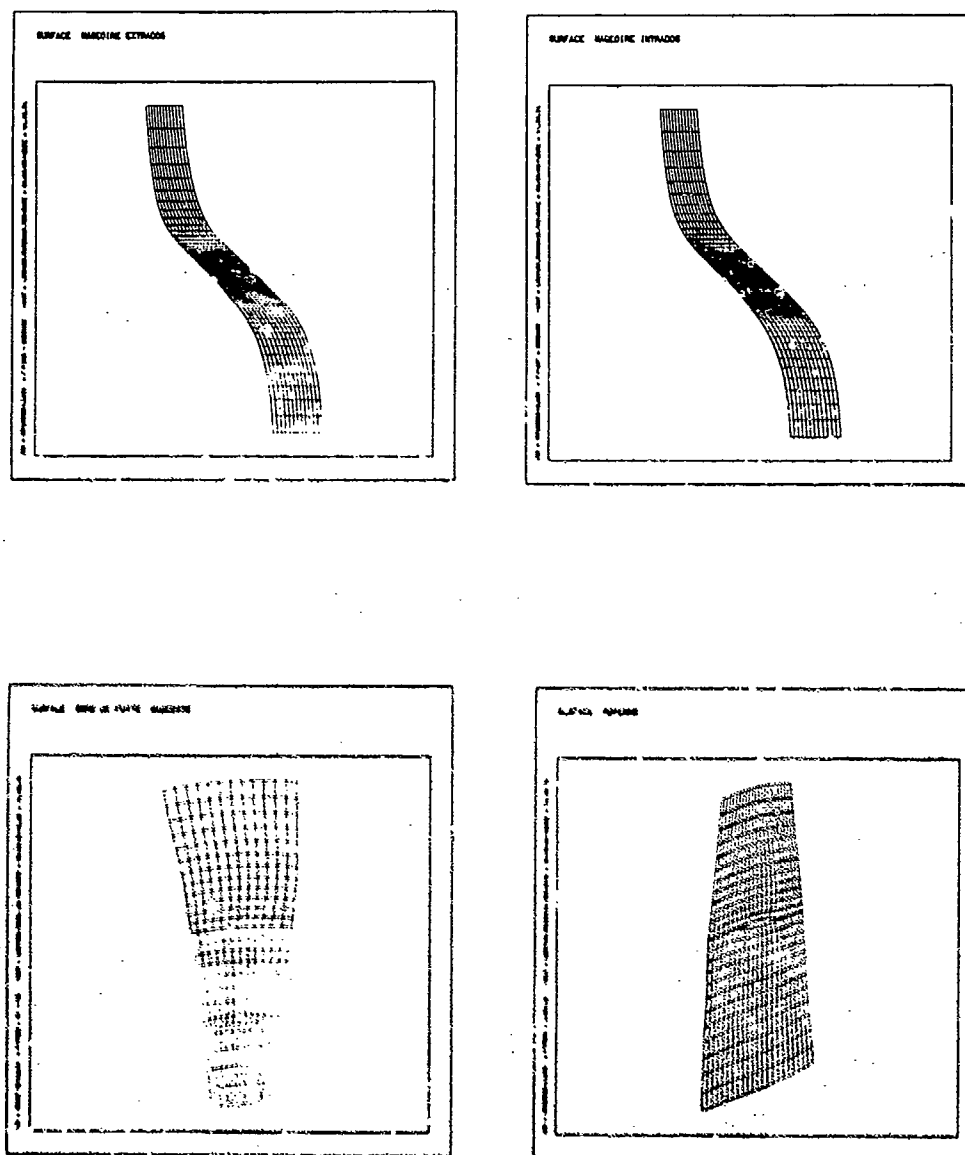
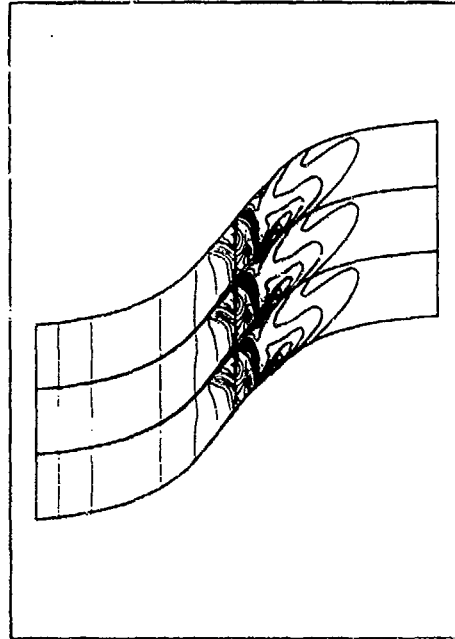


Fig 3. Maillage - Cas avec nageoire

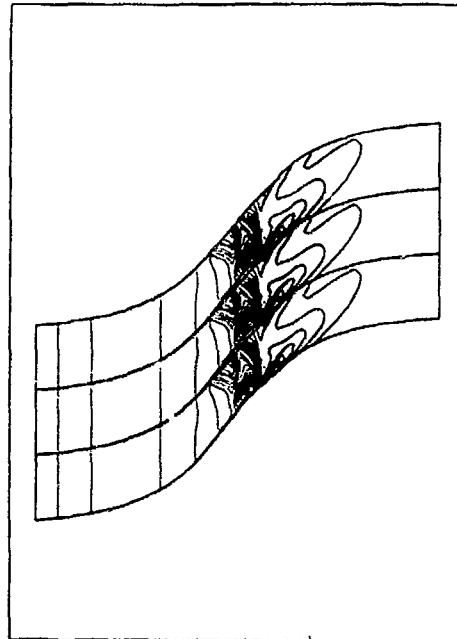
14-10

ZONE 8 COUPÉ 1



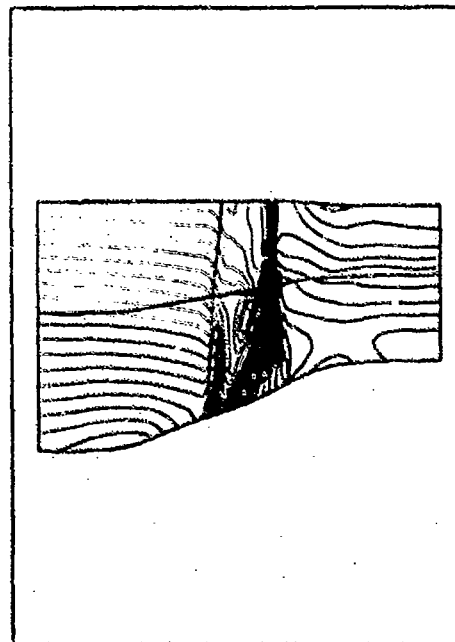
CALCUL INSTATIONNAIRE TRIDIMENSIONNEL - METHODE DES DOMAINES

ZONE 1 COUPÉ 2



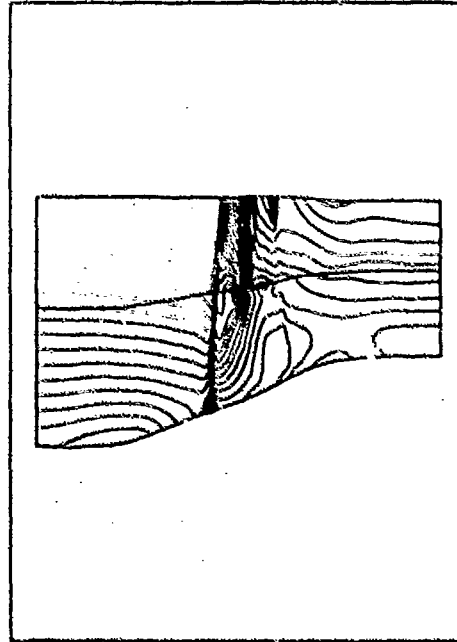
CALCUL INSTATIONNAIRE TRIDIMENSIONNEL - METHODE DES DOMAINES

COUPÉ 3



CALCUL INSTATIONNAIRE TRIDIMENSIONNEL - METHODE DES DOMAINES

COUPÉ 4



CALCUL INSTATIONNAIRE TRIDIMENSIONNEL - METHODE DES DOMAINES

Fig 4 - Lignes isobathes - Cas avec nappe

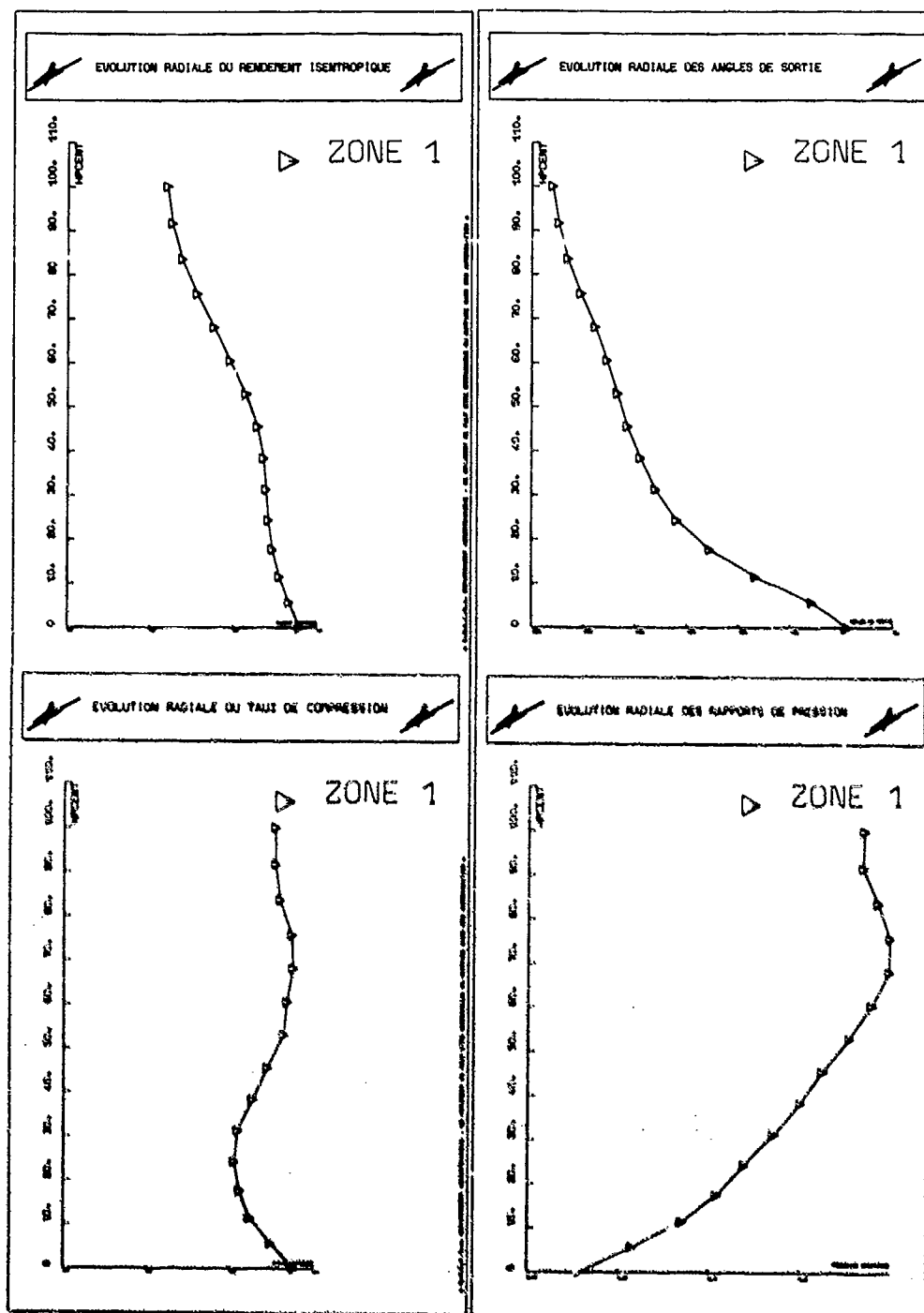


Fig 5. Répartitions radiales de paramètres globaux -

Coe sans nacelle

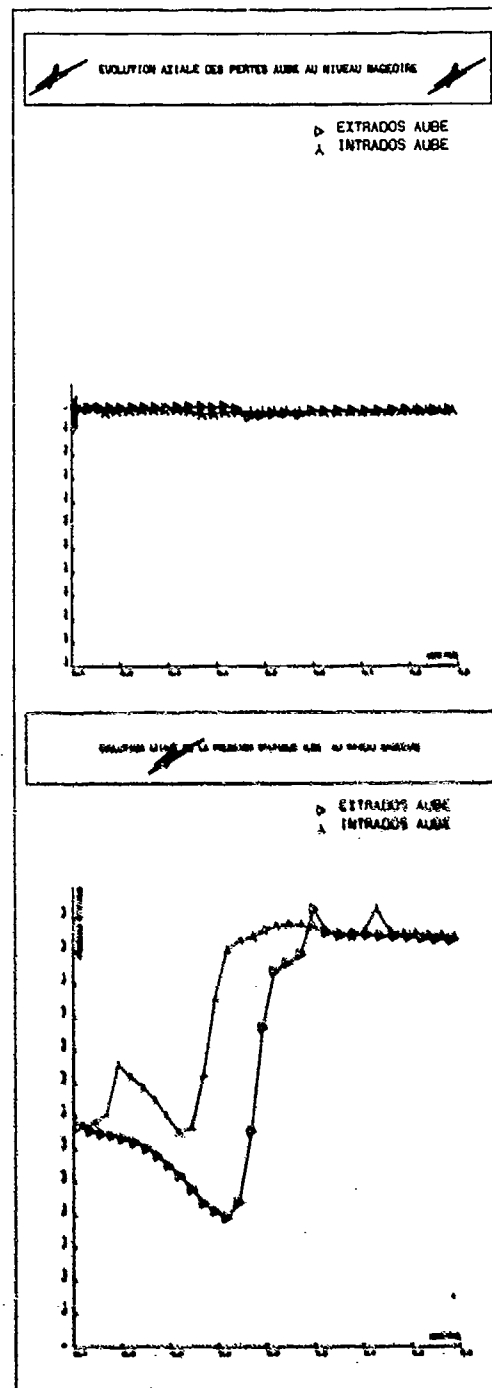


Fig. 6 - Répartitions axiales de variables locales -

Cas sans rageoire

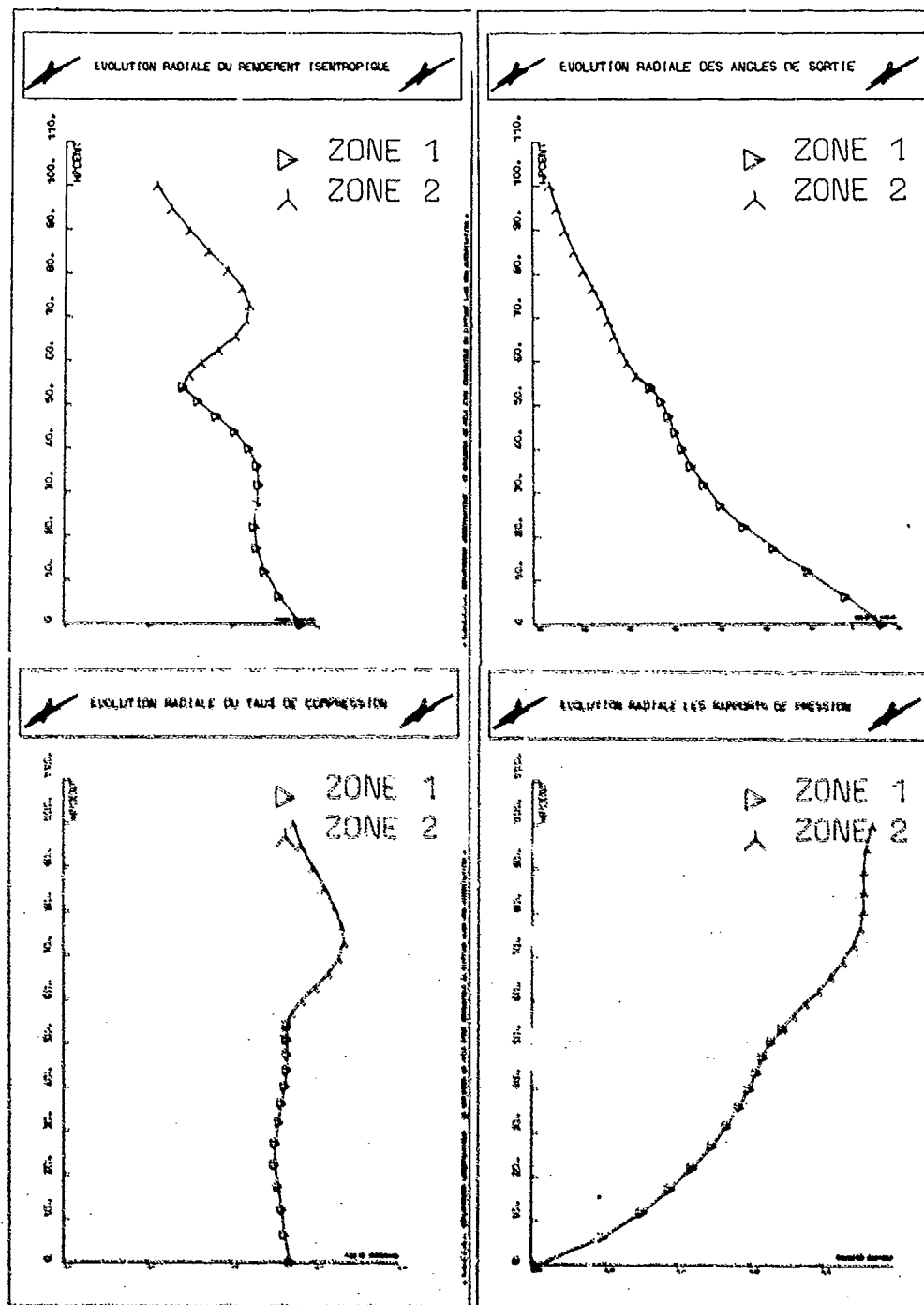


Fig. 7 Répartitions radiales de paramètres globaux -

Ces avec régime

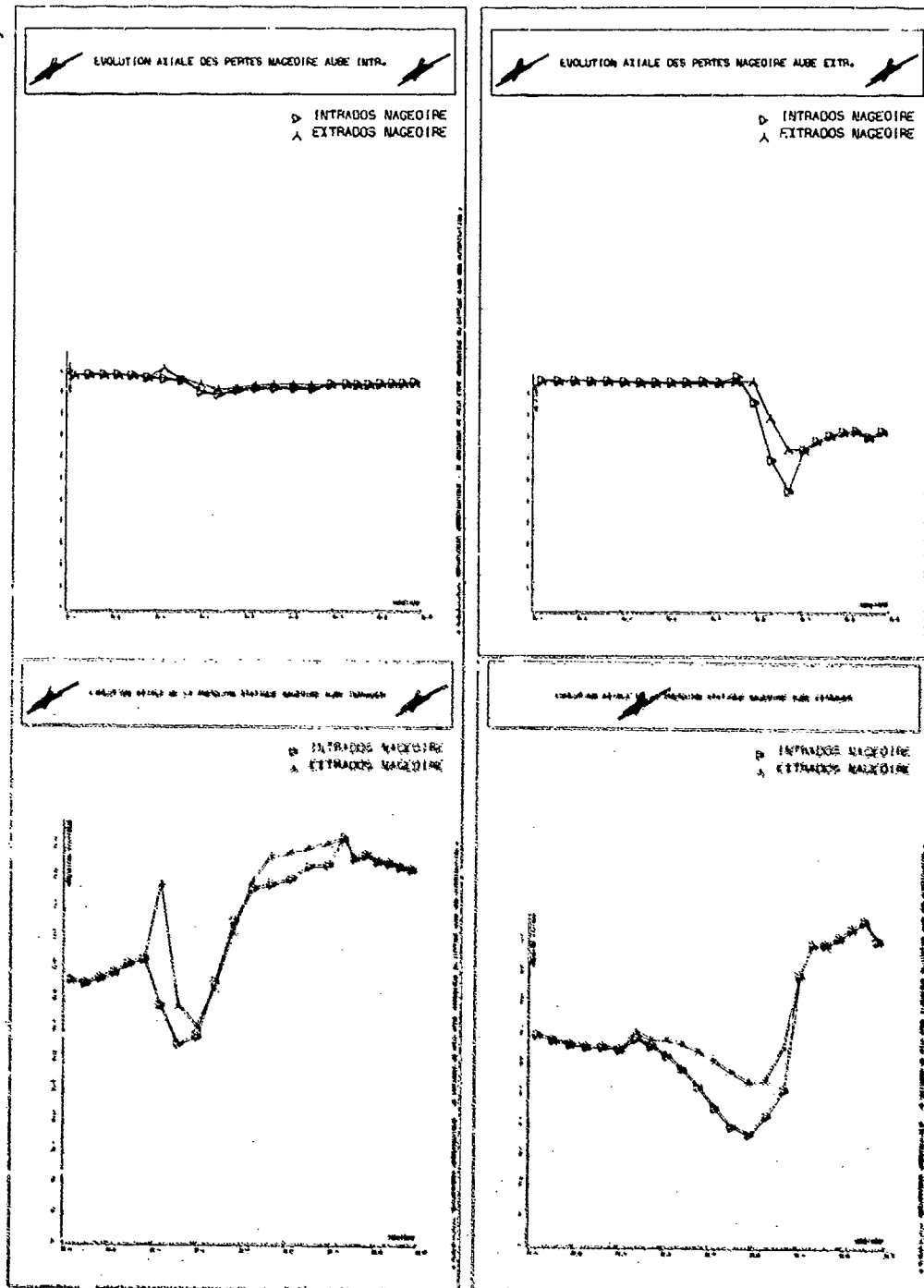


Fig. 8 Répartition axiale de variables locales

Ces avec nageoire

DISCUSSION

J.D.Denton, UK

I think that you said that you obtained 35% saving in computer time by using 2 levels of multigrid. I would have expected a much greater saving to about 1/3 of the original time. Is that what you meant to say?

Réponse d'Auteur

Le rapport de 35% est bien un gain en CPU; ces relativement modestes performances peuvent entre autre s'expliquer par:

- le calcul à chaque itération, (comptabilisé dans ces estimations dans la phase multigrid), des surfaces (il y en a 6) et des volumes de chaque "cube" élémentaire.
- La taille relativement élevée des mailles, pénalise l'évacuation des instationnarités à grande longueur d'onde.
- peut-être enfin par la complexité géométrique des cas traités.

H.Sto T, Switzerland

How did you prescribe the downstream boundary conditions for your two cases

- on the basis of a meridional flow (S2) computation?
- were they identical for both cases computed?
- was there a blockage factor considered for boundary-layer effects?

Réponse d'Auteur

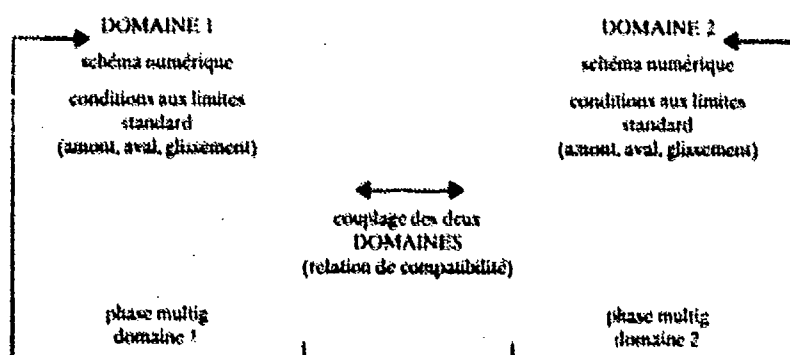
- Les conditions de pression aval, ainsi que l'initialisation viennent d'un calcul méridien ne prenant en compte que le blocage de l'aube. Nous n'avons pour ce cas introduit aucune perte par frottement.
- Néanmoins, au cours du calcul, seule la pression "avale-moyeu" est fixée. Un calcul simplifié d'équilibre radial ($dp = V^2/R dR$) permet d'obtenir la répartition aval et radiale de la pression statique.
- dans les deux cas, le champ méridien était le même (avec ou sans nageoire).

Ca.Hirsch, Be

Could you comment on the multidomain approach: How is the interaction defined, between the domains, and what is the effect on the overall accuracy.

Réponse d'Auteur

Le calcul s'effectue ainsi



AD-P005 515

A QUASI THREE DIMENSIONAL METHOD FOR THE CALCULATION OF TRANSONIC FLOWS IN TURBOMACHINES

Jörg Haller
Research Engineer
Universität Stuttgart
Institut für Luftfahrtantriebe
Pfaffenwaldring 6
D-7000 Stuttgart 80

Summary

A procedure based on the iterative coupling of flow calculations on S1 blade-to-blade stream surfaces and a flow calculation on an S2 hub-to-tip stream surface is described. The solutions on S1 surfaces of revolution are obtained by a time marching method in finite volume form, whereas a finite difference method is used for the S2 calculation. The finite difference method uses a stream function formulation based on a passage averaging technique in order to account for non-axisymmetric flows, especially with shocks inside a blade row. Sample calculations of a single-stage and a two-stage compressor are presented and compared with measurements.

List of symbols

b	geometrical displacement factor	w_r	radial velocity component
c_p	specific heat capacity at constant pressure	w_θ	circumferential velocity component
e	energy variable	w_z	axial velocity component
\hat{e}_r	unit vectors	z	axial coordinate
\hat{e}_θ		δ	relative flow angle
\hat{e}_z		θ	angular momentum
γ	momentum flux	Π	shear stress tensor
h_t	total enthalpy	ρ	density
j	rothalpy	ϕ	coordinate in circumferential direction
m	meridional coordinate	δ	dissipation
Ma	Mach number	ψ	stream function
p	pressure	ω	rotational speed
Q	heat per unit volume	∇	Nabla operator
r	radial coordinate		
R	gas constant	subscripts:	
R_e	right hand side energy equation	abs	absolute
R_g	right hand side momentum flux equation	rel	relative
R_θ	right hand side angular momentum equation	o	arbitrary reference conditions
R_ψ	right hand side stream function equation	r, θ, z	radial, circumferential, axial direction
v	relative velocity		

Introduction

Due to their high power concentration and pressure ratios, transonic compressors are widely used in modern gas turbines. The development of new components for gas turbines takes advantage of the rapidly growing ability to predict the flow through turbomachines by means of numerical calculations.

Since the three dimensional, unsteady and viscous flow through turbomachines cannot be analysed in this generality with the numerical methods available, simplified flow models are the basis of all calculation procedures. The majority of these numerical methods is restricted to two dimensional flow models, assuming steady flow conditions. Fully three dimensional methods have been developed, but their application is limited to isolated blade rows or single stages at best /1/. In order to reduce the required computer storage and calculation time, the flow is normally calculated either on an S2 hub-to-tip stream surface or on an S1 blade-to-blade stream surface. Some authors combine the computations on the S1 and S2 stream surfaces iteratively in order to calculate the influence of the bladeings more accurately, using a so called quasi three dimensional method /2/, /3/.

Many of these methods are not suited to calculate flows with Mach numbers close to unity because of singularities in the equations used, or are a priori restricted to subsonic or supersonic flows /4/, /5/.

This paper deals with a quasi three dimensional calculation procedure which has evolved out of a calculation method for the flow on an S2 stream surface, assuming axisymmetric flow. A modified version of this method has been coupled with a time marching method for blade-to-blade calculations in order to make it applicable to transonic flows in turbomachines.

Flow Model

All S1 and S2 stream surface calculations are based upon a theory developed by Wu /6/ which describes the steady, three dimensional flow through a blade row using solutions of iteratively coupled S1 and S2 stream surface calculations as shown in fig. 1. However, this theory is restricted to an isolated blade row. Owing to the relative rotation of two adjacent blade rows in a compressor or turbine stage, the S2 stream surfaces of the first blade row cannot be linked with the S2 stream surfaces of the second blade row, when steady flow conditions are assumed.

In order to calculate the flow through multistage turbomachines, a single S2 stream surface per blade row is used in the approach described here. Figure 2 shows this single S2 stream surface together with the S1 stream surfaces which are defined by rotating the streamlines in the meridional plane around the machine axis. The shape of the S2 stream surface can be obtained by averaging the flow variables on the S1 surfaces in circumferential direction, as will be described more detailed in one of the following chapters. In the iterative process of S1 and S2 calculations, the stream surface shapes are allowed to change. The calculation stops when the changes have fallen below a prescribed value. This flow model is called a quasi three dimensional flow model in this paper. The S2 stream surface is prescribed for the hub-to-tip calculation only in the blade row regions, whereas in the bladeless annular duct regions an additional equation for the angular momentum is solved.

Hub-to-Tip Calculation Procedure

This part of the quasi three dimensional system has its origin in a through flow method assuming axisymmetric flow /5/, /7/. The basic equation is a modification of Wu's equation. Similar equations are derived for rotor, stator and bladeless annular duct regions. As is usual in turbomachinery flow calculation, the stream function ψ , the total enthalpy h_t and the entropy s are used as main computational variables. The density is calculated out of the density-mass flow relation (see fig. 1) with the help of a Newton-Raphson iteration.

This original calculation procedure is applicable to purely subsonic or purely supersonic flows. Transonic flows cannot be treated because of the ambiguity in the density - mass flow relation. The method lacks of an adequate criterion for the location of the sonic line, where the density calculation has to switch from the subsonic branch in fig. 1 to the supersonic branch or vice versa. Another difficulty of the basic method is the representation of shocks inside the blade rows as shown in fig. 4. It is obvious that these shocks cannot be represented adequately by an axisymmetric flow model neglecting variations of the flow variables in circumferential direction.

Several modifications have been made in order to remove these deficiencies of the original method. Variations of the flow variables in circumferential direction can be taken into account by integrating the fundamental equations for three dimensional flows in circumferential direction as proposed by several authors /7/, /1/. In order to develop circumferentially integrated equations, the following averaged value of an arbitrary flow variable is introduced:

$$\bar{u}(r,z) = \frac{1}{\phi_1(r,z) - \phi_2(r,z)} \int_{\phi_1(r,z)}^{\phi_2(r,z)} u(r,\theta,z) d\theta \quad (11)$$

Hirsch and Hartge /1/ propose to introduce a second, mass averaged variable

$$\bar{u}(r,z) = \frac{1}{\phi_1(r,z) - \phi_2(r,z)} \frac{1}{\bar{\rho}(r,z)} \int_{\phi_1(r,z)}^{\phi_2(r,z)} u(r,\theta,z) \bar{\rho}(r,\theta,z) d\theta \quad (12)$$

Thus, flow variables can be separated into circumferentially averaged values and fluctuation terms similar to the treatment of variables in turbulent flows. This approach is especially helpful in shock regions as depicted in fig. 4 or in turbine blade regions with a sonic line. Regarding an idealized one dimensional flow on an S1 stream surface with a normal shock (see fig. 5) and assuming parallel streamlines in the meridional plane, an average Mach number can be defined which may decrease continuously in the shock region as shown in fig. 6. The curve crosses the critical value, although the average mass flux con-

responding to the Mach number distribution does not reach the critical value. In the original axisymmetric approach the critical Mach number corresponds to a critical mass flux, thus leading to inaccurate results in regions with shocks or sonic lines.

As is described by Hirsch and Warzee, the range of the averaging region extends from the suction side of one blade to the pressure side of the adjacent blade. The following circumferentially integrated equations can be derived by applying the averaging procedure of Hirsch and Warzee to the fundamental equations and switching from integral to differential notation:

$$\text{- continuity equation } V(\text{br}\bar{\rho}\bar{w}) = 0 \quad (3)$$

$$\text{- equation of motion } (\bar{w} \cdot \nabla) \bar{w} + 2\bar{w} \cdot \bar{\omega} + \frac{1}{\rho} (\bar{w} \cdot \bar{r}) + \frac{1}{\rho} \bar{V} p - \frac{1}{\rho} \bar{V} \Pi + \frac{1}{\text{br}\bar{\rho}} \nabla(\text{br}\bar{\rho} \bar{w}') = 0 \quad (4)$$

$$\text{- energy equation } \bar{w} \cdot \nabla \bar{e} = - \frac{1}{\rho} \bar{Q} + \frac{1}{\rho} \bar{\theta} + \frac{1}{\rho} \bar{w} \cdot \nabla \Pi - \frac{1}{\text{br}\bar{\rho}} \nabla(\text{br}\bar{\rho} \bar{w}') \quad (5)$$

The pressure gradient in the equation of motion is normally replaced by an entropy gradient and an enthalpy gradient, if a stream function formulation of the equations is used. In the method described here, the momentum flux variable

$$q = \rho w' + p \quad (6)$$

is used instead of the entropy as a main computational variable. It is better suited for the description of flows with shocks and allows to compute the density out of the main variables by solving a simple quadratic equation instead of the iterative procedure. The stream function equation can now be developed, using the following definition equation

$$\nabla \psi = -\text{br}\bar{\rho} \bar{w}_r \bar{e}_r + \text{br}\bar{\rho} \bar{w}_\theta \bar{e}_\theta \quad (7)$$

and projecting the equation of motion into a direction N orthogonal to the averaged velocity vector as shown in fig. 1. The transport equation for the momentum flux may be derived by projecting the equation of motion into the direction of the velocity vector \bar{e} . The angular momentum equation is derived by a projection into the circumferential direction. The averaging procedure is also valid in the bladeless duct if the integration is carried out over the whole circumference. Thus, the following set of equations can be established:

$$(1 - \bar{w}_\theta^2) \frac{d\bar{r}}{dl} + (1 + \bar{r}) \frac{d\bar{r}}{dl} = \bar{w}_\theta \quad \bar{r} = 1 + \frac{\bar{w}_\theta}{\bar{r}} \bar{w}_\theta^2 \quad (8)$$

$$\bar{w}_\theta \frac{d\bar{r}}{dl} = \bar{w}_\theta \quad (9)$$

$$\bar{w}_\theta \frac{d\bar{r}}{dl} = \bar{w}_\theta \quad (10)$$

The coordinates l and x are streamline oriented coordinates according to fig. 1. This set of equations is valid for rotor, stator and bladeless annular duct regions. In each of the three regions the variables have to be used in accordance with table 1. In the bladeless annular duct regions, the angular momentum equation has the form

$$\bar{w}_\theta \frac{d\bar{r}}{dl} = \bar{w}_\theta \quad \bar{r} = r \bar{w}_\theta, \text{ abs} \quad (11)$$

A complete description of the entire method can be found in [8].

TABLE 1

	ROTOR/STATOR	ANN. DUCT
\bar{w}_θ	$\frac{\bar{w}_\theta}{\bar{r}}$	$\frac{\bar{w}_\theta}{\bar{r}}$
\bar{e}	\bar{e}	$\bar{e}_{t, \text{abs}}$
\bar{q}	\bar{q}_{rel}	\bar{q}_{abs}

Numerical Approximation

The equations are discretized with a finite difference approximation of the derivatives. A nonorthogonal, contour adapted grid is used in the meridional plane, see fig. 8. In order to keep the discretisation schemes simple, this grid is transformed to an orthogonal equidistant grid shown in fig. 9.

The algebraic system of equations for the unknown stream function values at the grid points in one row $j = \text{const.}$ is solved by a successive line overrelaxation method. In order to ensure stability, centered discretisation schemes are used in the subsonic regime, whereas one sided discretisation schemes following the approximations of Murman and Cole [9] are applied in the supersonic regime. The transport equations are solved with an explicit method based on centered discretisation schemes.

Boundary Conditions

Assuming meridional Mach numbers below unity, the stream function distribution has to be prescribed at every boundary of the computational domain, see fig. 8. Normally the computational domain is chosen in a way that allows the assumption of uniform parallel flow at the inlet boundary. The hub and tip boundaries are treated as streamlines. At the exit boundary, the stream function distribution is not known a priori. Therefore it is assumed to be equal to the distribution calculated at the row of grid points next to the exit. Although a partial differential approximation is used for the solution of the transport equations, they are ordinary differential equations. The initial values for their integration are taken from the inlet boundary.

Density Calculation

In order to solve the main system of equations, the velocity components, temperatures, pressures and the density have to be calculated out of the main computational variables. In the bladeless duct regions, the following equations are used to develop a quadratic equation for the density calculation:

$$\frac{\partial \rho}{\partial \eta} = \rho \frac{\partial \ln \rho}{\partial \eta} \quad (121)$$

$$\ln \rho = \ln \rho_0 \left(1 - \frac{T}{T_0} \right) + \frac{1}{\gamma} \ln \frac{p}{p_0} + \frac{1}{\gamma} \ln \frac{\mu}{\mu_0} \quad (122)$$

$$\rho_0 = \rho_{0,0} \left(1 + \frac{1}{\gamma} \ln \frac{\mu}{\mu_0} \right) \quad (123)$$

Using nondimensional variables, this equation takes into account the fluctuation terms introduced by the averaging procedure:

$$\ln \rho = \ln \rho_0 + \frac{1}{\gamma} \ln \frac{p}{p_0} + \frac{1}{\gamma} \ln \frac{\mu}{\mu_0} \quad (124)$$

The variables λ , δ and ϵ are defined as follows:

$$\lambda = \frac{1}{\gamma} \ln \frac{p}{p_0} + \frac{1}{\gamma} \ln \frac{\mu}{\mu_0} \quad (125)$$

$$\delta = \frac{1}{\gamma} \ln \frac{\mu}{\mu_0} \quad (126)$$

$$\epsilon = \frac{1}{\gamma} \ln \frac{p}{p_0} \quad (127)$$

Figure 10 shows the graph of this equation. As can be shown easily, the maxima of the curves correspond to a critical meridional Mach number

$$\rho_{0,m} = \rho_0 \left(1 + \frac{1}{\gamma} \ln \frac{\mu}{\mu_0} \right) \quad (128)$$

In the rotor and stator regions the relative total enthalpy equation and the relative momentum flux equation are used besides eq. (121).

$$\rho_{rel} = \rho_{rel,0} \left(1 + \frac{1}{\gamma} \ln \frac{\mu}{\mu_0} \right) \quad (129)$$

$$\tilde{h}_{\text{rel}} = c_p (\tilde{T} - T_0) + \frac{1}{2} \tilde{w}_{\text{rel}}^2 + \frac{\rho \tilde{w}^2}{2\tilde{\rho}} \quad (21)$$

Here, the quadratic equation has the form

$$\Lambda \tilde{\epsilon}^2 - \Gamma \tilde{\epsilon} + \Omega = 0 \quad (22)$$

In this case Λ , Γ , and Ω are defined in a similar way as in the annular duct region, but with the relative variables for total enthalpy, momentum flux and velocity. The additional variable Ω may be defined with the help of the velocity component in circumferential direction calculated on the S1 stream surfaces:

$$\Omega = 1 + \frac{(1 - \frac{R}{2c_p}) \tilde{w}_\phi^2}{R T_0 (1 + \frac{\tilde{h}_{\text{rel}}}{c_p T_0})} \quad (23)$$

Again, this quadratic equation has a solution for $\tilde{\epsilon}$ corresponding to meridional Mach numbers below unity and another solution corresponding to meridional Mach numbers above unity. In order to avoid any ambiguity, the application of the method is restricted to flows with meridional Mach numbers below unity. This restriction seems to be reasonable because most of today's transonic turbomachines are operated in this regime.

Blade-to-Blade Calculation Procedure

Time marching methods solving the unsteady Euler equations are widely in use for blade-to-blade calculations. Their advantages are the shock capturing capabilities and the hyperbolic character of the unsteady Euler equations in both the subsonic and the supersonic regime, thus allowing the application of a single numerical solution procedure.

Using the equations for three dimensional flows as a starting point for the development of flow equations on S1 stream surfaces, a local coordinate system tangential to the S1 stream surface is introduced, see fig. 11. The S1 surface is regarded as the center surface of a thin stream sheet. With the following assumptions, the number of independent variables in the equations is reduced from three to two, namely the m and ϕ directions:

- no velocity component normal to the stream surface is admitted
- the momentum equation in the normal direction is not taken into account
- derivatives of the flow variables normal to the stream surface are neglected

The resulting system of equations can be written as follows

$$\int_V \frac{\partial U}{\partial t} dV + \oint_{\hat{A}} (\underline{F} \underline{e}_m + \underline{G} \underline{e}_\phi) \cdot d\hat{A} + \int_V \underline{H} dV + \underline{P} = 0 \quad (24)$$

the vectors having the following components

$$\underline{U} = \begin{pmatrix} \rho \\ \rho w_m \\ \rho w_\phi \end{pmatrix}, \quad \underline{F} = \begin{pmatrix} \rho w_m \\ \rho w_m^2 + p \\ \rho w_m w_\phi \end{pmatrix}, \quad \underline{G} = \begin{pmatrix} \rho w_\phi \\ \rho w_m w_\phi \\ \rho w_\phi^2 + p \end{pmatrix}, \quad \underline{H} = \begin{pmatrix} 0 \\ -(2\rho w_\phi + w^2 R \rho) \frac{dr}{dm} \\ 2\rho w_m \frac{dr}{dm} \end{pmatrix}, \quad \underline{P} = \begin{pmatrix} 0 \\ k \\ 0 \end{pmatrix} \quad (25)$$

Vector \underline{P} stands for the force exerted on the flow in meridional direction as a result of stream sheet thickness variations. \hat{A} is the surface of a volume element without the upper and lower cover surfaces of the stream sheet. The energy equation is replaced by the assumption of constant rothalpy in the rotating coordinate system or constant total enthalpy in the fixed coordinate system respectively. For the solution of the equations a finite volume method proposed by Lehthaus /10/ has been adopted.

Iterative Coupling of Hub-to-Tip And Blade-to-Blade Calculations

Having defined the total mass flow, the values of the flow variables at the inlet, the rotational speed and the machine geometry, the quasi three dimensional calculation begins with a calculation on an S2m stream surface. For this initial calculation, the distributions of the angular momentum and the shape of the stream surfaces in the blade region have to be estimated, while the fluctuation terms may be neglected.

Now the boundary conditions for the blade-to-blade calculations, the stream sheet thickness distribution and the streamline shape in the meridional plane can be determined. The blade-to-blade calculations furnish the angular momentum, the S2 stream surface geometry, and the fluctuation terms for the next hub-to-tip calculation. These cycles of alternating S2m and S1 calculations are repeated until changes of the flow variable values remain below a prescribed level. Typically three to four cycles are carried out.

Hub-to-Tip Stream Surface Generation

Different approaches for the S_{2m} stream surface generation can be found in the literature. Often the stream surface is defined as the surface dividing the mass flow between two adjacent blades into two equal parts [11]. In the present method another approach is used. The average flow direction can be defined with the averaged velocity components w_m and w_θ . This flow angle distribution can be integrated on several S_1 stream surfaces. In order to form the S_{2m} stream surfaces, these lines have to be stacked in the radial direction, as is illustrated in fig. 12. Here, the line connecting the centers of gravity of the profile areas is taken as a reference line for the radial stack.

Results

The method has been applied to a single-stage transonic compressor shown in fig. 13. This compressor is designed for a total pressure ratio of 1.51 at a rotor tip speed of 350 m/s and a rotor inlet Mach number at the tip of 1.1. Calculations have been made with a mass flow of 14.7 kg/s at 100% speed. Radial pressure and velocity distributions have been measured behind the rotor and the first stator by means of radial traverse probes [12]. In the meridional plane a computational grid with 11 x 81 points has been chosen. No heat transfer or friction losses have been regarded. Five blade-to-blade calculations on different S_1 stream surfaces equally dividing the mass flow have been made for the rotor and the first guide vane. In the region of the second guide vane, an axisymmetric approach without any blade-to-blade calculation has been applied.

Figures 14a and 14b show the distributions of the relative Mach number on the hub and the tip S_1 stream surfaces respectively. In the tip region a shock appears, extending from the leading edge of one blade to the suction side of the adjacent blade. The distribution of fluctuation terms in the rotor tip region is illustrated in fig. 15. In the shock region, they amount to almost 4% of the total pressure at the inlet, having a second maximum near the trailing edge.

The accuracy of the coupled calculation system can be examined by comparing the averaged Mach numbers obtained by the S_1 calculations with the corresponding Mach numbers of the S_{2m} calculations. In fig. 16 this comparison is made for the S_2 flow model based on the averaging procedure in circumferential direction, whereas an axisymmetric S_2 flow model is used in fig. 17, where differences in the results of S_1 and S_2 calculations appear. This comparison shows that a flow model based on a passage averaging technique is preferable to S_2 calculations.

In fig. 18 the calculated relative flow angle at the rotor exit is compared with measurements. Increased discrepancies are found in the endwall region, where the influence of the endwall boundary layer has not been taken into account. In the total pressure plot, fig. 19, similar discrepancies appear in the endwall region.

As a second test case, a NASA two-stage axial fan [13] with a design total pressure ratio of 2.8, a rotor tip speed of 442 m/s and a rotor inlet Mach number of 1.5 at the tip has been chosen. A 15 x 91 point grid has been used for the through flow calculations and a 17 x 51 point grid for the blade-to-blade calculations. Friction and heat transfer have again been neglected. Five blade-to-blade calculations on different S_1 surfaces have been made for every blade row. Figure 20 shows the streamline geometry in the meridional plane. The results depicted in fig. 21 to fig. 24 show generally good agreement with measurements.

Calculations were executed on a Cray 1/N computer. A typical run for a hub-to-tip calculation took 28 s, whereas 19 s were needed for a blade-to-blade calculation.

Conclusions

A quasi three dimensional system suited for the calculation of transonic flows through turbomachines has been developed. A through flow method based on circumferentially integrated equations has proven to be an appropriate means of treating flows with deviations from axisymmetry, especially in passage shock regions. Although restricted to flows without frictional losses so far, loss models based on the well known correlations or integral boundary layer methods could be adopted to predict the losses.

References

- 1/ Denton, J.D.
The Calculation of Fully Three Dimensional Flow Through Any Type of Turbomachine Blade Row
AGARD - LS - 140, 1985
- 2/ Jennions, I.C., Stow, P.
A Quasi-Three-Dimensional Turbomachinery Blade Design System
J. Eng. Gas Turbines and Power, Vol. 107, April 1985

- / 3/ Hirsch, Ch., Warzee, G.
An Integrated Quasi Three Dimensional Finite Element Calculation
Program for Turbomachinery Flows
ASME Paper 78 - GT - 56, 1978
- / 4/ Hüvel, B.
Berechnung der Strömung in Axialverdichtern mit einem 2D-Verfahren unter
Berücksichtigung der Seitenwandgrenzschicht und Sekundärströmung
Universität Stuttgart, Inst. f. Luftfahrtantriebe, Dissertation 1980
- / 5/ Hiebel, J.
Beitrag zur Berechnung von Unter- und Überschallströmungen unter
Berücksichtigung von Strömungsverlusten und Wärmeflüssen
Universität Stuttgart, Inst. f. Luftfahrtantriebe, Dissertation 1980
- / 6/ Wu, Ch.-H.
A General Theory of the Three-Dimensional Flow in Subsonic and Super-
sonic Turbomachines of Axial-, Radial-, and Mixed-Flow Types
NACA TN 2644, 1957
- / 7/ Sandel, W.
Viscous Effects and Heat Transfer in a Calculation Method for Axial-
symmetric Flow in Multistage Turbomachines Using the Stream Function
in: AGARD CP 351, Viscous Effects in Turbomachines, 1983
- / 8/ Simmler, H.
Ein Stromfunktionsverfahren zur rotationssymmetrischen Berechnung der
transsonischen Turbomaschinenströmung unter Berücksichtigung der Strömungs-
unterschiede in Umfangsrichtung
Universität Stuttgart, Inst. f. Luftfahrtantriebe, Dissertation 1986,
to be published
- / 9/ Murman, E.M., Cole, J.D.
Calculation of Plane Steady Transonic Flows
AIAA-J., Vol. 3/1, 1971
- / 10/ Lohthaus, P.
Berechnung der transsonischen Strömung durch ebene Turbinengitter nach
dem Zeit-Schritt-Verfahren
Technische Universität Braunschweig, Dissertation 1978
- / 11/ Lücking, P.
Numerische Berechnung der dreidimensionalen reibungsfreien und reibungs-
behafteten Strömung durch Turbomaschinen
RWTH Aachen, Dissertation 1982
- / 12/ Huck, W., Naglitsch, J., Stang, U.
Experimentelle Untersuchung einer transsonischen Axialverdichterstufe
Versuchsbericht Teil 1 (Bodenversuche)
Universität Stuttgart, Inst. f. Luftfahrtantriebe
ILA-82 A 02, 1982
- / 13/ Ruggeri, R.S., Densser, W.A.
Performance of a Highly Loaded Two-Stage Axial-Flow Fan
NASA TN-X-3076, 1974

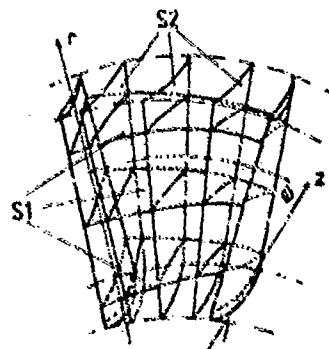


Fig. 1 Stream surface families proposed
by Wu

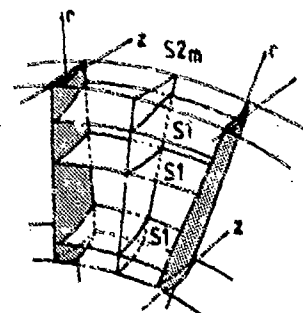


Fig. 2 Quasi three dimensional approach
using a single S_{2m} stream surface
and axisymmetric S_1 stream surfaces

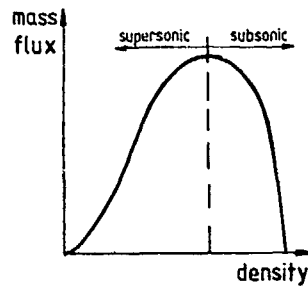


Fig. 3: Mass flux - density relation

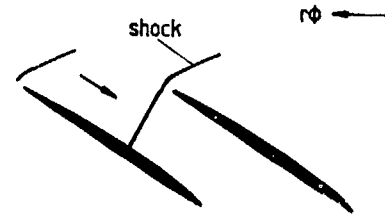


Fig. 4: Typical shock in a compressor blade

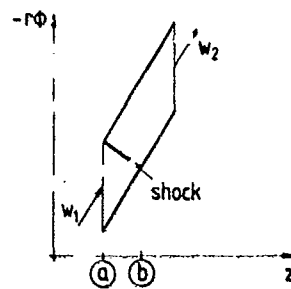


Fig. 5: Idealized, one dimensional flow on a SI surface with a shock

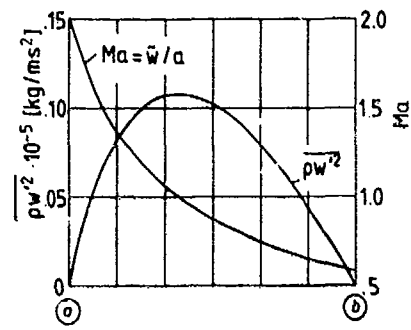


Fig. 6: Mach number and fluctuation terms in the shock region

BLADELESS DUCT	STATOR / ROTOR
<p> \mathbf{e}_t: Unit vector circumfer. direct. \mathbf{u}_m: Vector of averaged velocity \mathbf{n}: Normal vector $\mathbf{n} = \mathbf{e}_t \times \mathbf{u}_m$ $\mathbf{L} \parallel \mathbf{u}_m$ </p>	<p> \mathbf{n}: Stator normal direct. \mathbf{u}_m: Vector of averaged velocity \mathbf{n}: Normal vector $\mathbf{n} = \mathbf{n} \times \mathbf{u}_m$ $\mathbf{L} \parallel \mathbf{u}_m$ </p>

Fig. 7: Projection of the equation of motion

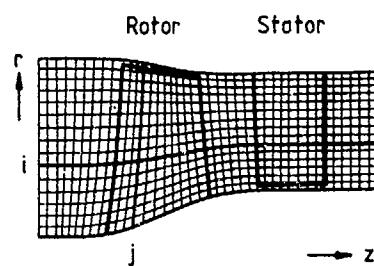


Fig. 8: Contour adapted grid

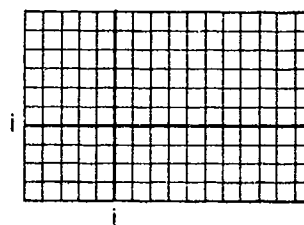


Fig. 9: Equidistant, orthogonal grid

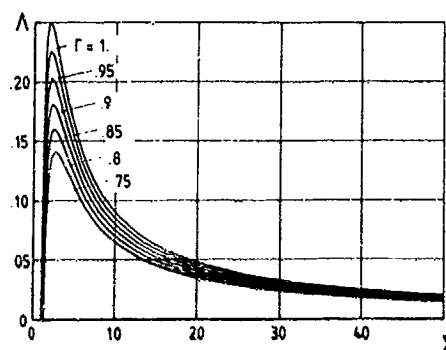
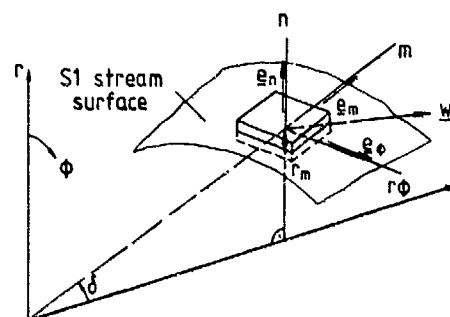
Fig. 10: Λ - ζ relation for $\kappa = 1.4$ with $r = f(\rho w^2)$ as curve parameter

Fig. 11: Local coordinate system for blade-to-blade calculations

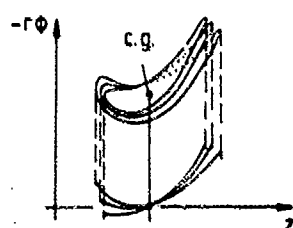


Fig. 12: radial stack of the S2m stream surface

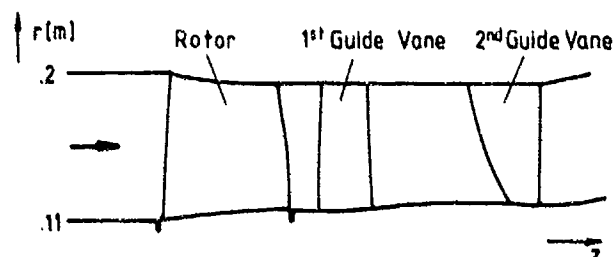
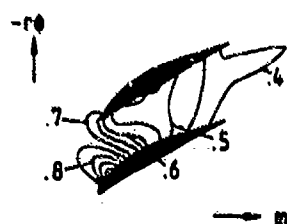
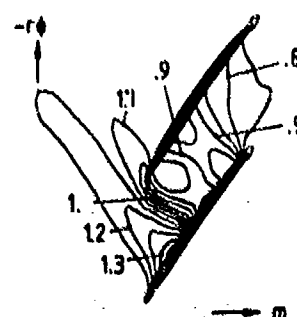


Fig. 13: Single-stage transonic compressor



a) Hub S1 stream surface



b) Tip S1 stream surface

Fig. 14: Relative Mach number distribution in the rotor

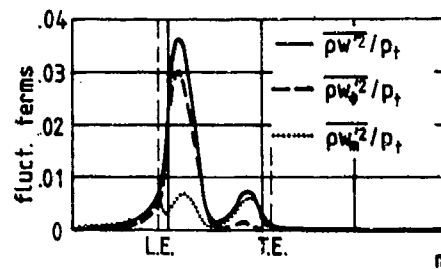


Fig. 15: Fluctuation terms evaluated on the tip S1 surface, normalized with the relative total pressure at the inlet

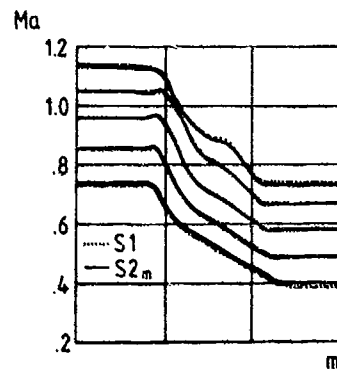


Fig. 16: Relative Mach number on 5 S1 surfaces; S1 solutions compared with circumferentially integrated S2m solutions

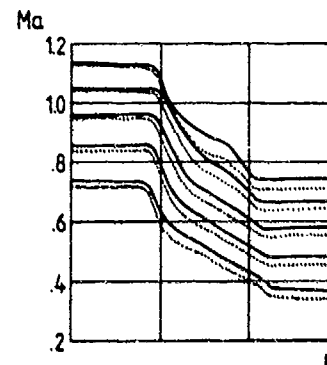


Fig. 17: Relative Mach number on 5 S1 surfaces; S1 solutions compared with axisymmetric S2m solutions

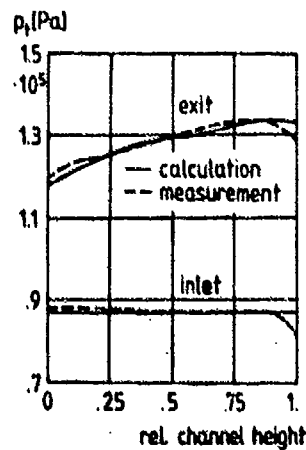


Fig. 18: Relative flow angle at rotor inlet and exit

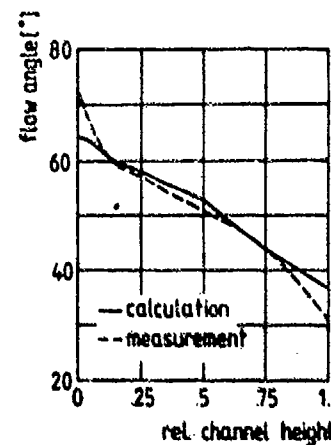


Fig. 19: Total pressure at rotor inlet and exit

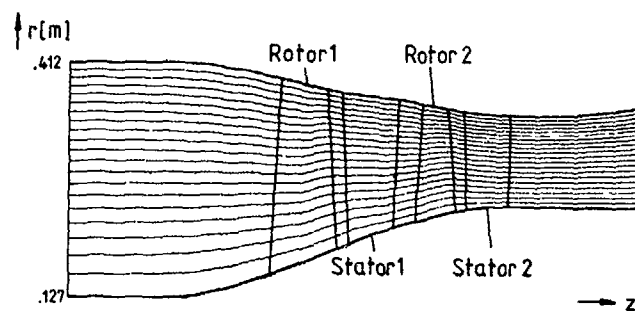


Fig. 20: NASA two-stage axial fan; streamline geometry

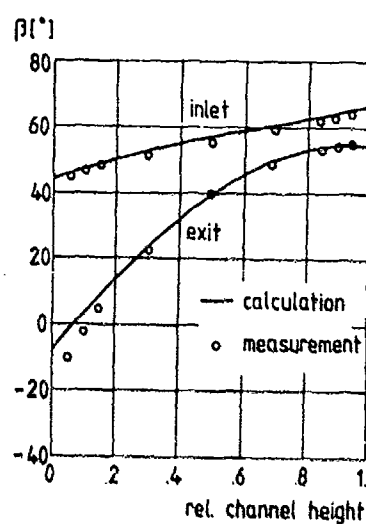


Fig. 21: Relative flow angle, rotor 1

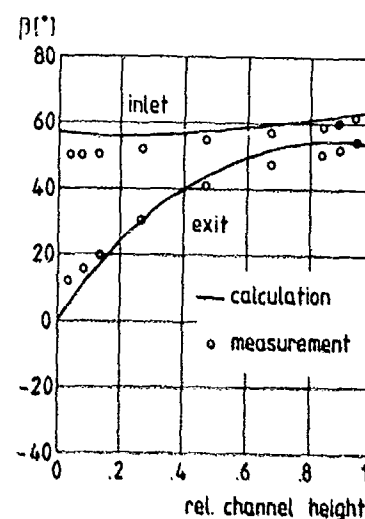


Fig. 22: Relative flow angle, rotor 2

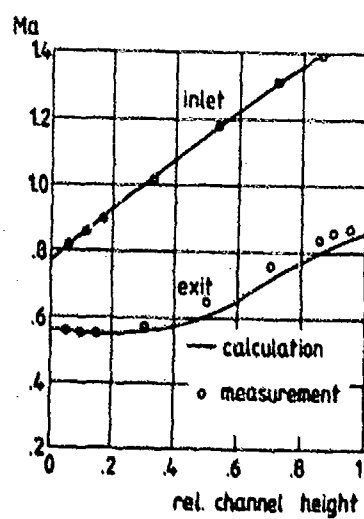


Fig. 23: Relative Mach number, rotor 1

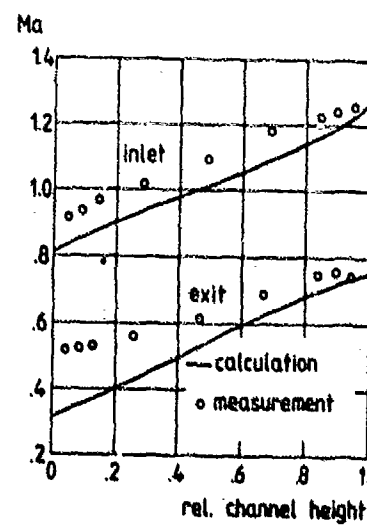


Fig. 24: Relative Mach number, rotor 2

DISCUSSION

J.D.Denton, UK

Did you have any loss model in your method other than the shock loss computed by the Euler calculation? If not, I do not think that you can expect good agreement with experiment for a single or multi-stage calculation.

Author's Reply

In this early stage of development we did not use any loss model. This will be done for the calculations to come.

P.Ramette, Fr

Do you plan to go to an adaptive grid in order to have a better shock capture?

Author's Reply

We have concentrated mainly on the development of the hub-to-tip calculation method. There are no plans at the present stage to use an adaptive grid which would increase the computation time considerably.

Ch.Hirsch, Be

What is the reason for the upwinding of the stream function in the S2 calculation since your approach, which fixes the relative tangential velocity, is elliptic for subsonic meridional Mach numbers?

Author's Reply

The tangential velocity is only used for the density calculation. The type of the stream function equation changes according to the relative Mach number in the rotor/stator region.

H.Stoff, Switzerland

Did you obtain your results on the basis of any empirical pressure loss input or input of endwall blockage? Are there any corrections for trailing-edge deviation? I presume that the term $\bar{p}w'^2$ contains empirical loss information (Fig.6).

Author's Reply

No empirical loss correlation or boundary layer blockage has been prescribed. The term $\bar{p}w'^2$ can be evaluated from the blade to blade results, even when the results are obtained with our Euler solver. See references 121 and 131 for further information.

F.Lebocuf, Fr

You take the fluctuations terms into consideration in your equations. Are they more important in the momentum or in the energy equation?

Author's Reply

They were not taken into account in the energy equation. They are important, for the momentum equation, in the shock region, amounting to 4% of the inlet total pressure.

F.Lebocuf, Fr

Prof. Hirsch has shown in an earlier paper, for a subsonic case, that those terms were not important in the momentum equation. You attribute their importance to the shock presence?

Author's Reply

Yes, and this is because of the flow pitch-wise asymmetry in this region (see Figure 4 or Figure 14 of the paper).

F.Lebocuf, Fr

Results from M.I.T. show that energy fluctuations are more important than momentum fluctuations. This is in contradiction with your results.

Author's Reply

I did not say that. I only say that I did not take them into account. I surely will have to do it in the future.



AD-P005 516

TRANSONIC THREE-DIMENSIONAL INVISCID CALCULATIONS IN TURBOMACHINES

F. Bassi

Politecnico di Milano
Dipartimento di Energetica
Piazza Leonardo da Vinci, 32
20133 Milano, Italy

M. Savini

CNPM/CNR
Viale Francesco Baracca, 69
20068 Peschiera Borromeo (MI), Italy

SUMMARY

This paper describes a finite volume Euler solver which has been applied to the calculation of the three-dimensional transonic flow field through straight cascades. The numerical algorithm, based on Jameson's approach, uses a centered space discretization, with explicit adaptive dissipation terms, and a three-stage Runge-Kutta method for the time integration; the convergence to the steady state solution may be enhanced by using local time step, residual smoothing, and enthalpy damping. The calculations were performed in a O-type grid, obtained by means of a constructive approach which guarantees good properties of smoothness, orthogonality, and resolution near the body. The computational code has been applied to two turbine blade cascades in transonic regime tested at von Karman Institute. Three-dimensional effects were introduced by imposing an inlet velocity profile normal to the endwall. The computational results show good agreement with the blades pressure experimental data and the code performed well in the prediction and development of the secondary flow vortices.

INTRODUCTION

The understanding and the prediction of the flow field within blade passages is a major problem in turbomachinery design. In the general case the flow is unsteady, turbulent and can be affected by relevant three-dimensional effects; moreover the flow is often transonic. Facing these problems, turbomachinery designers introduce various degrees of approximation in their analysis. In almost all cases the flow is considered two-dimensional; the influence of the viscosity is neglected at all or is taken into account with different levels of complexity, ranging from a boundary layer type formulation, in weak or strong interaction with the inviscid flow, to the compressible Navier-Stokes formulation with some kind of turbulence modelization.

Only recently numerical methods capable to solve the complete Navier-Stokes equations for three-dimensional turbulent flows have begun to appear, [1-5]. This is due both to the development of robust, reliable, accurate and fast numerical algorithms, e.g. the works of Mc Cormack, Beam and Warming, Jameson, Roe, Van Leer, and to dramatic improvement in computers performance. In the way of three-dimensional viscous calculations, the development of an Euler code can be considered an essential preliminary step to assess the properties of accuracy and robustness of the numerical algorithm. Moreover the shock capturing capability, the influence of the computational grid and the boundary conditions on the numerical results can be more easily analyzed. Notice that the computational results of an inviscid code can also give reliable predictions of blade pressure distribution, at least for accelerating flows in turbine blades.

The Euler code developed here is based on the explicit multi-stage Runge-Kutta algorithm introduced by Jameson et al. [6], and widely tested in a number of inviscid and viscous two-dimensional transonic calculations, both for internal and external flows, [7-9]. In the next sections the numerical solution of the governing equations is briefly outlined, and the grid generation technique and the boundary conditions treatment are presented. Finally computational results for two turbine blade cascades and some concluding remarks are given.

GOVERNING EQUATIONS AND NUMERICAL SOLUTION

The integral form of the Euler equations for a domain V with a fixed boundary S in a cartesian coordinate system (x, y, z) can be written in vector form as:

$$\frac{d}{dt} \int_V U dV + \int_S \mathbf{F} \cdot \mathbf{n} dS = 0 \quad (1)$$

where

$$W = \begin{bmatrix} \rho \\ \rho u \\ \rho v \\ \rho w \\ \rho E \end{bmatrix} \quad \vec{F} = \begin{bmatrix} \rho \vec{q} \\ \rho u \vec{q} + p \vec{i} \\ \rho v \vec{q} + p \vec{j} \\ \rho w \vec{q} + p \vec{k} \\ \rho E \vec{q} \end{bmatrix}$$

$$\vec{q} = u \vec{i} + v \vec{j} + w \vec{k}$$

$$E = e + \frac{1}{2} q^2$$

$$H = E + \frac{p}{\rho}$$

$$p = (\gamma - 1) \rho e$$

and $\vec{i}, \vec{j}, \vec{k}$ are unit vectors of the coordinate system, \vec{n} is the unit vector normal to the surface enclosing V , positive pointing outwards, u, v and w are the velocity components in x, y and z , ρ, p and E are respectively the density, pressure and total internal energy. The ratio of the specific heats γ is assumed constant and equal to 1.4.

The Eqn. (1) is applied to each hexahedral cell of the discretized domain. The numerical solution of Eqn. (1) follows the well known Jameson's scheme [6] and is briefly outlined below. By discretizing the surface integrals and by using the mean value theorem for the volume integral, a system of ordinary differential equations is obtained. The surface integrals are evaluated as arithmetic mean of the fluxes of adjacent cells. Thus the spatial discretization is second order accurate on a grid with slowly varying spacing. Second and fourth order artificial dissipation terms are added to the discretized form of Eqn. (1) in order to prevent oscillations near shocks and the even-odd decoupling. Note that the coefficient of the second order dissipative term is adapted to the local second difference of the pressure so that the second order accuracy of the scheme is not compromised in regions of smooth flow. The following explicit three-stage Runge-Kutta scheme has been used to advance the solution in time

$$W^{(k)} = W^{(0)} + a_k \frac{\Delta t}{V} [-C^{(k-1)} + D^{(0)}],$$

where C and D are respectively the net inviscid and adaptive dissipation contributions, evaluated as in Ref. [7], and $a_1 = a_2 = 0.6$. Observe that for computational efficiency the dissipative contribution is computed only once per time step, at the beginning of the Runge-Kutta cycle. If the steady state solution is of concern, the efficiency of the scheme can be improved by using local time step and a technique for implicit residual smoothing. If the flow has constant steady state total enthalpy, further improvement is obtained by means of an enthalpy damping technique.

COMPUTATIONAL GRID

The three-dimensional grid for cascades is obtained by stacking similar two-dimensional meshes in the z direction. The z distribution of similar meshes can be refined near the endwall. The two-dimensional mesh is algebraically generated. An O-type mesh was chosen in order to obtain the best resolution near the body and in the channel between blades without excessive distortion of the cells and without wasting many cells far from the blades. The use of an O-type mesh in the trailing-edge region may be questionable when solving the Euler equations; however, it should be noted that the unphysical effects of the artificial viscosity are confined in the trailing-edge region and in the wake and do not compromise the main results which one expects from an inviscid calculation on blade cascades, i.e. the blade pressure distribution and the downstream flow angle.

Briefly the grid generation here used defines a loop around the blade which consists of two periodic lines closed by cups upstream and downstream at prespecified distances from the blade. The position of the periodic boundaries is such that each point of these boundaries has the same distance from the blade surface of two adjacent blades. Once the external loop is formed, the points distribution on it is obtained in two steps: i) evaluation of the line integral of the inverse of the distances from the body; ii) interpolation of the curvilinear coordinate at constant fractional steps of the integral. The points

distribution on the body is also obtained in two steps: i) determination of the points where the straight lines from the outer loop intersect perpendicularly the blade surface; ii) smoothing of the points distribution so obtained in order to avoid abrupt variations of the distance between the points. The points on the two loops are then joined by means of splines in tension which form the second family of coordinate lines. By using these splines it is possible to obtain a family of lines which are normal to the blade surface and have two continuous derivatives across the periodic boundaries. Moreover intersections of lines of the same family are avoided acting on the tension factor. Finally the mesh point distribution on the 'normal' lines is given by a geometrical progression with variable ratio so as to have the second grid point of every 'normal' line at the same distance from the surface. This grid generation technique is very fast and leads to a 'well defined' grid as shown in Figs. 1 and 9. The only drawback (common to all O-type meshes) is the relative proximity of the 'far-field' to the blade; a point that could be important in a cascade with supersonic downstream conditions.

BOUNDARY CONDITIONS

Different types of boundary conditions must be set at the inflow and outflow of the domain, at the blade and endwall surfaces, at the midspan symmetry plane and at the periodicity surface. To improve the computational efficiency a strip of phantom cells is used at all boundaries.

Inflow boundary

According to characteristics theory, four variables can be specified at a subsonic inlet. We have chosen total enthalpy, flow direction (two angles) and entropy. Observe that these specifications correspond to the usual situation in wind tunnel experiments. The outgoing one-dimensional Riemann invariant, based on the u velocity component and on the sound speed in the first interior cell, gives the fifth relation necessary to determine the unknowns in the upstream boundary phantom cells. For computations inside blade rows, we considered that the axial direction was the most significant for the one-dimensional characteristics relations. In order to model the inlet boundary layer on the bottom wall, the entropy varies along the z direction so as to obtain the desired velocity profile. The assumption is made that the pressure is constant in the z direction. In this scheme the inlet entropy distribution varies if the inlet Mach number varies, and needs to be calculated at each time step.

Outflow boundary

As for the inflow boundary, the flow is considered one-dimensional in the x direction. With this assumption the characteristic relations allow to specify the Riemann invariant on the forward running characteristic, entropy, and the v and w velocity component from the interior of the domain. By giving the pressure at downstream infinity, one obtains the unknowns in the phantom cells. Notice that this boundary treatment is used also in those cells where the flow is incoming due to the shape of the downstream boundary and lets the pressure vary, to a certain extent, along the boundary as it happens in actual cascades.

Periodic and symmetry boundaries

At the periodic boundary cells, the variables are copied from those stored one pitch above or below, and at the midspan symmetry is enforced along the z direction.

Solid wall boundary

The solid wall boundary conditions are crucial in determining the amount of spurious entropy production along the body surface. The problem is not trivial and is still under investigation. In the present work the density in the phantom cells is extrapolated from the interior, and a reflection condition for the velocity is used. The normal momentum equation is solved for the pressure gradient at the wall, and this is used to obtain the pressure in the phantom cells.

TEST CASES AND RESULTS

Computational results for two transonic turbine cascades are presented and discussed. It is worth to mention that all calculations were performed on a supermini computer Gould 32/67 characterized by a peak velocity of 1.2 Mflops and a core memory of 4 Mbytes. The three-dimensional calculations started from a quasi-converged two-dimensional solution and were stopped at a 2.M.S. rate of change of density of $1.6E-4$. The convergence was reached for the two cases in about 500 time steps and the CPU time per step was 247 seconds. The first cascade is typical of a coolable gas rotor turbine section; the second one is a turbine nozzle characterized by a blunt leading-edge and a high stagger angle. Both cascades were tested at the von Karman Institute (Refs. [10-11]), and these experimental results are used to compare with the numerical ones. In both cases the computational grid was formed with $1024 \times 64 \times 12$ cells; the periodic boundaries extend for .5 and .8 of the axial chord upstream of the leading-edge and downstream of the trailing-edge respectively.

Fig. 1 shows the mesh used for the gas rotor turbine section. In order to assess the capability and accuracy of the method in describing three-dimensional effects, the endwall velocity profile shown in Fig. 2 was given as input for the upstream boundary. This test case was run with a pressure at downstream infinity corresponding to an isentropic Mach number of 1.21. However, due to the downstream boundary conditions treatment, the isentropic Mach number deduced from the arithmetic mean of the pressure values in the outflow boundary cells, resulted in a slightly lower value of 1.17. Fig. 3 presents the computed and experimental isentropic mach number on the blade surface at midspan. The agreement is fairly good, but the peak Mach number on the suction side is slightly underestimated due both to unsufficient mesh refinement and treatment of the trailing-edge region. In fact the isobars plot of Fig. 5 shows that the computed shocks at the trailing-edge are anticipated with respect to the reattachment shocks that appear in the Schlieren picture. A blade loading reduction at the endwall appears from Fig. 4 which compares midspan and endwall isentropic Mach numbers.

Fig. 7 gives the sequence of the secondary velocity vector plots in the plane sections shown in Fig. 6. As usual in the secondary flows representation, the vectors are the projection of the velocity vector at a point P onto a plane normal to the velocity vector at a point P' projection along z of the point P onto the midspan plane. The velocity vectors are all scaled by the inflow velocity. From the sequence of figures it is clearly visible the formation and the evolution of the passage vortex until it decays approaching the downstream boundary; in the left end corner of Figs. 7b and 7c it is even possible to see the suction leg of the horseshoe vortex which is rapidly damped by the passage vortex. Total pressure contours of Fig. 8 show the displacement of the low energy fluid from the pressure towards the suction side due to the vortex motion. In this picture one can also recognize that the spurious entropy production along the blade wall is limited to about 1% of the total pressure.

As a second test case the code was run for the turbine nozzle shown in Fig. 9. Observe that the grid generation technique outlined above performed well even for the complex body shape of this turbine blade. A calculation was performed for a downstream pressure corresponding to an isentropic Mach number equal to 1. As in the previous test case the velocity profile of Fig. 2 was given in input. The results of the blade isentropic Mach number, shown in Fig. 10, are in satisfactory agreement with the experimental data. Contrary to the former test case, the trailing-edge discretization behaves well; the computational results are clearly better than those obtained by Holmes and Tong, [12], who used a similar Euler code but modeled the trailing-edge as a wedge. The isobars plot of Fig. 11 confirms that the method captured well the system of shocks on the blade which appears in the Schlieren picture of Ref. [11]. In this cascade the evolution of secondary flows inside the channel is completely different than in the previous test case, as appears from the sequence of Fig. 13. In fact one can see that a true passage vortex doesn't develop and after the throat the secondary flows disappear at all. This behaviour can be explained considering the very low inlet vorticity, the relatively small deflection entirely accomplished in the entrance region, and the superposition of numerical errors.

As a final comment on the two test cases, we observed a full agreement between the computed outlet flow angles and the experimental ones.

CONCLUDING REMARKS

The Euler code developed proved, through severe tests, to be able to give some insight into the three-dimensional phenomena occurring in transonic turbine blades. Nevertheless this work must be regarded as the first step towards a deeper analysis, both theoretical and experimental; in this direction we have already started to move. Hopefully in the near future great effort will be devoted to the understanding of the three-dimensional features of transonic flows.

REFERENCES

1. Moore, J., Moore, J.: A Calculation Procedure for Three-Dimensional, Viscous, Compressible Duct Flow. Part I - Inviscid Flow Considerations, *Journal of Fluids Engineering*, Vol. 101, December 1979, pp. 415, 422.
2. Moore, J., Moore, J.: A Calculation Procedure for Three-Dimensional, Viscous, Compressible Duct Flow. Part II - Stagnation Pressure Losses in a Rectangular Elbow, *Journal of Fluids Engineering*, Vol. 101, December 1979, pp. 423, 428.
3. Chima, R. V.: Inviscid and Viscous Flows in Cascades with an Explicit Multiple-Grid Algorithm, *AIAA Journal*, Vol. 23, October 1985, pp. 1356, 1363.
4. Weinberg, B. C., Yang, H. J., McDonald, M., Shamroth, S. J.: Calculations of Two and Three-Dimensional Transonic Cascade Flow Fields Using the Navier-Stokes Equations, *Journal of Engineering for Gas Turbines and Power*, Vol. 108, January 1986, pp. 93, 102.
5. Schäfer, O., Frühauf, M. H., Sauer, B., Guggioits, M.: Application of a Navier-Stokes Analysis to Flows Through Plane Cascades, *Journal of Engineering for Gas Turbines and Power*, Vol. 108, January 1986, pp. 103, 111.

6. Jameson, A., Schmidt, W., Turkel, E.: Numerical Solutions of the Euler Equations by Finite Volume Methods Using Runge-Kutta Time-Stepping Schemes, AIAA paper no. 81-0204, 1981.
7. Bassi, F., Grasso, F., Jameson, A., Martinelli, L., Savini, M.: Solution of the Compressible Navier-Stokes Equations for a Double Throat Nozzle, Notes on Numerical Fluid Mechanics, Vieweg Verlag, to appear.
8. Bassi, F., Grasso, F., Savini, M.: Solution of the Compressible Navier-Stokes Equations by Using Embedded Adaptive Meshes, Lecture Notes in Physics, Springer Verlag, to appear.
9. Martinelli, L., Jameson, A., Grasso, F.: A Multigrid Method for the Navier-Stokes Equations, AIAA paper no. 86-0208, 1986.
10. Sieverding, C.: Experimental Data on Two Transonic Turbine Blade Sections and Comparison with Various Theoretical Methods, von Karman Institute, LS 59 "Transonic Flows in Turbomachinery", May 1973.
11. Sieverding, C., Van Hove, W., Bolatis, E., Gotthardt, H., Stark, U.: Description of Test Cases and Presentation of Experimental Results, von Karman Institute, LS 1982-05, "Numerical Methods for Flows in Turbomachinery Bladings", April 1982.
12. Holmes, D. G., Tong, S. S.: A Three-Dimensional Euler Solver for Turbomachinery Blade Rows, ASME paper no. 84-GT-79, 1984.

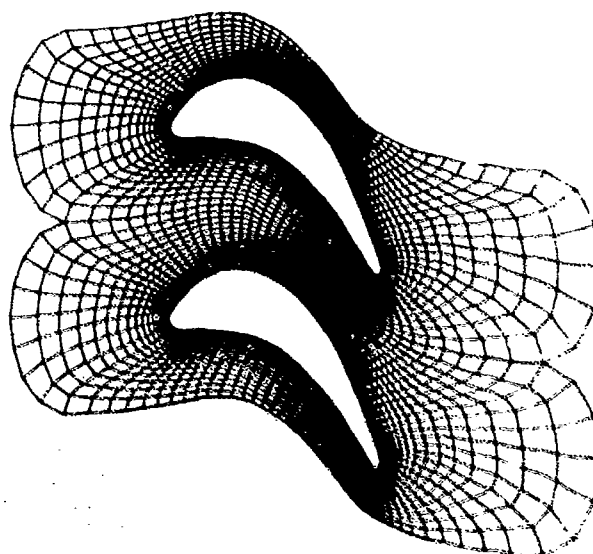


Fig. 1 Computational grid for the turbine rotor blade

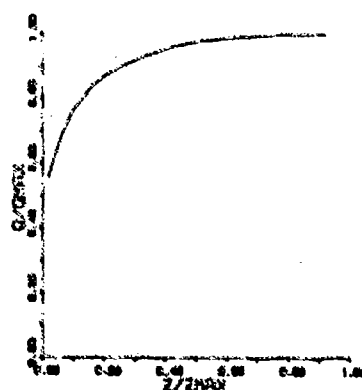


Fig. 2 Endwall inlet velocity profile

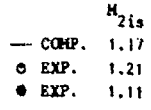


Fig. 5 Midspan isobars plot

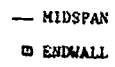


Fig. 4. Wideopen and endwall Mach number

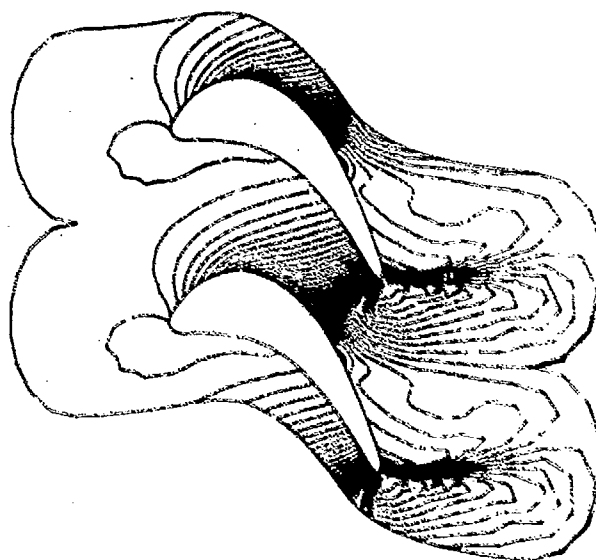
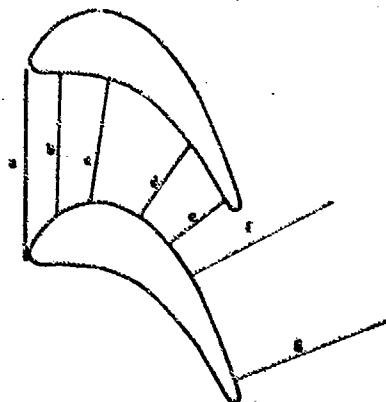


Fig. 6 Planes of secondary flows



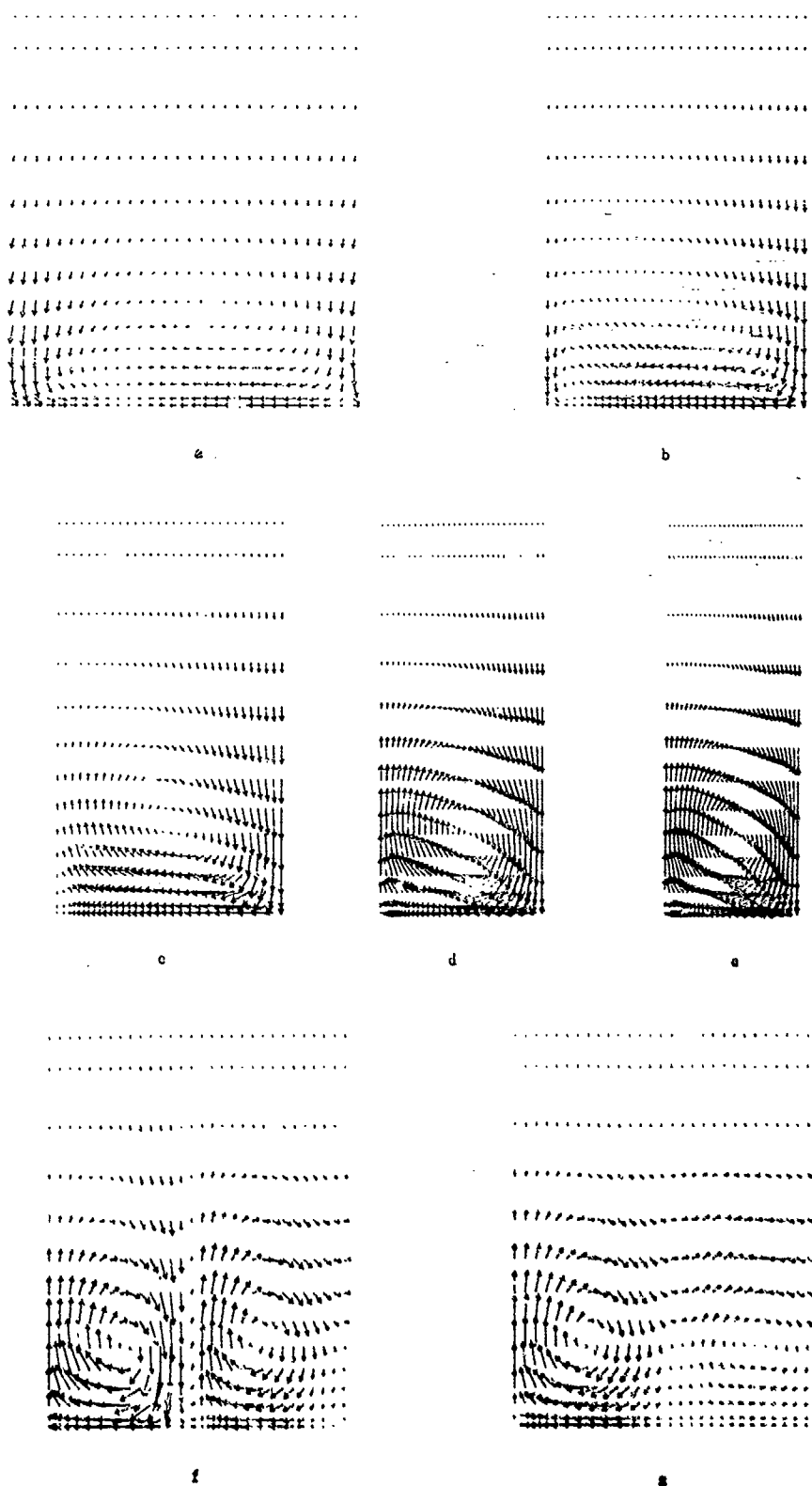


Fig. 7 Secondary flows development

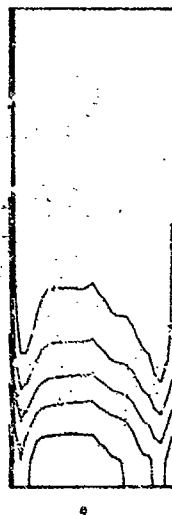


Fig. 8 Total pressure contours

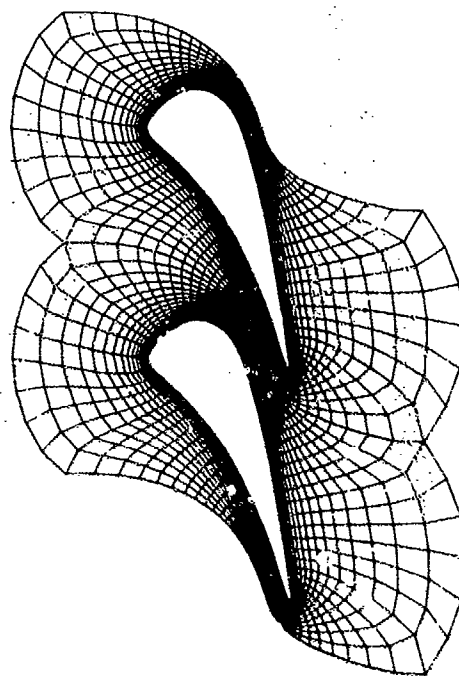


Fig. 9 Computational grid for turbine nozzle

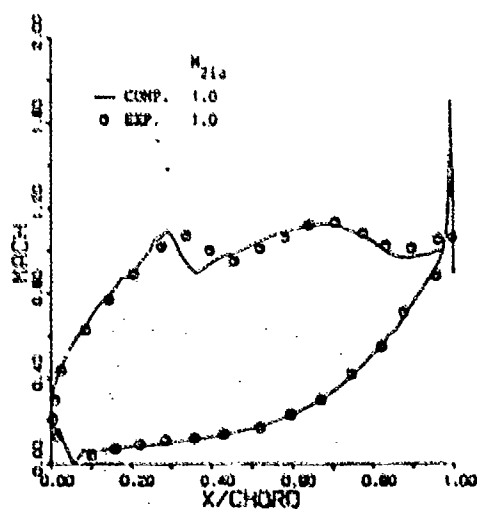


Fig. 10 Midspan isentropic Mach number

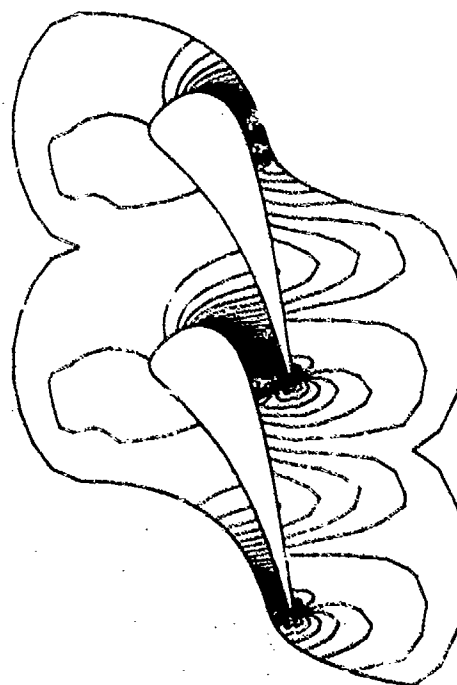


Fig. 11 Midspan isobars plot

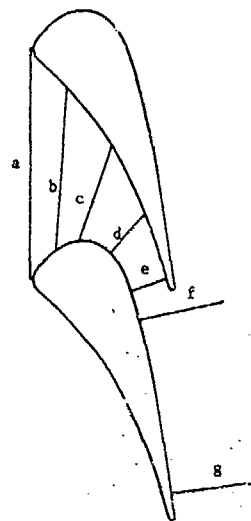


Fig. 12 Planes of secondary flows

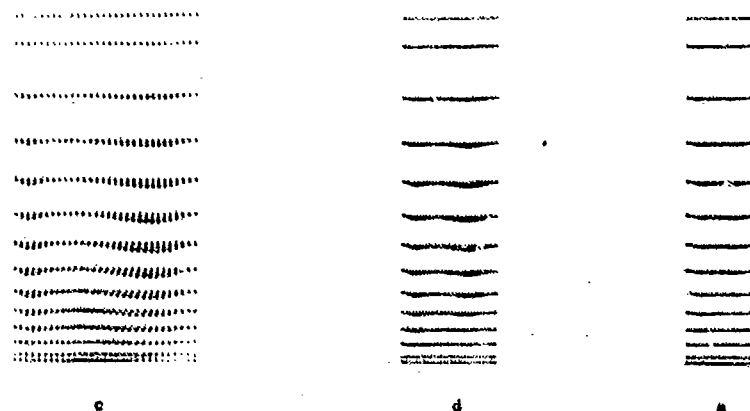
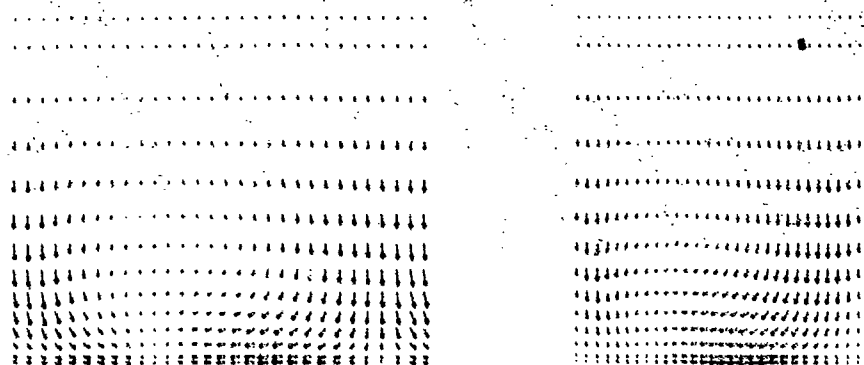


Fig. 13 Secondary flow development

DISCUSSION

P. Ramette, Fr

1. For downstream boundary conditions, you are assuming a constant pressure at downstream infinity. Where is your infinity? If it is of the order of a chord behind the blades, is the condition not too constraining?
2. You have a very large number of pressure measurements in Figure 10. Can you comment about the instrumentation, especially at the trailing edge? Are you doing the experiments on a real 3D turbine nozzle, or in a channel?

Author's Reply


1. We assumed that the pressure is constant outside the strip of phantom cells of the downstream boundary. The use of one dimensional Riemann invariants from infinity and from the interior of the domain, allows the pressure in the phantom cells to vary to a certain extent, as you can see from the isobar plots.
2. We have not done the experimental measurements. They were carried out at the von Kármán Institute.

Mr Kordulla, Ge

I would like to make a comment with respect to the interpretation of vortices simulated with the numerical solution of the Euler equations. I am not an expert in internal-flow predictions, but for external flow simulations with the Euler equations it is well known that vortices can only be generated by numerical diffusion, curved shocks or geometrical singularities unless vorticity is fed in with the inflow conditions. Therefore in internal flows without curved shocks vorticity can only be redistributed when introduced at the inlet. And one has to be quite careful when interpreting vortices in inviscid-flow solutions.

Author's Reply

I agree. In Euler calculations without shocks one can only follow the evaluation of vorticity given in input. If any vorticity is produced this is due to spurious entropy generation by numerical diffusion and/or rounding errors.



COMPUTATION OF TRANSONIC 2D CASCADE FLOW AND COMPARISON WITH EXPERIMENTS

H.-W. Happel, H. J. Dietrichs, K. Lehmann

MTU Motoren- und Turbinen-Union München GmbH
Dachauer Str. 665, 8000 München 50

SUMMARY

This paper describes a time-marching finite area method to obtain the steady 2D blade-to-blade solution along an axisymmetric stream surface with changing radius and stream tube thickness. The conservation laws are solved in a rotating frame. The numerical scheme is explicit and first order accurate in time and space. To achieve stability, explicit numerical viscosity is added. Three alternative methods of ensuring the zero normal velocity condition along the solid walls are analysed and their application is discussed. In order to increase the convergence speed, a sequential grid-refining procedure and a multiple-grid algorithm are used in the code. The accuracy and computational efficiency of the computer code are demonstrated for realistic blade geometries. The comparison with aerofoil measurements shows good agreement for turbine and compressor cascades.

NOMENCLATURE

a	speed of sound
A	JACOBIAN matrices of the quasi-linear form of the EULER equations
B	
B_n	stream tube thickness
C_i	correction vector
e_i	unit vector
e_{rot}	total internal energy with respect to the rotating frame
E	unit matrix
F_t	flux vector in meridional direction
G_t	flux vector in circumferential direction
H	source vector
h_{rot}	rothalpy
I_{2h}^h	prolongation operator from coarse (2h) to fine (h) mesh
J	JACOBIAN matrix of the transformation to curvilinear coordinates
m	coordinate in meridional direction
p	pressure
r	radius
R_h^{2h}	restriction operator from fine (h) to coarse (2h) mesh
t	time
U	state vector
V	control volume
w	relative velocity
\tilde{w}	contravariant velocity
ϵ	numerical viscosity coefficient
α	angle
γ	ratio of specific heats
η, ξ	curvilinear coordinates
λ	eigenvalue
ρ	density
ϕ	coordinate in circumferential direction
ω	angular velocity

Subscripts

Ch	solution along characteristics
Eu	EULER solution
i,k	grid point indices in m- and ψ -direction, respectively
m	in meridional direction
n	in normal direction
PS	along the pressure surface
SS	along the suction surface
t	in tangential direction
\mathbf{f}	in \mathbf{f} -direction
η	in η -direction
ψ	in circumferential direction

Superscripts

n	time level index
(\sim)	volume averaged value
(\rightarrow)	vector
(\wedge)	nonconservative formulation

INTRODUCTION

The development of modern gas turbine engines is characterized by the attempt, to reduce the number of stages in the turbomachinery components. The resulting increase of stage loading leads to transonic flow fields within the blade rows. Since the unsteady EULER equations are hyperbolic for subsonic as well as for supersonic Mach numbers, time-marching EULER codes are widely used for the prediction and analysis of transonic turbomachinery flow.

The fully 3D time-marching EULER codes, which are now becoming available, can only be applied to single blade rows or at maximum to one stage, Ref. 1. Therefore multi-stage turbomachines are designed by using a quasi 3D procedure, in which the fully 3D unsteady turbomachinery flow is approximated by calculating several 2D solutions along blade-to-blade surfaces (S1) as well as along hub-to-tip surfaces (S2) and iterating between the two kinds of 2D solutions, Ref. 2. In practice it is mostly acceptable, to perform only one hub-to-tip solution along one mean S_2 stream surface and several blade-to-blade solutions along axisymmetric S1 stream surfaces. In this approach the changing radius and the divergence of the S1 stream surfaces, which are provided by the averaged hub-to-tip throughflow or even ductflow calculation, must be taken into account. This is valid for subsonic and especially for transonic flow. Hence 2D transonic blade-to-blade solutions on cylindrical planes (Ref. 3) are not satisfactory and must be modified for the design of turbomachinery.

GOVERNING EQUATIONS

The unsteady 2D EULER equations are solved in integral form along an axisymmetric S1 stream surface with changing radius r and stream tube thickness B_n , Fig. 1. With respect to rotor blades the conservation laws are formulated in a rotating frame with constant angular velocity ω . Therefore centrifugal and CORIOLIS forces must be taken into account.

In the well known vector notation

$$\int_V \frac{\partial \vec{U}}{\partial t} B_n r dy dz + \int_S (\vec{F} B_n r dy - \vec{G} B_n dz) = \int_V \vec{H} B_n r dy dz$$

$$\vec{U} := \begin{bmatrix} g \\ g v_m \\ g r (v_y + \omega r) \\ g e_{rot} \end{bmatrix} \quad \vec{F} := \begin{bmatrix} g v_m \\ g v_m^2 + p \\ g r (v_y + \omega r) v_m \\ (g e_{rot} + p) v_m \end{bmatrix} \quad (1)$$

$$\vec{G} := \begin{bmatrix} g v_y \\ g v_m v_y \\ g r (v_y + \omega r) v_y + r p \\ (g e_{rot} + p) v_y \end{bmatrix} \quad \vec{H} := \begin{bmatrix} 0 \\ p \frac{0 \ln(B_n r)}{D_m} + g (v_y + \omega r)^2 \frac{0 \ln r}{D_m} \\ 0 \\ 0 \end{bmatrix}$$

the first row represents the continuity equation. The momentum equation in the second row contains a source term on the right hand side, which results from the centrifugal and CORIOLIS forces, the changing stream surface radius, the variation of streamtube thickness, and the use of cylindrical coordinates. In order to avoid additional source terms, the momentum equation in circumferential direction is replaced by the moment of momentum equation in axial direction. Furthermore, the total internal energy e_{rot} in the energy equation

$$e_{rot} := \frac{1}{\gamma - 1} \frac{p}{g} + \frac{1}{2} (v_y^2 + v_m^2 - (\omega r)^2) \quad (2)$$

is defined with respect to the rotating frame. Equation (2) being valid for a calorically perfect gas gives the closure relation for the static pressure in the flux and source terms.

In the 2D blade-to-blade solution uniform rothalpy h_{rot}

$$h_{rot} := \frac{\gamma}{\gamma - 1} \frac{p}{g} + \frac{1}{2} (v^2 + v_m^2 - (\omega r)^2) \quad (3)$$

is usually assumed in the inlet plane. That means, that in the adiabatic steady state solution h_{rot} is constant everywhere. Although the true time dependence of the transient solution is lost, the unsteady energy equation can be replaced by the assumption $h_{rot} = \text{constant}$. To obtain the correct steady state solution, it is only necessary to solve three transient conservations laws.

FINITE AREA DISCRETIZATION

Equation (1) is discretized in the physical domain consisting of one blade passage with up- and downstream periodic boundaries approximately along the flow direction, Fig. 2. The domain is divided into basic grid cells using quasi-streamlines and pitch-wise lines with non uniform spacing in circumferential and meridional direction.

The conservation principle is applied to overlapping finite area elements, Fig. 2. Each regular control element, which has a nodal point close to the center, is composed of four basic elements. Along the pressure and suction side including the leading and trailing edge the control area only consists of two basic elements.

PHYSICAL BOUNDARY CONDITIONS

In order to get a well posed problem, equation (1) must be completed by physically correct conditions along the boundaries of the computational domain, Fig. 2. The number of boundary conditions, which have to be imposed in the inlet and outlet plane, can be determined using the theory of characteristics. According to Ref. 4 three variables must be specified at the upstream boundary and only one at the downstream boundary. This is physically correct as long as the meridional velocity v_m in the outlet plane

is subsonic. If w_m is supersonic in the exit plane, all boundary conditions have to be specified in the inlet plane.

As supersonic meridional velocities usually do not occur in turbomachinery flow, in the inlet and outlet plane the following physical boundary conditions are imposed and held constant:

Inlet plane

- relative stagnation temperature,
- relative stagnation pressure, and
- relative flow angle (for subsonic inflow),

Outlet plane

- static pressure.

If the relative inflow Mach number is supersonic (but w_m is subsonic), the circumferential component of the relative velocity is held constant instead of the relative flow angle. Then the unique incidence condition is automatically satisfied as a part of the solution.

Along the solid walls of the aerofoil no mass and energy flux cross the surface, because the normal component of the velocity is zero everywhere. The transport of momentum and moment of momentum only consists of the pressure forces perpendicular to the surface.

NUMERICAL SCHEME

The numerical scheme is explicit and first order accurate in time and space. The first order accuracy in space is caused by the explicit numerical viscosity to achieve stability as well as by using half elements along the blade surfaces.

Defining a volume averaged state vector

$$\vec{U}_{i,k}^n := \frac{1}{\Delta V_{i,k}} \left[\int_V \vec{U}_n r dy dz \right]^n \quad (4)$$

of the control volume

$$\Delta V_{i,k} := \int_V r dy dz \quad (5)$$

and a lagging correction vector

$$\vec{C}_{i,k}^{n_0} := -(1 - \alpha) \left\{ \vec{U}_{i,k}^{n_0} - \vec{U}_{i,k}^n \right\} \quad (6)$$

the unsteady 2D EULER equations are discretized as

$$\vec{U}_{i,k}^{n+1} = \vec{U}_{i,k}^n + \vec{C}_{i,k}^{n_0} - \frac{\Delta t}{\Delta V_{i,k}} \left\{ \left[\int_S (\vec{F}_n r dy - \vec{G}_n dz) \right]^n - \left[\int_V \vec{H}_n r dy dz \right]^n \right\} \quad (7)$$

for the nodal point (i,k) close to the center of the control volume. The transport terms are positive for fluxes leaving the control surface.

In the so called damping surface technique (Ref. 5) the considerable numerical viscosity, which is introduced by the volume averaged state vector at time level n, is reduced by the lagging correction vector. This remains constant during N time steps and is then updated for the next period of iterations. With regard to convergence speed the number of iterations between two updates of the correction vector should be chosen as small as possible. In combination with a viscosity coefficient α in the range of about two percent the updating rate N should not be less than five iterations, because otherwise the calculation becomes unstable.

When the steady state solution is attained, the accuracy is mainly determined by the approximation used for the surface and volume integrals. Both are calculated for the basic elements assuming linear variation of the functions between adjacent nodal points.

NUMERICAL BOUNDARY RELATIONS

A 2D flow problem is determined at any point in space by a total of four state variables. Since at the inlet plane three physical boundary conditions are specified and at the outlet plane only one can be prescribed, the following numerical boundary relations are additionally used:

Inlet plane

- equality of the mass flow

in the inlet and the second plane,

Outlet plane

- equality of the mass flow,
- equality of the mass averaged rothalpy in the relative frame, and
- equality of the mass averaged moment of momentum with respect to the absolute frame

in the outlet and the last but one plane.

With the exception of the leading and trailing edge the periodic boundaries (upstream and downstream of the blades) are treated in the same way as the interior nodal points. Informations are combined from the upper and the lower boundary (AC and BD or EG and FH respectively, Fig. 2) to obtain the fluxes of a regular control element.

In order to apply the periodic condition even to the leading and trailing edge, special half elements are used, which only touch the blade surface at the leading and trailing edge nodal point, Fig. 2. The computed changes of the state vector are attached to the nodal points at the leading and trailing edge.

Although at the solid walls the physical boundary condition of zero normal velocity is imposed in the flux balance, the EULER solution usually gives a normal component of the velocity vector. Therefore in the computer program after each time step the following three options of correction:

- normal velocity method (Ref. 6),
- normal momentum method (Ref. 7), and
- normal compatibility method (Ref. 8)

are made available. For the formulation of the solid wall corrections it is convenient, to introduce a curvilinear coordinate system (f, η) such that the blade surfaces coincide with lines $f = \text{constant}$.

In the normal velocity method the normal component w_n of the velocity

$$w_n = \frac{\left(\frac{\partial u}{\partial \eta}\right) v_f - r \left(\frac{\partial v}{\partial \eta}\right) u_n}{\sqrt{r^2 \left(\frac{\partial v}{\partial \eta}\right)^2 + \left(\frac{\partial u}{\partial \eta}\right)^2}} \quad (8)$$

is cancelled and the kinetic energy of w_n is added isentropically to the static state. In this approach all changes of the state vector resulting from the flux balance of the half elements are directly attached to the nodal points at the blade surface.

In the normal momentum method the changes of the state vector are at first located at the centers of the half elements. Then the static pressure at the solid wall is predicted by applying the normal momentum equation

$$\begin{aligned} & \left(r^2 \left(\frac{\partial v}{\partial \eta} \right)^2 + \left(\frac{\partial u}{\partial \eta} \right)^2 \right) \frac{\partial p}{\partial f} + \left(r^2 \left(\frac{\partial v}{\partial f} \right) \left(\frac{\partial v}{\partial \eta} \right) + \left(\frac{\partial u}{\partial f} \right) \left(\frac{\partial u}{\partial \eta} \right) \right) \frac{\partial p}{\partial \eta} \\ & - \rho u^2 r^2 \det J \left(\left(\frac{\partial^2 v}{\partial \eta^2} \right) \left(\frac{\partial u}{\partial \eta} \right) - \left(\frac{\partial^2 u}{\partial \eta^2} \right) \left(\frac{\partial v}{\partial \eta} \right) \right) \\ & - \rho r \det J \left(r^2 \left(\frac{\partial v}{\partial \eta} \right) \left(\frac{\partial v}{\partial \eta} \right) u_\eta + \omega^2 \right) \\ & + 2 \left(\frac{\partial u}{\partial \eta} \right)^2 u_\eta \left(\left(\frac{\partial v}{\partial \eta} \right) u_\eta + \omega \right) \frac{Dr}{D\eta} \end{aligned} \quad (9)$$

between the center of the half element and the nodal point at the blade surface, where

$$\det J := \frac{\partial(y, z)}{\partial(\xi, \eta)} \quad (10)$$

is the JACOBIAN determinant and

$$w_\eta = \frac{1}{\det J} \left(- \left(\frac{\partial z}{\partial \xi} \right) \frac{v_\xi}{r} + \left(\frac{\partial y}{\partial \xi} \right) w_\xi \right) \quad (11)$$

is the contravariant velocity component being tangent to the solid wall.

Equation (9), relating the normal pressure gradient mainly to the curvature of the solid walls, can be derived by combining the momentum equations in meridional and circumferential direction

$$\frac{Dw_\eta}{Dt} - r \left(\frac{v_\xi}{r} + \omega \right)^2 \frac{Dr}{Dz} = - \frac{1}{\rho} \frac{\partial p}{\partial z} \quad (12)$$

$$r \frac{D}{Dt} \left(\frac{v_\xi}{r} \right) + 2 v_\eta \left(\frac{v_\xi}{r} + \omega \right) \frac{Dr}{Dz} = - \frac{1}{\rho r} \frac{\partial p}{\partial y} \quad (13)$$

keeping in mind, that in the relations between the physical and contravariant components of the velocity vector

$$\frac{v_\xi}{r} = \left(\frac{\partial y}{\partial \xi} \right) \frac{w_\xi}{r} + \left(\frac{\partial y}{\partial \eta} \right) w_\eta \quad (14)$$

$$w_\eta = \left(\frac{\partial z}{\partial \xi} \right) \frac{w_\xi}{r} + \left(\frac{\partial z}{\partial \eta} \right) w_\eta \quad (15)$$

the contravariant component w_η vanishes along the blade surface. Since the flow quantities of the nodal point at the solid wall must be substituted in the right hand side of equation (9), the correction procedure consists of a predictor and a corrector step. In both steps an isentropic relationship between the static values of density and pressure is assumed.

In the normal compatibility method it is assumed, that the EULER solution with $w_{\eta-Eu} \neq 0$ as well as the solution along characteristics with $w_{\eta-Ch} = 0$ have to fulfill the compatibility relations. Since only the boundary condition in the ξ -direction is maltreated, it is sufficient to derive the compatibility relations within a characteristic plane being parallel to the η -axis. The detailed derivation of the compatibility relations as well as the basic ideas of the so called postcorrection technique for improving the EULER solution at the end of a time step Δt are given in the appendix.

With the expression for the tangential component w_ξ of the velocity

$$w_\xi = \frac{\left(\frac{\partial z}{\partial \eta} \right) w_\eta + r \left(\frac{\partial y}{\partial \eta} \right) v_\eta}{\sqrt{r^2 \left(\frac{\partial y}{\partial \eta} \right)^2 + \left(\frac{\partial z}{\partial \eta} \right)^2}} \quad (16)$$

and assuming $w_{\eta-Ch} = 0$ the postcorrection equations may be written as

$$p_{Ch} - p_{Eu} = \int p_{\eta-Eu} \quad (17)$$

$$p_{Ch} - p_{Eu} = \frac{1}{2} (p_{Ch} - p_{Eu}) \quad (18)$$

$$v_{Ch} = v_{t-Eu} \quad (19)$$

The negative sign in equation (17) belongs to a left running characteristic from the flow field to the pressure side and the positive sign is valid for a right running characteristic carrying informations to the suction side. Equations (18) and (19) are the compatibility relations along the two characteristics with the slope $df/dt = W_g/r = 0$.

The normal momentum and the normal compatibility method have an advantage over the normal velocity method only on coarse grids. The improvements are comparable for fine grids with compressed mesh lines along the pressure and suction side. If the curvature of the solid walls is considerable, the normal momentum method should be preferred.

ACCELERATION OF CONVERGENCE

Since explicit time marching codes are time consuming with respect to the COURANT-FRIEDRICHS-LEWY (C.F.L.) condition, the convergence speed must be increased.

The simplest modification consists in replacing the unsteady energy equation by the steady one as mentioned before.

In connection with grid spacing it is very important to use local time steps being limited by the C.F.L. condition. This stability constraint states that the physical domain of dependence must be completely contained within the numerical domain of dependence, Fig. 3. That means, that the maximum time step is attained, when the sketched sonic circle touches the boundary of the control element. According to Fig. 3 the C.F.L. condition gives the maximum time step as

$$\Delta t \leq \frac{r_p (p_Q - p_p) \bar{e}_p \cdot \bar{e}_p}{q_p + \bar{v}_p \cdot \bar{e}_p} \quad (20)$$

where

$$\bar{e}_p = \sin \alpha \bar{e}_y - \cos \alpha \bar{e}_x \quad (21)$$

is the normal unit vector of the straight line \overline{QR} . In order to achieve a C.F.L. number close to unity everywhere, for each control area the minimum value of six possible time steps must be estimated. Since this calculation is very expensive with respect to computer time and the changing rate of Δt is very small, the number of time steps between two sequential updates can be chosen in the range of the number of grid lines in meridional direction.

Both improvements are implemented, because only the steady state solution is required and the true time dependence is not important.

The computer time is mainly reduced by using a grid-refining procedure and a multiple-grid algorithm.

The grid-refining proceeds in three sequential levels. The calculation starts on the coarsest mesh, where the solution is only performed at every fourth nodal point in both directions. After attaining convergence the solution is interpolated to the next finer grid and the iteration is continued.

At each level of grid-refining additionally a multigrid procedure is available. Due to the application of volume averaging the damping surface technique reduces all high-frequency errors in the order of one mesh width very quickly. Therefore, in coordination with the updating rate of the correction vector of the damping surface technique the two-level correction scheme is composed of a fixed number of iterations on the fine grid with mesh size h and one approximation of the residuals on the next coarser grid with mesh size $2h$.

The fine-to-coarse transfer operator R^{2h}_h (called restriction) consists of summing up the fluxes of the coarse control volume ΔV^{2h} using the already calculated values of the basic cells within it. To compute the coarse grid corrections

$$\Delta \bar{U}^{2h} = - \frac{\Delta t}{\Delta V} R_h^{2h} \left(\left(\int_S (\bar{F}(\bar{U}) \bar{B}_h r dy - \bar{G}(\bar{U}) \bar{B}_h dz) \right)^h - \left(\int_V \bar{H}(\bar{U}) \bar{B}_h r dy dz \right)^h \right) \quad (22)$$

local time steps Δt^{2h} are taken into account, which belong to the coarse mesh.

For returning to the fine grid linear interpolation is applied as a coarse-to-fine transfer operator I_h^{2h} (called prolongation). Then the state vector at all nodal points of the fine grid $2h$ is replaced by

$$\bar{U}_{i,k}^{n+1} = \bar{U}_{i,k}^n + \bar{C}_{i,k}^{n_0} \frac{h}{2h} (\Delta \bar{U}^{2h}) \quad (23)$$

using the damping surface technique.

The main purpose of this correction scheme, being only valid for linear problems, is the rapid propagation of the fine grid corrections throughout the computational domain. The savings in computer time are about 70 percent and the low truncation error of the fine grid discretization is maintained.

APPLICATION AND COMPARISON WITH EXPERIMENTS

The computer code containing all the features described in the previous chapters has been developed for routine application. A large amount of experience has been accumulated over the past several years, when it was used for design work at an average rate of about five applications per day. The quality of the results may vary with the problem. Typical examples for turbine and compressor flow will be discussed to demonstrate the accuracy, the computational efficiency, and the limitations of the method.

To compare the computed results with 2D aerofoil measurements the isentropic Mach number distributions along the pressure and suction side is used, because the static pressure is least affected by the numerical viscosity. For all test cases the computational fine mesh is composed of 145×37 nodal points with different spacing between the pressure and suction surface as well as at the leading and trailing edge.

Fig. 4 presents the isentropic Mach number distribution of a turbine stator blade at a downstream supersonic Mach number of 1.32 and shows good agreement with experimental data. The experiments were carried out at DFVLR Göttingen. The predicted exit flow angle is within a half degree of the test result. The comparison between a Schlieren photograph and computed isodensity lines in Fig. 5 is satisfactory. The trailing edge shock on the pressure side (a) is captured quite well, however the intensity decreases toward the suction side, becoming practically zero after the reflection (b) in contrast to reality. This is due to the neglected friction effects in the calculation. Following the explanations in Ref. 9 the boundary layer thickness would effectively change the curvature on the suction side in real flow leading to compression waves. This process would be amplified by the shock boundary layer interaction resulting in the structures observed in the Schlieren. The strong suction side shock at the trailing edge (c) is in good agreement with the experiment.

Fig. 6 shows the comparison of the isentropic Mach number distribution of a turbine rotor blade over the relative surface length, Ref. 10. The exit Mach number of the plane cascade test is in the range of 0.99. The data agree quite well except at 60 percent suction surface length, where a laminar separation bubble occurs in the experiment. This is caused by the interaction of the trailing edge shock of the adjacent aerofoil with the suction side boundary layer. As this mechanism is not included in the inviscid calculation, the computed shock is stronger. But the predicted shock position differs slightly from the experimental result. The shock can be clearly seen in the isodensity contours, which are plotted in Fig. 8. Fig. 7 presents a second measurement in comparison with the first one, where cooling air is ejected at a position of about 35 percent relative suction side length. The ejection produces a disturbance in the local Mach number distribution and causes an earlier boundary layer transition, resulting in a weaker interaction of the shock with the boundary layer. In this case the measured values of strength and position of the shock are in excellent agreement with the inviscid prediction in Fig. 6.

Fig. 9 compares the computed and measured Mach number distribution of a compressor rotor blade at a slightly supersonic inlet Mach number of about 1.09. All compressor cascade measurements were performed at DFVLR Köln. The computed isopressure contours

in Fig. 10 show the detached shock at the leading edge. Although the computed shock is smeared over several grid points, the shock location is predicted quite well. The difference between the computed and measured shock strength results mainly from friction effects. The growing boundary layer on the suction side upstream of the shock decreases the curvature of the wall, leading to a weaker supersonic expansion. The increase of the boundary layers downstream of the shock within the flow channel produces a blockage, which explains the higher Mach number level along the pressure side as well as along the suction side behind the shock in the experiment. The overall trends of the Mach number distributions are in good agreement.

Fig. 11 presents the calculated and measured Mach number distribution of a compressor cascade with precompression at the front part of the suction side. The experimentally observed inlet conditions, Mach number of 1.50 and flow angle of 150 degrees corresponding to unique incidence, are computed exactly. The intended flow pattern at the design point is characterized by a precompression at the beginning of the suction side with converging Mach lines at the leading edge of the adjacent profile and an oblique shock, which starts at the leading edge and hits the suction surface at about 75 percent relative chord length. That means, that this part of the suction side cannot be affected by the adjacent pressure side. Accordingly the Mach number distribution results only from the geometrical shape of the suction side upstream of the oblique shock and can be predicted analytically using the theory of characteristics. The additionally shown comparison between this analytical prediction and the time-marching EULER solution agrees quite well. This excellent agreement can also be seen in the isopressure contours of Fig. 12. With the exception of the strong supersonic expansion at the round leading edge the discrepancy between the measurement and the inviscid calculations of the Mach number distribution results from the boundary layer behaviour upstream of the oblique shock. Due to the growing thickness of the boundary layer the wall curvature increases along the compression part, resulting in a stronger deceleration, and decreases along the expansion part, leading to a weaker acceleration. The difference between the experimental data and the computed Mach number distribution along the pressure side is considerable, because the flow field downstream of the oblique shock is sensitive to the back pressure in the outlet plane. The location as well as the strength of the normal shock, which starts at the trailing edge of the suction side and hits the pressure side at about 55 percent relative chord length (Fig. 12), differ from the calculation. In order to move the computed shock approximately to the measured position, a considerable increase of the static pressure would be required in the outlet plane, leading to an exit Mach number in the range of 0.63 in contrast to the measured value of about 0.85.

CONCLUDING REMARKS

The described 2D time-marching EULER code is integrated in a quasi 3D approach and can be effectively applied for design and analysis of 3D turbomachinery flow.

The comparison of the 2D test cases has shown, that the prediction of the 2D inviscid blade-to-blade solution is in good agreement with the measurements, if the friction effects are weak and mainly concentrated in the boundary layers without separation. Further improvements for these applications can be achieved by the implementation of an iterative routine between the inviscid EULER solution and a boundary layer calculation. This is valid for transonic turbine cascades and for the inlet part of transonic as well as supersonic compressor cascades.

ACKNOWLEDGEMENT

The work was supported within research programs of the German Bundesministerium der Verteidigung. The permission to publish the results is greatly acknowledged.

REFERENCES

- Ref. 1 DENTON, J. D.: "An improved time-marching method for turbomachinery flow calculation", ASME paper 82-GT-239 (1982)
- Ref. 2 WU, C. H.: "A general theory of three-dimensional flow in subsonic and supersonic turbomachines of axial-, radial- and mixed-flow types", NACA TN 2604 (1952)
- Ref. 3 McDONALD, P. W.: "The computation of transonic flow through two-dimensional gas turbine cascades", ASME paper 71-GT-89 (1971)
- Ref. 4 CCPALARRISHMAN, S. BOZZOLA, N.: "Numerical representation of inlet and exit boundary conditions in transient cascade flow", ASME paper 73-GT-33 (1973)
- Ref. 5 COUSTON, M., McDONALD, P. W., SMOLDEREN, J. J.: "The damping surface technique for time dependent solutions to fluid dynamic problems", VKI TN 109 (1975)
- Ref. 6 DENTON, J. D., SINGH, U. K.: "Time marching methods for turbomachinery flow calculation", VKI lecture series 1979-7 (1979)

- Ref. 7 RIZZI, A.: "Numerical implementation of solid body boundary conditions for the EULER equations", ZAMM Vol. 58, pp. 301 - 304 (1978)
- Ref. 8 NEEF, T. de: "Treatment of boundaries in unsteady inviscid flow computations", Delft U. of Tech. Dep. of Aerosp. Engng. Rep. LR-262 (1978)
- Ref. 9 HOORMOUZIADIS, J., LICHTFUSS, H.-J.: "Modern technology application to compressor and turbine aerodynamics", Seventh I.S.A.B.E. Symposium papers, Beijing, China (1985)
- Ref. 10 KLOCK, R., HOEISEL, H., DIETRICH, H.J., HOLMES, A.T.: "The boundary layer behaviour of an advanced gas turbine rotor blade under the influence of simulated film cooling", AGARD CP-390 (1985)

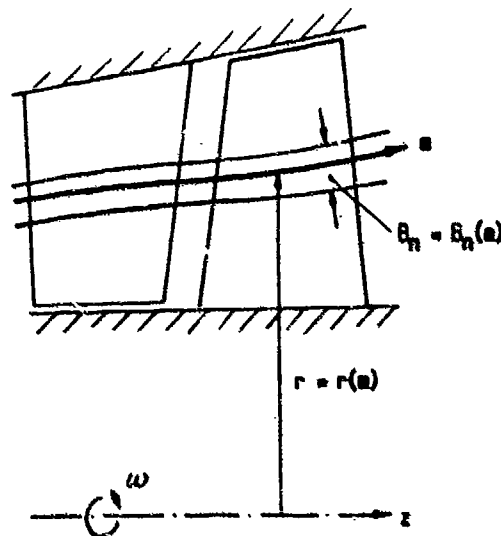


Fig. 1 Hub-to-tip plane of an axial turbine stage

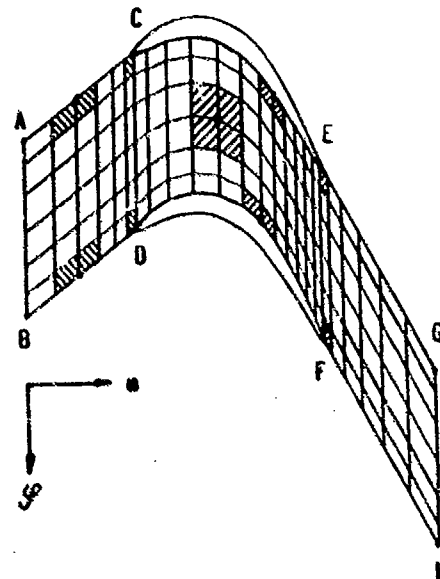


Fig. 2 Finite area discretization (coarse grid is for illustrative purposes only)

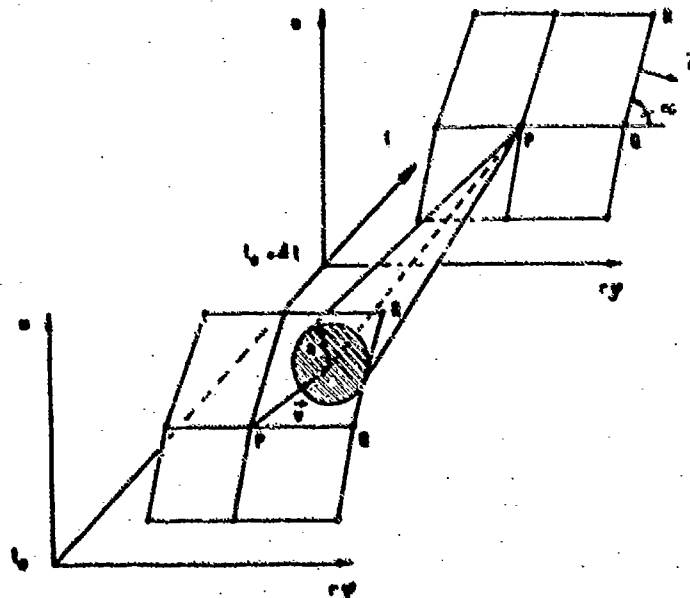


Fig. 3 COURANT-FRIEDRICHS-LEWY stability condition

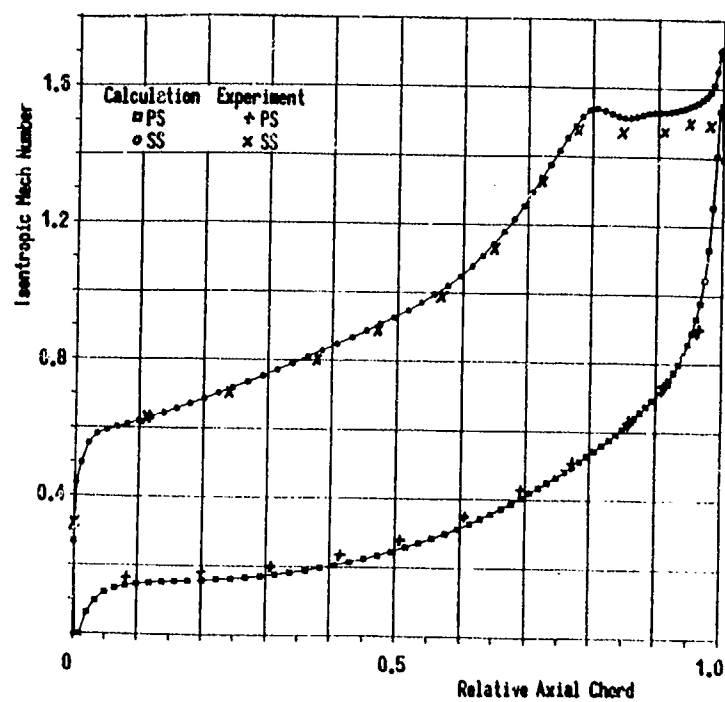


Fig. 4 Isentropic Mach number distribution along the pressure and suction surface of a turbine stator blade

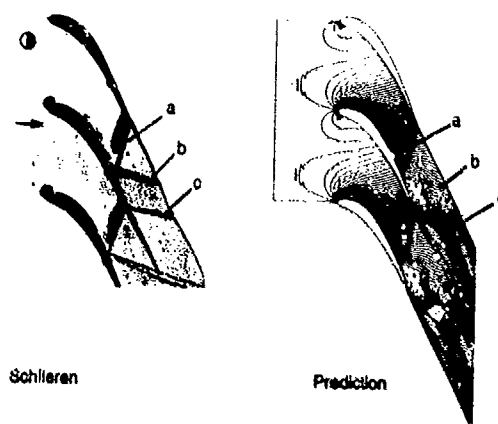


Fig. 5 Comparison between a Schlieren photograph and computed isodensity lines of a turbine stator blade

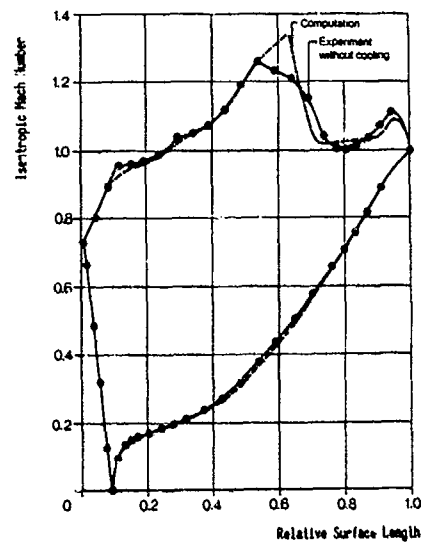


Fig. 6 Isentropic Mach number distribution along the pressure and suction surface of a turbine rotor blade

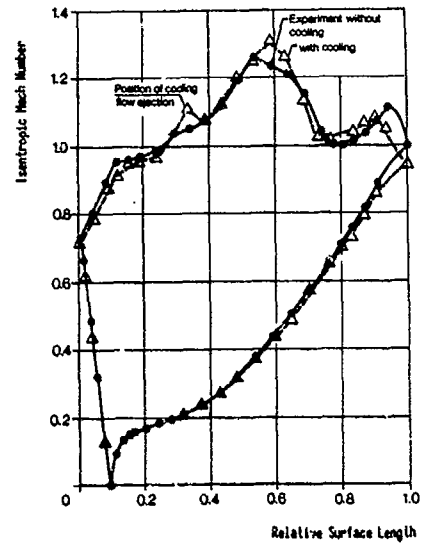


Fig. 7 Comparison between the measured isentropic Mach number distribution with and without ejection of cooling air

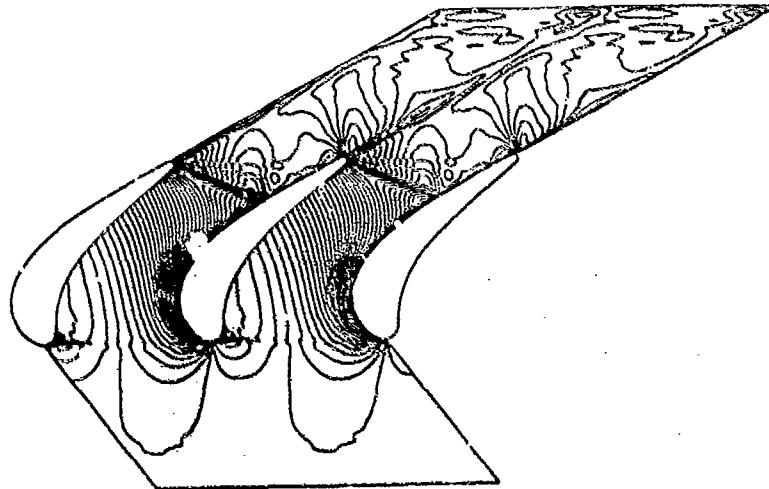


Fig. 8 Computed isodensity lines of a turbine rotor

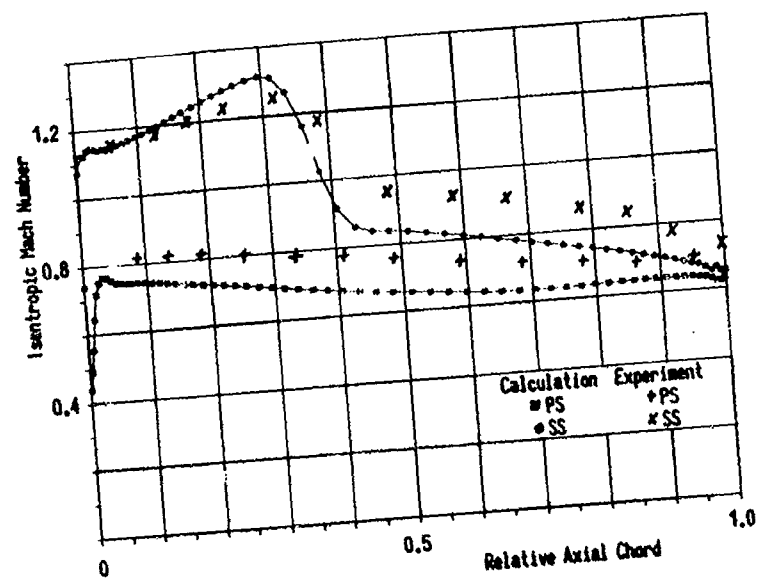


Fig. 9 Isentropic Mach number distribution along the pressure and suction surface of a transonic compressor cascade

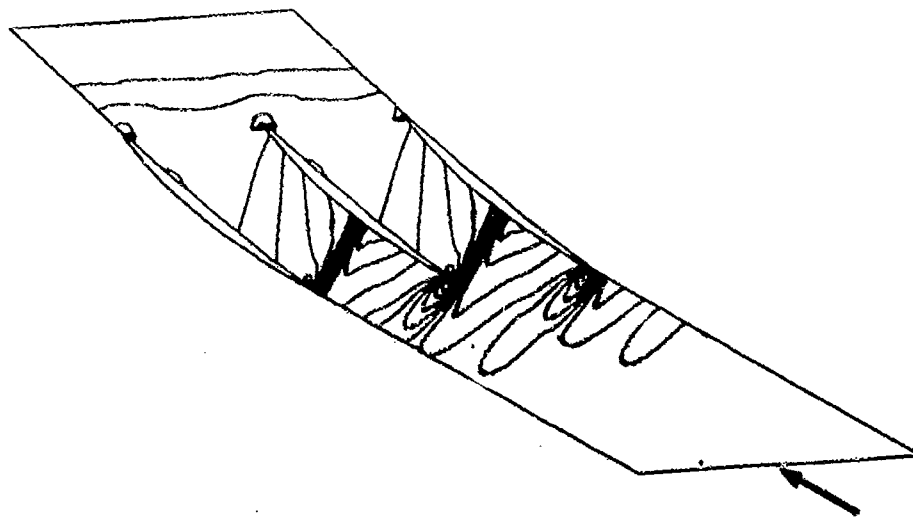


Fig. 10 Computed isopressure lines of a transonic compressor cascade

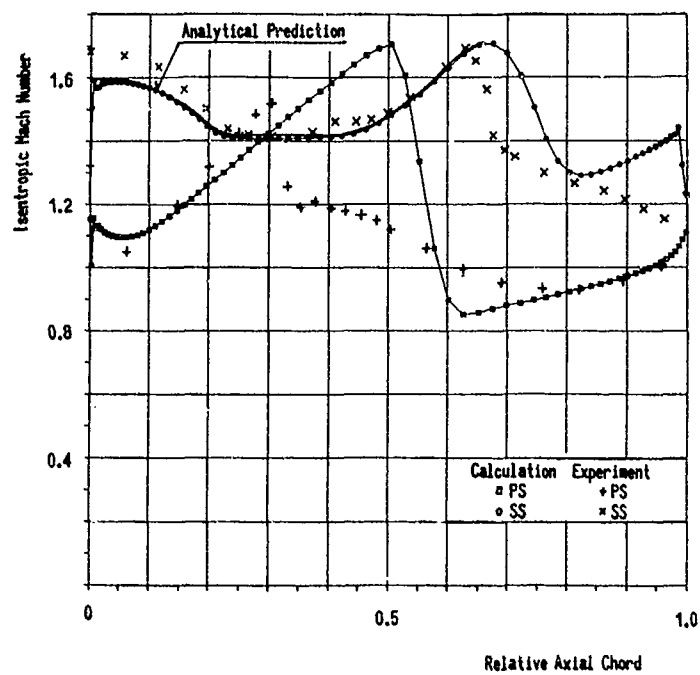


Fig. 11 Isentropic Mach number distribution along the pressure and suction surface of a supersonic compressor cascade

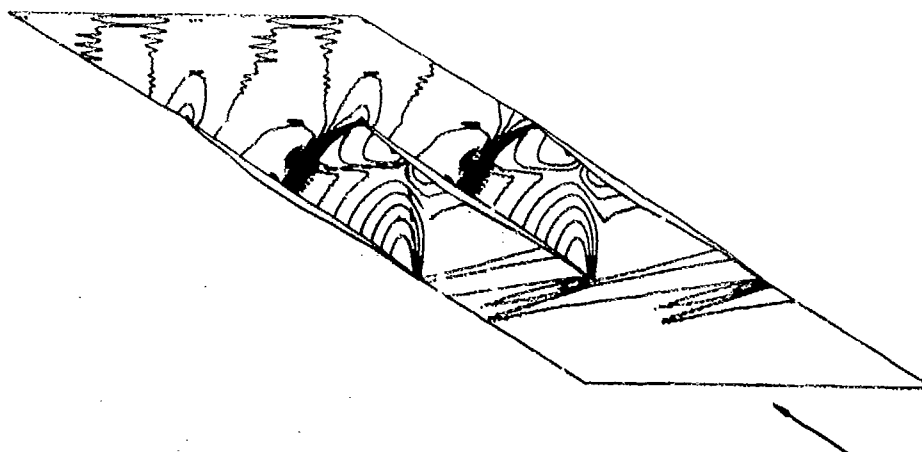


Fig. 12 Computed isopressure lines of a supersonic compressor cascade

APPENDIX POSTCORRECTION TECHNIQUE

In the normal compatibility method (called postcorrection technique) it is supposed, that the EULER solution with a normal velocity component $w_n \neq 0$ as well as the solution along characteristics with a vanishing normal component $w_n = 0$ have to satisfy the corresponding compatibility equations. This means, that the postcorrection technique is based on the equivalence of the governing unsteady EULER equations and of the compatibility relations along characteristic surfaces. Therefore, if we write the latter twice, once for the results as obtained from the discretization of the EULER equations and again for the exact characteristic solution, the postcorrection relations are obtained by subtracting one equation from the other, assuming that the discretizations of the corresponding spatial derivatives are equal for both sets of compatibility equations.

Since the JACOBIAN matrices of the corresponding quasi-linear formulation of equation (1) contain only a few zero elements, the determination of the eigenvalues is very cumbersome. Therefore we consider the quasi-linear form of the nonconservative EULER equations

$$\frac{\partial \vec{U}}{\partial t} + \hat{A} \left[\frac{\partial \vec{U}}{\partial m} \right]_{s, y} + \frac{\hat{B}}{r} \left[\frac{\partial \vec{U}}{\partial \varphi} \right]_{s, m} = \vec{H}$$

$$\vec{U} := \begin{bmatrix} B_n r g \\ w_m \\ w_y \\ B_n r p \end{bmatrix} \quad \hat{A} := \begin{bmatrix} w_m & B_n r g & 0 & 0 \\ 0 & w_m & 0 & \frac{1}{B_n r g} \\ 0 & 0 & w_m & 0 \\ 0 & B_n r g a^2 & 0 & w_m \end{bmatrix} \quad \hat{B} := \begin{bmatrix} w_y & 0 & B_n r g & 0 \\ 0 & w_y & 0 & 0 \\ 0 & 0 & w_y & \frac{1}{B_n r g} \\ 0 & 0 & B_n r g a^2 & w_y \end{bmatrix}$$

$$\vec{H} := \begin{bmatrix} 0 \\ \frac{(B_n r p)}{(B_n r g)} \frac{D \ln(B_n r)}{Dm} + (w_y + w_r)^2 \frac{D \ln r}{Dm} \\ - w_m (w_y + 2 w_r) \frac{D \ln r}{Dm} \\ - w_m (B_n r p) (\gamma - 1) \frac{D \ln(B_n r)}{Dm} \end{bmatrix}, \quad (\text{A.1})$$

keeping in mind, that both formulations have the same eigenvalues due to an existing similarity transformation between the conservative and the nonconservative state vector.

In order to facilitate the derivation of the compatibility relations, it is convenient to introduce a curvilinear coordinate system (f, η) such that the blade surfaces coincide with lines $f = \text{constant}$.

The application of the chain rule to equation (A.1) yields

$$\frac{\partial \vec{U}}{\partial t} + \hat{A} \left[\frac{\partial \vec{U}}{\partial \eta} \right]_{s, f} + \frac{\hat{B}}{r} \left[\frac{\partial \vec{U}}{\partial f} \right]_{s, \eta} = \vec{H} \quad (\text{A.2})$$

with the JACOBIAN matrices

$$\hat{A} := \frac{\hat{A}}{r} \frac{\partial \eta}{\partial y} + \hat{B} \frac{\partial \eta}{\partial m} \quad (\text{A.3})$$

and

$$\frac{B}{r} := \frac{\hat{A}}{r} \frac{\partial f}{\partial y} + \hat{B} \frac{\partial f}{\partial m} \quad (A.4)$$

Introducing the contravariant velocity components

$$\frac{W_f}{r} = \frac{w_y}{r} \frac{\partial f}{\partial y} + w_m \frac{\partial f}{\partial m} \quad (A.5)$$

$$W_\eta = \frac{w_y}{r} \frac{\partial \eta}{\partial y} + w_m \frac{\partial \eta}{\partial m} \quad (A.6)$$

the JACOBIAN matrices of the transformation can be written as

$$A := \begin{bmatrix} W_\eta & B_n r g \frac{\partial \eta}{\partial m} & B_n r g \frac{1}{r} \frac{\partial \eta}{\partial y} & 0 \\ 0 & W_\eta & 0 & \frac{1}{B_n r g} \frac{\partial \eta}{\partial m} \\ 0 & 0 & W_\eta & \frac{1}{B_n r g} \frac{1}{r} \frac{\partial \eta}{\partial y} \\ 0 & B_n r g a^2 \frac{\partial \eta}{\partial m} & B_n r g a^2 \frac{1}{r} \frac{\partial \eta}{\partial y} & W_\eta \end{bmatrix} \quad (A.7)$$

$$\frac{B}{r} := \begin{bmatrix} \frac{W_f}{r} & B_n r g \frac{\partial f}{\partial m} & B_n r g \frac{1}{r} \frac{\partial f}{\partial y} & 0 \\ 0 & \frac{W_f}{r} & 0 & \frac{1}{B_n r g} \frac{\partial f}{\partial m} \\ 0 & 0 & \frac{W_f}{r} & \frac{1}{B_n r g} \frac{1}{r} \frac{\partial f}{\partial y} \\ 0 & B_n r g a^2 \frac{\partial f}{\partial m} & B_n r g a^2 \frac{1}{r} \frac{\partial f}{\partial y} & \frac{W_f}{r} \end{bmatrix} \quad (A.8)$$

Since the derivatives in the η -direction can be calculated with sufficient accuracy, and the blade surfaces hinder us only in the space differentiation in f -direction, it is only necessary for the derivation of the postcorrection relations to consider the corresponding one-dimensional problem

$$\frac{\partial \vec{U}}{\partial t} + \frac{B}{r} \left[\frac{\partial \vec{U}}{\partial f} \right]_{s, \eta} = 0. \quad (A.9)$$

This means, that we focus on a particular set of characteristic planes, which are parallel to the η -axis and whose slopes in time $\lambda = df/dt$ are the eigenvalues of the matrix B/r . Solving the eigenvalue problem $\det(B/r - \lambda E) = 0$, we obtain the four

eigenvalues

$$\lambda_{1/2} = \frac{W_f}{r}$$

$$\lambda_{3/4} = \frac{W_f}{r} \mp \sqrt{\frac{1}{r^2} \left(\frac{\partial f}{\partial \varphi} \right)^2 + \left(\frac{\partial f}{\partial m} \right)^2} a \quad (A.10)$$

Taking into account the left and right eigenvectors associated with these four eigenvalues, the corresponding compatibility relations can be written as:

$$\frac{d(B_n r \rho)}{dt} - \frac{1}{a^2} \frac{d(B_n r p)}{dt} = 0 \quad (A.11)$$

$$\frac{1}{r} \frac{\partial f}{\partial \varphi} \frac{dw_m}{dt} - \frac{\partial f}{\partial m} \frac{dw_\varphi}{dt} = 0 \quad (A.12)$$

$$\frac{\partial f}{\partial m} \frac{dw_m}{dt} + \frac{1}{r} \frac{\partial f}{\partial \varphi} \frac{dw_\varphi}{dt} \mp \frac{\sqrt{\frac{1}{r^2} \left(\frac{\partial f}{\partial \varphi} \right)^2 + \left(\frac{\partial f}{\partial m} \right)^2}}{B_n r \rho a} \frac{d(B_n r p)}{dt} = 0 \quad (A.13)$$

with the total derivative operator

$$\frac{d}{dt} = \frac{\partial}{\partial t} + \frac{d^*}{dt} \frac{\partial}{\partial f} \quad (A.14)$$

along a straight line parallel to the t - f -plane on the characteristic plane parallel to the η -axis. The negative sign in equation (A.13) belongs to the left running characteristic plane (λ_3) and the positive sign is valid for the right running characteristic plane (λ_4).

Substituting the results of the EULER solution (subscript Eu) as well as the exact values of the characteristic solution (subscript Ch) into the equations (A.11) up to (A.13) and subtracting the corresponding equations yields

$$\left\{ \left(\frac{\partial \rho}{\partial t} \right)_{Ch} - \left(\frac{\partial \rho}{\partial t} \right)_{Eu} \right\} - \frac{1}{a^2} \left\{ \left(\frac{\partial p}{\partial t} \right)_{Ch} - \left(\frac{\partial p}{\partial t} \right)_{Eu} \right\} = 0 \quad (A.15)$$

$$\frac{1}{r} \frac{\partial f}{\partial \varphi} \left\{ \left(\frac{\partial w_m}{\partial t} \right)_{Ch} - \left(\frac{\partial w_m}{\partial t} \right)_{Eu} \right\} - \frac{\partial f}{\partial m} \left\{ \left(\frac{\partial w_\varphi}{\partial t} \right)_{Ch} - \left(\frac{\partial w_\varphi}{\partial t} \right)_{Eu} \right\} = 0 \quad (A.16)$$

$$\frac{\partial f}{\partial m} \left\{ \left(\frac{\partial w_m}{\partial t} \right)_{ch} - \left(\frac{\partial w_m}{\partial t} \right)_{Eu} \right\} + \frac{1}{r} \frac{\partial f}{\partial y} \left\{ \left(\frac{\partial w_y}{\partial t} \right)_{ch} - \left(\frac{\partial w_y}{\partial t} \right)_{Eu} \right\} + \frac{\sqrt{\frac{1}{r^2} \left(\frac{\partial f}{\partial y} \right)^2 + \left(\frac{\partial f}{\partial m} \right)^2}}{\rho a} \left\{ \left(\frac{\partial p}{\partial t} \right)_{ch} - \left(\frac{\partial p}{\partial t} \right)_{Eu} \right\} = 0. \quad (A.17)$$

These postcorrection relations are valid for the assumption, that the spatial derivatives in the f -direction are equal for both solutions. Substituting the contravariant velocity component w_f from equation (A.5), equation (A.17) can be written as

$$\frac{1}{r} \left\{ \left(\frac{\partial w_f}{\partial t} \right)_{ch} - \left(\frac{\partial w_f}{\partial t} \right)_{Eu} \right\} + \frac{\sqrt{\frac{1}{r^2} \left(\frac{\partial f}{\partial y} \right)^2 + \left(\frac{\partial f}{\partial m} \right)^2}}{\rho a} \left\{ \left(\frac{\partial p}{\partial t} \right)_{ch} - \left(\frac{\partial p}{\partial t} \right)_{Eu} \right\} = 0 \quad (A.18)$$

Due to the assumption, that the state variables satisfy all boundary conditions at the beginning of the time step and w_{f-ch} is zero at any time along the solid walls, we obtain the following relations

$$\rho_{ch} - \rho_{Eu} = \frac{1}{a^2} (p_{ch} - p_{Eu}) \quad (A.19)$$

$$\frac{1}{r} \frac{\partial f}{\partial y} w_{m-ch} - \frac{\partial f}{\partial m} w_{y-ch} = \frac{1}{r} \frac{\partial f}{\partial y} w_{m-Eu} - \frac{\partial f}{\partial m} w_{y-Eu} \quad (A.20)$$

$$\pm (p_{ch} - p_{Eu}) = \frac{\rho a}{\sqrt{\frac{1}{r^2} \left(\frac{\partial f}{\partial y} \right)^2 + \left(\frac{\partial f}{\partial m} \right)^2}} \left(\frac{w_f}{r} \right)_{Eu} \quad (A.21)$$

for correcting the EULER solution at the end of the time step.

Taking into account the relations between the transformation metrics and the metrics of the inverse mapping we obtain finally the equations (17), (18), and (19).

DISCUSSION

J.D.Denton, UK

I think that your solutions are very impressive, especially for the turbine blades. However, it is well known that the shock structure at the trailing edge of a turbine blade is determined by viscous effects and the results from an inviscid solution depend greatly on how they are modelled. Can you please explain how you modelled this trailing edge flow?

Author's Reply


We do not change the real airfoil geometry of the trailing edge for computational purposes. We only use a very fine grid spacing at the leading as well as at the trailing edge and apply no further model at the rounded trailing edge.

Mr Korduila, Gc

I have a question concerning the quality of the solution for the compressor flow. Usually, thinking of solutions with first order of accuracy in space one assumes that the solutions are very dissipative (smearing of shocks, etc.). The isobars in Figure 10, however show many oscillations. Could you comment on this?

Author's Reply

The substitution of the correction vector (Eq.6) into the discretisation (Eq.7) gives a better insight in the damping surface technique. When the steady state solution is marched, the correction vector becomes nearly constant. This means that the damping surface technique will be simplified to an EULER-LAX combination with very small artificial viscosity due to the use of 2 values in the range of 2% for the interior nodal points of the fine grid.



A NUMERICAL STUDY OF UNSTEADY FLOW EFFECTS
IN A SUPERSONIC COMPRESSOR CASCADE

by

Scott M. Richardson

AFWAL/POTX
Wright-Patterson AFB, OH 45433
USAAbstract

Recent experimental evidence exists which suggests that compressor cascades operating supersonically may pass a higher mass flow with a periodic inflow condition than with the thermodynamically equivalent mass-averaged steady condition. Since most compressor design methods rely on the use of an axi-symmetric analysis, any excursion in mass flow caused by blade row interactions will not be accounted for in the design. In the present study the two-dimensional Navier-Stokes equations are solved using the MacCormick explicit algorithm to obtain the flow in a subsonic rotor cascade for both periodic and steady flow inlet conditions. A new outflow boundary condition is presented to model the unsteady cascade exit flow conditions by using localized heat addition to produce a choke point near the downstream boundary. A computational study of the wake model parameters used in the periodic inlet boundary condition is performed to determine their effect on the cascade mass flow swallowing capacity.

Nomenclature

b	wake half width
c	speed of sound
D	scaling length
e	specific energy
E,F	vector fluxes in the mean flow equations
k	thermal conductivity
K_1	characteristic variables
m	mass flow
M	Mach number
P_0	total pressure
p	pressure
q	heat
R	gas constant
s	streamwise direction
t	time
T	static temperature
T_0	total temperature
u,v	velocity components
U	dependent variable flux vector
w	wheel speed
x	axial dimension
y	tangential dimension
α	stator flow angle
γ	ratio of the specific heats
δ	streamtube contraction

- ϵ turbulent eddy viscosity
- λ second viscosity coefficient (0.6μ for air)
- μ molecular viscosity coefficient
- ρ density
- σ normal stress
- τ shear stress
- ω vorticity

Subscripts

- a absolute coordinate frame
- i inviscid value or inner turbulence model viscosity
- o outer turbulence model viscosity
- r relative coordinate frame
- te trailing edge conditions
- w wall quantities
- ∞ freestream conditions

Introduction

One of the problems presently faced by designers of modern transonic and supersonic compressors is a method to account for the unsteadiness which naturally occurs within the moving blade rows of the machine. Examples of this unsteadiness are flow turbulence, blade row interactions, rotating stall, and surge. Of these, the blade row interaction effects have the most impact on normal design point compressor operation. As noted by Wennerstrom [1], recent experimental evidence exists which might support the conclusion that a compressor cascade operating supersonically may pass a higher mass flow with periodic inflow conditions than with the equivalent mass-averaged steady inflow conditions. Since modern compressor design methods rely on the use of an axis-symmetric analysis, and therefore treat all quantities in a mass-averaged way, any excursion in flow rate caused by this type of blade row interaction effect would not be accounted for during design. As shown in Fig. 1, this may cause the downstream rotor to overflow which would, in the case of supersonic rotors which have a nearly vertical characteristic, create a large reduction in the pressure ratio and efficiency produced by the stage.

An example of this situation is the Allison High Flow Compressor as reported by Bettner and Alverson [2]. In this machine all five rotors were operating with inlet relative Mach numbers equaling or exceeding unity at the tip, with stages two and three operating supersonically across the entire span. At the design stator setting the second stage exhibited flow capacity higher than the design intent by approximately six percent. It was necessary to close down the upstream stator to achieve the design pressure ratio and efficiency.

The only previous computational study of this problem was made by Scott [3] who performed Navier-Stokes calculations on the same second stage compressor cascade as used in this study. For the operating condition that was examined, the results indicate that the unsteady mass flow is approximately three percent higher than the steady case when using an inlet wake profile derived from experiment. Other numerical examinations of the blade row interaction problem, notably those by Mitchell [4] and Hodson [5], have used the inviscid time-marching method of Denton [6] to investigate the blade surface static pressure and velocity amplitude and phase relationships at the wake passing frequency. Although these calculations produced reasonable agreement with experiment, they are limited by both the use of the inviscid equations of motion and the first order time accuracy of the time-marching scheme.

The computations in the present analysis are performed for a stream surface at approximately 90% of the blade span for the second stage of a high performance supersonic compressor. At this spanwise location the inlet Mach number is approximately 1.33. Although this design is not necessarily typical of those in operation in many compressors today, it is typical of designs which may appear in future compressors requiring high pressure ratios and high flow rates. A generalized distribution of upstream total pressure is used to model wakes from an upstream stator row. Using this model, the wakes are varied in both depth and width to show their effect on the cascade mass flow capacity. In order to realistically model the actual compressor, the differing number of rotor and upstream stator blades must also be taken into account. This is done in the present study by calculating over four rotor passages to represent the approximately 3:4 stator to rotor blade ratio in the actual machine. Other blade ratios are also calculated to obtain the information about the effect of wake passing frequency on the mass flow capacity.

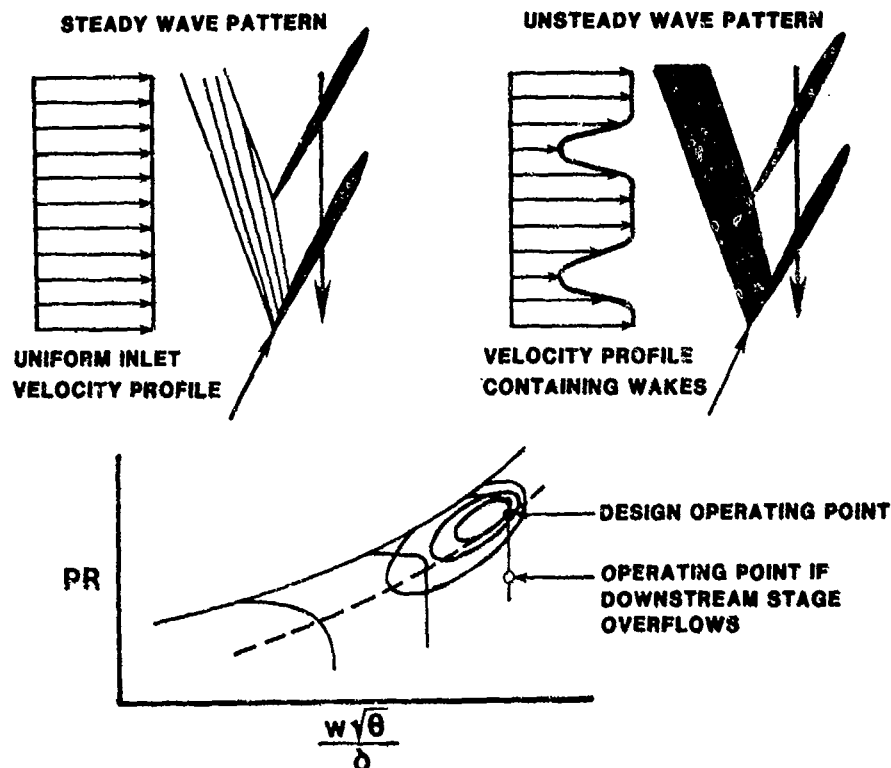


Figure 1: Blade Row Interaction Effect on Compressor Design Point.

Equations

The unsteady flowfield resulting from blade row interaction in a transonic or supersonic compressor is by definition complex, consisting of unsteady shock patterns, shock-boundary layer interactions, and separation regions. In order to capture both the inviscid and viscous flow features, the governing equations used for this analysis are the unsteady two-dimensional Reynolds averaged Navier-Stokes equations written in a quasi-three-dimensional formulation. These equations are written in terms of the mass-averaged variables for general curvilinear coordinates as follows:

$$U_t + \frac{1}{\delta}(U_x + V_y) = 0 \quad (1)$$

where the vector components are:

$$U = \begin{bmatrix} \rho \\ \rho u \\ \rho v \\ \rho e \end{bmatrix} \quad E = \begin{bmatrix} \delta \rho u \\ \delta \rho u^2 - \sigma_{xx} \\ \delta \rho uv - \tau_{xy} \\ \delta \rho ue - u\sigma_{xx} - v\tau_{xy} - \dot{q}_x \end{bmatrix} \quad F = \begin{bmatrix} \delta \rho v \\ \delta \rho uv - \tau_{xy} \\ \delta \rho v^2 - \sigma_{yy} \\ \delta \rho ve - v\sigma_{yy} - u\tau_{xy} - \dot{q}_y \end{bmatrix} \quad (2)$$

and the stress components are given by:

$$\begin{aligned} \sigma_{xx} &= (2\mu+1)\frac{\partial(\delta u)}{\partial x} + \lambda\frac{\partial(\delta v)}{\partial y} - \delta p & \sigma_{yy} &= (2\mu+1)\frac{\partial(\delta v)}{\partial y} + \lambda\frac{\partial(\delta u)}{\partial x} - \delta p \\ \tau_{xy} &= \mu\left(\frac{\partial(\delta u)}{\partial y} + \frac{\partial(\delta v)}{\partial x}\right) & \dot{q}_x &= k\frac{\partial(\delta T)}{\partial x} & \dot{q}_y &= k\frac{\partial(\delta T)}{\partial y} \end{aligned} \quad (3)$$

Auxiliary relationships used are the equation of state for a perfect gas, Sutherland's viscosity relation, and the molecular Prandtl number for air, $Pr=0.72$. Streamtube contraction is applied in the axial direction through the use of the contraction factor, $\delta(x)$. The contraction profile is taken directly from streamline pattern determined in the axis-symmetric method used to design the cascade. In the present calculation this contraction is approximately 38% through the blade passage.

Turbulence Model

The turbulence model employed is a modified form of the Baldwin-Lomax algebraic eddy viscosity model [7]. Although this model was originally developed for steady flow situations it is used in this unsteady problem for lack of a model better suited to unsteady flow calculations. Two separate flow regions are assumed in the implementation of the turbulence model, the blade boundary layer region and the wake region downstream of the cascade. In the blade boundary layer region, a two layer formulation is used. In the inner layer the turbulent eddy viscosity is given by the Prandtl-Van Driest expression:

$$\epsilon_1 = \rho (KYD)^2 |\omega| \quad (4)$$

where

$$D = 1 - \exp \left[-Y \left(\frac{\rho |\omega|}{\mu} \right)^{1/4} / 26 \right] \quad (5)$$

$|\omega|$ is the magnitude of the vorticity, Y is the distance normal to the blade surface, and $K=0.40$ is the von Karman constant. In the outer region of the boundary layer, the turbulent eddy viscosity is given by:

$$\epsilon_0 = \rho K C_{cp} F_{\max} Y_{\max} F_{KLEB} \quad (6)$$

where $F_{\max} = \max(Y|\omega|D)$, Y_{\max} is the value of Y where F_{\max} occurs,

$$F_{KLEB} = \left[1 + 5.5 (C_{KLEB} Y / Y_{\max})^6 \right]^{-1} \quad (7)$$

and $K = 0.0168$, $C_{cp} = 1.6$, $C_{KLEB} = 0.3$. The turbulence model switches from the inner to the outer model at the first point at which $\epsilon_1 \geq \epsilon_0$. Downstream of the blades the turbulent eddy viscosity is computed by taking an exponential decay of the eddy viscosity values calculated at the blade trailing edge using the following expression:

$$\epsilon(x) = \epsilon(x_{te}) \exp \left(\frac{x_{te} - x}{\lambda} \right) \quad (8)$$

In practice, the application of the turbulence model in the blade boundary layer region is limited to an area of the grid within a third or a quarter of the blade pitch from the blade surface. This is to minimize the calculation of Y_{\max} at mid-passage locations due to the influence of the strong passage shocks in the cascade. Also, it is the author's experience that applying the turbulence model throughout the blade passage leads to an inordinate damping of the unsteady effects in the passage.

Numerical Procedure

The algorithm used in the present study is McCormick's alternating direction explicit scheme. This is a predictor-corrector method which includes fourth-order numerical smoothing in order to reduce numerical oscillations. A detailed description of the algorithm may be found in [9].

The present analysis also includes the use of two grids, a coarse grid (22 x 52) to allow rapid initial convergence, and a finer final grid (40 x 103) for better resolution of shock patterns and increased accuracy of the final solution. The solution is initiated on the coarse grid and the majority of the convergence occurs there. The results of the coarse grid are then interpolated into the fine mesh and the solution is allowed to re-converge. For multiple blade solutions a converged single blade passage solution is first obtained with steady inlet conditions. This solution is then duplicated and examined in the remaining blade rows before the unsteady flow calculations are initiated. The convergence criteria used to obtain the steady state solution was defined to be less than a 0.1% change in the cascade mass flow at the blade leading edge plane. For unsteady calculations, the leading edge plane mass flow is monitored for convergence to a periodic state.

Boundary Conditions

The proper specification of boundary conditions continues to be of major concern in the calculation of both steady and unsteady flow. In the calculation of steady flows where the inlet relative Mach number is supersonic, as in the present case, one must satisfy the unique incidence condition and it is usual to specify the upstream stagnation pressure and temperature and either the inlet relative Mach number or the relative wheel speed. This is done by either specifying the quantities directly or by using a characteristic variables approach [3,9,10]. While having a superior ability to allow pressure waves moving upstream to exit the computational domain, the characteristic method does have the disadvantage that although the solution converges to the correct values of the Riemann invariants, it may not necessarily attain the

correct values of the stagnation quantities. It must be recognized however, that no set of inlet boundary conditions will guarantee that the program results match all upstream conditions when the inlet quantities are completely defined. It is often necessary to adjust the specified quantities to achieve the desired cascade inlet flowfield with the user having the control of the priority of the different parameters.

In the case of unsteady inlet conditions the situation is even less clear. For the upstream wake effects, the typical method is to specify the wake in terms of a velocity or stagnation pressure distribution in the wake relative reference frame (rotor absolute reference frame). Additional assumptions usually made are to hold the wake relative stagnation temperature and stator exit flow angle constant while using the static pressure obtained from the solution. This may be viewed as applying the usual subsonic flow inlet conditions but in the absolute reference frame. Quantities in the reference frame relative to the cascade may then be obtained through application of the usual velocity triangle relationships.

In the present study, both steady and unsteady flow calculations are made using the characteristic variables approach. This method is necessary because the downstream boundary condition used directly effects mass flow rather than exit static pressure. During convergence to a steady state, this downstream condition must be adjusted to obtain the desired cascade back pressure causing a series of pressure waves to propagate upstream and exit the computational domain at the inlet plane. The unsteady characteristic variable boundary condition is then used for the wake calculations with the wake profile given by a generalized variation in the absolute stagnation pressure of the form:

$$P_{01} = P_0(y') = (P_{01} - P_0)_{\max} \left[1 - \left(\frac{y'}{b} \right)^{1.5} \right]^2 \quad (9)$$

where b is half the wake width and y' is the circumferential distance measured from the wake centerline. The values of the Riemann invariants, K_1 , are given by (9):

$$K_1(\theta) = \frac{P_0}{P_0^*} = \frac{(RT_0)^{1/2}}{P_0^{1/2}} = \frac{P}{P_0^{1/2}}$$

$$K_2(\theta) = u \tan \alpha + v$$

$$K_3(\theta) = \frac{P}{P_0^{1/2}} = u \quad (10)$$

$$\frac{dK_1}{d\theta}(\theta) = \frac{1}{P_0^{1/2}} \left(\frac{dP_0}{d\theta} - u \right) = 0$$

Satisfying these four conditions gives the density, static pressure, and absolute velocity components at the inlet plane (i.e. the stator exit flow variables). The rotor inlet values are then obtained through the normal velocity triangle relations (by simply adding the wheel speed to the circumferential velocity component).

Downstream boundary conditions are also altered in the case of unsteady inlet flows. For steady flows, the normal method is to assume that the exit boundary is sufficiently far downstream that the static pressure can be taken to be uniform. This assumes that the inlet stagnation pressure is uniform, which, as noted above, is not the case for an incoming wake profile. The correct downstream condition for unsteady inlet flows allows the exit plane static pressure to be non-uniform, but with a specified average value. Since the static pressure distribution is obtained from the solution, the downstream condition must also come from the solution. One method to do this is to model the physical throttling process that occurs in an actual cascade test. When a cascade or blade row is throttled its mass flow is reduced resulting in an increase in the level of the downstream static pressure. Therefore, the introduction of a physical choke point in the flow downstream of the blade row with supersonic exit conditions at the grid exit plane should produce the same results. An approach using this method, which has been successful, was used by Scott [3] who introduced a second row of bodies downstream of the cascade to act as a variable area nozzle. While this method produces the desired pressure rise, the method does not easily generalize to three dimensions, and the upstream potential effect of the nozzles on the cascade flow has not yet been fully explored. An alternative approach, which has been developed in this effort, is to model the choke point through the introduction of heat sources across the pitch at some axial location downstream of the blade row and apply supersonic conditions at the exit plane. The effect of these sources, as shown in Fig. 2, is to cause the exit flow near the sources (the axial component of which is subsonic) to move along the Rayleigh line until it reaches the sonic point which is the point of maximum heating for that mass flow. At this point the flow has become choked and any additional heat input will cause the flow to remain choked, but move to a lower mass flow. The value of the heat sources is calculated using the Rayleigh flow equations and the flowfield parameters taken from the results of a calculation done for the cascade using a supersonic exit condition. Once the value of heat addition per unit mass flow required to choke the flow has been determined, the actual heat source

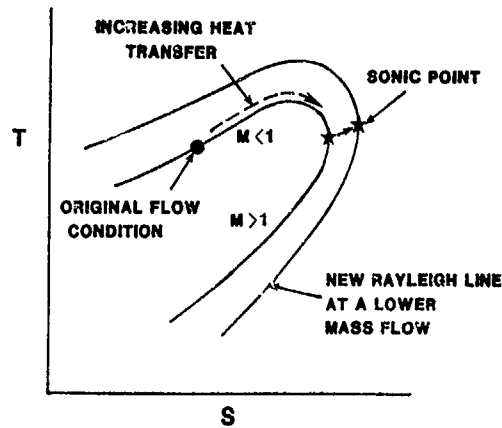


Figure 2: Thermal Choking Boundary Condition.

value is calculated at each time step taking into consideration the local mass flow and grid dimensions. Of course, this value of heat addition will only choke the original supersonic outflow (which has the highest mass flow rate) and the value of heat addition must be adjusted (upwards) to obtain the desired pressure rise as the solution proceeds. Normally, this adjustment is done during the coarse grid iterations and thus may be accomplished rather rapidly. Alternatives to the heat source method used here is the introduction of sources of mass flow or friction (Fanno flow), or a localized contraction in the streamtube thickness. These other methods have been used with the heat sources yielding the best results.

Other boundary conditions required in the solution of the Navier-Stokes equations are the solid boundary conditions and blade row periodicity. At the blade surface the no-slip condition is required and the normal derivatives of both pressure and temperature are zero. For the case of the present investigation the specification of the periodicity conditions must also take into account the differing numbers of stator and rotor blades. This may either be done using a time-lagged periodic condition [11] or by calculating over several blade passages. In the present study the latter method was used because, although it does require more computer storage, it provides for faster convergence than the time-lagged method. Boundary conditions used in the present investigation are summarized in Fig. 3.

The Grids

The computational mesh used consists of quasi-streamlines and quasi-pitchwise lines arranged to produce near-orthogonality at all grid boundaries. A method based on that of Sorenson [12] is used to generate this mesh by solving Poisson's equation. This method was modified to allow redistribution of grid lines up- and downstream of the blade row to remove regions which contain undesired pitchwise clustering or depletion of grid lines. The resulting grid has a smooth overall distribution while retaining grid near-orthogonality at the blade surfaces. The coarse grid used in the

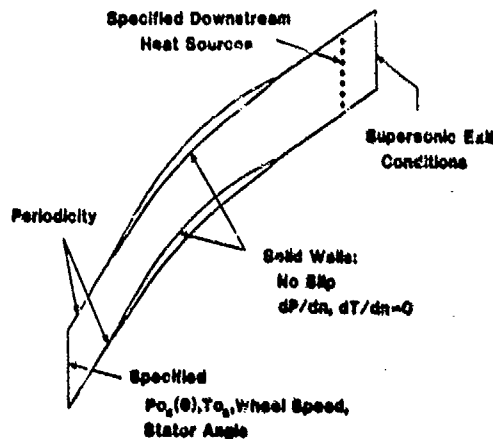


Figure 3: Boundary Condition Summary.

calculations is generated by removing every other grid line in both directions from the fine grid. This grid is shown in Fig. 4 which also includes a detail of the fine grid at the blade leading edge. An advantage of this type of grid is that a blade with a blunt leading edge is more correctly modeled than a grid using straight pitchwise grid lines. This will allow a more correct treatment of the bow shock which forms at the blade leading edge.

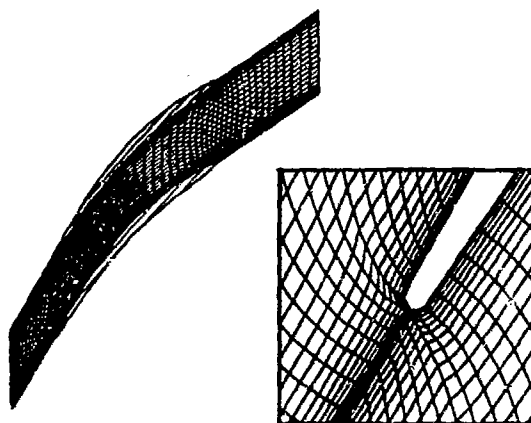


Figure 4. Coarse Computational Grid With Fine Grid Leading Edge Detail.

Sample Calculations

To provide a better understanding of the unsteady flow phenomena that arise in the blade wake interaction, samples of both steady and unsteady flow calculations are presented. The steady flow example is provided to show that while the leading edge mass flow has converged to the required steady state criteria, the resulting flowfield is far from steady. The steady solution is obtained after convergence on both the coarse and fine grids using the wake upstream boundary conditions with a wake depth of zero. Using a zero wake depth, the boundary condition remains valid for steady flow while allowing any effects of the wake boundary condition to be removed during convergence. As can be seen from Fig. 5, which presents the results from a single blade calculation 200 iterations apart, large vortices are periodically generated and shed along the suction surface near the trailing edge. This results in a small regular oscillation in the leading edge plane mass flow although this does not cause any visible unsteadiness in the upstream shock pattern in the inlet region. Note that while the calculation presented here is for a single blade row, two blade passages are presented to emphasize the periodicity in the inlet shock structure. The large concentration of contours near the exit plane indicates the presence of the heat sources used in the downstream boundary condition.

Once the steady solution has been obtained, calculations using the unsteady upstream boundary condition are initiated. The results of a sample calculation of the unsteady wake flow in four blade passages are presented in Fig. 6. This figure shows a "snapshot" of the four blade passage solution showing both stagnation pressure and Mach number contours. The effect of the wakes is clearly evident in the Mach number contours as a variation in the inlet shock structure and movement in the foot of the passage shock between passages. Of particular note is the way in which the wakes are chopped into individual segments which remain isolated as they pass through the blade row. This is most visible in the stagnation pressure contours where pockets of lower stagnation pressure may be seen convecting through the blade passage.

The Parameter Study

In order to examine the effect of various wake parameters on the unsteady mass flow swallowing capacity of a compressor rotor a generalized wake stagnation pressure profile is used. As mentioned previously, this profile is specified so that the wake width, defect depth, and wake spacing may be easily varied. During the parameter study the wake shape was kept constant with variations made in the wake depth and the stator rotor blade ratio. To model different blade ratios, calculations were made with several combinations of rotor blade passages and upstream stator wakes. The blade ratio is expressed as S/R where S is the number of stator wakes and R is the number of rotor blade passages calculated. The ratios used were 1:1, 2:3, and 3:4 (which approximates the actual machine value). The specification of a constant wake shape and different blade ratios exposes the rotor to wakes that all look the same but which are spaced differently. The wake depths used were 5, 10, and 15% of the inviscid value of the stagnation pressure, P_{01} , used in the wake description (9). The wake widths used were 13.1, 26.7, and 40% of the stator spacing in the 3:4 blade ratio case. These values were chosen to give a wake shape approximating that found experimentally. To maintain a thermodynamically equivalent inlet condition a separate analysis was

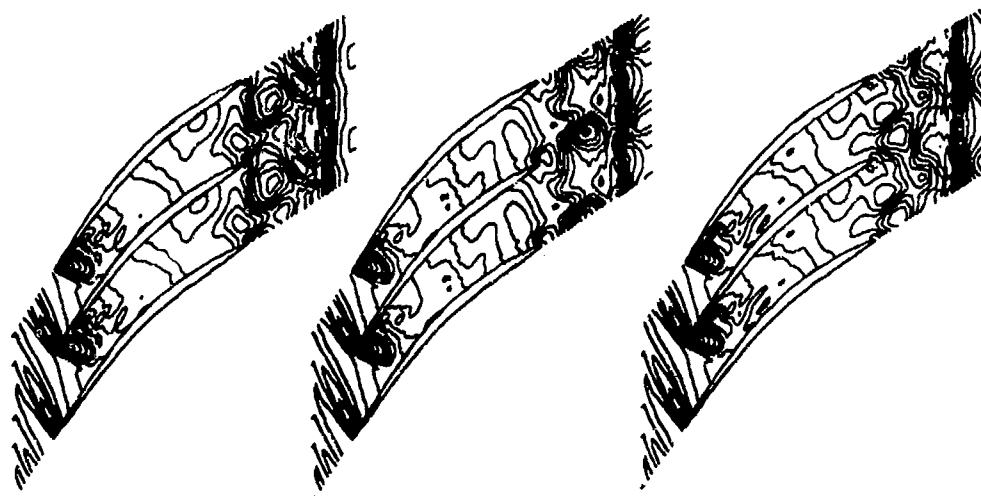


Figure 5: Static Pressure Contours of the Steady State Solution.

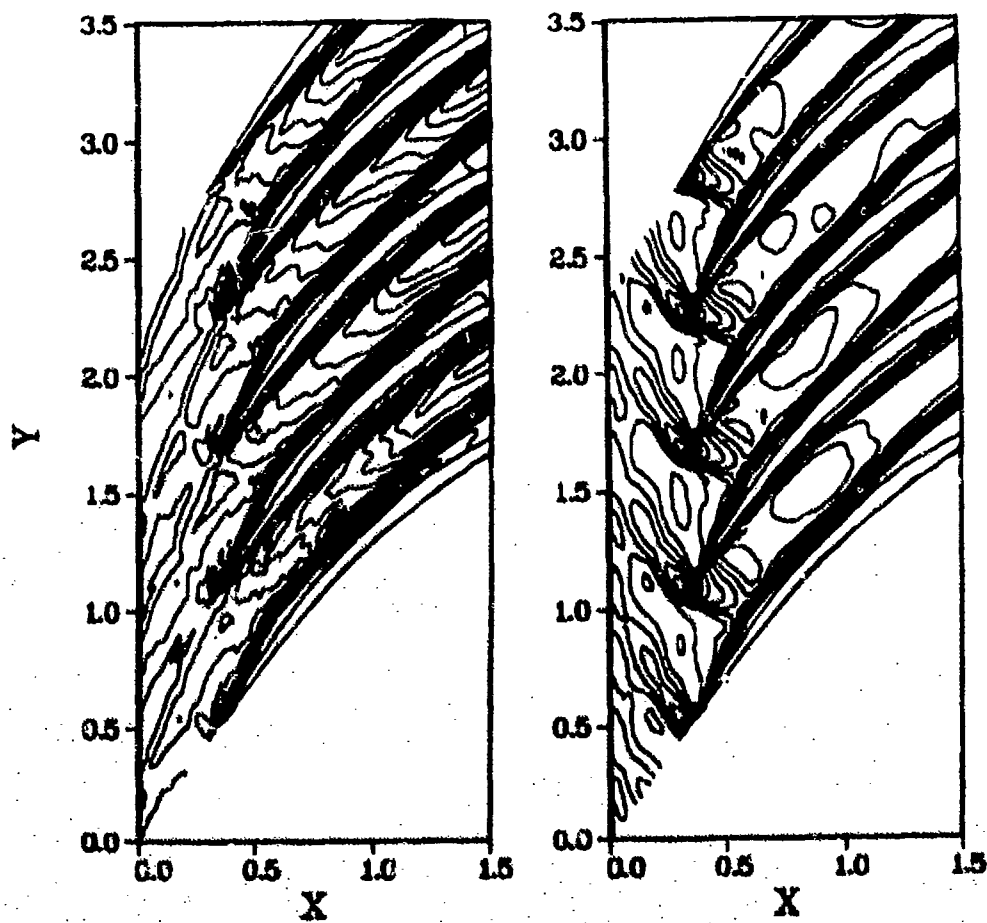


Figure 6: Stagnation Pressure and Mach Number Contours for the Unsteady Solution.

performed to calculate the mass averaged flow values at the inlet plane by integrating the stagnation pressure profile while holding the absolute stagnation temperature, static pressure, stator flow angle, and wheel speed constant. This provided the inviscid value of stagnation pressure which was specified in the wake profile to produce a mass-averaged inlet stagnation pressure equivalent to the steady state value.

The results of this parameter study are shown in Figures 7 and 8. The effect of the upstream blade wakes is to increase the mass flow swallowing capacity in the case of smaller wakes and decrease the mass flow for the largest wake. This change in mass flow capacity is also found to be nearly independent of the stator-rotor blade ratio. The increase in capacity may be understood by again considering Fig. 6 which shows the results for the 5% wake depth, 3:4 blade ratio case. This figure shows that the foot of the passage shock experiences a periodic movement into the passage, resulting in a localized increase in mass flow for that passage. This movement is perhaps due to interference between the wake and the upstream shock structure, causing a reduction in the shock strength. As the wake depth increases the "negative jet" effect of the wake is no longer compensated for by the movement of the passage shock. For larger wakes, this "negative jet" effect occupies a sufficient portion of the passage to cause the overall mass flow deficit. It is expected that the mass flow capacity of the blade row will decrease further for deeper wakes.

Conclusions

This paper has presented the results of a computational study of the effect of blade wake parameters on the mass-flow swallowing capacity of a transonic compressor rotor. The results of this study indicated that in a typical close-coupled stage the presence of upstream stator wakes can cause a downstream rotor row to overflow by as much as four percent. The parameter study showed that the amount of this overflow reaches a maximum for the smaller of the wakes studied and becomes a mass flow deficit as the wake deepens. Those results indicate that the presence of blade row wake interactions does effect the mass flow swallowing capacity of a transonic cascade. By not taking these effects into account, the compressor designer may miss the original mass flow objectives of the designed machine.

Acknowledgements

The author would like to thank Dr. A. J. Wennerstrom for providing direction and useful advice during the development of this study. Appreciation is also expressed to the Computational Aerodynamics Group, AFVAL/FIMMA, for their continued support and assistance.

References

1. Wennerstrom, A. J., "Low Aspect Ratio Axial Flow Compressors: Why and What it Means," Third Cliff Garrett Turbomachinery Award Lecture, Society of Automotive Engineers, October, 1986.
2. Bettner, J. L., and Alverson, R. F., Turbine Engine High Flow Compressor, AFAPL-TR-77-23, Air Force Aero Propulsion Laboratory, Wright-Patterson AFB, Ohio, 1977.
3. Scott, J. N., "Numerical Solution of Unsteady Flow in a Compressor Rotor Cascade," AIAA Paper 85-0133.
4. Mitchell N. A., "A Time-Marching Method of Unsteady Two-Dimensional Flow in a Blade Passage," CUEB/A-Turbo/TR 100, Cambridge University, 1980.
5. Hodson, H. P., "An Inviscid Blade-to-Blade Prediction of a Wake-Generated Unsteady Flow," ASME Paper 84-GT-43.
6. Denton, J. D., "An Improved Time Marching Method for Turbomachinery Flow Calculation," ASME Paper 83-GT-239.
7. Baldwin, B., and Lomax, H., "Thin Layer Approximation and Algebraic Model for Separated Turbulent Flows," AIAA Paper 78-257.
8. McCormick, R. W., and Baldwin, B. S., "A Numerical Method for Solving the Navier-Stokes Equations with Application to Shock-Boundary Layer Interactions," AIAA Paper 75-1.
9. Scott, J. N., and Hankey, W. L., "Navier-Stokes Solutions of Unsteady Flow in a Compressor Rotor," Journal of Turbomachinery, Transactions of the ASME, Vol. 108, No. 2, October 1986.
10. McKenna, P. J., Graham, J. E., and Hankey, W. L., The Role of Far-Field Boundary Conditions in Numerical Solutions of the Navier-Stokes Equations, AFVAL TR-87-3019, Air Force Wright Aeronautical Laboratories, Wright-Patterson AFB, OH, Sept. 1982.
11. Erdos, J. I., and Ainsner, E., Computation of Unsteady Transonic Flows through Rotating and Stationary Cascades, NASA-CN-2900, 1977.
12. Sorenson, R. L., A Computer Program to Generate Two-Dimensional Grids About Airfoils and Other Shapes by Use of Poisson's Equation, NASA-TN-81198, 1980.

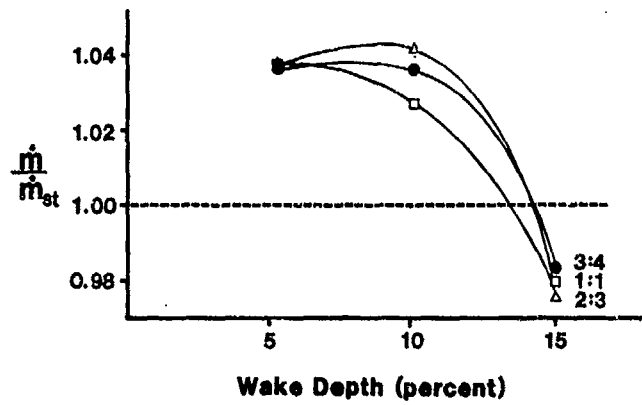


Figure 7: Variation in Cascade Mass Flow with Wake Depth.

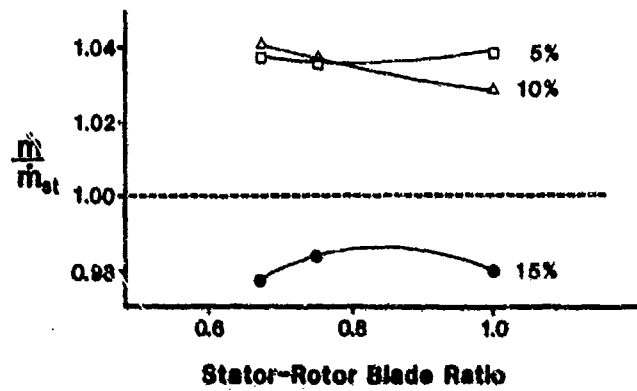


Figure 8: Variation in Cascade Mass Flow with Stator-Rotor Blade Ratio.

DISCUSSION

P. Ferrand

Avez vous etudier votre ecoulement instationnaire sur un seul canal interaube ou sur plusieurs; dans le premier cas quelle condition de periodicite instationnaire imposez vous?

Avez vous fait une analyse de la frequence du sillage a l'aval de la grille? Retrouvez vous la meme vitesse de defilement que celle que vous imposez a l'amant? N'y a t'il pas d'interaction entre la perodicite spatiale des aubes (nombre d'aubes) et la periodicite temporelle.

Author's Reply

The calculations were performed for several different numbers of blade passages. In multi-passage cases, the periodicity condition is imposed only at the top and bottom of the multiple passage "block." The other blade passage boundaries within this "block" are then treated as any other internal grid line.

The shedding frequency was not directly studied although it was noted that for steady inflow conditions (no wakes) in a multiple passage case the downstream wake structure varies from passage to passage apparently due to randomness in the calculated separation point.

T. Derrien

Could you develop or give some references about quasi-3D formulation where viscous terms and turbulent modelling are included?

Author's Reply

References which have included a description of a quasi-3D formulation are those of Scott[9] and Schafer, et. al. [13], although neither of these describe any contraction effects in the turbulence modelling.

The quasi-3D formulation used in the present study takes into account the streamtube contraction in both the mean flow and viscous terms of the governing equations. The contraction is also taken into account in the turbulent modeling since the viscosity used in the viscous terms is a combination of both the molecular and turbulent viscosities as described in [8]. Additionally, contraction effects are also found in the artificial damping terms which use second-derivatives of pressure to monitor the spatial change in the solution.

[13] Schafer, O., et. al., "Application of a Navier Stokes Analysis to Flows Through Plane Cascades," ASME Paper 85-GT-56.

J. G. Moore

While the calculated mass flow rates were sensitive to wake size they were insensitive to the wake frequency. Does this indicate that the variation in mass flow rate could be calculated with a steady flow calculation or quasi-steady calculation where the wakes are considered fixed in space relative to the rotor?

Author's Reply

Although the mass flow values presented do show an insensitivity to wake frequency it should be noted that these values are averages of the unsteady mass flow obtained from the solution. The time history of the mass flow at the leading edge plane of each blade passage was recorded and then averaged to give the values in Figures 7-8. While this average was fairly steady in time, the individual blade passage mass flows had considerable fluctuation with increasing amplitude as the upstream wake deepened. Therefore a quasi-steady analysis perhaps be done by placing a stationary wake profile at several circumferential locations relative to the blade passage and then averaging the results of the separate mass flows.

H. P. Hedson

Would the author please explain why the centre lines of the wakes appear to be oriented with the rotor relative flow direction.

Author's Reply

Part of the wake orientation is due to the rotor operating with a counter-swirling inlet flow of approximately 20 degrees. A more likely reason is that there exists some deficiency in the numerical algorithm which causes the wake flow to move in the direction of the grid lines in the inlet region.



A NUMERICAL STUDY OF THE 3D FLOWFIELD IN A
TRANSONIC COMPRESSOR ROTOR WITH A MODELLING
OF THE TIP CLEARANCE FLOW

W.N. Dawes,
Whittle Laboratory,
Maddingley Road,
Cambridge CB3 0DY,
U.K.

SUMMARY

Modelling the complex flowfield in a transonic axial compressor rotor is a considerable but worthwhile challenge for flow prediction methods. This paper describes a computer code aimed at solving the equations of three dimensional viscous compressible flow in turbomachine geometries.

The code is applied to the study of the flowfield in a transonic axial compressor rotor at design speed at both maximum flow and towards stall. The rotor was designed at DFVLR and tested using laser two-focus velocimetry. The rotor has a hub-tip ratio of 0.5 and design speed of 20260 rpm. At the design point the rotor pressure ratio is 1.626 and the mass flow 17.1 kg/s.

The predicted flowfield is compared with the laser measurements and the performance of the code discussed. In addition the discussion highlights the changes in the predicted endwall and tip clearance flows as the rotor operating point is moved towards stall.

INTRODUCTION

There are large inefficiencies in transonic compressor rotors, especially towards the endwalls. Minimising the weight and drag of an aeroengine requires the mass flow per unit frontal area to be maximised. This forces designers to use high axial Mach numbers and low hub-tip ratios. The latter means that the rotor flowfield will be highly three-dimensional and the former means that complex shock structures may exist. One of the reasons for shortfall in efficiency is undoubtedly the complex 3D coupling between the inviscid bulk flow and shock system and the blade and endwall boundary layers.

The stage pressure ratio is a strong function of tangential blade Mach number M_t and the stage temperature rise increases with the square of M_t (with corresponding variation of stage pressure ratio). Thus the fan of a typical high bypass turbofan engine with a stage pressure ratio of 1.6 to 1.7 will run with $M_t = 1.6$ at the tip and at an axial Mach number of 0.7. The performance of this fan has a significant impact on the overall performance of the engine. At 1% point increase in fan efficiency is worth about 0.7% points saving in a.f.c.

Conventional viscous/shock loss mechanisms do not seem able to account for the apparent measured inefficiency of the outboard supersonic part of a transonic fan [1]. Kerrebroek discusses additional loss mechanisms which may be active. They include strong radial flow in the rotor wakes (enhancing flow non-uniformity and mixing losses); flow unsteadiness relative to the rotor (possibly due to rotor-stator interaction); shock-induced boundary layer interactions; and tip clearance flows. It is known that tip clearance has a significant effect on efficiency. Rotor loss coefficients are not only increased in the tip region itself but also as far as 30% of span inboard from the tip. An increase in clearance to span ratio of 1% point may lead to an efficiency penalty of 1 to 2% points. It is also believed that the flow in the clearance region plays a key role in determining the stability of the stage. Measurements show large reductions in stall margin for quite small increases in clearance.

To understand these complex phenomena it seems essential to develop fully three dimensional flow models with appropriate allowance for viscous effects. The current paper outlines an efficient implicit algorithm solving the 3D compressible Reynolds averaged Navier-Stokes equations in turbomachinery geometries. The code is then used to study the flowfield in a low hub-tip ratio axial-flow transonic compressor rotor with a modelling of the tip clearance flow. The predicted flowfield is compared with laser velocimetry measurements. The behaviour of the predicted clearance flow is discussed.

EQUATIONS OF MOTION

The three-dimensional Reynolds averaged Navier-Stokes equations are written in finite volume form and cast in the blade-relative frame using cylindrical coordinates (r, θ, x) [2]:

$$\frac{\partial}{\partial t} \oint_{VOL} \bar{U} dVOL = \oint \bar{H} \cdot d\bar{A} \bar{R} \bar{E} \bar{A} + \oint \rho \bar{S} dVOL \quad (1)$$

where

$$\bar{U} = \begin{bmatrix} \rho \\ \rho W_x \\ r \rho W_\theta \\ \rho W_r \\ \rho E \end{bmatrix} \quad \bar{H} = \begin{bmatrix} \rho \bar{q} \\ \rho W_x \bar{q} + \bar{\tau} \hat{i}_x \\ r \rho W_\theta \bar{q} + \bar{\tau} \hat{i}_\theta \\ \rho W_r \bar{q} + \bar{\tau} \hat{i}_r \\ \rho I \bar{q} \end{bmatrix} \quad \bar{S} = \begin{bmatrix} 0 \\ 0 \\ -2\Omega r W_r \\ \frac{W_\theta^2}{r} + r\Omega^2 + 2\Omega W_\theta \\ 0 \end{bmatrix}$$

with $\bar{q} = W_x \hat{i}_x + W_r \hat{i}_r + W_\theta \hat{i}_\theta$, the relative velocity; Ω = rotation speed; $\bar{\tau}$ = the stress tensor (containing both the static pressure and the viscous stresses); and $I = c_p T_{e,rel} - \frac{1}{2}(\Omega r)^2$, the rothalpy. The system is closed by an equation of state

$$p = \rho(\gamma - 1)(E - 0.5(\bar{q} \cdot \bar{q} - (\Omega r)^2))$$

and a mixing length turbulence model patterned after Baldwin and Lomax [3].

NUMERICAL SOLUTION PROCEDURE

Finite Volume Formulation

The governing equations (1) are written in integral conservation form and the numerical discretization is designed to mimic this. We divide the computational domain into hexahedral cells and store the variables $\bar{U} = (\rho, \rho W_x, r \rho W_\theta, \rho W_r, \rho E)$ at cell centers (ijk) . The integrals in the equations are replaced by discrete summation around the faces of the computational cell.

$$\frac{\Delta \bar{U}_{ijk}}{\Delta t} VOL_{ijk} = \sum_{CELL(ijk)} \bar{H} \cdot \bar{A} \bar{R} \bar{E} \bar{A} = P(\bar{U})_{ijk} + \rho S_{ijk} \Delta VOL_{ijk} \quad (2)$$

Fluxes through cell faces are found by linear interpolation of density, velocity, etc., between cell centers and so the formal spatial accuracy is second order on smoothly varying meshes and global conservation is ensured. Viscous stresses are computed by defining a local curvilinear coordinate system and the chain rule.

Artificial Viscosity

An adaptive artificial viscosity term recommended by Jameson [4] is added to the discretized equations (2) to control odd-even point solution decoupling and to suppress oscillations in regions with strong pressure gradients. Equation (2) becomes

$$\frac{\Delta \bar{U}_{ijk}}{\Delta t} VOL_{ijk} = P(\bar{U})_{ijk} + \bar{D}(\bar{U})_{ijk} \quad (3)$$

where \bar{D} is the dissipative operator.

The artificial viscosity term has the form

$$\bar{D}(\bar{U}) = \bar{D}_I + \bar{D}_J + \bar{D}_K$$

where \bar{D}_I , \bar{D}_J , and \bar{D}_K represent the contributions from each of the curvilinear coordinate directions. Each contribution is written in conservation form as, for example

$$\bar{D}_I = d_{i+1/2jk} - d_{i-1/2jk}$$

The right-hand side terms have the form

$$d_{i+1/2jk} = \frac{\Delta VOL}{\Delta t} \epsilon_{i+1/2jk}^{(2)} (U_{i+1jk} - U_{ijk}) - \epsilon_{i+1/2jk}^{(4)} (U_{i+2jk} - 3U_{i+1jk} + 3U_{ijk} - U_{i-1jk}) \quad (4)$$

The coefficients $\epsilon^{(2)}$ and $\epsilon^{(4)}$ are determined by the flow in a self-adaptive manner

$$\epsilon_{i+1/2jk}^{(2)} = K^{(2)} \text{AMIN1} (0.5, (\pi_{ijk} + \pi_{i+1jk}) * 0.5)$$

$$\epsilon_{i+1/2jk}^{(4)} = \text{AMAX1}(0., (K^{(4)} - \alpha \epsilon_{i+1/2jk}^{(2)}))$$

where

$$\pi_{ijk} = |p_{i+1jk} - 2p_{ijk} + p_{i-1jk}| / (p_{i+1jk} + 2p_{ijk} + p_{i-1jk})$$

In the current effort we have used values for constants of $K^{(2)} = 1$, $K^{(4)} = 0.01$, $\alpha = 2$. Numerical experimentation showed that the dissipation in directions normal to solid boundaries should be set to zero to avoid masking the physical viscosity.

Boundary Conditions

A variety of boundary conditions is employed in the current study.

At inflow, total temperature and pressure are fixed and either flow angle or absolute swirl velocity held constant depending on whether the relative flow is subsonic or supersonic. At outflow the hub static pressure is fixed and radial variation derived from the simple radial equilibrium equation.

The finite volume mesh is constructed so that cell faces lie on solid surfaces (blades, hub, and casing) and along the periodic boundaries up and downstream of the blade row. Consequently, cells adjacent to periodic boundaries are updated just as if they were interior cells with the flux across the periodic boundary formed from linear interpolation between variables stored at the centers of the cells on either side of the boundary.

For cells adjacent to solid boundaries, zero fluxes of mass, momentum, and energy are imposed through the cell face aligned with the solid boundary. In addition, boundary conditions must be devised for the wall static pressure and wall shear stress; these two, acting on the wall cell face, are used in updating the momentum and energy equations for the cells adjacent to the solid walls. Wall static pressure is found by setting the derivative of pressure normal to the wall equal to zero. This is an accepted high Reynolds number approximation to solving the normal momentum equation. To prescribe the wall shear stress we use the velocities stored at cell centers adjacent to the wall and the known zero value of velocity on the wall to compute the velocity gradients at the wall. These gradients together with the wall viscosity are used with a locally defined curvilinear coordinate system to compute the wall shear stresses. If the mesh spacing near the wall is too coarse to resolve the boundary layer then wall shear stresses are set to zero.

Preprocessed Algorithm

The discretized equations are time-marched using an implicit preprocessed algorithm described in references [5] and [6]. In outline, we define a residue, R^* , by the two steps:

$$\begin{aligned} R_{ijk} &= \frac{\Delta t}{\Delta VOL_{ijk}} (P_{ijk}^n + D_{ijk}^n) \\ \bar{U}_{ijk} &= U_{ijk}^n + R_{ijk} \\ R_{ijk} &= \frac{\Delta t}{\Delta VOL_{ijk}} (P_{ijk}^n + D_{ijk}^n) \end{aligned} \quad (5)$$

We then update the variables by solving the implicit set of equations:

$$\begin{aligned} [I - c_i \frac{\Delta t^2}{\Delta VOL^2} \lambda_i^2 \delta_{ii}^2] [I - c_j \frac{\Delta t^2}{\Delta VOL^2} \lambda_j^2 \delta_{jj}^2] \\ [I - c_k \frac{\Delta t^2}{\Delta VOL^2} \lambda_k^2 \delta_{kk}^2] \Delta U = R^* \end{aligned} \quad (6)$$

where c_i , c_j and c_k are free parameters (of order unity), λ_i , λ_j and λ_k are the spectral radii of the Jacobians associated with the convective fluxes in the i , j and k directions, and δ_{ii}^2 , for example, represents $(\phi_{i+1} - 2\phi_i + \phi_{i-1})$. The left-hand side is factored into three tridiagonal matrices for efficient inversion.

Although in principle the algorithm can be made stable for any size time step by suitable choice of the free parameters, ϵ_I , ϵ_J and ϵ_K , in practice it is found that there is an optimum range of time steps which leads to minimum number of steps to convergence. Extensive numerical experimentation for a range of geometries showed that larger time steps required larger values of ϵ for stability and that after a certain point the solutions became too smoothed during the transient, delaying convergence. It was found that CFL numbers in the range 2 - 5 were optimal with associated values of ϵ equal to unity. For the results presented in this paper, the CFL number was 2 and $\epsilon_I = \epsilon_J = \epsilon_K = 1$.

Multigrid convergence acceleration

The present effort is concerned with steady solutions so a multigrid acceleration technique [4], [7] is used. The basic principal of multigrid is to take advantage of the fact that the finite volume residue, \bar{R}_{ijk} (equation 5), has errors over the whole range of wavelengths which can be supported by the mesh. The time marching algorithm, equation (6), is efficient at eliminating the short wavelength components of this error, but much less so for higher wavelengths. So we define a succession of ever coarser meshes, typically by deleting every other mesh line, derive an appropriate representation of the residue on each mesh and use the basic time marching solver, equation (6), to reduce the level of the error associated with the current mesh. Thus, sweeping through the meshes should allow each of the wavelengths in the residue error to be attacked with optimum efficiency. The multigrid recipe is as follows:

- (i) Update finest mesh variables using the basic time marching solver, equation (6), represented by

$$L^h \Delta U^h = R^h(U^h) + P^h \quad (7)$$

Here U^h is the variable (ρ, p, v_x etc.) on the finest mesh, h , R^h is the fine mesh residue, L^h is the fine mesh implicit operator, ΔU^h is the correction to the fine mesh variables,

$$U^h = U^h + \Delta U^h \quad (8)$$

and P^h is the forcing function (zero on the finest mesh).

- (ii) Collect residues and variables to the next mesh, the $2h$ mesh, using a suitable collection operator, I_h^{2h} , and define a forcing function P^{2h} :

$$\begin{aligned} U^{2h} &= I_h^{2h} U^h \\ P^{2h} &= I_h^{2h} R^h(U^h) - R^{2h}(U^{2h}) \end{aligned} \quad (9)$$

The collection operator performs a volume weighted average to maintain conservation

$$I_h^{2h} U^h = \sum U^h \Delta VOL^h / \sum \Delta VOL^h \quad (10)$$

with the sum being over the fine mesh cells gathered together to form the next mesh cell. This procedure also eliminates error with twice the wavelength of the fine mesh which cannot be supported on the next mesh.

- (iii) Update current mesh variables using the basic time marching solver

$$L^{2h} \Delta U^{2h} = R^{2h}(U^{2h}) + P^{2h} \quad (11)$$

The forcing function guarantees fine mesh accuracy by causing the coarse mesh solution to be driven by the fine mesh residues.

- (iv) Prolong the coarse mesh corrections to the finest mesh using a prolongation operator, I_h^{2h} and update the finest mesh variables

$$U^h = U^h + I_h^{2h} \Delta U^{2h} \quad (12)$$

This prolongation must not reintroduce errors on the finest mesh eliminated in step (i)

This multigrid procedure is illustrated by application to the 2D test case of transonic shocked flow past a channel hump (the shock is strong enough to cause the boundary layer to separate). The basic fine mesh is 51×25 and two levels of coarsening give meshes of 41×13 and then 21×7 . Predicted Mach number contours and velocity vectors are shown in Fig. 1. convergence histories are shown in Fig. 2. Roughly speaking, the first level of multigrid halves the number of time steps to convergence; introducing the second level produces similar improvements. Further levels, however, give no further gains as the meshes are just simply too coarse.

APPLICATION TO THE TRANSONIC COMPRESSOR ROTOR

The code is applied to the study of the three-dimensional flowfield in the axial flow single stage transonic compressor rotor tested using laser-two-focus velocimetry at the DFVLR [8,9]. The compressor rotor has an inlet tip diameter of 0.4 m, a hub-tip ratio of 0.5, and tip solidity of 1.34. The design total pressure ratio is 1.626 with a mass flow of 17.1 kg/s at 20260 rpm. The compressor flow path with the laser velocimeter measuring stations is shown in Fig. 3; the compressor stage performance is shown in Fig. 4 with the maximum efficiency point indicated.

The computations were performed with an attempt to resolve the tip clearance flow. A $17 \times 41 \times 17$ finite volume mesh was used, illustrated in Fig. 5. The mesh is refined exponentially near blade suction and pressure surfaces and in the radial direction cells are concentrated near the casing and stretched away toward the hub. The blade tip is treated rather crudely by simply reducing the blade thickness smoothly to zero and then applying periodic boundary conditions between the tip itself and the casing. The tip clearance was taken to be 1.5 mm, i.e. 1.5 percent span; the actual value is not known. Only two cells are used in the clearance region because of computer storage constraints. Nevertheless it is believed that, at least to a first approximation, something of the nature of the clearance flow can be resolved. Again because of storage constraints, no attempt was made to model the hub boundary layer and an inviscid solid surface boundary condition imposed. It is believed that this will not affect the solution over the majority of the blade height but clearly may affect the computed mass flow-pressure rise characteristics of the stage. The mesh spacing is fine enough near blade surfaces and casing for the centers of cells adjacent to the solid surfaces to be at $Y^+ = 10$. This gives marginally acceptable resolution.

The code executes at about 5×10^{-3} s per unit point per time step on a Perkin-Elmer 3230 minisystem ($= 5 \times 10^{-3}$ s on an IBM 370). Using a spatially varying time step with CFL number around 2 and one level of multigrid, 750 time steps were used to achieve acceptable convergence (rms pointwise $\sum H(p_{w_x}) \cdot dAREA$ less than 1×10^{-6}).

PRESENTATION AND DISCUSSION OF RESULTS (1) Maximum efficiency point

Figures 6-9 compare contours of computed relative Mach number with the laser measurements at each of four spanwise stations. The relative inflow Mach number varies from around 0.95 near the hub to about 1.4 toward the casing and there is a corresponding spanwise variation of flow character. At 18 percent span the flow accelerates to just sonic before shockfree compression. At 45 percent span the relative inflow is just supersonic and a well-resolved detached bow shock forms. At this point flow is spilling from one passage to the next and local incidence at the leading edge is high. Considering the coarseness of the computational mesh, the resolution of the expansion-shock pattern is considered to be good. At 68 percent span, the relative inflow Mach number is higher and the bow shock is now attached to the leading edge. At 89 percent span the measurements indicate a weak oblique shock followed by diffusion to the subsonic exit flow whereas the computations show a rather stronger shock with somewhat less downstream diffusion.

In general considering the complexity of the flow and the coarseness of the mesh the level of agreement is considered to be encouraging. Toward the exit plane the computed Mach numbers tend to be lower than those measured particularly toward the hub. This discrepancy is partly due to the coarse mesh underestimating the blockage. However, the discrepancy also arises because the mixing length turbulence model contains no correction for the stabilizing effect of convex curvature, which tends to relaminarize the boundary layer [10] on the aft part of the suction surface. Thus, toward the hub the turning is overpredicted and Mach number level too low.

Computed and measured contours of relative Mach number in the cross-flow plane near the blade stacking axis, plane 11 in Fig. 3, are compared in Fig. 10. The predicted high Mach number region in the casing-suction surface corner associated with the leakage jet is clearly resolved but smaller in spatial extent than that measured.

Figure 11 shows predicted contours of relative Mach number and relative velocity vectors in a blade-blade plane just near the casing actually in the clearance region. The bow shock causes a large pressure difference across the blade tip which drives a strong jet from the pressure side to the suction side starting at the leading edge. This jet meets and deflects the incoming flow along a clearly visible interaction zone passing from the leading edge to about midchord on the pressure surface. Over the aft half of the passage the flow is nearly circumferential representing a considerable axial blockage. Figure 12 shows velocity vectors just near the suction surface. This shows the strong vortex associated with the clearance flow and the strongly disturbed casing endwall boundary layer profile.

The interaction zone between the leakage flow and the incoming flow corresponds to the rollup of the tip leakage into a vortex whose core represents a region of high loss. Figure 13 shows predicted entropy contours at several axial stations starting at the leading edge. A loss core can be seen, moving across the pitch following the line of the interaction zone.

Figure 14 shows a shadowgraph taken in a plane near the casing of a similar transonic compressor rotor [11]. Labelled on the figure is the bow shock and the strong vortex arising from the tip clearance flow. A similar result and interpretation has been reported in [1]. This experimental evidence provides strong support for the physical realism of the present computed flow.

One of the key parameters in understanding the effect of clearance flows on compressor stability is the state of the casing endwall boundary layer [11]. Not only the circumferential average is of interest but also any local thickening. Figure 15 shows contours of axial velocity in axial stations from the leading edge to the wake. This gives a qualitative picture of the development of endwall blockage and shows that although downstream of the blade row (where conventional measurements are made) the axial blockage is more or less circumferentially uniform, within the blade passage substantial pitchwise variation exists. The endwall blockage is seen to develop from the leading edge near the suction side and steadily grow across the passage until reaching the pressure side.

(ii) Maximum flow point

This picture changes in the flowfield computed at a lower back pressure with the compressor rotor operating near to the maximum flow point. Figure 16 shows contours of computed relative Mach number at 89% span station. The blade incidence is now negative and the shock has been swallowed. Figure 17 shows predicted contours of relative Mach number and relative velocity vectors in a blade-blade plane just near the casing, actually in the clearance region. The clearance flow and tip leakage vortex have moved aft to correspond to the new shock position. This is to be expected and there is some experimental evidence for the leakage vortex and the passage shock location moving in sympathy [11]. The strong distortion in the Mach number contours is due to the strongly distorted total pressure (loss) field associated with the leakage vortex. Contours of axial velocity at several axial stations, shown in Figure 18, suggest that there is less circumferential non-uniformity than in the earlier maximum efficiency point case (Figure 15), but that growth of the blockage is much more abrupt.

CONCLUSIONS

An efficient code solving the compressible Navier-Stokes equations in turbomachinery geometries has been developed.

Results are presented for the flow in a low hub-tip transonic compressor rotor with an attempt to model the tip clearance flow. Despite using a relatively coarse mesh which supports only marginally acceptable resolution, generally good agreement with laser velocimeter measurements is obtained.

A strong tip leakage vortex is predicted, in good qualitative agreement with experimental evidence. This leakage vortex moves in sympathy with the passage shock. The predicted development of axial blockage on the casing endwall through the machine shows strong circumferential non-uniformity within the blade passage. This non-uniformity appears greater at the maximum efficiency point than at the maximum flow point. It is speculated, therefore, that compressor instability may develop in response to an increasingly non-uniform blade-blade variation of endwall blockage as the operating point is moved towards stall.

REFERENCES

- [1] Kerrebrock, J.L., "Flow in Transonic Compressors" AIAA Journal, Vol. 19, No. 4, 1980.
- [2] Sarathy, K.P., "Computation of Three-Dimensional Flowfields Through Rotating Blade Rows and Comparison with Experiment" ASME Journal of Engineering for Power, Vol. 104, 1982.
- [3] Baldwin, B., and Lomax, H., "Thin Layer Approximation and Algebraic Model for Separated Turbulent Flows" AIAA Paper No. 78-257, 1978.
- [4] Jameson, A., and Baker, T.J., "Multigrid Solution of the Euler Equations for Aircraft Configurations", AIAA Paper No. 84-0093, 1984.
- [5] Dawes, W.N. "A pre-processed implicit algorithm for 3D viscous compressible flow" Notes on Numerical Fluid Mechanics, Vol. 12, Vieweg 1986.
- [6] Dawes, W.N. "Application of full Navier-Stokes solvers to turbomachinery flow problems" VKI Lectures Series 2: Numerical techniques for viscous flow calculations in turbomachinery bladings, Jan 1986.
- [7] Brandt, A. "Multi-level adaptive solutions to boundary-value problems" Math. Comp. Vol. 31, No. 138, 1977.
- [8] Weyer, H.B., and Dunker, R., "Laser Anemometry Study of the Flowfield in a Transonic Compressor Rotor", AIAA Paper No. 78-1, 1978.
- [9] Dunker, R., Strinning, P.E., and Weyer, H.B. "Experimental Study of the Flowfield within a Transonic Axial Compressor Rotor by Laser Velocimetry and Comparison with Throughflow Calculations", ASME Paper No. 77-gt-28, 1977.
- [10] Adams, E.W., and Johnston, J.P. "A mixing length model for the prediction of convex curvature effects on turbulent boundary layers" ASME J. of Eng. for Gas Turbines and Power, Vol. 106, pp 142, 1984.
- [11] Freeman, C., "Tip Clearance Effects in Axial Turbomachines" VKI Lectures Series LS-05, 1984.

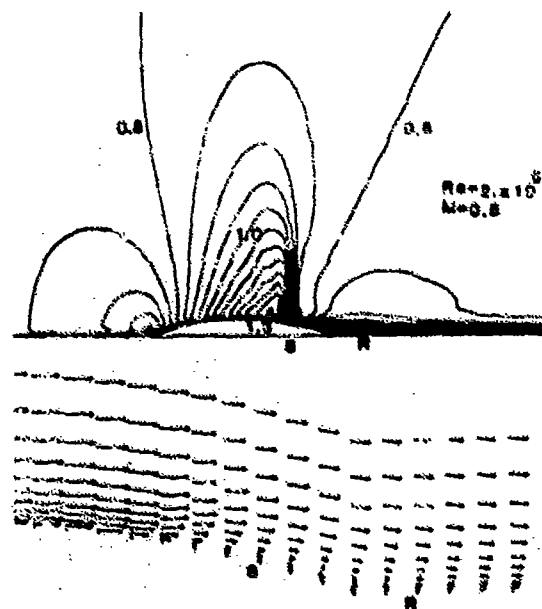


Fig.1 Computed Mach numbers and velocities for a channel hump

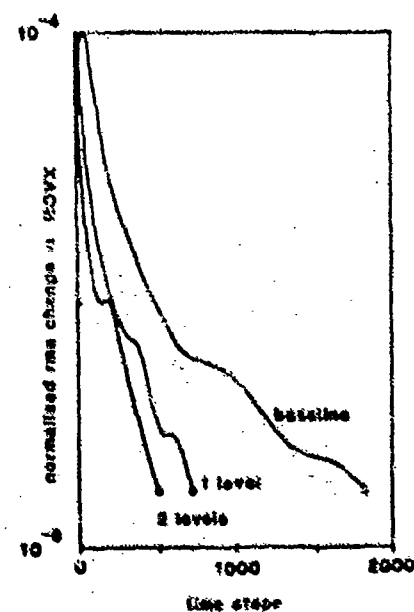


Fig.2 Convergence histories

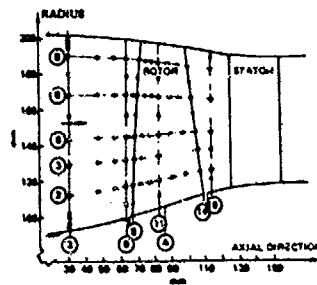
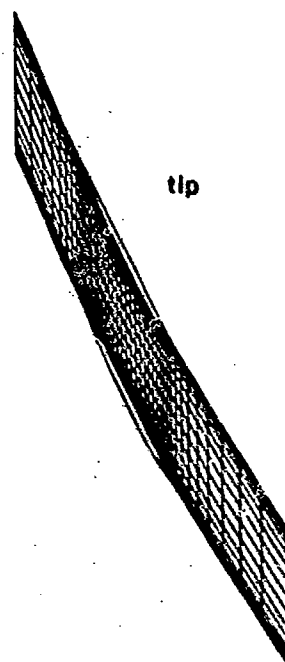
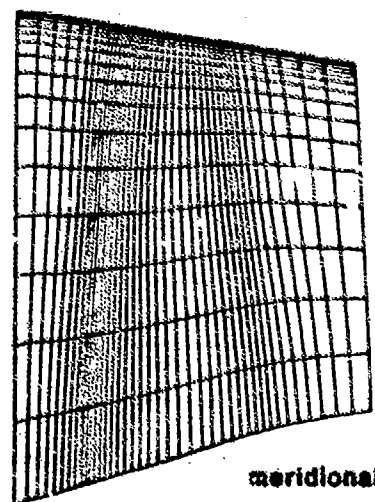


Fig.3 Flowpath and laser measuring stations



tip



meridional

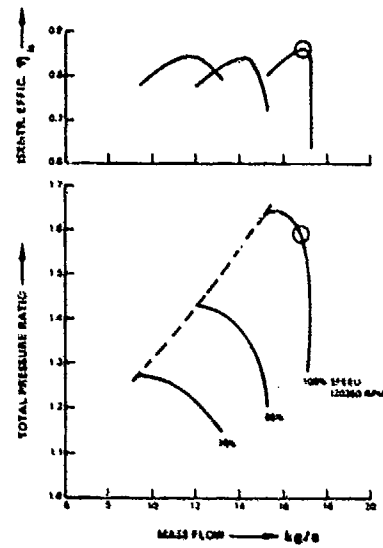
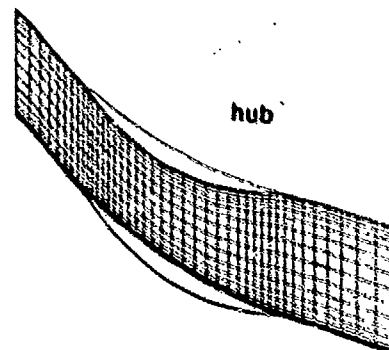
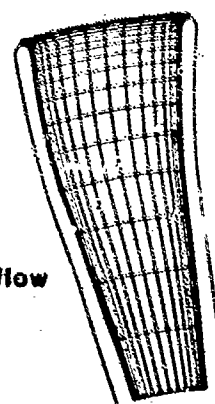


Fig.4 Stage performance

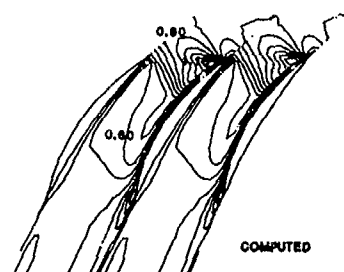
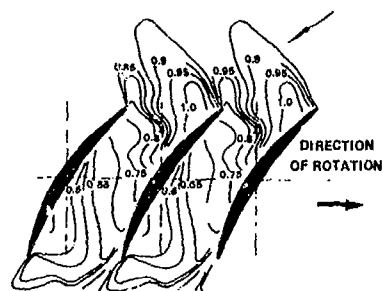


hub

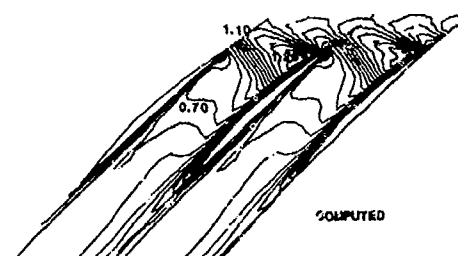
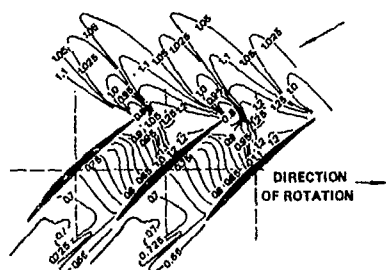


cross-flow

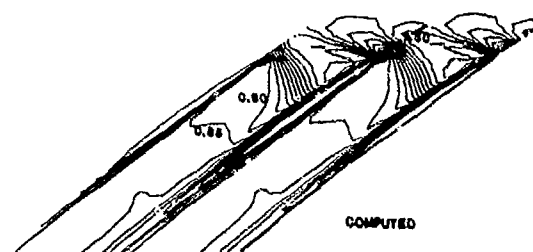
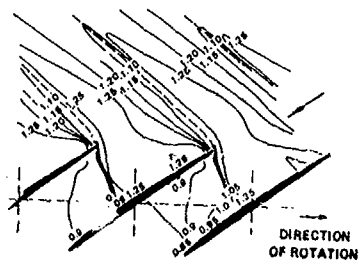
Fig.5 Computational mesh



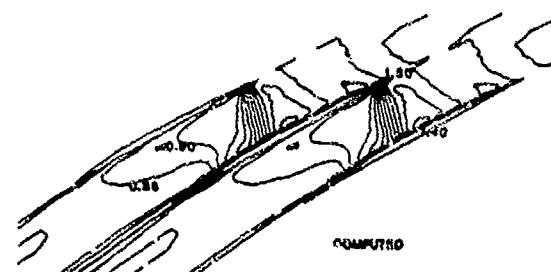
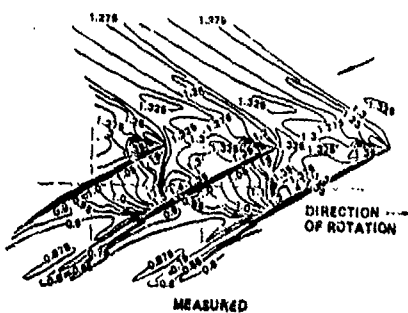
18% span



45% span



68% span



89% span

Figs. 8-9 Contours of relative Mach number

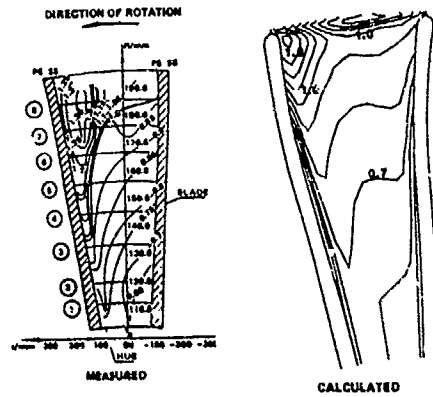


Fig.10 Contours of relative Mach number in Plane 11

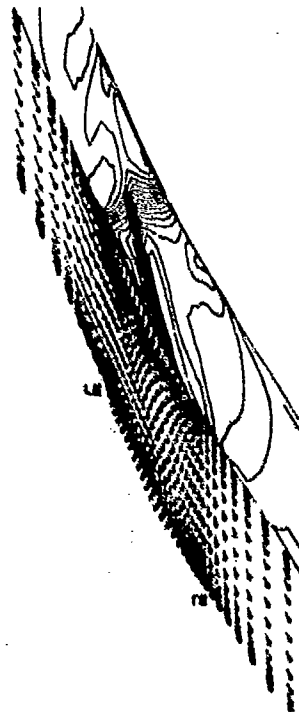


Fig.11 Relative Mach numbers and velocity vectors in the clearance region

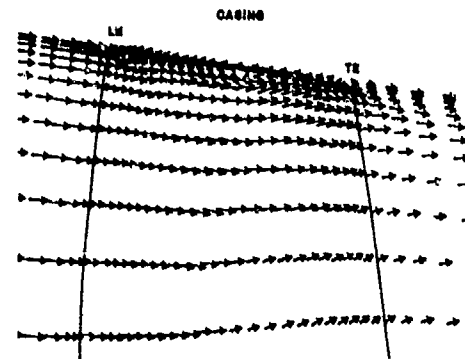


Fig.12 Velocity vectors near the suction surface

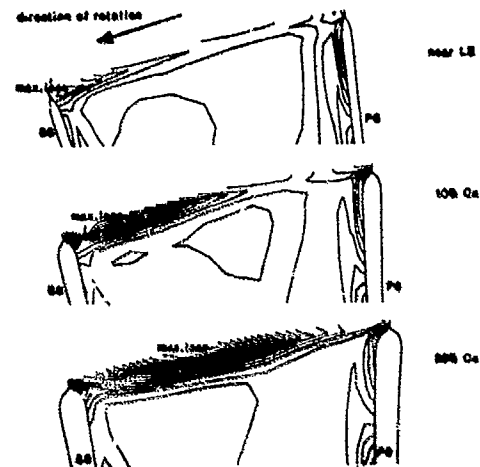


Fig.13 Contours of entropy

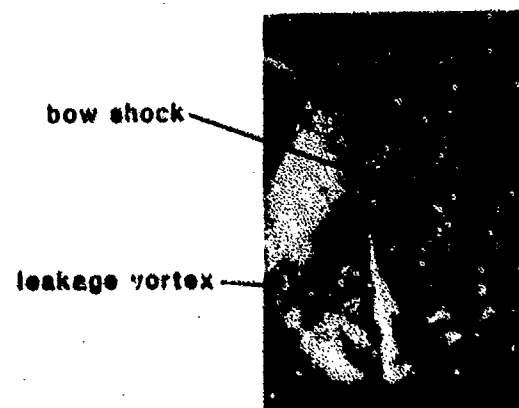


Fig.14 Shadowgraph taken near the casing of a similar transonic compressor

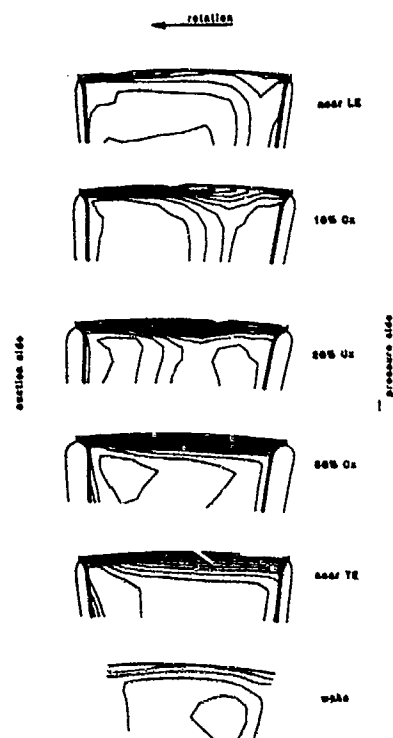


Fig. 15 Contours of axial velocity at several axial stations at the max. efficiency point

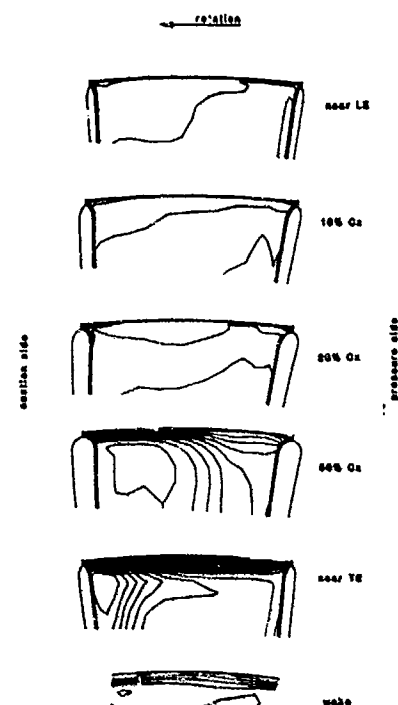


Fig. 18 Axial velocities near the maximum flow point

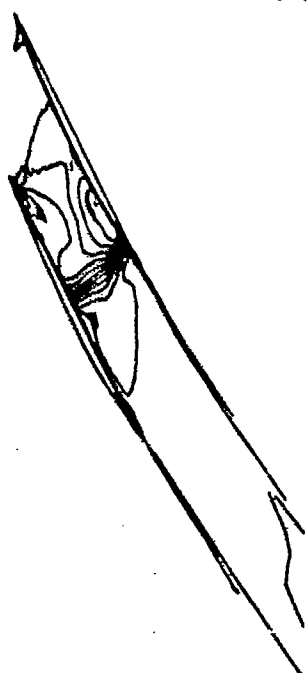


Fig. 16 Mach numbers at 80% span for an operating point near maximum flow

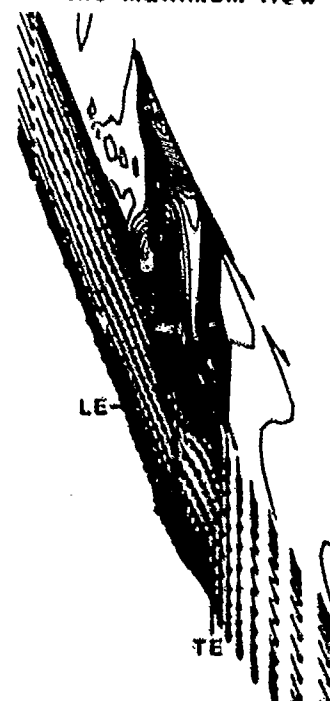


Fig. 17 Mach nos. and velocities in the clearance region near the max. flow point

DISCUSSION

J. Moore, US

In the multigrid method, you said it was not easy taking the changes calculated for the coarse grid back to the fine grid. Could you explain how you do this for the non-uniform grid region near the walls?

Author's Reply

It is important not to re-introduce short wavelength error when adding coarse mesh changes to fine mesh variables. I use a point-Jacobi smoother to distribute the coarse mesh changes into the fine mesh.

Mr Hourmouziadis, Ge

Looking at your full results for the two operating points, could you give a physical explanation for the behaviour of the clearance flows?

Author's Reply

The leaking flow is more vigorous at maximum flow and so the deficit created is more substantial.

Mr Hourmouziadis, Ge

Why is it more vigorous?

Author's Reply


At the maximum point you see very little flow deficit from where the flow has leaked. You see this deficit much more strongly for the other case. You would have expected it the other way round. But at maximum flow the pressure ratio across the blades downstream of the shock is in fact greater than at maximum and so drives a more vigorous leakage albeit over a smaller fraction of chord.

Mr Hourmouziadis, Ge

Do you suggest that the mass flow through the clearance is lower on the high pressure case?

Author's Reply

The distance on which the leakage occurs is much larger in the H.P. case so the mass flow is bigger.



CALCUL D'ÉCOULEMENTS INTERNES A GRAND NOMBRE DE REYNOLDS PAR RESOLUTION NUMERIQUE DES EQUATIONS DE NAVIER-STOKES

L. Cambier, B. Escande et J-P. Vuilliot

OFFICE NATIONAL D'ETUDES ET DE RECHERCHES AEROSPATIALES
BP 72, 92322 CHATILLON CEDEX (France)

RESUME

L'exposé est consacré au calcul d'écoulements turbulents à grand nombre de Reynolds par résolution numérique des équations de Navier-Stokes moyennées et complétées par un modèle de turbulence, et à la présentation de résultats concernant l'aérodynamique interne.

La méthode de calcul est brièvement rappelée; elle se caractérise par la mise en oeuvre d'une approche par sous-domaines et par l'utilisation d'un schéma numérique simple combiné à une technique de sous-maillage par dichotomie pour la description fine des couches visqueuses. On présente des résultats de calcul d'écoulements transsoniques turbulents, avec lois de paroi, pour une configuration industrielle relative à une grille de compresseur à divers régimes de fonctionnement. Dans une dernière partie, des données expérimentales détaillées pour le problème de l'interaction onde de choc-couche limite dans un canal transsonique plan sont mises à profit pour comparer un modèle de turbulence algébrique et un modèle (k, ϵ).

1. INTRODUCTION

Les écoulements dans les turbomachines aéronautiques sont particulièrement sensibles aux effets dus à la viscosité du fluide et l'amélioration, au moindre coût, des performances de telles machines passe par la mise en oeuvre de méthodes de calcul permettant de prédire ces effets le plus précisément possible. La détermination par voie numérique d'écoulements aussi complexes ne peut, le plus souvent, être effectuée par des méthodes de calcul simples fondées sur le seul effet de déplacement des parois, mais nécessite le développement de méthodes moins sommaires prenant en compte la forte interaction entre les régions de fluide parfait et les couches dissipatives. Pour atteindre cet objectif, deux voies principales sont actuellement ouvertes: les méthodes indirectes de couplage fort fluide parfait-fluide visqueux (voir, par exemple, la communication de Le Bailleur et Blaise [1]), les méthodes directes de résolution des équations de Navier-Stokes. C'est à ce dernier type qu'appartient la méthode exposée dans la présente communication. Les techniques de résolution des équations de Navier-Stokes, appliquées aux turbomachines, sont en cours de développement dans plusieurs laboratoires et ont fait l'objet récemment d'assez nombreuses publications (par exemple [2] à [8]).

Aux grands nombres de Reynolds, la simulation numérique des écoulements visqueux se heurte à la difficulté de représenter au mieux deux phénomènes fondamentaux: la turbulence et la faible épaisseur des couches dissipatives. Pour ce qui concerne la prise en compte de la turbulence, il n'est pas envisageable à moyen terme et pour des applications industrielles de mettre en oeuvre des méthodes de simulation directe de la turbulence, il faut avoir recours à la modélisation. A l'heure actuelle, il existe une grande diversité de modèles de turbulence (modèles algébriques, modèles à une ou plusieurs équations de transport, "Algebraic Stress Model", etc.), mais aucun de ces modèles ne s'est encore véritablement imposé par un accord avec l'expérience satisfaisant pour des configurations d'écoulement variées. La faible épaisseur des couches visqueuses pariétales induit une évolution très rapide de la vitesse et des grandeurs turbulentes, la discrétisation des gradients de ces quantités exige alors l'utilisation d'un maillage fin au voisinage des parois, conduisant à des coûts de calcul élevés, en particulier pour les méthodes astreintes à un critère de stabilité. L'emploi de lois de paroi universelles constitue un palliatif de cette difficulté, couramment utilisé. On notera également que les coûts de calcul peuvent être notablement réduits grâce à une approche par sous-domaines (voir, par exemple, [9]) dans laquelle les équations de Navier-Stokes ne sont résolues que dans des sous-domaines de faible étendue contenant les couches visqueuses.

La présente communication est consacrée au calcul d'écoulements turbulents à grand nombre de Reynolds par résolution des équations de Navier-Stokes moyennées et complétées par un modèle de turbulence, et à la présentation de résultats concernant l'aérodynamique interne. La méthode numérique qui sera brièvement rappelée se caractérise par la mise en oeuvre d'une approche par sous-domaines et par l'utilisation d'un schéma explicite simple combiné à une technique de sous-maillage par dichotomie pour la description fine des couches visqueuses. On présente des résultats de calcul d'écoulements transsoniques turbulents pour une configuration industrielle relative à une grille de compresseur supersonique à divers régimes de fonctionnement. Ces calculs ont été effectués à l'aide d'un modèle de turbulence algébrique de longueur de mélange et à l'aide de lois de paroi

simples. Dans une dernière partie, des données expérimentales détaillées pour le problème de l'interaction onde de choc-couche limite dans un canal plan sont mises à profit pour comparer un modèle de longueur de mélange et un modèle à deux équations de transport pour l'énergie cinétique de la turbulence et son taux de dissipation.

2. MODELISATION DES ECOULEMENTS COMPRESSIBLES TURBULENTS

Dans ce paragraphe, on rappelle le modèle mathématique mis en oeuvre pour la simulation numérique d'écoulements bidimensionnels compressibles turbulents. Ce modèle, tout à fait classique, est fondé sur l'opération de moyenne en temps des équations de Navier-Stokes instantanées (pour le vecteur vitesse et l'énergie totale par unité de masse, il s'agit de moyennes pondérées par la masse volumique), les termes relatifs aux corrélations entre quantités fluctuantes étant ou bien négligés ou bien modélisés par l'introduction du tenseur de Reynolds $\overline{\tau}_{Ri}$, du flux de diffusion turbulente d'enthalpie de densité \overline{q}_i et de l'énergie cinétique de turbulence k . Pour une présentation détaillée de cette opération de moyenne, le lecteur pourra se reporter à [10].

2.1 Equations de Navier-Stokes moyennées

Les équations de Navier-Stokes, permettant de décrire l'écoulement moyen, se présentent sous la forme intrinsèque suivante:

$$(2.1) \quad \begin{aligned} \frac{\partial \rho}{\partial t} + \operatorname{div}(\rho \mathbf{V}) &= 0 \\ \frac{\partial \rho \mathbf{V}}{\partial t} + \operatorname{div}(\rho \mathbf{V} \otimes \mathbf{V}) &= \operatorname{div}(\overline{\sigma} + \overline{\tau}_R) \\ \frac{\partial \rho E}{\partial t} + \operatorname{div}(\rho E \mathbf{V}) &= \operatorname{div}[(\overline{\sigma} + \overline{\tau}_R) \cdot \mathbf{V} - \overline{q} - \overline{q}_t] \end{aligned}$$

Dans ces expressions, ρ et \mathbf{V} désignent respectivement la masse volumique et la vitesse de l'écoulement moyen. E est l'énergie totale moyenne par unité de masse, c'est à dire la somme de l'énergie interne moyenne e , de l'énergie cinétique du mouvement moyen et de l'énergie cinétique du mouvement turbulent:

$$(2.2) \quad E = e + \frac{V^2}{2} + k.$$

Les équations (2.1) relatives à la conservation de la masse, de la quantité de mouvement et de l'énergie, sont à compléter par les lois de comportement du fluide considéré, par des lois d'état et par un modèle de turbulence.

Pour un fluide classique, et compte tenu de l'hypothèse de Stokes $3\lambda + 2\mu = 0$, les lois de comportement exprimant le tenseur des contraintes $\overline{\sigma}$ et la densité de flux de chaleur \overline{q} , s'écrivent:

$$(2.3) \quad \begin{aligned} \overline{\sigma} &= -\left(p + \frac{2}{3}\mu \operatorname{div} \mathbf{V}\right) \mathbf{I} + \mu \left[\nabla \mathbf{V} + (\nabla \mathbf{V})^T \right] \\ \overline{q} &= -\chi \nabla T. \end{aligned}$$

où p et T désignent la pression statique et la température absolue de l'écoulement moyen. Les coefficients μ et χ sont les coefficients de viscosité et de conductibilité thermique.

Les lois d'état traduisent les propriétés thermodynamiques du milieu considéré que nous supposons être un gaz parfait à chaleurs spécifiques constantes de rapport $C_p/C_v = \gamma$, et permettent d'exprimer la pression p ainsi que les coefficients μ et χ grâce aux relations suivantes:

$$(2.4) \quad \begin{aligned} p &= (\gamma - 1)\rho e = (C_p - C_v)\rho T \\ \mu &= \mu_0 \left(T/T_0\right)^n \frac{1 + 110/T_0}{1 + 110/T} \\ \chi &= \frac{\mu C_p}{Pr} \end{aligned}$$

où Pr est le nombre de Prandtl que nous supposons constant $Pr = 0.725$.

Les modèles de turbulence mis en oeuvre pour les résultats numériques présentés aux paragraphes 4 et 5 sont du type "viscosité tourbillonnaire". Le tenseur de Reynolds $\overline{\tau}_{Ri}$ et le flux \overline{q}_i sont reliés aux gradients de l'écoulement moyen par des expressions analogues à (2.3), c'est à dire:

$$(2.5) \quad \bar{\tau}_R = -\left(\frac{2}{3}\rho k + \frac{2}{3}\mu_t \operatorname{div} \bar{V}\right) \bar{I} + \mu_t \left[\nabla \bar{V} + (\nabla \bar{V})^T\right]$$

$$\bar{q}_t = -\frac{C_p \mu_t}{Pr_t} \nabla T.$$

A ce stade, la modélisation de la turbulence se réduit à l'évaluation de trois quantités scalaires: l'énergie cinétique de turbulence k , le coefficient de viscosité turbulente μ_t , et le nombre de Prandtl turbulent Pr_t . Nous avons utilisé deux modèles de turbulence: un modèle algébrique de longueur de mélange et un modèle à deux équations de transport. Ces deux modèles sont décrits dans les deux paragraphes qui suivent.

Dans la mise en oeuvre numérique décrite au paragraphe 3, les différentes grandeurs intervenant dans les équations de Navier-Stokes sont rendues sans dimension à l'aide de trois grandeurs de référence: une longueur L_0 , la vitesse du son a_0 et la masse volumique ρ_0 du fluide dans les conditions d'arrêt à l'infini amont. Les coefficients sans dimension de viscosité et de conductibilité thermique effectives (notés à l'aide d'un tilde) sont définis par les expressions:

$$\tilde{\mu}_t = \tilde{\mu} + \tilde{\mu}_t = \frac{1}{Re_0} \frac{\mu}{\mu_0} + \frac{\mu_t}{\rho_0 a_0 L_0}$$

$$\tilde{\chi}_t = \frac{\tilde{\mu} C_p}{Pr} + \frac{\tilde{\mu}_t C_p}{Pr_t} = \left(\frac{1}{Pr Re_0} \frac{\mu}{\mu_0} + \frac{1}{Pr_t} \frac{\mu_t}{\rho_0 a_0 L_0} \right) C_p,$$

où $Re_0 = \rho_0 a_0 L_0 / \mu_0$ désigne le nombre de Reynolds. Dans toute la suite, on ne considère que des quantités sans dimension et la notation tilde est omise.

2.2 Modèle de turbulence de longueur de mélange

Ce modèle est fondé sur le concept de longueur de mélange introduit par Prandtl. La formulation que nous avons utilisée est une extension du modèle initialement développé dans le cadre de l'approximation de couche limite par Michel et al [11]: on néglige l'énergie cinétique de turbulence dans les expressions de l'énergie totale (2.2) et du tenseur de Reynolds (2.5), le nombre de Prandtl turbulent est supposé constant $Pr_t = 0,9$ et le coefficient de viscosité turbulente est donné par,

$$(2.6) \quad \mu_t = \rho l^2 F^2 |\bar{\Omega}|,$$

où $\bar{\Omega}$ désigne le tourbillon ($\bar{\Omega} = \operatorname{Rot} \bar{V}$), l est la longueur de mélange et F est la fonction correctrice de sous couche visqueuse. La longueur de mélange l , rapportée à l'épaisseur δ de la couche limite est donnée comme une fonction universelle du rapport η/δ (η désignant la distance à la paroi) par:

$$(2.7) \quad l/\delta = 0,085 \ln \left(\frac{K}{0,085} \frac{\eta}{\delta} \right).$$

où K est la constante de Karman ($K=0,41$). La fonction correctrice F est destinée à représenter l'évolution de la turbulence depuis la zone où elle est pleinement établie jusqu'au film laminaire proche de la paroi où elle s'annule, elle a pour expression

$$(2.8) \quad F(\zeta) = 1 - \exp(-\sqrt{\zeta/20K})$$

$$\zeta = \rho l^2 \frac{\mu + \mu_t}{\mu^2} |\bar{\Omega}|.$$

On notera que la définition de la variable intermédiaire ζ fait intervenir le coefficient μ_t et que, par conséquent, la détermination de μ_t à l'aide de la relation (2.6) nécessite la résolution d'une équation implicite. Dans la pratique, cette équation est résolue par une méthode de point fixe.

On notera également que l'épaisseur δ de la couche limite intervient directement dans ce modèle de turbulence. Cette échelle de longueur est tout à fait adaptée aux calculs classiques de couche limite, en revanche, lorsqu'on utilise les équations de Navier-Stokes, on passe continuellement de la couche visqueuse à la région de fluide parfait et la détermination de δ est posée quelques problèmes.

Le modèle qui vient d'être décrit est spécifique des couches dissipatives de parois, dans le cas d'un aillage, nous avons adopté un modèle très simple pour lequel le coefficient de viscosité turbulente est donné par:

$$(2.9) \quad \mu_t = \rho l^2 |\bar{\Omega}|, \quad l = 0,14 \delta.$$

Cette formulation présente toutefois la particularité, peu physique, d'imposer un niveau de turbulence anormalement faible au centre du sillage où le tourbillon est pratiquement nul.

2.3 Modèle de turbulence à deux équations de transport

Dans ce modèle, l'échelle de vitesse U et l'échelle de longueur L intervenant dans la définition du coefficient de viscosité turbulente sont déterminées en fonction de l'énergie cinétique de turbulence k et de son taux de dissipation ϵ par:

$$U = k^{1/2} \quad \text{et} \quad L = k^{3/2} \epsilon^{-1},$$

de telle sorte que μ_t a pour expression,

$$(2.10) \quad \mu_t = C_p \rho \frac{k^2}{\epsilon},$$

où C_p est une constante sans dimension.

Les deux équations aux dérivées partielles permettant le calcul de k et ϵ se présentent sous la forme suivante:

$$(2.11) \quad \begin{aligned} \frac{\partial \rho k}{\partial t} + \text{div}(\rho k \mathbf{V}) &= \text{div} \left(\frac{\mu_t}{\alpha_k} \nabla k \right) + \overline{\mathcal{P}_k} - \overline{\mathcal{D}_k} \\ \frac{\partial \rho \epsilon}{\partial t} + \text{div}(\rho \epsilon \mathbf{V}) &= \text{div} \left(\frac{\mu_t}{\alpha_\epsilon} \nabla \epsilon \right) + C_1 \frac{\epsilon}{k} \overline{\mathcal{P}_k} - C_2 \rho \frac{\epsilon^2}{k}, \end{aligned}$$

où α_k , α_ϵ , C_1 et C_2 sont des constantes sans dimension. Les valeurs numériques des cinq constantes intervenant dans ce modèle de turbulence (eq. 2.10 et 2.11) sont celles proposées par Launder [12] et sont indiquées dans le tableau suivant.

C_p	α_k	α_ϵ	C_1	C_2
0,09	1,00	1,30	1,57	2,00

Il est classique de distinguer les différents rôles joués par chacun des termes des équations (2.11). Pour chacune de ces deux équations, le membre de gauche correspond au transport par l'écoulement moyen de la quantité considérée, quant aux trois termes du membre de droite, ils expriment respectivement une "diffusion" par l'écoulement fluctuant, une "production" proportionnelle au travail des contraintes de Reynolds au cours de la déformation due à l'écoulement moyen et une "dissipation".

Il est admis que les équations (2.11) pour k et ϵ ne sont valables que dans les régions où la turbulence est pleinement établie. En revanche, dans les régions proches des parois où l'effet de la viscosité moléculaire est prépondérant devant l'effet de la turbulence ou du même ordre de grandeur, les équations (2.11) ne rendent pas compte de façon satisfaisante des phénomènes physiques et il convient de modifier le modèle de turbulence défini par (2.10) et (2.11) (modèle dit (k, ϵ)). Ceci peut être réalisé par modification des équations (2.11) en y incluant des termes supplémentaires où intervient explicitement le coefficient de viscosité moléculaire μ . Il est également possible, et c'est la solution que nous avons retenue, d'utiliser le modèle algébrique du paragraphe 2.2 dans le voisinage immédiat des parois et le modèle (k, ϵ) lorsque la turbulence est tout à fait développée, le passage du premier modèle au second s'effectuant lorsque le rapport μ_t/μ est supérieur à une certaine valeur. Dans les applications numériques présentées au paragraphe 5, cette valeur critique a été prise égale à 10, ce qui correspond à un nombre de Reynolds turbulent (défini avec l'échelle de vitesse U et l'échelle de longueur L)

$$Re_t = \frac{\rho k^{3/2} \epsilon^{-1}}{\mu} = \frac{1}{C_p} \frac{\mu_t}{\mu} \quad \text{de l'ordre de } 100.$$

2. METHODE NUMERIQUE

2.1 Schéma aux différences finies

Pour les équations de Navier-Stokes, le système instationnaire (2.1) est intégré pas à pas en fonction du temps à l'aide d'un schéma aux différences finies, explicite, de type "prédicteur-correcteur". La discrétisation spatiale des équations est réalisée directement dans le plan physique à l'aide d'une technique décrite dans [13] et [14]. Le

schéma peut être considéré comme une généralisation du schéma explicite de MacCormack [15] dont la simplicité est bien connue.

Le principe de cette discrétisation en espace est le suivant. Les dérivées partielles $\partial\phi/\partial x$ et $\partial\phi/\partial y$ d'une fonction $\phi(x, y)$ sont approchées en un noeud M du maillage par les expressions suivantes obtenues à l'aide d'une formule de Green :

$$(3.1) \quad \left(\frac{\partial\phi}{\partial x}\right)_M = \frac{\int_{\partial\Omega} \phi n_x d\sigma}{\int_{\partial\Omega} x n_x d\sigma}, \quad \left(\frac{\partial\phi}{\partial y}\right)_M = \frac{\int_{\partial\Omega} \phi n_y d\sigma}{\int_{\partial\Omega} y n_y d\sigma},$$

où les intégrales de contour sont calculées le long du bord $\partial\Omega$, de normale $\vec{n}=(n_x, n_y)$, d'un domaine élémentaire Ω contenant le point M. Ces formules sont obtenues en approchant la valeur de $\partial\phi/\partial x$ (resp. $\partial\phi/\partial y$) en M par la valeur moyenne des dérivées partielles $\partial\phi/\partial x$ (resp. $\partial\phi/\partial y$) d'une approximation ϕ de la fonction ϕ , définie sur Ω . La détermination complètes des approximations (3.1) nécessite donc la connaissance du domaine Ω et de la fonction $\phi(x, y)$. On notera que, dans les formules (3.1), l'orientation de la normale \vec{n} est indifférente.

Le schéma aux différences utilisé est construit à l'aide de deux couples d'opérateurs aux différences finies décentrés (δ_x, δ_x') et (δ_y, δ_y') , définis par les relations (3.1) en prenant pour domaine Ω , d'une part, le triangle MSE (Fig. 1) et, d'autre part, le triangle MNO, et en supposant la fonction ϕ linéaire sur chacun de ces deux triangles. On notera que ce schéma de discrétisation ne fait appel qu'aux coordonnées des noeuds du maillage.

Dans le système de coordonnées cartésiennes (x, y) , les équations (2.1) s'écrivent sous la forme condensée suivante:

$$(3.2) \quad \frac{\partial f}{\partial t} + \frac{\partial F}{\partial x} + \frac{\partial G}{\partial y} = 0,$$

où f est la colonne des inconnues $(\rho, \rho u, \rho v, \rho E)^T$ et où les "flux" F et G peuvent s'exprimer comme la différence de deux termes, $F=F_1-F_2$ et $G=G_1-G_2$, l'indice "1" étant relatif aux termes de fluide parfait et l'indice "2" correspondant aux termes dissipatifs. Le niveau de temps étant repéré par l'indice "n" ($t^n=n\Delta t$), et la valeur fournie par le prédicteur, constitué par le premier pas en temps, étant notée " $n+1$ ", le schéma s'écrit:

$$(3.3) \quad \begin{aligned} f^{n+1} &= f^n - \Delta t (\delta_x F^n + \delta_y G^n) \\ f^{n+1} &= 1/2 \left[f^n + f^{n+1} - \Delta t (\delta_x F^{n+1} + \delta_y G^{n+1}) \right] \end{aligned}$$

Les dérivées intervenant dans la contribution F_2 (resp. G_2) du "flux" F (resp. G) sont approchées par les opérateurs (δ_x, δ_x') au premier pas (prédicteur) et par les opérateurs (δ_x, δ_x') au second pas (correcteur).

Le critère de stabilité du schéma explicite (3.3) retenu pour les calculs présentés a pour expression

$$(3.4) \quad \Delta t = \eta \min \left[\frac{\lambda}{V + a}, \frac{\rho \lambda^2}{2\gamma (\mu/Pr + \mu_t/Pr_t)} \right],$$

où η est un coefficient numérique de l'ordre de l'unité introduit en raison du caractère approché de ce critère, et où λ est une longueur caractéristique de la taille de la maille.

Le schéma numérique a été décrit pour les équations de Navier-Stokes. Pour la résolution des équations d'Euler, ($\mu=0, \mu_t=0$), le même schéma (3.3) a été mis en oeuvre avec ($F_2=0, G_2=0$). Le critère de stabilité correspondant se réduit à:

$$(3.5) \quad \Delta t = \eta \frac{\lambda}{V + a}$$

Notons enfin que dans le cas du modèle de turbulence décrit au paragraphe 2.3, les deux équations de transport déterminant k et ϵ se présentent sous une forme analogue au système (3.2) moyennant l'introduction d'un second membre non nul, et sont discrétisées par le schéma (3.3). Le critère de stabilité (3.4) a été conservé dans ce cas.

2.3 Viscosité artificielle

Pour assurer la stabilité du schéma et capturer correctement les discontinuités de l'écoulement dans les régions de fluide parfait, deux termes de dissipation sont ajoutés aux équations, de la manière suivante:

$$(3.6) \quad f^{n+1} = f_{sch}^{n+1} + D_0(f^n) + D_1(f^n),$$

où la notation "sch" caractérise les valeurs obtenues après application du schéma (3.3).

Le terme $D_0(f^n)$ est un terme linéaire de lissage ajouté à toutes les équations et a pour expression:

$$(3.7) \quad D_0(f^n) = -(Q_{10} \delta_i^{(4)} f^n + Q_{j0} \delta_j^{(4)} f^n),$$

où l'opérateur aux différences quatrièmes $\delta_i^{(4)}$ est défini par: $\delta_i^{(4)} f = f_{i+2} - 4f_{i+1} + 6f_i - 4f_{i-1} + f_{i-2}$, et où Q_{10} et Q_{j0} sont des coefficients numériques.

Le terme $D_1(f^n)$ correspond à une dissipation non linéaire qui n'est ajoutée qu'à l'équation de quantité de mouvement. Par exemple, la composante de D_1 suivant Ox s'écrit:

$$(3.8) \quad (D_1)_x = \Delta t \left\{ \frac{Q_{11}}{4h_i} \left[(\rho_{i+1,j} + \rho_{i,j}) |u_{i+1,j} - u_{i,j}| (u_{i+1,j} - u_{i,j}) - (\rho_{i,j} + \rho_{i-1,j}) |u_{i,j} - u_{i-1,j}| (u_{i,j} - u_{i-1,j}) \right] + \frac{Q_{j1}}{4h_j} [\dots] \right\},$$

où h_i (resp. h_j) est l'inverse du nombre de noeuds de maillage suivant l'indice "i" (resp. "j") dans le sous-domaine considéré, et où Q_{11} et Q_{j1} sont des coefficients numériques.

3.3 Technique de sous-maillage par zones

L'important raffinement de maillage au voisinage de la paroi, nécessaire dans le cas d'un écoulement à grand nombre de Reynolds pour représenter les forts gradients de vitesse dans la direction transversale, est généralement obtenu au moyen d'une contraction analytique. Cependant, le rapport de raffinement local ne peut dépasser une certaine valeur pour des raisons de précision, ce qui conduit à un très grand nombre de mailles. Afin de remédier à cet inconvénient, on utilise la technique suivante de sous-maillage par zones proposée et développée par Viviani et Ghazali dans [16].

A un maillage présentant dans le plan physique (x, y) une contraction régulière, est associé un maillage uniforme dans le plan de calcul (X, Y) , c'est à dire à pas constant ΔY . A partir de ce maillage de base dans le plan de calcul, la technique de sous-maillage par zones consiste à diviser par deux la taille en Y de la maille d'une zone à la suivante en allant vers la paroi. Le maillage obtenu par retour dans le plan physique combine alors les effets de la contraction analytique et de cette dichotomie.

Les zones étant repérées par un entier q variant de 1 à Q , avec $q=1$ à la paroi, la taille $\Delta Y^{(q)}$ de la maille en Y dans la zone q est donnée par

$$(3.9) \quad \Delta Y^{(q)} = \frac{\Delta Y}{2^{q-1}}.$$

Cette technique permet une rapide transition entre un maillage relativement grossier à l'extérieur de la couche limite et un maillage très fin dans la sous-couche visqueuse, tout en conservant un maillage régulier dans chaque zone. On trouvera dans la référence [17] une étude détaillée de l'optimisation du maillage par zones permettant, pour une épaisseur donnée de la maille à la paroi, de choisir les différents paramètres intervenant dans cette méthode de maillage de façon à minimiser le coût du calcul.

Le raccord de deux zones adjacentes est assuré par recouvrement. Le domaine de dépendance numérique du schéma de McCormack (3.3) appliqué aux équations de Navier-Stokes s'étendant sur deux mailles dans chaque direction, le schéma ne peut être écrit dans la zone q que pour les lignes $l=3$ à $L^{(q)}-2$, où l est l'indice local repérant les lignes de maillage de la zone q et variant de 1 à $L^{(q)}$ dans la direction des Y croissantes. Les valeurs $f_l^{(q)}$ des inconnues f sur les lignes $l=1, 2, L^{(q)}-1$ et $L^{(q)}$ sont obtenues par transfert ou interpolation à partir des valeurs de f dans les zones adjacentes $(q-1)$ et $(q+1)$, comme le montre la figure 2. La formule d'interpolation utilisée est la suivante:

$$(3.10) \quad f_l^{(q)} = 1/16 \left[-f_l^{(q+1)} + 9(f_l^{(q+1)} + f_l^{(q-1)}) - f_l^{(q-1)} \right]$$

Enfin un procédé adéquat de balayage en temps des zones est mis en oeuvre de manière à utiliser dans chaque zone un pas de temps proche du pas de temps maximum propre à chaque zone. Cette technique est fondée sur le choix pour la zone q d'un pas de temps $\Delta t^{(q)}$ proportionnel à $\Delta Y^{(q)}$, soit d'après (3.9).

$$(3.11) \quad \Delta t^{(q)} = 2^{1-q} \Delta t^{(1)}.$$

où $\Delta t^{(Q)}$ est le pas de temps utilisé dans la zone externe. Ce choix correspond approximativement à la valeur optimum dans chaque zone, si la stabilité est gouvernée par le critère "fluide parfait" (3.5), ce qui est le cas dans les calculs présentés aux paragraphes 4 et 5. Afin d'avancer en temps de manière coordonnée entre les différentes zones, le nombre d'itérations devant être effectuées dans une zone q pour une itération dans la zone Q est $N^{(q)} = 2^{Q-q}$. La progression des itérations dans les différentes zones est indiquée sur le diagramme de la figure 3 correspondant à un sous-maillage en quatre zones. Ce diagramme décrit un cycle, c'est à dire l'ensemble des itérations effectuées dans les différentes zones pour une itération (pas de temps $\Delta t^{(Q)}$) dans la zone Q .

Pour accélérer la convergence du processus itératif, on utilise dans les sous-domaines "Euler" la technique classique du pas de temps local. En revanche, dans les sous-domaines "Navier-Stokes", le pas de temps ne varie dans une zone donnée qu'en fonction de l'indice "i".

3.4 Lois de paroi

Le calcul du tenseur des contraintes visqueuses à la paroi se fait généralement par discrétisation des dérivées de vitesse. Toutefois, aux très grands nombres de Reynolds, on observe qu'à la frontière de la sous-couche laminaire, la vitesse peut atteindre une fraction notable de la vitesse à l'extérieur de la couche visqueuse. Une description correcte de l'écoulement nécessite alors que la taille de la maille voisine de la paroi soit inférieure à l'épaisseur de la sous-couche laminaire, c'est à dire que le premier point de maillage soit à une distance η de la paroi telle que la distance réduite η^* définie par $\eta^* = \rho u_* \eta / \mu$ soit inférieure à 3 (u_* désigne la vitesse de frottement définie à partir de la tension de cisaillement τ_s à la paroi par la relation: $\tau_s = \rho u_*^2$).

Lorsque le nombre de Reynolds est élevé, la distance η correspondant à $\eta^* = 3$ est très petite, et le nombre Q de zones de sous-maillage nécessaire devient très important. Au cours d'un cycle, le nombre d'itérations effectuées dans la zone la plus proche de la paroi est égal à 2^{Q-1} , ce grand nombre d'itérations est lié à la faible valeur du pas de temps correspondant à la très petite taille de la maille à la paroi, et conduit alors à un coût de calcul très élevé.

Une approche plus économique consiste à représenter la vitesse par une loi de paroi universelle qui permet de calculer les contraintes à la paroi sans discrétiser les dérivées de vitesse. L'idée de base pour obtenir ces lois de paroi est d'admettre qu'il existe une région de la couche limite proche de la paroi où la tension de cisaillement $\tilde{\tau}$ est constante, égale à sa valeur à la paroi τ_s ($\tilde{\tau}$ est le tenseur des contraintes laminaires et turbulentes, \tilde{n} et $\tilde{\tau}$ désignent respectivement le vecteur unitaire normal à la paroi orienté vers l'extérieur du domaine de calcul, et le vecteur unitaire tangent à la paroi tel que $(\tilde{n}, \tilde{\tau})$ soit direct). Cette région, appelée couche interne, est elle-même classiquement (voir, par exemple, [18]) divisée en trois sous-couches selon l'importance relative des contraintes laminaires et des contraintes turbulentes: i) la sous-couche laminaire limitée à $\eta^* < 3$ et dans laquelle μ est négligeable devant μ_t , ii) une zone intermédiaire allant de $\eta^* = 3$ à $\eta^* = 40$, appelée communément sous-couche tampon, et dans laquelle μ_t et μ sont de même ordre, iii) la sous-couche logarithmique définie à partir de $\eta^* = 40$ jusqu'à la limite supérieure de la couche interne, et dans laquelle μ_t est grand devant μ .

Si V_i^* désigne la composante de la vitesse réduite dans la direction \tilde{i} ($V_i^* = V_i / u_*$), il existe pour une couche limite incompressible des lois simples reliant V_i^* et η^* dans les sous-couches laminaire et logarithmique.

Dans la sous-couche laminaire, la loi de vitesse s'écrit

$$(3.12) \quad V_i^* = \eta^*.$$

et dans la sous-couche logarithmique, elle a pour expression,

$$(3.13) \quad V_i^* = \frac{1}{K} \log(\eta^*) + C.$$

où K est la constante de Karman et C une constante d'intégration. En revanche, dans la sous-couche tampon, il n'existe pas de loi universelle simple reliant V_i^* et η^* .

Dans les calculs présentés au paragraphe 4, nous avons utilisé les lois (3.12) et (3.13) valables en incompressible, la masse volumique variant assez peu au voisinage de la paroi pour les écoulements transsoniques considérés. Nous avons admis également que la sous-couche tampon pouvait être décrite jusqu'à une valeur $\eta_0^* = 11.225$ par la loi linéaire (3.12), la continuité de V_i^* en η_0^* impose alors la valeur de la constante $C = 5.449$. En définitive, connaissant la vitesse tangentielle V_i au premier point de maillage non situé sur la paroi, les lois (3.12) et (3.13) permettent de déterminer la valeur τ_s de la tension de cisaillement à la paroi. Notons que nous avons appliqué ces lois même dans les régions décollées en fixant le signe de τ_s au signe de V_i .

La valeur de η^* au premier point de maillage varie selon la région de l'écoulement et s'annule même en un point de décollement ou de recollement. C'est pour cette raison qu'il est nécessaire d'utiliser soit la loi linéaire, soit la loi logarithmique, selon que η^* est inférieur ou supérieur à η_0^* . Cependant, on ne connaît pas la valeur de η^* a priori puisque η^* dépend de τ_s qui est l'inconnue. Cette difficulté peut être résolue en remarquant, d'une part, que V_i^* est une fonction croissante de η^* , et, d'autre part, que le produit $V_i^* \eta^* = \rho V_i \eta / \mu$ est indépendant de τ_s , donc connu. Le choix entre la loi linéaire (3.12) et la loi logarithmique (3.13) s'effectue alors en comparant la quantité $\rho V_i \eta / \mu$ à la valeur η_0^{*2} . La détermination de τ_s s'effectue explicitement dans le cas de la loi

linéaire; en revanche, dans le cas de la loi logarithmique, nous avons utilisé une méthode de Newton pour résoudre l'équation implicite donnant r_p .

En pratique, le maillage est défini de telle sorte que la taille de la maille près de la paroi corresponde à une valeur maximum de η^+ de l'ordre de 30. Ceci permet, par rapport à un calcul sans loi de paroi, de diminuer d'au moins trois le nombre Q de zones de sous-maillage, et donc de diviser le nombre d'itérations effectuées dans la zone la plus proche de la paroi par un facteur au moins égal à 2^3 , soit 8.

3.5 Traitement des conditions aux limites et des raccords entre les sous-domaines

La technique de traitement des conditions aux limites et des raccords décrite dans ce paragraphe a été utilisée dans les applications numériques présentées aux paragraphes 4 et 5 pour toutes les frontières, à l'exception des parois et des frontières internes séparant deux sous-domaines "Navier-Stokes". Cette technique est fondée sur les propriétés des systèmes hyperboliques en temps; son application au cas d'une frontière interne Σ séparant un sous-domaine "Euler" et un sous-domaine "Navier-Stokes" exige donc que les effets dissipatifs soient négligeables au voisinage de Σ de telle sorte que les équations de Navier-Stokes se réduisent pratiquement aux équations d'Euler. La technique de traitement des conditions aux limites a été proposée dans [13]; son application au raccord entre sous-domaines a été décrite dans [9]. L'extension au cas de sous-domaines se recouvrant présentée dans [19] ne sera pas envisagée ici; le lecteur intéressé trouvera des applications de cette extension en approximation de fluide parfait dans [19] et [3].

3.5.1 Principe de la méthode

Le principe de la technique de traitement des conditions aux limites et des raccords peut être énoncé comme suit.

En un point P d'une frontière Σ , éventuellement mobile, d'un sous-domaine D_i , le système hyperbolique à résoudre est remplacé par un système équivalent formé par les relations de compatibilité (ou relations caractéristiques) associées à la normale unitaire \vec{V} à Σ en P , orientée par exemple vers l'extérieur de D_i . Ces relations de compatibilité peuvent être interprétées comme des équations de transport le long de directions particulières du plan (\vec{V}, t) . Parmi les relations de compatibilité écrites en P , on ne retient que celles qui traduisent un transport de l'intérieur de D_i vers l'extérieur. La solution au point P est alors obtenue en complétant ces relations de compatibilité, soit par des conditions aux limites si Σ est une frontière externe, soit par des conditions de raccord si Σ sépare le sous-domaine D_i d'un autre sous-domaine D_j . Le cas d'un système hyperbolique en temps quelconque est décrit dans [9] et [20]. Nous allons développer ici la technique de traitement des conditions aux limites et des raccords dans le cas des équations d'Euler bidimensionnelles.

3.5.2 Relations de compatibilité pour les équations d'Euler

Les quatre relations de compatibilité associées à la normale \vec{V} peuvent s'écrire sous la forme remarquable suivante

$$(3.14) \quad \omega^{(i)} \left(\frac{\partial g}{\partial t} + \lambda^{(i)} \frac{\partial g}{\partial \vec{V}} \right) = S_i^{(i)} \quad i=1,4$$

Les valeurs propres $\lambda^{(i)}$ rangées par ordre croissant ont pour expression

$$(3.15) \quad \lambda^{(1)} = V_x - a, \quad \lambda^{(2)} = \lambda^{(4)} = V_x, \quad \lambda^{(3)} = V_x + a \quad (V_x = \vec{V} \cdot \vec{D})$$

Les quatre composantes de g sont des variables indépendantes décrivant l'état du fluide, g est une fonction bivariée des variables conservatives f . Si on choisit $g = (\rho, V_x, V_y, p)^T$, où \vec{f} est le vecteur unitaire normal à \vec{V} et $V_y = \vec{V} \cdot \vec{Z}$, les coefficients $\omega^{(i)}$ des relations de compatibilité ont alors des expressions très simples, soit:

$$(3.16) \quad \omega^{(1)} = (0, -\rho a, 0, 1) \quad \omega^{(2)} = (0, 0, 1, 0) \quad \omega^{(3)} = (-a^3, 0, 0, 1) \quad \omega^{(4)} = (0, \rho a, 0, 1)$$

Dans les relations de compatibilité (3.14), $\partial/\partial \vec{V} = \vec{V} \cdot \partial/\partial \vec{x}$, représente la dérivation le long de la direction \vec{V} , et les membres de droite $S_i^{(i)}$ ne contiennent que des dérivées le long du vecteur \vec{f} tangent à Σ . Lorsque les variables sont connues dans le sous-domaine D_i à l'instant t_0 , les dérivées le long de \vec{f} sont également connues, et les relations de compatibilité peuvent alors être considérées comme des équations de transport le long des directions caractéristiques de pente $1/\lambda^{(i)}$ du plan (\vec{V}, t) .

Soit w la vitesse normale de déplacement du point P . Selon le principe énoncé en 3.5.1, on ne retient que les relations de compatibilité traduisant un transport de l'intérieur de D_i vers l'extérieur, c'est à dire les relations (3.14) correspondant aux valeurs propres $\lambda^{(i)}$ vérifiant l'inégalité

$$(3.17) \quad \lambda^{(i)} \geq w$$

L'examen des expressions (3.15) des valeurs propres $\lambda^{(i)}$ montre que la position de ces valeurs propres par rapport à w ne dépend que de la valeur du nombre de Mach normal relatif $M_n^* = (V_n - w)/c$ à comparer à -1, 0 et +1.

3.5.3 Discrétisation des relations de compatibilité

En pratique, la discrétisation d'une relation de compatibilité se fait directement dans le maillage utilisé pour l'application du schéma courant (3.3). Le principe de cette discrétisation est décrit dans [13] et [9]. Les relations de compatibilité (3.14) s'expriment alors très simplement sous la forme discrétisée suivante.

$$(3.18) \quad \omega^{(i)*} g^{*+1} = \omega^{(i)*} g^*, \quad i=1,4,$$

où la notation g^* désigne la valeur de g calculée à partir des valeurs de $\rho, \rho V, \rho E$ données par le schéma numérique courant appliqué au point P. Notons que g^* ne vérifie en général pas les conditions aux limites ou les conditions de raccord.

Avec le choix $g = (\rho, V_n, V_t, p)^T$, les coefficients $\omega^{(i)}$ sont donnés par les relations (3.16), et les quatre relations de compatibilité discrétisées s'écrivent:

$$\begin{aligned} \rho^{*+1} - (\rho a)^* V_n^{*+1} &= \rho^* - (\rho a)^* V_n^* \\ V_t^{*+1} &= V_t^* \\ (3.19) \quad p^{*+1} - (a^2)^* \rho^{*+1} &= p^* - (a^2)^* \rho^* \\ p^{*+1} + (\rho a)^* V_n^{*+1} &= p^* + (\rho a)^* V_n^* \end{aligned}$$

3.5.4 Cas d'une coupure artificielle fixe

Ce cas est le seul type de frontières de raccord intervenant dans les applications présentées aux paragraphes 4 et 5. La solution $(\rho, \rho V, \rho E)$ est alors continue à travers la frontière Σ séparant deux sous-domaines D_1 et D_2 , et les conditions de raccord expriment simplement la continuité des variables. On montre aisément que la solution au point P est obtenue à l'aide du système linéaire (3.19) dans lequel les quantités intermédiaires notées ** sont calculées soit dans le sous-domaine D_1 si la relation de compatibilité correspondante traduit un transport de D_1 vers D_2 , soit dans le sous-domaine D_2 dans le cas contraire.

4. ÉCOULEMENT DANS UNE GUILLE D'AUBES PLANE

4.1 Cas de calcul

L'application présentée dans ce paragraphe est relative à l'écoulement bidimensionnel dans une grille de compresseur supersonique étudiée à la SNECMA. La longueur de référence L_0 choisie pour l'encombrement axial d'une aube, le nombre de Reynolds (défini au paragraphe 3.2) est égal à $Re_0 = 800000$. Les calculs ont été effectués pour trois valeurs de la contre-pression aval, et pour un même écoulement axial caractérisé par un nombre de Mach $M_1 = 1.58$ et un angle d'incidence $\alpha_1 = 65.6^\circ$.

4.2 Découpage en sous-domaines

Le domaine de calcul (Fig. 4) est limité par deux frontières de périodicité situées sensiblement au milieu de deux canaux interaubes consécutifs, par une frontière amont parallèle au front de grille et par une frontière aval approximativement perpendiculaire à l'écoulement. Ce domaine est découpé en cinq sous-domaines de la manière suivante. Les sous-domaines $D_1^{(1)}$ et $D_2^{(1)}$, dans lesquels sont résolues les équations de Navier-Stokes, sont situés le long de l'intrados et de l'extrados de l'aube et se prolongent vers l'aval de part et d'autre de la ligne de maillage L_0 issue du bord de fuite. Le reste du domaine de calcul est divisé en trois sous-domaines où sont résolues les équations d'Euler complètes: un sous-domaine $D_3^{(1)}$ situé en amont du front de grille, et deux sous-domaines $D_4^{(1)}$ et $D_5^{(1)}$ s'étendant de part et d'autre de l'aube, jusqu'à la frontière de périodicité.

4.3 Conditions aux limites

À la paroi de l'aube, on impose l'adhérence du fluide ainsi que la valeur de la température. La pression est déterminée en supposant nulle sa dérivée suivant la tangente à la ligne de maillage $L_0 = \text{const.}$ passant par le point considéré, etiquement normale à la paroi.

Sur la frontière amont, les conditions généralisées et la vitesse tangentielle calculée à partir de M_1 et de α_1 sont imposées. L'écoulement est obtenu à l'aide de ces trois conditions aux limites complétées par la relation de

compatibilité correspondant à une propagation de l'information de l'intérieur du domaine de calcul vers l'extérieur (voir paragraphe 3.5).

Sur la frontière aval, ainsi que sur l'arc AB (Fig. 4) de la frontière latérale du domaine de calcul n'ayant pas d'homologue par périodicité, on applique une condition de "non-réflexion", qui s'écrit:

$$(4.1) \quad \frac{\partial p}{\partial t} - \rho a \frac{\partial V_n}{\partial t} = 0,$$

où V_n désigne la composante de la vitesse suivant la normale à la frontière, orientée vers l'extérieur du domaine de calcul. On remarque que cette condition (4.1), qui conduit à un problème mathématique bien posé [21], ne fixe pas la valeur de la pression statique sur la frontière aval, mais que celle-ci peut varier dans le temps en fonction de la vitesse normale. Les autres grandeurs caractéristiques de l'écoulement sont obtenues à l'aide des trois relations de compatibilité devant être utilisées.

Enfin la condition de périodicité est appliquée sur les deux frontières latérales du domaine de calcul (excepté l'arc AB); son traitement s'effectue de la même façon que celui d'une coupure entre deux sous-domaines.

4.4 Description des calculs

Les calculs ont été effectués à l'aide du modèle de longueur de mélange et en appliquant les lois de paroi décrites au paragraphe 3.4. Les conditions initiales résultent d'un calcul effectué en approximation de fluide parfait qui, en outre, permet d'une part de limiter l'écart entre la contre-pression initiale et la contre-pression à convergence dû à l'application de la condition de non-réflexion (4.1), et d'autre part de déterminer par une technique d'ajustement la ligne de maillage L_2 comme étant la ligne de courant issue du bord de fuite de l'aube. Ce dernier point permet d'assurer qu'à très grand nombre de Reynolds, le sillage visqueux est contenu dans les sous-domaines "Navier-Stokes", sans qu'il soit nécessaire d'en augmenter exagérément l'étendue transversale.

Le tableau suivant indique les valeurs de la contre-pression aval (p_2/p_1) caractéristiques des trois calculs (notés respectivement a, b et c), ainsi que les valeurs du nombre de Mach (M_2), de la pression d'arrêt (p_0) et de la direction (α_2) de l'écoulement aval. Ce dernier n'étant pas uniforme (à la différence de l'écoulement amont) les grandeurs aval sont en fait obtenues à l'aide d'une opération de moyenne.

	a	b	c
M_1		1.58	
α_1		65.5°	
p_2/p_1	0.297	0.337	0.458
M_2	1.40	1.39	1.04
p_0/p_1	0.946	0.926	0.900
α_2	66.1°	68.8°	67.7°

Pour les écoulements a et b, les maillages (Fig. 5) des sous-domaines "Euler" $D_1^{(1)}$, $D_1^{(2)}$ et $D_1^{(3)}$ comportent respectivement $210 \times 13 = 2730$ nœuds, $48 \times 7 = 336$ nœuds et $210 \times 13 = 2730$ nœuds, chacun des sous-domaines "Navier-Stokes" est constitué de deux zones de sous-maillage (§ 3.3) et comporte $164 \times 20 = 3280$ nœuds distincts. L'écoulement c qui correspond à la contre-pression la plus élevée, présente en aval des couches visqueuses plus épaisses que pour les écoulements a et b, et par conséquent les sous-domaines "Navier-Stokes" ont été agrandis dans la direction transversale. Ils sont encore constitués de deux zones de sous-maillage, mais comportent $164 \times 24 = 3936$ nœuds distincts. Par construction, les sous-domaines $D_1^{(1)}$, $D_1^{(2)}$ et $D_1^{(3)}$ comportent respectivement $210 \times 12 = 2520$ nœuds, $48 \times 9 = 432$ nœuds et $210 \times 12 = 2520$ nœuds. L'épaisseur des sous-domaines "Navier-Stokes" correspond à trois mailles "Euler" pour les cas a et b, et quatre mailles "Euler" pour le cas c. Dans ce dernier cas, la maille joignant la paroi à une épaisseur égale à environ 0.002 (on rappelle que la

longueur de référence est l'encombrement a (al). A la traversée des coupures séparant un sous-domaine "Euler" et un sous-domaine "Navier-Stokes" (par exemple, $D_1^{(1)}$ et $D_2^{(1)}$), la taille de la maille subit une réduction d'un facteur cinq dans la direction transversale; cette discontinuité de la métrique ne pose pas de problème numérique particulier grâce à la technique de raccord entre sous-domaines utilisée (§ 3.5).

4.5 Présentations des résultats numériques

Les champs d'écoulements calculés pour les trois valeurs de la contre-pression du tableau précédent sont illustrés par les figures 6 à 8 représentant les cartes du nombre de Mach. Bien que cela n'apparaisse pas sur ces figures et alors que toutes les caractéristiques de l'écoulement ne sont pas fixées sur la frontière amont (§ 4.3), l'examen des résultats numériques montre que l'écoulement en amont du bord d'attaque est indépendant de la contre-pression aval. Pour les deux plus faibles valeurs de la contre-pression, l'écoulement reste entièrement supersonique dans la région de fluide parfait; la contre-pression croissant (passage du cas a au cas b), le choc oblique issu du bord de fuite de l'aube a pivoté vers l'amont et son intensité a augmenté, conduisant à un fort épaissement de la couche limite intrados qui se trouve alors destabilisée à la limite du décollement. Pour la plus grande valeur de la contre-pression (cas c), des zones subsoniques apparaissent dans la région de fluide parfait et on constate une structure de choc en "X" qui résulte de la réflexion singulière du choc du bord de fuite sur l'intrados de l'aube, induisant un décollement de la couche limite intrados et un fort épaissement du sillage.

Cette analyse des trois écoulements est confirmée par l'examen des figures 9 à 11 qui représentent l'évolution de la pression statique sur l'aube et le long de la ligne de maillage L_3 qui se situe approximativement au centre du sillage. De plus, pour le cas c , la figure 11 présente une comparaison avec un calcul effectué en approximation de fluide parfait, et, comme il était prévisible, les effets visqueux se traduisent essentiellement par un déplacement vers l'amont des ondes de choc qui, aux parois, se transforment en compressions continues de plus faible intensité.

Les figures 12 à 14 représentent l'évolution de l'épaisseur de déplacement des couches limites intrados et extrados. On observe que seule la partie aval de la couche limite extrados a été fortement modifiée par l'augmentation de la contre-pression. Ces figures mettent également en évidence qu'au voisinage du bord de fuite, les couches limites intrados et extrados subissent des évolutions inverses, résultant respectivement d'une détente et d'une compression de l'écoulement.

Enfin la figure 15 représente des profils de vitesse à l'intrados de l'aube, à l'extrados et dans le sillage calculés pour le cas c , mettant en évidence le décollement puis le recollement de la couche limite intrados en aval du choc.

Le calcul de cet écoulement c effectué, rappelons-le, avec deux zones de sous-maillage dans les sous-domaines "Navier-Stokes" et un nombre total de points de maillage égal à 13344 a nécessité 8000 cycles pour atteindre une convergence satisfaisante, ce qui correspond à 1850 secondes de temps CPU sur un ordinateur CRAY-1S.

5. COMPARAISON DE MODELES DE TURBULENCE POUR UNE INTERACTION ONDE DE CHOC-COUCHE LIMITE EN CANAL.

5.1 Cas de calcul

Des simulations numériques de l'interaction d'une onde de choc avec une couche limite turbulente dans un canal bidimensionnel symétrique ont été présentées dans [22] et [23] pour une situation de décollement naissant, et pour une situation de décollement étendu. Les résultats obtenus avec le modèle algébrique § 2.2 puis avec le modèle (k, ϵ) (§ 2.3) ont fait l'objet de comparaisons avec des mesures détaillées obtenues à l'aide d'un Vélocimètre Laser à deux composantes [24]. Nous reprenons ici la comparaison portant sur l'interaction avec décollement étendu, dont les résultats sont les plus significatifs. En effet, bien que la configuration étudiée ne représente pas totalement la complexité des écoulements dans les turbomachines, elle apparaît comme un cas d'épreuve très significatif pour les modèles de turbulence.

La longueur de référence L_0 choisie étant la hauteur maximale du canal, le nombre de Reynolds est égal à: $Re_0 = 2,078 \cdot 10^6$.

5.2 Décomposition en sous-domaines

Le canal considéré, étant symétrique, le domaine de calcul (Fig. 16), limité de façon naturelle par la paroi inférieure et l'axe de symétrie, est divisé en deux sous-domaines de la façon suivante. Une coupure Σ longitudinale sépare un sous-domaine D_1 , jouxtant la paroi et contenant la couche visqueuse, d'un sous-domaine D_2 , où les effets visqueux sont négligeables et où les équations d'Euler remplacent les équations de Navier-Stokes.

5.3 Conditions aux limites

A la paroi, on impose l'adhérence du fluide ($v = v_n = 0$) et un flux de chaleur nul ($\partial \epsilon / \partial \eta = 0$). La pression est calculée par discrétisation de la composante de l'équation de quantité de mouvement suivant la tangente à la ligne de maillage $X = \text{const.}$ passant par le point considéré de la paroi.

Sur l'axe de symétrie (frontière de D_1) on impose une condition de glissement qui, à convergence, est équivalente en fluide parfait à la condition de symétrie.

Sur la frontière amont de D_1 et de D_2 , les conditions génératrices et la direction de l'écoulement sont imposées. L'écoulement est obtenu à l'aide de ces trois conditions aux limites complétées par une relation de compatibilité.

Enfin, sur la frontière aval de D_1 et de D_2 , la pression statique est fixée et les autres grandeurs sont obtenues à l'aide des trois relations de compatibilité devant être utilisées. La position de l'onde de choc dépend essentiellement de la valeur de la pression statique imposée à l'aval.

Compte tenu du caractère convectif des équations (2.11), k et ϵ sont fixés à des valeurs k_{\min} et ϵ_{\min} sur la frontière amont, et sont extrapolés sur la frontière aval; et, sur la coupure Σ , k et ϵ sont fixés aux valeurs k_{\min} et ϵ_{\min} lorsque le fluide va de D_1 vers D_2 et sont calculés par le schéma numérique lorsque le fluide va dans la direction opposée. Les valeurs k_{\min} et ϵ_{\min} sont choisies très petites et de telle sorte que $\mu_1/\mu = 10^{-8}$, mais non nulles pour éviter que les termes de production des équations (2.11) ne soient singuliers. De plus, sur la frontière aval, la quantité imposée est alors une "pression" p^* définie comme la contrainte normale moyenne, c'est à dire : $p^* = p + 2/3 \rho k$.

5.4 Description des calculs

Un premier calcul de l'interaction onde de choc-couche limite a été effectué avec le modèle de longueur de mélange, à partir de conditions initiales correspondant à un écoulement non visqueux monodimensionnel. La pression statique imposée sur la frontière aval a été ajustée à une valeur $p_2 = 0,667 p_0$ de façon à faire coïncider au mieux l'onde de choc calculée avec l'onde de choc expérimentale. Cette valeur diffère de la valeur expérimentale $p_{2exp} = 0,648 p_0$, pour une part en raison des effets tridimensionnels dus à la présence de couches limites latérales dans l'expérience. Le maillage utilisé (Fig. 16) comprend $181 \times 13 = 2353$ noeuds dans D_1 , et $181 \times 53 = 9593$ noeuds distincts dans D_2 . Le maillage de D_2 comprend huit zones de sous-maillage, le premier point de calcul est à une distance réduite $\eta^+ = 2,4$ et le rapport des tailles dans la direction transversale y d'une maille proche de la paroi et d'une maille proche de l'axe de symétrie est égal à 0,003. Des essais numériques ont montré qu'un resserrement de maillage plus important dans la direction y ne modifie pas la solution, et les calculs peuvent ainsi être considérés comme assez précis pour valider une comparaison entre des modèles de turbulence.

Un deuxième calcul de l'interaction, avec le modèle (k, ϵ) , a été effectué dans le même maillage. L'état initial pour ce calcul correspond à la solution obtenue avec le modèle de longueur de mélange, les valeurs de k et ϵ étant calculées à partir du champ de viscosité turbulente à l'aide des relations suivantes:

$$(5.1) \quad \begin{aligned} k &= \frac{\overline{u'v'}}{0,3} \quad \epsilon = -\overline{u'v'} \left(\frac{\partial u}{\partial y} + \frac{\partial v}{\partial x} \right) \\ \overline{u'v'} &= \frac{\mu_t}{\rho} \left(\frac{\partial u}{\partial y} + \frac{\partial v}{\partial x} \right) \end{aligned}$$

Dans la région proche de la paroi où le modèle (k, ϵ) est remplacé par le modèle algébrique, les relations (5.1) sont également utilisées pour donner des valeurs à k et ϵ . La pression imposée à l'aval a la même valeur que dans le calcul avec modèle algébrique.

5.5 Présentation des résultats numériques et comparaison avec l'expérience

L'examen des cartes du nombre de Mach calculé à l'aide des deux modèles (Fig. 17) permet de constater que la région d'interaction est beaucoup plus étendue avec le modèle (k, ϵ) qu'avec le modèle de longueur de mélange. L'écoulement calculé par le modèle (k, ϵ) présente une onde de choc ayant une structure en "X" bien définie correspondant à une région décollée nettement plus importante (comme le confirme l'examen de la figure 18 représentant les lignes de courant). La position de l'onde de choc est sensiblement plus en amont que celle calculée par le modèle algébrique.

En raison de ce décalage, les comparaisons quantitatives qui suivent seront effectuées en considérant une abscisse relative $x - x_0$, où x_0 désigne l'origine de l'interaction définie comme le point où la pression pariétale commence à croître.

Les distributions de pression pariétale ainsi tracées (Fig. 19) montrent que la compression prédite par le modèle de longueur de mélange est trop raide alors que l'accord avec l'expérience est bien meilleur avec le modèle (k, ϵ) . En particulier, le plateau de la distribution expérimentale, caractéristique d'une région décollée, est bien représenté par le calcul avec le modèle (k, ϵ) , alors qu'il n'apparaît pas avec le modèle algébrique.

Cependant, la distribution d'épaisseur de déplacement $\delta^+(x - x_0)$ (Fig. 20) prédite par le modèle (k, ϵ) n'est en bon accord avec l'expérience que dans la première partie de l'interaction, le retour à l'équilibre étant en revanche mal décrit. Pour le modèle de longueur de mélange, le bon accord apparent de $\delta^+(x - x_0)$ avec la distribution expérimentale est dû en fait à une compensation des imperfections des profils de vitesse calculés, représentés sur

la figure 21. L'examen de cette figure confirme également que les profils de vitesse obtenus avec le modèle (k, ϵ) ne coïncident avec l'expérience que dans la partie amont de l'interaction alors que le processus de relaxation en aval n'est pas correctement prédit. Cette mauvaise description de l'écoulement en aval de l'interaction conduit à une surévaluation de la longueur du décollement par le modèle (k, ϵ) . On peut constater toutefois que la valeur de la vitesse externe obtenue par le calcul (k, ϵ) présente un bon accord avec les mesures pour les quatre profils de vitesse présentés.

L'examen des profils de tension de cisaillement turbulente (Fig. 22) montre que les deux modèles prédisent une croissance trop rapide du maximum de la tension de cisaillement au début de l'interaction. En revanche, dans la partie aval de l'interaction, le modèle de longueur de mélange conduit à une décroissance trop rapide de ce maximum, alors que le modèle (k, ϵ) prédit un processus de relaxation trop lent. Pour les résultats avec le modèle (k, ϵ) , on a également effectué une comparaison entre les profils d'énergie cinétique de turbulence calculés et les profils expérimentaux (Fig. 23) mettant en évidence une sous-évaluation de k , en particulier dans la première partie de l'interaction.

Les principales conclusions se dégageant des comparaisons présentées sont les suivantes. L'inadaptation généralement admise du modèle de longueur de mélange à représenter de grandes régions décollées est confirmée. Le modèle (k, ϵ) améliore grandement la prédiction de la pression pariétale, et donne une bonne représentation de la première partie de l'interaction. Cependant, plus en aval, la solution obtenue par ce modèle présente des différences notables avec l'expérience et, en particulier, une trop lente relaxation vers un nouvel état d'équilibre. Un tel désaccord est sans aucun doute dû à une mauvaise prédiction des tensions turbulentes, ce qui peut remettre en cause le concept de viscosité tourbillonnaire pour des interactions aussi fortes.

Le calcul de l'écoulement avec le modèle algébrique et huit zones de sous-maillage a nécessité 5000 cycles pour obtenir une position stable de l'onde de choc, ce qui correspond à cinq heures de temps CPU sur ordinateur CRAY-1S. Ce coût, admissible pour un calcul où l'on veut comparer des modèles de turbulence de manière fine à l'exclusion de toute autre approximation, est en revanche inacceptable pour des applications de type industriel comme celles présentées au paragraphe 4, où des lois de paroi avaient permis d'augmenter considérablement la taille de la maille à la paroi, et donc de diminuer fortement la durée du calcul.

REFERENCES

- [1] J.C. LE BALLEUR et D. BLAISE - Méthode numérique d'interaction visqueux-non visqueux pour les écoulements internes décollés et l'interaction couche limite-onde de choc - Communication à la présente réunion.
- [2] V. IYER and E. Von LAVANTE - Numerical Solutions of Viscous Transonic Flow in Turbomachinery Cascades - AIAA Paper 85-0007, jan. 1985.
- [3] L. CAMBIER and J.P. VEUILLLOT - Application of a Multi-Domain Approach for the Computation of Compressible Flows in Cascades - 7th Int. Symposium on Air Breathing Engines, Beijing, 9/13 sept. 1985 - ONERA TP No 1985-116.
- [4] R.V. CHIMA - Inviscid and Viscous Flows in Cascades with an Explicit Multiple-Grid Algorithm - AIAA J., Vol. 23, No 10, pp. 1556-1563, oct. 1985.
- [5] W.N. DAWES - Computation of Off-Design Flows in a Transonic Compressor Rotor - ASME J. of Engineering for Gas Turbines and Power, Vol. 108, No 1, pp. 144-150, jan. 1986.
- [6] O. SCHAFER, H.H. FRUHAUF, B. BAUER and M. GUGGOLZ - Application of a Navier-Stokes Analysis to Flows through Plane Cascades - ASME J. of Engineering for Gas Turbines and Power, Vol. 108, No 1, pp. 103-111, jan. 1986.
- [7] B.C. WEINBERG, R.J. YANG, H. McDONALD and S.J. SHAMROTH - Calculations of Two and Three Dimensional Transonic Cascade Flow Fields Using the Navier-Stokes Equations - ASME J. of Engineering for Gas Turbines and Power, Vol. 108, No 1, pp. 93-102, jan. 1986.
- [8] R.L. DAVIS, R.H. NI and J.E. CARTER - Cascade Viscous Flow Analysis Using the Navier-Stokes Equations - AIAA Paper 86-0033, jan. 1986.
- [9] L. CAMBIER, W. GHAZZI, J.P. VEUILLLOT et H. VIVIAND - Une approche par domaines pour le calcul d'écoulements compressibles - 5th Int. Symposium on Computing Methods in Applied Sciences and Engineering, Versailles, Dec. 1981, in "Computing Methods in Applied Sciences and Engineering, V", R. Glowinski and J.L. Lions Ed., North Holland Publishing Company, 1982 - ONERA TP No 1981-143.
- [10] H. VIVIAND - Traitement des problèmes d'interaction fluide parfait-fluide visqueux en écoulement bidimensionnel compressible à partir des équations de Navier-Stokes - Conférence AGARD/VKI, 20/24 fév. 1978 - ONERA TP No 1978-4.
- [11] R. MICHEL, C. QUEMARD et R. DURANT - Application d'un schéma de longueur de mélange à l'étude des couches limites turbulentes d'équilibre - ONERA NT No 154, 1969.
- [12] W.P. JONES and B.E. LAUNDER - The Prediction of Laminarization with Two-Equation Model of Turbulence - Int. J. of Heat and Mass Transfer, Vol. 15, pp. 301-314, 1972.
- [13] H. VIVIAND et J.P. VEUILLLOT - Méthodes pseudo-instationnaires pour le calcul d'écoulements transsoniques - ONERA Publication No 1978-4, 1978 (English Version ESA TT 549).
- [14] H. HOLLANDERS and H. VIVIAND - The Numerical Treatment of Compressible High Reynolds Number Flow - Computational Fluid Dynamics, Vol. 2, Kollmann Ed., Hemisphere Publ. Corp., Washington, 1980 -

ONERA TP No 1979-22.

- [15] R.W. MacCORMACK - The Effect of Viscosity in Hypervelocity Impact Cratering - AIAA Paper 69-354, 1969.
- [16] H. VIVIANI and W. GHAZZI - Numerical Solution of the Navier-Stokes Equations at High Reynolds Numbers with Applications to the Blunt Body Problem - Lecture Notes in Physics, 59, Springer Verlag, pp. 434-439, 1976 - ONERA TP No 1977-17.
- [17] W. GHAZZI et H. VIVIANI - Optimisation de maillage pour le calcul des écoulements visqueux à grand nombre de Reynolds - La Recherche Aéronautique, No 1985-2, pp. 81-87, 1985.
- [18] P. BRADSHAW (Ed.) - Turbulence - Topics in Applied Physics, Vol. 12, Springer Verlag, chapt. 1/2, 1976.
- [19] L. CAMBIER, F. DUSSON et J.P. VEUILLOT - Méthodes multi-domaines pour les équations d'Euler. Applications pour des sous-domaines avec recouvrement - La Recherche Aéronautique, No 1985-3, pp. 181-186, 1985.
- [20] L. CAMBIER, W. GHAZZI, J.P. VEUILLOT et H. VIVIANI - A Multi-Domain Approach for the Computation of Viscous Transonic Flows by Unsteady Type Methods - Recent Advances in Numerical Methods in Fluids, Vol. III : Viscous Flow Computational Methods, W.G. Habashi Ed., Pineridge Press, 1984 - ONERA TP No 1985-66.
- [21] G.W. HEDSTROM - Non-Reflecting Boundary Conditions for Non Linear Hyperbolic Systems - J. Comp. Physics, No 30, 1979.
- [22] B. ESCANDE and L. CAMBIER - Turbulence Modeling in Transonic Interactions - Symposium IUTAM sur les Interactions ondes de choc-couches cisailées turbulentes, Ecole Polytechnique, Palaiseau, 9/11 sept., 1985 - ONERA TP No 1985-128.
- [23] B. ESCANDE et L. CAMBIER - Simulation numérique d'interactions onde de choc-couche limite turbulente par résolution des équations de Navier-Stokes - Colloque sur les Ecoulements Turbulents Compressibles, Poitiers, 10/13 mars 1986 - ONERA TP No 1986-16.
- [24] J. DELERY - Experimental Investigation of Turbulence Properties in Transonic Shock-Boundary Layer Interactions, AIAA J., Vol. 21, No 2, 1983 - ONERA TP No 1983-157.

REMERCIEMENTS

Le travail, objet de la présente communication, a été réalisé avec le soutien financier de la Direction des Recherches, Etudes et Techniques de la D.G.A..

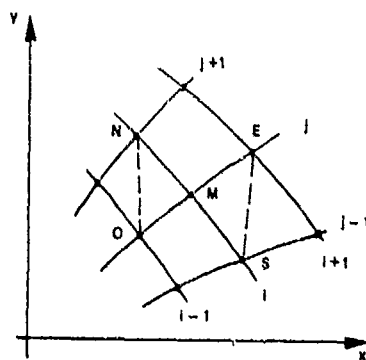
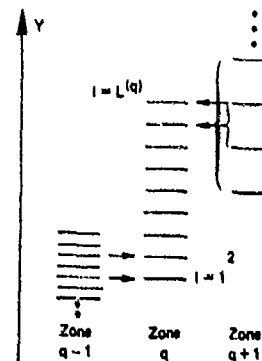


Fig. 1 - Discretisation directe dans le plan physique.

Fig. 2 - Sous-maillage par dichotomie et raccord des zones.



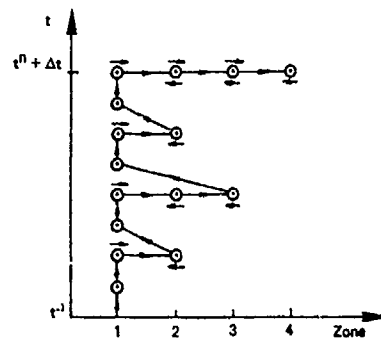


Fig. 3 — Balayage des zones au cours d'un cycle ($Q = 4$).

Fig. 4 — Grille de compresseur supersonique.
Décomposition du domaine de calcul en cinq sous-domaines.

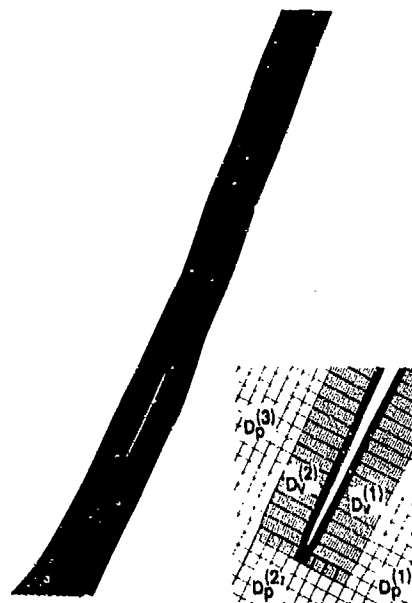
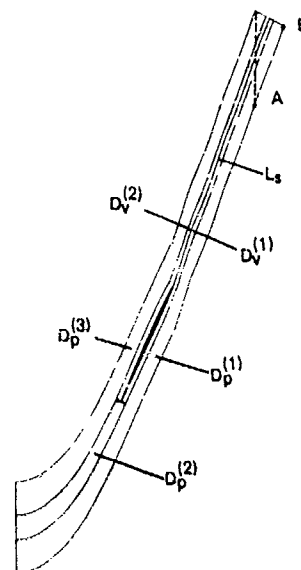


Fig. 5 — Grille de compresseur supersonique.
Maillage des cinq sous-domaines.

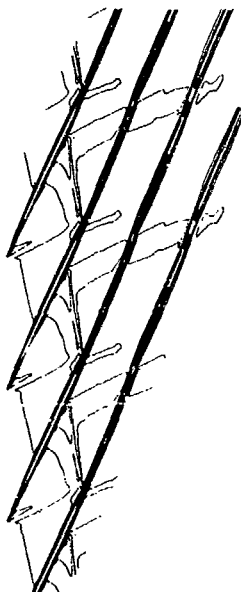


Fig. 6 — Grille de compresseur supersonique. Ecoulement a.
Courbes iso-nombre de Mach ($\Delta M = 0,1$).

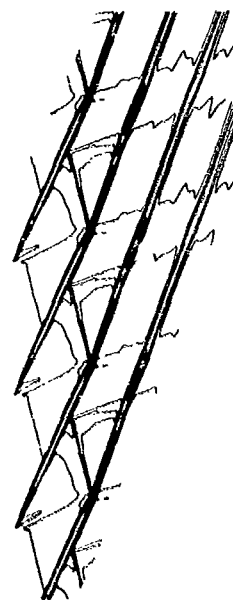


Fig. 7 — Grille de compresseur supersonique. Ecoulement b.
Courbes iso-nombre de Mach ($\Delta M = 0,1$).

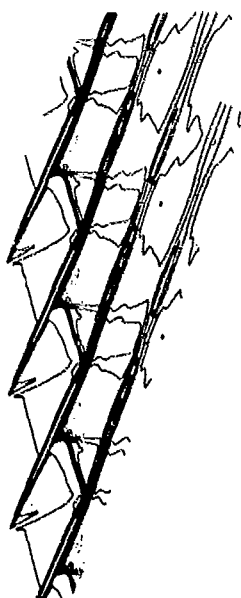


Fig. 8 — Grille de compresseur supersonique. Ecoulement c.
Courbes iso-nombre de Mach ($\Delta M = 0,1$).

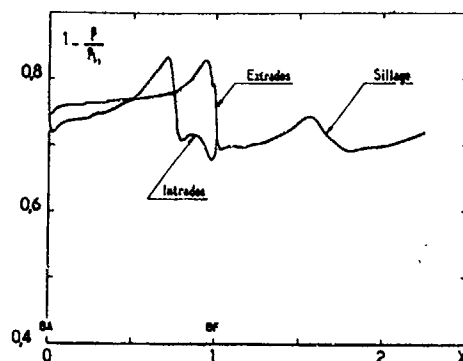


Fig. 9 — Grille de compresseur supersonique. Ecoulement a. Distribution de pression sur l'aube et dans le sillage.

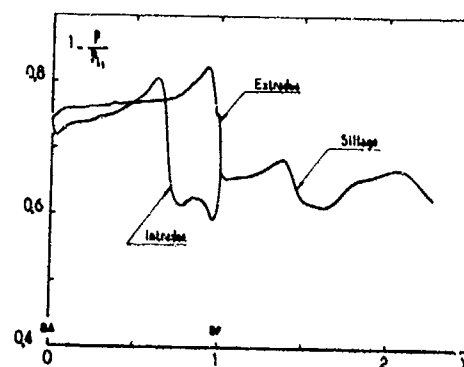


Fig. 10 — Grille de compresseur supersonique. Ecoulement b. Distribution de pression sur l'aube et dans le sillage.

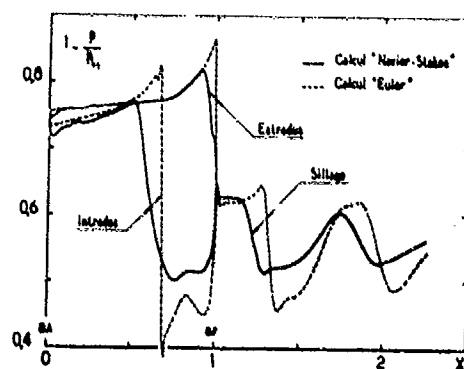
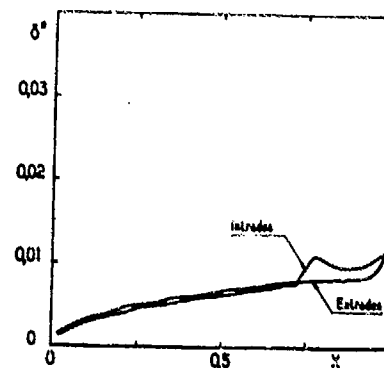


Fig. 11 — Grille de compresseur supersonique. Ecoulement c. Distribution de pression sur l'aube et dans le sillage. Comparaison avec un calcul en fluide parfait.

Fig. 12 — Grille de compresseur supersonique. Ecoulement a. Epaisseur de déplacement.



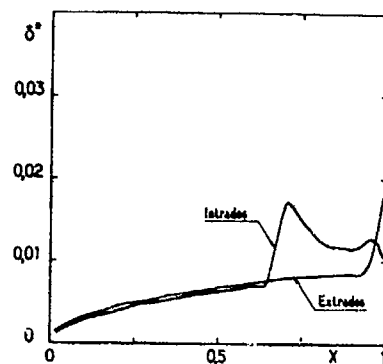


Fig. 13 — Grille de compresseur supersonique.
Ecoulement b. Epaisseur de déplacement.

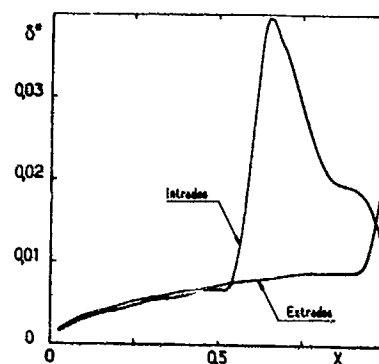


Fig. 14 — Grille de compresseur supersonique.
Ecoulement c. Epaisseur de déplacement.

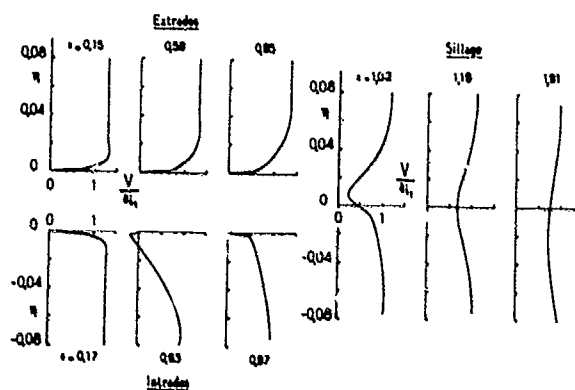
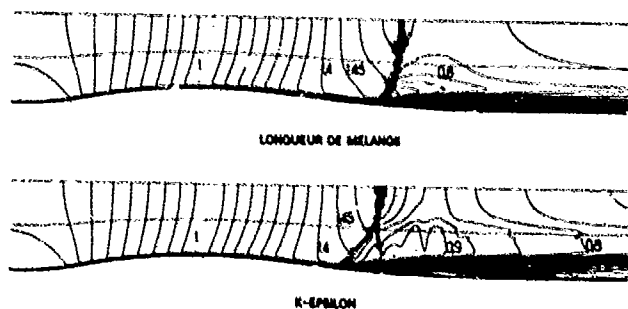


Fig. 15 — Grille de compresseur supersonique. Ecoulement c.
Profils de vitesse sur l'aube et dans le sillage.



Fig. 16 — Canal plan. Maillages des deux sous-domaines.



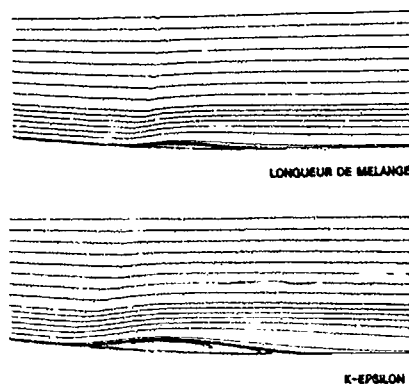


Fig. 18 - Canal plan. Lignes de courant au voisinage de la zone décollée.

Fig. 19 - Canal plan. Distribution de pression pariétale.

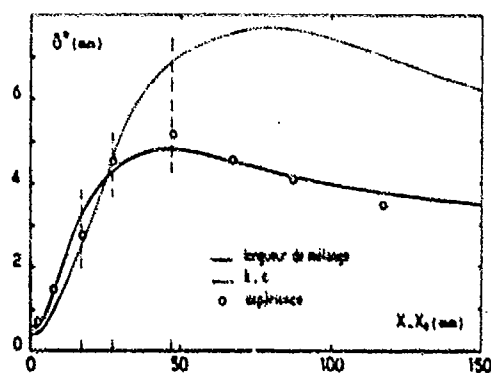
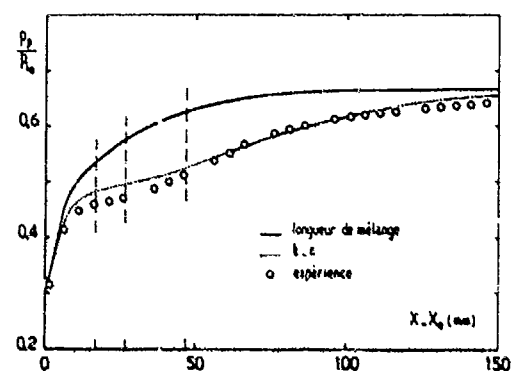
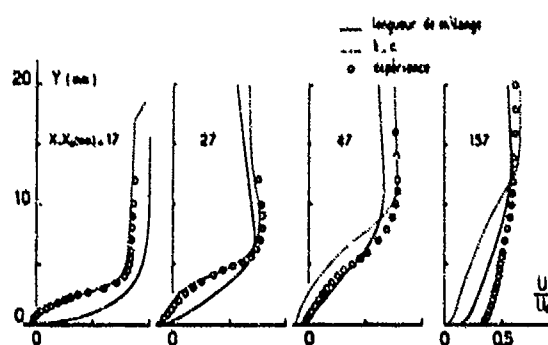


Fig. 20 - Canal plan. Distribution d'épaisseur de déplacement.

Fig. 21 - Canal plan. Profils de vitesse.



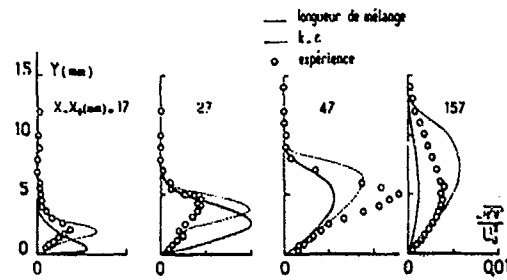


Fig. 22 — Canal plan. Profils de tension de cisaillement turbulente.

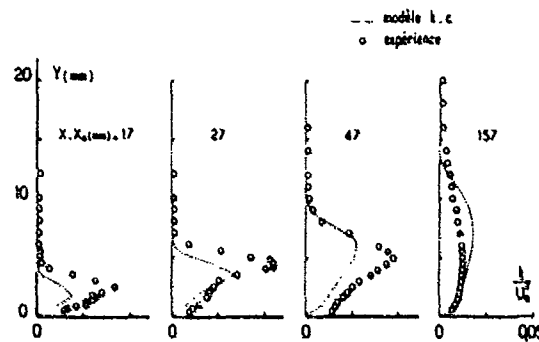


Fig. 23 — Canal plan. Profils d'énergie cinétique de turbulence.

DISCUSSION

H. Stoff, Switzerland

La Figure 17 montre un choc en forme de λ près de la séparation des domaines de calcul visqueux et non-visqueux. Il se pose la question de savoir comment vous imposez la taille du domaine de calcul visqueux en considérant le résultat obtenu après.

Réponse d'Auteur

La technique de raccord entre les divers sous-domaines, fondée sur l'utilisation des relations caractéristiques (ou relations de compatibilité), exige que la frontière séparant deux sous-domaines soit située dans une région où les effets visqueux sont négligeables. Dans tous les calculs présentés (grilles d'ube, canal 2D), la position des interfaces séparant deux sous-domaines est fixée a priori. On vérifie, a posteriori, que les couches visqueuses sont effectivement confinées à l'intérieur des sous-domaines "Navier-Stokes". Cette vérification s'effectue par simple examen des courbes iso-nombre de Mach. Une solution plus satisfaisante mais de mise en oeuvre plus complexe, consisterait à ajuster, au cours du calcul itératif, la géométrie des interfaces à celle des frontières des couches visqueuses.

AD-P005 520

SOME TURBOMACHINERY BLADE PASSAGE ANALYSIS METHODS -
RETROSPECT AND PROSPECT

D Carrahar⁺ and T R Kingston^{*}

⁺ Manager
Theoretical Science Group
Rolls-Royce plc
P O Box 3
Filton
Bristol BS12 7QE

^{*} Senior Technology Engineer
Theoretical Science Group
Rolls-Royce plc

Summary

The development of time marching methods to analyse blades started at Rolls-Royce in the mid seventies, when sufficient computing power was becoming available. It was recognised that such methods had much to offer, especially for transonic and supersonic flows. Since then several different algorithms have been developed to predict both quasi-3D and 3D flows. At present the time-marching methods are used to solve the unsteady Euler/Navier-Stokes equations to produce a time steady solution.

Future developments are aimed towards predicting loss accurately, and to investigate unsteady effects such as vortex shedding and incoming wakes.

Nomenclature

c	local speed of sound in air = $\sqrt{\gamma RT}$
C_p	specific heat at constant pressure
C_v	specific heat at constant volume
e	specific internal energy = $C_v T$
E	total specific energy = $e + \frac{V^2}{2}$
h	stream tube height
H	total enthalpy
I	rothalpy = $H - \Omega r V_\theta$
k	conductivity
m	meridional distance
p	pressure
P_r	molecular Prandtl number, 0.72
P_{rt}	turbulent Prandtl number, 0.90
q	heat conduction flux = $-k \nabla T$
r, θ, z	polar coordinates
R	gas constant
s	arc length on blade surface
S	surface area
t	time
T	temperature
V	absolute velocity vector
W	relative velocity vector $W_\theta = V_\theta - \Omega r$
β	"hade" angle of stream surface of revolution to axial direction
δ^*	boundary layer displacement thickness
ρ	density
Ω	rotational speed (rad/sec)

γ	ratio of specific heats = C_p/C_v
ϵ	turbulent eddy viscosity
μ	laminar molecular viscosity
$\underline{\sigma}$	total stress tensor
$\underline{\pi}$	viscous stress tensor = $\underline{\sigma} + p\mathbf{I}$
ΔV	elemental volume

Subscripts

0	total conditions
abs	absolute
rel	relative
r, θ , z	components in polar coordinates
m	meridional component
1	upstream conditions
i, j, k	local grid coordinates (in z, θ , r directions)

1. Introduction

During the last ten to fifteen years time-marching methods, for internal turbomachinery flow problems, have progressed continuously. Originally applied to two-dimensional cascade flows with the restriction of an inviscid gas, to the present day when three-dimensional, viscous flow problems, in both steady and unsteady states, are being attempted. Hand-in-hand with the development of the methods has been the major developments of computers, and the increase in the size of the memory which they may access. The roles have reversed several times, in that at times methods have been running ahead of available computing power, whereas at other times computing power has raced ahead of the methods development. Time marching in this context refers to a method which solves the unsteady compressible equations of continuity, energy, and either the inviscid (Euler) or viscous (Navier-Stokes) equations of motion expressed in conservation form, viz.

$$\text{Continuity} \quad \frac{\partial}{\partial t}(\rho Y) + \nabla \cdot (\rho Y \mathbf{V}) = 0 \quad (1)$$

$$\text{Momentum (Navier-Stokes)} \quad \frac{\partial}{\partial t}(\rho Y \mathbf{V}) + \nabla \cdot (\rho Y \mathbf{V} \mathbf{V}) - \nabla \cdot \underline{\sigma} = 0 \quad (2)$$

$$\text{Energy} \quad \frac{\partial}{\partial t}(\rho Y E) + \nabla \cdot (\rho Y H \mathbf{V}) + \nabla \cdot \underline{q} - \nabla \cdot (\underline{\pi} \cdot \mathbf{V}) = 0 \quad (3)$$

The solution is advanced in time ("marched") to yield either a fine steady (asymptotic solution), or to provide an unsteady (time accurate) solution. The first applications of time-marching for steady state solutions, to the flow patterns inside turbomachines, were based upon solving the finite difference form of the partial differential equations. Without special treatment of the conservation variables, this discretization suffers accuracy problems, particularly in the regions of solid boundaries and shock waves. This can be overcome by use of so called iso-parametric transformations, but a simpler method is to discretize the equations using a 'finite area' method as described originally by P W McDonald (1971) for two-dimensional flow, and its natural extension, the 'finite volume' method for three-dimensional flow (Appendix A). McDonald's finite area method for two-dimensional flow was relatively slow on the computers of the day, due mainly to solving on over-lapping hexagonal elements. It was also limited to solving the isentropic density - pressure relationship, the most serious result of which was that only weak shock-waves could be accommodated. J D Denton (1974) overcame these two problems by using a simplified grid structure (the "sheared" grid), stabilising the procedure using upwinding and downwinding with correction factors to achieve greater accuracy in the steady state, and introducing the ideal gas equation instead of the isentropic equation. The result of these innovations was that engineering accuracy could be achieved in acceptable computer run times, and shocks of any strength could be captured with their respective losses of total pressure predicted.

It was with this proven capability, that the first author embarked in 1975 on writing his initial time-marching program for turbomachinery flows.

In the present paper only explicit formulations of the equations are presented, as pursued by the authors. The methods developed are for both quasi-3D and full 3D flow. Blades are normally designed and analysed in sections, being essentially 2D with allowance made for radius and stream tube height variation. The complete 3D blade definition is achieved by stacking these "sections", from hub to casing. An analysis of the blade is then undertaken to examine the 3D nature of the flow, which may result in a re-stack of the sections, or their re-design.

2. Quasi Three-Dimensional (Q-3D) Flow

In the design stage of axial flow turbines or compressors it is convenient to describe the flow as being confined to assumed axisymmetric streamtubes, their definition being provided by a previous throughflow analysis. The flow is essentially 2D but confined to a meridional stream-surface (defined in figure 1), with the expansion of the streamtube described by a parameter h , termed the streamtube height.

The equations solved are those of Inviscid flow, expressed in conservation form, for a relative frame of reference. In addition for convenience the unsteady energy equation is not solved, and instead replaced with the assumption of isothermal flow, thus:

$$\frac{\partial U}{\partial t} + \frac{1}{rh} \frac{\partial F}{\partial m} + \frac{\partial G}{\partial \theta} + B = 0 \quad (4)$$

$$\underline{U} = \begin{bmatrix} \rho \\ \rho W_m \\ \rho W_\theta \end{bmatrix}, \quad \underline{F} = \begin{bmatrix} rh\rho W_m \\ rh(p + \rho W_m^2) \\ rh\rho W_\theta W_m \end{bmatrix}, \quad \underline{G} = \begin{bmatrix} h\rho W_\theta \\ h\rho W_\theta W_m \\ rh(p + \rho W_\theta^2) \end{bmatrix}$$

$$B = \begin{bmatrix} 0 \\ -\frac{\rho \sin \beta (W_m + \Omega r)^2}{r} - \frac{\rho}{rh} \frac{\partial (rh)}{\partial m} \\ 2\rho r \Omega W_m \sin \beta \end{bmatrix}$$

This system of equations is closed by combining the energy and perfect gas equations.

$$p = \rho RT = \rho R(T_{tot} - \frac{W^2}{2C_p}) \quad (5)$$

The relative total temperature $T_{tot}(m)$ is given by conservation of enthalpy h on the inviscid, non-conducting stream surface.

$$T_{tot} = T_{tot,1} + \frac{\Omega^2}{2C_p}(r^2 - r_1^2) \quad (6)$$

Several time-marching schemes have been written to solve equations 1-3, and are collectively known as TITAN (Time Iterative Analysis), and for simplicity we shall refer to them as TITAN 1, 2 and 3. The basic mesh for each is an 'H' or 'sheared' grid fixed in the relative frame (figure 2, shown for a left handed set of coordinates following normal turbomachinery practice), which has the great virtue of simplicity, and is adequate for most practical problems. Boundary conditions have to be applied for ABCDEFGH. AB and GH are the upstream periodic or repeating boundaries, CD and EF the downstream, and conservation variables are equalised at each meridional grid point.

AB¹C and EF¹D are solid boundaries where flow tangency is enforced for an Euler formulation of the equations, or 'no-slip' for a Navier-Stokes (viscous) formulation. At the upstream plane AH three conditions are necessary, the relative total pressure and temperature, and either the relative flow angle for subsonic flow, or the relative swirl velocity for supersonic flow. Downstream DE just has a pitchwise constant static pressure specified.

In the present formulation the changes for equation 4 are evaluated by finite volumes, by application of Gauss' theorem, as indicated in Appendix B.

Solution Algorithms

TITAN 1 (1975)

The method is essentially based on Denton's (1974) original cell centred scheme. Figure 3.1 shows a typical element 1234, extending over two (equal) pitchwise (θ) grid spacings, and overlapping half of the adjoining element. Changes in the conservation variables are obtained at the centroid C of 1234 by a finite volume method (Appendix B), with special treatment for boundary elements. Aerodynamics at the point P (necessary for flux calculations) are obtained by second order accurate interpolation formulae

from the cell centred variables, but to ensure stability pressures have to be biased upstream, and density and momenta downstream.

The scheme tends to be robust but unfortunately allows no reverse flows, leading edge problems being overcome by use of a cusp.

TITAN 2 (1979)

This is a scheme similar to, but developed prior to Denton's 'A' scheme (1982). It was devised in order to attempt more accurate solutions without the need for more mesh points, or an appreciable increase in computer run times. Spurious total pressure changes are more severe at solid boundaries due to the calculations being essentially one-sided, and because generally the largest gradients of the flow variables occur at these boundaries. The treatment in TITAN 2 provides a means of controlling the accuracy at the boundary without detrimentally affecting the rest of the solution. This is achieved by maintaining the isentropic distribution of relative total pressure on the walls, unless a discontinuity is detected (Appendix C). The algorithm of TITAN 2 is such that limited amounts of reverse flow are possible, and the need for a leading edge cusp is removed. Unfortunately, the algorithm of TITAN 2 cannot be extended to three-dimensions neither is it acceptable for large amounts of reverse flow such as those present in boundary layers.

The scheme is node based using non-overlapping elements, such as 1234 in figure 3.2. The change of density at node 1 (1,j) is given by:

$$\Delta \rho_{1j} = \frac{1}{2} (\delta \rho_{1,j-1} + \delta \rho_{1j}) \quad (7)$$

and the changes of ρu or ρw (denoted by 'F' below) at node 1,j is given by:

$$\Delta F_{1j} = \frac{1}{2} (\delta F_{1,j-1} + \delta F_{1j}) \quad (8)$$

with special treatment for boundary elements. The different treatment of density and momenta is in order to ensure stability.

TITAN 3 (1982-0)

As blade design philosophy changed, bringing with it higher physical blade loadings and their distribution, so the need for higher accuracy in analysis methods became apparent. In addition the need to be able to compute reverse flows, further accelerated the introduction of a new scheme, TITAN 3. This provided the necessary accuracy, as well as significant savings in computer run time.

TITAN 3 is a Ni (1981) type Lax-Wendroff scheme, employing a multiple-grid technique for convergence acceleration to the steady stage. It is node based and employs a second order accurate Taylor expansion formulation to update the conservation variables, viz.

$$\delta U = \frac{\partial U}{\partial t} \Delta t + \frac{1}{2} \frac{\partial^2 U}{\partial t^2} \Delta t^2 + O(\Delta t^3) \quad (9)$$

Substitution of equation 9 into 4, with a change in the order of differentiation yields (with the first order change denoted by ΔU)

$$\delta U = -\left(\frac{1}{\Delta t} \frac{\partial F}{\partial x} + \frac{1}{\Delta t} \frac{\partial G}{\partial y} + B\right) \Delta t - \left(\frac{1}{\Delta t} \frac{\partial}{\partial x} \left(\frac{\partial F}{\partial t} \Delta t\right) + \frac{1}{\Delta t} \frac{\partial}{\partial y} \left(\frac{\partial G}{\partial t} \Delta t\right) + \frac{\partial B}{\partial t} \Delta t\right) \frac{\Delta t^2}{2}$$

$$\delta U = -\Delta U - \left(\frac{1}{\Delta t} \frac{\partial}{\partial x} \left(\frac{\partial F}{\partial t} \Delta U\right) + \frac{1}{\Delta t} \frac{\partial}{\partial y} \left(\frac{\partial G}{\partial t} \Delta U\right) + \frac{\partial B}{\partial t} \Delta U\right) \frac{\Delta t^2}{2} \quad (10)$$

The terms $\frac{\partial F}{\partial t}$, $\frac{\partial G}{\partial t}$, $\frac{\partial B}{\partial t}$ are termed the Jacobians, and are simply analytic functions of the current aerodynamics. Consider the grid shown in figure 3.3, the first order change at C for element 1234 is evaluated by finite volume, and similarly at A, B, D. The first order change at node 1 is then simply given by an average of the changes at A, B, C and D. The second order change for node 1 is evaluated from the element

ABCD, using the previously calculated first order changes ($\Delta U, A, B, C, D$).

This second order change could be evaluated by finite volumes, but in the present formulation we choose to save storage and use finite differences. It is also advantageous to introduce a spatial marching process, whereby variables are updated in axial planes. Thus in figure 3.3, for element 1234, the calculated fluxes use updated variables at 3,4 and old (previous time step) values at 1 and 2. Thus one complete iteration involves marching downstream and then back upstream, introducing a semi-implicit nature to the scheme. This ensures the upstream and downstream boundary conditions are propagated quickly through the flow field, hence speeding convergence.

As given by Ni (1981) rapid convergence can be achieved for steady flow problems, by use of the multiple-grid method. The calculation mesh can be decomposed into successively coarser meshes by deletion of every other grid line. Following the update of the variables on the fine mesh, further time steps are taken on each coarser mesh. Even faster convergence can be achieved by using grid refinement, in combination with multiple-gridding.

General Features

(1) Boundary Layers

Adequate inclusion of the effects of boundary layers must be achieved for most problems, and in the present method a "transpiration" technique is used. The usual inviscid equations are solved, but a modification to the solid and downstream periodic boundary conditions are made due to the presence of the boundary layer. Figure 4 shows a boundary layer on a blade surface (calculated from the inviscid velocity distribution). It can be seen that a transpiration of normal momentum $(\rho w)_s = \int (\rho w)_s ds$ refers to the slip (inviscid) surface momentum, satisfied on the control volume. This approach has the advantage over the usual method, in that the computational mesh does not have to be modified for the calculation.

The coding has been set up so that several different boundary layer methods, both integral and differential, can be used. The integral methods have the great virtue of being fast and simple, whilst the differential methods can allow the inclusion of phenomena such as film cooling.

The technique of using a "direct mode" is used for rapid boundary layer growth is observed, for example separation of the boundary layer on compressor blade suction side. The alternative "inverse mode", has not so far been pursued.

(2) Kutta Condition

For turbine cascade calculations the Kutta condition is satisfied, by equalizing the circulation around the trailing edge circle blend points.

(3) Mixing

For the present calculations a mixing calculation is carried out at the exit of the cascade. This includes the effects of base pressure, and the effects of the flow field into downstream where it is assumed conditions are uniform.

3. Three-Dimensional Flow

For axial flow machinery problems it is convenient to express equations 1-3 in a cylindrical polar set of coordinates. Thus in the absolute frame we have:

$$\frac{\partial \rho}{\partial t} + \left(\frac{1}{r} \frac{\partial F}{\partial r} + \frac{1}{r} \frac{\partial G}{\partial \theta} + \frac{\partial H}{\partial z} + B \right) - \left(\frac{1}{r} \frac{\partial F'}{\partial r} + \frac{1}{r} \frac{\partial G'}{\partial \theta} + \frac{\partial H'}{\partial z} + B' \right) = 0 \quad (11)$$

A

B

Where the terms designated 'A' constitute the Euler (inviscid) equations, and 'B' the additional terms due to viscosity and heat conduction, with

$$B = \left[\begin{array}{c} \frac{\partial \rho}{\partial t} \\ \frac{\partial \rho u}{\partial t} \\ \frac{\partial \rho v}{\partial t} \\ \frac{\partial \rho e}{\partial t} \end{array} \right]$$

$$F = \begin{bmatrix} r\rho V_r \\ r(p + \rho V_r^2) \\ r\rho V_r V_\theta \\ r^2\rho V_r V_\theta \\ r\rho H V_r \end{bmatrix}, \quad G = \begin{bmatrix} \rho V_\theta \\ \rho V_\theta V_r \\ \rho V_\theta V_\theta \\ r(p + \rho V_\theta^2) \\ \rho H V_\theta \end{bmatrix}, \quad H = \begin{bmatrix} \rho V_z \\ \rho V_z V_r \\ p + \rho V_z^2 \\ r\rho V_z V_\theta \\ \rho H V_z \end{bmatrix}, \quad R = \begin{bmatrix} 0 \\ -\frac{p}{r} + \rho V_\theta^2 \\ 0 \\ 0 \\ 0 \end{bmatrix},$$

$$F' = \begin{bmatrix} 0 \\ r\pi_{rr} \\ r\tau_{rz} \\ r^2\tau_{r\theta} \\ r(\pi_{rr}V_r + \tau_{r\theta}V_\theta + \tau_{rz}V_z - q_r) \end{bmatrix}, \quad G' = \begin{bmatrix} 0 \\ \tau_{r\theta} \\ \tau_{\theta z} \\ r\pi_{\theta\theta} \\ \tau_{r\theta}V_r + \pi_{\theta\theta}V_\theta + \tau_{\theta z}V_z - q_\theta \end{bmatrix},$$

$$H' = \begin{bmatrix} 0 \\ \tau_{rz} \\ \pi_{zz} \\ r\tau_{z\theta} \\ \tau_{rz}V_r + \tau_{z\theta}V_\theta + \pi_{zz}V_z - q_z \end{bmatrix}, \quad R' = \begin{bmatrix} 0 \\ -\pi_{\theta\theta} \\ 0 \\ 0 \\ 0 \end{bmatrix},$$

$$\sigma_{rr} = -p + 2(\mu + \epsilon)\left(\frac{\partial V_r}{\partial r} - \frac{1}{3}\nabla \cdot V\right)$$

$$\sigma_{\theta\theta} = -p + 2(\mu + \epsilon)\left(\frac{1}{r}\frac{\partial V_\theta}{\partial \theta} + \frac{V_r}{r} - \frac{1}{3}\nabla \cdot V\right)$$

$$\sigma_{zz} = -p + 2(\mu + \epsilon)\left(\frac{\partial V_z}{\partial z} - \frac{1}{3}\nabla \cdot V\right)$$

$$\pi_{rr} = \sigma_{rr} + p$$

$$\pi_{\theta\theta} = \sigma_{\theta\theta} + p$$

$$\pi_{zz} = \sigma_{zz} + p$$

$$\tau_{\theta z} = \tau_{z\theta} = (\mu + \epsilon)\left(\frac{1}{r}\frac{\partial V_\theta}{\partial z} + \frac{\partial V_z}{\partial \theta}\right)$$

$$\tau_{rz} = \tau_{zr} = (\mu + \epsilon)\left(\frac{\partial V_r}{\partial z} + \frac{\partial V_z}{\partial r}\right)$$

$$\tau_{r\theta} = \tau_{\theta r} = (\mu + \epsilon)\left(\frac{\partial V_\theta}{\partial r} - \frac{V_\theta}{r} + \frac{1}{r}\frac{\partial V_r}{\partial \theta}\right)$$

$$q = -k\nabla T = -\frac{k}{C_v}\nabla e = -\gamma\left(\frac{\mu}{P_r} + \frac{\epsilon}{P_\theta}\right)\nabla e$$

$$q_r = -\gamma\left(\frac{\mu}{P_r} + \frac{\epsilon}{P_\theta}\right)\frac{\partial e}{\partial r}$$

$$q_\theta = -\gamma\left(\frac{\mu}{P_r} + \frac{\epsilon}{P_\theta}\right)\frac{1}{r}\frac{\partial e}{\partial \theta}$$

$$q_z = -\gamma\left(\frac{\mu}{P_r} + \frac{\epsilon}{P_\theta}\right)\frac{\partial e}{\partial z}$$

$$e = E - \frac{(V_r^2 + V_\theta^2 + V_z^2)}{2}$$

This system of equations is closed by the perfect gas law $p = \rho RT$, a suitable viscosity formula and an eddy viscosity model.

Equation 11 is expressed in an absolute frame but generally we are looking for a time steady solution in a relative frame (i.e. for the flow in rotor passage), and thus we make use of the following relationship for \underline{U} .

$$\frac{\partial_{rel} \underline{U}}{\partial t} = \frac{\partial_{abs} \underline{U}}{\partial t} + \Omega \frac{\partial \underline{U}}{\partial \theta} \quad (12)$$

Combining 11 with equation 12 yields

$$\begin{aligned} \frac{\partial_{rel} \underline{U}}{\partial t} + \frac{1}{r} \frac{\partial F}{\partial r} + \frac{1}{r} \frac{\partial (G - \Omega r U)}{\partial \theta} + \frac{\partial H}{\partial z} + B \\ - \frac{1}{r} \frac{\partial F'}{\partial r} - \frac{1}{r} \frac{\partial G'}{\partial \theta} - \frac{\partial H'}{\partial z} - B' = 0 \end{aligned} \quad (13)$$

Equation 13 is solved explicitly by finite volumes on a suitable grid. This consists of radially stacked Q-3D streamwise surfaces (figure 2), and is shown in figure 5 (again shown as a LH set for convenience). At the inlet surface the boundary conditions are distributions of absolute total pressure, absolute total temperature and absolute swirl angle for subsonic flow, or absolute swirl velocity for supersonic flow, and in addition the distribution of radial flow angle. Downstream the static pressure is given. This may be input in several ways, including a complete specification of the distribution or allowing the solution to satisfy simple radial equilibrium. Again at solid boundaries (blade, hub and casing) we enforce tangency (Euler) or no-slip (viscous), and in addition, a wall temperature or gradient (heat transfer) distribution, if we solve the unsteady energy equation.

TITAN 4 (1978)

This is a three-dimensional version of TITAN 1 which is based upon the original Denton scheme (1974). Only the inviscid equations of motion (designated 'A' in equation 11) are solved. Although inviscid, a loss distribution can be specified which models to some extent the total pressure loss associated with the presence of boundary layers.

Multiple-grid techniques (similar to Denton) may be used to enhance the convergence rate to a steady solution. As with the TITAN 1 code, no large reverse flow can be calculated and a cusp is employed to alleviate leading edge problems.

TITAN 5 (1984)

In a similar way that quasi-3D algorithms developed to meet new design requirements, so the need for an improved 3-D code became apparent. TITAN 5 is the three-dimensional counterpart of TITAN 3, but extended to be a full Navier-Stokes solver, when required. In similar fashion, the change in the vector \underline{U} over the time step Δt is approximated by taking the first two terms of the Taylor series expansion.

The equations are discretized using finite volumes for the first order changes ($\Delta \underline{U}$), and finite differences for the second order changes. To speed up convergence a grid refinement technique is used, and also a spatial marching process, as outlined for TITAN 3. In variance to the Q-3D, if boundary layer inclusion is required, then we solve the full Navier-Stokes equations (A and B in equation 11). This necessitates the local refinement of the grid near solid boundaries, in order to resolve the flow gradients. Although this requires many more grid points, and hence increases the computational overhead, it should permit the calculation of blade loss. A Baldwin and Lomax (1978) turbulence model is incorporated, with a specified start and end of transition. The unsteady energy equation allows the prediction of heat transfer at the walls, but in certain instances (inviscid, constant rothalpy) it is not solved, which not only saves computer time, but reduces truncation errors.

4. Comparison with Test Results

(1) 2D Results

The example presented is of a high exit angle HP NGV mid section profile, tested in 2D cascade at AVA Göttingen supersonic wind tunnel (Jaspel, 1977). The cascade geometry is shown in figure 6. This was tested over a range of exit Mach numbers, for which pressure distribution, schlieren and downstream traverse were collected.

For comparison purposes only one exit Mach number case (= 0.99), at design incidence, is presented. Both TITAN 1 and 3 were run without boundary layers, and the corresponding Mach number distributions are shown in figure 7, together with the isentropic test points. The computational grid used for both was the same, having 20 pitchwise and 35 blade calculation points. It can be seen that TITAN 3 predicts the distribution well, apart from the overshoot in Mach number on the suction surface (which could be expected without boundary layer inclusion). The run time for TITAN 3, using multiple gridding, was less than half that for TITAN 1, for the same convergence.

Further use of the TITAN 1 program, this time for a compressor example is presented by Nabeisael and Seyb (1986).

(2) 3D Results

Some of the results of the three-dimensional calculation method (TITAN 5) are compared with the test of the flared RD turbine rotor cascade described in Camus et al (1983). This cascade is planar with one end wall flared to give an increase in the bulk flow area across the blade.

At the time that this calculation was performed the turbulence model, indicated in Section 3, had not been included but nevertheless a viscous gas flow, at high Reynold's number, was calculated. In order to model the planar cascade, a radius more than a hundred times greater than the blade span was input. The grid used is extremely coarse for a Navier-Stokes calculation ($18 \times 20 \times 64$) but the grid spacing has been chosen such that the finest definition occurs near the solid boundaries. As a result, large variations in the grid sizes of adjacent elements occur with some elements being of the order of ten times larger by volume, figures 8 and 9. Some shock definition has been lost as a consequence of coarsening the grid in this way.

Figures 10 and 11 show a comparison between the isentropic Mach numbers at the blade surfaces. In each case the isentropic exit Mach number is maintained at 1.2 and this accounts for the calculated peak Mach numbers being different in the inviscid and viscous cases. The measured static pressures were taken along lines which were parallel to the lower wall, whereas the calculated values were on the mesh points shown in figure 9. No attempt has been made to interpolate either result to obtain exact correspondence since only general trends were required at this stage. It is expected that the calculated viscous results would be improved with a finer grid, and with the inclusion of the Baldwin and Lomax (1978) turbulence model.

In order to show the extremely complex flow patterns in the region of the cascade walls, calculated 'streak' lines at .12 per cent of the span away from the plane end wall are shown in figure 12. Major features such as the 'saddle' point upstream of the leading edge, the generation and transport of the horseshoe vortex and the movement of the fluid from pressure to suction surface are apparent.

5. Discussion and Future Work

The need for better blade analysis methods has prompted the rapid development of both quasi-3D and 3D time marching algorithms. TITAN 3 and TITAN 5, although much more complex than the previous methods, still produce solutions to comparable problems in less or similar computer run times. Computer speed and storage have also advanced, and with this it has been possible to analyse problems in more detail. The use of finer meshes also decreases the spurious entropy changes (manifested as a loss or gain in total pressure) present in the final solution. In addition fine meshes are the only way to resolve small scale features of the flow.

Figure 13 shows the development of computational methods by the authors, and possible future work. Calculation of 'steady' flows is well in hand using the existing TITAN codes, predominantly TITAN 3 and 5. It should however be emphasised that particular solution algorithms may not be optimum for every flow problem, and thus constant reappraisal becomes necessary. For instance it may well be better to use an implicit formulation in the boundary layer regions. Current effort is directed towards reasonable loss calculations, and understanding loss mechanisms, such as the flow around trailing edges. Time marching however offers the possibility to calculate time accurate unsteady or periodic flows. Probably the most obvious unsteady problem is that of a rotor-stator configuration, either in 2D or 3D, and this is currently being addressed. Future work will certainly be aimed at trying to resolve smaller scale structures, and to tackle the problems of unsteady flow.

Acknowledgements

M Poole for help with the 2D predictions. The authors wish to express their thanks to Rolls-Royce for permission to publish this paper. The opinions expressed are those of the authors, and do not necessarily represent those of Rolls-Royce.

References

- | | |
|---------------|--|
| McDonald, P W | "The computation of transonic flow through two-dimensional gas turbine cascades".
ASME 71-GT-89, 1971. |
| Denton, J D | "A time marching method for two and three dimensional blade to blade flow".
Aero. Res. Co., R & N 3775, 1974. |
| Denton, J D | "An improved time marching method for turbomachinery flow calculation".
ASME 82-GT-239, 1982. |

- Ni, R H "A multiple grid scheme for solving the Euler equations".
AIAA paper 81-1025, June 1981.
- Baldwin, B S & Lomax, H "Thin-layer approximation and Algebraic model for separated turbulent flows."
AIAA paper 78-257, Jan. 1978.
- Jaspal, R Rolls-Royce private communication 1977.
- Hoheisel, H and Seyb, N J "The boundary layer behaviour of a highly loaded compressor cascade at transonic flow conditions", AGARD 68th (B) specialists' meeting on transonic and supersonic phenomena in turbomachines, Munich 10-12 Sept. 1986.
- Camus, J J, Denton J D, Soulis, J V, Scrivener, C T J "An experimental and computational study of transonic three-dimensional flow in a turbine cascade".
ASME 83-GT-12, 1983.

APPENDIX A

The Finite Volume (Area) Technique

Consider a model equation given by:

$$\frac{\partial f}{\partial t} + \nabla \cdot F(f) = 0 \quad (A1)$$

expressing the conservation of a variable f in an Eulerian frame of reference. The finite volume method makes use of Gauss' theorem to express the volume integral as a surface integral bounding a volume ΔV .

$$\nabla \cdot F(f) = \lim_{\Delta V \rightarrow 0} \frac{1}{\Delta V} \int_{\Delta V} F \cdot n \, ds \quad (A2)$$

where n is the outward unit normal to ΔV . Thus the time derivative may be expressed as

$$\frac{\partial f}{\partial t} = -\nabla \cdot F = \lim_{\Delta V \rightarrow 0} \frac{1}{\Delta V} \int_{\Delta V} F \cdot n \, ds \quad (A3)$$

The new f at a time level $n+1$ is related to that at the previous time level n by:

$$f^{n+1} = f^n + \delta f \quad (A4)$$

where

$$\delta f = -\frac{\Delta t}{\Delta V} \int_{\Delta V} F \cdot n \, ds \quad (A5)$$

APPENDIX B

Finite Volume Formulation of Q-3D Equations

Applying Gauss's theorem (or Green's theorem in the plane) to equation 4 yield

CONTINUITY

$$\frac{\Delta m}{\Delta t} = -\frac{1}{\Delta V} \sum_{m=1}^M [(\rho u_m)_n (h r \delta \theta)_n - (\rho u_m)_n (h \delta m)_n] \quad (B1)$$

m-momentum

$$\frac{\Delta_{rel}(\rho W_m)}{\Delta t} \approx -\frac{1}{\Delta V} \sum_{n=1}^N [(p + \rho W_m^2)_n (hr \delta \theta)_n - (\rho W_m)_n (hr \delta m)_n] + \frac{\rho (W_\theta + \Omega r)^2 \sin \beta}{r} + \frac{\rho}{\Delta V} \sum_{n=1}^N (hr \delta \theta)_n \quad (B2)$$

θ (angular) momentum

$$\frac{\Delta_{rel}(\rho r W_\theta)}{\Delta t} \approx -\frac{1}{\Delta V} \sum_{n=1}^N [(\rho W_m r W_\theta)_n (hr \delta \theta)_n - (p + \rho W_m^2)_n (hr \delta m)_n] - 2\rho \Omega r W_m \sin \beta \quad (B3)$$

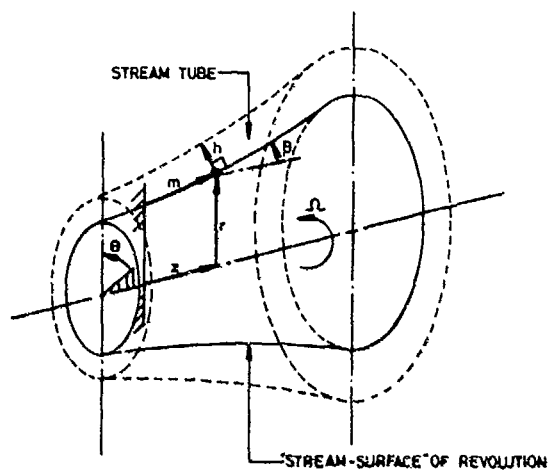
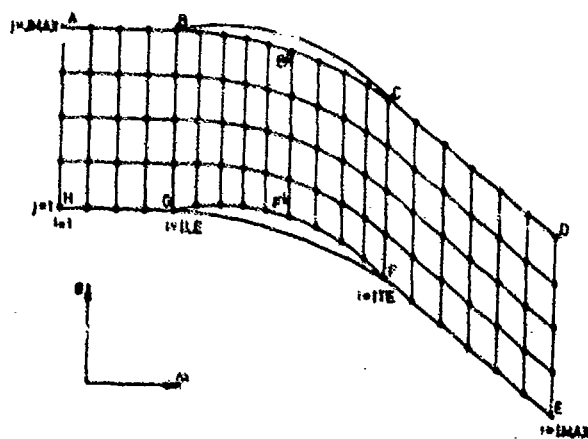
Where the summation is for all sides of the Q-3D grid element, and the fluxes are positive w.r.t. the outward normal, the elemental volume $\Delta V = hr \delta m \delta \theta$, and the overbar indicates a mean quantity at the centre of the element.

APPENDIX CTreatment of Solid Boundaries in TITAN 2

In 2D inviscid flow the solid boundaries are flow streamlines, and in the absence of shocks the total pressure should be conserved along the blade surfaces. In Q-3D the situation is the same except that the isentropic relative total pressure is a function of radius only. Thus in the present formulation the total relative pressure condition is forced at boundaries, unless an increase in static pressure ratio between nodes greater than 1.3 indicates the presence of a shock. In such a case the total pressure downstream (suffix 2) can be related to that upstream (suffix 1) by the relationship

$$\frac{P_{02}}{P_{01}} = \left(\frac{(\gamma+1) \frac{P_1}{P_1} + (\gamma-1)}{(\gamma-1) \frac{P_1}{P_1} + (\gamma+1)} \right)^{\frac{\gamma}{\gamma-1}} \left(\frac{P_1}{P_1} \right)^{-\frac{1}{\gamma-1}} \quad (C1)$$

P_{02} is now used to provide the new variation of isentropic relative total pressure distribution on the blade, until the next shock is detected.

FIGURE 1. DEFINITION OF QUASI-3D GEOMETRYFIGURE 2. QUASI-3D STREAMWISE MESH

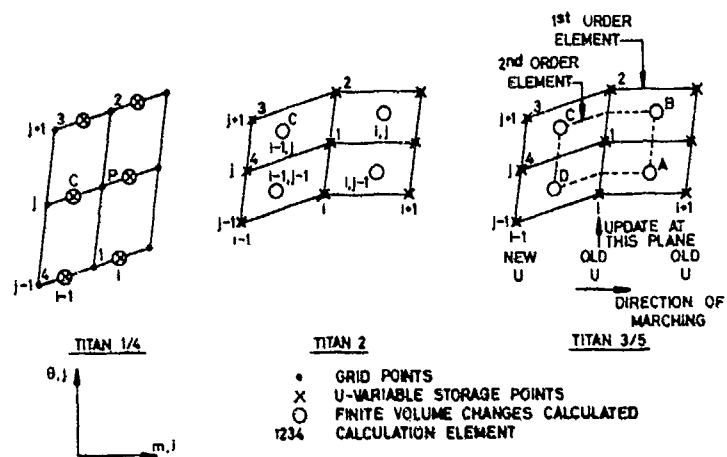


FIGURE 3. COMPARISON OF COMPUTATIONAL DOMAINS FOR QUASI-3D/3D CALCULATIONS

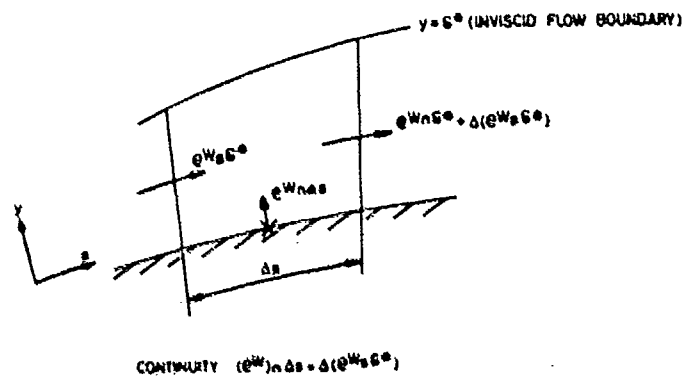
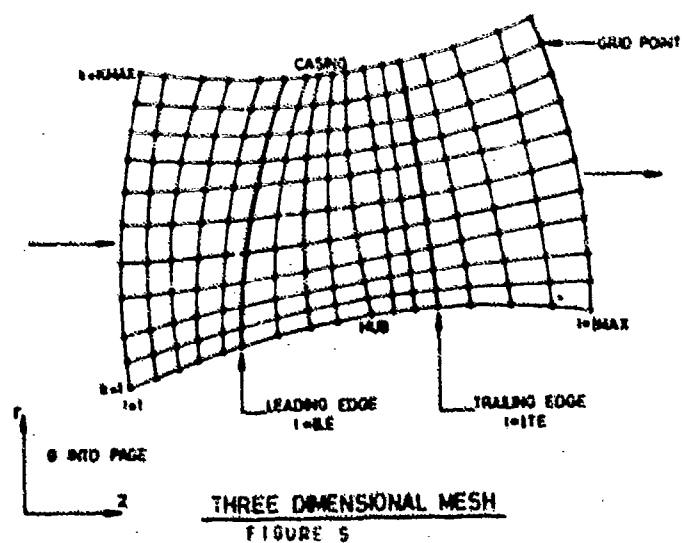
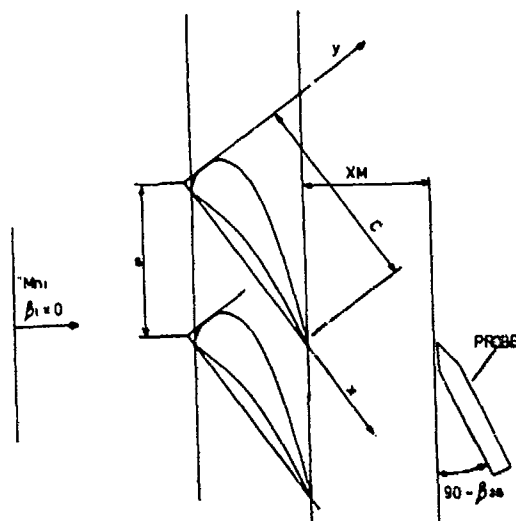


FIGURE 4. BOUNDARY LAYER TRANSPIRATION MODEL





$C = 60 \text{ MM}$
 $\mu/c = 0.762$
 $\text{BETA } S = 37.0$
 $\text{BETA } 1 = 0, -10, -5, +10^\circ$
 $\text{XM} = 24 \text{ MM}$
 $\text{BETA } 2 = 70^\circ$

FIGURE 6. N3V CASCADE GEOMETRY

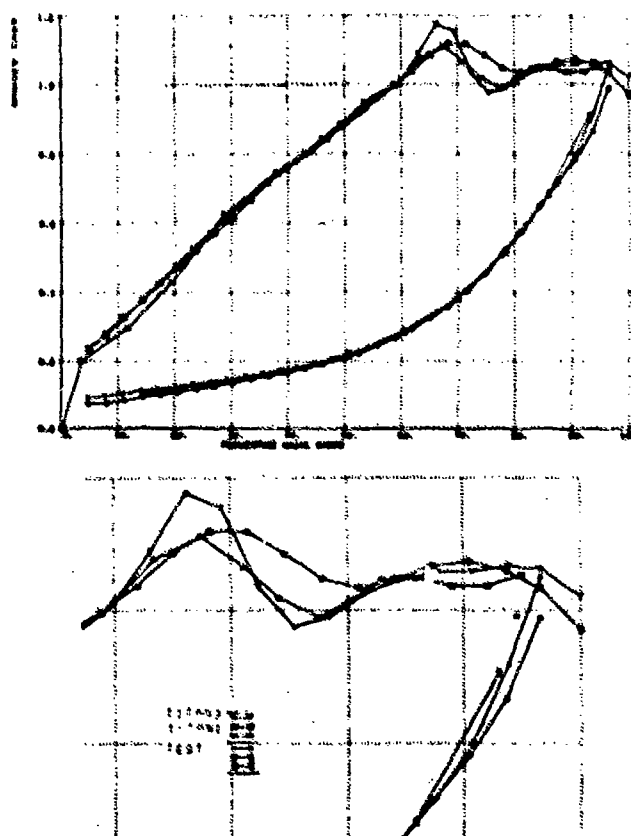


FIGURE 7. COMPARISON OF TEST RESULTS WITH TEST RESULTS

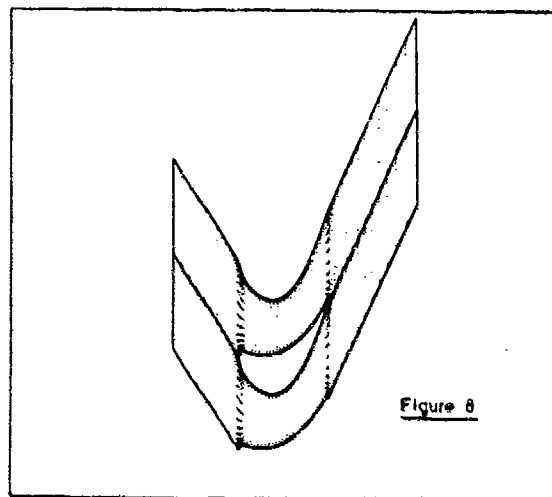


Figure 8

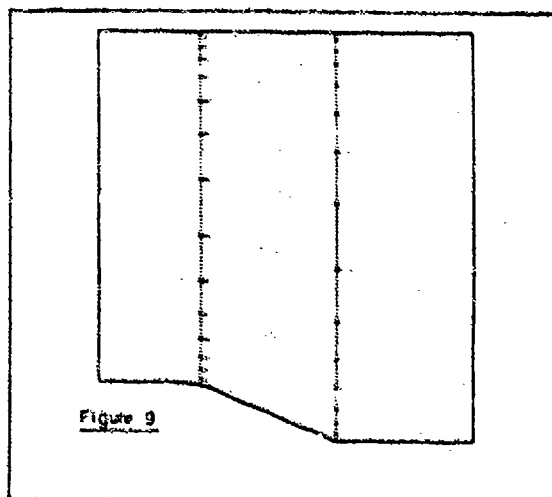


Figure 9

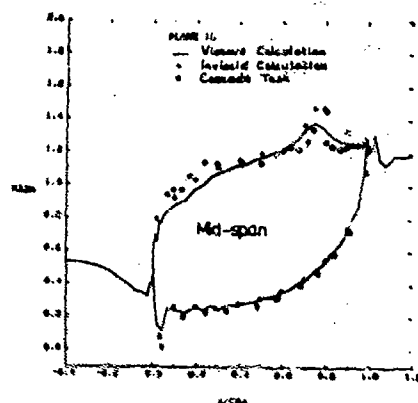


Figure 10

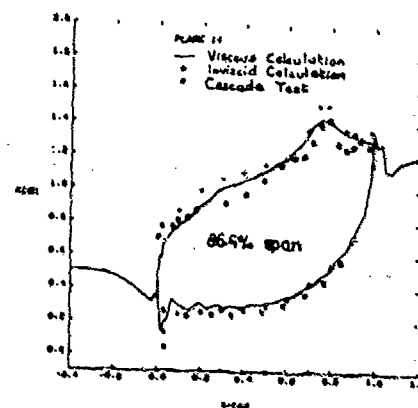


Figure 11

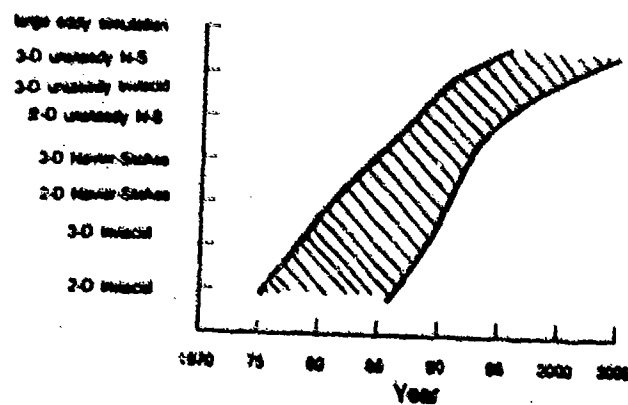
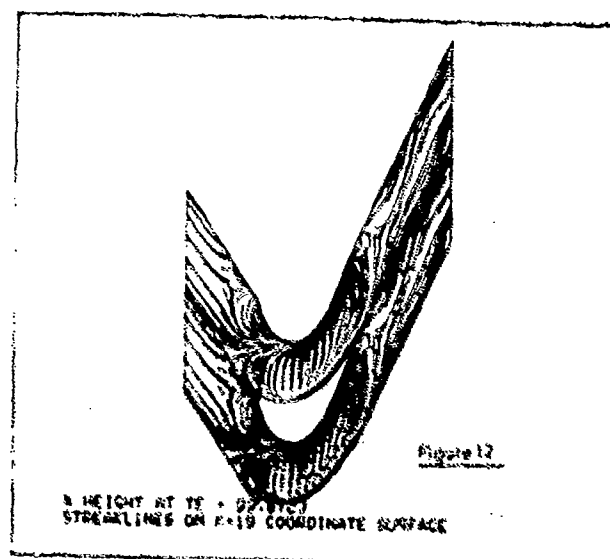


Figure 13 Development of time-matched capabilities

DISCUSSION

P. Ramette, Fr

1. Does your grid refinement technique use a fixed grid or an adaptive grid (which is refined by gradients' considerations)?
2. For turbulence modelling, you are using a Baldwin and Lomax model. Do you think you would have a better modelisation for turbulences by some K, ϵ models, and do you plan to go to $K, -\epsilon$ models?
3. In the last figure of your paper, showing a prospective view in the future, you are painting out Large Eddy Simulation techniques in year 2000. How do you feel about those LES techniques?

Author's Reply

1. The grid is fixed, with successively coarser grids being obtained by deletion of every other grid line in all directions, starting conditions on a finer grid are obtained by simple linear interpolation.
2. We use the Baldwin and Lomax model because it is a simple one and well documented in the open literature. Certainly there may be advantages from using a K, ϵ model, but no plans exist at present to implement such a model in our codes.
3. We will keep an open mind and see how things develop with regard to LES, but nothing is certain.

J. Hourmouzliadis, Gr

You have mentioned the application of a coupled inviscid/boundary layer blade to blade prediction method. How do you solve the problem of gradient discontinuities at the wall which are produced by laminar/turbulent transition in simple models?

Author's Reply

Generally we will carry out of some sort of smoothing of such kinks, by means of curve fitting; if however we believe such a discontinuity in gradient is physically correct, then we would do nothing as long as the scheme remained stable.

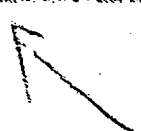
H. Stoll, Switzerland

The title of your paper mentions "blade passage methods" in general, but your test cases show turbine examples only. Could you comment on experience in compressor design?

Author's Reply

For quasi 3D flow a considerable amount of compressor work has been undertaken. Typical of this is the results presented by Hahnel and Siegl at this meeting, for a double cascade air compressor. Reasonable success can be achieved at design conditions, but because of limitations in the direct mode coupling of the boundary layer into the scheme, off design cannot be handled so well.

In 2D, the methods presented have been used extensively by compressor designers for many years, in check blade final design, and hence many evaluations have been carried out. Certainly many more evaluations are required, and this will be addressed in the near future.



DETERMINATION DE LA REGION DE CAPTATION D'UNE GRILLE D'AUBES SUPERSONIQUE

par Georges MEAUZE

Office National d'Etudes et de Recherches Aérospatiales
29, avenue de la Division Leclerc
92320 CHATILLON (France)

RESUME

Les conditions d'existence et les propriétés du phénomène d'incidence unique, bien connues dans le cas d'une grille d'aubes supersonique, sont tout d'abord rappelées et ensuite étendues au cas très général d'une grille sur une surface de courant de rayon et d'épaisseur variable. Le cas particulier d'une grille radiale est étudié en détail.

A partir de ces considérations il est possible d'optimiser la région de captation d'une grille d'aubes supersonique en réduisant au mieux les pertes par chocs.

ABSTRACT

Unique incidence phenomenon, well known for supersonic straight cascades, is analyzed and extended in the general case of a cascade of a stream-surface with variable radius and thickness. The special configuration of a radial cascade is studied in details.

From this analysis, it is possible to point out some rules for the optimisation of the entrance part of supersonic cascades.

1 - INTRODUCTION

Cet article présente une description générale des phénomènes aérodynamiques qui apparaissent dans la région de captation des grilles d'aubes supersoniques.

Le comportement de l'écoulement, bien connu dans le cas d'une grille plane, est tout d'abord rappelé ainsi que ses conséquences principales : indépendance du domaine amont par rapport à l'aval, et incidence unique. Ce rappel qui comporte une analyse qualitative de l'influence de la géométrie de la zone de captation de l'aubage est nécessaire avant la généralisation au cas d'une coupe supersonique d'une roue fixe ou mobile sur une nappe de courant à rayon variable. Le cas d'une grille radiale a été choisi pour illustrer cette généralisation.

L'analyse des conditions d'existence de l'incidence unique ainsi que l'influence de la forme de la région de captation est complétée par les schémas des différents écoulements possibles.

Les considérations générales analysées dans cet article permettent de déduire des directives pour la conception de profils d'aubages supersoniques présentant des pertes réduites.

2 - HYPOTHESES ET CONSIDERATIONS GENERALES

On considère un écoulement permanent relatif à une grille d'aube (repère mobile si la grille tourne, repère absolu si la grille est fixe).

La vitesse (relative) au rayon d'entrée de la grille est supersonique mais sa composante normale est subsonique.

Il est indispensable pour étayer les raisonnements qui suivent, de se référer aux lignes de courant de l'écoulement "uniforme" ou "naturel" qui s'établirait en absence de tout aubage en supposant une uniformité aximutale.

Pour l'écoulement plan, ces lignes de courant sont des droites parallèles entre elles.

Mais pour le cas général, les lignes de courant naturelles sont courbes. la vitesse et l'angle évoluant en fonction du rayon, leur géométrie est déterminée par la résolution de l'équation de continuité et de conservation du produit $R V_\theta$ et la prise en compte d'une évolution transversale connue de l'épaisseur de la nappe de courant ainsi que la présence éventuelle de pertes au sein du fluide, simulée par exemple par la donnée d'une évolution de la pression d'arrêt.

3 - RAPPEL DES PARTICULARITES DE L'ÉCOULEMENT DANS LE CAS D'UNE GRILLE PLANE

3.1 - Indépendance des domaines amont et aval. Effet du pas relatif

Bien que la composante axiale de la vitesse soit subsonique, les perturbations qui proviennent de l'aval et remontent l'écoulement sont arrêtées par la grille si les aubes sont suffisamment rapprochées et si l'écoulement reste amorcé.

Considérons, en effet, une grille plane "transparente", c'est-à-dire constituée de profils plats infiniment minces orientés suivant la direction de l'écoulement incident β , la composante axiale étant subsonique.

Cette dernière condition implique que les lignes de Mach (ou caractéristiques) montantes, dont l'angle avec le vecteur vitesse V est $\alpha_1 = \arcsin(1/M_1)$, sont inclinées de plus de 90° par rapport à l'axe et ainsi que toute perturbation faible issue d'un point P du champ "remonte" l'écoulement dans un secteur angulaire (C) limité par les demi-droites $(+90^\circ)$, $(\beta + \alpha_1)$ comme cela est indiqué sur la figure 1. Les perturbations provenant de l'aval et qui remontent l'écoulement jusqu'à la grille en suivant les caractéristiques C^* inclinées de l'angle $\beta + \alpha_1$ par rapport à la normale au front de grille, se réfléchissent lorsqu'elles rencontrent une paroi de l'ailette.

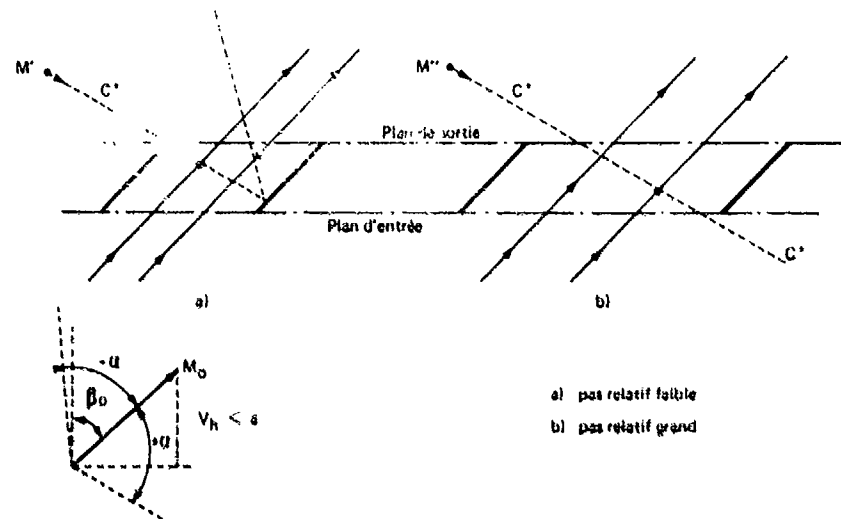


Fig. 1. EFFET DU PAS RELATIF SUR LA DÉPENDANCE DE L'AMONT PAR RAPPORT À L'AVANT

Elles ne peuvent alors traverser la grille que dans un couloir $L-L'$ dont l'existence est liée au pas de la grille. Il apparaît ainsi que l'écoulement amont est totalement indépendant du domaine aval si le pas relatif de la grille est suffisamment faible.

Dans ce cas, le même raisonnement montre que seule une partie de l'extrados de l'ailette comprise entre le bord d'attaque A' et le point de départ B' de la caractéristique montante passant par le bord d'attaque A'' de l'aube supérieure a une influence possible sur le domaine amont (fig. 2).

Il est clair que toute modification de la géométrie de l'aube en aval de B' n'a aucun effet sur l'écoulement amont. Ainsi l'écoulement incident est totalement indépendant de la forme de l'intrados en totalité et de l'extrados en partie de B' , dans la mesure où il n'y a pas blocage de l'écoulement ou formation de choc détaché au bord d'attaque.

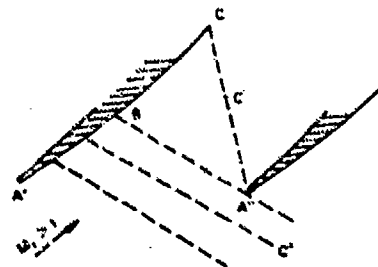


Fig. 2. INFLUENCE PARTIELLE DE L'EXTRADOS SUR L'AMONT

3.2 - Écoulement par ondes simples. Incidence unique

Le phénomène analysé ci-dessus laisse entrevoir que lorsque l'écoulement à l'entrée de la grille est supersonique et amorcé il n'existe qu'un seul régime possible à l'amont compatible avec le profil de l'extrados de l'aube A'B' pour un nombre de Mach M_1 donné, ou bien pour une vitesse de rotation donnée dans le cas d'une roue.

Dans le cas d'un extrados A'B' plan avec un dièdre pointu au bord d'attaque, il est bien connu que l'écoulement incident est uniforme et qu'il est parallèle à l'extrados.

Remarquons que l'écoulement amont est régi par les lois d'ondes simple si l'on néglige en première approximation l'intensité d'éventuelles ondes de chocs puisque les caractéristiques descendantes proviennent d'un écoulement uniforme M_1, β_1 à l'infini amont. Cela signifie que les caractéristiques montantes sont des lignes de Mach et sont donc rectilignes.

Ce régime par ondes simples demeure jusqu'à la caractéristique C- issue du bord d'attaque A' (fig. 2) et en particulier l'écoulement sur l'extrados ne dépend que de la pente locale de A' à C'.

Cette remarque permet d'établir aisément le schéma de l'écoulement dans le cas où le départ de l'extrados est de forme convexe ou concave avec un bord d'attaque pointu.

Considérons le cas d'un extrados convexe (fig. 3) et prenons l'exemple d'une grille semi-infinie alimentée par un écoulement (M_1, β_1) à l'infini amont.

Selon les valeurs respectives de β_0 et β_1 , un choc ou un faisceau de détente prend naissance en A₁ : en aval de A₁ se développe une détente par onde simple. Le long de la ligne de Mach B₁A₂, l'écoulement a la direction β_A . Son nombre de Mach est plus élevé qu'à juste en aval de A₁. En A₂, il y a nécessairement apparition d'une onde de choc à l'extrados puisque $\beta_0 > \beta_A$, de même en A₃ et pour les aubes suivantes. L'écoulement amont est ainsi traversé par une suite d'ondes de choc et de zones de détente qui amortissent d'ailleurs les chocs au fur et à mesure que l'on remonte vers l'infini amont.

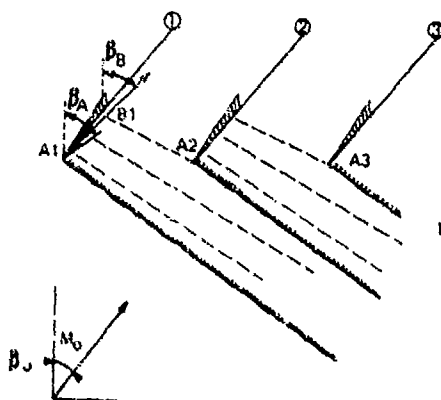


Fig. 3. SCHEMA DE L'ÉCOULEMENT AMONT POUR UN EXTRADOS CONVEXE

Dans le cas d'un extrados concave (fig. 4) on retrouve la même structure d'écoulement amont sauf que les faisceaux de détente sont issus des bords d'attaque alors que les ondes de choc proviennent d'une focalisation d'ondes de compression issues de A₁.

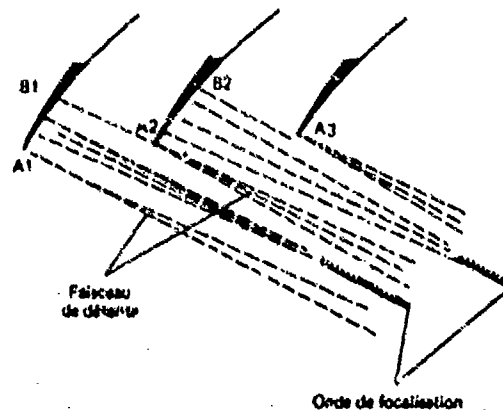


Fig. 4. SCHEMA DE L'ÉCOULEMENT AMONT POUR UN EXTRADOS CONCAVE

En toute rigueur, l'intensité des ondes de chocs ne peut pas être négligée au voisinage de la grille mais elle doit être évanescence quand on s'éloigne vers l'amont, pour qu'un écoulement soit possible. En effet, si l'on considère un tube de courant passant dans un canal interaube donné il traverse une suite de chocs et les pertes qui se cumulent doivent rester limitées.

Il n'y a pas de démonstration simple possible du principe de l'incidence unique à cause de la présence de ces chocs, mais on conçoit facilement qu'après un nombre limité de canaux s'établisse une périodicité de l'écoulement et qu'en remontant vers l'infini amont on retrouve un écoulement quasi-uniforme dont la direction β_1 est intermédiaire entre β_A et β_B .

Le point B variant selon le niveau du nombre de Mach, cet angle moyen β_1 dépend en réalité du Mach moyen M_1 .

Les méthodes de calcul exactes confirment parfaitement cette analyse et sont indispensables pour déterminer la relation $\beta_1 = f(M_1)$. Une première approximation qui est empiriquement bien vérifiée consiste à admettre que l'angle β_1 de l'écoulement à l'infini amont est égal à la demi-somme des angles β_A et β_B .

Une seconde approximation consiste à déterminer l'incidence unique de l'écoulement amont en écrivant d'une part la conservation du débit, et d'autre part, la propriété d'écoulement par onde simple, entre l'infini amont (M_1) et la ligne de Mach montante B_1A_2 (fig. 3).

$$\rho_1 V_1 A_1 \overline{A_1 A_2} \cos \beta_1 = \rho' V' A' \overline{A' B'} \cos \alpha'$$

$$\omega(M_1) = \omega(M_1) + \beta_1 - \beta_3$$

Il convient ici d'établir une remarque importante sur la conception des profils d'aubes supersoniques.

Il est bien connu que si l'on souhaite une compression par choc droit, celui-ci ne peut être stable que dans une partie divergente et il est a priori intéressant de s'inspirer des techniques d'optimisation des prises d'air supersoniques. On peut alors distinguer deux types de profils selon qu'il y a ou non "compression interne", autrement dit selon que le col (ou section minimale) se situe à l'entrée ou à l'intérieur du canal interaube. Malheureusement le principe de la compression externe qui a pour but de ralentir l'écoulement supersonique entre l'amont et le col situé à l'entrée du canal interaube, just avant la formation d'un choc droit dont l'intensité est réduite, ne présente pas d'intérêt dans le cas des grilles d'aube supersoniques. En effet, par définition la compression externe correspond à un tube de courant divergent à partir de la section d'entrée du canal interaube (fig. 5).

A_2C_1 représente la section d'entrée du canal interaube.

θ_{2A} est l'angle du dièdre de bord d'attaque.

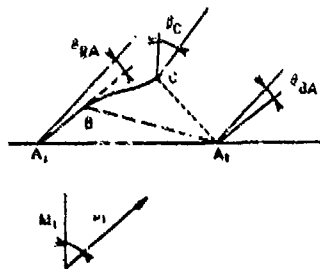


Fig. 5. SCHEMA D'UNE GRILLE A COMPRESSION EXTERNE

L'évolution de B_1 à C_1 peut correspondre à une rampe de compression isentropique focalisant ou non en A_2 ; ou bien elle peut comporter un dièdre ou bien une onde de choc oblique passant par A_2 ou un peu en aval.

Dans le cas d'un écoulement pratiquement bidimensionnel, puisque la section doit croître par définition en aval de A_2C_1 , l'angle β_1 de la paroi de l'extrados en aval de C_1 doit nécessairement être inférieur à $\beta_1 = \theta_{2A}$.

Remarquons que si l'écoulement est convergent transversalement, l'angle β_1 est a fortiori plus petit. Par contre si l'écoulement est divergent, cette condition ne sera plus respectée mais par contre le ralentissement de l'écoulement accompli en amont de A_2C_1 sera alors fortement atténué voire même supprimé.

Il est clair que, en amont de A_2C_1 , nous restons en présence d'un écoulement par ondes simples même s'il existe une onde de choc due, soit à la focalisation, soit à la présence d'un dièdre entre B_1 et C_1 . En effet l'intensité de cette onde de choc sera nécessairement faible puisque la déviation ψ correspondante doit être telle que la réflexion du choc en A_2 soit possible ; cette condition s'écrit : $\psi + \theta_{2A} < \text{déviation limite correspondant à } M_1$.

Dans ces conditions il est évident que, quelle que soit l'évolution du profil entre B_1 et C_1 , le nombre de Mach à la paroi en aval de C_1 sera nécessairement plus élevé que M_1 puisque l'angle de "Buseman" aura globalement augmenté. Cela condamne toute possibilité de compression externe unique ; il est alors nécessaire d'utiliser le principe de la compression interne si l'on souhaite former une onde de choc droite avec un nombre de Mach inférieur à celui en amont de la grille.

3.3 - Influence du bord d'attaque

Considérons tout d'abord un extrados plat avec un bord d'attaque pointu (fig 6a) ; la présence obligatoire d'un dièdre donne naissance à une onde de choc oblique faible, attachée, si l'angle du dièdre est inférieur à la déviation limite correspondant au nombre de Mach local juste en amont du bord d'attaque. Dans le cas d'un angle supérieur (fig. 6b), il y a formation d'un choc courbe, détaché, avec apparition d'une zone subsonique dont l'étendue n'est pas négligeable à l'intrados. Le détachement du choc crée aussi une zone subsonique beaucoup plus limitée à l'extrados. La branche supérieure de l'onde de choc, qui remonte l'écoulement, s'atténue assez rapidement pour redevenir une ligne de Mach, mais interagit avec le domaine amont et a pour effet d'augmenter légèrement l'angle d'incidence unique, c'est-à-dire de diminuer le débit.

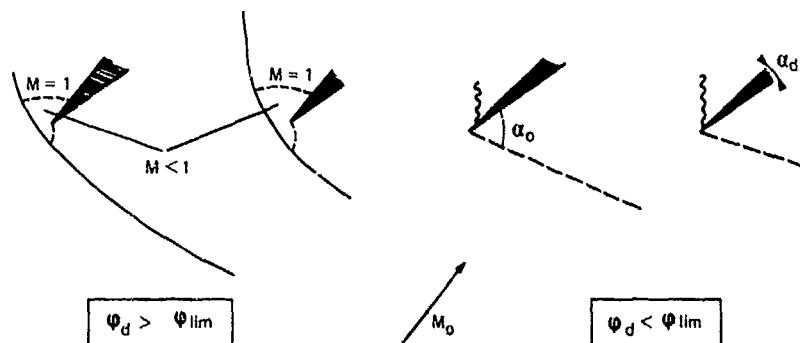


Fig. 6. EFFET DU DIÈDRE DE BORD D'ATTAQUE

Dans la réalité, un dièdre parfait n'est jamais réalisé, mais il existe toujours un arrondi de bord d'attaque (fig. 7) qui donne lieu à un choc détaché avec une zone subsonique très réduite qui reste à l'échelle du rayon de bord d'attaque, sauf pour des nombres de Mach très proche de 1. Ce phénomène qui n'a pratiquement aucun effet dans le cas où l'angle du dièdre est supérieur à la déviation limite, modifie la configuration dans le cas contraire. Les principales conséquences sont les suivantes :

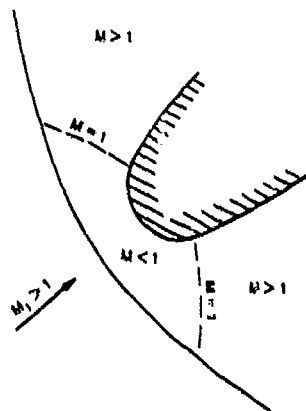


Fig. 7. EFFET DE L'ARRONDI DE BORD D'ATTAQUE

- par rapport à la solution choc oblique attaché, il y a création de pertes supplémentaires dues à la présence de la partie de l'onde de choc détachée de forte intensité. Même pour des très petits rayons, ces pertes ne sont pas négligeables ; elles sont chiffrées dans les références [1] et [2] ;
- la branche externe à la grille interagit avec le domaine amont et augmente l'angle d'incidence unique. Une étude paramétrique de cet effet a été effectuée dans le cas de profils en forme de plaque plane, par STARKEN [3]. Les abaques présentés donnent une très bonne approximation de l'effet de bord d'attaque arrondi et reste valable pour des dièdres faibles ;
- la distance de détachement du choc qui reste à l'échelle du rayon est négligeable quand celui-ci est réduit, par contre, la courbure de la branche interne à la grille provoque un écart non négligeable entre le point d'impact C de l'onde détachée et celui de l'onde attachée, sur l'extrados du canal considéré (fig. 8).

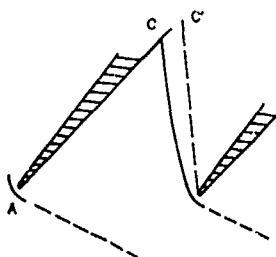


Fig. 8. EFFET D'ONDE DE CHOC DETACHEE

D'une façon générale, la présence des ondes de chocs dues à l'épaisseur de l'arondi de bord d'attaque d'une part, et à la convexité ou concavité de la partie initiale de l'extrados d'autre part, est néfaste et ne présente a priori aucun intérêt. Il est préférable d'utiliser des profils ayant la partie AB de l'extrados plate, ou plus précisément épousant la ligne de courant naturelle dans le cas général, avec des bords d'attaques le plus fin possible.

Le principe d'incidence unique montre que c'est la première partie de l'extrados d'une roue qui impose le débit maximum traversant la roue, pour une vitesse de rotation donnée.

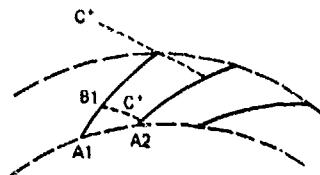
4 - GENERALISATION AU CAS DES GRILLES RADIALES

4.1 - Conditions d'indépendance des domaines amont et aval

Nous avons choisi d'illustrer cette généralisation dans le cas d'écoulements centrifuges qui peuvent être souvent supersonique à l'entrée des grilles, alors que cela est beaucoup plus rare pour les écoulements centripètes.

Considérons une grille radiale constituée d'aubes infiniment minces et épousant les lignes de courant de l'écoulement "naturel" de façon à n'apporter aucune perturbation (fig. 9).

Fig. 9. GRILLE RADIALE "TRANSPARENTÉ"



Le principe d'existence de l'incidence unique reste identique ainsi que le comportement général du phénomène bien qu'il soit compliqué par l'évolution radiale de l'écoulement.

Une condition supplémentaire peut apparaître par suite de l'évolution radiale du nombre de Mach qui peut diminuer et devenir subsonique comme cela est le cas pour une grille fixe.

La condition pour qu'il y ait strictement indépendance de l'amont par rapport à l'aval est que la caractéristique C^* issue du bord d'attaque A_2 rencontre l'extrados de l'aube inférieure en B_1 avant d'atteindre le cercle où le nombre de Mach devient sonique comme dans le cas d'une grille fixe (fig. 10).

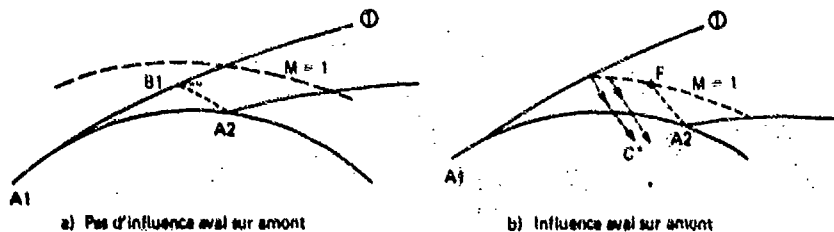


Fig. 10. EFFET DU PAS SUR LA DEPENDANCE DE L'AMONT PAR RAPPORT A L'AVANT DANS UNE GRILLE RADIALE FIXE

L'écoulement est alors bloqué.

L'écoulement amont et en particulier son incidence ne dépend que de la géométrie de la partie de l'entraxe A_1B_1 et d'une condition amont telle que le nombre de Mach, ou la vitesse tangentielle. Le régime d'incidence unique subsiste tant que le régime reste amorcé (choc en aval de A_2).

Si la caractéristique C^* issue de A_2 rejoint le cercle sonique avant de rencontrer l'extrados (1), il existe des caractéristiques C^* issues de la ligne sonique qui influencent le domaine amont. Or toute modification aval change la forme de cette ligne sonique et par conséquent le domaine amont.

Par exemple, si l'on baisse la pression aval, la ligne sonique aura tendance à reculer et le débit augmentera jusqu'à ce que le point de rencontre F de la caractéristique C^*A_2 avec la ligne sonique atteigne l'extrados (1). Le régime d'incidence unique sera alors établi. On peut illustrer cette variation de débit à l'aide du cas particulier suivant : comme le montrent les calculs, la géométrie des lignes de courant naturelles reste pratiquement inchangée pour des variations modérées du niveau des nombres de Mach. Ainsi, dans la mesure où la condition amont correspond à une invariance de l'angle, la ligne sonique reste pratiquement circulaire et son déplacement en fonction de la variation de la pression aval P_2 est aisément déterminé par le calcul des lignes naturelles.

Mais si la condition amont ne correspond pas à une invariance de l'angle, la déformation de la ligne sonique en fonction de P_2 devient très complexe. En particulier l'écoulement à l'amont de la grille n'est plus "uniforme" azimutalement.

On remarque que dans ce qui précède la ligne sonique ne correspond en aucun cas à un blocage de l'écoulement. L'apparition du blocage n'est liée qu'à l'existence du point B_1 . Par contre, dans le cas d'une aube réelle, il pourra apparaître un blocage prématuré dû à un col interne mais dans ce cas il y aura nécessairement une zone subsonique avant ce col. En toute rigueur, il n'y aura blocage que si la configuration des caractéristiques à l'aval du col et rejoignant la ligne sonique est indépendante des conditions à l'aval.

4.2 - Effet de courbure (par rapport à l'écoulement naturel) de l'extrados

Dans le cas d'un écoulement radial, la concavité et la convexité n'ont plus de sens mais les phénomènes restent les mêmes que pour l'écoulement plan, selon que l'extrados est plus ou moins courbe que la ligne de courant naturelle.

Si l'on considère le cas où l'extrados est moins courbe (fig. 11) que la ligne de courant naturelle, il y a formation d'un choc oblique au bord d'attaque, suivi d'un gradient sur l'extrados ayant tendance à donner une accélération ou bien une moindre compression par rapport à l'évolution naturelle. Le nombre de Mach est plus élevé juste en amont du B.A. que dans le cas d'un écoulement naturel ayant même incidence unique et même nombre de Mach au rayon d'entrée.

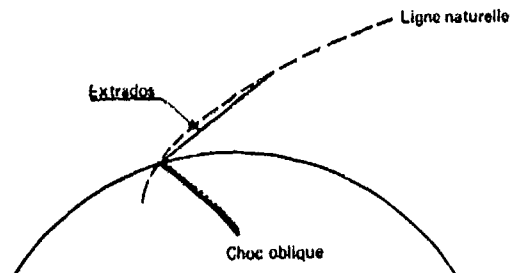


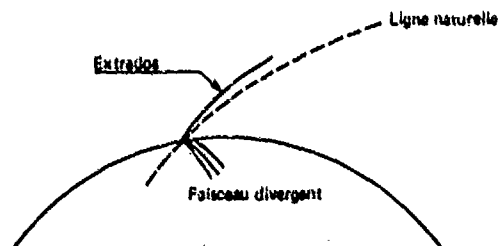
Fig. 11. EFFET DE COURBURE REDUITE DE L'EXTRADOS DANS UNE GRILLE RADIALE

L'angle β_1 de l'incidence unique est inférieur à l'angle du B.A. à l'extrados.

Les ondes de choc obliques qui remontent l'écoulement amont peuvent s'intensifier (cas des grilles fixes) et provoquer des pertes inutiles.

Si l'extrados est plus courbé que la ligne de courant naturelle (fig. 12), il a formation d'une détente au bord d'attaque, suivi d'une compression (ou d'une moindre détente) pouvant créer une focalisation des caractéristiques montantes et donner lieu à un choc oblique à l'amont. Le niveau du nombre de Mach est diminué juste en amont du bord d'attaque mais l'angle d'incidence unique est supérieur à l'angle du B.A. à l'extrados.

Fig. 12. EFFET DE COURBURE ACCENTUEE DE L'EXTRADOS DANS UNE GRILLE RADIALE



4.3 - Influence du bord d'attaque

Cette influence est tout à fait similaire à celle évoquée précédemment pour le cas plan. Nous précisons seulement que la présence d'un dièdre pointu ou émoussé ne change rien au phénomène de blocage, toujours lié à l'existence du point B_1 sauf s'il y a un col interne. S'il existe un choc détaché de bord d'attaque avec une petite zone subsonique, la caractéristique C^* à considérer est celle provenant du point $M = 1$ à l'intrados (point D) (fig. 13).

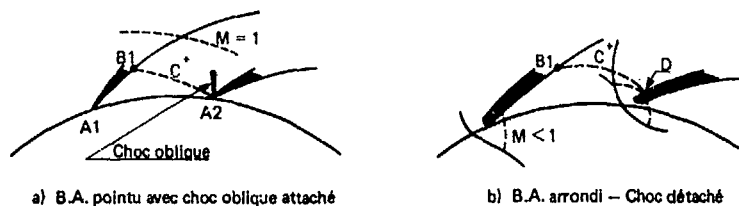


Fig. 13. EFFET DE BORD D'ATTAQUE POUR UNE GRILLE RADIALE

4.4 - Schémas d'écoulement possibles

Les différents types d'écoulements qui peuvent exister de façon stable sont bien connus dans le cas des grilles planes et sont facilement transposables au cas des grilles radiales, mais il peut être intéressant de les préciser ici.

Les figures décrites ci-après résument les diverses configurations que l'on peut rencontrer dans une grille radiale avec bord d'attaque arrondi.

4.4.1 - Régime en incidence unique. Choc fort dans le canal (fig. 14)

Le débit est fixé, la variation de la pression aval, "pilote" le choc fort dans le canal.

Quand l'impact du choc C sur l'intrados atteint le point D il y a désamorçage et le débit va diminuer si P_2 augmente.

On notera qu'il peut exister une zone subsonique sur l'extrados avec un léger choc éventuel (fig. 15).

Dans ce cas, quand P_2 augmente, le point G peut atteindre la ligne sonique en H avant que C n'atteigne D. Il n'y a alors plus de régime d'incidence unique, le débit diminue si P_2 augmente.

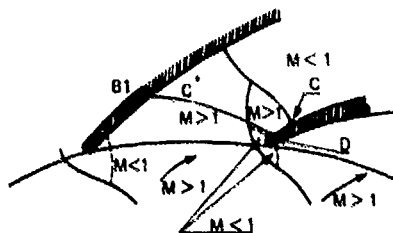
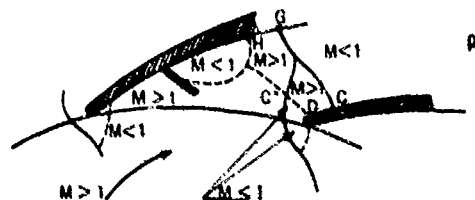


Fig. 15. SCHEMA II D'UNE GRILLE RADIALE EN REGIME D'INCIDENCE UNIQUE

Fig. 14. SCHEMA I D'UNE GRILLE RADIALE EN REGIME D'INCIDENCE UNIQUE



4.4.2 - Régime transsonique

Il n'y a pas de choc traversant tout le canal.

Le débit est fixé ou non selon l'existence du point B1. (Dans le cas de la figure 16 la caractéristique C* atteint la ligne sonique avant l'extrados, et le débit n'est pas fixé). Mais le désamorçage ne sera pas à proprement parler atteint que quand le point C rejoindra le point D. Il n'y a plus de point sonique à l'intrados.

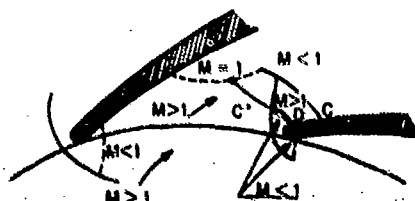


Fig. 16. SCHEMA D'UNE GRILLE RADIALE EN REGIME TRANSSONIQUE (DEBIT NON FIXE)

Les configurations désamorçées sont illustrées par les schémas des figures 17 et 18.

(Le "choc" peut comporter une petite zone sonique pouvant aller jusqu'à l'extrados) (fig. 18).

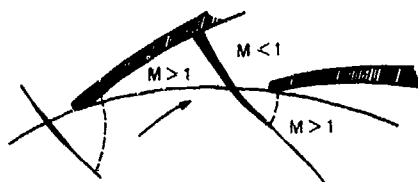
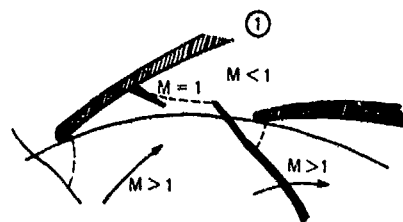


Fig. 17. SCHEMA I D'UNE GRILLE RADIALE EN REGIME DESAMORCE

Fig. 18. SCHEMA II D'UNE GRILLE RADIALE EN REGIME DESAMORCE



4.4.3 - Régime bloqué par col interne

Deux cas peuvent se présenter :

- soit le col interne est plus grand que la section critique correspondant à l'une des configurations ci-dessus à la limite du désamorçage ; dans ce cas, une configuration amorcée (compatible avec le col) s'établit et restera figée tant que le col aval restera amorcé ;
- soit le col aval est inférieur à la section critique correspondant à la configuration à la limite de l'amorçage, il empêche alors le débit maximum de s'établir et force une configuration désamorcée. Cela peut être le cas si l'épaisseur de B.A. est relativement trop importante ou si le dièdre est trop grand.

Deux configurations de régime désamorcé et bloqué peuvent être imaginées selon que le choc détaché rejoint ou non la ligne sonique entre l'intrados et l'extrados (fig. 19 et 20). On notera en outre qu'une petite zone subsonique (après un léger choc transsonique) peut éventuellement exister sur l'extrados.

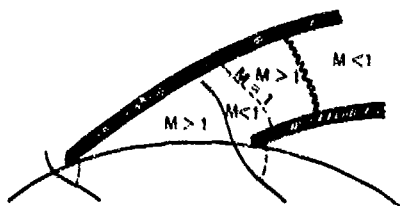
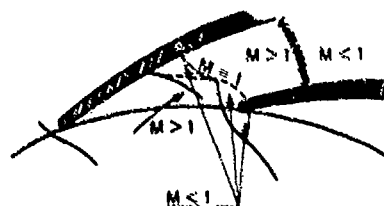


Fig. 19. SCHEMA I D'UNE GRILLE RADIALE DESAMORCEE ET BLOQUEE PAR COL INTERNE

Fig. 20. SCHEMA II D'UNE GRILLE RADIALE DESAMORCEE ET BLOQUEE PAR COL INTERNE



5 - DIRECTIVES GENERALES POUR L'OPTIMISATION DE GRILLES D'AUBES SUBSONIQUES A FORT TAUX DE COMPRESSION

L'obtention d'un taux de compression élevé dans un compresseur nécessite des ralentissements très importants de l'écoulement relatif dans les canaux interaubes.

En particulier pour les coupes où l'écoulement relatif à l'entrée du canal interaube est supersonique, les vitesses à la sortie sont subsoniques : le passage de l'écoulement supersonique à l'écoulement subsonique se fait par l'intermédiaire d'un système plus ou moins compliqué d'ondes de choc se terminant obligatoirement, en absence de phénomènes visqueux, par des ondes de choc droites au voisinage des parois du canal interaube. Or, il est bien connu que plus le nombre de Mach, juste en amont d'un choc droit est élevé, plus le ralentissement local est important. A partir d'une certaine valeur comprise entre 1,35 et 1,4, mais souvent voisine de $M = 1,37$, pour une couche limite turbulente, celle-ci ne peut plus supporter le ralentissement. Il se produit alors un décollement important, associé à un nouveau système d'ondes de choc, et qui entraîne des pertes importantes.

Si on considère alors, la famille des profils fréquemment utilisés où la section du tube de courant traversant la grille est constamment divergente, le nombre de Mach M' de l'écoulement non visqueux en amont du choc droit est nécessairement plus élevé que M_1 . Ainsi toutes les coupes comportant de tels profils, avec un écoulement relatif à l'entrée du canal supérieur à 1,37 conduisent nécessairement à des pertes élevées (la valeur de 1,37 doit en fait être diminuée pour tenir compte de la divergence du tube de courant entre M_1 et M').

Si l'on veut réduire ces pertes, il est nécessaire de ralentir l'écoulement en supersonique avant le choc droit, tout au moins auprès des parois. Comme nous l'avons rappelé plus haut cela ne peut être envisagé que grâce à une compression interne de l'écoulement.

Mais il est avant tout indispensable de rappeler l'observation importante qui suit : cela n'a pas de sens de vouloir optimiser (au sens des pertes) un diffuseur supersonique, c'est-à-dire correspondant à un écoulement supersonique donné à l'entrée, le débit étant ainsi fixé, pour un niveau de pression aval donné. En effet, le fait de se donner cette pression aval équivaut à se donner les pertes. L'exemple de la prise d'air pitot monodimensionnelle illustre bien cet effet.

Considérons une prise d'air pitot de section d'entrée A_1 et alimentée par un écoulement supersonique M_1 ; soit A_2 la section à l'aval et P_2 la pression statique dans la section A_2 . Supposons que le régime est amorcé, il y a ainsi choc droit dans la partie divergente (fig. 21).

Fig. 21 SCHEMA D'UNE PRISE D'AIR PITOT MONODIMENSIONNELLE



Rappelons que le débit peut s'écrire sous la forme :

$$Q = K \frac{P_1 A_1}{\sqrt{T_1}}$$

avec K = coefficient dépendant de C_p et γ

P_1 = pression d'arrêt

A_1 = section critique

T_1 = température d'arrêt

La variation de la température d'arrêt relative ne dépend que de l'évolution du rayon et de la vitesse de rotation.

Ainsi la conservation du débit entraîne la conservation du produit $\frac{P_1 A_1}{\sqrt{T_1}}$

$$\text{soit} \quad \frac{P_1 A_1}{\sqrt{T_1}} = \frac{P_2 A_2}{\sqrt{T_2}}$$

En utilisant les notations $\Xi(M) = A/A_1$

et $\omega(M) = P/P_1$

on peut écrire

$$\frac{P_1}{P_2} = \frac{A_2}{A_1} \frac{\omega_2}{\omega_1} \frac{\Xi_1}{\Xi_2} \frac{\sqrt{T_1}}{\sqrt{T_2}}$$

soit

$$\frac{P_1}{P_2} = \frac{A_2}{A_1} \frac{\omega_2}{\omega_1} \frac{\Xi_1}{\Xi_2} \frac{\sqrt{T_1}}{\sqrt{T_2}} \quad (1)$$

D'autre part, on peut écrire

$$\frac{P_2}{P_1} \frac{A_1}{A_2} = \frac{P_2}{P_1} \frac{A_1}{A_2} \frac{\sqrt{T_1}}{\sqrt{T_2}} = \omega_2 \Xi_2 \frac{\sqrt{T_1}}{\sqrt{T_2}}$$

soit

$$\frac{P_2}{P_1} = \frac{A_2}{A_1} \omega_2 \Xi_2 \frac{\sqrt{T_1}}{\sqrt{T_2}} \quad (2)$$

Ainsi l'équation (2) montre que si P_2 est donné, cela revient à imposer le produit $\omega \Xi$ et donc le nombre de Mach M_2 . La relation (1) montre alors que le rapport des pressions d'arrêt est déterminé ; par conséquent imposer P_2 revient à imposer les pertes.

La présence de la viscosité du fluide ne change strictement rien à ce raisonnement : en fluide non visqueux, les pertes seront dues uniquement aux ondes de choc (un choc droit dans le cas de la prise d'air pitot). En fluide visqueux, il y aura partage entre les pertes par viscosité (frottement) interaction choc-couche limite et choc dont l'intensité sera plus faible qu'en fluide non visqueux.

La seule optimisation possible consiste à minimiser les pertes au point juste avant le désamorçage, c'est-à-dire avant la diminution du débit. Pour la prise d'air pitot, cela correspond au choc droit dans la section d'entrée A_1 , la perte en fluide non visqueux étant celle due au choc M_0 .

L'optimisation consiste alors à ralentir au préalable l'écoulement supersonique afin qu'au désamorçage l'intensité du choc soit plus faible. La pression statique P_2^{**} au désamorçage sera plus élevée que celle P_2^* de la prise d'air non optimisée : pour $P_2 = P_2^*$ les deux prises d'air auront les mêmes pertes, pour $P_2 = P_2^{**}$ la prise d'air non optimisée aura un débit inférieur.

Une des conclusions de la remarque importante rappelée ci-dessus, est qu'il faut faire très attention quand on compare différents diffuseurs supersoniques. En particulier, si l'on impose les mêmes conditions de sortie (par exemple par la présence des étages suivants) pour des mêmes conditions d'entrée, il n'y aura aucune différence entre diverses solutions du point de vue du rendement, par contre les marges pourront être différentes.

Si l'on utilise un diffuseur optimisé, il est nécessaire que les conditions aval soient compatibles avec cette optimisation.

Compte tenu des observations et remarques établies précédemment il est possible de dégager des directives générales pour la conception des profils.

Pour une première ébauche du profil, il est conseillé de construire la première partie de l'extrados du profil comme une ligne de courant naturelle. On choisira un rayon de bord d'attaque le plus petit possible afin d'éviter un blocage et des pertes éventuelles.

Il faut alors distinguer deux cas selon qu'une compression interne est jugée nécessaire ou pas.

a) Cas sans compression interne

Compte tenu d'une évolution d'épaisseur donnée, liée à des problèmes technologiques, on peut construire la première partie de l'intrados. On peut alors définir le reste de l'extrados en s'éloignant progressivement de la ligne de courant naturelle à partir de la région de la section d'entrée ou du point de départ B de la caractéristique C^+ aboutissant au B.A. de l'aube suivante, de façon à éviter le blocage dû à l'intrados, et à assurer une direction à l'aval sur le rayon de sortie choisi ou pour une corde donnée. On termine enfin l'intrados selon la loi d'épaisseur envisagée.

Un calcul direct permettra alors de vérifier qu'il n'y a pas de blocage par col interne, et aussi d'estimer l'écart entre l'incidence calculée et celle souhaitée.

A ce stade, l'emploi de la méthode inverse peut être intéressant pour modifier la répartition obtenue sur l'extrados dans la région d'entrée mais aussi pour la partie subsonique : plusieurs calculs seront toutefois nécessaires pour adapter au mieux les conditions d'entrée.

b) Cas avec compression interne

La compression interne peut se faire par une compression à partir du point B (fig. 21) avec un dièdre ou une légère rampe de compression déviant l'écoulement de ψ par rapport à la ligne de courant naturelle suivie auparavant par l'extrados. Mais il y a aussi la compression due au dièdre de bord d'attaque conduisant à un niveau de Mach M_2 .

Dans la majorité des cas il paraît judicieux de positionner le col (section minimale) au voisinage du pied D l'onde de compression issue du bord d'attaque A_2 de l'intrados de l'aube adjacente. On remarque qu'il y a plusieurs compromis possible entre la déviation ψ en B et le dièdre de B.A. pour donner un même niveau de Mach M_2 au col. Une étude paramétrique facile à faire est très utile pour le choix de ce compromis. Ensuite il faut respecter la possibilité d'amorcer cet écoulement supersonique dans le convergent avec éventuellement une certaine marge. Cela est facile à établir dans la théorie monodimensionnelle qui est applicable pour une grille si le nombre de Mach reste à peu près uniforme juste avant le col, mais devient plus difficile à prévoir si la configuration est tridimensionnelle.

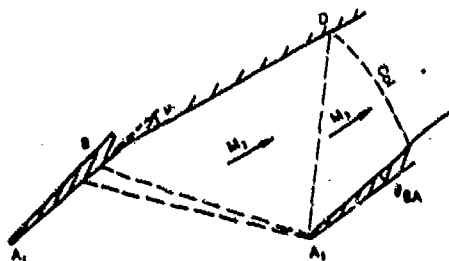


Fig. 22 SCHEMA DE LA REGION DE CAPTATION D'UNE GRILLE SUPERSONIQUE

Enfin il faut prévoir une partie divergente en aval du col qui contiendra le choc principal mais cette divergence doit rester modérée pour éviter une réaccélération trop brutale et perdre ainsi le bénéfice de la compression interne préalable. Il reste enfin à fermer le profil mais cela est lié à la déflexion globale de l'écoulement désiré. Le pas relatif résulte ainsi de la conception du canal interaube. Plusieurs grilles ont été définies et expérimentées. Un résultat est présenté en [2].

6 - CONCLUSION

Les conditions d'existence et les propriétés du phénomène d'incidence uniques bien connues dans le cas d'une grille plane d'aubes supersoniques ont été étendues au cas très général d'une grille à rayon variable et notamment au cas d'une grille radiale. L'analyse qualitative des diverses configurations aérodynamiques ainsi que les effets principaux de la forme de la région de captation des aubages permettent de déduire des directives générales pour la conception de profils en réduisant au mieux les pertes.

REFERENCES

- [1] - LE MEUR A. - Computation of blade cascade aerodynamic losses due to detached shock waves. 6ème ISABE, Paris, 6-11 juin 1983.
- [2] - FOURMAUX A. et LE MEUR A. - Analyse des pertes dues aux ondes de chocs - 68th AGARD-PEP, Munich, septembre 1986.
- [3] - STARKEN H., SCHREIBER H., YONG XING Z. - Mass flow limitation of supersonic blade rows due to leading edge blockage - ASME Paper n° 84-GT-233.

DISCUSSION

H.A.Schreiber, Ge

You explained the principle relationship of M_1 and β_1 for the configuration of a radial cascade. Can you give some quantitative data, on how this M_1 and β_1 relationship looks in a real radial cascade configuration?

Author's Reply

The analysis presented in the paper is only qualitative and I can't give you any quantitative data. I have checked by using a 2D Euler Code that all phenomena happened. But it is only in the simple case of an isolated cascade and not in the real radial configuration.

In the case of a radial diffuser, there is a strong interaction between stator and rotor, and the flow is unsteady and very complicated.

In the case of a radial rotor, without any row at the entrance, I am sure that the analysis and optimisation suggestion can be applied.

DOWNSTREAM FLOW ANGLE CORRELATIONS FOR TURBINE CASCADES IN SUBSONIC AND TRANSONIC FLOW CONDITIONS

by

W. Rieß
P. Dalbert
Institut für Strömungsmaschinen
Universität Hannover

Appelstr. 9
D-3000 Hannover
Germany

P.-A. Gieß
H.-J. Heinemann
Inst. für Exp. Strömungsmechanik
Deutsche Forschungs- und Versuchsanstalt
für Luft- und Raumfahrt
Bunsenstr. 10
D-3400 Göttingen
Germany

SUMMARY

Extensive experimental and theoretical investigations of different turbine cascades have been performed within the transonic Mach number range. Some problems related to measurements in rectilinear cascades are discussed. From the done flow field calculations using a 2-d time-marching Euler code limitations can be determined when applying the computer code itself as well as when comparing the calculated data with experimental ones. Experimental and theoretical results within the subsonic Mach number range are used to check the accuracy of "simplified methods" for calculating the downstream flow angle.

1. INTRODUCTION

The great variety of possible and applicable turbine blade profile forms has precluded so far the accumulation of systematic and rather exhaustive aerodynamic data, as are available for axial compressor blades - at least in the subsonic regime. Therefore, as well as for the development and optimisation of new profile forms as for the detailed calculation of multi-stage turbine bladings, methods are necessary for the sufficiently exact calculation of

- outlet angle
- aerodynamic loss coefficient

in the whole subsonic-compressible and - mainly for gas turbines - in the transonic flow regime in the great numbers of cases, where pertinent experimental data are not available.

Loss calculation has made progress by combined application of modern cascade flow and boundary layer methods. Outlet angle calculation by flow field methods still comprises some uncertainties, mainly connected with the formulation of the trailing edge condition, and the practical application seemingly encounters often some doubt. Furthermore it necessitates a not negligible effort in the preparation and the execution of computer calculations and, consequently, the turbo machine industry still prefers to apply widely different "simplified methods" - e.g. the well known Sine Law for the calculation of outlet angle. All of these are based on balances of mass flow and momentum in the outlet region of the cascade and necessitate various simplifying assumptions.

Because of the differing experiences in application of "simplified methods" and, to some extent, of modern cascade flow calculation methods, a research project was initiated by Forschungsvereinigung Verbrennungskraftmaschinen (FVV) and carried out jointly by Institut für Strömungsmaschinen (IFS), Universität Hannover, and Institut für Experimentelle Strömungsmechanik (SM-ES) at Deutsche Forschungs- und Versuchsanstalt für Luft- und Raumfahrt (DFVLR), Göttingen. It comprises:

- experimental investigation of downstream flow angle, loss coefficient and pressure distribution for several cascades in the transonic regime (DFVLR, chapter 2),

- flow field calculation using a transonic time marching procedure and comparison with experimental data (DFVLR, chapter 3),
- experimental investigation of downstream flow angle, loss coefficient and pressure distribution for several cascade geometries in the subsonic-compressible regime (IfS, chapter 4),
- flow field calculations using a subsonic-compressible finite difference method and comparison with experimental data (IfS, chapter 5),
- comparison of downstream flow angle data from several "simplified methods" with experimental results for more than thirty different turbine cascades (IfS, chapter 6).

The project resulted in a deepened insight in the potential and the limitations of the different methods and a better understanding of the aerodynamic characteristics of turbine cascades.

2. EXPERIMENTAL INVESTIGATIONS ON TRANSONIC TURBINE CASCADES

At DFVLR the experimental task within the scope of this project has been to re-measure three different profiles in one cascade geometry each and a fourth profile in six different cascade geometries. All these cascades have been investigated for the design incidence flow angle and within the downstream Mach number range $0.2 < Ma < 1.3$. From the obtained wake traverses, surface pressure distributions and Schlieren photographs documented in [6] a few examples are taken to discuss some typical problems of transonic turbine cascade flow.

2.1 Test facility

A detailed description of the test-facility for rectilinear cascades (EGG) of DFVLR, Göttingen is given in [1]. The cascade assembly drawn to scale is shown in *FIGURE 1* for a hub-section cascade. The width of the flow channel which is equal to the height of the cascade blades is 125 mm. In general, the profile chord length is 60 mm and therefore the aspect ratio is 2.08. There are approximately 6 blades in the flow field in the case of stator cascades and up to 15 in the case of rotor cascades.

Some blades of the cascade are fixed into glass panes to allow the Schlieren pictures to be taken. For surface pressure distribution measurements, one of the blades is substituted by an instrumented one. For this subject the panes of glass in the cascade rig are replaced by steel plates.

2.2 Upstream flow

In the upstream flow field total pressure, total temperature, and humidity of the air are measured in the settling chamber. The upper and lower walls of the rectangular nozzle can be adjusted in horizontal and vertical direction and can be set to angles up to $\pm 4^\circ$ relative to the centre line. These adjustments are used to set the inlet flow conditions to periodicity as well as possible. The wall static pressure can be measured in a plane parallel to the cascade inlet front at 96 positions distributed over all blade passages on one instrumented side-wall. Values from 47 ports are acquired, D1 to D47 in fig. 1.

Through holes on the opposite side wall in the very same plane, the incidence angle can be measured with a wedge probe at 7 different locations, W1 to W7. The check of this angle is necessary because experience has shown that the actual incidence angle can differ by up to $\pm 2^\circ$ from the geometric one. The incidence angle distribution as well as the static pressure distribution show a remarkable dependence on the position of the upper and lower walls.

With the adjustable walls variations in the flow angle can be kept within the range of some tenth of a degree. In *FIGURE 2* the distribution of the inlet Mach number based on static pressures, D8 to D42, and total pressure in the settling chamber

shows that, for two flow conditions, the distribution is quite uniform except for the region close to the upper and lower walls.

FIGURE 3 shows the dependence of inlet Mach number on outlet Mach number. The choking Mach number is about 0.5 corresponding to a downstream Mach number of about 0.9. For higher flow accelerations no changes in the upstream flow occur.

Tests lead to higher inlet Mach numbers than can be expected for 2-d flow [2]. This is due to the relatively long inlet duct which causes a turbulent boundary layer of about 30 mm thickness on both sides. In the future an adaptive nozzle will be used which is shorter in order to approximate 2-d flow conditions better.

2.3 Downstream flow

Usually, downstream of the cascade, the flow is not guided by walls and therefore free shear layers originate from both the top and bottom blades. The interference of obstacles crossing the whole channel in the downstream supersonic flow field is demonstrated by Schlieren pictures (flash duration: 50 nsec) in FIGURE 4. Four pitches downstream cylinders of different diameters are inserted. Severe distortions of the flow are evident even if the diameter of the cylinder is only about twice of the blade's trailing edge thickness. This was taken into account by designing the probe with a long axial stem and mounting the probe support as far downstream as possible, [3]. In FIGURE 5 Schlieren pictures show the probe head within the flow.

A wedge-type probe, [3], specially designed for tests in the complex supersonic cascade flow fields is traversed at a fixed angle. From the probe's readings the local values for total and static pressure and flow angle are evaluated within the calibration range for the flow angle of $\pm 6^\circ$.

In FIGURES 6 and 7 sample measured distributions of local flow angle, total pressure and Mach number are shown for a stator cascade. In the case of subsonic flow results are shown for about 7 different pitches beginning from the free shear layer at the bottom. About 2 pitches from this boundary the wakes are almost identical. The rig consists of two more blades. For those blades measurements could not be provided due to the restrictions of the support system. This would be possible with the system in use today because the downstream area is now covered with 800 mm instead of the previous 314 mm.

In the supersonic case the flow is often less periodic. The expansion around the trailing edges can lead to a smaller flow angle at the bottom blade and to a higher one at the top blade. This may cause an angle gradient in the flow field.

Trailing edge shocks are reflected from the free shear layer and its influence on the flow pattern can be considerable, especially when causing additional shock boundary layer interactions or flow separation at the blades. For the example given in the figure the results for the 3 pitches of the centre blades show a quite periodic outlet flow field, which may not be achieved in all cases.

Additional reasons for deviations of the flow behind different pitches are due to the unavoidable imperfections of the hardware. Formerly blades were manufactured by copy-machining from a template. For some years the blades have been wire-eroded from brass which is a more precise method. The actual shape of the instrumented blade is measured with a ZEISS UMM 500 and is compared with the desired contour. Usually, deviations normal to the surface are within 5/100 mm. These maximum deviations occur at the leading edge and trailing edge, respectively. They are primarily due to the technology used to instrument the blade, [1]. An important geometric quantity is the throat, c^* , i.e. the shortest distance between two adjacent blades, fig. 1; numbers differ up to 3/10 mm. For calculating the 1-d theoretical choking Mach number, an averaged value of c^* is used.

From the data of the inhomogeneous flow in the traverse plane, the properties of an equivalent uniform downstream flow are obtained by applying the equations of conservation of mass, momentum and energy [4]. Results of data for downstream flow angle, total pressure loss and axial velocity density ratio as functions

of downstream Mach number are given in *FIGURES 8 to 10* for the cascade shown in *fig. 1*.

2.4 Pressure distribution

In *FIGURE 11* a measured surface pressure distribution is shown. The pressure coefficient

$$(1) \quad c_{p1}^* = [p_k^* - p_1^*] / p_1^* \quad \text{and} \quad p_1^*/p_{01} = [2/(\kappa+1)]^{\kappa/(\kappa-1)}$$

is plotted versus the axial length of the cascade, XA/LA . In *FIGURE 12* the pressure distribution cp_1^* is plotted versus YA/LU , the coordinate perpendicular to the axial direction, and combined with the corresponding Schlieren picture which allows an easy comparison.

Exemplarily, the suction side flow behaviour is discussed: the flow is accelerated from the stagnation point at $YA/LU = 0.4$ continuously up to $YA/LU = 0.0$. An area of recompression/expansion follows up to $YA/LU = 0.3$. From there the flow is accelerated up to $YA/LU = 0.7$ where the trailing edge shock from the adjacent blade is reflected which causes a shock boundary layer interaction. Further downstream the flow is decelerated and finally forms a shock at the trailing edge.

By integrating pressure distributions aerodynamic forces on the blades can be determined. These values can be cross-checked with those evaluated from data reduction of the wake flow measurements. In *FIGURE 13* results are shown for the normal force coefficient, normal to the chord direction, and for the tangential force coefficient. Only the results for the first seem to agree quite well. The deviations are related to the fact that friction forces are taken into account by probe measurements but not by static pressure measurements on the blades.

3. THEORETICAL INVESTIGATIONS OF TRANSONIC TURBINE CASCADES

At DFVLR the theoretical task of the project has been to perform flow field calculations applying a 2-d time-marching Euler code for seven different cascades for subsonic and transonic downstream Mach numbers. These data have been used to determine limitations of the application of the computer code itself as well as to check some assumptions which are necessary for "simplified methods" to calculate the angle of the homogeneous downstream flow. Some typical results are discussed and compared with experiments.

3.1 Computer code

A finite volume method, [2], is used to solve the time-dependent Euler equations for 2-d compressible flow. The boundary conditions prescribed in the computer code are total pressure, total temperature and direction of the homogeneous flow upstream of the cascade and the static pressure downstream. The spatial discretization is based on a H -grid which is systematically refined in four steps. Refinement is done by doubling the number of quasistreamlines as well as the number of nodes on a quasistreamline. In *FIGURE 14* a second mesh consisting of relatively widely spaced grid points is shown. From the final solution of the coarser grid initial values for the next finer one are interpolated. The values of the homogeneous flow are calculated using the conservation laws according to [4] after each time interval.

Formerly the vanishing local pressure change on the blade contour was used to define a criterion for the "steady state" solution with iteration in time. For this project the "steady state" was based on the vanishing changes of the homogeneous downstream flow quantities, [5]. These time-dependent values approach the "steady state" with variations of decreasing amplitude. In *FIGURE 15* the "steady state" values for the four grids after 40, 80, 160 and 320 time intervals are shown for downstream flow angle, pressure loss coefficient, upstream and downstream Mach number and the axial velocity density ratio. Allowing deviations from this "steady

state" value of about $\Delta\beta_2 \pm 1.0^\circ$, $\pm 0.5^\circ$, $\pm 0.25^\circ$ or $\pm 0.1^\circ$, in the four meshes respectively, as the maximum amplitudes for the downstream flow angle then the "steady state" is approximated sufficiently after 10, 20, 40 and 80 time intervals. The accuracy achieved for the other flow quantities is given in the figure, too. There is a significant change of the steady state values in the first three meshes, while in the finest mesh only local values vary, especially near the leading and trailing edge, [5]. If one takes into account that the experimental error in general corresponds to the accuracy prescribed in the third mesh, the accuracy of the final solution is sufficient.

3.2 Application of the computer code

• Surface pressure distribution

In *FIGURE 16* the surface pressure distribution for a low subsonic downstream Mach number in cascade 10.1.2 with the designed blades is shown. The comparison of experimental and calculated data indicates some significant deviations marked by arrows. Another calculation using Katsanis' code, [6], results in a very similar pressure distribution with irregularities at the same locations. In the case of transonic downstream Mach number in fig. 11 the corresponding deviations are to be seen.

The two main reasons which cause these deviations are first the inaccuracies of the manufactured blades forming the cascade 10.1.2I and second 3-d effects because of the side-wall boundary layers resulting in an axial velocity density ratio μ not equal to 1.0. The irregularities of the surface pressure distribution vanish when the actual cascade 10.1.2I is computed, fig. 11 and 16. The remaining difference to the experimental values can be reduced again by introducing the axial velocity density ratio from the measurements given in fig. 10 to the code. This leads to a remarkable agreement of experimental and calculated data for both subsonic as well as for transonic downstream Mach number.

The calculated blade force coefficients determined from homogeneous flow quantities on one hand and from pressure distributions on the other give nearly the same results, fig. 13. In spite of the abovementioned deviations in the pressure distribution, after integration the calculated results for cascade 10.1.2 and experimental ones for cascade 10.1.2I agree quite well.

• Influence of blade variations

The blades used in the basic cascade 10.1.2 have very thin trailing edges, i.e. low values of d/t see *TABLE 1*, and a curved suction side downstream of the throat. The variation of the flow field due to changes of the blade's suction side and trailing edge have been investigated in cascades 10.SSV1 and 10.SSV2. The blade shapes in *FIGURE 17* indicate the increase of the trailing edge diameter, the reduction of the curvature of the suction side and identical contours up to the throat. Therefore the geometry of the cascade variations has been chosen to give the same flow channel up to the throat as in cascade 10.1.2. Due to the different chord length of the blades the pitch chord ratios in tab. 1 are slightly different.

In fig. 17 the calculated pressure distributions for a downstream Mach number of $Ma_{2is} = 0.670$ are shown. There is an increase of the velocity level on the blade surface related to the increase of the trailing edge thickness. The difference between the pressure distributions for the two cascade versions is less than that between the basic one and version 10.SSV2. Due to the unchoked flow condition the whole flow field is influenced by the thick trailing edge. The stronger expansion around the thicker trailing edges causes the increasing differences between the local pressure maximum and minimum. Based on this expansion there is an upstream shift of the crossing of the pressure curves of the suction and the pressure side. In *FIGURE 18* the experimental results for other flow conditions indicate the same behaviour. In the case of transonic downstream Mach number, i.e. for a choked cascade, there are identical pressure distributions up to the throat, *FIGURE 19*. Moreover the pressure distributions indicate an increasing strength of the shock reflected on the suction side with increasing trailing edge thickness.

In the throat, constant flow velocity and constant flow direction perpendicular to the throat, are assumed when using "simplified methods" to calculate the angle

of the homogeneous downstream flow. For cascade 10.SSV2 the local flow direction in the throat calculated by the time marching procedure (TMP) indicates significant deviations from this assumption, see *FIGURE 20*. This may be related to the thick trailing edge but in cascade 3.1.1, having blades with thin trailing edges, there are remarkable differences, too. In addition the local flow velocity varies by about $\pm 10\%$ from an averaged value, [5]. As the abovementioned assumptions are not proven by the time-marching procedure in these cases significant differences between the downstream flow angle calculated using one of the "simplified methods" and experimental results may be expected.

3.3 Homogeneous flow quantities

• Upstream flow

For cascade 10.1.2 the homogeneous upstream flow indicates that the experimental upstream Mach number is higher than the corresponding calculated one, fig. 3, due to side-wall boundary layers in the wind tunnel. Correcting the geometric cross-section with the displacement thickness a corrected experimental inlet Mach number for 2-d flow can be calculated. The results from the flow field calculation for cascade 10.1.2 and 10.1.2I using $\mu = 1.00$ fit this curve quite well. On the other hand it is possible to take into account different cross-sections in calculation planes 1 and ME and linear interpolation in-between and to perform a quasi-3-d calculation corresponding to the experimental value μ not equal to 1.00. The result for cascade 10.1.2I is an upstream Mach number close to that of the experiment.

Due to the thick trailing edges of the blades in cascades 10.SSV1 and 10.SSV2 the mass flow changes for subsonic downstream Mach number $Ma_{2is} = 0.67$. There is a significant difference for the basic cascade and the variations, while the two variations have nearly the same upstream Mach number. The expansion around the thicker trailing edges results in a higher level of the contour velocities and therefore more mass flows through the cascade. To increase the mass flow in cascade 10.1.2 to that value the isentropic downstream Mach number has to be increased to $Ma_{2is} = 0.70$.

• Downstream flow

From the local flow quantities in calculation plane ME the values of the homogeneous downstream flow are computed. For the basic cascade 10.1.2 the downstream flow angle in fig. 8 from experiment and calculation fit to the same curve. This is related to the fact that the values of the pressure loss coefficients, ζ (ZETA), in fig. 9 are close to each other, i.e. for the subsonic case numerical losses due to smoothing the solution and for the transonic case numerical losses and predicted shock losses are comparable to the measured ones. All this is related to the thin trailing edge of the blades.

For the cascades having blades with thicker trailing edges the downstream flow angle in fig. 8 increases. This can be seen in the case of the blade variations as well as in the case of the actual blade. The corresponding pressure loss coefficients in fig. 9 increase as well. When smoothing the expansion around a thick trailing edge obviously from the subsonic case the numerical viscosity increases. This gives a hint for the necessity of a wake model to be incorporated in the procedure especially for thick trailing edges.

For the axial velocity density ratio, μ (MY), in fig. 10 it can be seen that the calculated values are close to 1.00, while the experimental ones are significantly different. As mentioned above this is because of the higher upstream Mach number due to side-wall boundary layers. If these geometric modifications of the flow channel are introduced to the code the calculated values are close to the experimental ones.

4. EXPERIMENTAL INVESTIGATIONS ON SUBSONIC TURBINE CASCADES

Parallel to the transonic cascade investigations described above measurements and calculations in the subsonic-compressible range were conducted at IfS, Hannover.

For two different profiles geometrical modifications of the outlet part of the suction side combined with an increase of the trailing edge thickness were investigated in a range of downstream Mach number of 0.2 to about 0.8. Wake traverses and surface pressure measurements were made and in addition some L-2-F velocity measurements in the throat area for comparison with flow field calculations. A few results are presented here.

4.1 Test Facility

The cascade tunnel used is of the suction type. It is shown in *FIGURE 21*. The blades of 240 mm length are mounted between two circular side wall plates which can be rotated so that the outlet flow is directed roughly vertically downwards. One of the side plates is made of steel and comprises the probe insert and traversing provisions, furthermore the outlets for the static pressure taps on the blades. The other side plate has a glass insert and allows measurements with a L-2-F anemometer between the blades and behind the cascade. With a blade chord length between 80 and 100 mm the aspect ratio realized is 2.4 to 3. Because of the limited airflow capacity available a rather limited number of six to eight blades constituted the cascade.

The flow channel consists of two fixed, sector-shaped side walls and two adjustable guide plates which are set at the intended angle. The quality of the inlet flow is controlled by static pressure taps all along the guide plates and in front of the cascade. The uniformity of the inlet flow is remarkably good. The side wall boundary layers are according to our measurements thin.

Since the outlet plenum is not sufficiently large for an undisturbed free jet outlet, the flow behind the cascade is protected against uncontrollable influences from the direct environment by adjustable guide plates. This, however poses the problem to avoid influencing the flow, especially the outlet angle. This problem was - in most cases sufficiently to satisfaction - solved by using pressure taps on the guide plates and behind the cascade for adjusting the guide plates to a nearly uniform pressure distribution. Nevertheless, this configuration of cascade tunnel will always pose operational problems. A further operational limitation results from the expansion of the more or less moist air in the cascade which leads to spontaneous condensation under transonic flow conditions and a falsification of the results. The outlet Mach number has to be limited to about 0.8.

4.2 Downstream Flow

For the determination of the outlet flow a wedge-type five-hole probe (*FIGURE 22*) was used. The long axial stem built according to DFVLR experiences minimizes the interference of the holder with the flow. The probe is traversed at a fixed angle. The flow direction is calculated from the calibration factors. Because of the geometrical limitations at the tunnel the traversing travel was only about two pitches lengths which is not enough to smooth out statistical scattering. In the subsonic region, however, the results were quite satisfactory.

Measurements were made - among others - for the cascade configurations described above (fig. 5 and 17 resp.). *FIGURE 23* shows local distributions of the flow angle, total and static pressure and Mach number. The decrease of uniformity and periodicity with increasing trailing edge thickness is obvious. The comparison of the parameters flow angle β_{22} , loss factor ξ and inlet Laval number La_1 - all calculated from the test data also according to [4] - with the same data from the DFVLR measurements is shown in *FIGURE 24*. The differences, keeping in mind some unavoidable shortcomings of the IFS measurements, are rather small and the general compatibility is good. Similarly good agreement has been found for the blade pressure distributions which is not shown here in detail.

5. THEORETICAL INVESTIGATIONS OF SUBSONIC TURBINE CASCADES

5.1 Computer Code

For the calculation of subsonic-compressible flow fields in turbine cascades a finite difference method for calculation of the stream function acc. to Katsanis, [6], was used after some adaptations to our problem. The solutions yields the 2-d subsonic-compressible, frictionless flow field for a given geometry and given inflow and outflow conditions. Contour Mach numbers up to 0.7 could well be handled.

5.2 Application of the computer code

It is well known that methods like this demand an additional information defining the total circulation around the profiles to render a correct solution, i.e. the outlet angle should be available as input which poses some problems in all cases where experimental data are not already available. Test calculations for a number of different cascades with prescription of three or four slightly differing outlet angle values showed, that - provided the calculating net and the contour point spacing are fine enough at the trailing edge - the "correct" outlet angle value can quite easily be deducted by visual inspection of the pressure distribution diagrams with some experience. A "normal" closure of the pressure curve at the trailing edge is a good indicator. It seems highly probable that the introduction of an extra iteration level in the code which satisfies p.e. identical velocity (or static pressure) at the both end points of the halfcircle of a non-zero thickness trailing edge, will allow the direct calculation of a flow field with an outlet angle correct to a few tenth of a degree (see fig 16). Experience showed, as mentioned already for the time marching method, that high accuracy for the geometrical input data is indispensable for a quality solution. Small differences cause considerable disturbances in the solution (fig. 16).

Very important, too, for the comparison of measured and calculated contour pressure distribution curves is the introduction of the experimental value of the axial velocity density ratio into the calculation, if it deviates - as often - sensibly from unity. *FIGURE 25* shows results with and without correction.

6. DOWNSTREAM FLOW ANGLE CORRELATION

6.1 "Simplified Methods" for Outlet Flow Angle Calculation

Almost since the beginning of turbomachine theory the need for methods for the theoretical prediction of the outlet flow angle covering a large variety of profile forms and a great range of operating conditions was felt. In course of time a host of - in principle - quite generally applicable methods was developed, beginning with the famous Sine Law, described p.e. in a modern form in [8]. Further exist the Tangent Law, [9], and it's more generalized form in [14], the methods of Fricke, [10], and Oedegard, [11], which take into account the compressibility of the fluid and finally, also classical example, the Jet Deflection Law, [12], for transonic conditions only.

The practical experiences with all these methods were differing widely. The deviations from experimental data seemed somewhat erratic and unpredictable. The research project the results of which are reported here very partially, was started originally in order to check the results and the accuracy of all these "simplified methods" for the calculation of outlet flow angle in a wide range of profile form and operating conditions against proven experimental results of high quality and thus decide their practical applicability. Experimental data were collected or produced for about 60 cascade configurations with more than 30 different profile forms. *FIGURE 26* gives a synoptical presentation of the cascade characteristics in a inflow - outflow angle manner. *FIGURE 27* shows the range of outlet flow Mach number resp. Laval number covered by the experimental data.

For all cases the outlet flow angle was calculated according to all the "simplified methods" cited above (except [14]), if applicable for variable outlet Mach number, and compared with the experimental data. Three typical examples of the comparison are presented in *FIGURES 28 to 30*.

A case of good agreement for a turbine cascade with rather high deflection shows *fig. 28*. Although the Sine Law value differs by more than 5% the Tangent Law and the Oedegard method coincide nearly perfectly and the Fricke method agrees quite well. Even the decrease and increase of the flow angle with outlet Mach number is very well reproduced. Only the values according to the Jet Deflection Law are far off, as in most cases investigated.

Fig. 29 for a seemingly similar cascade reveals a quite different situation. The Sine Law gives at least a good mean value, the result of the Fricke method is very good, while Tangent Law and Oedegard differ somewhat more. *Fig. 30*, finally, for a quite normal profile form, shows enormous differences in the subsonic range. Especially the variation of outlet flow angle with Mach number is overestimated by all methods dramatically. In the transonic range, however, good agreement exists, which is true for quite a number of cases.

As a resume of the complete investigation it can be stated that no one of the "simplified methods" applied showed a sufficient agreement with experimental results all over the range considered. The differences are differing widely, a correlation with cascade geometry or other relevant parameters could not be found.

6.2 Critical Review of "Simplified Methods"

All the "simplified methods" investigated here are based on the application of the conservation laws for mass flow and momentum in a "control area" limited by the throat of the cascade and a plane with assumed homogeneous flow behind the cascade as shown in *FIGURE 31*. The mass flow and momentum balances are influenced by the conditions along the boundaries of the control area. Only the influences of the rearward stagnation stream lines cancel each other because of the periodicity. The pressure forces in the throat, Kp_a , on the rearward suction side, Kp_s , on the trailing edge, Kp_B , and in the outlet flow plane, Kp_2 , further the mean velocity vectors in the throat, w_a , and in the outlet flow plane, w_2 , and eventually the friction force, R , on the suction surface enter into the balance equations. Since detailed values for all these quantities are never available for a simplified calculation of the outlet flow angle, the different "simplified methods" apply different assumptions to overcome this inherent problem. These assumptions are described in detail in the pertinent publications cited above; a synopsis is given in [13].

Since the conservation equations for mass flow momentum introduced in the "simplified methods" are inherently correct, any differences between the values calculated by this way and the real values can only be due to the fact, that the mentioned assumptions are not met. A closer examination of this question might reveal the reasons for the experienced deviations and show perhaps means for an improved "simplified method" through a better understanding.

Therefore an extensive study comparing the assumptions of the different "simplified methods" with the real values of the relevant quantities along the boundaries of the control area extracted from numerical flow field calculations and special cascade measurements, as reported above, was conducted and detailed results are reported in [13]. It was found generally, that the constitutive assumptions of the "simplified methods" for calculation of the outlet flow angle are nearly never fulfilled and considerable differences exist. Relatively small modifications in cascade geometry may result in considerable changes of the numerical values of the boundary quantities. Systematic correlations between cascade geometry and the relevant quantities for the balance equations valid for a large range of cascade geometry and operating conditions were not found. This does not exclude the possibility to define such correlations for a small range of geometry variations, i.e. to use "simplified methods" with correction factors or functions for similar "profile families" in a satisfactory and safe way. The necessary corrections, however, have to be determined empirically for each case.

The efforts to correlate the outlet flow angle to specific details of cascade geometry - unsuccessful as they were - led, however, to the formulation of a new general correlation of acceptable accuracy. The ratio of the effective mean outlet flow angle, β_2 , to the outlet flow angle, $\beta_2 \sin$, calculated according to the Sine Law is correlated to the contraction of the flow channel near the throat expressed as angle γ explained in *FIGURE 32*. The general tendency is well defined, the accuracy is a few percent, based on about 15 cascade configurations.

7. CONCLUSION

Modern numerical methods for the calculation of cascade flow fields render satisfactory results in the compressible-subsonic as well as in the transonic region, as long as boundary layer separation does not occur. For comparison with experimental data the use of the actual and accurate cascade geometry and the experimental value of the axial velocity density ratio in the calculation is indispensable.

With appropriate treatment of the trailing edge - even with considerable thickness - either by introduction of suitable wake flow models or assumptions into the computer code or by competent judgement of the results and controlled adaption of the input data, these calculating methods will render values for the outlet flow angle with an accuracy sufficient for industrial demands, i.e. of a few tenth of a degree.

"Simplified methods" for the calculation of the outlet flow angle, based on mass flow and momentum balance with generalized assumptions for the outlet area of a cascade only, are not capable to take sufficiently into account the real flow field and the specific nature of the boundary conditions and will hardly ever achieve the necessary accuracy. Application of these methods is only advisable within narrow ranges of cascade geometry and with empirically determined corrections or adaptations.

References

- [1] Heinemann, H.-J. The Test-Facility for Rectilinear Cascades (EGG) of the DFVLR
DFVLR Bericht IB 222 - 83 A 14 (1983)
- [2] Lehthaus, F. Berechnung der transsonischen Strömung durch ebene Turbinengitter nach dem Zeitschrittverfahren
VDI-Forschungsheft 686, S. 5-24
VDI-Verlag, Düsseldorf (1978)
- [3] Klock, R. The Transonic Flow Through a Plane Turbine Cascade as Measured in Four European Wind Tunnels
Lehthaus, F. ASME Journal of Engineering for Gas Turbines and Power, Vol. 108, p. 285-292, (1986)
Baines, N.
Sieverding, C.
- [4] Amecke, J. Anwendung der transsonischen Ähnlichkeitsregel auf die Strömung durch ebene Schaufelgitter
VDI-Forschungsheft 540, S. 16-28
VDI-Verlag, Düsseldorf (1970)
- [5] Gies, P.-A. Theoretische Untersuchungen mit Hilfe eines 2-d-Zeitschrittverfahrens an drei Turbinengittern
DFVLR Bericht IB 222 - 85 A 35 (1986)
- [6] Katsanis, Th. Computer program for Calculating Velocities and Streamlines on a Blade-to-Blade Stream Surface of a Turbomachine
NASA TN D - 4525 (1968)

- [7] Dalbert, P. Untersuchung der Strömung und der Verluste an Turbinen-schaufelgittern zur Bestimmung des Abströmwinkels
Abschlußbericht zum FVV-Forschungsvorhaben
"Abströmwinkel II"
FVV-Heft Nr. 368 (1985)
- [8] Bammert, K. Der Einfluß verdickter und verdünnter Turbinenschaufeln
Sonnenschein, H. auf die Gittereigenschaften
Archiv für das Eisenhüttenwesen 38 (1967),
Nr. 4, S. 287
- [9] Traupel, W. Prediction of Flow Outlet Angle in Blade Rows with
Conical Stream Surfaces
ASME Paper 73-GT-32 (1973)
- [10] Fricke, H. Beitrag zur Ermittlung des Abströmvektors aus Turbinen-
gittern für den unter- und überkritischen Bereich
VDI-Bericht Nr. 264 (1976), S. 25 pp.
- [11] Oedegard, S. Der Abströmwinkel von Turbinenleitschaufeln als Funktion
der Machzahl und der Teilung
Mitt. Inst. f. Strahlantriebe und Turboarbeitsma-
schinen, RWTH Aachen, Nr. 74-04 (1974)
- [12] Traupel, W. Die Strahlablenkung in der vollbeaufschlagten Turbine
Mitt. Inst. Therm. Turbomaschinen, ETH Zürich,
Nr. 3 (1956), S. 27 pp.
- [13] Dalbert, P. Der Abströmwinkel von Turbinen-Schaufelgittern,
Leistungsfähigkeit und Grenzen von Berechnungsverfahren
Dissertation, Universität Hannover (1986)
- [14] Bräunling, W. Prediction of Flow Outlet Angle in Rotating Annular Turbine
Cascades with Conical Stream Surfaces in Subsonic and
Transonic Flow Regimes
Thermische Strömungsmaschinen '85, Bochum 17/18. Sept. 1985
VDI Verlag, Düsseldorf (1985)

Acknowledgments

The investigations have been initiated by Forschungsvereinigung Verbrennungs-kraftmaschinen e.V. (FVV), Frankfurt/Main, and have been sponsored by Ministry of Economics via Arbeitsgemeinschaft Industrieller Forschungsvereinigungen e.V. (AIF), Köln. The authors wish to thank Mr. H. Bals, Kraftwerk-Union/Mülheim, chairman of the FVV working group, and Dr. F. Lehthaus, DFVLR/Göttingen, head of the cascade group, for intensive discussions when performing the FVV contract.

cascade	β_s	t/l	β_1	c^*/t	d/t
3.1.1	49.0°	0.680	94.0°	0.4489	0.0115
10.1.2	70.0°	0.600	130.0°	0.5458	0.0159
10.1.2I	70.0°	0.600	130.0°	0.5458	-
10.SSV1	70.0°	0.586	130.0°	0.5460	0.0789
10.SSV2	70.0°	0.593	130.0°	0.5460	0.0473
17.1.1	71.0°	0.499	118.0°	0.4246	0.0673

TABLE 1: Geometrical values of the investigated cascades

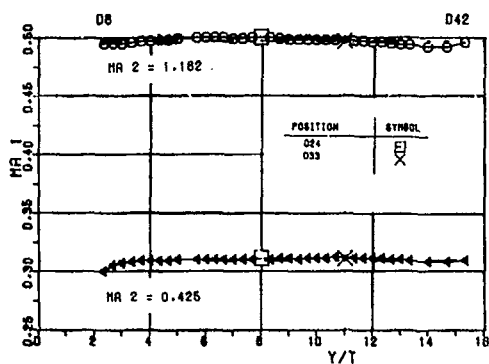


FIGURE 2: Inlet Mach number distribution versus inlet nozzle hight

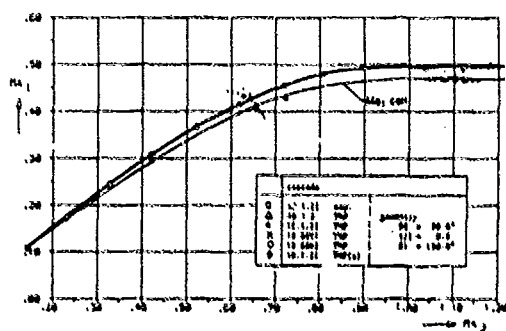
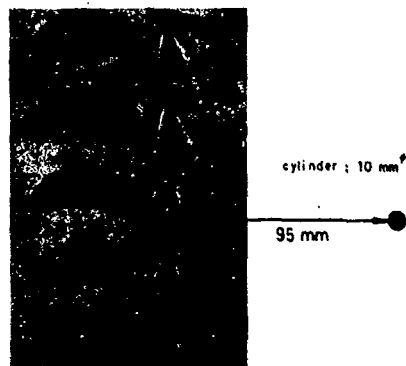


FIGURE 3: Upstream Mach number of homogeneous flow

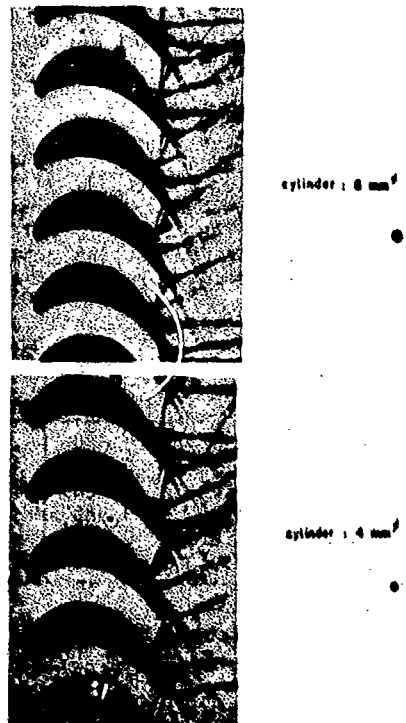


FIGURE 4: Cylinders in a downstream supersonic cascade flow ($M_\infty \approx 1.2$)

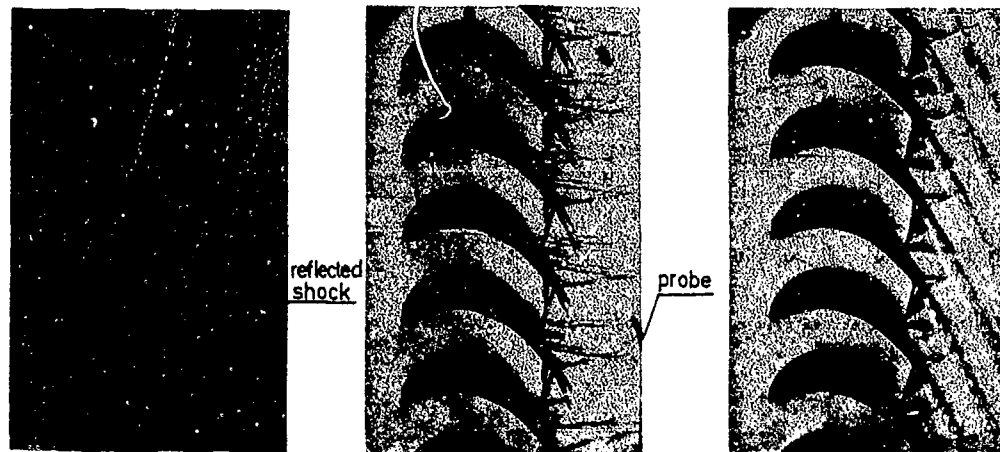


FIGURE 5: Wedge-probe, supported with the new probe-holder

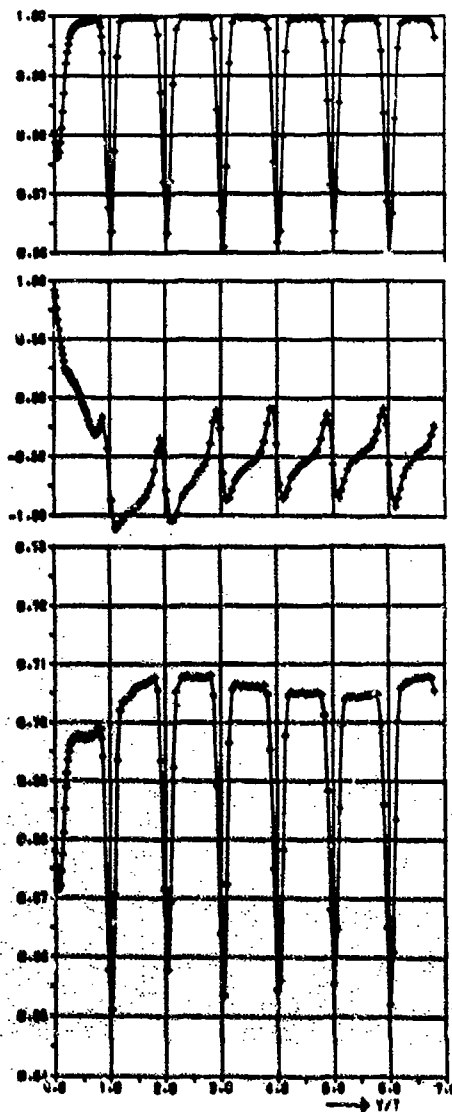


FIGURE 6: Local flow quantities (subsonic)

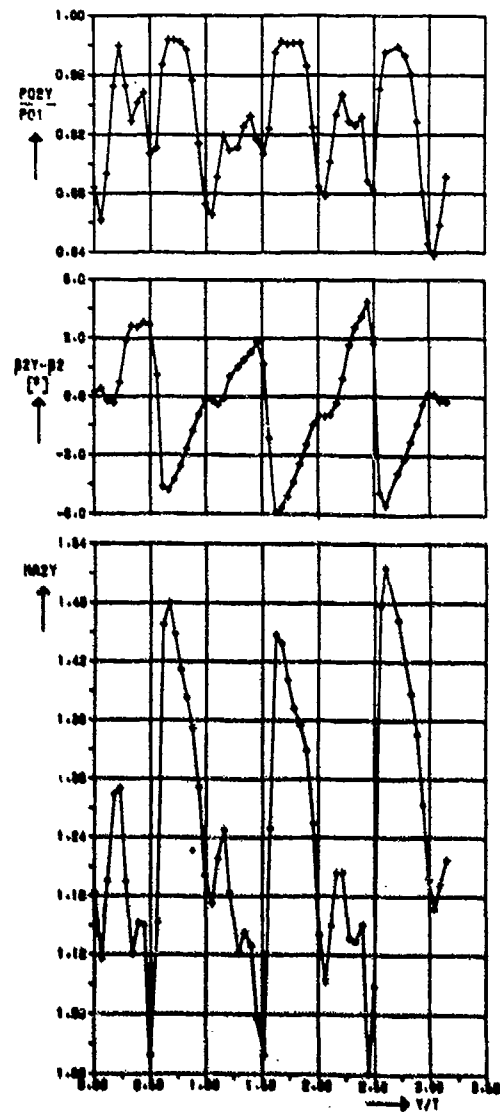


FIGURE 7: Local flow quantities (supersonic)

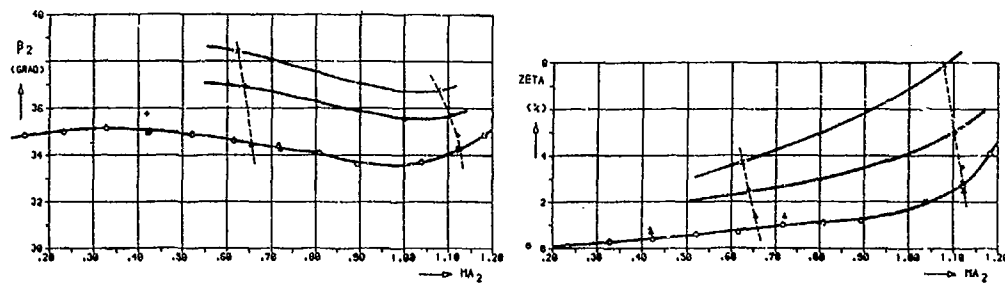


FIGURE 8: Downstream flow angle of homogeneous flow

FIGURE 9: Total pressure loss coefficient of homogeneous flow

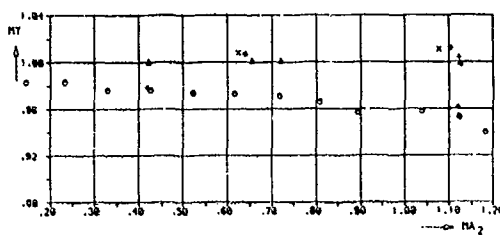


FIGURE 10: Axial velocity density ratio of homogeneous flow

cascade			geometry	
○	10.1.21	exp.	85	70.0°
△	10.1.21	THP	85	70.0°
+	10.1.21	THP	85	70.0°
x	10.55V1	THP	81	130.0°
◇	10.55V2	THP	81	130.0°
◆	10.1.21	THP(u)		

Symbols used in fig. 8, 9 and 10

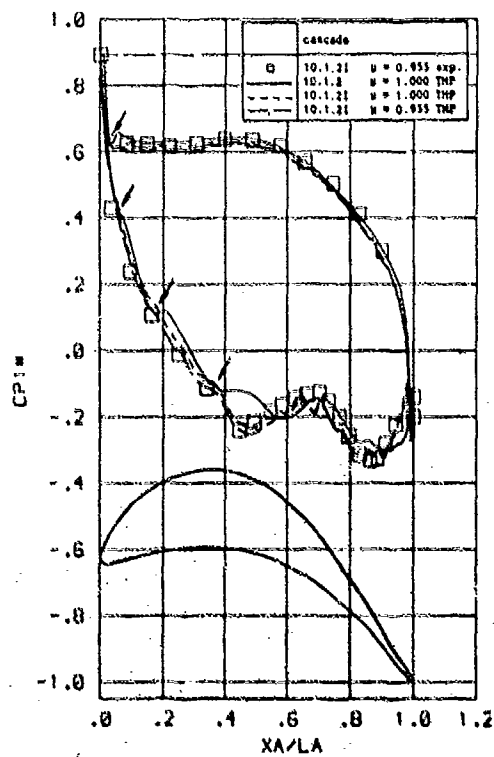


FIGURE 11: Surface pressure distribution
($N_{212u} = 1.144$)



FIGURE 12: Surface pressure distribution with
Schlieren picture

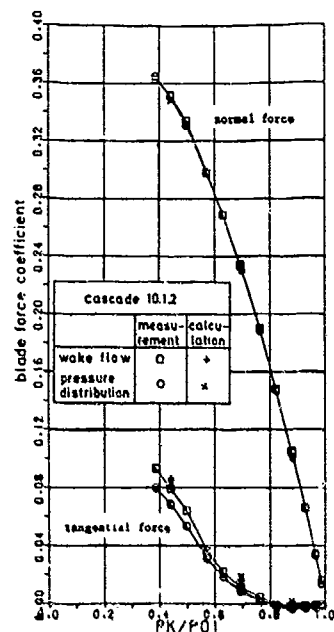


FIGURE 13: Blade force coefficients

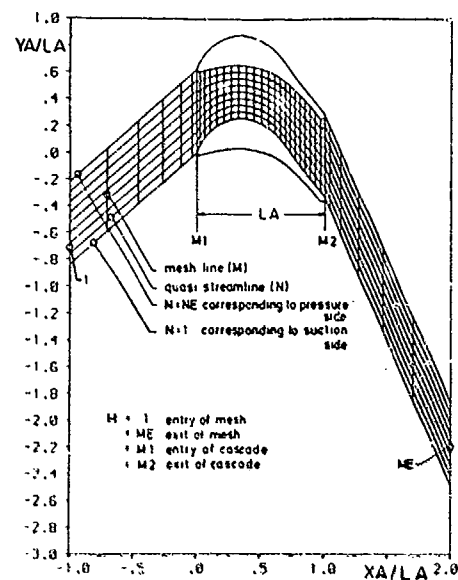


FIGURE 14: Definitions within the computational mesh

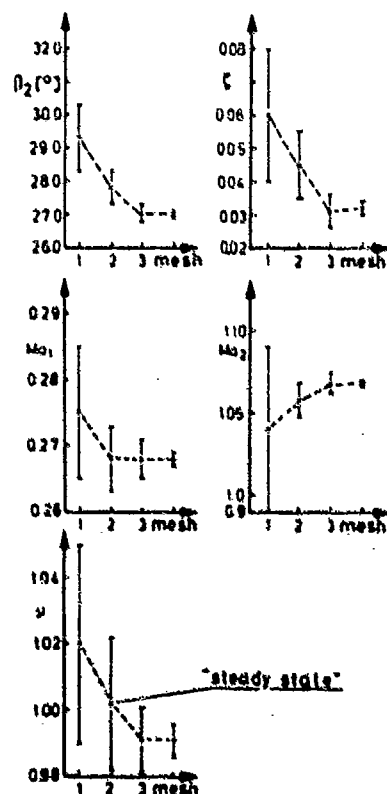
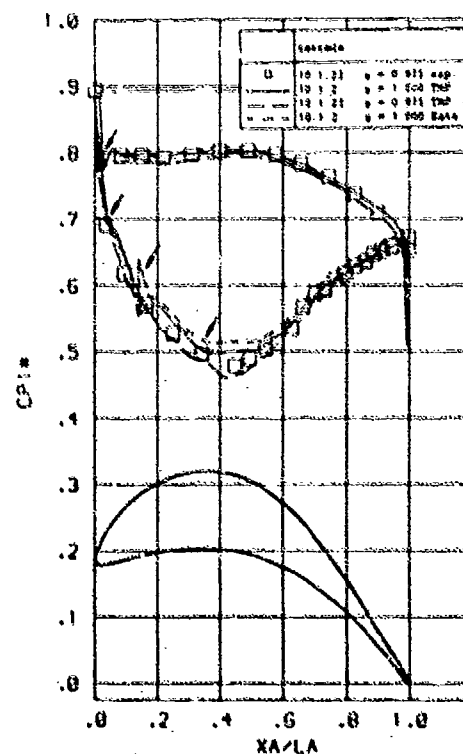


FIGURE 15: Maximum deviation from the steady state solution after 10, 20, 40 and 80 time intervals corresponding to the four meshes

FIGURE 16: Surface pressure distribution ($Re_{215} = 0.433$)

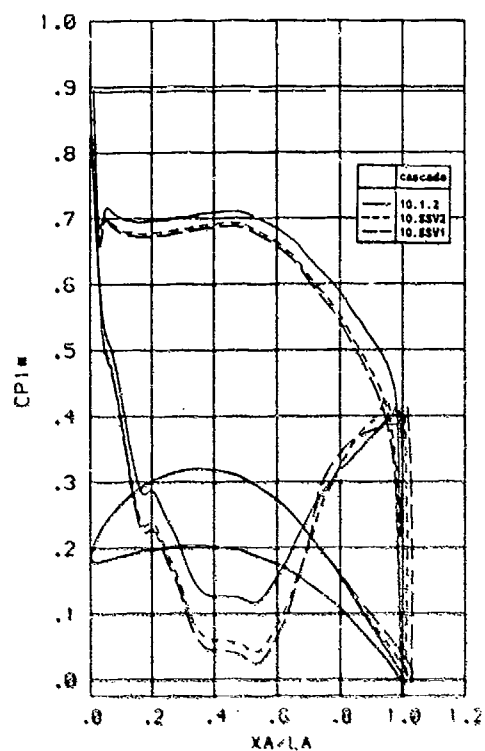


FIGURE 17: Surface pressure distribution
($Na_{21a} = 0.670$)

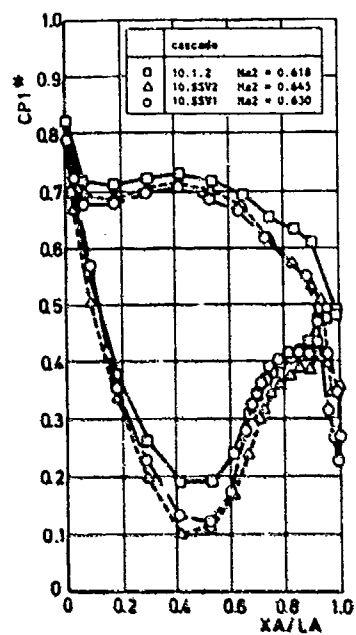


FIGURE 18: Surface pressure distribution from
experiments

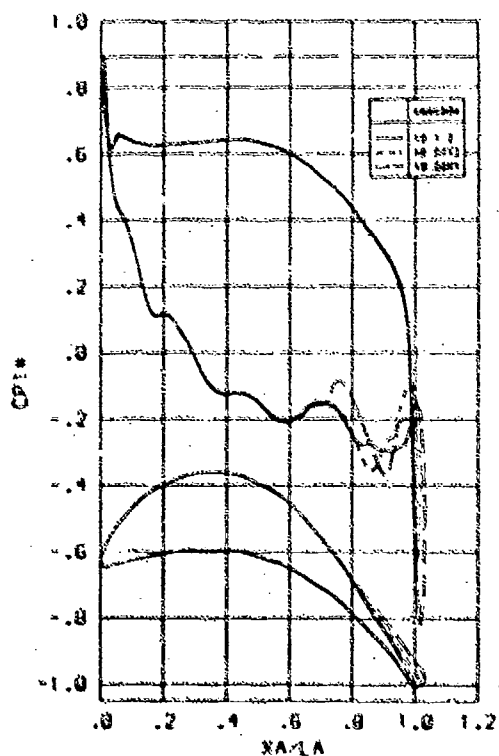


FIGURE 19: Surface pressure distribution
($Na_{21a} = 1.144$)

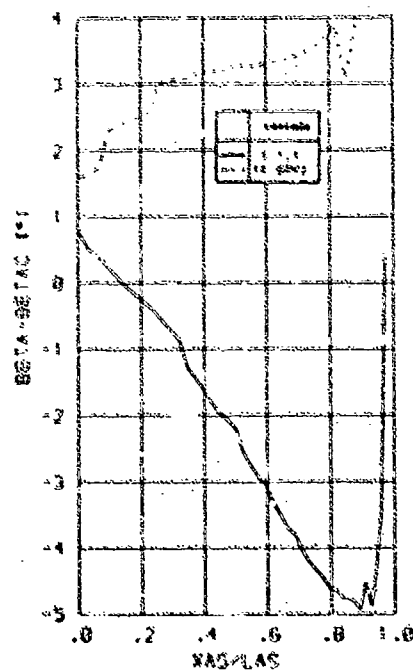


FIGURE 20: Deviation of the local flow direction
from perpendicular flow through the throat

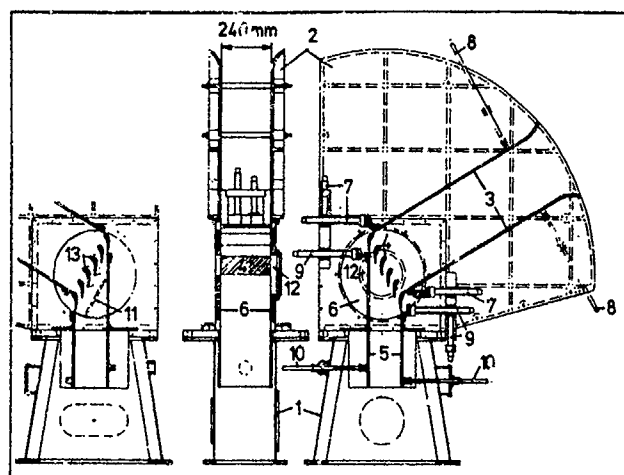


Fig. 21
Suction-type Cascade
Wind Tunnel (IfS Hannover)

- 1 - Outlet Plenum
- 2 - Side Walls
- 3 - Inlet Guide Plates
- 4 - Cascade
- 5 - Outlet Guide Plates
- 6 - Cascade Holding Plate
- 7, 8, 9, 10 - Adjusting Screws
- 11 - Probe Slot
- 12 - Window
- 13 - Pressure Meas. Profiles

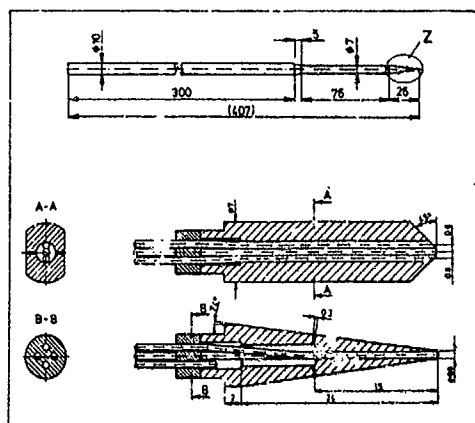


Fig. 22 Wedge-Type Five Hole Probe

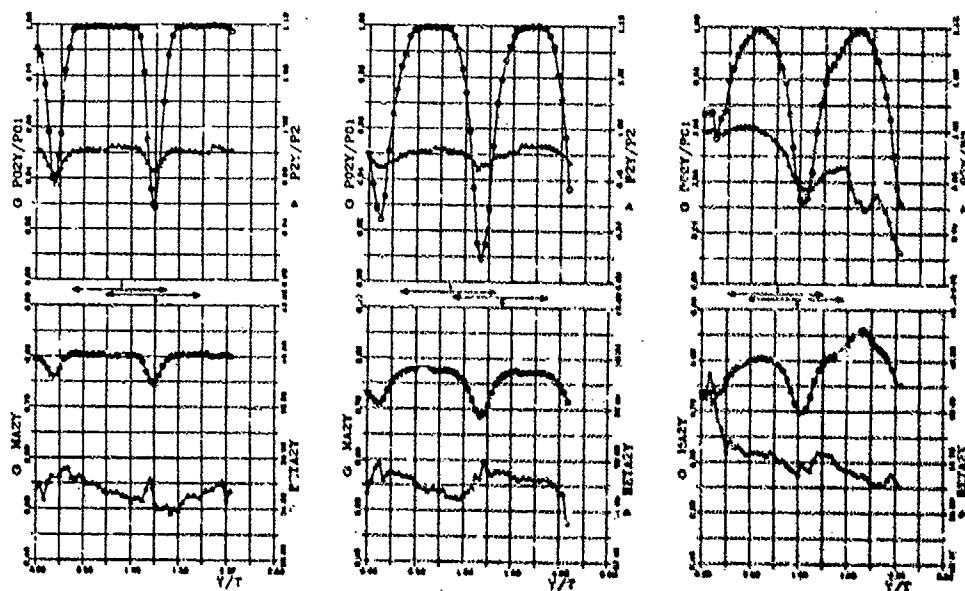


Fig. 23 Downstream flow of Cascade 10.1.2 with Ratio of
Trailing Edge to Pitch 0.016; 0.04; 0.075

P02 - Total Pressure MA2 - Outlet Mach No.
P2 - Static Pressure BETA2 - Outlet Angle

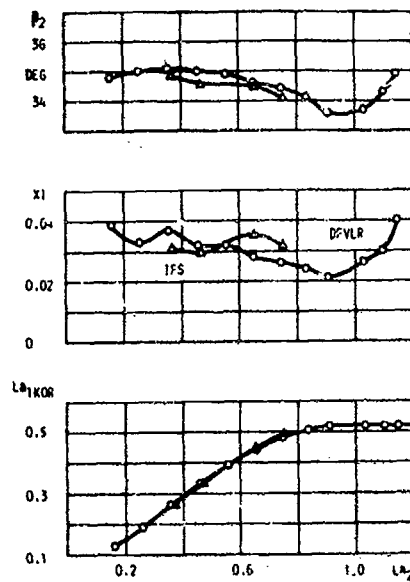


Fig. 24 Comparison of Test Results of Cascade 10.1.2

La_2 - Outlet Level Nb.
 XI - Loss Coefficient
 P_2 - Outlet Angle
 La_1 - Inlet Level Nb. (corrected)

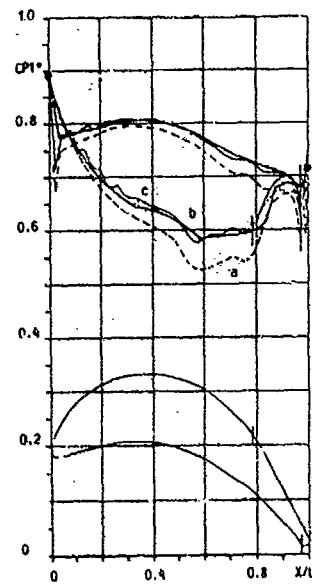


Fig. 25 Comparison of Measured and Calculated Pressure Distribution for Cascade 17.1.1

a - Katsanis-Calculation
 b - Katsanis-Calc. with Correction
 c - Experimental

$$La_1 = Ma_1^2 = \frac{Ma^2}{1 + \frac{\gamma-1}{\gamma+1} (Ma^2 - 1)}$$

for ideal gases with constant specific heat

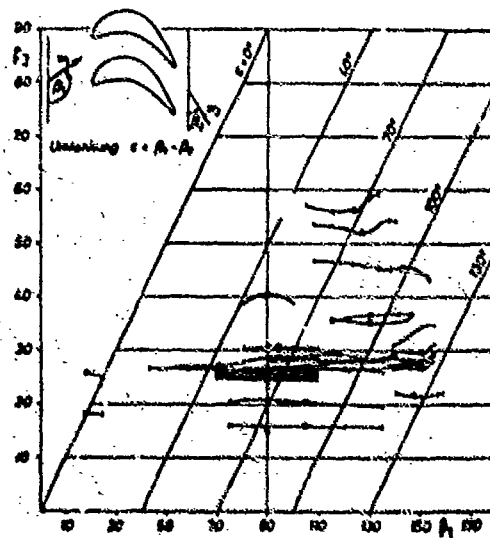


Fig. 26 Flow Angle Characteristic of Investigated Cascades

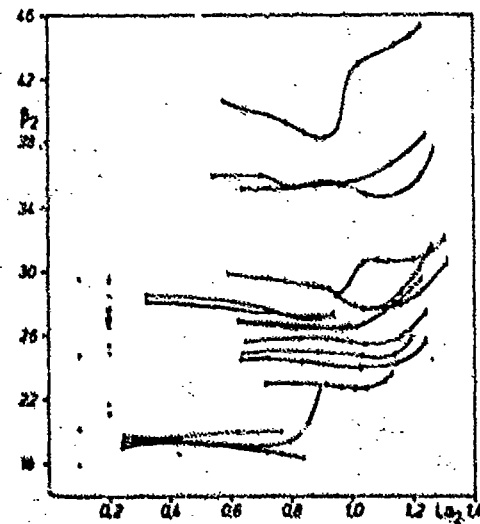


Fig. 27 Level Number Range of Investigated Cascades

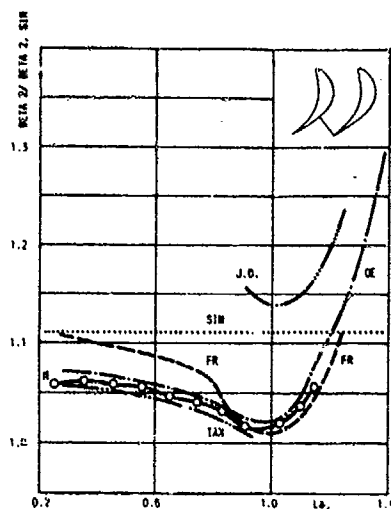


Fig. 28
Outlet Flow Angle vs. Outlet Laval Number for Cascade 10.1.2, Comparison of Measurement with Simplified Calculations

SIN - Sine Law OE - Oedegard
TAN - Tangent Law FR - Fricks
J.D. - Jet Deflection M - Measurements (DFVLR)

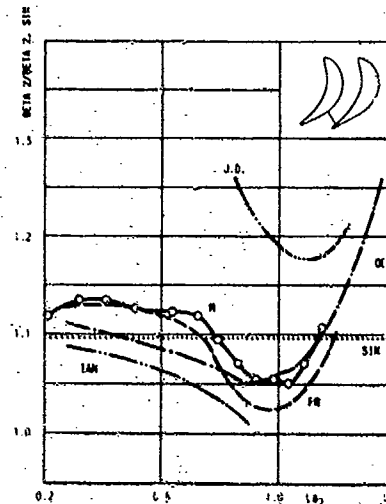


Fig. 29 Outlet Flow Angle vs. Outlet Laval Number for Cascade 17.1.1 (see Fig. 28)

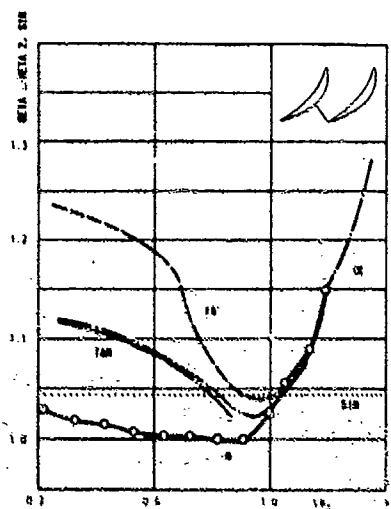


Fig. 30 Outlet Flow Angle vs. Outlet Laval Number for Cascade 3.1.1 (see Fig. 28)

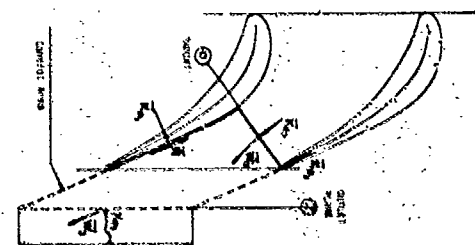


Fig. 31 Control Area for "Simplified Methods" with Relevant Parameters

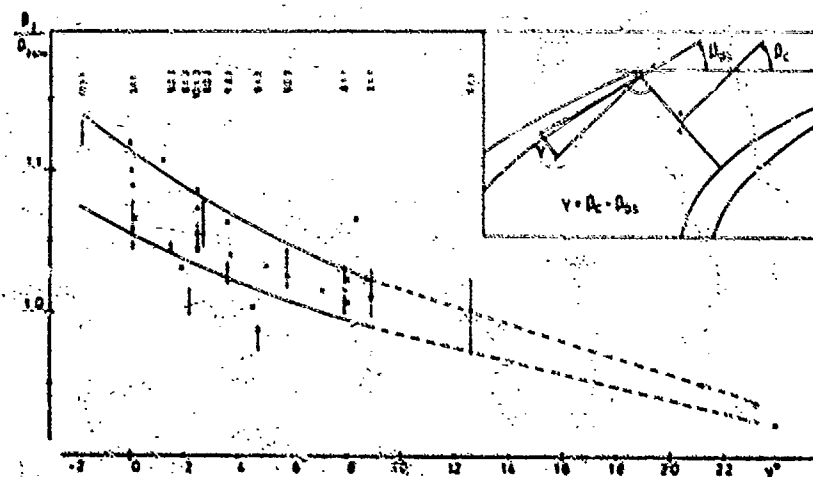


Fig. 32
Outlet Flow Angle
Correlation vs.
Contraction Angle
of Flow Channel

DISCUSSION

H.A. Schreiber, Ge

We know that the AVDR can have a strong influence on the downstream flow angle. Have you considered the AVDR influence in the β correlation?

Author's Reply

The correlation presented in Figure 32 is at present purely empirical and no corrections are included. The correction proposed is surely possible, but we did not work on this further refinement of the correlation, because we are not convinced of the general applicability of any correlation based only on simple geometric parameters.

J.D. Denton, UK

In Figures 28, 29, 30 why is the value of $\beta_2/\beta_1 \sin$ equal to 1 for the sine rule?

Did you make any comparisons of the outlet angle predictions from the computational methods with the measurements?

If not I think that it would be a very useful exercise.

Author's Reply

$\beta_1 \sin$ is taken from the simple sine law

$$\beta_1 \sin = \sin a/t$$

a = throat width

t = pitch

SIN in the diagrams is the result of a corrected sine law as presented in Reference 8 or in Traupel: Termische Turbomaschine, which takes into account the trailing edge thickness.

The downstream flow angles calculated by the time-marching code compare in general well with experimental data; see Figure 8 of the paper. The subsonic Katsanis code demands actually to specify the downstream angle. An iterative calculation based on visual judgement of the pressure distribution calculated around the trailing edge normally gives results accurate to a few tenths of a degree. Introduction of a suitable outflow condition into the Katsanis code seems well possible as described in the paper.



A SHOCK LOSS MODEL FOR SUPERCRITICAL SUBSONIC FLOWS IN TRANSONIC AXIAL FLOW COMPRESSORS

R.J. Dunker

DFVLR, Institut für Antriebstechnik
Postfach 90 60 58, D-5000 Köln 90
Federal Republic of Germany

SUMMARY

This investigation was aimed at developing more sophisticated shock models to be incorporated in an off-design performance prediction method for transonic axial flow compressor stages for more accurate flow prediction. Primary emphasis was given to the improvement of shock models used for evaluating the shock losses, especially, at supercritical subsonic, but also at supersonic inflow conditions. The newly developed and refined methods were verified by calculating, investigating and analysing the losses of compressor cascades, as well as of a transonic axial flow compressor.

LIST OF SYMBOLS

A_{HSS} straight shock extension (see Fig. 13); m
d shock distance ahead of leading edge (see Fig. 4); m
l chord length; m
Ma, M Mach number
r_{le} leading edge radius; m
r_{ss} suction surface radius of 1st blade element; m
z_{ss} straight distance measured between leading edge and assumed shock impingement point on suction surface
β relative flow angle measured acute against axial direction; deg.
β local inclination angle of blade contour measured against axial direction; deg.
θ difference angle of inclination in shock impingement point and sonic point; deg.
ω total pressure loss coefficient, $\omega = (P_{01} - P_{02}) / (P_{01} - P_1)$

Subscripts

0 total condition; related to camber line
1 condition far upstream of cascade front; at inlet
1_{seq} indicating transition between circular arc of the leading edge and that of the suction surface
bow related to the bow shock
C intersection point of 1st captured Mach wave and detached shock
E emanating point on suction surface of 1st captured Mach wave
H assumed shock end point
ink incompressible
krit critical
og at the upper limit, i.e. at near sonic condition
p related to the passage shock
sh concerning the shock
SP sonic point
SH shock impingement point
tot total

INTRODUCTION

For aero gas turbines transonic axial flow compressors represent a good compromise between power concentration per stage on the one hand, efficiency, weight and size on the other hand. Fig. 1 shows a sketch of a typical transonic axial compressor stage. One of the characteristic features of the flow in such a compressor stage is the formation of complicated 3-dim. shock fronts, as illustrated in principle in Fig. 2. Moreover the shock front considerably changes its extension, position and intensity depending on the operating point of the compressor. This is shown schematically in Fig. 3 in a 2-dim. view, whereby the through flow is characterized by mixed subsonic/supersonic flow fields. When the operating point of the compressor is shifted through the part load range towards full load conditions, the inflow conditions to and the corresponding flow field around a midsection of the rotor blade, for instance, pass through all flow conditions shown in this Fig. 3 and in Fig. 5. Due to the complicated flow behaviour in transonic compressors it is difficult to analyse these flow fields and to make accurate performance predictions at off-design conditions. This is especially true for the determination of the shock losses at supercritical inflow conditions. Therefore work was undertaken at DFVLR in order to derive improved methods for shock loss prediction in the range of supercritical subsonic, as well as for supersonic inflow Mach numbers, which can be incorporated into performance prediction methods.

As the mathematical treatment of the models is very lengthy, only a brief description of their main features and capabilities as well as a comparison with experimental results will be given below. For more details the interested reader is referred to [1].

SHOCK MODEL FOR SUPERSONIC INFLOW CONDITIONS

For local supersonic inflow conditions a shock model has been adapted, which was originally developed by Starken [2] for cascade flow. It is based on the work of Levine [3] and Moeskel [4].

AD-P005 522

In order to incorporate the supersonic shock loss model into a performance prediction procedure Starke's model has been refined and simplified to some extent, however the basic ideas have been kept. This method also serves as a basis for the prediction of shock losses at supercritical subsonic inflow conditions. The method provides the unequivocal dependency between inflow Mach number at supersonic flow, flow angle and shock position, not only for the unique-incidence- and spill point condition, respectively, but also at off-design conditions, i.e. for detached shock as is shown in Fig. 4. The shock is separated into two parts, a passage shock and a bow wave. This method is based on simple wave flow using the Prandtl-Meyer-expansion as other supersonic methods known from the open literature. It delivers informations on the location of the sonic point on the suction surface, on the 1st captured Mach wave, on the shock impingement point on the suction surface, on the lateral shock extension, on the distance of the shock wave ahead of the leading edge of the neighbouring blade and on the stagnation streamline shift and finally enables to evaluate the shock loss. At the moment depending on the calculation procedure used the adapted method can be employed at supersonic Mach numbers above $Ma_1 \geq 1.01$.

SHOCK MODEL FOR SUPERCRITICAL SUBSONIC INFLOW CONDITIONS

Most current methods for shock loss predictions in the supercritical velocity range use correlations or interpolations. The real local supersonic flow field and the terminating shock (see Fig. 3a, 3b and 6) are not directly taken into account in most cases, but rather the shock losses either are evaluated by correcting the profile losses for compressibility effects or are determined using extrapolation of those shock losses, which are calculated at sonic or low supersonic inflow conditions by the aid of other methods. In order to improve that unsatisfactory situation two methods have been developed, one is called the semi-empirical-correlative model and the second is designated as the gasdynamic model. Here the first one will be primarily dealt with. Afterwards the gasdynamic model will be shortly explained.

Flow Model

The derivation of a suitable flow model is based on experimental results from compressor- and cascade investigations. Detailed examples of which for supercritical inflow conditions can be found e.g. in the presentation by Schreiber [5].

The flow model must provide informations on

- the actual critical Mach number corresponding to the reference and off-design inlet flow angle (see Fig. 5); if the shock loss shall be determined individually matching any off-design operating point;
- the local supersonic flow region and its variations with the inflow conditions, i.e. the shift of the sonic point and of the shock impingement point along the suction surface, the lateral extension of the shock across the adjacent blade channels, or the shape and location of the sonic line.

Some of these features are illustrated in Figs. 3a,b and in Fig. 6.

The flow within the local supersonic region is characterized by left and right running Mach waves, which are curved as the local velocity and the speed of sound are varying from point to point. As far as the shocks are weak, one can assume that the flow field in the subsonic region is not influenced by the supersonic one. Hence the supersonic region can be treated independently. If the profile contour is convex, as e.g. for a DCA-blade, the left and right running Mach lines are expansion and compression waves, respectively. Part of the expansion waves are impinging on the sonic line, where they are reflected as compression waves. Some of them are reaching the suction surface thereby reducing the expansion, other expansion and compression waves are striking the downstream shock. Because of this flow behaviour the assumption of a Prandtl-Meyer-expansion, i.e. a simple wave flow, as has been done for the supersonic shock model, is only a coarse approximation. This problem is discussed in more detail e.g. for single airfoils in [6] and for cascade flow in [7].

Determination of the Critical Mach Number Limit

Up to the critical Mach number one can assume, that the blade pressure distribution is similar to that one for incompressible flow. However, as in general the blade pressure distribution is unknown, the pressure coefficient is determined depending on the ratio of the maximum local velocity on the blade contour and of the inlet velocity, assuming that the maximum velocity is equal to the speed of sound. Therefore:

$$(1) \quad Ma_{1,lim} = \sqrt{\frac{2}{\gamma-1} \left\{ \left[\frac{\left(\frac{v_{max}}{v_1} \right)^2}{\left(\frac{2}{\gamma-1} \right)^{\frac{\gamma}{\gamma-1}} + \left(\frac{v_{max}}{v_1} \right)^2} - 1 \right]^{\frac{\gamma-1}{\gamma}} - 1 \right\}}$$

This holds for the incompressible reference inlet flow angle β_1 (see Fig. 5) as well as for the given actual inlet flow angle β at off-design condition, as far as the maximum velocity v_{max} is known. At positive incidence inflow condition the incompressible maximum velocity on the blade suction surface is determined in the same way as it is done for the diffusion factors D , D_u , and D_{∞} , i.e. using the well known correlations [8,9,10,11]. At negative incidence angles these correlations are valid only in a limited sense, because then the velocity distribution on the pressure side has to be observed, too.

As it is rather difficult to check the validity of this procedure for example by means of numerical blade-to-blade flow calculations, Schlieren pictures have been used in order to evaluate the critical inflow conditions, which have been obtained from cascade tests in [12] on rotor blade sections of the DVL 030 transonic axial compressor stage.

One example is given in Fig. 7 with an inlet flow angle at high positive incidence (see Fig. 5, too). Taking into account the difficulties of the evaluation of Schlieren photos the shock extension and the shock impact point, measured straight from the blade leading edge, were estimated from the numerous Schlieren pictures for different test conditions. It was assumed that these values decline to zero as function of inlet Mach number at constant inlet flow angle, each, when the critical inflow conditions are reached. Before the results are discussed, some uncertainties have to be mentioned, which exist for this estimation. The intensity, extension and smearing of the shock depends on focussing the Schlieren optic and is further influenced by the actual 3-dim. flow through the cascade wind tunnel (wall boundary layers, shock bending). Additionally the estimation is certainly subjectively conducted by the interpreter.

Fig. 8 shows the dependency on the inlet Mach number of the distance z_{ss}/l between the blade leading edge and the shock impingement point, which varies nearly linearly with constant inlet flow angle. Concerning the distance measurements it should be remarked, that in case of high positive incidence angles problems arise, if the shock shifts upstream to the leading edge region.

Fig. 9 shows the extension A_{ss}/l of the shock as functions of the inlet Mach number and the inlet flow angle, which vary nearly linearly with flow Mach number. Of the two quantities evaluated from the Schlieren pictures, z_{ss}/l and A_{ss}/l , the latter is considered to be more reliable.

Fig. 10 shows an inlet flow angle-Mach number diagram into which the results on the critical inflow Mach number have been entered. The tendencies of both extrapolations agree quite well considering the data scattering. The limiting critical Mach number line has a strong gradient as function of inlet flow angle, especially at off-design conditions.

These results are now used to check the values for the critical Mach number which can be deduced from the above mentioned correlations for the diffusion factors and which are illustrated in Fig. 10, too. As can be seen best agreement between correlative prediction and measured values can be reached for those relations which correspond to the well known equivalent diffusion factor D_{eq} . This is additionally ascertained by the results from other cascades, i.e. MCA-profiles, NACA-65 profiles and controlled diffusion blades. Judging from these results it seems that the critical Mach number limit can be obtained with sufficient reliability from the correlative prediction method for D_{eq} .

Location of the Sonic Point on the Blade Surface

Due to the lack of sufficiently accurate informations on the position of the sonic point resort has been made to relevant investigations on single airfoils made by Thompson and Wilby [14]. Also using profiles which are composed of circular arcs they deduced the similarity of the velocity distribution along the suction surface with that one of a circular cylinder, whereby for the airfoil the sonic point can be located on the leading edge or suction surface circular arc.

For the case without angle of attack Fig. 11, taken from [14], illustrates the angular change in position of the sonic point, i.e. θ_s , dependent on the inflow Mach number, which is related to the inflow direction and stagnation point, respectively. The distribution is only approximatively in particular considering the sudden transition in curvature from leading edge to suction surface.

For the case of non-zero incidence the location of the sonic point is determined firstly by the location of the stagnation point itself and secondly by its position relative to the stagnation point.

In order to circumvent the difficulties in determining the stagnation point with varying angles of attack, here, resort is made, that at sonic condition the sonic point position itself is known approximatively from the supersonic shock model for any inlet flow angle, which is at least larger than that one corresponding to the unique-incidence condition. By that the distribution in Fig. 11 can be converted to a relative quantity with reference to the sonic condition. As an example of the cascade section R030-4 at 45 percent rotor blade height the results of sonic point positions, i.e. local inclination angle of blade contour θ_{ss} , at supercritical inflow Mach number are shown in the upper part of Fig. 12 for different inlet flow angles.

Determination of the Shock Extension on
Based on the results of the evaluation of the Schlieren pictures, shown in Fig. 9, the following relation for the shock extension can be formulated:

$$(2) \quad \frac{A_{ss}}{l} = \frac{A_{ss}}{A_{ss,0}} \cdot \frac{M_{0,0} \sin \alpha_{0,0}}{M_{0,0} \sin \alpha_{0,0}} \cdot \left(\frac{A_{ss}}{A_{ss,0}} \right)_{\alpha=0}$$

As mentioned before the straight shock extension A_{ss}/l between shock impingement point on the suction surface and the assumed shock and is considered. This simplification is justified, because in all Schlieren observations the detached shock was only marginally curved.

It should be mentioned that, in order to get an approximative solution for the whole range of flow conditions concerned, the discontinuity, which is theoretically produced at $M_{0,0} = 1$, has been consciously left out of consideration by assuming the linear distribution. Thus the upper limiting value of the shock extension can be taken from the lower one of the supersonic shock model, dependent on inlet flow angle, each, whereas at critical Mach numbers the shock extension is zero.

Evaluating the Shock Position

The determination of the shock position is based on the experimental results of z_{ss}/l , shown in Fig. 8, and again the upper limit value is taken from the supersonic shock model. For known blade geometries the values of z_{ss}/l are converted to the equivalent local

inclination angles β_{ss} of the blade contour. These are plotted for different inflow angles in the lower part of Fig. 12. The values are supplemented by additional data elaborated from blade pressure distributions belonging to tests with side wall suction [13]. In spite of the data scattering a clear tendency can be gathered from Fig. 12 due to the numerous measuring values. This allows to establish a correlation, whereby two limiting conditions have to be observed. At the critical Mach number limit the sonic point and the vanishing shock impact point have to coincide; at sonic condition, i.e. Ma_{0g} , the distribution for β_{ss} should pass over to those values calculated by the supersonic shock model, as these can be directly evaluated without being based on experimental results. For the correlation itself it is more general and appropriate, to define a relative angle θ , relating the change of the shock position with inlet Mach number to the position of the sonic point. Considering the above mentioned conditions and taking into account the experimental results for β_{ss} the relation for the relative difference angle θ is composed of a linear interpolation term and a superimposed sinusoidal variation. As mentioned before the complete derivation and description of the corresponding equations is documented in [1].

In the lower part of Fig. 12 the described correlation for the shock position angle β_{ss} is plotted together with the experimental results on which it was based. It can be seen that a sufficient fitting is achieved. A similar agreement has been obtained for other blade sections at 68 and 89 percent blade height of the rotor R030. Thus an approximative method is now available for the estimation of the change of the shock position. Before turning now to the determination of the corresponding shock losses the discussion of Fig. 12 shall be completed. Two limiting values are illustrated in the diagram, i.e. β_{ss0} and β_{ssg} . The blade contour angle β_{ssg} characterizes the transition point between leading edge and suction surface circular arc. This angle is of interest here for estimating in particular, whether the sonic point lies on the leading edge or on the suction surface. The angle β_{ss0} indicates the shock position farthest downstream possible, if the shock extends over more than one blade channel and is assumed being straight, perpendicular on the blade suction surface and tangential to the leading edge of the neighbouring blade. For those measuring results, which lie below this limiting line and which represent flow conditions near subsonic and essentially near supersonic choke margin, it means, that oblique passage shocks exist for these test conditions. This could also be seen from the corresponding Schlieren pictures.

Flow Conditions ahead of the Shock and Determination of the Shock Losses

After having described how to evaluate the shock extension and shock position it is furthermore necessary to specify the flow conditions ahead of the shock for determining the shock losses. For this purpose the local supersonic flow region is first treated as a simple wave flow, which can be afterwards corrected by considering the attenuating effects on the supersonic expansion caused by the reflection of expansion waves on the sonic line.

In Fig. 13 the geometrical conditions and the corresponding specifications are illustrated as they are subsequently used.

Based on the simple wave flow assumption the mass flow rate over the shock is approximately evaluated by calculating the mass flow over the left running Mach wave, which emanates from point G in Fig. 13 and which strikes the "end point" of the shock H. Taking into account the relations of the Prandtl-Meyer-expansion and the corresponding geometrical conditions, as shown in Fig. 13, a system of equations can be established, by which the mass flow dependent on the Mach number Ma_0 can be determined iteratively. The corresponding mathematical formulation is described in [1]. Concerning the real flow conditions this method is only reasonable, because the mass flow rate over the shock can be estimated with sufficient validity.

As the inlet mass flow for one blade passage far upstream of the cascade front is known, too, the ratio between the mass flow passing over the shock and the latter one can be calculated.

If the ratio of the mass flows is lower than 1, it can be concluded that only a limited passage shock exists, which according to the shock model above is assumed to be straight and perpendicular on the suction surface. For the Mach number ahead of the shock an average value is assumed, which is determined as the arithmetic mean of the Mach numbers in point H and in the shock impingement point, i.e. Ma_0 and Ma_{0g} , respectively (see Fig. 13). The latter can be calculated by the already mentioned correlation for the suction surface inclination angle β_{ss} using the simple wave flow assumption. Using this averaged Mach number ahead of the shock the total pressure ratio and hence the shock loss can be calculated. Because, as mentioned before, the mass flow passing over the shock is less than the total mass flow through the blade passage, a mass averaging is applied to the shock loss.

For the case that the ratios of the mass flows over the shock and over one blade passage far upstream is larger than 1 the shock is assumed to be composed of a normal passage shock and a detached oblique shock or a bow wave, respectively, as is illustrated in Fig. 14. As the shock position and the shock extension are prescribed by the above mentioned correlations, the division and consequently the shock losses are calculated for the two corresponding parts independently.

The division is given by the 1st captured Mach wave, running through points E and C. That mass flow rate which is determined for one blade passage far upstream of the cascade has to pass over that Mach line E-C. In order to fulfill the above mentioned mass flow condition the points E on the suction surface and the intersection point C with the shock, suchlike with the stagnation streamline, has to be evaluated iteratively depending on the Mach number Ma_0 . The equations set up for this procedure are omitted here and can be found in [1].

The shock loss caused by the passage shock part is determined afterwards in the same way as described above.

Bow Shock

For the determination of the flow conditions ahead of and over the bow shock part the already mentioned model of Moeckel [4], which is used in Starcken's method [2], too, is applied in a similar, however simplified way.

Like in these references it is assumed that the bow wave is described by a hyperbola, whose apex is located in point C (see Fig. 14), and that constant flow conditions exist ahead of the bow wave, which correspond to those in point C. Then, as is illustrated in Fig. 14, the axis of the hyperbola has the direction of the flow angle in point C, i.e. β_{ss} , and a kink can be observed in point C for the shock. The asymptote of the hyperbola is determined by the 1st captured Mach wave, i.e. Ma_{ss} .

Fig. 14 shows also, that on the left running branch of the hyperbola the point S is located, which is a projection of the above mentioned point H, which itself is used to determine the straight shock extension A_{ss} . Considering the above mentioned constant flow conditions ahead of the bow wave, it is assumed here that in point S the inlet Mach number Ma_{ss} is decelerated to sonic condition over the oblique shock. Based on that it is further assumed that the total pressure losses over the bow shock beyond point S are marginal.

As a simplification to Starcken's and Moeckel's models [2,4] the shock distance ahead of the blade leading edge, the distance C-S and the stagnation streamline shift Δy (see Fig. 14) are indirectly prescribed by the shock position angle β_{ss} , the shock extension, as well as by the conditions along the 1st captured Mach wave, which has been determined before independently from the bow shock model.

Based on the afore mentioned assumptions and conditions and taking into account the relations for the oblique shock near sonic conditions the geometric function of the hyperbola, the mass flow rate and the flow conditions over the bow shock can be approximately determined. As with the supersonic shock model it is assumed that the total pressure ratio over the bow shock is represented by that one along a representative mean streamline. As is described in [4] this one is determined by the condition $y''_M = y''_S/2$ for the 2-dim. case.

If the mass flow rate over the bow shock is larger than the inlet mass flow corresponding to one blade passage, the total pressure ratio calculated before is assumed to be approximately representative for the whole bow shock. However in case, if the mass flow rate over the bow shock is less, a mass averaging is applied to the total pressure ratio.

After having determined the individual losses associated with the two parts of the shock wave, i.e. the passage shock and the bow wave, their addition yields the total pressure loss of the whole shock front.

Possibility for Taking into Account the Influence of Real Flow Effects on the Supersonic Flow Region

As has been discussed above and as is illustrated in Fig. 6 the local supersonic region and, also, the flow acceleration along the suction surface is influenced by the compression waves coming from the sonic line. By this interfering effect the above described simplified evaluation becomes more complicated. However, in principle and at least the attenuating effect on the supersonic expansion along the suction surface can be taken into account in the following way.

Based on blade pressure distributions of cascades with transonic inflow conditions Fottner in [7] developed a method in order to estimate the attenuation of the supersonic expansion, whereby monotonous accelerations up to the terminating shock were considered. The correlation describes the local values of actual velocity and the static blade pressure, respectively, along the blade suction surface. The relative geometrical difference angle, i.e. the angle between sonic point and the actual point considered, is related to the corresponding Prandtl-Meyer-angle, which is determined by the local flow condition. Incorporating the associate correction function of Fottner [7] into the present calculation procedure lower values for the interesting flow Mach numbers are calculated for all cases considered, i.e. for Ma_{ss} , Ma_{ss} , as well as for Ma_{ss} . Also the position of the characteristic points G, E and C are affected, whereas the shock position and the shock extension remain unchanged. The use of this correction results in shock losses which are considerably lower than with the simple wave assumption.

GASDYNAMIC SUPERCRITICAL SHOCK MODEL

Since all correlative methods suffer from a limited range of application and in order to check the calculated different amounts mentioned just before, a second method has been developed which makes use of gasdynamic laws as far as possible. Therefore it should be more generally valid. Only the main differences compared to the correlative method described above are given below, for further informations see [1].

The only prerequisite which is postulated for the gasdynamic model is the validity of the linear dependence of the mass flow over the shock on the inlet Mach number, which had been worked out in the correlative model.

Considering conservation of mass flow the shock is fitted in the flow field, such that the shock position can be calculated. The terminating shock is assumed to be always straight and perpendicular on the blade suction surface. Contrary to the correlative model sonic condition is considered in the end point of the shock. Furthermore for evaluating the flow field ahead of the shock a linear distribution of the flow direction between the shock impingement point and the shock end point is assumed. In order to consider the interference of expansion and compression waves the Mach number distribution is approximated by an expansion curve, which is similar to an epicycloid. The whole calculation of the shock must be done iteratively and it includes also the attenuating effect.

CALCULATION RESULTS

Fig. 15 illustrates the order of magnitude of shock losses, which can be calculated with the new correlative model for a cascade section at 45 percent blade height of the transonic rotor R030. The results are plotted as a function of inlet Mach number Ma , and the inflow angle β . In order to get a smooth transition to the supersonic shock losses the supercritical shock losses have been calculated in this particular example without considering the attenuation of the supersonic expansion, i.e. using the simple wave assumption. As consequence, the calculated losses may be somewhat higher than in reality, however the relative partition of the total shock losses between the individual contributions of the passage shock and the bow wave are retained. The latter two parts of the shock losses are plotted in the middle and the upper diagram of Fig. 15, the total shock loss is given in the lowest diagram.

Fig. 15 generally illustrates that the total shock loss as well as the two individual contributions increase with increasing inflow angle β . Furthermore, contrary to methods in current use, e.g. for the supercritical range the correlation of Jansen, Moffat [15] and for the supersonic range of Miller, Lewis, Hartmann [17], it can be seen that the losses associated with the bow shock are not marginal. This holds particularly for highly positive inflow angles at high subsonic and supersonic Mach numbers. However, as the shock extension reduces to less than one blade passage, the shock loss fraction of the bow wave tends to zero. As this example shows, the Mach number range, over which only a limited passage shock exists, is rather large.

COMPARISON BETWEEN SHOCK LOSS PREDICTIONS AND EXPERIMENTAL RESULTS

Using again the cascade section at 45 percent blade height of the transonic rotor R030 as an example, the total shock losses which can be calculated with the correlative model are compared with experimental results. Additionally these results are compared with loss predictions obtained with methods currently in use for axial compressor performance prediction [15,16].

The above mentioned cascade was the only one, for which sufficiently accurate experimental shock loss evaluations were available in the transonic flow regime, i.e. from about critical inlet Mach number up to the design inlet Mach number of 1.09.

The measured cascade losses as well as the shock losses of this cascade have been obtained by Schreiber [12,13], also they are discussed in his paper [5] for this meeting, together with the method of separating the shock losses from the total losses measured.

Fig. 16 illustrates the comparison between calculated and measured shock losses dependent on the upstream Mach number Ma , for three inflow angles β , 57.60 and 63°, which nearly range from unique incidence to positive blade stall (compare again Fig. 5). The experimental results achieved with side wall suction [13] and those without side wall suction [12] are characterized by the full and the open symbols, respectively. The calculated results with the new correlative shock model for supercritical inflow condition and those for the adapted supersonic model are indicated by the thin and thick drawn lines respectively.

As can be seen from Fig. 16 the agreement between the shock losses evaluated with the correlative supercritical model and with the supersonic model- and those experimentally analysed is quite satisfying. As can be further observed in Fig. 16 -in the lower diagram- at high positive inflow direction, i.e. for β 63°, the shock losses evaluated from the measurements lie above the distribution of the calculated ones. That holds true for the supercritical as well as for the supersonic range. A probable cause for this observation is that in this case noticeable losses occur, which are induced by boundary layer separation, such that it is made difficult to separate the shock losses by the experimental evaluation method used [13].

The dashed line in Fig. 16 indicates the shock losses which are calculated using the correlation of Jansen, Moffat [15]. One can see that for all three inlet flow angles this correlation underpredicts the shock losses. This holds also in the range of supersonic inlet Mach numbers for the method of Miller, Lewis, Hartmann [17], the results of which are indicated by the connected triangular symbols. The latter method is also often used in compressor performance predictions, e.g. [16]. Particularly for high inlet flow angles β 60° this underestimation becomes significant.

A similarly satisfying, or even better agreement as mentioned above between calculated and experimentally analysed shock losses is obtained with the gasdynamic supercritical method. Discussing these results in detail would go beyond the scope of this paper, however the comparison is documented in [1].

CONCLUSION

A new shock loss model was presented, which has been developed for the purpose of off-design performance prediction of transonic axial flow compressors. This method enables to calculate the losses associated with shock waves as well as to determine qualitatively the shock position at flow conditions to blade elements ranging from unique-incidence up to stall inflow direction with subsonic axial and relative supersonic or particularly supercritical velocities. In this context empirical correlations for prediction of reference and off-design critical inflow Mach numbers have been proved by comparison with cascade results. In a first step at flow conditions with relative supersonic velocities a method, which allows to evaluate shock losses for unique-incidence condition and for detached shock waves, has been adapted to off-design performance calculations in compressors. The shocks are composed of a normal passage shock and a bow shock. Based on results of this method at sonic inflow conditions and starting from experimental results in cascades a correlative model has been developed which can predict the shock losses in the Mach number range between critical and sonic conditions depending on inflow direc-

tion. It takes into account the variation of the sonic point on the blade surface, the shock position and shock extension. The method has been proved by cascade results and has been incorporated into a loss prediction procedure of off-design calculation methods. Furthermore the new correlative shock model has been supplemented by a second model, which is based on gasdynamic considerations and which can be used more generally.

REFERENCES

- [1] Dunker, R.J. "Theoretical and Experimental Investigations on Shock Losses in Transonic Axial Flow Compressors", to be published as DFVLR-Research Report (DFVLR-FB) (in German).
- [2] Starken, H. "Untersuchungen der Strömung in ebenen Überschallverzögerungsgittern", DLR-Forschungsbericht 71-99, 1971.
- [3] Levine, P. "Two-Dimensional Inflow Conditions for a Supersonic Compressor with Curved Blades", J. of Appl. Mech., Vol. 24, No. 2, 1957.
- [4] Moeckel, W.E. "Experimental Investigation of Supersonic Flow with Detached Shock Waves for Mach Numbers between 1.8 and 2.9", NACA RM E50D05, 1950.
- [5] Schreiber, H.A. "Experimental Investigations on Shock Losses of Transonic and Supersonic Compressor Cascades", Paper 68 B-11, AGARD 58th (B) Specialists' Meeting of the PEP on "Transonic and Supersonic Phenomena in Turbomachines", Neubiberg, Germany, 10-12 Sept. 1966.
- [6] Pearcey, H.H. "Some Effects of Shock-Induced Separation of Turbulent Boundary Layers in Transonic Flow Past Airfoils", ARC RM No. 3108, 1959.
- [7] Fottner, L. "Ein halbempirisches Verfahren zur Bestimmung der reibungsbehafteten transsonischen Schaufelgitterströmung mit Einfluß von Überschallfeldern und Verdichtungsstößen", Dissertation TH München, 1970.
- [8] Herrig, L.J.; Emery, J.C.; Erwin, J.R. "Systematic Two-Dimensional Cascade Tests of NACA 65-Series Compressor Blades at Low Speeds", NACA TN 3916, 1957.
- [9] "Aerodynamic Design of Axial-Flow Compressors", NACA-S7-36, 1963.
- [10] Lieblein, S. "Loss and Stall Analysis of Compressor Cascade", J. of Basic Eng., Trans. ASME, Series D, 1957, pp. 387-400.
- [11] Koch, C.C.; Smith, L.H. Jr. "Loss Sources and Magnitudes in Axial-Flow Compressors", J. of Eng. for Power, Trans. ASME, Series A, Vol. 98, No. 3, 1976, pp. 411-424.
- [12] Schreiber, H.A. "Untersuchungen am Verdichtergitter L030-4 bei schallnahen Zustrommachzahlen", DFVLR-Interner Bericht IB 352-79/10, 1979.
- [13] Schreiber, H.A. "Experimentelle Untersuchung des Verdichtergitters L030-4 mit Variation des axialen Massenstromdichteverhältnisses im transsonischen Machzahlbereich", DFVLR-Interner Bericht IB 325/4, 1981.
- [14] Thompson, N.; Wilby, D.G. "Leading-Edge Supersonic Velocity Peaks and the Determination of the Velocity Distribution on an Airfoil in a Sonic Stream", Paper 14 in Transonic Aerodynamics, AGARD-CP-15, Sept. 1968.
- [15] Jansen, W.; Moffat, W.C. "The Off-Design Analysis of Axial Flow Compressor", J. of Eng. for Power, Trans. ASME, Oct. 1967, pp. 433-442.
- [16] Davis, W.R. "Axial Flow Compressor Analysis Using a Matrix Method (Revision)", Carleton University ME/A 73-1, 1973.
- [17] Miller, G.R.; Lewis, G.W.; Hartmann, M.J. "Shock Losses in Transonic Compressor Blade Rows", J. of Eng. for Power, Trans. ASME, Series A, Vol. 83, 1961.

FIGURES

Fig. 1: Sketch of a transonic axial flow compressor

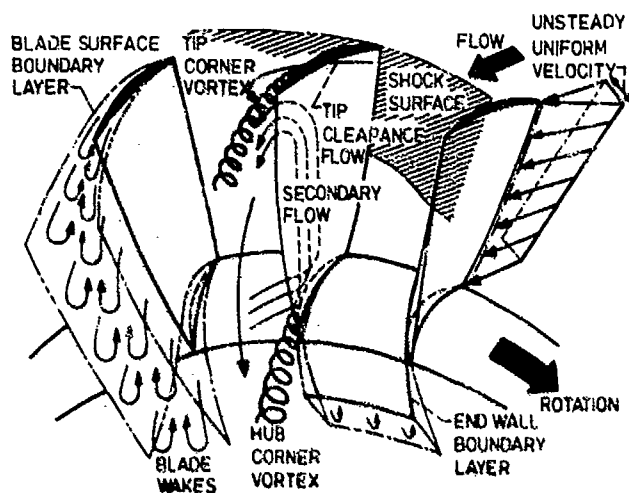
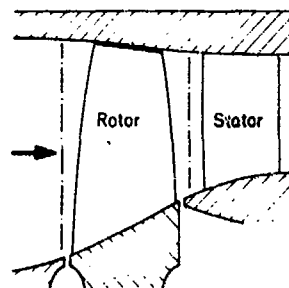


Fig. 2: Complex flow phenomena in compressors

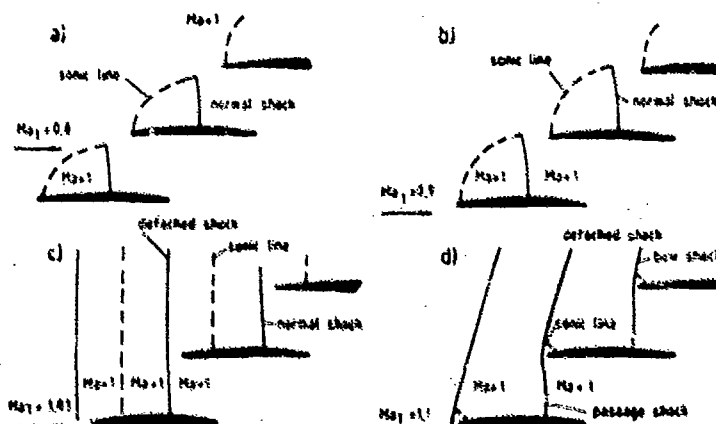


Fig. 3: Flow pattern of a transonic compressor blade section at supercritical, subsonic and supersonic inflow conditions

--- representing $P_2 = P_{2\text{opt}}$
 — representing $P_2 > P_{2\text{opt}}$

shock

Δy

stagnation streamline

1st captured Mach wave

Mach wave

A graph showing the upstream flow angle β_1 (in degrees) versus the upstream Mach number Ma_1 for the R 030-GS4 rotor blade. The y-axis ranges from 46° to 70° in increments of 4°. The x-axis ranges from 0.6 to 1.4 in increments of 0.1. The graph includes several data series and curves:

- rotor blade element data at leading edge:** A series of data points showing a decreasing trend from approximately 66° at $Ma_1 = 0.7$ to 61° at $Ma_1 = 1.1$. Labels include "n=70% n_b ", "85%", "92.5%", and "100% speed line".
- limit of Moore:** A dashed line connecting the rotor blade data points to a lower set of points.
- design point:** A specific point marked with a circle at approximately $Ma_1 = 1.05$ and $\beta_1 = 58^\circ$.
- unique incidence:** A curve starting from the design point and extending to the right.
- limits for linear 2-dim cascade:** A region bounded by two curves, one above and one below the unique incidence curve.
- chocking:** A region at the bottom left of the graph, below the lower limit curve.
- sinus-variation for $\beta_{1,red}$:** A curve at the bottom of the graph, starting around 48° and increasing to 54°.
- Pressure P_0 :** A horizontal dashed line at approximately 57°.
- $Ma_1 = Ma_{turb}$:** A label near the limit of Moore curve.

$$Ma_{1krit} \leq Ma_1 < 1.0$$

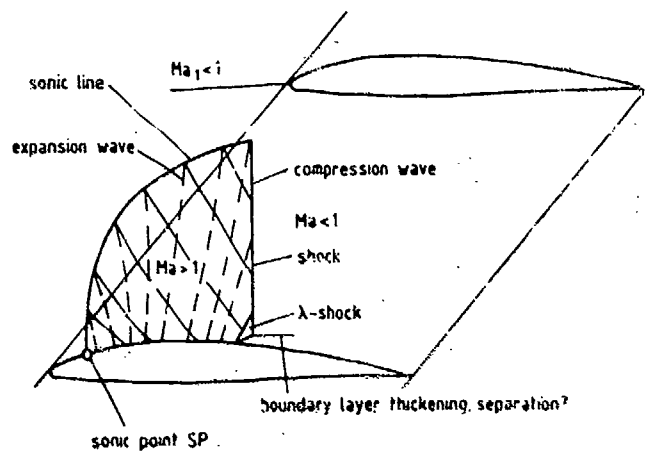


Fig. 6: Schematic view of the local supersonic flow field for supercritical inflow condition

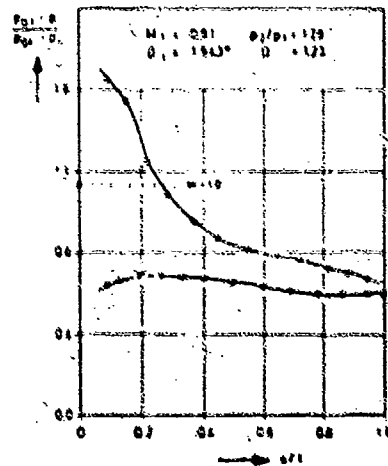


Fig. 7: Blade pressure distribution and Schlieren picture for the cascade section R071-4 of test case 106 (ref. [10]) with high positive inlet flow angle near blade stall (s. Fig. 5)

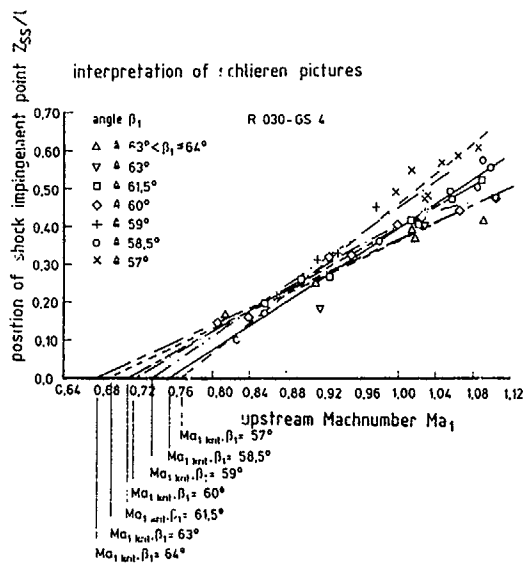


Fig. 9: Shock extension A_{HSS}/l evaluated from Schlieren pictures at supercritical flow conditions for the cascade section R030-4

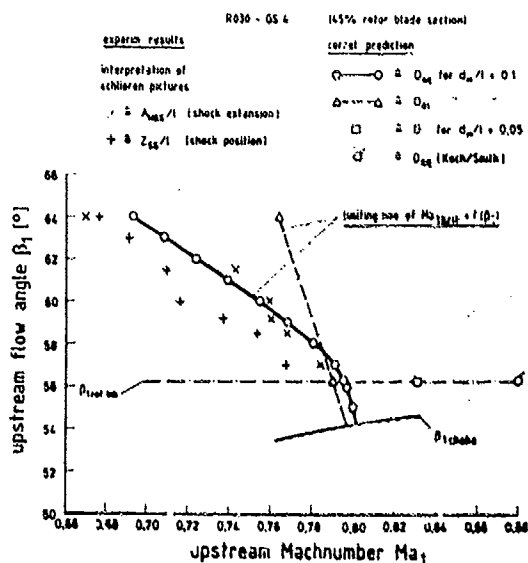
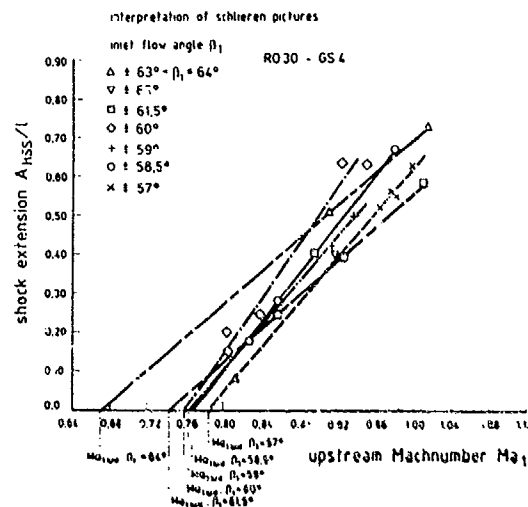


Fig. 10: Limiting curve for the critical Mach number and the evaluation of the conditions $A_{HSS}/l=0$ and $Z_{SS}/l=0$ as function of upstream flow angle β_1 for the cascade section R030-4

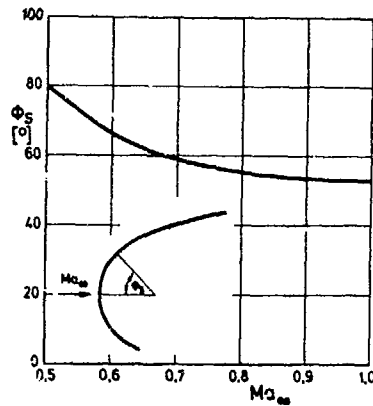


Fig. 12: Position of sonic point on the blade suction surface, i.e. β_{SP} , and comparison of shock positions, i.e. β_{SS} , evaluated from measurements and calculated with the correlative supercritical shock model and the adapted supersonic shock model for cascade section R030-4

Fig. 11: Shifting of sonic point for a single airfoil with non-incidence condition as function of Mach number (ref. [14])

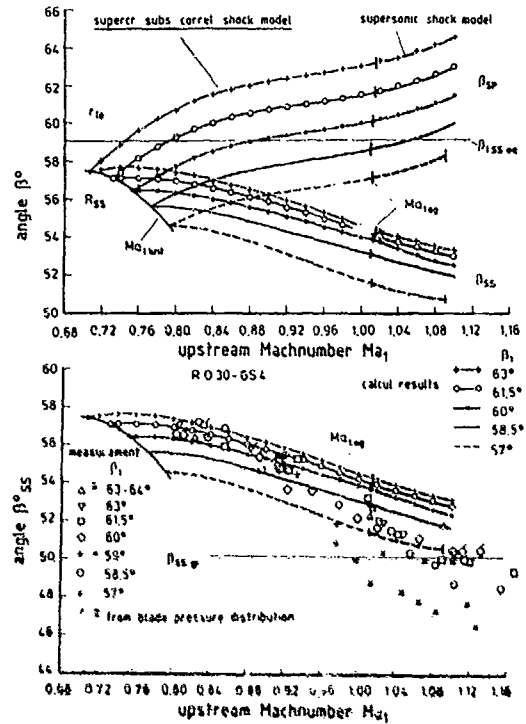


Fig. 13: Sketch of the correlative supercritical shock model and descriptions for determining the Mach wave G-H, used to estimate the mass flow rate over the shock, and the 1st captured Mach wave E-C, if the shock extends beyond one blade passage

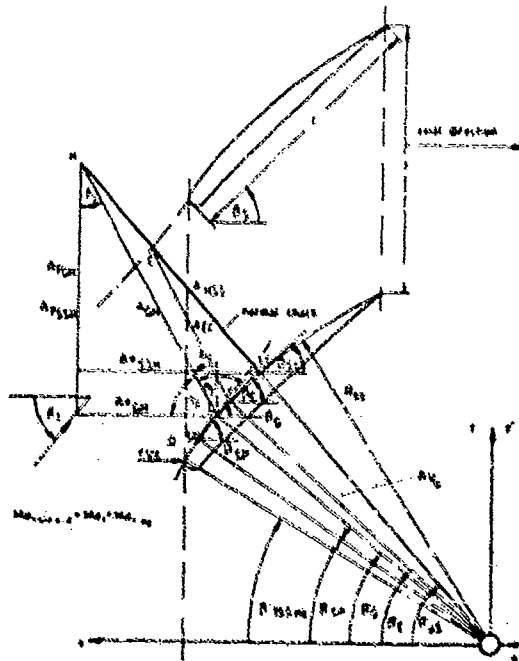


Fig. 14: Detached bow wave model and corresponding descriptions used for the correlative supercritical shock model

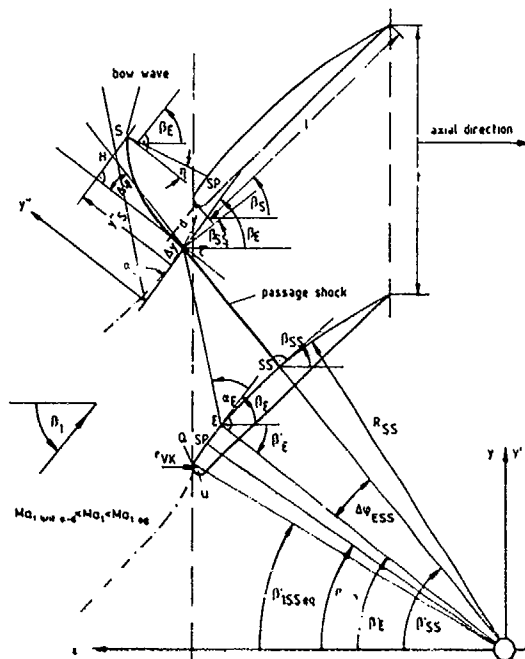
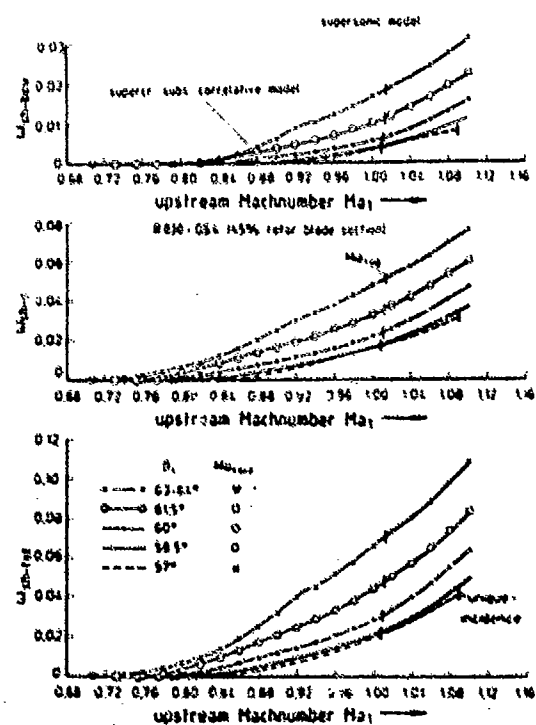


Fig. 15: Total shock loss coefficient and its fractions for different upstream flow angles β_1 calculated with the correlative supercritical shock model and the adapted supersonic shock model (upper part: fraction of the bow shock; middle part: fraction of the passage shock; lower part: total shock loss)



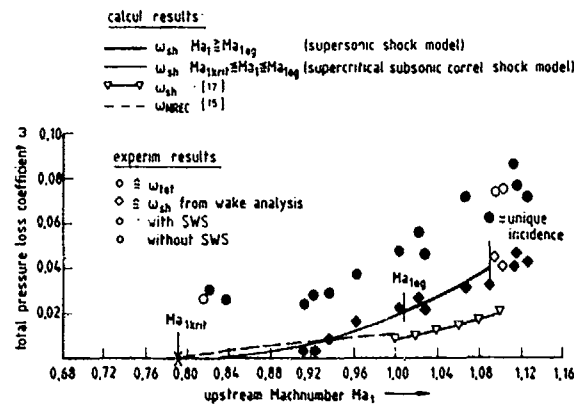
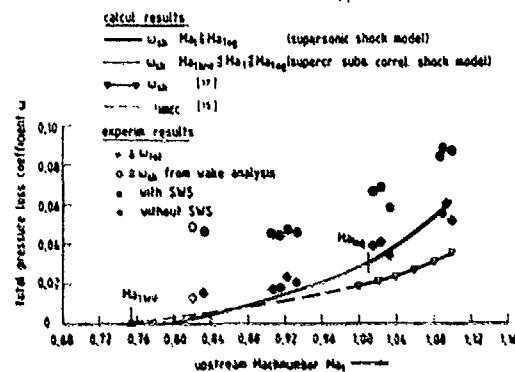
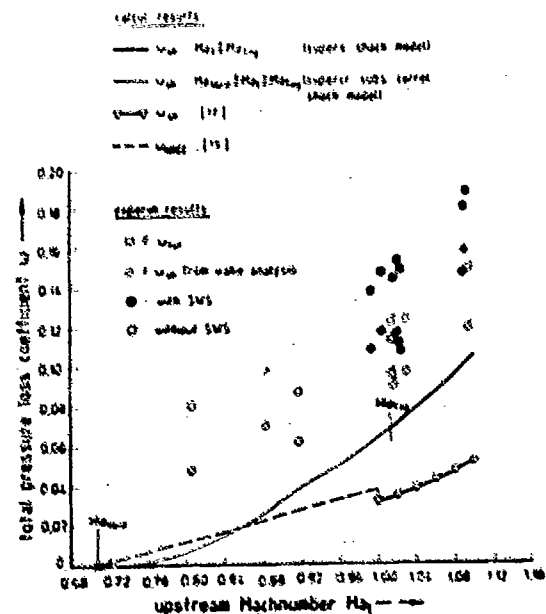
R 030 - GS 4 $\beta_1 = 57^\circ$ 

Fig. 16: Comparison of total shock loss coefficient analysed from cascade measurements and calculated using current methods as well as with the correlative supercritical shock model

R 030 - GS 4 $\beta_1 = 60^\circ$ 

and with the adapted supersonic shock model dependent on upstream Mach number (open symbols: cascade tests without side wall suction; full symbols: with side wall suction)

R 030 - GS 4 $\beta_1 = 61^\circ$
 $17.63^\circ < \beta_1 < 84.1^\circ$ 

DISCUSSION

P. Ramette, Fr

For your flow model, shown in Figure 4 of your paper, one can see a shift of shock waves and stagnation streamline depending on whether the downstream pressure P_2 is optimum or larger than optimum, for off design condition. There is a shift for the stagnation streamline, but not for the stagnation point. How do you explain that the stagnation point is not shifted, and what are your assumptions for this stagnation point?

Author's Reply

Figure 4 is a sketch illustrating the main features of the supersonic shock model. Looking closer to it, a marginal shift of stagnation point is indicated. However the stagnation point is not considered in the method, but only the intersection of the 1st captured Mach wave and of the shock, suchlike of the stagnation streamline, is considered, i.e. points C and C' in Figure 4. Point C divides the shock into a passage shock fraction and a bow wave fraction. Point C is determined taking into account the conditions for the 1st captured Mach wave and the distance of the bow wave ahead of the blade leading edge, as indicated in the upper part of Figure 4, as well as the stagnation streamline shift, if the back pressure is larger than optimal. For determining the distance of the shock, i.e. of the bow wave, ahead of the blade an adaptation of Moeckel's method (4) is used. Moeckel's model has been developed for single symmetrical bodies.

P. Ramette, Fr

But your profiles are asymmetrical.

Author's Reply

Beyond point C only the left running branch of the bow wave is considered taking into account the blade leading edge and the suction surface circular arcs, only, and treating that as a symmetrical aerofoil. As has been shown by Starken (2), Moeckel's bow shock model has proved an acceptable approximation for the cascade case.



AD-P005 523

COMPARISON BETWEEN INVERSE DESIGNED (PVD) AIRFOILS AND STANDARD SERIES AIRFOILS FOR HIGH LOADED AXIAL TURBINE NOZZLE APPLICATION

by

M. Horsmann and M. Schmidt
KHD-Luftfahrttechnik GmbH
Hohemarkstr. 60-70
D-6370 Oberursel 1, Germany

Summary

Guide vane profiles with transonic flow regions in the flow field have been developed for a high loaded one stage axial turbine. The profiles were designed in two different ways: first, using standard design techniques and second, using an inverse design method, where the profile shape is computed from prescribed velocity distributions (PVD).

The results of both design methods will be presented. Comparison is made by using another computer program system to calculate the velocity distributions in the flow field, the boundary layer parameters, and the profile losses.

The computed results of our first application of an inverse design method on axial turbine guide vanes show that improvements can be made.

Nomenclature

a^*	critical sonic velocity	β	flow angle
c	absolute velocity	β_s	stagger angle
c^*	Laval number c/a^*	δ_1	displacement thickness
L	chord length	w	loss coefficient
L_{ax}	axial width of cascade	<u>Subscripts</u>	
p	static pressure	LE	leading edge
R	radial coordinate	PS	pressure side
s	arc length along streamlines	SS	suction side
t	cascade gap, pitch	TE	trailing edge
U	circumferential direction	t	total
X, Y	blade coordinate system	1, 2	upstream and downstream station
z	axial direction		

1. Introduction

For reasons of power concentration the mass flow through modern turbomachines is increased. This leads to high through-flow velocities with the occurrence of local supersonic regions. When returning from supersonic to subsonic velocities, shocks will be present which may cause separation of the boundary layer and therefore high losses. With a careful blade profile design it is possible to avoid or at least reduce the intensity of the shocks and therefore lower losses will result.

With the conventional design of turbine cascades the profile shapes are computed by means of a profile systematic. A desired local influence on the blade shape to avoid shocks is not possible directly, but has to be checked in an iterative process with a blade-to-blade calculation. As there are several parameters in the profile systematic to influence the blade shape this can be quite an expenditure of work. Using the inverse design method by Schmidt [1] the profile shape is computed from a prescribed velocity distribution around the unknown profile. The velocity distribution has to be altered until an appropriate blade shape is received.

In the paper presented some results of the design of guide vane profiles using these two methods are compared and discussed.

2. Aerodynamic design

2.1 Definition of cascade geometry

The upstream and downstream flow conditions and vector diagrams for the guide vane profiles to be designed, result from the given mass-flow, speed and possible geometric constraints. Flow angles β_1 and β_2 and upstream Laval number c_1^* (see Fig.1) are considered constant along the blade height. Assuming a constant pressure and temperature distribution an almost linear velocity distribution c_x will result, i.e. transonic velocity at the hub and a high subsonic velocity at the shroud.

2.2 Meridional plane

To achieve the necessary circumferential velocity component at the required downstream vector diagram, a decreasing channel height has to be realized resulting in a rapid axial acceleration. For simple boundary conditions a linear shroud contour between leading and trailing edge of the blade is assumed. When referenced to hub, mid-span or shroud cross-sections in Figure 2, we should understand developed cylindrical cross-sections at these positions.

3. Comparison of conventional and inverse design

3.1 Conventionally designed profile cross-sections

When conventionally designed the profile cross-sections are calculated from a few characteristic profile data such as camber, maximum thickness, position of maximum camber and thickness, etc. An analytical superposition of computed camberline and thickness-distribution leads to the profile shape. In the program then the geometric throat conditions, spacing and angle, are estimated for several stagger angles. Varying the throat conditions for each stagger angle, the downstream conditions, angle, velocity and pressure loss can be calculated (Refs. (9,10)). If the desired downstream vector is prescribed the stagger necessary can be interpolated. Figure 3 shows the resulting profile cross-sections of hub, mid-span and shroud. Either by an expensive experiment or using a blade-to-blade calculation the velocity distribution and boundary layer development can be checked. If the results are not satisfactory the design procedure might have to be repeated.

3.2 Profile design with an inverse design method

The above mentioned iterative and time consuming method for high loaded cascades may be replaced by an inverse profile design method. Using this method not only upstream and downstream conditions but also the velocity distributions along suction and pressure side are to be prescribed. Doing this, that profile shape will be calculated, which should show the given velocity distributions.

3.2.1 Prescribed velocity distribution

Solving the inverse problem a computer program was used that had been developed in a FVV sponsored research program (2,3). The calculation algorithm needs the prescription of the Laval-number distribution along the stagnation streamlines and suction- and pressure-sides of the still unknown flow channel between two blades. The Figure 4b shows such a prescribed velocity distribution for the mid-span profile. There is a residual circulation downstream of the blade corresponding to a part of the necessary turning.

The shapes for the prescriptions of the velocity distributions along hub and shroud look similar and are shown in Fig. 4c and Fig. 4a respectively. The suction velocity at the hub exceeds sonic speed at about mid-chord, and downstream velocity is supersonic as wanted from the aerodynamic design. At midspan and shroud the whole suction velocity is subsonic. At the front stagnation points the prescribed velocities cannot be reduced to zero, since the numerical method does not permit this singular point. At the rear stagnation points the problem does not appear, since they do not exist physically owing to the wake.

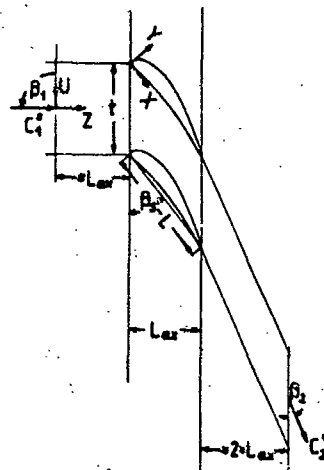


Fig. 1: Guide vane cascade geometry

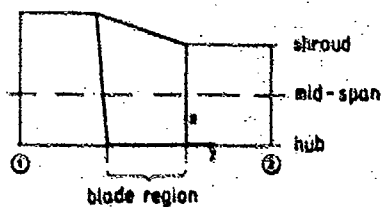


Fig. 2: Meridional plane

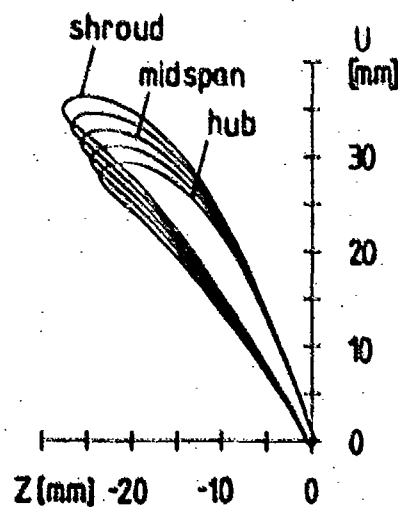


Fig. 3: Standard designed profiles

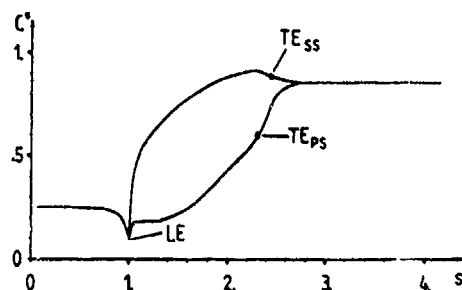


Fig. 4a: Shroud velocity prescription

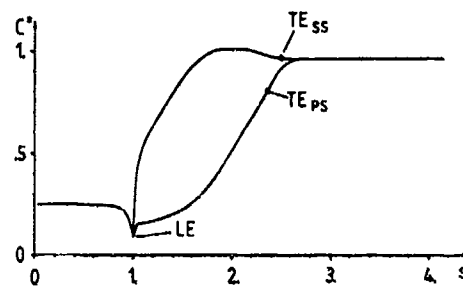


Fig. 4b: Mid-span velocity prescription

3.2.2 Results of inverse design

The computer program ISGAV [4] solves the potential equation for the given problem and calculates the so-called potential-profile. Deviations from a 2-D flow (see Fig. 2 no parallel end walls) will be taken into account by an axial velocity-density ratio. The potential-profiles for the three cross-sections are presented in Figs. 5a - 5c.

The contour shapes will result by shifting the calculated channel walls by one pitch. The plotted symbols mark the positions of the leading and trailing edge of the blade, resulting from the prescription. The coincidence of the superposed stagnation streamlines is a measure for matching of the periodic conditions.

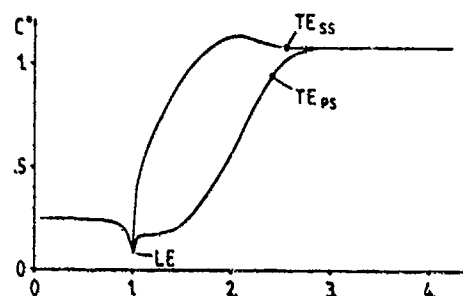


Fig. 4c: Hub velocity prescription

3.2.3 Staggered metal profiles

As mentioned before the shown contour shapes are results of a potential flow calculation. For receiving the real metal profiles the boundary layer displacement-thickness has to be subtracted. The computer program for the design of the inverse profile [4] is therefore linked to a boundary layer calculation program by McNally [5]. This integral method solves the boundary layer equations and the computed displacement-thickness is subtracted after a smoothing procedure from the potential profile. The smoothing procedure is necessary especially in the region near the transition point laminar-turbulent.

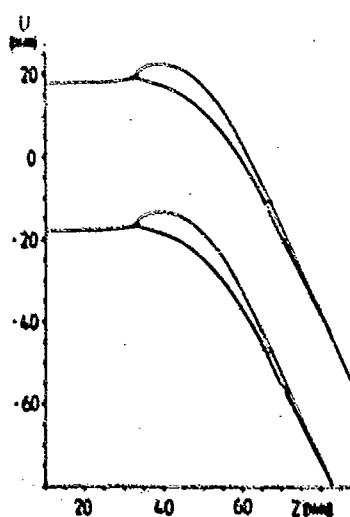


Fig. 5a: Calculated contours at shroud section

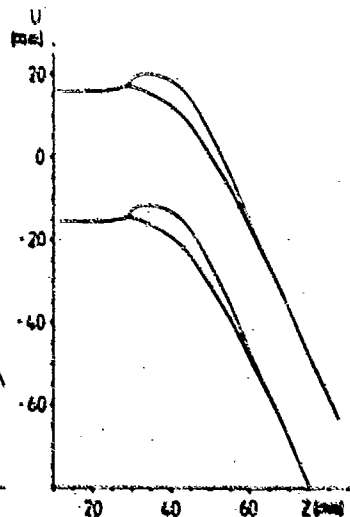


Fig. 5b: Calculated contours at mid-span section

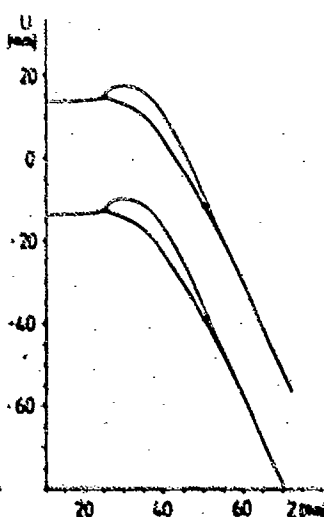


Fig. 5c: Calculated contours at hub section

After smoothing the resulting contour, which is sometimes necessary near the stagnation point and adjusting a trailing edge rounding to the profile the cross-sections shown in Fig. 6 were obtained. The hub, mid-span and shroud profiles were computed using the inverse design method, the others were obtained by an interpolation procedure.

3.3 Analytical calculations

For an analytical calculation of the cascade flow a FFEM-program system [6] is at our disposal. This computer program has also been developed in the mentioned FVV sponsored research program. With the program system called NEUTRAK the two-dimensional, inviscid, irrotational steady state flow in axial cascades is computed. Local supersonic regions are allowed, but upstream and downstream conditions have to be subsonic. Due to the last restriction it is not possible to calculate the flow at the hub cross-section, as downstream conditions are not subsonic. The comparison of the two bladings will be made only for the mid-span profiles, as the expenditure of computing time for all cross-sections would be rather high.

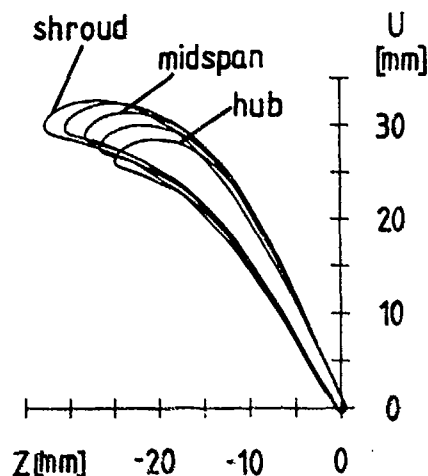


Fig. 6: Inverse designed profiles

With the data of the metal profile as input to the NEUTRAK-program the potential flow around the profile is calculated. Using the resulting velocity distribution in a boundary layer calculation procedure (in the linked program GRENZ) the displacement-thicknesses at suction and pressure side can be estimated and superposed to the profile. A new potential flow calculation with the data of the thus thickened profile leads to the inviscid velocity distribution around the given profile. By means of boundary-layer parameters as well as interpolated trailing edge velocity and flow angles, viscous downstream conditions are calculated in the program NACHLA, about two pitches behind the trailing edge. Additionally a loss coefficient is calculated defined for turbine flows as follows:

$$\omega = \frac{P_{t1} - P_{t2}}{P_{t2} - P_2}$$

3.3.1 Calculated velocity distributions

Fig. 7 shows the calculated velocity (Laval-number) distributions for suction and pressure side of the conventional blade profile design. The stagnation point does not coincide with the grid point $x/L = 0$, but is located at about 3% on the pressure side distance. The intersection of the velocities at the profile and indicates that the flow angle required and used for the calculation is not realized exactly.

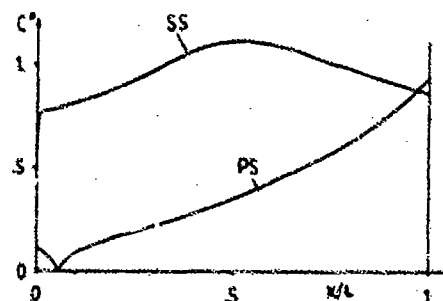


Fig. 7: Calculated Laval-number distributions for the conventional blade design

In Fig. 8 the corresponding velocity distribution for the inverse blade profile design is shown. Additionally some points of the prescribed velocity distribution are shown. A fairly good agreement between prescribed and calculated velocity distribution with a max. difference of 3% can be stated.

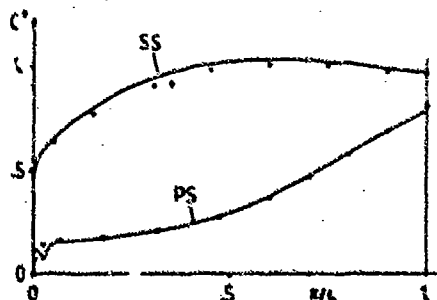


Fig. 8: Calculated and prescribed (o) Laval-numbers for the inverse blade design

3.4 Boundary layer and loss calculations

The calculated boundary layer displacement thicknesses of both the conventional and the inverse profile design are shown in Fig. 9 and Fig. 10, respectively. In the area of transition point laminar-turbulent the development of the displacement thickness is smoothed by a four point spline algorithm to receive a steady contour shape when superposing the displacement thickness to the metal contour.

Turbulent boundary layer separation does not occur on both profiles at the calculated design point. At other configurations

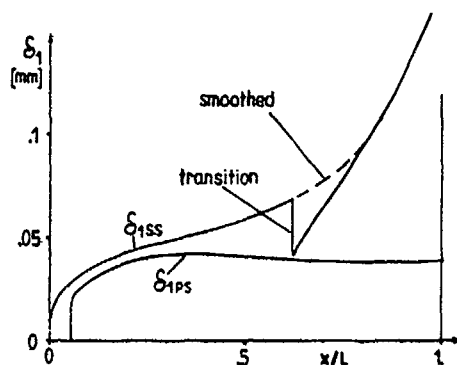


Fig. 9: Displacement thicknesses
conventional blade design

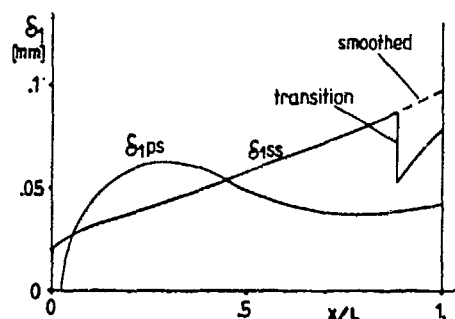


Fig. 10: Displacement thicknesses
inverse blade design

or at off-design where separation may occur, the development of the boundary layer downstream of the separation point is calculated by using a half-empirical separation model by Fottner [7] and Grahl [8]. From the downstream calculations with the program NACHLA the following values for the loss coefficient result (Fig. 11).

For the inverse designed profile the calculated loss coefficient at the design point is about 26% lower than for the conventional profile design.

4. Results and conclusions

Comparing the calculated velocity distributions it is obvious that the conventional design has a higher loading than the inverse profile near the leading edge. The higher loading causes higher losses at off-design with positive incidence as can be seen in Fig. 11. In the case of negative incidence the loss behaviour of the conventional profile is slightly better than that of the inverse one, but on a higher level. Altogether it seems that the gain in loss behaviour of the inverse designed profile has to be paid by a somewhat smaller working range, compared to that of the conventional designed one.

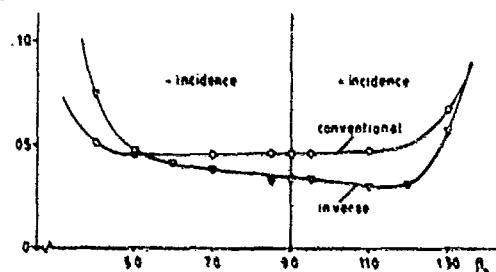


Fig. 11: Calculated loss coefficients

It has to be mentioned that the loss coefficient calculations have been done at the plane two axial chord lengths downstream of the trailing edge of the cascade (see Fig. 1). Experimental values often are lower because they are estimated just behind the trailing edge where the flow is not yet mixed out.

The downstream calculation position is very important for the flow angle calculation too. Far behind (two axial chord lengths) the trailing edge, in the case of the inverse profile one computes for the downstream flow angle $\theta_s = 25.8^\circ$ whereas for the conventional profile one gets $\theta_s = 26.5^\circ$. The calculations in the trailing edge plane however, yield for the inverse profile $\theta_{tr} = 26.8^\circ$ and for the conventional profile $\theta_{tr} = 25.4^\circ$. This surprising result can be explained by the fact that the difference in the trailing edge velocities between suction and pressure side is positive in the case of the inverse design (Fig. 5) but it is negative in the conventional case (Fig. 7). In the first case this leads to an additional positive turning in the downstream mixing region and in the second case to a negative turning respectively.

Summarizing it can be stated that improvements can be made by means of the inverse profile design but the method is rather time consuming at the present. Thus an inverse design is only justified exceptionally causing therefore the lack of experience using this method. Potential for optimizing the inverse design procedure is expected. Modifying the conventional camber-systematic in such a manner that profile shapes similar to those of the inverse design are generated, may be a compromise for the time being.

5. References

- [1] Schmidt, E. Computation of Supercritical Compressor and Turbine Cascades with a Design method for Transonic Flows. Trans. ASME, vol. 102, 1980, pp. 68-74.
- [2] Schmidt, E. Verlustarme, superkritische Verdichterprofile. Teil 1: Auslegung. FVV-Forschungsbericht 344-1, 1984.

- [3] Weber, A.
Rechter, H.
Starken, H. Verlustarme, superkritische Verdichterprofile, Teil II: Nachrechnung, Experiment. FVV-Forschungsbericht 344-2, 1984.
- [4] Schmidt, E. Inverses Schaufelgitterauslegungsrechenprogramm ISGAV 18.0-0584. Institut für Aero- und Gasdynamik der Universität Stuttgart, 1984.
- [5] McNally, W.D. FORTRAN Program for Calculating Compressible Laminar and Turbulent Boundary Layers in Arbitrary Pressure Gradients. NASA TN D-5681, 1970.
- [6] Weber, A.
Rechter, H. Verlustarme, superkritische Verdichtergitter, Programmbeschreibung zu Teil II. FVV-Vorhaben Nr. 266, DFVLR - Forschungsbericht IB-325-07-84, 1984.
- [7] Fottner, L. Ein halbempirisches Verfahren zur Bestimmung der reibungsbehafteten transsonischen Schaufelgitterströmung mit Einschluß von Überschallfeldern und Verdichtungsstößen. Dissertation TU München, 1970.
- [8] Grahl, K.
Benra, F.K.
Foitzik, R. Theoretische Untersuchung zur optimalen Verstellung der Geometrie von Verzögerungsgittern. Fortschrittsbericht der VDI-Zeitschrift, Reihe 7, Nr. 65, 1982.
- [9] Fricke, H. Beitrag zur Ermittlung des Abströmvektors aus Turbinengittern für den unterkritischen und überkritischen Bereich. VDI-Bericht 264, 1976, pp. 25-30.
- [10] Christiani, J. Überlegungen zur Bestimmung der Abströmwinkel aus Turbinengittern. VDI-Bericht 572.1, 1985, pp. 149-166.



REPORT DOCUMENTATION PAGE			
1. Recipient's Reference	2. Originator's Reference	3. Further Reference	4. Security Classification of Document
	AGARD-CP-401	ISBN 92-835-0413-5	UNCLASSIFIED
5. Originator	Advisory Group for Aerospace Research and Development North Atlantic Treaty Organization 7 rue Ancelle, 92200 Neuilly sur Seine, France		
6. Title	TRANSONIC AND SUPERSONIC PHENOMENA IN TURBOMACHINES		
7. Presented at	the Propulsion & Energetics Panel 68th(B) Specialists' Meeting held in Munich, Germany. 10-12 September 1986.		
8. Author(s)/Editor(s)	Various		9. Date March 1987
10. Author's/Editor's Address	Various		11. Pages 362
12. Distribution Statement	This document is distributed in accordance with AGARD policies and regulations, which are outlined on the Outside Back Covers of all AGARD publications.		
13. Keywords/Descriptors	<div style="display: flex; justify-content: space-between;"> <div style="width: 45%;"> <p>Blade design</p> <p>Boundary layer interaction</p> <p>Heat transfer</p> <p>Laser anemometry</p> <p>Shock induced losses</p> </div> <div style="width: 45%;"> <p>Shock structure in turbomachines</p> <p>Supersonic flow in engines</p> <p>Three-dimensional engine flow</p> <p>Transonic flow in engines</p> <p>Unsteady flow in turbomachines</p> </div> </div>		
14. Abstract	<p>The Conference Proceedings contain 24 papers presented at the Propulsion & Energetics Panel 68th(B) Specialists' Meeting on Transonic and Supersonic Phenomena in Turbomachines, which was held 10-12 September 1986 in Munich, Germany.</p> <p>The Specialists' Meeting was arranged in the following sessions: Experimental Data on Shock Structures (4); Shock Induced Losses Including Shock Boundary Layer Interaction (8); Computational Results (7); and Blade Design Methods (5). Questions and answers of the discussions follow each paper.</p> <p>In order to maintain high efficiency and reliability of advanced engines with high speed in compressors and turbines, a deep understanding of the influence of transonic and supersonic phenomena is essential. The meeting was aimed at providing a contribution to this goal.</p>		

<p>AGARD Conference Proceedings No. 401 Advisory Group for Aerospace Research and Development, NATO TRANSONIC AND SUPERSONIC PHENOMENA IN TURBOMACHINES Published March 1987 362 pages</p> <p>The Conference Proceedings contain 24 papers presented at the Propulsion & Energetics Panel 68th(B) Specialists' Meeting on Transonic and Supersonic Phenomena in Turbomachines, which was held 10-12 September 1986 in Munich, Germany.</p> <p>The Specialists' Meeting was arranged in the following sessions: Experimental Data on Shock Structures (4); P.T.O.</p>	<p>AGARD-CP-401</p> <p>Blade design Boundary layer interaction Heat transfer Laser anemometry Shock induced losses Shock structure in turbomachines Supersonic flow in engines Three-dimensional engine flow Transonic flow in engines Unsteady flow in turbomachines</p>	<p>AGARD-CP-401</p> <p>Blade design Boundary layer interaction Heat transfer Laser anemometry Shock induced losses Shock structure in turbomachines Supersonic flow in engines Three-dimensional engine flow Transonic flow in engines Unsteady flow in turbomachines</p>
<p>AGARD Conference Proceedings No. 401 Advisory Group for Aerospace Research and Development, NATO TRANSONIC AND SUPERSONIC PHENOMENA IN TURBOMACHINES Published March 1987 362 pages</p> <p>The Conference Proceedings contain 24 papers presented at the Propulsion & Energetics Panel 68th(B) Specialists' Meeting on Transonic and Supersonic Phenomena in Turbomachines, which was held 10-12 September 1986 in Munich, Germany.</p> <p>The Specialists' Meeting was arranged in the following sessions: Experimental Data on Shock Structures (4); P.T.O.</p>	<p>AGARD-CP-401</p> <p>Blade design Boundary layer interaction Heat transfer Laser anemometry Shock induced losses Shock structure in turbomachines Supersonic flow in engines Three-dimensional engine flow Transonic flow in engines Unsteady flow in turbomachines</p>	<p>AGARD-CP-401</p> <p>Blade design Boundary layer interaction Heat transfer Laser anemometry Shock induced losses Shock structure in turbomachines Supersonic flow in engines Three-dimensional engine flow Transonic flow in engines Unsteady flow in turbomachines</p>

<p>Shock Induced Losses Including Shock Boundary Layer Interaction (8); Computational Results (7); and Blade Design Methods (5). Questions and answers of the discussions follow each paper.</p> <p>In order to maintain high efficiency and reliability of advanced engines with high speed in compressors and turbines, a deep understanding of the influence of transonic and supersonic phenomena is essential. The meeting was aimed at providing a contribution to this goal.</p> <p>ISBN 92-835-0143-5</p>	<p>Shock Induced Losses Including Shock Boundary Layer Interaction (8); Computational Results (7); and Blade Design Methods (5). Questions and answers of the discussions follow each paper.</p> <p>In order to maintain high efficiency and reliability of advanced engines with high speed in compressors and turbines, a deep understanding of the influence of transonic and supersonic phenomena is essential. The meeting was aimed at providing a contribution to this goal.</p> <p>ISBN 92-835-0143-5</p>
<p>Shock Induced Losses Including Shock Boundary Layer Interaction (8); Computational Results (7); and Blade Design Methods (5). Questions and answers of the discussions follow each paper.</p> <p>In order to maintain high efficiency and reliability of advanced engines with high speed in compressors and turbines, a deep understanding of the influence of transonic and supersonic phenomena is essential. The meeting was aimed at providing a contribution to this goal.</p> <p>ISBN 92-835-0143-5</p>	<p>Shock Induced Losses Including Shock Boundary Layer Interaction (8); Computational Results (7); and Blade Design Methods (5). Questions and answers of the discussions follow each paper.</p> <p>In order to maintain high efficiency and reliability of advanced engines with high speed in compressors and turbines, a deep understanding of the influence of transonic and supersonic phenomena is essential. The meeting was aimed at providing a contribution to this goal.</p> <p>ISBN 92-835-0143-5</p>

AGARD

NATO  OTAN

7 rue Ancelle • 92200 NEUILLY-SUR-SEINE

FRANCE

Telephone (1)47.38.57.00 • Telex 610 176

**DISTRIBUTION OF UNCLASSIFIED
AGARD PUBLICATIONS**

AGARD does NOT hold stocks of AGARD publications at the above address for general distribution. Initial distribution of AGARD publications is made to AGARD Member Nations through the following National Distribution Centres. Further copies are sometimes available from these Centres, but if not may be purchased in Microfiche or Photocopy form from the Purchase Agencies listed below.

NATIONAL DISTRIBUTION CENTRES

BELGIUM

Coordonateur AGARD — VSL
Etat-Major de la Force Aérienne
Quartier Reine Elisabeth
Rue d'Evere, 1140 Bruxelles

CANADA

Defence Scientific Information Services
Dept of National Defence
Ottawa, Ontario K1A 0K2

DENMARK

Danish Defence Research Board
Ved Idrætsparken 4
2100 Copenhagen Ø

FRANCE

O.N.E.R.A. (Direction)
29 Avenue de la Division Leclerc
92320 Châtillon

GERMANY

Fachinformationszentrum Energie,
Physik, Mathematik GmbH
Kernforschungszentrum
D-7514 Eggenstein-Leopoldshafen

GREECE

Hellenic Air Force General Staff
Research and Development Directorate
Holargos, Athens

ICELAND

Director of Aviation
c/o Flugrad
Reykjavik

ITALY

Aeronautica Militare
Ufficio del Delegato Nazionale all'AGARD
3 Piazzale Adenauer
00144 Roma/EUR

LUXEMBOURG

See Belgium

NETHERLANDS

Netherlands Delegation to AGARD
National Aerospace Laboratory, NLR
P.O. Box 126
2600 AC Delft

NORWAY

Norwegian Defence Research Establishment
Attn: Biblioteket
P.O. Box 25
N-2007 Kjeller

PORTUGAL

Portuguese National Coordinator to AGARD
Gabinete de Estudos e Programas
CLAF
Base de Alfragide
Alfragide
2700 Amadora

TURKEY

Milli Savunma Bakanligi (MSB)
ARGE Daire Bakanligi (ARGE)
Ankara

UNITED KINGDOM

Defence Research Information Centre
Kentigern House
65 Brown Street
Glasgow G2 8EX

UNITED STATES

National Aeronautics and Space Administration (NASA)
Langley Research Center
M/S 180
Hampton, Virginia 23665

THE UNITED STATES NATIONAL DISTRIBUTION CENTRE (NASA) DOES NOT HOLD STOCKS OF AGARD PUBLICATIONS, AND APPLICATIONS FOR COPIES SHOULD BE MADE DIRECT TO THE NATIONAL TECHNICAL INFORMATION SERVICE (NTIS) AT THE ADDRESS BELOW.

PURCHASE AGENCIES

National Technical
Information Service (NTIS)
5285 Port Royal Road
Springfield
Virginia 22161, USA

ESA/Information Retrieval Service
European Space Agency
10, rue Mario Nikis
75015 Paris, France

The British Library
Document Supply Division
Boston Spa, Wetherby
West Yorkshire LS23 7BQ
England

Requests for microfiche or photocopies of AGARD documents should include the AGARD serial number, title, author or editor, and publication date. Requests to NTIS should include the NASA accession report number. Full bibliographical references and abstracts of AGARD publications are given in the following journals:

Scientific and Technical Aerospace Reports (STAR)
published by NASA Scientific and Technical
Information Branch
NASA Headquarters (NIT-40)
Washington D.C. 20546, USA

Government Reports Announcements (GRA)
published by the National Technical
Information Service, Springfield
Virginia 22161, USA



Printed by Specialised Printing Services Limited
40 Chigwell Lane, Loughton, Essex IG10 3TZ

ISBN 92-835-0413-5